

Investigating the Functional Requirement of *Nedd4L* for Mammalian Hearing

A thesis presented for the degree of Doctor of Philosophy (DPhil)

Trinity Term (2021)

Jamie Kwok Hung Lee

Department of Physiology, Anatomy and Genetics, Linacre College, University of Oxford

Mammalian Genetics Unit, MRC Harwell Institute

Supervisors: Dr. Mike Bowl (Mammalian Genetics Unit, MRC Harwell Institute)

Professor Steve Brown (Mammalian Genetics Unit, MRC Harwell Institute)

Professor Victoria Bajo Lorenzana (Department of Physiology, Anatomy and Genetics, University of Oxford)

Word Count: 49, 404



ABSTRACT

The function of the NEDD4 (Neuronal Cell Expressed, Developmentally Downregulated, 4) E3 Ubiquitin Ligase protein family members, NEDD4L and NEDD4, has previously been studied. However, their potential involvement in the mammalian auditory system was only recently indicated. As such, studies were undertaken to investigate the requirement of *Nedd4l* and *Nedd4* in the process of hearing using constitutive and conditional knockout (KO) mouse models. Auditory characterisation of *Nedd4l* KO mice identified an early-onset hearing loss by 3-weeks of age, which progresses to profound deafness by 8-weeks of age. Pathological assessment identified fewer synapses between inner hair cells and afferent neurons in 3-week old *Nedd4l* KO mice, and a subsequent progressive degeneration of hair cell bundles and spiral ganglion neurons. Molecular characterisation discovered decreased abundance of αENaC subunit in *Nedd4l* KO mice and identified NKCC1 as a potential NEDD4L substrate, suggesting that impaired endolymphatic ion homeostasis may contribute to the auditory dysfunction in *Nedd4l* KO mice. In addition, auditory phenotyping indicates that *Nedd4* KO mice experience a high-frequency hearing loss, which is first detected by 8-weeks of age. These studies highlight the importance of the NEDD4L and NEDD4 ubiquitin ligase proteins in supporting auditory function. However, further investigations are required to fully elaborate upon their essential roles in mammalian hearing.

ACKNOWLEDGEMENTS

First and foremost, I would like to express my deepest gratitude to my supervisors Dr. Mike Bowl, Professor Victoria Bajo Lorenzana and Professor Steve Brown, for their continued support, guidance, insights and patience throughout my DPhil studies.

Thank you to the UKRI and MRC for funding my DPhil studies. I would like to extend my thanks to the MRC Harwell Institute, especially to the past and present members of the Sensorineural Hearing Loss team with whom I had the honour of working with, for their insight and mentorship. Thank you to Sherylanne Newton for editing and providing feedback on my thesis. I must also acknowledge the core facilities (GEMs, Protein Core, Histology Teams, Bioimaging Facility) for their expertise and assistance, and all the staff in Mary Lyon Centre Ward 4 and 5, who cared for all my mouse lines. Thank you to my fellow DPhil students, for their uplifting and supporting presence throughout my studies. All have made significant contributions to the progression of my DPhil research, for which I am extremely grateful for their time and efforts.

Thank you to my treasured family and friends, who have stood by me and provided encouragement, companionship, and wisdom throughout my DPhil studies. I would particularly like to thank my partner, Kelly Casey, for all your love and support, and for reminding me that every day provides new opportunities to learn, succeed and thrive.

To my Mum and Dad, Mei and Ping Lee, I am eternally grateful for your sacrifices, all the opportunities you provided me, and for continually challenging me to shoot for the stars. This DPhil would not have been possible if you had not pushed me to be the best that I can be; it is as much yours, as it is mine.

TABLE OF CONTENTS

ABSTRACT 2
ACKNOWLEDGEMENTS 3
TABLE OF CONTENTS 4
LIST OF FIGURES 9
LIST OF TABLES 17
ABBREVIATIONS 18
1 INTRODUCTION 22
1.1 Mammalian Auditory System 22
1.1.1 Peripheral Auditory System 22
1.1.2 Central Auditory System 24
1.2 Mammalian Inner Ear Physiology 26
1.2.1 Inner Ear Physiology 26
1.2.2 Hair Cell Bundle and MET 28
1.2.3 K^+ Recycling and the Endocochlear Potential 32
1.2.4 Ribbon Synapses 35
1.3 Cochlear Innervation 39
1.3.1 Afferent Neurons: Type I Neurons 40
1.3.2 Afferent Innervation: Type II Neurons 41
1.3.3 Efferent Innervation: LOC 42
1.3.4 Efferent Innervation: MOC 42
1.4 Cochlear Development 44
1.4.1 OoC Development 45
1.4.2 SGN Development 46
1.5 Mouse Models of Hearing Loss 47
1.5.1 Utilization of Mouse Model Organisms in Auditory Research 47
1.5.2 Methods of Characterising Mouse Auditory Function 48
1.5.3 Contributions to the Genetics of Hearing Loss 50
1.6 Ubiquitination in Hearing 53
1.6.1 Ubiquitination 53
1.6.2 NEDD4 E3 Ubiquitin Ligase Proteins 54
1.6.3 E3 Ubiquitin Ligases in Cochlear Function 55
1.7 Research Aims 57
2 MATERIALS AND METHODS 59
2.1 Mouse Lines and Phenotyping Tests 59
2.1.1 IMPC-generated KO Alleles 59
2.1.2 Mouse Husbandry 60
2.1.3 ABR Tests 60

2.1.4 ABR Wave Analysis 61
2.1.5 DPOAE Tests 62
2.1.6 Vestibular Swim Tests 63
2.2 Cochlear *Ex Vivo* Experiments 65
2.2.1 Cochlear Dissections 65
2.2.1.1 Schedule 1 Cull of Mice 65
2.2.1.2 Obtaining Cochlear Tissue from Postnatal-aged Mice 65
2.2.1.3 Fine Dissection of Cochlear Tissue 65
2.2.1.4 Obtaining Embryonic Tissue 65
2.2.2 Cryosectioning of Cochlear Tissue 66
2.2.3 Haematoxylin and Eosin (H&E) Staining and Nuclei Counts 66
2.2.3.1 Tissue Preparation: Fixation and Decalcification 66
2.2.3.2 Tissue Preparation: Automated Dehydration, Clearance and Paraffin Impregnation Processing 67
2.2.3.3 Tissue Preparation: Paraffin Embedding and Microtome Sectioning 68
2.2.3.4 H&E Staining 68
2.2.3.5 Imaging and SGN Nuclei Counts 69
2.2.4 SEM 70
2.2.4.1 Tissue Preparation: Fixation, Decalcification and Dissection 70
2.2.4.2 Tissue Preparation: Osmium Processing and Dehydration 70
2.2.4.3 Tissue Preparation: Critical Point Drying (CPD), Mounting and Sputter Coating 71
2.2.4.4 Imaging 72
2.2.5 Immunohistochemistry 72
2.2.5.1 Wholemount Staining 72
2.2.5.2 Cryosection Staining 73
2.2.5.3 Inverted Confocal Microscopy 74
2.2.6 X-Gal Stains 75
2.3 Molecular Experiments 76
2.3.1 Quantitative PCR (qPCR) Genotyping 76
2.3.2 PCR Assays 80
2.3.2.1 RNA Isolation 80
2.3.2.2 cDNA Synthesis 81
2.3.2.3 PCR Amplification 81
2.3.2.4 DNA Agarose Extraction and Amplicon Sequencing 82
2.3.3 Protein Experiments 83
2.3.3.1 Protein Isolation 83
2.3.3.2 Protein Concentration Quantification 83
2.3.3.3 Western Blots 84
2.3.3.4 Immunoprecipitation 85
2.3.4 MS 86
2.3.4.1 Protein Band Excision and Trypsination 86

2.3.4.2 High Performance Liquid Chromatography and Tandem MS 87
2.3.4.3 gEAR Database Scraping 88
2.4 MEFs Culture 89
2.4.1 Common Techniques 89
2.4.1.1 Trypsin Incubation 89
2.4.1.2 Passaging 89
2.4.1.3 Counting MEFs 90
2.4.1.4 Freezing MEFs 90
2.4.1.5 Thawing MEFs 90
2.4.2 Generation of MEFs 91
2.4.3 MEFs Treatment 92
2.4.3.1 Cre Treatment 92
2.4.3.2 Cre-CQ Cotreatment 93
2.4.3.3 MG132 Treatment 93
2.4.4 DNA Extraction 93
2.4.5 Protein Extraction 94
2.4.5.1 Whole Cell Protein Lysates 94
2.4.5.2 Membrane and Cytosolic Fractions 94
3 AUDITORY CHARACTERISATION OF *NEDD4L* 96
3.1 Introduction 96
3.2 Results 101
3.2.1 NEDD4L Expression in Cochlear Tissue 101
3.2.1.1 NEDD4L Transcript and Protein Expression 101
3.2.1.2 Spatiotemporal Expression of NEDD4L 103
3.2.2 Viability of *Nedd4l*$^{tm1b/tm1b}$ Mice 107
3.2.3 Auditory Phenotyping of *Nedd4l*$^{tm1b/tm1b}$ Mice 110
3.2.3.1 ABR Tests 110
3.2.3.2 ABR Wave Analysis 113
3.2.3.3 DPOAE Tests 118
3.2.4 Vestibular Phenotyping of *Nedd4l*$^{tm1b/tm1b}$ mice 120
3.2.5 Cochlear Pathology of *Nedd4l*$^{tm1b/tm1b}$ mice 121
3.2.5.1 Progressive Loss of Hair Cell Bundles 121
3.2.5.2 Progressive Loss of SGN Nuclei 127
3.2.5.3 Assessment of Afferent IHC Ribbon Synapses 131
3.2.5.4 Assessment of Cochlear Innervation 134
3.2.6 Cochlear-Specific cKO of *Nedd4l* 136
3.2.6.1 Generation of the Auditory Phenotyping Cohort 136
3.2.6.2 Auditory Phenotyping 139
3.2.6.3 Cochlear Pathology 142
3.2.7 Hair Cell-Specific cKO of *Nedd4l* 144
3.2.7.1 Generation of the Auditory Phenotyping Cohort 144

3.2.7.2 Auditory Phenotyping 145
3.2.7.3 Cochlear Pathology 147
3.3 Discussion 149
3.3.1 *Nedd4l* is a Deafness-Causing Gene 149
3.3.2 Cochlear Synaptopathy of *Nedd4l*$^{tm1b/tm1b}$ mice 149
3.3.3 Requirement of *Nedd4l* in IdCs 152
3.3.4 Haploinsufficiency of *Nedd4l* in Mammalian Hearing 155
4 INVESTIGATION OF NEDD4L COCHLEAR SUBSTRATES 158
4.1 Introduction 158
4.2 Results 160
4.2.1 Decreased ENaC Expression in *Nedd4l*$^{tm1b/tm1b}$ Cochlear Tissue 160
4.2.2 NEDD4L Antibodies are Unsuitable for Immunoprecipitation 161
4.2.3 Cre Treatment of *Nedd4l*$^{tm1c/tm1c}$ MEFs 165
4.2.3.1 Proposed Anti-Ubiquitinated Protein Immunoprecipitations 165
4.2.3.2 FBS Impairs Cre-Mediated *in vitro* Recombination 166
4.2.3.3 CQ does not Aid *in vitro* Recombination 168
4.2.3.4 Inconsistent Efficacy of Nedd4l^{tm1c} In Vitro Recombination 172
4.2.4 Use of *Nedd4l*$^{tm1b/tm1b}$ MEFs to Identify Nedd4l *In Vivo* Cochlear Substrates 174
4.2.4.1 *Nedd4l*$^{tm1b/tm1b}$ MEFs are Suitable Model 174
4.2.4.2 Subtle Changes to the Ubiquitinated Proteins in *Nedd4l*$^{tm1b/tm1b}$ MEFs 176
4.2.4.3 MG132 Treatment did not Aid Selection of Protein Bands 179
4.2.5 In silico Analysis of Potential NEDD4L cochlear substrates 183
4.2.5.1 Identification of Potential NEDD4L Substrates 183
4.2.5.2 In Silico Analysis of Potential Substrate Expression in Cochlear Tissue 186
4.2.5.3 Investigation of Previously Reported NEDD4L Substrates 190
4.3 Discussion 193
4.3.1 Potential Non-Canonical Regulation of ENaC by NEDD4L 193
4.3.2 Cochlear Function of Potential NEDD4L Cochlear Substrates 195
4.3.3 Suitability of MEFs to Identify NEDD4L Cochlear Substrates 197
4.3.4 Underreporting of NEDD4L Cochlear Substrates 199
5 AUDITORY CHARACTERISATION OF *NEDD4* 201
5.1 Introduction 201
5.2 Results 207
5.2.1 Auditory Characterisation of *Myo15*-Driven cKO *Nedd4* Mice 207
5.2.1.1 Generation of the Auditory Phenotyping Cohort 207
5.2.1.2 Auditory Phenotyping of *Myo15*-driven *Nedd4* cKO Mice 208
5.2.1.3 Cochlear Pathology of *Myo15*-driven *Nedd4* cKO Mice 210
5.2.2 Auditory Characterisation of *Sox10*-driven *Nedd4* cKO Mice 212
5.2.2.1 Generation of the Auditory Phenotyping Cohort 212
5.2.2.2 Auditory Phenotyping of *Sox10*-driven *Nedd4* cKO Mice 215

5.2.2.3 Cochlear Pathology of *Sox10*-driven *Nedd4* cKO Mice 217
5.3 Discussion 219
5.3.1 *Nedd4* is a Potential Deafness-Causing Gene 219
5.3.2 The Role of *Nedd4* Function in Cochlear Tissue 221
6 DISCUSSION 224
6.1 Auditory Dysfunction of *Nedd4l*$^{tm1b/tm1b}$ Mice 224
6.1.1 IMPC-Generated *Nedd4l*^{tm1b} KO Null Allele 225
6.1.2 NEDD4L Cochlear Expression 226
6.1.3 NEDD4L and TM Function 228
6.1.4 Endolymphatic Ion Homeostasis in *Nedd4l*$^{tm1b/tm1b}$ Mice 229
6.1.4.1 Further Investigation of ENaC and NKCC1 Activity in *Nedd4l*$^{tm1b/tm1b}$ Mice 232
6.2 Increased Purinergic Signalling in *Nedd4l*$^{tm1b/tm1b}$ Mice? 235
6.2.1 Cochlear Synaptopathy 236
6.2.2 Decreased ENaC Abundance 238
6.2.3 Investigating Puringeric Signalling Pathways 239
6.3 Characterisation of *Nedd4* in Mammalian Cochlear Function 241
6.4 Further Auditory Characterisation of *Nedd4* 243
6.5 Conclusion 246
BIBLOGRAPHY 247
APPENDIX 287

LIST OF FIGURES

Figure 1.1: The Peripheral Auditory System. 23

Figure 1.2: The auditory pathway, from the cochlea of the Peripheral Auditory System to the auditory cortex of the Central Auditory System. 24

Figure 1.3: The Organ of Corti and the mechanoreceptive hair cell population. 27

Figure 1.4: Development of hair cell bundles. 30

Figure 1.5: Tip links are required stereocilia bundle deflection and MET channel opening. 31

Figure 1.6: K^+ ion flux through cochlear tissues. 33

Figure 1.7: Presynaptic ribbon structures at the hair cell basolateral membrane. 36

Figure 1.8: Overview of the cochlear afferent and the efferent innervation. 39

Figure 1.9: Development of the inner ear between E11.5 – 17.5. 45

Figure 1.10: Overview of the ABR test. 49

Figure 1.11: Overview of the DPOAE test. 50

Figure 1.12: Diagrammatic representation of the IMPC-generated alleles strategy. 52

Figure 1.13: The ubiquitination of substrates and the diversity of polyubiquitin chains. 54

Figure 2.1: Overview of the osmium processing and dehydration to prepare samples for SEM. 71

Figure 2.2: Overview of the different IMPC-generated and Cre driver mouse lines and the genomic location where the different qPCR genotyping assays are targeted against. 79

Figure 3.1: Diagrammatic representation of the domain structure of the short and long isoforms of NEDD4L protein. 96

Figure 3.2: Summary of relevant results of IMPC phenotyping of *Nedd4l*$^{tm1b/tm1b}$ mice. 97

Figure 3.3: Diagrammatic representation of the *Nedd4l* KO alleles generated by the IMPC. 98

Figure 3.4: Molecular characterisation of NEDD4L transcript and protein expression in cochlear tissue. 102

Figure 3.5: Spatiotemporal investigations of *Nedd4l* expression in cochlear tissue. 104

Figure 3.6: Immunohistochemistry stains against NEDD4L in cochlear tissue. 106

Figure 3.7: *Nedd4l*$^{tm1b/tm1b}$ mice experience sub-viability issues. 107

Figure 3.8: Both female and male *Nedd4l*$^{tm1b/tm1b}$ mice are not significantly lighter than *Nedd4l*$^{+/+}$ and *Nedd4l*$^{tm1b/+}$ mice. 109

Figure 3.9: Auditory dysfunction of *Nedd4l*$^{tm1b/tm1b}$ mice. 111

Figure 3.10: Sexual dimorphism of auditory dysfunction of *Nedd4l*$^{tm1b/tm1b}$ mice.... 113

Figure 3.11: Diminished ABR waveform of *Nedd4l*$^{tm1b/tm1b}$ mice. 114

Figure 3.12: Diminished ABR wave latency and amplitude recorded from *Nedd4l*$^{tm1b/tm1b}$ mice..... 116

Figure 3.13: Disruptions to both PAS and CAS function is attributable to the auditory phenotypes of *Nedd4l*$^{tm1b/tm1b}$ mice. 118

Figure 3.14: OHC dysfunction of *Nedd4l*$^{tm1b/tm1b}$ mice. 119

Figure 3.15: Vestibular function appears unaffected in *Nedd4l*$^{tm1b/tm1b}$ mice. 120

Figure 3.16: Hair cell morphology unaffected at P16-aged *Nedd4l*$^{tm1b/tm1b}$ mice. 122

Figure 3.17: Hair cell bundle morphology unaffected in 3-weeks old *Nedd4l*$^{tm1b/tm1b}$ mice. 123

Figure 3.18: Loss of basal hair cells in 8-weeks old *Nedd4l*$^{tm1b/tm1b}$ mice..... 124

Figure 3.19: Loss of hair cell bundles and sensory epithelium morphology in 6-month old *Nedd4l*$^{tm1b/tm1b}$ mice..... 125

Figure 3.20: Progressive loss of IHC and OHC bundles in *Nedd4l*$^{tm1b/tm1b}$ mice. 126

Figure 3.21: Cochlear morphology was unaffected in P16-aged *Nedd4l*$^{tm1b/tm1b}$ mice. 127

Figure 3.22: Cochlear morphology was unaffected in 3-week old *Nedd4l*$^{tm1b/tm1b}$ mice. 128

Figure 3.23: Loss of SGN in 8-week old *Nedd4l*$^{tm1b/tm1b}$ mice. 129

Figure 3.24: Further loss of SGNs in 6-month old *Nedd4l*$^{tm1b/tm1b}$ mice. 130

Figure 3.25: Progressive loss of SGN in *Nedd4l*$^{tm1b/tm1b}$ mice. 131

Figure 3.26: Decreased number of matched ribbon synapses at inner hair cells in *Nedd4l*$^{tm1b/tm1b}$ mice..... 133

Figure 3.27: Clustered α-Parvalbumin abundance in IHCs of *Nedd4l*$^{tm1b/tm1b}$ mice. . 135

Figure 3.28: Unspecific expression of the *Sox10-Cre* transgene in non-*Sox10* expressing cochlear tissues. 137

Figure 3.29: Non-Mendelian ratio of the genotype of mice born through the generation of *Sox10*-driven, cKO *Nedd4l* mice. 138

Figure 3.30: 3-Week old *Nedd4l*$^{tm1c/+}$*; Sox10-Cre*$^{+}$ mice display low frequency hearing loss. 139

Figure 3.31: *Nedd4l*$^{tm1c/+}$*; Sox10-Cre*$^{+}$ mice experience variable profound hearing loss. 140

Figure 3.32: Reduced DPOAE response of *Nedd4l*$^{tm1c/+}$*; Sox10-Cre*$^{+}$ mice. 141

Figure 3.33: A *Sox10*-driven, cKO *Nedd4l* mouse displayed profound loss of auditory function. 142

Figure 3.34: Cochlear morphology appears unaffected in *Nedd4l*$^{tm1c/+}$*; Sox10-Cre*$^{+}$ mice. 143

Figure 3.35: Mendelian ratio of genotypes of mice born through the generation of *Myo15*-driven, *Nedd4l* cKO mice. 144

Figure 3.36: *Myo15*-driven loss of *Nedd4l* does not cause profound hearing loss. . . 146

Figure 3.37: Reduced DPOAE response of both *Nedd4l*$^{tm1c/tm1c}$*; Myo15-Cre*$^{-}$ and *Nedd4l*$^{tm1c/tm1c}$*; Myo15-Cre*$^{+}$ mice. 147

Figure 3.38: Cochlear morphology appears unaffected in *Nedd4l*$^{tm1c/tm1c}$; *Myo15-Cre*$^{+}$ mice. 148

Figure 3.39: gEAR Database: scRNA-seq reported *Nedd4l* expression in mouse cochlear tissue. 153

Figure 3.40: Variable level of *Sox10-Cre* transgene expression. 154

Figure 4.1: Decreased αENaC subunit protein abundance in *Nedd4l*$^{tm1b/tm1b}$ mice. . 160

Figure 4.2: Proposed workflow of Cre treatment of *Nedd4l*$^{tm1c/tm1c}$ MEFs to identify *in vivo* NEDD4L substrates. 162

Figure 4.3: *Nedd4l*$^{tm1c/tm1c}$ MEFs express NEDD4L protein. 163

Figure 4.4: Immunoprecipitation reactions against NEDD4L are unspecific. 164

Figure 4.5: FBS impairs Cre-mediated recombination of *Nedd4l*$^{tm1c/tm1c}$ MEFs. 167

Figure 4.6: Co-treatment of Cre and CQ does not recapitulate previously observed effectiveness of *in vitro* recombination. 169

Figure 4.7: Chloroquine does not increase efficacy of recombination of the *Nedd4l*^{tm1c} allele. 171

Figure 4.8: Inconsistent levels of *Nedd4l* recombination in Cre-treated *Nedd4l*$^{tm1c/tm1c}$ MEFs. 173

Figure 4.9: *Nedd4l*$^{tm1b/tm1b}$ MEFs do not express NEDD4L protein. 175

Figure 4.10: Subtle differences in protein ubiquitination in *Nedd4l*$^{tm1b/tm1b}$ MEFs... 178

Figure 4.11: Proposed workflow for proteasome inhibitor, MG132, treatment of *Nedd4l*$^{tm1b/tm1b}$ MEFs. 181

Figure 4.12: Unique protein bands in MG132-treated *Nedd4l*$^{+/+}$ MEFs could not be detected following an anti-ubiquitinated immunoprecipitation. 182

Figure 4.13: Overview of sorting MS protein hits to identify potential NEDD4L substrates. 184

Figure 4.14: gEAR Database: scRNA-seq reported *Nedd4l* expression in mouse cochlear tissue. 187

Figure 4.15: gEAR Database: transcript expression of potential NEDD4L substrates *Itga9*, does not overlap with *Nedd4l* transcript expression in P1-aged mouse cochlear epithelial tissue. 188

Figure 4.16: gEAR Database: location of transcript expression of potential NEDD4L substrates, *Nemf* and *Smarcad1* is ubiquitously expressed in P1-aged mouse cochlear epithelial tissue. 189

Figure 4.17: gEAR Database: the location of transcript expression of potential NEDD4L substrates, *Slc12a2* and *Aak1*, in P1-aged mouse cochlear epithelial tissue. 190

Figure 4.18: gEAR Database: the location of transcript expression of the previously reported NEDD4L substrates, Potassium Voltage-Gated Channel Subfamily Q Member 1 and Occludin. 192

Figure 5.1: Diagrammatic representation of the IMPC-generated *Nedd4* KO alleles. 203

Figure 5.2: Summary of relevant results of IMPC-performed phenotyping of *Nedd4*$^{tm2b/+}$ mice. 204

Figure 5.3: gEAR Database: reported transcriptomic data regarding *Nedd4* expression in mouse cochlear tissue..... 206

Figure 5.4: Generation of *Myo15*-driven *Nedd4* cKO mouse litters produced a Mendelian ratio of mice. 207

Figure 5.5: *Myo15*-driven *Nedd4* cKO mice display normal ABR thresholds. 209

Figure 5.6: Decreased DPOAE levels of *Myo15*-driven *Nedd4* cKO mice. 210

Figure 5.7: 4-month old, *Nedd4*$^{tm2c/tm2c}$*; Myo15-Cre*$^{+}$ mice show no loss of cochlear structures. 211

Figure 5.8: *Sox10*-driven, homozygous *Nedd4* cKO is a lethal mutation..... 213

Figure 5.9: *Nedd4*$^{tm2c/tm2c}$*; Sox10-Cre*$^{-}$ mice are lighter than other mice in the *Sox10*-driven *Nedd4* cKO phenotyping cohort. 214

Figure 5.10: *Nedd4*$^{tm2c/tm2c}$*; Sox10-Cre*$^{-}$ mice display a high-frequency hearing loss phenotype..... 216

Figure 5.11: Decreased DPOAE levels of Nedd4$^{tm2c/+}$; Sox10-Cre^{-} and *Nedd4*$^{tm2c/+}$*; Sox10-Cre*$^{+}$ mice in response to high frequency stimuli. 217

Figure 5.12: Histological sections of *Nedd4*$^{tm2c/+}$*; Sox10-Cre*$^{+}$ cochlear tissue appears similar to control *Nedd4*$^{tm2c/+}$*; Sox10-Cre*$^{-}$ mice..... 218

Figure 6.1: scRNA-seq data of *Nedd4l* transcripts in the cochlear lateral wall. 227

Figure 6.2: Hypothesised increased endolymphatic [K^+] and [Na^+] in *Nedd4l*$^{tm1b/tm1b}$ mice. 230

Figure 6.3: Pharmacological treatment of *Nedd4l*$^{tm1b/tm1b}$ mice. 233

Figure 6.4: Increased endolymphatic [ATP] in *Nedd4l*$^{tm1b/tm1b}$ mice. 235

Figure 6.5: Increased [Ca^{2+}_i] at IHC and OHC of *Nedd4l*$^{tm1b/tm1b}$ mice. 237

Figure 6.6: Decreased ENaC activity via activation of $P2Y_4$ receptors at RM. 239

LIST OF TABLES

Table 2.1: Scoring criteria for vestibular swim tests. 64

Table 2.2: Sequences of the Forward and Reverse Primers, and the probe for the different qPCR genotyping assays. 77

Table 3.1: The average weight of mice in the *Nedd4l*$^{tm1b/tm1b}$ phenotyping cohort. 108

Table 3.2: Summary of the ABR wave I – IV latency and amplitude linear regression analyses. 117

Table 4.1: The 31 protein hits identified by MS of FK2-immunoprecipitated protein fraction band 1a, prepared from *Nedd4l*$^{+/+}$-derived MEFs. 186

Table 4.2: The 10 protein hits identified by MS of FK2-immunoprecipitated membrane protein fraction band 2a, prepared from *Nedd4l*$^{+/+}$-derived MEFs. 186

Table 5.1: The body weight of female and male mice of each genotype born in the *Sox10*-driven *Nedd4* cKO phenotyping cohort. 214

ABBREVIATIONS

ABR: Auditory Brainstem Response

ACh: Acetylcholine

AMPA: α-Amino-3-Hydroxy-5-Methyl-4-Isoxazolepropionic Acid

ANFs: Auditory Nerve Fibres

ATP: Adenosine Triphosphate

AGC: Automatic Gain Control

BM: Basilar Membrane

C2: Ca^{2+}-dependent, Phospholipid-Binding

Ca^{2+}: Calcium Ion

Ca^{2+}_i: Intracellular Calcium Ion

CAS: Central Auditory System

CDH23: Cadherin 23

cKO: Conditional Knockout

Cl^-: Chloride Ions

ClC: Chloride Channel

CPD: Critical Point Drying

Cre-ER: Tamoxifen-inducible, Ubiquitous-expressing Cre transgene

CROSC: Conditionally Reprogrammed Otic Stem Cells

CVG: Cochleovestibular Ganglion

DAG: Diacylglycerol

DAPI: 4', 6-diamidino-2-phenylinodole

dB SPL: Decibel Sound Pressure Level

dPBS: Dulbecco's Phosphate Buffered Saline

DPOAE: Distortion Product Otoacoustic Emission

E: Embryonic Day

ESCs: Embryonic Stem Cells

E1 Protein: E1 Ubiquitin-Activating Protein

E2 Protein: E2 Ubiquitin-Conjugating Protein

E3 Ligase: E3 Ubiquitin-Ligase Protein

EDTA: Ethylenediamine Tetracetic Acid

ENaC: Epithelial Sodium Channel

EP: Endocochlear Potential

FGF: Fibroblast Growth Factor

GABA: γ-aminobutyric acid

GPI: Glycosylphosphatidylinositol

H&E: Haematoxylin and Eosin

HECT: Homologous to the E6-AP Carboxyl-Terminus

IDA: Industrial Denatured Alcohol

IdC: Interdental Cell

IHCs: Inner Hair Cells

iKO: Inducible Knockout

IS: Inner Sulcus

IMPC: International Mouse Phenotyping Consortium

IP_3: Inositol 1, 4, 5-triphosphate

K: Lysine

KI: Knock-In

KO: Knockout

K^+: Potassium Ion

LOC: Lateral Olivocochlear

MAPK: Mitogen-Activated Protein Kinase

MET: Mechanoelectrical Transduction

MEFs: Mouse Embryonic Fibroblast Cells

MOC: Medial Olivocochlear

MS: Mass Spectrometry

MS/MS: Tandem Mass Spectrometry

***Myo15-Cre*:** *Myo15* expression-driven, *Cre* KI allele

Na^+: Sodium Ion

Na^+, K^+-ATPase: Na^+-K^+-ATPase Channel

NDP: NanoZoomer Digital Pathology

NEDD4: Neuronal Cell Expressed, Developmentally Downregulated 4

NEDD4L: Neuronal Cell Expressed, Developmentally Downregulated 4, Like

NF200: Neurofilament Heavy Polypeptide

NKCC: Na^+-K^+-Cl^- Channel

OCT: Optimal Cutting Temperature

OHCs: Outer Hair Cells

OS: Outer Sulcus

O/N: Overnight

P: Postnatal Day

PAS: Peripheral Auditory System

PB: Phosphate Buffer

PBS: Phosphate-Buffered Saline

PBS-T_{100}: PBS with 0.1% Triton X-100

PCDH15: Protocadherin 15

PD: Prosensory Domain

PFA: Paraformaldehyde

PI: Protease Inhibitors

PIP_2: Phosphatidylinositol 4,5-bisphosphate

PKC: Protein Kinase C

PLC: Phospholipase C

PolyUb: Polyubiquitin

PVH: Periventricular Heterotopia

PY: Proline-Tyrosine

qPCR: Quantitative Polymerase Chain Reaction

RM: Reissner's Membrane

Re: dB: Suprathreshold

RRP: Readily Releasable Pool

RT: Room Temperature

RT-PCR: Reverse Transcription Polymerase Chain Reaction

SC: Supporting Cells

SEM: Scanning Electron Microscope

SGN: Spiral Ganglion Neuron

SL: Spiral Ligament

SLim: Spiral Limbus

SNARE: Soluble N-Ethylmaleimide-Sensitive Fusion Protein Attachment Protein Receptors

SNV: Single Nucleotide Variants

***Sox10-Cre*:** *Sox10* promoter-driven, *Cre* transgene

SR: Spontaneous Activity Rate

SV: Stria Vascularis

TDT: Tucker Davis Technology

TM: Tectorial Membrane

Ub: Ubiquitin

WC: Whole Cell

1 INTRODUCTION

1.1 Mammalian Auditory System

The peripheral auditory system (PAS) can be anatomically divided into three sections, the outer, middle and inner ear (Figure 1.1). It functions to direct, amplify and send the acoustic stimuli that we hear from our surrounding environment towards processing centres found in brainstem, midbrain, thalamus and temporal cortex of the central auditory system (CAS). Tonotopic (frequency-based) gradients in biophysical properties, cytoarchitecture and neural activity are detected in the auditory system to allow specific portions of the auditory system to specifically respond to stimuli of a specific frequency.

1.1.1 Peripheral Auditory System

The outer ear is composed of the pinna and auditory canal which funnels sounds from our environment towards the middle ear. The middle ear consists of the tympanic membrane (ear drum) and three ossicular bones (malleus, incus, stapes) oscillates due to the vibrational energy of incoming sounds (Figure 1.1). The ossicle bones amplify the acoustic stimuli from the outer ear, culminating in the stapes stimulating a fluid wave within the perilymphatic spaces of the cochlea and vestibular system of the inner ear (Nakajima *et al.*, 2009). The cochlea and vestibular system, which are responsible for the sense of hearing and balance respectively, both possess mechanoreceptive elements that can transform stimuli into an electrochemical form. In the cochlea specifically, the vibrational properties of acoustic stimuli are transduced into graded action potentials that are sent along the auditory nerve to the CAS for higher auditory processing (Figure 1.2) (Hudspeth & Corey, 1977).

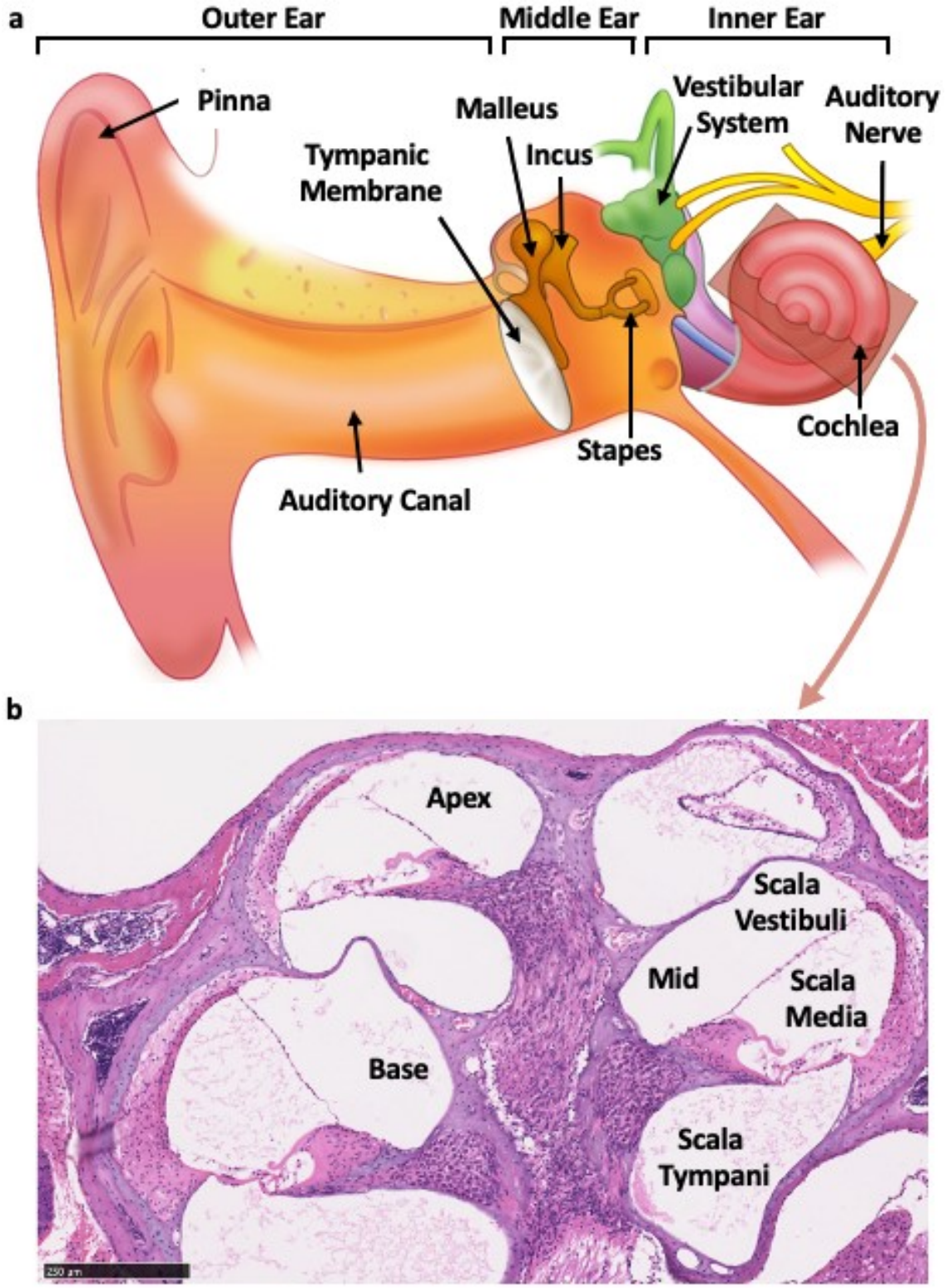

Figure 1.1: The Peripheral Auditory System. The outer, middle and inner ear partition of the Peripheral Auditory System (a) and a cross section of the cochlea, which captures the cochlea apical, mid and basal turns (b). **(a)** The outer ear (pinna and auditory canal) funnel acoustic stimuli towards the tympanic membrane and ossicles (malleus, incus and stapes) of the middle ear. The stapes bone transmits sounds towards the cochlea and vestibular system of the inner ear. The cochlea perceives and transduces the acoustic stimuli towards the Central Auditory System along the auditory nerve. Figure image is adapted from Delhez *et al.*, 2020. **(b)** A H&E-stained section of the cochlea, showing the apex, mid and base of the cochlea. The Scala Vestibuli, Media and Tympani which run the entire length of the cochlea can also be seen. Scale bar = 250µm.

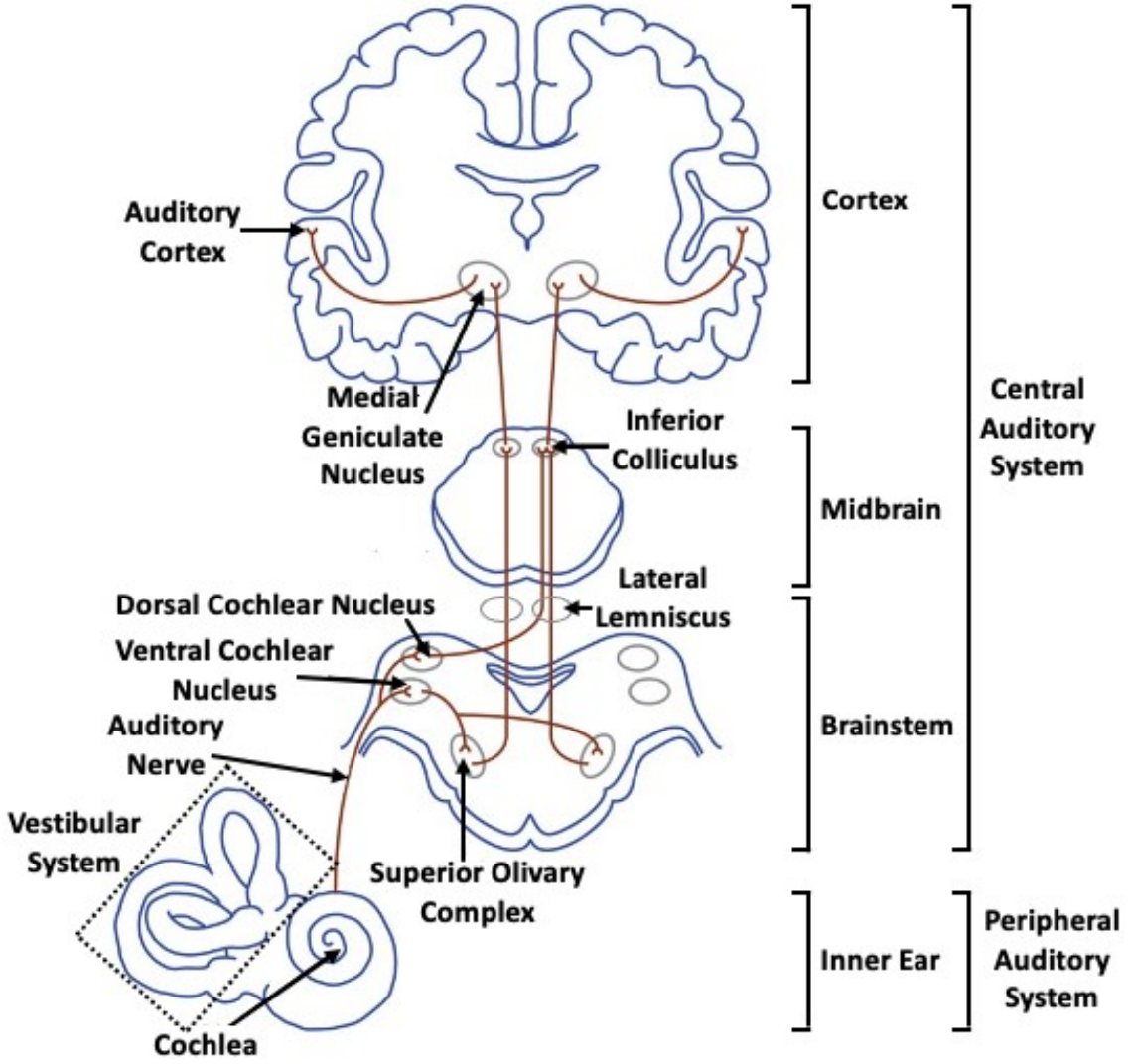

Figure 1.2: The auditory pathway, from the cochlea of the Peripheral Auditory System to the auditory cortex of the Central Auditory System. Acoustic stimuli processed by the cochlea of the Peripheral Auditory System is sent towards the Central Auditory System for higher processing. Sounds are processed at specific regions of the CAS: the Cochlear Nucleus, the Superior Olivary Complex, the Lateral Lemniscus and Inferior Colliculus and Medial Geniculate Nucleus. Auditory stimuli along with other sensory stimuli, are processed in the auditory cortex. Figure image adapted from Butler & Lomber, 2013.

1.1.2 Central Auditory System

The CAS is composed of six specific nuclei: the cochlear nucleus, superior olivary complex and lateral lemniscus nuclei in the brainstem, the inferior colliculus which is found in the midbrain, and the medial geniculate body of the thalamus, and the auditory cortex in the temporal lobe (Figure 1.2; Central Auditory System) (Nordeen *et al.*, 1983). In brief, central auditory processing does not just involve the sequential ascension of acoustic stimuli from one nucleus to the next, it is a highly connected network that also

contains descending pathways that allow modulation and refinement of central auditory processing (Shore *et al.*, 1991). This is not limited to the CAS, as the superior olivary complex also extends efferent processes to the cochlea to modulate the intensity of its output (Brown *et al.*, 1983). Another dimension of complexity to central auditory processing exists through the integration of sounds detected by the left and right cochleae. Both cochleae send graded potentials to the ipsilateral cochlear nucleus through the auditory nerve (i.e. the left cochlea sends graded potentials to the left side of the cochlear nucleus) and will project neurons to contralateral side of the CAS (i.e. to the opposite side) (Sanes, 1990; Moore, 1988). Along with the auditory cortex, the CAS disentangles and processes the complexities of incoming sounds such as determining the spatial location of the source of sounds, processing complex sounds like speech and integrating input from other sensory systems (Figure 1.2) (Masterton, 1992; Rauschecker, 2012; Komura *et al.*, 2005).

1.2 Mammalian Inner Ear Physiology

1.2.1 Inner Ear Physiology

Cochlear transduction of acoustic stimuli begins with vibrations of the stapes at the membrane-covered opening of the inner ear (the oval window) which induces a fluid wave in the perilymph-filled ducts of the cochlea. Beginning at the base of the cochlea, the fluid wave travels to the cochlear apex and back to the basal turns via the scala vestibuli and tympani respectively, where it reaches another membrane-covered opening (round window). This induces the traveling wave, a sinusoidal wave motion in the basilar membrane (BM), a collagen-based structure that runs the entire length of the cochlea (Békésy, 1960; Wenzel *et al.*, 2007). Due to the non-uniform physical properties of the BM (increased width, weight and decreased tautness from base to apex), the frequency of incoming sounds dictates where the peak of the traveling wave occurs (Békésy, 1960). Low frequency sounds peak at the cochlear apex whereas high frequency sounds peak around basal regions of the cochlea. The peak of the traveling wave deflects a specific portion of the organ of Corti (OoC) and the mechanoreceptive stereocilia bundles found atop the approximately 16000 hair cells in humans that run the length of the cochlea (Schwander *et al.*, 2010). Stereocilia bundle deflection is aided by the tectorial membrane (TM), which is found directly above the OoC and applies a shearing force onto bundles (Figure 1.3a).

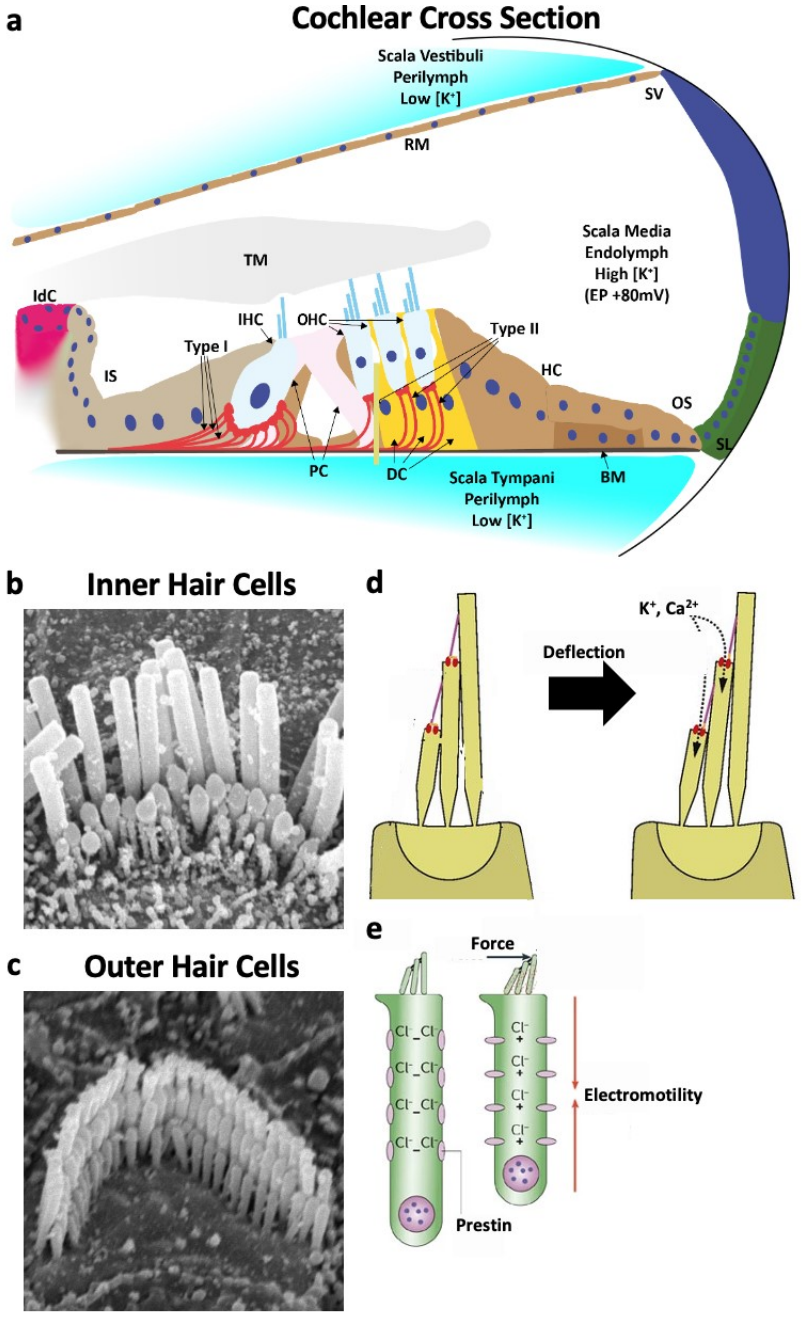

BM: Basilar Membrane; **DC:** Deiters Cell; **HC:** Hensen's Cells; **IdC:** Interdental Cell; **IHC:** Inner Hair Ce
IS: Inner Sulcus; **OHC:** Outer Hair Cells; **OS:** Outer Sulcus; **PC:** Pillar Cells; **RM:** Reissner's Membrar
SL: Spiral Ligament; Stria Vascularis; **TM:** Tectorial Membrane

Figure 1.3: The Organ of Corti and the mechanoreceptive hair cell population. **(a)** A cross-section showing the different cell types found within cochlear tissue. **(b, c)** Image of an IHC and OHC bundle taken at 5000x and 7000x magnification, respectively. Two rows of stereocilia, "V" shape and staircase-like architecture can be seen in the IHC bundle, whereas the OHC bundle has three rows of stereocilia and a "W" shape. OHC also have a staircase-like architecture. **(d)** Overview of hair cell bundle deflection which leads to the opening of MET channels found at the tip of the smaller row of stereocilia. Consequently, bundle deflection results in depolarisation of both population of hair cells. Opening of MET channels permits the entry of K^+ and Ca^{2+} ions into hair cells. Figure image adapted from Bartsch *et al.*, 2019. **(e)** Overview of the laterally-localised Prestin protein which confers the electromotile properties of OHCs. Deflection of OHC bundles (force) and OHC depolarisation results in the shortening of OHC somatic length. When OHC bundles are not deflected and OHC hyperpolarise, the OHC lengthen returns to its original size. Figure image adapted from Fettiplace & Hackney, 2006.

Sensory hair cells can be divided into two populations, a single row of inner hair cells (IHCs) which transduce acoustic stimuli into graded action potentials and three rows of outer hair cells (OHCs) that amplify incoming sounds (Figure 1.3a). Upon their deflection, mechanoelectrical transduction (MET), non-selective cation channels (MET channels) are opened, allowing the influx of potassium (K^+) and calcium (Ca^{2+}) ions into hair cells, causing graded depolarisation in proportion to the extent of bundle deflection (Hudspeth & Corey, 1977; Corey & Hudspeth, 1979). IHC depolarisation results in exocytosis of glutamate-containing vesicles to stimulate action potentials in innervating afferent fibres. Changes in OHC potential results in lengthening and shortening of OHC somatic length for cochlear amplification.

1.2.2 Hair Cell Bundle and MET

On the apical surface of IHCs and OHCs are highly ordered rows of actin-based stereocilia bundles that are arranged in a staircase-like architecture (Figure 1.3b, c). IHC bundles contain two rows of stereocilia and the bundle has a "V" shape which is responsible for the propagation of acoustic stimuli to the CAS (Figure 1.3b). OHC bundles are composed of three rows of stereocilia and have a "W" shape and in response to changes in their membrane potential, OHCs change in length to amplify the output of IHCs (Figure 1.3c) (Dallos *et al.*, 2008). This electromotility is attributed to the expression and localisation of the protein Prestin at the OHC lateral membrane, which confers to the longitudinal shortening and extension of OHCs in response to its depolarisation and hyperpolarisation respectively (Figure 1.3e) (Belyantseva *et al.*, 2000; Liberman *et al.*, 2002; Ashmore, 1987).

Although morphological and physiological differences exist between bundles on both hair cells, they share a common developmental process. To orientate stereocilia bundles perpendicular to the cochlear length, a transient microtubule-based protrusion known as the kinocilium is found at the centre of primordial hair cells (Jones *et al.*, 2008). Concurrent with hair cell polarisation and migration of the kinocilium to the hair cell periphery is the formation of stereocilia from microvilli structures that neighbour the kinocilium. Through the activity of non-muscle myosin proteins (e.g. Myosin 15a and Myosin 7) to deliver proteins such as Whirlin, Twinfilin-2 and Espin for the maturation of microvilli into stereocilia through increases in length and width, with those closest to the kinocilium growing the tallest (Figure 1.4) (Belyantseva *et al.*, 2005; Peng *et al.*, 2009; Sekerková *et al.*, 2011). Further refinement of bundles occurs postnatally, as the number of rows and of stereocilia decreases between Postnatal day (P) 0 to the onset of hearing in the mouse (at P12) (Lim & Anniko, 1985; Lelli *et al.*, 2016).

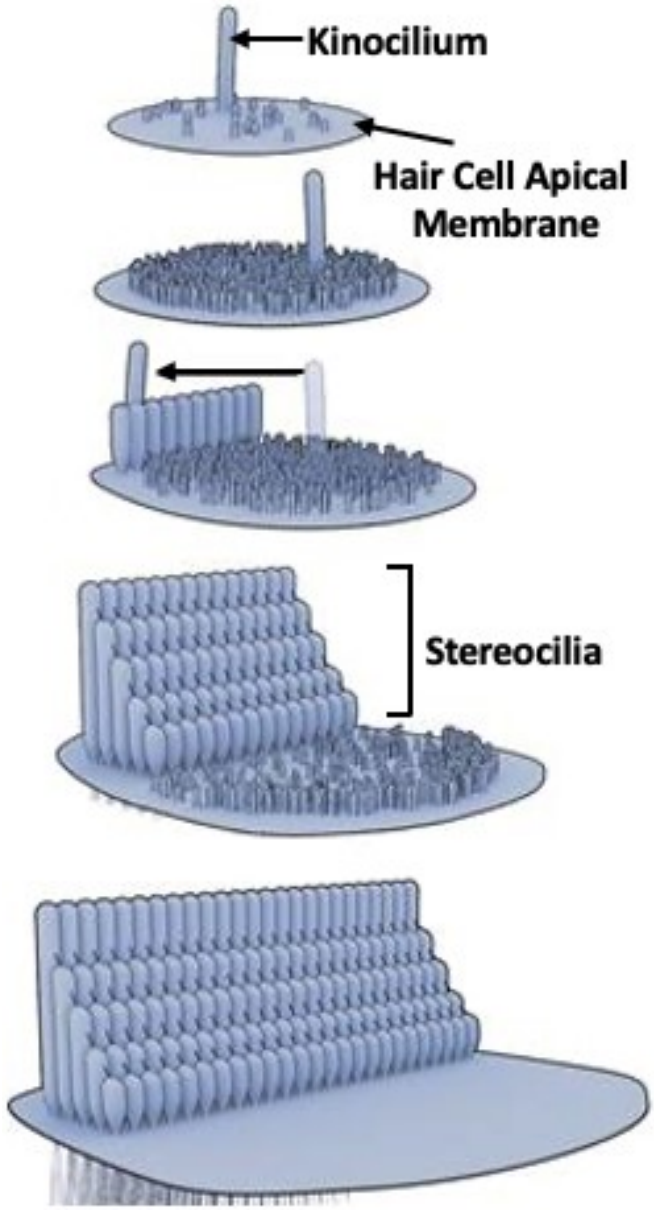

Figure 1.4: Development of hair cell bundles. The formation of hair cell bundles on IHCs and OHCs requires the kinocilium which properly orients stereocilia bundles. The kinocilium migrates to periphery of the hair cell apical membrane and microvilli protrusions extend to form stereocilia. The microvilli closest to the kinocilium growing the tallest, which establishes the staircase-like architecture of bundles. At early postnatal ages, the rows of stereocilia are pruned. Figure image adapted from Schwander *et al*., 2010.

Coordinated bundle deflection towards the tallest row of stereocilia is required to open MET channels, which are found at the tip of the shorter rows of stereocilia (Figure 1.3d) (Beurg *et al.*, 2009; Hudspeth & Corey, 1977). To ensure that bundles are properly organised, numerous connections within hair cell bundles are found along the length of stereocilia hair cell bundles, with the most crucial being tip links (Figure 1.5) (Hackney &

Furness, 2013). This stereociliary linkage is composed of a homodimer of Protocadherin 15 (PCDH15) protein found at the tip of shorter rows of stereocilia, which interacts in a Ca^{2+}-dependent fashion with a homodimer of Cadherin 23 (CDH23) protein that is found along the length of taller stereocilia (Ahmed *et al.*, 2006; Siemens *et al.*, 2004; Kazmierczak *et al.*, 2007). Anchoring CDH23 and PCDH15 in place are upper and lower tip link densities, which consist of scaffolding proteins such as SANS and Harmonin (Grati & Kachar, 2011).

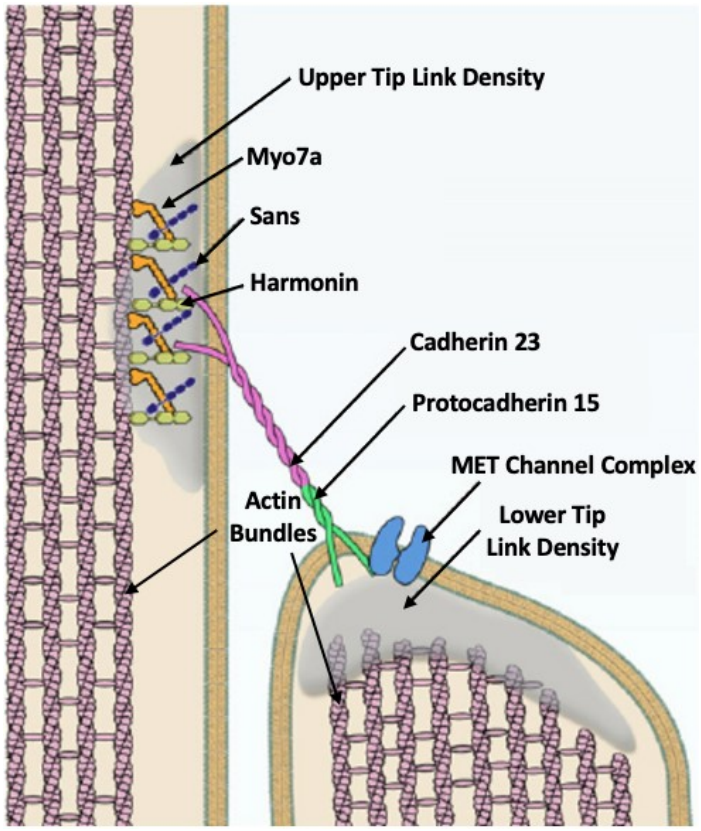

Figure 1.5: Tip links are required stereocilia bundle deflection and MET channel opening. Overview of the CDH23-PCDH15 heterotetrametric, tip link complex which connects the tip of shorter stereocilia to a longer stereocilium in the same bundle. Pcdh15 interacts with the shorter tip link and the MET channel complex, which is believed to be comprised of the TMC1, TMC2, TMIE and TMHS proteins. CDH23 interacts with the longer stereocilium and interacts with the Sans and Harmonin proteins which anchor CDH23 and the upper tip link density in place. Figure image adapted from Grati & Kachar, 2011.

Tip links are crucial for transmission of the mechanical forces of bundle deflection to the opening of MET channels, which is demonstrated by the concurrent absence of MET channel current or the onset of progressive hearing loss in models (*in* or *ex vivo*) where

tip links are chemically or genetically disrupted (Assad *et al.*, 1991; Basu *et al.*, 2016; Palma *et al.*, 2001; Schwander *et al.*, 2009; Alagramam *et al.*, 2011; Pepermans *et al.*, 2014). Additional evidence for the functional requirement of tip links in MET channel gating, is the observed interactions between PCDH15 and the MET channel complex (Xiong *et al.*, 2012; Maeda *et al.*, 2014; Zhao *et al.*, 2014). Proteins believed to constitute the MET channel complex, TMHS, TMIE and TMC1/2, are found at the tip of shorter stereocilia, correlating with the location of the MET channel and with PCDH15. In their absence, MET channel current is disrupted or absent (Xiong *et al.*, 2012; Zhao *et al.*, 2014; Kawashima *et al.*, 2011; Kurima *et al.*, 2015).

1.2.3 K^+ Recycling and the Endocochlear Potential

Opening of the MET channel complex leads to an influx of K^+ and Ca^{2+} influx into hair cells. This is driven by the electrochemical gradient between the endolymph-filled scala media and the underlying perilymph-filled scala tympani, which bathes the apical and basolateral surfaces of HCs, respectively (Figure 1.6a). The reciprocal ionic concentration of K^+, sodium (Na^+) and Ca^{2+} (157mM, 1mM and 20µM respectively) of the endolymph, to that found in the perilymph (4mM K^+, 148mM Na^+ and 1.3mM Ca^{2+}), establishes an electrochemical gradient and a ~100mV potential difference (known as the endocochlear potential (EP)) (Wangemann & Schacht, 1996; Steel & Bock, 1980). Upon MET channel opening, the electrochemical gradient and the EP influence K^+ and Ca^{2+} influx into hair cells, with the EP being the principal K^+ ion influx driving force (Chan & Hudspeth, 2005). Tight junctions are found between hair cells and adjacent supporting

cells (SCs) to maintain the distinction between the scala media and tympani (Wilcox *et al.*, 2001; Nakano *et al.*, 2009).

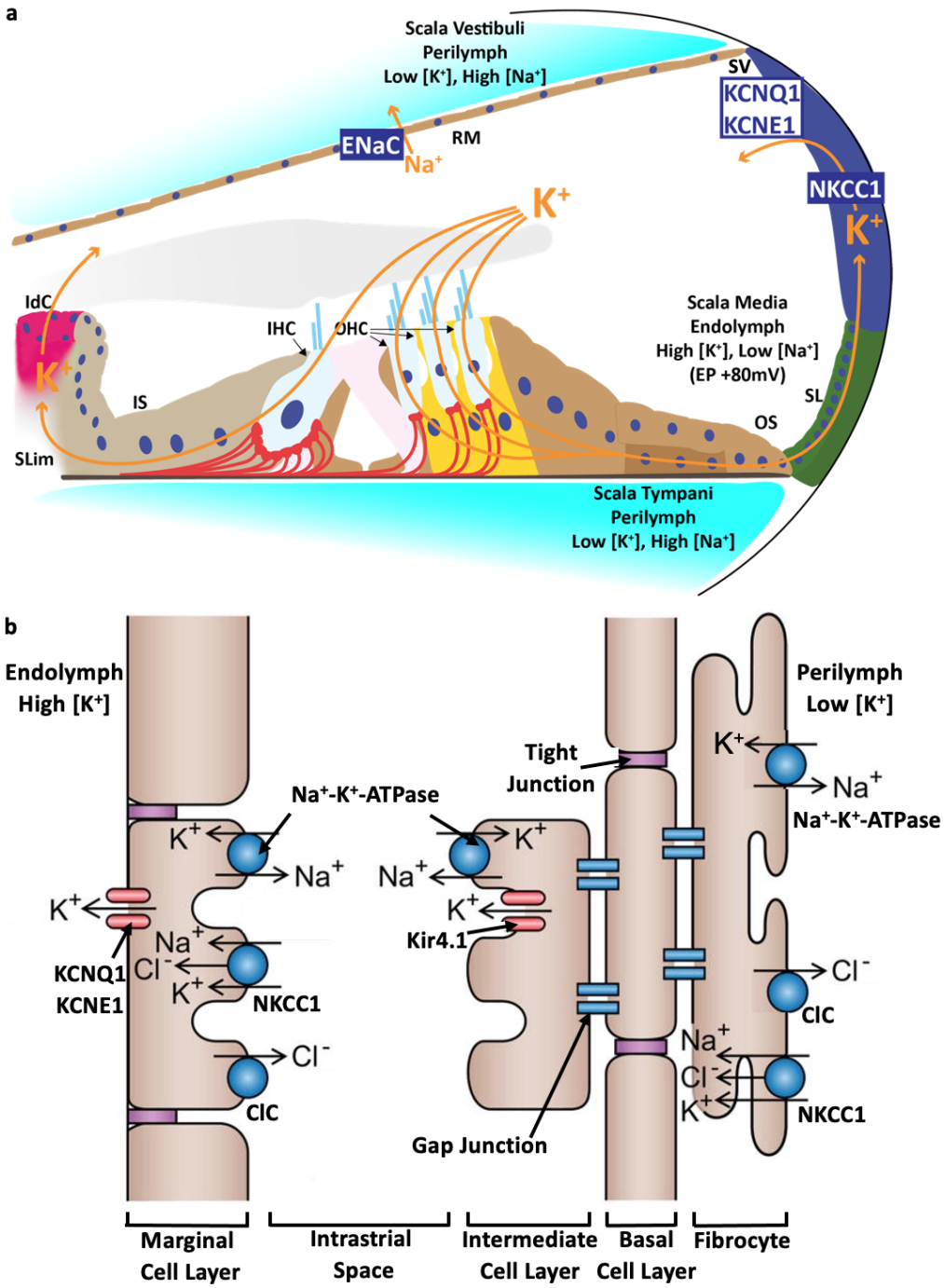

IdC: Interdental Cells; **IHC:** Inner Hair Cells; **IS:** Inner Sulcus; **OS:** Outer Sulcus; **RM:** Reissner's Membrane; **SL:** Spiral Ligament; **SLim:** Spiral Limbus; **SV:** Stria Vascularis

Figure 1.6: K^+ ion flux through cochlear tissues. **(a)** The K^+ concentration gradient between the Scala Media and Tympani (157 and 4mM, respectively) and the resultant EP drives K^+ flux into HCs following their depolarisation. Return of K^+ ions back into endolymphatic spaces occurs through the lateral (SL and SV) or medial (SLim and IdC) pathways. **(b)** Diagrammatic representation of the marginal, intermediate and basal cell layer of the SV. Coupled activity of the NKCC1, Na^+-K^+-ATPase and ClC channels results in transport of K^+ ions out from the perilymph and into the SV. Kir4.1 channels push K^+ ions out of the intermediate layer where they are moved into the marginal cell layer by more NKCC1, Na^+-K^+-ATPase and ClC channels. K^+ ions are then transported back into endolymphatic spaces by KCNQ1/KCNE1 channels. Figure image adapted from Fettiplace, 2017.

Following hair cell depolarisation, K^+ ion are cleared from hair cells along concentration gradients into the perilymph via basally located KCNQ4 channels (Kharkovets *et al.*, 2006). However, for sustained MET and cochlear function, preservation of the endolymphatic K^+ ionic concentration and the EP is crucial. To this end, a network of channel proteins found within the cochlear lateral wall maintains the ionic composition of endolymphatic spaces (Figure 1.6b). K^+ uptake from the perilymph into spiral ligament (SL) fibrocytes is facilitated by the coupled activity of the Na^+-K^+-ATPase, NKCC (Na^+-K^+-Chloride ion (Cl^-)) and Cl^- channels (ClC) (Schulte & Steel, 1994; Mizuta *et al.*, 1997; Wangemann *et al.*, 1995; Crouch *et al.*, 1997). This ensures maximal K^+ ion uptake from the perilymph and allows it passive movement through to the intermediate cell layer of the stria vascularis (SV) (Figure 1.6b; Intermediate Cell Layer – Fibrocyte).

A large potential difference exists between the high K^+ ion concentration ($[K^+]$) of the intermediate cells, and the low $[K^+]$ of the neighbouring intrastrial space, which drives Kir4.1-mediated K^+ ion transport out of intermediate cells (Figure 1.6b; Intermediate Cell Layer) (Salt *et al.*, 1987; Hibino *et al.*, 1997). As such, the intermediate cell apical membrane is regarded as the origin of the EP (Marcus *et al.*, 2002). The mechanisms of marginal cell K^+ ion uptake from the intrastrial space mirrors the SL fibrocytes, in that marginal cell K^+ ion influx is achieved through the coupled activity of Na^+-K^+-ATPase, NKCC and ClC (Figure 1.6b; Marginal Cell Layer) (Delpire *et al.*, 1999; Estévez *et al.*, 2001; Rickheit *et al.*, 2008; Schulte & Steel, 1994; Wangemann *et al.*, 1995). Consequently, this maintains the EP and the low intrastrial fluid $[K^+]$, in relation to the intermediate cells. Finally, KCNQ1/KCNE1 channels permit K^+ ions return back into the endolymph, thus completing the cycle of K^+ transport (Neyroud *et al.*, 1997; Rickheit *et al.*, 2008).

1.2.4 Ribbon Synapses

Sounds are continuously being encoded by the cochlea. To aid in this process, presynaptic ribbon (ribbon synapse) structures are found at the basal hair cell presynaptic membrane active zone, which facilitate the high release rate of glutamate-containing vesicles onto the underlying afferent neuron fibres (Figure 1.7) (Moser & Beutner, 2000; Glowatzki & Fuchs, 2002). Ribbon synapses are electron-dense structures with numerous vesicles tethered to its surface and are found in IHCs in varied abundance along the cochlear length, and sparingly in OHCs (Smith & Sjöstrand, 1961; Lenzi & Von Gersdorff, 2001; Meyer *et al.*, 2009; Martinez-Monedero *et al.*, 2016). In addition to displaying differences in ribbon synapse along the OoC, the ribbon synapses found within a single IHC display morphological differences to one another. For example, ribbon synapses found on the modiolar surface of IHCs are larger than those found on the pillar surface (Figure 1.7). Inverse relationships are also found along the same modiolar-pillar gradient with regards to the size of postsynaptic glutamate receptors found on the type I afferent neurons (Liberman *et al.*, 2011; Liberman & Liberman, 2016). Furthermore, the morphologically different presynaptic ribbons will mediate glutamate exocytosis onto specific subpopulations of type I afferent neurons with defined physiological properties (discussed further in 1.3.1: Afferent Neurons: Type I Neurons) (Liberman, 1982; Petitpré *et al.*, 2018; Shrestha *et al.*, 2018; Sun *et al.*, 2018).

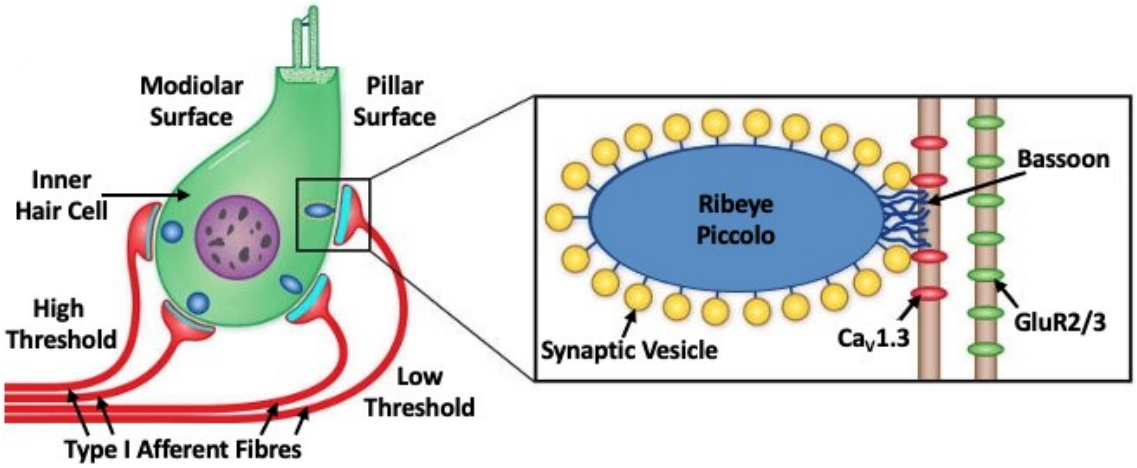

Figure 1.7: Presynaptic ribbon structures at the hair cell basolateral membrane. Overview of the IHC basolateral membrane and the innervating Type I Fibres. Fibres contacting the IHC pillar surface have low spontaneous activity compared to the high spontaneous activity fibres that contact the IHC modiolar surface. The pre- and postsynaptic membrane are magnified. At the presynaptic membrane, is the presynaptic ribbon with numerous glutamate-filled vesicles tethered to its surface. Ca^{2+} influx via $Ca_V1.3$ channels permits rapid glutamate exocytosis into the synaptic cleft between the pre- and postsynaptic membrane. At the postsynaptic membrane, glutamate stimulates the glutamate-receptive GluR2 and GluR3 channels. Figure image adapted from Fettiplace, 2017.

The extent of hair cell bundle deflection and depolarisation results in a graded release of glutamate. Upon depolarisation, L-type, voltage-gated $Ca_V1.3$ channels mediate Ca^{2+} influx in close proximity to ribbon synapses, generating domains of intracellular Ca^{2+} (Ca^{2+}_i) (Brandt *et al.*, 2003; 2005). In turn, this stimulates a graded release of membrane-associated, readily releasable pool (RRP) of glutamate-containing vesicles within 10 milliseconds of hair cells depolarisation (Moser & Beutner, 2000; Frank *et al.*, 2009; Pangrsic *et al.*, 2015; Chakrabarti *et al.*, 2018). In response to prolonged acoustic stimuli, ribbon synapses are believed to be involved in replenishment of the RRP, thus allowing a synchronous and sustained release of glutamate from hair cells (Frank *et al.*, 2010; Pangšrič *et al.*, 2010; Michalski *et al.*, 2017; Khimich *et al.*, 2005; Moser & Beutner, 2000). The hair cell presynaptic membrane and the proteins that constitute the ribbon synapse are unique compared to non-sensory synapses. Many proteins that are required for synaptic function in non-sensory neuronal tissues are superfluous to auditory ribbon synapse function (Safieddine *et al.*, 2012). Some traditional presynaptic scaffolding

proteins such as Bassoon and Piccolo are required for hair cell vesicle exocytosis (Figure 1.7) (Regus-Leidig *et al.*, 2013; Khimich *et al.*, 2005). Transcription and translation of vesicular fusion SNARE (Soluble N-Ethylmaleimide-Sensitive Fusion Protein Attachment Protein Receptors) proteins such as SNAP-25, Syntaxin 1 and Synaptobrevin 1 are detectable in cochlea hair cells (Safieddine & Wenthold, 1999; Uthaiah & Hudspeth, 2010). However, their functional role in hair cell synaptic transmission is questionable; ablation of SNARE protein function through genetic or chemical means does not disrupt Ca^{2+} influx, glutamate exocytosis or replenishment of the RRP (Nouvian *et al.*, 2011). Similar incongruencies were also observed in the expression of some members of the Ca^{2+}-sensing, Synaptotagmin proteins (1, 2 and 7) and their functional role in ribbon synapses (Beurg *et al.*, 2010; Johnson *et al.*, 2010). Whilst Synaptotagmin 1 is required for sustained vesicular release at early postnatal ages, loss of Synaptotagmin 2 or 7 has no effect on vesicular release (Beurg *et al.*, 2010). Instead of Synaptotagmin proteins, hair cell proteins express the Ca^{2+}-sensing Otoferlin protein, which is also required for the replenishment of the RRP (Johnson & Chapman, 2010; Roux *et al.*, 2006; Michalski *et al.*, 2017). Ribbon synapses require the protein Ribeye, which aggregates to itself and interacts with other ribbon synapse proteins (Magupalli *et al.*, 2008). In its absence, ribbons are lost which correlates with less vesicles associated to the active zone membrane and a decreased summed response of the afferent neuron to a sound stimulus (Becker *et al.*, 2018; Jean *et al.*, 2018; Buchwald & Huang, 1975).

The postsynaptic membrane is more conventional compared to the presynaptic membrane, with scaffold proteins such as PSD-95, Shank and Homer are all present at the postsynaptic membrane (Cheng *et al.*, 2006; Davies *et al.*, 2001; Martinez-Monedero

et al., 2016). Found alongside such aforementioned proteins are the α-Amino-3-Hydroxy-5-Methyl-4-Isoxazolepropionic Acid (AMPA) class glutamate receptors such as GluR2, 3 and 4 (Matsubara *et al.*, 1996; Ruel *et al.*, 2000). Glutamate stimulation of AMPA receptors permits non-selective cation influx, thus stimulating synchronised excitatory postsynaptic action potentials along afferent neurons towards the CAS (Figure 1.7). Other classes of glutamate receptors (Kainate, NMDA and metabotropic) are also found within cochlear tissues but are more likely to be involved in the modulation of afferent neuron activity rather than generating excitatory action potentials (Niedzielski & Wenthold, 1995; Peppi *et al.*, 2012; Ruel *et al.*, 2008; Peng *et al.*, 2004).

1.3 Cochlear Innervation

Cochlear tissue is innervated by afferent and efferent fibres to send action potentials to and receive feedback from the CAS, respectively (Figure 1.8). Two distinct afferent neuron populations exist in the spiral ganglion neurons (SGNs) of the cochlea, with type I and II afferents receiving glutamatergic signals from either IHC or OHC respectively (Figure 1.8; green and purple fibres) (Berglund & Ryugo, 1987). As previously discussed, glutamate release onto type I afferents allows the propagation of acoustic stimuli to the CAS (Glowatzki & Fuchs, 2002). On the other hand, there is evidence to suggest that type II afferents can be activated by Adenosine Triphosphate (ATP) neurotransmitter to mediate auditory nociception within the cochlea (Weisz *et al.*, 2009; Liu *et al.*, 2015; Flores *et al.*, 2015; Maison *et al.*, 2016).

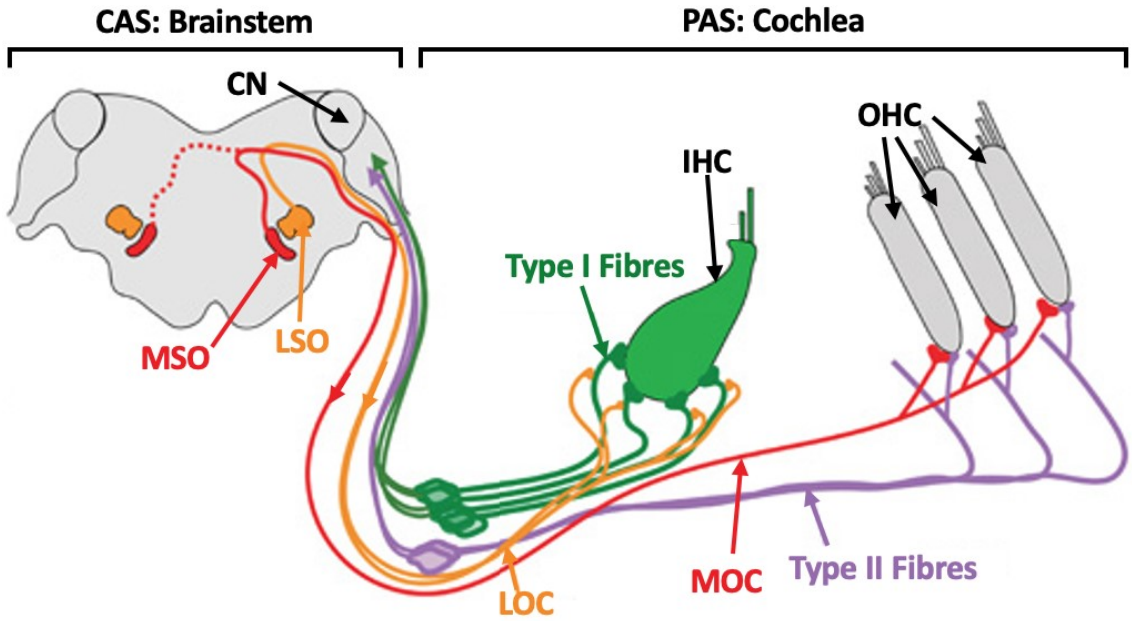

CAS: Central Auditory System; **CN:** Cochlear Nucleus; **IHC:** Inner Hair Cell; **LOC:** Lateral Olivocochlear; **LSO:** Lateral Superior Olive Fibre; **MOC:** Medial Olivocochlear Fibre; **MSO:** Medial Superior Olive; **PAS:** Peripheral Auditory System

Figure 1.8: Overview of the cochlear afferent and the efferent innervation. Two populations of afferent fibres innervate cochlear tissues, the Type I (green) and II (purple) fibres contact IHC and OHC, respectively. Two populations of efferent fibres also innervate cochlear tissue, which descend from the SOC of the CAS. LOCs (orange) specifically descend from the LSO and make axodendritic connection with Type I afferent fibres. MOCs (red) originate from the MSO and make axosomatic connection with OHCs directly. Figure Image adapted from Webber *et al.*, 2021.

Two efferent fibres also co-exist within cochlear tissue and are required for the protection of cochlear function, by modulating its output (Rajan & Johnstone, 1988; Darrow *et al.*, 2007). Both efferent systems, the lateral and medial olivocochlear (LOC and MOC, respectively), originate from distinct regions of the superior olivary complex and form axodendritic and axosomatic connection with type I afferents and OHCs respectively (Figure 1.8; LOC and MOC) (Guinan *et al.*, 1983). It is believed that cochlear efferent innervation modulates and protects auditory function against damage (Maison *et al.*, 2010). Investigations in which the LOC and MOC fibres are surgically severed, there were fewer functional inner hair cell ribbon synapses and higher sensitivity to noise-exposure threshold shifts (Darrow *et al.*, 2007). The LOC and MOC can modulate activity of the auditory nerve and cochlear amplification, respectively.

1.3.1 Afferent Neurons: Type I Neurons

Each IHC is innervated by 5 – 30 myelinated, type I afferent fibres, with each fibre receiving glutamate from an individual presynaptic ribbon (Figure 1.7) (Liberman, 1980). The Type I afferent populations, which constitutes an overwhelming majority of the total SGN population, can be subdivided further based upon their anatomical, physiological and transcriptional differences to each other (Liberman, 1982; Sun *et al.*, 2018; Petitpré *et al.*, 2018; Shrestha *et al.*, 2018). Ultimately this allows the cochlea to be sensitive to dynamic range of sounds and be able to perceive acoustic stimuli in noisy environments (Winter *et al.*, 1990). These differences include the thickness of the afferent fibre, the rate of spontaneous activity (SR) when not acoustically stimulated and its auditory threshold (the lowest amplitude of sound necessary to record an action potential) (Liberman, 1978). The relationship between these factors is evident along the modiolar-

pillar axis along the basolateral IHC membrane (Liberman, 1982). Type I afferents which contact the IHC pillar surface are thicker, display higher SR and lower auditory thresholds than those that contact on the modiolar surface; medium SR and auditory threshold neurons contact the modiolar surface (Liberman, 1982). Through single cell RNA sequencing (scRNA-seq) of type I afferent SGNs, neurons with different physiological properties have distinct transcriptional profiles. For instance, type I afferents which contact the IHC pillar membrane highly express the *Calb2* and *Pcdh20* gene (Sun *et al.*, 2018; Petitpré *et al.*, 2018; Shrestha *et al.*, 2018).

1.3.2 Afferent Innervation: Type II Neurons

Recording of type II afferent electrophysiological behaviour has been challenging and as such, much less is known about them (Robertson, 1984; Weisz *et al.*, 2009). Type II afferent fibres extend across the OoC before turning and extending towards the cochlear base whilst innervating numerous OHCs (Perkins & Morest, 1975; Berglund & Ryugo, 1987; Weisz *et al.*, 2012) . Type II afferents have been dubbed 'silent' due to the observed lack of spontaneous activity under resting conditions and their unresponsive nature in response to loud stimuli (Robertson, 1984; Weisz *et al.*, 2009). More recently, electrophysiological recording of type II afferent fibres suggests that a coordinated glutamate release from numerous OHCs is required to measure their activity (Weisz *et al.*, 2012; Weisz *et al.*, 2009; Martinez-Monedero *et al.*, 2016; Weisz *et al.*, 2014). In addition, type II afferents are also responsive to the ATP neurotransmitter, which mediates its electrophysiological activity in damaged cochlea (Nakagawa *et al.*, 1990; Weisz *et al.*, 2009; Liu *et al.*, 2015). Reports have also detailed the increased endolymphatic ATP concentration and expression of ATP-responsive purinergic

receptors in OHCs following cochlear damage, which collectively suggests that type II afferents are involved in pain perception in cochlear tissue (Munoz *et al.*, 2001; Wang *et al.*, 2003).

1.3.3 Efferent Innervation: LOC

Investigation of LOC efferents function has identified that they can either enhance or suppress type I afferent postsynaptic activity over long durations (Groff & Liberman, 2003). These opposing physiological outcomes are believed to due to the range of neurotransmitters that LOC fibres are capable of releasing (Eybalin, 1993; Puel, 1995; Maison *et al.*, 2002; Darrow *et al.*, 2006; Dickerson *et al.*, 2016). Application of the Acetylcholine (ACh) neurotransmitter increased the rate of type I afferent postsynaptic rate of spontaneous activity (Felix & Ehrenberger, 1992). Cholinergic LOC fibres are also receptive to the Calcitonin Gene-related Protein neurotransmitter, which has been shown to enhance the amplitude of type I afferent postsynaptic activity (Dickerson *et al.*, 2016). Conversely, application of γ-aminobutyric acid (GABA) neurotransmitter or a Dopamine receptor agonist has been shown to dampen type I afferent fibre activity (Felix & Ehrenberger, 1992; Arnold *et al.*, 1998; d'Aldin *et al.*, 1995). Phenotypic characterisation of Dopamine receptor KO mouse models has demonstrated increased amplitudes of type I afferent postsynaptic activity and susceptibility to noise-induced auditory threshold shifts (Maison *et al.*, 2012).

1.3.4 Efferent Innervation: MOC

The MOC efferent system can cause rapid repression of the OHC-mediated cochlear amplification in response to incoming sounds (Blanchet *et al.*, 1996; Vetter *et al.*, 1999; Vetter *et al.*, 2007). This effect is mediated by the ACh neurotransmitter but like the LOC

efferent system, other neurotransmitters like GABA are also involved in MOC efferent function (Batta *et al.*, 2004; Maison *et al.*, 2006; Schrott-Fischer *et al.*, 2007; Wedemeyer *et al.*, 2013). Mechanistically, this occurs through basally located nicotinic α9 and α10 receptors, which allow Ca^{2+} influx into OHC and subsequently stimulates their hyperpolarisation (Housley & Ashmore, 1991; Elgoyhen *et al.*, 1994; Elgoyhen *et al.*, 2001; Vyas *et al.*, 2020; Fuchs & Murrow, 1992). Consequently, this is expected to affect the Prestin-mediated electromotility and cochlear amplification function of OHCs (Frolenkov, 2006). Mouse models with increased activity of α9 receptor, either through a point mutation or increased abundance were more resistant to noise-induced hearing loss when exposed to damaging levels of acoustic stimuli (Maison *et al.*, 2002; Taranda *et al.*, 2009).

1.4 Cochlear Development

Cochlear tissue derives from an ectodermal tissue known as the otic placode of the ectoderm, which first develops at around Embryonic Day (E) 9 (Anniko & Wikström, 1984). Following invagination of the otic placode into the otocyst, development of the cochlear tissue begins with the protrusion of the cochlear duct form the ventral surface of the otocyst (Figure 1.9a; E11.5) (Sai & Ladher, 2015; Driver & Kelley, 2020). A *Sox2*-expressing region of the cochlear duct known as the prosensory domain (PD) eventually gives rise to the hair cells and surrounding cells of the OoC (Figure 1.9a; E12.5) (Kiernan *et al.*, 2005; Dabdoub *et al.*, 2008). Through a combination of Fibroblast Growth Factor (FGF) and Notch-mediated lateral inhibition signals (JAG1 protein), different regions of the PD are specified towards different cochlear cell fates (Pirvola *et al.*, 2002; Kiernan *et al.*, 2006; Brooker *et al.*, 2006; Ono *et al.*, 2014). By E13.5, the PD of the developing cochlear duct has distinct boundaries of FGF10, $p27^{Kip1}$ and Bone Morphogenic Protein 4 (BMP4) which eventually forms the inner sulcus (IS), OoC and outer sulcus (OS), respectively (Ohyama *et al.*, 2010; Chen & Segil, 1999; Morsli *et al.*, 1998).

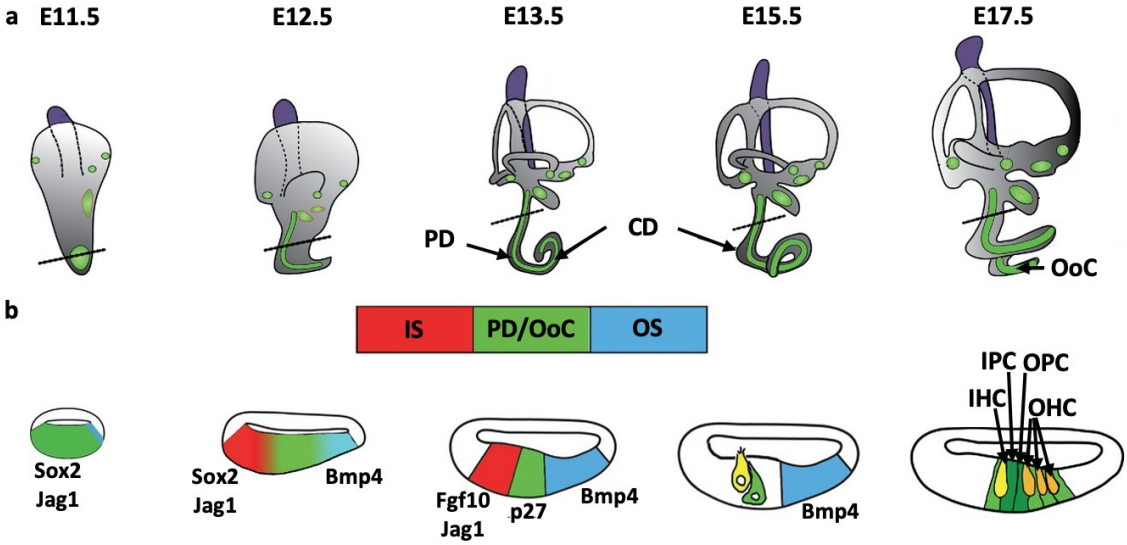

CD: Cochlear Duct; **IHC:** Inner Hair Cell; **IPC:** Inner Pillar Cell; **IS:** Inner Sulcus; **OHC:** Outer Hair Cell; **OoC:** Organ of Corti **OPC:** Outer Pillar Cell; **OS:** Outer Sulcus; **PD:** Prosensory Domain

Figure 1.9: Development of the inner ear between E11.5 – 17.5. **(a)** The developing cochlea protrudes from the ventral surface of the developing otocyst. Extension of the cochlear duct occurs concurrently with the extension of the PD along the cochlear duct. The PD contains progenitors that give rise to the numerous specialised cells of the OoC. Black lines through the developing cochlear duct indicate which corresponding cochlear cross-section view is shown below in (b). **(b)** Cochlear cross-section view of the developing cochlear duct, with different regions of the PD showing expression of specific transcription factors and signalling molecules. At E11.5, the PD expresses the SOX2 transcription factor and the Notch signalling ligand, JAG1. At E12.5, SOX2 and JAG1-expressing regions of the PD begin to demark the primordial IS. The opposite region expresses the BMP4 which marks the primordial OS. In between the SOX2/JAG1 and BMP4 expressing regions is where the OoC will form. At E13.5, the PD which eventually gives rise to the OoC begins to express the cell cycle inhibitor protein $p27^{Kip1}$. At basal cochlear turns at E17.5, the OoC has adopted its highly organised structure, with IHC and OHC and surrounding SCs. Figure image adapted from Basch *et al.*, 2016.

1.4.1 OoC Development

Formation of the OoC and hair cells begins with the expression of the cell cycle inhibitor protein, $p27^{Kip1}$, in the PD which is expressed in an apical-to-basal gradient (Figure 1.9; E13.5, E15.5) (Chen & Segil, 1999). The pattern of $p27^{Kip1}$ expression coincides with the exit from the cell cycle and cell proliferation, which is first observed at the apical cochlear turn (Lee *et al.*, 2006). Differentiation of hair cells begins at around E13.5-14.5 and occurs along an opposing gradient to cell-cycle exit; cells of the PD that are fated to become hair cells first express the *Atoh1* transcription factor at mid-basal cochlear regions (Chen & Segil, 1999; Chen *et al.*, 2002; Bermingham *et al.*, 1999). Alongside hair cell fate specification, *Atoh1* expression also drives SC differentiation through lateral inhibition signals which prevents excessive formation of hair cells (Woods *et al.*, 2004;

Lanford *et al.*, 1999; Zheng *et al.*, 2000). Ultimately, PD cells which receive the inhibitory signals eventually develop into SCs (Murata *et al.*, 2006).

1.4.2 SGN Development

SGNs derive from the cochleovestibular ganglion (CVG) which is a collection of *Neurog1* and *Neurod1* expressing precursors that have delaminated away from the developing otic placode (Ma *et al.*, 1998; Kim *et al.*, 2001). CVG progenitors which eventually form the SGNs, proliferate alongside the developing cochlear duct and become post-mitotic in basal-to-apical gradient (Matei *et al.*, 2005; Koundakjian *et al.*, 2007). Hair cell innervation by SGNs begins around E12.5 – 15.5, with basal PD regions being infiltrated by both type I and II afferents (Koundakjian *et al.*, 2007). Whilst hair cells differentiation and their innervation occur concurrently, migration of afferent fibres to the PD is independent of OoC development; developing cochlear tissue of *Atoh1* KO mice are still innervated (Fritzsch *et al.*, 2005; Pan *et al.*, 2011). To ensure proper IHC and OHC innervation, repulsive interactions between Erythripoietin-Producing Hepatocellular Carcinoma (Eph) and Neuropilin receptors, and Ephrin and Semaphorin ligands respectively, are required (Defourny *et al.*, 2013; Coate *et al.*, 2015). Establishing proper afferent innervation of hair cells is necessary for the proper axodendritic and axosomatic efferent innervation supplied by the LOC and MOC respectively (Webber *et al.*, 2021).

1.5 Mouse Models of Hearing Loss

1.5.1 Utilization of Mouse Model Organisms in Auditory Research

Model systems are required to further our understanding of human physiological processes, providing a system which to study the pathological consequences of disease. The mouse has been an invaluable model organism that is utilised in many fields of biomedical research due to their genetic, anatomical and physiological similarities to humans (Rosenthal & Brown, 2007; Mouse Genome Sequencing Consortium, 2002). Auditory research is no different as the mouse is the most popular mammalian model organism (Ohlemiller *et al.*, 2016). The anatomical and physiological processes of hearing in mice are incredibly similar to humans, thus making it an appropriate model to study human deafness and develop therapeutic options that ameliorate loss of cochlear function (Ahituv & Avraham, 2002; Ren *et al.*, 2019). This is reflected in the numerous reports detailing the rescue of auditory dysfunction in mouse models of human deafness through gene therapy approaches (Akil *et al.*, 2012; Pan *et al.*, 2017; Isgrig *et al.*, 2017; Emptoz *et al.*, 2017; Akil *et al.*, 2019; Yeh *et al.*, 2020).

Considerations to the background strain must be made when mice are utilized as model organisms in auditory research. Inbred strains such as C57BL/6N mice, are at least 98.6% identical across the genome, eliminating any genetic heterogeneity between mice (isogenic) (Beck *et al.*, 2000; Justice *et al.*, 2011; Yoshiki & Moriwaki, 2006). Therefore, when assessing the phenotypic consequences of a genetic mutation introduced onto an inbred strain (congenic), there is greater confidence in attributing any pathological consequences to the genetic mutation (Justice *et al.*, 2011). However, there are inherent differences in the auditory function of different inbred mouse strains which can

constrain their use in auditory research (Zheng *et al.*, 1999; Johnson *et al.*, 2006). For example, a guanine to adenine synonymous polymorphism at nucleotide 753 on the *Cdh23* gene (*Cdh23*^{ahl}) was identified in many mouse strains including C57BL/6N mice (Johnson *et al.*, 2000; Noben-Trauth *et al.*, 2003). These mice experience an early-onset, high-frequency hearing loss between 3 – 6 months of age unlike the CBA strain, which is commonly utilised strain in auditory research (Zheng *et al.*, 1999; Johnson *et al.*, 2000; Kane *et al.*, 2012). To make the C57BL/6N background more suitable for auditory research, a "repaired" C57BL/6N background strain, which does not carry the *Cdh23*^{ahl} allele, has been generated which does not experience the aforementioned hearing loss (Mianné *et al.*, 2016).

1.5.2 Methods of Characterising Mouse Auditory Function

Numerous auditory phenotyping tests are utilised to investigate the auditory function of mice, including Auditory Brainstem Response (ABR) and Distortion Product Otoacoustic Emission (DPOAE) tests (Figure 1.10,Figure 1.11 respecitvely) (Zheng *et al.*, 1999; Martin *et al.*, 2007). ABR tests are used to assess the propagation of acoustic stimuli, by recording the electrical response at different points along the auditory brainstem which generates an "ABR trace" (Figure 1.10b) (Hardisty-Hughes *et al.*, 2010). Five characteristic ABR waves are present in ABR traces recorded in mice, which are commonly attributed to the activity in the auditory nerve (wave I), cochlear nucleus (wave II), superior olivary complex (wave III), lateral lemniscus (wave IV) and inferior colliculus (wave V) (Figure 1.10) (Buchwald & Huang, 1975). By presenting mice with a range of acoustic stimuli of varying intensities, the "auditory threshold" of a mouse can be determined, which is the lowest intensity acoustic stimuli that elicits an ABR trace

with identifiable ABR waves. Latency and amplitude measures recorded from specific ABR waves can indicate auditory dysfunction at specific points along the auditory pathway. DPOAE tests assesses OHC function by measuring their otoacoustic emissions, which derives from their ability to amplify acoustic stimuli (Figure 1.11) (Kemp, 2002). In general, the acoustic distortion product ($2f_1$-f_2) is measured when presenting two discreet tones (f_1 and f_2) with a frequency ratio (f_2/f_1) of 1.2. Measuring the amplitude of the DPOAE provides an objective measure of whether OHC function is compromised (Figure 1.11a) (Kemp, 1978; Gaskill & Brown, 1990).

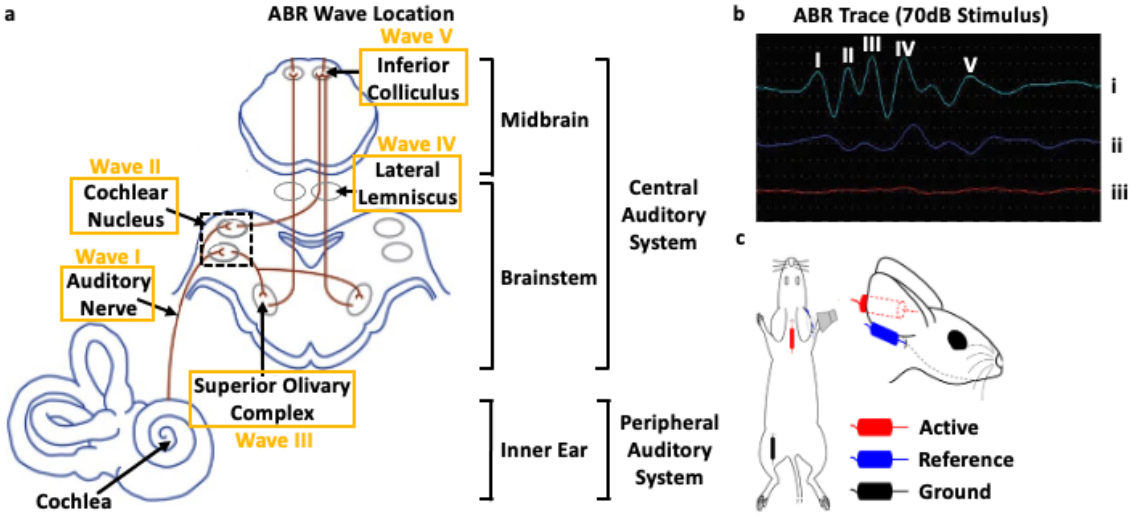

Figure 1.10: Overview of the ABR test. **(a, b)** The ABR test records the progression of acoustic stimuli through the auditory system. The characteristic ABR waves I – V are commonly attributed to the Auditory Nerve, Cochlear Nucleus, Superior Olivary Complex, Lateral Lemniscus and Inferior Colliculus, respectively. **(bi-iii)** Example ABR traces recorded in response to a 70dB stimulus. Traces i, ii and iii show examples of normal hearing, moderate and severe hearing loss, respectively. **(c)** Schematic of where different probes are placed in mice for ABR tests. Figure images (a) and (b) were adapted from Butler & Lomber, 2013 and Hardisty-Hughes *et al.*, 2010.

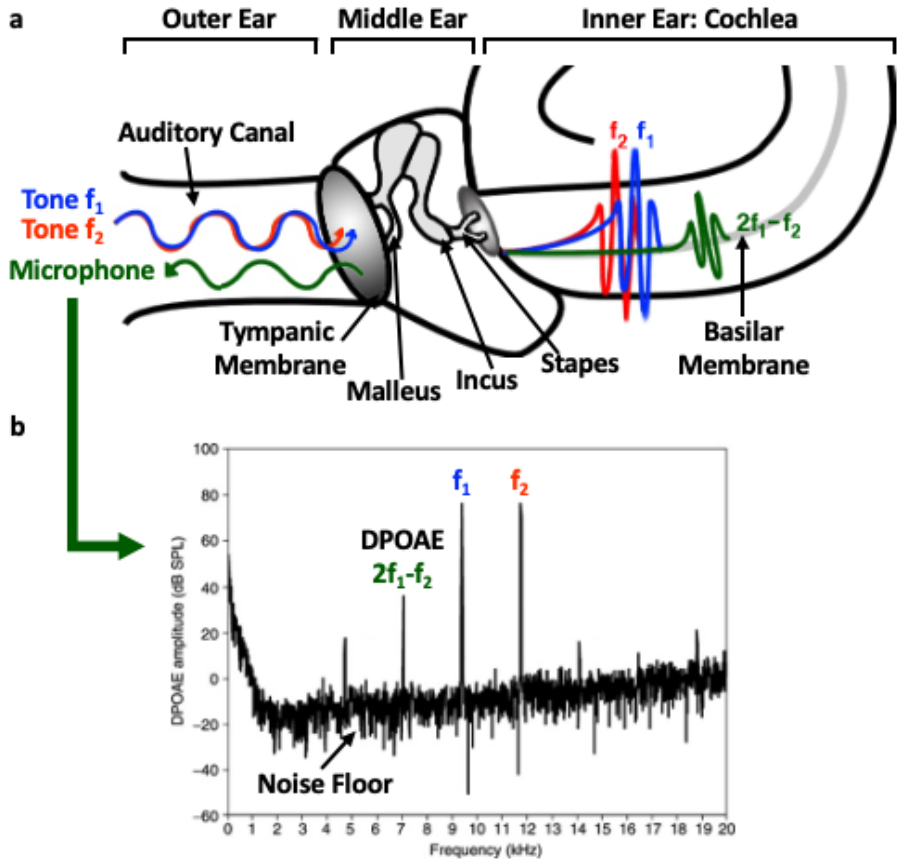

***Figure 1.11: Overview of the DPOAE test*. (a)** The DPOAE test assesses outer hair cell function by presenting two tones, f_1 and f_2, and recording the resulting distortion product generated by OHCs. **(b)** The recorded distortion product from mice, has a specific frequency which is related to the frequency of f_1 and f_2, by the expression "$2f_1$-f_2". Figure image adapted from Martin *et al.*, 2006.

1.5.3 Contributions to the Genetics of Hearing Loss

Mouse models are also commonly used as they can be genetically modified easily. The ability to generate genetic mutant lines to investigate the functional requirement of specific genes in the process of hearing has been crucial to understanding the genetic landscape of mammalian hearing. One method of introducing genetic mutations into the mouse genome is by using ENU (N-Ethyl-N-Nitrosourea), a chemical mutagen that introduces random point mutations (Russell *et al.*, 1979; Justice *et al.*, 1999). As recently demonstrated by the Harwell Ageing Screen, this approach has been able to identify many mice deafness models that display a diverse range of hearing loss phenotypes (Potter *et al.*, 2016; Carrott *et al.*, 2016; Chessum *et al.*, 2018; Agnew *et al.*, 2018; Dunbar

et al., 2019). For example, the *cello* deafness mouse model carries a nonsynonymous point mutation in the *Ikzf2* gene, which causes an early-onset hearing loss due to OHC dysfunction and decreased expression of OHC-specific proteins, Prestin and Oncomodulin (Chessum *et al.*, 2018). On the other hand, the *trombone* deafness model which carries a nonsynonymous point mutation in the *Slc4a10* gene, develop a late onset, progressive hearing loss, attributable to the disruptions to the SV and the EP (Potter *et al.*, 2016).

Large scale, reverse genetic screens have also been able to identify novel candidate deafness-causing genes, as demonstrated by the International Mouse Phenotyping Consortium (IMPC) (Bowl *et al.*, 2017). The IMPC aims to characterise every mouse protein-coding gene by generating mouse models that are homozygous carriers for a gene-specific, KO null allele, which are then entered into a broad-based phenotyping pipeline (Skarnes *et al.*, 2011; Brown & Moore, 2012). These KO null mouse models using embryonic stem cells (ESCs) that are electroporated with a gene-specific targeting vector, which introduces a "KO first" allele that disrupts "critical exons" present in all protein isoforms of a specific gene and gene function (Figure 1.12) (The International Mouse Knockout Consortium, 2007; Testa *et al.*, 2004; Skarnes *et al.*, 2011). ESCs are then injected into C57BL/6N-derived blastocysts (Pettitt *et al.*, 2009). Auditory function of KO null mouse models are assessed at 14-weeks of age by ABR (Brown & Moore, 2012). From a cohort of 3006 IMPC-generated, KO null mouse lines, the IMPC was able to identify 67 candidate deafness-causing genes, of which 52 were novel candidates that had no published literature describing their role in the mammalian process of hearing (Bowl *et al.*, 2017). One candidate, is the *Nedd4l* (*Neuronal Cell Expressed,*

Developmentally Downregulated 4, Like) gene which is encodes an E3 Ubiquitin (Ub) Ligase protein (E3 Ligase), that is most known for its ubiquitination of the Epithelial Sodium Channel (ENaC) (Kamynina *et al.*, 2001). The role of *Nedd4l* in auditory function will be explored in later chapters.

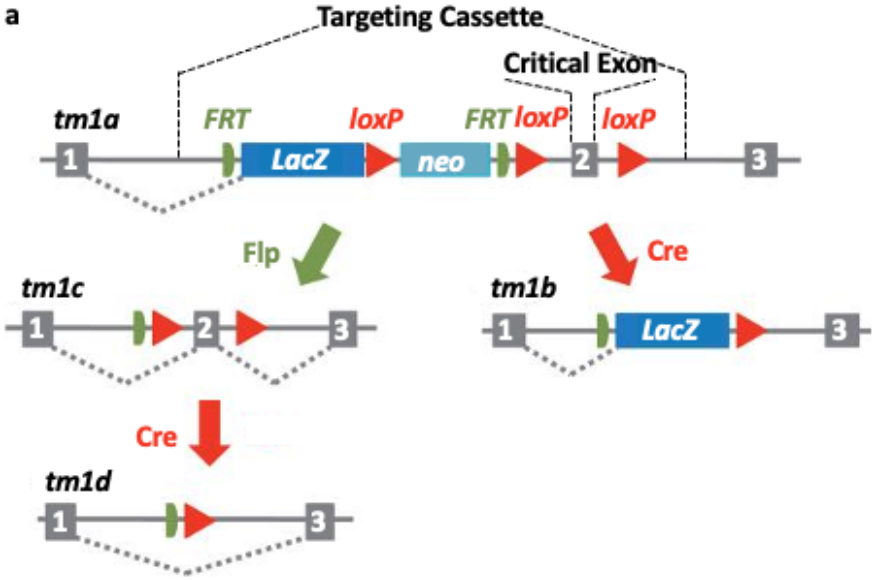

Figure 1.12: Diagrammatic representation of the IMPC-generated alleles strategy. The *tm1a* "KO First" allele is generated through the introduction of a gene trap cassette into a specific gene, in ES cells. The cassette introduces a *lacZ* reporter gene, and various *FRT* and *loxP* recombination sites. Cre-mediated recombination of the *tm1a* allele generates a *tm1b* KO null allele of a gene; the critical exon is removed, and *lacZ* reporter gene expression is under the endogenous control of the targeted gene. Flp-mediated recombination eliminates the *lacZ* reporter gene-trap cassette generates the *tm1c* allele, where the critical exon is flanked by *loxP* sites. Subsequent introduction of Cre recombinase generates the *tm1d* KO null allele. Figure image adapted from Skarnes *et al.*, 2011.

1.6 Ubiquitination in Hearing

1.6.1 Ubiquitination

Ubiquitination is a fundamental cellular process in which a substrate protein is modified through the covalent attachment of a small 76-amino acid protein onto the sidechain of a Lysine (K) residue. Modification of protein substrates with a Ub moiety is a three-step reaction process (Figure 1.13a). In the first reaction, the E1 Ub-Activating Protein (E1 protein) catalyses the activation of a Ub protein with ATP, to generate a high-energy, E1 protein-Ub intermediate complex (Haas *et al.*, 1982). The complex provides kinetic and steric advantages for the transfer of activated Ub from the E1 protein-Ub intermediate, onto the E2 Ub-Conjugating Protein (E2 protein), which is required for the second reaction of the ubiquitination process (Pickart *et al.*, 1994; Olsen & Lima, 2013). In the final stage of the ubiquitination process, E3 ligases interacts with Ub-conjugated, E2 proteins to catalyse the transfer of Ub onto protein substrates (Kamadurai *et al.*, 2009; Pruneda *et al.*, 2012).

Protein can be ubiquitinated in numerous ways. For example, the addition of a single Ub moiety (monoubiquitination) onto histone proteins induces conformational changes in chromatin structure, ultimately leading to changes in gene transcription (Minsky *et al.*, 2008; Zhu *et al.*, 2011). Once monoubiquitinated, additional Ub moieties can then be added onto the Ub that was initially bonded to substrates at one of seven K residues (K6, K11, K27. K29, K33, K48, K63) to form polyubiquitin (polyUb) chains (Figure 1.13b, c). Polyubiquitination of proteins is involved in several cellular processes. K63-linked polyUb chains are involved in initiating immune response, the DNA damage response and the turnover of mitochondria (Laplantine *et al.*, 2009; Liu *et al.*, 2018; Richard *et al.*,

2020). The most well-known effect of polyUb is its proteolytic properties, which marks proteins for degradation through non-K63-linked polyUb chains, with K48-linked polyUb chains being the most abundant degradative polyUb signal (Xu *et al.*, 2009).

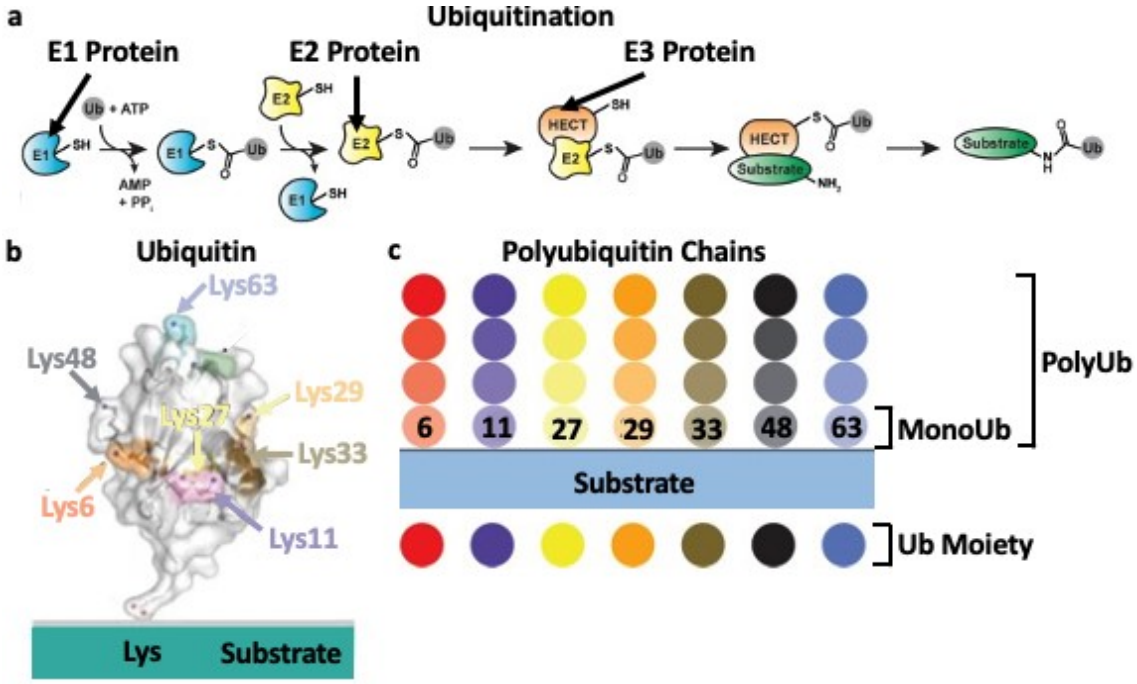

***Figure 1.13: The ubiquitination of substrates and the diversity of polyubiquitin chains*. (a)** The three reaction process of ubiquitination. In the first reaction, interactions between the E1 protein and Ub along with an ATP molecule generates a high energy, E1 protein-Ub intermediate. This activates Ub for further reactions in the ubiquitination process. In the second reaction, the activated Ub moiety is conjugated to the E2 protein. In the third reaction, the HECT-domain containing E3 ligase catalyses the addition of Ub onto a substrate protein. **(b)** The structure of the Ub protein, with the seven K residues highlighted (Protein Data Bank: 1UBQ). **(c)** The possible homotypic, polyUb chains that can be covalently attached to substrate proteins. Figure images adapted from Swatek & Komander, 2016 and Deol *et al.*, 2019.

1.6.2 NEDD4 E3 Ubiquitin Ligase Proteins

The NEDD4L protein is a member of the Neuronal Cell Expressed, Developmentally Downregulated 4 (NEDD4) family of E3 Ub ligase proteins, which all have the same protein domains (Ingham *et al.*, 2004). The N-terminus of NEDD4 proteins have a Ca^{2+}-dependent, Phospholipid-Binding (C2) domain, which has been found in many membrane-associated proteins such as Protein Kinase C (PKC) and Synaptotagmin proteins (Nalefski & Falke, 1996). NEDD4 proteins also contain a variable number of WW substrate binding domains which, canonically bind to Proline-Tyrosine (PY) motifs (Sudol

et al., 1995; Persaud *et al.*, 2009; Hatstat *et al.*, 2020). At the C-terminal of NEDD4 proteins is the catalytic HECT (Homologous to the E6-AP Carboxyl-Terminus) domain, an evolutionary conserved domain that is present in proteins found in found in yeast, mice and humans (Ingham *et al.*, 2004; Huibregtse *et al.*, 1995).

As its name suggests, NEDD4L shares some similarities with the NEDD4 protein. Most notably, a comparison between a NEDD4L isoform which does not contain the C2 domain, shares 78% of its amino acid sequence with NEDD4 protein (Harvey *et al.*, 2001). There is some capacity for NEDD4L and NEDD4 to interact with the same proteins *in vitro*, which includes the $Na_V1.2$ and 1.7, NEDD4-binding protein 1 and some E2 proteins (Fotia *et al.*, 2004; 2006). However, there is more evidence to suggest that the NEDD4L is a distinct protein rather than being a functionally redundant NEDD4 protein. Phylogenetically, orthologous NEDD4L proteins from different model organisms have a greater degree of similarity to each other than the orthologous NEDD4 protein from the same species (Harvey *et al.*, 2001). In addition, NEDD4L has very distinct functional requirements compared to NEDD4. Previously generated and described KO null *Nedd4l* mice show pulmonary and renal dysfunction which is characterised by the increased activity of ENaC channel (Boase *et al.*, 2011; Kimura *et al.*, 2011; Henshall *et al.*, 2017). On the other hand, NEDD4 is required for development, as mice that are homozygous for *Nedd4* KO null alleles experience embryonic lethality (Cao *et al.*, 2008; Liu *et al.*, 2009; Kawabe *et al.*, 2010).

1.6.3 E3 Ubiquitin Ligases in Cochlear Function

The role of ubiquitination in the mammalian cochlear function has not been studied extensively. Some published articles have described the functional requirement of

different E3 ligases and their degradative signals in cochlear function and development. For example, the HUWE1 E3 ligase is involved in regulating the ATOH1 transcription factor, with an additional row of IHCs when *Huwe1* is knocked out specifically in cochlear prosensory progenitors and developing SCs. However, no auditory dysfunction could be detected by ABR or DPOAE tests (Cheng *et al.*, 2016). Interactions between the MDM2 E3 ligase and the transcription factor p53 is also required for cochlear development, as evident by the dysmorphic cochlear morphology observed in E18.5-age, otic placode-specific *Mdm2* KO mice (Laos *et al.*, 2017). Loss of the NEDD4 E3 ligases, SMURF1 and SMURF2, affected the asymmetric cellular distribution of the planar cell polarity protein PRICKLE1, and consequently results in disorganised hair cell stereocilia bundles (Narimatsu *et al.*, 2009). The FBXO2 E3 ligase has been shown to be required for cochlear function, as *Fbxo2* KO null mice experience a progressive hearing loss phenotype from 2-months of age. Loss of auditory function and observed degeneration of IS cells, OoC and SGN fibres was attributed to the increased expression of the Connexin 26 protein and disrupted membrane junctions of supporting Claudius' cells (Nelson *et al.*, 2007).

1.7 Research Aims

The discovery that the E3 ligase, *Nedd4l* is a novel, candidate deafness-causing gene represents an interesting opportunity to further investigate the role of ubiquitination in cochlear function. NEDD4L protein is known for ubiquitinating membrane proteins for degradation, most notably ENaC (Goel *et al.*, 2015). As previously discussed, membrane proteins are required in various cochlear tissues, such as the MET channel complex in hair cell stereocilia bundles, voltage-gated ion channels in synaptic transmission of auditory stimuli at the base of hair cells and transporter proteins required for K^+ recycling pathways in the cochlear lateral wall (Cunningham & Müller, 2019; Safieddine *et al.*, 2012; Wangemann, 2006).

To verify and elucidate the functional requirement of *Nedd4l* in the mammalian process of hearing, I conducted auditory characterisation of IMPC-generated *Nedd4l* KO mouse models through a combination of auditory phenotyping techniques (ABR, DPOAE). In addition, I assessed the cochlear morphology via Scanning Electron Microscopy (SEM), Haematoxylin and Eosin (H&E)-stained and Immunohistochemistry (Chapter 3). To identify the underlying molecular mechanisms that results in auditory dysfunction in *Nedd4l* KO mice, a Mass Spectrometry (MS) approach was taken to identify potential NEDD4L substrates in cochlear tissues (Chapter 4).

Furthermore, in a recently published article, whole exome sequencing of patients who experience adult-onset hearing loss, identified potential causative single nucleotide variants (SNVs) in the *Nedd4* gene (Lewis *et al.*, 2018). Given the relation to the *Nedd4l* gene, I also assessed the potential requirement of *Nedd4* in mammalian auditory function using *Nedd4* KO mice that carry IMPC-generated alleles (Chapter 5).

Collectively, investigations into the functional requirement of both *Nedd4* and *Nedd4l* genes will expand our knowledge of what role ubiquitination plays in the mammalian auditory system.

2 MATERIALS AND METHODS

All reagents, solutions, antibodies and equipment used in the experiments described in this chapter are detailed in the APPENDIX.

All statistical analysis was conducted using GraphPad Prism 7.0 software and only when $n \geq 3$, for all genotypes compared. When comparing the averaged data from mice of three different genotypes, Ordinary one-way ANOVA with multiple comparisons tests were performed. Sidak's multiple comparison tests were performed if data from mice of a specific genotype was compared to others. Otherwise, Tukey's multiple comparisons tests were performed. Unpaired T-tests with Welch's corrections were performed when comparing data from mice of two different genotypes. Chi-square tests were performed to test if the ratio of mice of each genotype, was different to the expected Mendelian ratios. Non-linear regression analysis was conducted to analyse ABR wave data and is described in 2.1.4.

2.1 Mouse Lines and Phenotyping Tests

2.1.1 IMPC-generated KO Alleles

The IMPC *Nedd4* and *Nedd4l* mutant alleles were generated via a computer-assisted design (Skarnes *et al.*, 2011). In short, IMPC alleles were generated via the electroporation of a gene-specific targeting vector into C57BL/6N embryos. Critical exons were selected for mutagenesis, based on their presence in all gene transcript variants and in the event of their removal, disruption to at least 50% of the protein-coding sequence. The targeting vector included gene-specific 5' and 3' homology arms, numerous *FRT* and *loxP* recombination sites, *neomycin* resistance gene and the *lacZ* trapping element. Introduction of Cre or Flp recombinase generated the *lacZ*-tagged

tm1b or *floxed tm1c* alleles respectively. Introduction of Cre recombinase to the *floxed tm1c* allele produced the KO *tm1d* alleles.

2.1.2 Mouse Husbandry

All mice were housed in the Mary Lyon Centre and maintained under specific pathogen-free conditions in individually ventilated cages, with environmental conditions as outlined in the Home Office Code of Practice. Mice were kept in a light: dark cycle of 12: 12 (hours) with the room temperature kept between 20 - 24°C, and 55% humidity. Food and water were sterilised and filtered, *ad libitum*. Wood bedding, shredded paper and a cardboard tube were placed into cages for their enrichment. Mice were housed with littermates until they were weaned (P21), before being housed with mice of the same sex and similar age. Both male and female animals were used for all experiments.

2.1.3 ABR Tests

Mice were anaesthetised by an intraperitoneal injection with a mixture of ketamine (100 mg/mL at 10% v/v) and xylazine (20 mg/mL at 5% v/v) at a dosage of 0.1 ml/10g mouse body mass in sterile water. Mice were placed in a heat-box until sedated, which was confirmed by lack of pedal and lunge reflex. Mice were moved into a sound attenuating chamber (Small Device enclosure) and placed on a heated mat to maintain body temperature at 37°C. Recording electrodes (F-E2-12) were placed sub-dermally over the vertex (active), right mastoid (reference) and left femoral region (ground). Viscotears was administered to both eyes to prevent irritation from prolonged sedation. An overview of electrode positioning is depicted in Figure 1.10c.

Acoustic stimuli were delivered monoaurally to the right ear at a distance of 1.5cm via a ES1 free field transducer controlled by TDT SigGen/BioSig software using the Tucker

Davis Technology (TDT) system III RZ6 hardware (TDT, Alachua, FL, USA). The same systems also collected, amplified and averaged the ABR responses. Four different acoustic stimuli were presented to mice; either a 0.1ms broadband click of alternating polarity or tone-burst stimuli at 8, 16 and 32 kHz, which were presented at rate of 21/sec for 300 averages or 42.5/sec for 1000 averages respectively. The response to all stimuli was recorded for 10ms after the onset. Stimuli were presented at 90dB SPL (decibel sound pressure level) followed by decreasing steps of 5 or 10db SPL, until an ABR threshold could be visually determined by the absence of all characteristic ABR waves. Thresholds were also scored by a second person who was blind to genotype, for confirmation of the correct threshold determined.

Once ABR tests were completed, mice were removed from the sound attenuating chamber and administered a subcutaneous injection of atipamezole (Antisedan™) with a 1mg/kg body weight dosage, to accelerate recovery from sedation.

2.1.4 ABR Wave Analysis

Averaged ABR traces recorded in response to broadband click stimuli were extracted using the TDT SigGen/BioSig software. Extracted traces included those recorded at and above the auditory threshold (i.e. auditory threshold determined to be 30dB SPL, all traces recorded in response to a broadband click stimulus at 30dB SPL and louder were extracted).

A custom-made “auto-cursor” configuration file was used to extract data regarding the five characteristic ABR wave latencies and amplitudes. For each ABR wave, the file identifies and places cursors at the highest and lowest point along the trace within a specific time frame. On rare occasions, I manually altered where cursors were placed if

the file did not accurately place them at a wave peak or trough. Wave latency was determined by the time of a peak's highest point. The amplitude of individual waves was calculated by the difference between the wave's peak and trough voltage. Both latency and amplitude were averaged by genotype and plotted against suprathreshold (Re: dB), whereby 0 Re: dB refers to the auditory threshold. Inter-wave latency and amplitude ratios between ABR Wave IV and I was calculated by subtracting the Re: dB recorded latency, or dividing the Re: dB recorded amplitudes, respectively.

Latency, amplitude and calculated inter-wave data was analysed via non-linear regression analysis. Two analyses were conducted. One determined whether a first- or second order (null and alternative hypothesis, respectively) curve could adequately describe the data. The other determined whether a single, shared curve or individual curves (null and alternative hypothesis, respectively) could adequately describe the data from mice of different genotypes. If a single shared curve could describe the data recorded from mice of different genotypes, it was plotted on the graph.

2.1.5 DPOAE Tests

Mice were anaesthetized by intraperitoneal injection with a mixture of (100 mg/mL at 10% v/v), xylazine (20 mg/mL at 5% v/v) and acepromazine (2 mg/mL at 8% v/v) in sterile water and administered 0.1mL /10g mouse body weight. The acepromazine was added to provide surgical levels of anaesthesia. Once this was achieved, as demonstrated by the absence of a pedal reflex, a sufficient portion of the pinna was removed to allow unobstructed access to the external auditory meatus. Mice were then placed on a heated mat inside a sound attenuating chamber. The DPOAE probe assembly, consisted of an ER10B+ low-noise probe microphone to measure the DPOAE near the tympanic

membrane, and two separate MF1 speakers attached to the probe by small lengths of plastic tubing. A pipette tip was placed over the end of the probe assembly and it was inserted into the ear canal.

In-ear calibration was performed before each test. DPOAE tests were performed using frequency-specific tone-burst stimuli ranging from 6 to 32kHz in 2kHz increments, with the TDT RZ6 System 3 hardware and BioSig RZ software (TDT, Alachua, FL, USA). Stimuli consisted of 2 tones, f1 and f2, which were centred around the test frequency at a ratio of f2/f1 = 1.2 and of a constant level where f1 was 65 dB SPL and f2 was 55 dB SPL. The f1 and f2 tones were presented continuously, and a Fast-Fourier Transform was performed on the average response of 356 epochs (each ~21 ms). The level of the 2f1-f2 DPOAE response was recorded and the noise floor calculated by averaging the 10 frequency bins either side of the 2f1-f2 frequency.

2.1.6 Vestibular Swim Tests

Mice were individually placed in a bath of milliQ water that had been warmed and maintained at 25°C. The water bath was deep enough so that mice could not stand up in the bath and large enough that they had enough room to swim in all directions. Mice were placed into a bath for a sufficient amount of time so that their swimming behaviour could be assessed and scored, based on the criteria outlined in Table 2.1 (Hardisty-Hughes *et al.*, 2010). Mice were immediately removed if they displayed signs of distress. Tests were recorded so that they could scored by a second person, blind to genotype.

Score	Behaviour
0	Swims. Mouse body is elongated, and the tail propels in a flagella-like motion.
1	Irregular swimming. Includes: vertical swimming, swimming in a circle, swimming on side (left/right preference should be noted), swimming in an unbalanced manner (tail is raised and beats in an unstable manner).
2	Immobile floating. May follow or proceed brief disorientation.
3	Underwater tumbling. Mouse is unable to maintain a balanced body position and continuously tumbles.

Table 2.1: Scoring criteria for vestibular swim tests. The typical swimming behaviour associated with each score is shown, with higher scores indicating more compromised swimming ability.

2.2 Cochlear *Ex Vivo* Experiments

2.2.1 Cochlear Dissections

2.2.1.1 Schedule 1 Cull of Mice

All mice were culled via cervical dislocation in accordance with the age-appropriate, Home Office Personal Licence Schedule 1 cull methods. Regardless of the mouse's age, death was confirmed by the cessation of circulation.

2.2.1.2 Obtaining Cochlear Tissue from Postnatal-aged Mice

To extract postnatal-aged inner ear tissue, mice were culled as described in 2.2.1.1. Mice were then decapitated and then the skull was skinned. Head tissue was then bisected along the sagittal plane. The brain was removed, and the inner ear was located via the semi-circular canals. The inner ear was removed from the skull and if still covered by the bulla, this was removed. Under a microscope, the stapes was removed from the oval window, before perforating it and the round window. The appropriate fixative was perfused through the cochlear membranous labyrinth through the cochlear apex, ensuring that it flowed out of the windows. Cochlear tissue was then placed into a sufficient amount of fixative to cover cochleae.

2.2.1.3 Fine Dissection of Cochlear Tissue

To expose the OoC and the hair cells, cochlear tissue was fine dissected under a microscope. The otic capsule, SL, SV and TM was removed to expose the cochlear duct and hair cell bundles at all cochlear turns.

2.2.1.4 Obtaining Embryonic Tissue

To obtain embryos, pregnant mice were first culled as described in 2.2.1.1. Once death was confirmed, the pregnant mice were laid on their back and incisions were made to expose the abdominal cavity. The uterus containing all the embryos were removed and

placed into ice cold PBS. Embryos were removed from the uterus tissue and culled by decapitation, after the umbilical cord was severed. The embryonic head was then placed into an appropriate fixative. A limb was also taken from embryos for genotyping purposes.

2.2.2 Cryosectioning of Cochlear Tissue

To cryoprotect tissue, they were incubated in 30% sucrose solution overnight (O/N) at 4°C. Cryoprotected tissue was then removed from the sucrose solution, blotted on tissue paper to remove as much of the sucrose solution as possible and placed into moulds filled with Optical Cutting Temperature (OCT) solution. Cochlear tissue was left in OCT O/N at 4°C, or until cochleae had sunk to the bottom of the moulds, ensuring that OCT had penetrated throughout the cochlea.

To freeze samples, a bath of dry ice and acetone was prepared. To obtain a mid-modiolar section of postnatal-aged cochlear tissue, where all cochlear turns would be visible in a single section, cochlea were orientated perpendicular to the length of the moulds. Embryonic tissue was orientated so that sagittal cryosections would be obtained. Moulds were then placed in the dry ice-acetone bath until the OCT solution had completely frozen, as signified by the appearance of a small dome on the frozen OCT surface. 12µm thick sections were cut using a cryostat microtome, placed onto Superfrost Plus™ Adhesion slides and stored at -20°C.

2.2.3 Haematoxylin and Eosin (H&E) Staining and Nuclei Counts

2.2.3.1 Tissue Preparation: Fixation and Decalcification

Mice were culled as previously described in 2.2.1.1. Mice were then decapitated and skinned. Head tissue was then bisected along the sagittal plane and then placed into

pots containing 25mL of 10% neutral buffered formalin, ensuring that tissue was completely submerged. Tissue was left in fixative for at least 48 hours before subsequent steps. Head tissue was decalcified using 18% D.F.B decalcifying agent for 3 days, or until the skull was soft.

2.2.3.2 Tissue Preparation: Automated Dehydration, Clearance and Paraffin Impregnation Processing

To process samples for microtome sectioning, decalcified head tissue was placed into the Excelsior AS processor, which automates the dehydration, clearance and molten paraffin wax impregnation treatment processes. Automated processing of head tissue takes 22 hours in total to complete and performed under vacuum, at 350 mbar below atmospheric pressure. Dehydration and clearance steps were also performed at 30°C, and the molten paraffin wax impregnation steps was performed at 63°C.

Samples were first dehydrated in a series of increasing concentrations (volume/volume) of Industrial Denatured Alcohol (IDA). Samples were dehydrated in 70%, 90% and four rounds of 100% IDA. For each step, fresh IDA solution was used, with each dehydration step lasting for an hour and 45 minutes. Dehydrated samples then underwent three rounds of clearance with 100% xylene, to remove lipids and residual IDA from the dehydration process. The first two xylene steps last for an hour and 30 minutes each, whilst the last round of xylene treatment lasted for two hours. Cleared tissue was then placed into three molten wax impregnation steps, to ensure that paraffin wax had sufficiently penetrated through the head and into the cochlea. The first two impregnation step lasts for two and the last step lasting three hours.

2.2.3.3 Tissue Preparation: Paraffin Embedding and Microtome Sectioning

Following automated processor, wax-impregnated head tissue was then embedded into a paraffin wax block using an Histostar Embedding Centre set to 68°C. Molten paraffin wax was dispensed into the mould and the processed head tissue was placed into the wax. To obtain mid-modiolar cochlear sections, head tissue was orientated so that they would be sectioned along the sagittal plane. Labelled cassettes were placed atop of the wax-filled moulds, and both were moved onto a cold plate and left until the paraffin wax had completely set into blocks. Moulds were removed form embedded tissue and the excess wax was then trimmed using a Paratrimmer™.

Wax-embedded head tissue was mounted onto a Rotary Microtome, where 5µm sections were cut and then moved into a prewarmed water bath set to 45°C to remove creases in the sections. Pre-labelled slides were placed into the water bath, underneath the section as to not disrupt the section, and gently lifted out of the water bath so that the sections adhere to the slides. Slides were placed in a draining rack and placed into an oven prewarmed 37°C to dry O/N.

2.2.3.4 H&E Staining

H&E staining of paraffin sections was performed using an Automatic Stainer which dewaxes and stains sections with Haematoxylin and Eosin solutions. To dewax sections, slides were loaded into staining racks and underwent three washes in 100% xylene (the first, second and final wash lasted for 10, five and one minute, respectively), four washes in IDA (three washes in 100% alcohol followed by a single wash in 70% alcohol, with each wash lasting one minute) and then quickly washed in water.

Sections were stained with freshly filtered haematoxylin Gills III for five minutes. Sections were washed in water for one minute, before being briefly washed in 70% alcohol containing 1% hydrochloric acid to remove excess haematoxylin stain from the cytoplasmic regions of the cells. Sections were washed in water again for one minute, placed in a saturated lithium carbonate solution intensify the nuclear stain, before being washed in water again for another minute. Sections were then moved into filtered 1% AQ Eosin Y solution for three minutes to counter stain tissue. Sections were washed in water for 30 seconds and then washed four times, two minutes per wash, in 100% isopropanol alcohol to remove any residue water from stained sections.

Following H&E staining, sections were then mounted in Clearium solution and 24mm x 22mm coverslips were applied atop of sections.

2.2.3.5 Imaging and SGN Nuclei Counts

Images of H&E-stained cochlear sections were taken using the NanoZoomer RS scanner. Before being imaged, sections were observed under a brightfield microscope to ensure that all cochlear turns were visible. Once slides were chosen, they were loaded into the scanner in batches of six, to acquire an image of the H&E-stained head tissue. Using the Hamamatsu NanoZoomer Digital Pathology (NDP) scanning software (Hamamatsu), the area of acquisition was selected to encompass the entire head section, including brain and cochlea tissue. Scans of stained sections were viewed on the NDP.view 2 software, and 20x magnification images with 100µm scale bars, of the apical, mid and basal cochlear turns were taken.

To count the SGN nuclei in the images of H&E-stained sectioned cochlear tissue, the ImageJ “point tool” was utilized. A 50 x 50µm square in Rosenthal’s canal was drawn

and only SGN nuclei that were completely within the square were counted. The density of SGN nuclei was obtained by dividing the number of SGN nuclei counted by the area of the square (2500µm^2).

2.2.4 SEM

2.2.4.1 Tissue Preparation: Fixation, Decalcification and Dissection

Mice were culled and inner ear tissue was obtained as described in 2.2.1.1 and 2.2.1.2 respectively and fixed using 2.5% Glutaraldehyde in 0.1M Phosphate buffer (PB). Inner ear tissue was fixed O/N at 4°C. Tissue was washed three times with PB for 15 minutes per wash, at room temperature (RT). Samples were placed in 4.3% EDTA in PB solution at 4°C until soft. Cochleae were washed three times with PB for 15 minutes per wash before the sensory epithelium was exposed as detailed in 2.2.1.3. Fine dissected cochleae were returned back into PB.

2.2.4.2 Tissue Preparation: Osmium Processing and Dehydration

Fine dissected cochleae were placed into baskets and stacked onto a common stem for automated osmium processing and dehydration using the Leica Automated Tissue Processor. For osmium treatment, samples were treated twice with 1% Osmium Tetroxide solution in 0.1M sodium cacodylate solution, with a treatment in filtered 1% Thiocarbohydrazide solution (dissolved in ddH_2O) in between. After each treatment, samples were washed in fresh ddH_2O seven times before moving onto the next step. Samples were then dehydrated in an increasing ethanol series with the following concentrations: 25%, 40%, 60%, 85%, 95% and 100%; an additional 100% ethanol series was also included. Samples were incubated at 4°C for 45 mins in each solution, with exceptions to the 100% incubations which lasted 30 minutes each. The dehydration

series ends in storage in 100% acetone, at 4°C. An overview of the Osmium processing and dehydration steps are depicted in Figure 2.1.

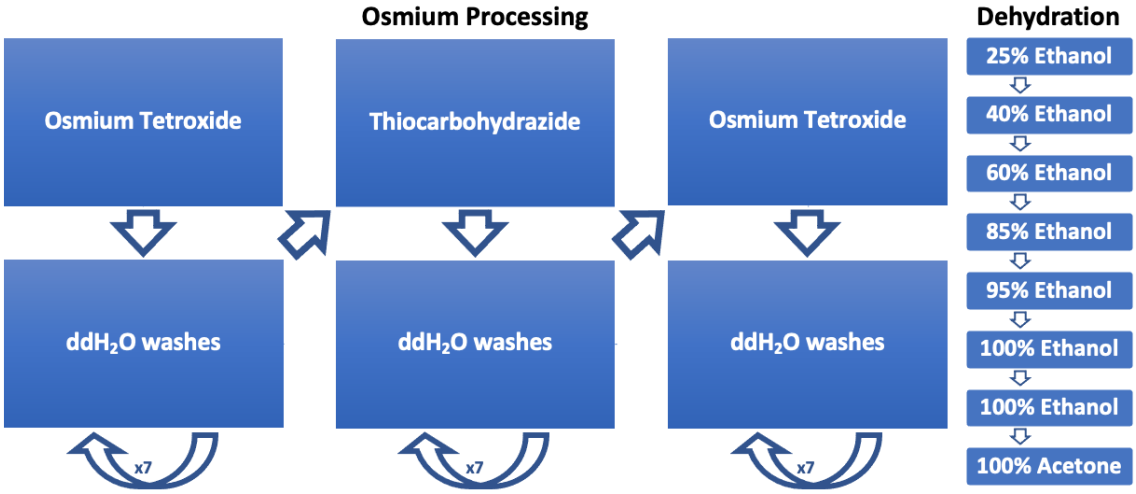

Figure 2.1: Overview of the osmium processing and dehydration to prepare samples for SEM.

2.2.4.3 Tissue Preparation: Critical Point Drying (CPD), Mounting and Sputter Coating

Dehydrated samples were loaded into the chamber of a CPD Machine and submerged in acetone. Liquid CO_2, which is miscible with acetone, was then supplied to the machine, and subsequently purged to remove acetone from the samples. This process was repeated to ensure the complete replacement of acetone with liquid CO_2. To dry samples, the machine's "CO_2 in", "exchange", "heat" and "gas out" settings were all set to medium. Following CPD, samples are mounted on a carbon disc which was stuck atop of a metal stub. Using a dab of silver paint, dried samples were removed from the baskets and mounted in an upright orientation on the stub so that hair cell bundles could be visualised by the electron microscope. Samples were then sputter coated in platinum using a Quorum Q150RS sputter coater twice to ensure that all cochlear surfaces would be electrically conductive to be visualised using the electron microscope.

2.2.4.4 Imaging

The Joel LSM-6010 SEM was configured to image coated, biological specimens. The Joel InTouchScope™ software was used to orientate loaded samples to obtain a suitable view of the sensory epithelium and hair cell bundles, change the SEM imaging parameters and to focus images. Micrographs of the sensory epithelium which contained both inner and outer hair cell bundles were taken at 2500x, with the spot size adjusted to 30.

2.2.5 Immunohistochemistry

2.2.5.1 Wholemount Staining

Mice were culled and inner ear tissue was obtained as described in 2.2.1.1 and 2.2.1.2 respectively, using filtered 4% Paraformaldehyde (PFA) in PBS to fix the cochlear tissue. Tissue was fixed for 1 hour on ice at RT, before being washed three times with PBS for 10 minutes per wash. The cochlear sensory epithelium was fine dissected as described in 2.2.1.3. In addition, the sensory epithelium was dissected away from the central modiolus bone and the vestibular system and placed into the well of a 96-well plate, which contained PBS.

Dissected tissue was washed three times with PBS with 0.1% Triton X-100 (PBS-T_{100}) for 10 minutes, and then submerged in blocking solution for 1 hour. Cochleae were incubated with primary antibody (diluted in blocking solution) O/N at 4°C. After primary antibody incubation, tissue was washed with PBS-T_{100} a further three times for 10 minutes per wash, before being incubated with fluorophore-conjugated secondary antibodies (diluted in blocking solution) for 1 hour. Tissue was washed three times with PBS-T_{100}, and then mounted on slides with Slowfade™ antifade mountant. Coverslips were placed atop of tissue and secured down with nail varnish.

Different staining conditions were required when staining against ribbon synapse at the IHC afferent nerve. Cochleae was washed using a PBS + 0.3% Triton X-100 solution and blocked with a 5% donkey serum solution instead. Both antibody incubations were performed at 37°C; 96-well plates were wrapped with multiple layers of parafilm to prevent evaporation of the antibody solutions.

2.2.5.2 Cryosection Staining

Mice were culled and inner ear tissue was obtained as described in 2.2.1.1 and 2.2.1.2 respectively and fixed using filtered 4% PFA in PBS, O/N at 4°C. Samples were washed three times with PBS for 15 minutes at RT, then decalcified in a 4% EDTA solution in PBS, at 4°C, until soft. Samples were then washed three times again with PBS and then cryosectioned as described in 2.2.2. Sections were removed from -20°C freezer and briefly left to thaw. Slides were placed in a coplin jar filled with 4% PFA for 10 minutes, and then washed three times with PBS-T_{100} for 10 minutes per wash. Slides were then placed into a humidity chamber and borders were drawn around cochlear sections using a Hydrophobic Barrier PAP pen. Sections were blocked with a blocking solution for 1 hour. Sections were incubated with primary antibody (diluted in fresh blocking solution) O/N, at 4°C.

Following the primary antibody incubation, slides were placed back into a coplin jar and washed three times with PBS-T_{100}, for 10 minutes per wash. Slides were placed in the humidity chamber again and sections were incubated with fluorophore-conjugated secondary antibodies diluted in blocking solution, for 1 hour at RT. Slides were washed three times with PBS-T_{100}, for 10 minutes. Cochlear sections were incubated with the DAPI (4', 6-diamidino-2-phenylinodole) nuclear stain (diluted in PBS-T_{100} at 1:30,000) in

the humidity chamber for 5 minutes, and then washed another three times in a coplin jar. Coverslips with Slowfade™ antifade mountant were applied over sections and secured with nail varnish.

2.2.5.3 Inverted Confocal Microscopy

Immunohistochemistry images were captured using a Zeiss LSM 710 fluorescence microscope (Zeiss) and the Zeiss Zen Black software to change the imaging parameters of the confocal microscope. Slides of stained tissue were loaded onto the microscope upside down, and the region of interest of the tissue was located using the eyepiece. To acquire an image, the fluorophore and DAPI channels were loaded and the "best signal" setting was selected to reduce cross-talk between channels. The pinhole size for each channel was adjusted so the optical section thickness was the same for all channels; for images taken at 20x and 63x magnification, section thickness was set to 1.9µm and 0.8µm respectively. The gain and digital offset were appropriately set, in order to maximise the intensity of fluorescence. All images displayed were captured with the frame size, average and pixel speed/dwell time set to 2048 x 2048, 8 and 0.79µs respectively. To capture z-stack images, the focus was adjusted to set the first and last image of the stack and the optical section of each image captured in a z-stack was set to 0.61µm and 0.23µm for z-stack images taken at 20x and 63x magnification, respectively. The "Regions" mode was selected so that only the region of interest is imaged when z-stacks were acquired. Post-acquisition, the ImageJ software installed with the "Bioformats" plugin was used to open and process Z-stack images to acquire maximum intensity projection of Z-stack images and add suitably sized scale bars.

2.2.6 X-Gal Stains

All tissue obtained for X-Gal staining was fixed in filtered 4% PFA in PBS, at 4°C. To obtain postnatal-aged cochlear tissue, mice were culled and inner ear obtained, as described in 2.2.1.1 and 2.2.1.2 respectively, and fixed for 1 hour at RT. Inner ear tissue was washed three time with PBS, for 15 minutes per wash. Embryonic head tissue was obtained as detailed in 2.2.1.4 and left in fixative for 24 hours at 4°C, to ensure sufficient fixation. Embryonic head tissue was then washed three times with PBS, for 1 hour per wash. Samples of all ages were then incubated in *lacZ* staining solution for 48 hours, at 37°C. Due to the photosensitivity of X-Gal in the staining solution, samples were wrapped in foil to keep samples in the dark.

Following incubation in lacZ staining solution, samples were washed three time with PBS and post-fixed with filtered 4% PFA in PBS for 1 hour at RT. Samples were washed three times again. Samples were then decalcified, processed and cryosectioned as described in 2.2.2. X-Gal-stained sections were imaged using the widefield Zeiss Axio Observer Z1 microscope. Z-stacks of brightfield and differential interference contrast images (DIC) images were processed using the extended focus function in the Zen Blue software (Zeiss). Subsequently brightfield and DIC images were combined in Adobe Photoshop.

2.3 Molecular Experiments

2.3.1 Quantitative PCR (qPCR) Genotyping

All mice were genotyped by multiple qPCR assays, performed by the MRC Harwell Institute Genotyping, Expression and Mutation Screens core facility. In addition to gene-specific primers, a Taqman™ oligonucleotide probe was also used which contains a FAM fluorescent label to measure the progression of qPCR amplification.

Genotyping of mice was performed using DNA extracted from either from ear-clip or limb tissue taken from embryonic or adult mice respectively. Samples were placed into individual wells of a 96-well plate, to which 50µL of Sample-to-SNP™ Lysis Solution was added to each sample, ensuring that they were submerged in solution. An adhesive film was placed atop the 96-well plate and then spun at 3000rpm for 1 minute. The plate was placed into a PCR block and incubated at 95°C (lid set to 110°C) and spun again for 1 minute at 3000rpm. 50µL of Sample-to-SNP™ DNA stabilising solution was added to samples and the plates placed onto a shaker for 1 minute to mix the solution. Following an additional spin at 3000rpm for 1 minute, 10µL crude DNA lysate was added to 90µL ddH_2O and mixed thoroughly to make a 1:10 dilution ready for use in qPCR reactions.

10µL qPCR reactions were set up using a TouchTools™ PCR Wizard automated processor, which loads 2.5µL of crude DNA lysate and 7.5µL of qPCR reaction mastermix into individual wells of a 384-well plate. The mastermix is composed of: 5µL ABI GTX TaqmanTM mastermix, 0.225µL of 20µM forward and reverse internal control *Dot1L* primers, 0.2µL of 5µM *Dot1L* probe, 0.3µL of the gene specific TaqmanTM expression assay which utilises the FAM dye (FAM, 5µM probe, 15µM forward and reverse primer) and 1.55µL of water. Primer-probes utilized for qPCR assays are detailed in Table 2.2.

.

Assay	Forward Primer Sequence	Reverse Primer Sequence	Probe Sequence
Dot1L Control	GCCCCAGCACGACCATT	TAGTTGGCATCCTTATGCTTCATC	CCAGCTCTCAAGTCG
Nedd4 BP	CACACACATGCACACACATACAAC	TGTACCGATCAAGCTGGACAT	CTAATAGCTGTATTTCACGTAAAACA
Nedd4 FRT-loxP	AGGCGCATAACGATACCACGATA	TGCTATACGAAGTTATCTCGACGA	TCCGAAGTTCCTATTCTCTAGA
Nedd4l CR	GTCAACCACAACAACAGGAGTA	CACAGCATCCCTGCCATCTG	CAGTGGCACCGACCCAGCTTG
Nedd4l lacZ	CTCGCCACTTCAACATCAAC	TTATCAGCCGGAAAACCTACC	TCGCCATTTGACCACTACCATCAATCC
Nedd4l BP	TGTTGCCTTGTGGCACTATG	GGGAGGCAAGGTGACTCAAG	TCTCCTAGGATTACTGAGGTGTGCGT
Nedd4l FRT-loxP	AGGCGCATAACGATACCACGATA	TGCTATACGAAGTTATCTCGACGA	TCCGAAGTTCCTATTCTCTAGA
Myo15 WT	TCCAAGCAGTGTCTCCAAGTC	GGGCCTTCTTCCCCTTCTTC	CCTGAACCTGTGACACCTGCCC
Myo15 Mut	TCCAAGCAGTGTCTCCAAGTC	CCTCTTCTTCTTGGGCACCATG	CCTGAACCTGTGACACCTGCCC
Sox10 Mut	GTGGGCGTTGGGCTCTTC	TGCGAACCTCATCACTCGTT	CCATGGTGCCCAAGAAGAAGAGGA

Table 2.2: Sequences of the Forward and Reverse Primers, and the probe for the different qPCR genotyping assays.

384-well plates were placed into the ABI 7900 PCR machine and run using the following qPCR programme: a 95°C hold stage for 20 seconds, before undergoing 40 cycles of 95°C for 1 second and 60°C for 20 seconds. Following completion of the qPCR programme, amplification plots were viewed using the QuantStudio™ 7 Real-Time PCR system software to check the exponential phase of the amplification plot, the CT values, successful amplification of the *Dot1L* control and determine the genotypes of samples. Numerous qPCR assays were run using different primers-probe combinations which amplify different regions of the allele, as shown in Figure 2.2. To genotype the the constitutive *Nedd4l* KO null allele (*Nedd4l*^{tm1b}), a "*CR*" and a "*lacZ*" assays were run; the *CR* assay was designed against the critical region of the *Nedd4l* gene (including the

targeted exons) and the *lacZ* assay against the *lacZ* gene. To genotype the *floxed Nedd4l* allele (*Nedd4l*^{tm1c}), the "*BP*" and "*FRT-loxP*" assays were used. The BP assay was designed against the most 3' *loxP* recombination site and the surrounding endogenous *Nedd4l* sequence. The *FRT-loxP* assay was designed against the sequence surrounding the *FRT* and l*oxP* recombination sites following generation of the *Nedd4l*^{tm1c} allele (Figure 2.2a). The IMPC-generated floxed *Nedd4* allele was also generated using similarly designed assays as shown in Figure 2.2b. Genotyping of the *Myo15*-driven *Cre* (*Myo15-Cre*) knock-in (KI) and *Sox10*-driven (*Sox10-Cre*) *Cre* transgenic mouse lines were also genotyped using primers-probe combination as shown in Figure 2.2c and Figure 2.2d respectively. For use of the "*Mut*" assay to genotype the *Myo15-Cre* allele, the presence of the *Cre recombinase* prevents successful amplification, whereas in the wild type *Myo15* allele the primers-probe combination is in close proximity for successful amplification.

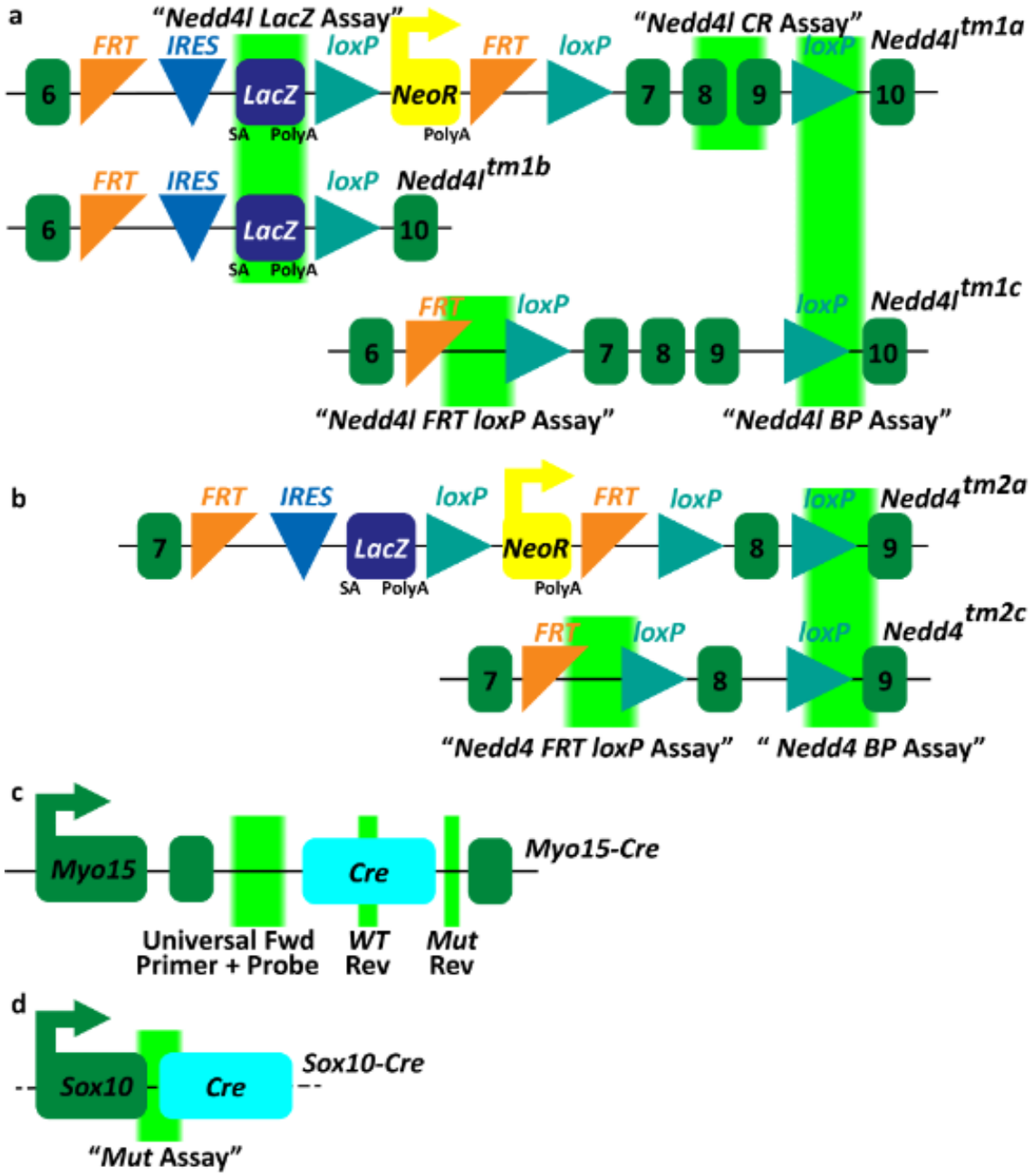

Figure 2.2: Overview of the different IMPC-generated and Cre driver mouse lines and the genomic location where the different qPCR genotyping assays are targeted against. **(a)** The *Nedd4l*^{tm1a}, *Nedd4l*^{tm1b} and *Nedd4l*^{tm1c} alleles and the different genotyping assays. The "*Nedd4l lacZ* Assay" and "*Nedd4l CR* Assay" are designed against the *lacZ* cassette and the critical region respectively. The "*Nedd4l FRT loxP* Assay" is designed against a recombinant sequence around the *FRT* and *loxP* recombination site after Flippase-mediated recombination has removed the *lacZ* cassette. The "*Nedd4l BP* Assay" are designed against the *loxP* recombination site and the surrounding endogenous genomic sequence from the *Nedd4l* gene. **(b)** The *Nedd4*^{tm2a} and *Nedd4*^{tm2c} allele and the "*Nedd4 FRT loxP* Assay" and "*Nedd4 BP* Assay", which is designed in a similar fashion to the "*Nedd4l FRT loxP* Assay" and "*Nedd4l BP* Assay". **(c)** An overview of the *Myo15-Cre* allele. Genotyping for the *Myo15-Cre* allele involves the "*WT*" and "*Mut*" assay which utilises a Universal Forward primer and probe for both assays. The reverse primers for the *WT* and *Mut* assay are designed against sequences in the *Cre recombinase* coding sequence and the endogenous *Myo15* genomic sequence located after the Cre recombinase, respectively. **(d)** An overview of the *Sox10-Cre* transgene and the "*Mut* Assay". Regions highlighted in green denote the genomic regions where primers-probes are designed against.

2.3.2 PCR Assays

2.3.2.1 RNA Isolation

Mice were culled and inner ear tissue was obtained as described in 2.2.1.1 and 2.2.1.2 respectively, but not fixed as previously outlined. The cochlea was removed from the vestibular system and placed into 500µL of RNAlater. To isolate RNA, cochlear tissue was blotted to remove as much RNAlater as possible and then placed into Precellys tube. To the tubes, a mixture of 350µL Buffer RLT supplemented with ß-mercaptoethanol (10µL per 1mL of RLT) and 5µL carrier RNA diluted in Buffer RLT (4ng/µL) was added. Tissue was homogenized using a Precellys Homogenizer set to 5000 rpm, cooled on ice and then homogenized again at 5000 rpm, with each step lasting 20 seconds.

Following homogenization, the Precellys tube containing homogenized cochlear tissue was centrifuged for 3 minutes at the maximum speed. The supernatant was transferred into a RT-equilibrated gDNA Eliminator Column and centrifuged for 30 seconds at 10,000x rpm. The columns were discarded, and an equal volume of 70% ethanol was added to the flowthrough in the collection tube, ensuring that the mixture was thoroughly mixed. The flowthrough-ethanol mixture was added into a RNeasy MiniElute Column and centrifuged for 15 seconds at 10,000x rpm. For all subsequent steps, the flowthrough was discarded. 700µL of Buffer RW1 was added to RNeasy columns and centrifuged for 15 seconds at 10,000x rpm. 500µL of Buffer RPE was added to RNeasy columns and centrifuged again for 15 seconds at 10,000x rpm. 500µL of 80% ethanol was added to the column and centrifuged for a further 2 minutes at 10,000x rpm. Following replacement of the collection tube, columns were centrifuged for 5 minutes at the maximum speed to dry out the membranes as much as possible.

To obtain RNA, dried columns were placed in fresh Eppendorf tubes and 14µL of RNAase-free water was added to the column membrane. Tubes and columns were centrifuged at the maximum speed for 1 minute to elute RNA. The RNA concentration was quantified using an Epoch microplate spectrophotometer that had set to quantify single strand RNA.

2.3.2.2 cDNA Synthesis

For each cDNA synthesis reaction, 200ng of RNA was used per 20µL cDNA synthesis reaction. RNA samples were diluted in RNase-free water if required, ensuring that the volume of diluted RNA did not exceed 8µL. For each synthesis reaction, 10µL and 2µL of Reverse Transcription Reaction and Enzyme mixture were added to diluted RNA samples. Reaction mixtures were made up to 20µL using RNase-free water. cDNA synthesis reaction mixtures were placed in a PCR thermocycler set to a specific cDNA synthesis programme. Reaction mixtures were heated at 25°C for 10 minutes, 50°C for 30 minutes, 85°C for 10 minutes.

2.3.2.3 PCR Amplification

20µL PCR were made in 96-well plates. For Reverse Transcription PCR (RT-PCR) against the *Nedd4l* isoforms, 10µL of Hotshot Diamond PCR mastermix, 1.25µL each of 10µM forward and reverse primers, 2.5µL of 2ng/µL cDNA and 5µL of ddH_2O were added. Amplicons generated from the long, C2 domain-containing or the shorter C2-less *Nedd4l* isoforms were amplified using the primer combination Long-Fwd (GCAGAAGGACAGAGGGT) and Long-Rev (TCGCTGGCTCCAAATATG), and Short-Fwd (GGATTCCTCTTCCATTCTTGC) and Short-Rev (GAGCCTGTGATTAGATGGATTTACC), respectively.

For PCR against the *Nedd4l*^{tm1c} allele, the same PCR reaction mix was used with some exceptions. DNA extracted from cultured mouse embryonic fibroblast cells (MEFs) were used as template instead (MEFs DNA extraction described in 2.4.4). To amplify specific regions of the *Nedd4l*^{tm1c} allele, the following primers were used: P1 (GGAGATAGTATCACCTCACC), P2 (CCACATCCTACTAGCTTAGAG), P3 (TCCTGCGACCTAGAAGGTGAGGC), P4 (GAGTCACTGTAACTAATGG) and P5 (GGCTTGAGTCACCTTGCCTCC) (Binding location detailed in Figure 4.5c).

Reaction mixtures were centrifuged briefly, before being placed into a PCR thermocycler and the run on the programme: 95°C for 3 minutes, 44 cycles of the following steps: 95°C for 30 seconds, 60°C for 30 seconds and 72°C for 30 seconds, before a final step at 72°C for 4 minutes. PCR products were run out on a 2% agarose gel and imaged using a ChemiDoc imaging system to visualise amplicon bands. Amplicon bands were cut from agarose gel for extraction of DNA using the Geneclean® II kit.

2.3.2.4 DNA Agarose Extraction and Amplicon Sequencing

Gel slices were weighed to determine their approximate volume and then placed into an Eppendorf tube, to which 3 volumes of NaI solution was added (i.e., if the gel slice has weighed 10mg, 30µL of NaI was added). The gel slice-NaI mixture was incubated at 55°C until the agarose had completely dissolved. Once dissolved, 5µL of GLASSMILK® reagent was added and briefly vortexed before a further incubation at RT for 5 minutes, with occasionally agitation of the mixture to prevent resuspension of the GLASSMILK® reagent. The mixture was centrifuged at 14,000 x g for 5 seconds and the resulting supernatant was discarded. The GLASSMILK® pellet was resuspend in 500µL of wash buffer and centrifuged again for 5 seconds, at 14,000 x g; this process was repeated once

more. An additional centrifugation at 14,000 x g for 5 seconds was performed to dry the pellet, before being resuspended in 10µL of TE buffer. The mixture was centrifuged at 14,000 x g for 30 seconds and the supernatant was placed into a clean Eppendorf tube. Extracted PCR products were then submitted for Sanger sequencing (Source Bioscience, Oxford). Sequences were analysed using SeqMan Pro (DNASTAR) software and the online BLAST tool (blast.ncbi.nlm.nih.gov).

2.3.3 Protein Experiments

2.3.3.1 Protein Isolation

Mice were culled and inner ear tissue was obtained as described in 2.2.1.1 and 2.2.1.2 respectively, with the additional step of removing the cochlea from the vestibular system and not placing tissue into fixative. To homogenise the cochlear tissue, they were placed into Precellys tubes that contained RIPA buffer that had been supplemented with protease inhibitors (PI). Tissue was homogenised at 5000 rpm for 20 seconds and left placed on ice until the froth settles. This process was repeated until cochleae were fully homogenised. Precellys tubes were centrifuged at 12000rpm for 10 minutes, at 4°C, and the supernatant containing the protein lysate was transferred to fresh Eppendorf tubes.

2.3.3.2 Protein Concentration Quantification

Protein lysate concentrations were quantified by the Biorad DC assay, which required the preparation of duplicate protein standards. Standards were prepared by a 1:2 serial dilution series using BSA protein in ddH_2O, starting from 10mg/mL and ending at 0.15mg/mL. A blank consisting of ddH_2O was also included at the end of the protein standards. 5µL of the duplicate protein standards and duplicates of the extracted protein lysates were loaded into individual wells of a 96-well plate. To each loaded well, 25µL of Reagent A' was added, followed by 200µL of Reagent B. The 96 well plate was

wrapped in foil and left in the dark for 15 minutes to allow the colourimetric assay to complete. Any bubbles in the loaded wells were popped before loading the 96 well plate into an Epoch BioTek spectrophotometer, which was set to 750nm to detect the blue colour change of the DC assay. Protein concentrations were accepted if the BSA protein standard fitted line r^2 value ≥ 0.97. Following quantification, protein lysates were stored at -80°C indefinitely.

2.3.3.3 Western Blots

LDS sample buffer and reducing agent were added to protein lysates and placed on a heatblock set to 70°C, 10 minutes. Reduced samples were briefly centrifuged and loaded along with a protein ladder, into precleared wells of a 4-12% Bis-Tris polyacrylamide gel, that had been placed in a western blot gel tank and filled with fresh MOPS buffer. Samples were electrophoresed at 200 volts, until the migration front had reached the base of the gel. Proteins on the 4-12% Bis-Tris gel were transferred to a nitrocellulose membrane using a transfer cassette that was loaded into to the gel tank. The cassette was submerged in transfer buffer (20x Transfer Buffer, 50mL methanol and 500µL antioxidant), and ran at 30 volts for 1 hour. Following transfer, the membrane was incubated with Ponceau to confirm a successful transfer of proteins onto the membrane. Once protein bands were observed, the Ponceau was removed and the membrane was washed with ddH_2O several times until the ddH_2O ran colourless.

Membranes were blocked in 5% (non-fat) milk solution at RT for 1 hour. The membrane was incubated O/N with primary antibodies (Appendix Table 4) diluted in 5% milk solution, at 4°C. The membrane was washed four times with TBS with 0.1% Tween20 (TBS-T_{20}) for 5 minutes per wash, and then incubated with Goat Anti-Rabbi IgG (H + L)

horseradish peroxidase -conjugated, secondary antibodies diluted in 5% milk solution for 2 hours, at RT. The membrane was washed another four washes with TBS-T_{20}.

To visualise protein bands, ECL Select blotting reagent was applied to membranes for 3 minutes and then wrapped in clingfilm, ensuring that no bubbles were trapped. The HRP chemiluminescent protein bands on the membrane were imaged using the ChemiDoc™ imaging system (Bio-Rad) that was set to capture an autoexposure image. A brightfield image of the membrane was also taken to capture the protein ladder, so that the molecular weight of bands could be determined. Protein band intensity was determined using ImageJ and normalised to the relative intensity of α-actin protein bands.

2.3.3.4 Immunoprecipitation

20µL of protein G Sepharose beads were transferred to an Eppendorf and washed with 500µL of lysis buffer that was originally used to extract the protein lysates that will be used for immunoprecipitation. Beads were centrifuged for 1 minute at 1000x g, and the supernatant was removed without disrupting the protein beads. Protein lysates were added to the beads and incubated for 2 hours at 4°C, with constant mixing. Beads were centrifuged for 1 minute at 1000x g and the supernatant, containing the precleared protein lysates, was transferred to a fresh Eppendorf and beads were discarded. Precleared lysates were incubated with FK2 antibody O/N at 4°C, with constant mixing.

Following antibody incubation, protein lysates were added to another 20µL of washed protein G beads and incubated together for 3 hours at 4°C, with constant mixing. The protein lysates-beads mixture was centrifuged for 1 minute at 1000x g, and the supernatant was removed without disrupting the protein beads. Beads were washed

three times, with 500µL of lysis buffer originally used to extract the protein lysates, centrifuged for 1 minute at 1000x g and the supernatant was removed.

Immunoprecipitated proteins was released from protein G beads by adding LDS sample buffer and reducing agent and placed on a heatblock set at 95°C for 5 minutes. If the mixture was viscous, ddH_2O was added. The supernatant containing immunoprecipitated proteins was removed, ensuring that the beads were not disturbed. Proteins were loaded into precleared wells of a 3-8% Tris-Acetate (TA) gel that had been placed in a western blot gel tank and filled with fresh TA buffer. Proteins were electrophoresed at 200 volts until the gel front had reached the base of the gel, and then incubated in Coomassie Stain for 15 minutes at RT. The gel was washed with ddH_2O and left O/N at 4°C. The ddH_2O was replaced and a brightfield image of the Coomassie-stained gel was taken using the ChemiDoc™ imaging system.

2.3.4 MS

2.3.4.1 Protein Band Excision and Trypsination

Following Coomassie stains of the 3 – 8% TA gel, the protein banding pattern was inspected, in search of protein bands that were unique to that lane and that were not present in control conditions. Unique bands were cut out of the Coomassie-stained 3 – 8% TA gel and placed into individual Eppendorf tubes. Excised gel was sent to the University of Birmingham, Advanced MS Facility Services for HPLC-MS/MS.

To prepare protein samples for HPLC-MS/MS, proteins were extracted from the excised gel bands, trypsin digested and then desalted. In order extract proteins from the gel, the excised band was cut into smaller pieces, to which 40µL of 100mM ammonium bicarbonate (pH 8) was added. Subsequently 50µL 10mM dithiothreitol was added to

10µL of extracted proteins, and incubated in a pre-warmed heatblock set to 56°C for 30 minutes. Samples were subsequently cooled to RT, to which 50µL 50mM iodoacetamide was added, mixed thoroughly and incubated at RT for 30 minutes. 50µL of trypsin gold (Promega, 6ng/µL) was added to samples and incubated at 37°C, O/N.

Proteins were desalted using Millipore C18 ZipTips. Tips were prepared for use by pre-wetting with 100% acetonitrile, and rinsed twice with 10µL 0.1% formic acid. Tips were used to pipette samples ten times, throughout the sample volume. Tips were washed thrice with 0.1% formic acid to remove excess salt, before peptides were eluted in 10µL of 50% acetonitrile/0.1% formic acid solution. Eluted peptides were dried to remove the acetonitrile, and resuspended in 0.1% formic acid solution.

2.3.4.2 High Performance Liquid Chromatography and Tandem MS

UltiMate® 3000 HPLC series was used for peptide concentration and separation. Samples were trapped on an Acclaim™ PepMap™ 100 C18 precolumn (5µm particle size, 100Å pore size, 300µm diameter x 5mm length) and separated in Nano Series™ Standard Columns (75µm diameter x 15cm length), packed with a PepMap™ 100 C18 column (3µm particle size, 100Å pore size). The gradient used was from 3.2% to 44% solvent B (0.1% formic acid in acetonitrile) for 30 minutes. The column was then washed with 90% mobile phase solvent B before re-equilibrating at 3.2% mobile phase solvent B.

Separated peptides were directly eluted (~350nL/min) via a Triversa Nanomate nanospray source into a Q Exactive™ (QE) HF Orbitrap mass spectrometer. The QE HF spray voltage was set to 1.7kV through Triversa NanoMate and heated capillary at 275°C. The mass spectrometer performed a full Fourier Transform-MS scan (m/z 360−1600) and a subsequent Higher-Energy Collisional Dissociation (HCD) Tandem MS

(MS/MS) scans of the 20 most abundant ions with dynamic exclusion set to 15 seconds. Full scan mass spectra were recorded at a resolution of 120,000 at 200 m/z and Automatic Gain Control (AGC) target of 3×106. Precursor ions were fragmented in HCD MS/MS with resolution set up at 15,000, a normalized collision energy of 28 and AGC target of 1x105. The width of the precursor isolation window was 1.2 m/z and only multiple charged precursor ions were selected for MS/MS. Spectra were acquired for 56 minutes.

The MS and MS/MS scans were searched against the Uniprot database using the Protein Discovery 2.2 software, Sequest HT algorithm (ThermoFisher). Variable modifications were deamidation (on Asparagine and Glutamine residues), oxidation (on Methionine residue) and phosphorylation (on Serine, Threonine and Tyrosine residues). The precursor mass tolerance was 10ppm and the MS/MS mass tolerance was 0.02Da. Two missed cleavages were allowed, and data was filtered with a false discovery rate of 0.01. Only proteins with at least two high confidence peptides were considered.

2.3.4.3 gEAR Database Scraping

To efficiently look at the expression of several candidate *in vivo* NEDD4L substrates in the gEAR database, a python code (Python™ 3.8.2) was written to navigate the gEAR database (umgear.org) and save images of the appropriate tSNE plots. When run, the code would open the gEAR database website, search for the gene that encodes for a candidate NEDD4L protein substrate in the scRNA-seq dataset posted by the Kelley lab, acquire images of the tSNE plots and save them to the appropriate folder (Kolla *et al.*, 2020). The code used is described in the APPENDIX.

2.4 MEFs Culture

All MEFs culture experiments were performed in a sterilised, laminar flow hood. All the reagents and equipment used were sprayed with 100% ethanol before being placed into the hood. All solutions were incubated in a pre-warmed 37°C water bath until warmed before use. Gloves were also sprayed with 100% ethanol before conducting experiments in the hood.

2.4.1 Common Techniques

2.4.1.1 Trypsin Incubation

MEFs were washed with dPBS and incubated in 0.05% trypsin/EDTA for 2 minutes or until cells had detached from the bottom of the flask or well (assessed visual inspection under a brightfield microscope), and culture media was added to prevent degradation of MEFs. Suspensions of MEFs were gently pipetted to ensure dissociation of cells, before being transferred into a falcon tube. MEFs were centrifuged at 1200rpm, for 3 minutes at RT, and the media was removed without disruption of the cell pellet.

2.4.1.2 Passaging

Cells were passaged once cultures were deemed to be 80 – 90% confluent via inspection under the microscope. MEFs were incubated with trypsin as described in 2.4.1.1 and the pellet was resuspended in 1mL culture media for each flask of MEFs that had been treated with 0.05% trypsin/EDTA. If MEFs were passaged from an individual well of a 6-well plate, the whole suspension was added to a single T75 flask containing 12mL of culture media. If MEFs were passaged from a T75 flask, the volume of MEFs suspension used to seed a T75 flask was dependent on subsequent experiments; for the expansion of MEFs population into more T75 flasks, an equal amount of the cell suspension was used to seed flasks (i.e., to expand 1 T75 to 5 T75 flasks, 0.2mL was added to each new

flask containing media culture). The following day, the culture media was replaced with fresh media.

2.4.1.3 Counting MEFs

The number of MEFs in a given suspension was calculated using the concentration of cells, as determined by the Invitrogen Countess II, and the total volume of said suspension. 100µL each of the MEFs suspension and Trypan Blue stain were combined and mixed by gentle pipetting. 10µL of the cell suspension-stain mixture was loaded into both "A" and "B" chambers of the Countess™ Cell Counting Chamber Slide. Both chambers were loaded into the Countess II machine, to obtain an average concentration (cells/mL) of the alive, dead and the combined total of cells.

2.4.1.4 Freezing MEFs

MEFs were incubated with 0.05% trypsin as described in 2.4.1.1. The cell pellet was resuspended in 1mL of culture media for each flask of MEFs that had been treated with 0.05% trypsin/EDTA. 0.5mL of the cell suspension and freezing media was added to a cryovial and then placed into an isopropanol-containing Mr Frosty™ freezing container. The container is placed in the -80°C freezer for 24 hours, before cryovials were placed into long term storage in a liquid nitrogen container.

2.4.1.5 Thawing MEFs

Frozen MEFs were removed from storage and thawed in a pre-warmed 37°C water bath, until a few ice crystals remained. Cells were transferred into a 15mL falcon tube and 10mL of culture media was added, pipetting gently to avoid damaging the cells. MEFs were centrifuged at 1200rpm, for 3 minutes at RT, and the media was removed without disrupting the cell pellet. The pellet was homogenised in 1mL culture media and then

added to a T75 flask that contained 10mL of culture media, before being placed in the incubator. The following day, the culture media was replaced with fresh media.

2.4.2 Generation of MEFs

MEFs were generated from E14.5-aged embryos. Pregnant mice were culled and the embryos were obtained as described in 2.2.1.1 and 2.2.1.4, respectively. Instead of placing the head into the appropriate fixative solution, it along with the visceral organs and limbs were discarded. The remaining embryonic tissue was washed again in ice-cold dPBS, before being placed into a 15mL falcon tube containing ice-cold dPBS, on ice.

Embryonic tissue was placed in sufficient amount of 0.25% Trypsin/EDTA solution to submerge the tissue, and manually dissociated using spring-loaded surgical scissors and scalpel blade. To ensure sufficient homogenisation, embryonic tissue was also pipetted. Homogenised tissue was incubated in a 37°C water bath for 15 minutes, with regular inversions. Digested tissue was centrifuged at 1200rpm, for 5 minutes at RT, and the media was decanted without disrupting the cell pellet.

The pellet was homogenised with 1mL of culture media for each embryo used, and 1mL aliquots were added to individual wells of a 6-well plate that contained 2.5mL culture media. Cells were dispersed equally across the well by moving 6-well plates in a back-and-forth motion vertically and horizontally, before being placed into the incubator. The following day, MEFs were washed using dPBS and fresh culture media was added. MEFs were grown to 80 – 90% confluency and then passaged into T75 flasks, as described in 2.4.1.2.

Multiple populations of MEFs were generated. MEFs that were wild type (*Nedd4l*$^{+/+}$), heterozygous (*Nedd4l*$^{tm1b/+}$) or homozygous (*Nedd4l*$^{tm1b/tm1b}$) for the *Nedd4l*^{tm1b} were

generated using embryos generated from a timed intercross breeds between *Nedd4l*$^{tm1b/+}$ mice. During embryonic dissection, a limb was taken for genotyping purposes. MEFs were also generated from embryos homozygous for the *floxed* *Nedd4l*^{tm1c} allele (*Nedd4l*$^{tm1c/tm1c}$), through timed intercross breeds between *Nedd4l*$^{tm1c/tm1c}$ mice. No tissue was taken for genotyping, as all embryos have the same *Nedd4l*$^{tm1c/tm1c}$ genotype.

2.4.3 MEFs Treatment

MEFs were treated with different reagents. For *in vitro* recombination experiments using *Nedd4l*$^{tm1c/tm1c}$ MEFs, a recombinant Cre protein and/or lysosomotrophic Chloroquine (CQ) treatment was performed. Homozygous *Nedd4l*$^{tm1b/tm1b}$ MEFs were treated with the proteasomal inhibitor, MG132.

2.4.3.1 Cre Treatment

The recombinant Cre recombinase protein includes the cell-penetrating peptide sequence and nuclear localisation signal, to ensure its uptake into *Nedd4l*$^{tm1c/tm1c}$ MEFs by macropinocytosis and migrates towards the nucleus (Fawell *et al.*, 1994a). The supplied amount of recombinant Cre protein varied by batch, so the molar concentration was calculated before MEFs were treated. Prior to Cre treatment, *Nedd4l*$^{tm1c/tm1c}$ MEFs were passaged and seeded into 6-well plates, at a density of $3x10^5$ cells/ well, and allowed to adhere to the well base O/N. The following day, MEFs were washed with dPBS to remove as much residual FBS from MEFs, which has previously been shown to decrease the efficiency of *in vitro* recombination (Lin *et al.*, 2004; Wadia *et al.*, 2004).

As the concentration (mg/mL) of Cre supplied varied by lot, the volumes required to treat MEFs with Cre differed between different treatments. Cre was diluted to the required working concentration in culture media without FBS and was added to wells. Following treatment, the Cre-containing media was removed, cells were washed with dPBS and culture media which contained FBS was added to treated cells. Treated cells were expanded for protein extraction.

2.4.3.2 Cre-CQ Cotreatment

CQ has previously been utilized to aid delivery of Cre protein into cells (Seglen *et al.*, 1979; Fawell *et al.*, 1994a; Wadia *et al.*, 2004). 200mM stock CQ solution was made up using sterile H_2O and stored at -20°C. MEFs were treated with Cre as described in 2.4.3.1, but with the addition of chloroquine into the media. During treatment, 200mM CQ was further diluted to a working 50µM concentration. Due to the known toxicity of chloroquine treatment, Cre treatment duration was reduced to 4 hours (Seglen *et al.*, 1979; Wadia *et al.*, 2004).

2.4.3.3 MG132 Treatment

MG132 was dissolved in sterile, cell culture grade DMSO to make a 10mM stock solution, which was diluted further to a working concentration of 10µM in culture media. *Nedd4l*$^{tm1b/tm1b}$ MEFs were incubated with MG132-containing culture media for 8 hours and then washed with dPBS.

2.4.4 DNA Extraction

MEFs were incubated in trypsin as described in 2.4.1.1. Cell pellets could either be frozen at -20°C and DNA could be extracted later or homogenised in 200µL PBS and transferred to 1.5mL Eppendorf tubes. 20µL proteinase K was added to samples before adding 200µL of AL buffer. Tubes were shaken vigorously for 15 seconds before being briefly

centrifuged. Tubes were incubated in a pre-warmed heating block set to 56°C, for 10 minutes, with occasional mixing to ensure proper dispersion of the lysed cells. 200µL of 100% ethanol was added to each sample, before being shaken again for 15 seconds and briefly centrifuged. The supernatant in each tube was transferred into separate DNeasy Mini Spin column, which were placed atop of a 2ml collection tube, and centrifuged for 1 minute at 6,000 x g; the flow-through in the collection tube was discarded. 500µL AW2 buffer was added to the columns and centrifuged for a further 3 minutes at 20,000 x g; the collection tube and flow-through were discarded.

To elute DNA, columns were placed atop individual 1.5mL Eppendorf tubes and 200µL of AE buffer was added to the centre of each column membrane. Columns were incubated for 1 minute at RT, and then centrifuged for 4 minutes, at 6000rpm. DNA concentration was determined as using a BioTek™ Epoch spectrophotometer.

2.4.5 Protein Extraction

2.4.5.1 Whole Cell Protein Lysates

MEFs were incubated with trypsin as described in 2.4.1.1; pellets can be stored at -80°C indefinitely. Pellets were homogenised in 1mL of ice-cold, M-PER lysis buffer which had been supplemented with PI. Cells were placed on ice for 30 minutes and inverted every 10 minutes, before being centrifuged at 13000 rpm for 30 minutes. The resulting supernatant containing the protein lysates was then transferred to pre-chilled Eppendorf tubes. Protein concentration was determined as described in 2.3.3.2.

2.4.5.2 Membrane and Cytosolic Fractions

Culture media was removed and 1.5mL of PI-supplemented dPBS was added to MEFs, before using a sterile cell scraper to manually dissociate cells from the base of flasks. The MEF cell-dPBS suspension was transferred into falcon tubes and centrifuged at

1200rpm for 3 minutes, at RT. The supernatant was removed without disrupting the cell pellet underneath. The pellet was washed with 3mL dPBS and centrifuged again at 1200rpm for 3 minutes at RT twice, with the supernatant removed in between washes. To extract the cytosolic fraction from MEFs, 750µL of PI-supplemented Permeabilization buffer of the MEM-PER Extraction kit was added to homogenise the cell pellet and then briefly vortexed. Samples were incubated for 10 minutes at 4°C, whilst being constantly mixed, before being centrifuged for 15 minutes at 16000 x g at RT. The resulting supernatant (cytosolic fraction) was removed, making sure not to disrupt the pellet, and placed into pre-chilled Eppendorf tubes and stored at -80°C. To extract the membrane fraction, 250µL of PI-supplemented Solubilization buffer of the MEM-PER Extraction kit was added to homogenise the pellet. If not fully homogenised, additional PI-supplemented Solubilization buffer was added in 100µL increments to the pellet, until the pellet was completely homogenised. Samples were incubated for 30 minutes temperature at 4°C whilst being constantly mixed, before being centrifuged for 15 minutes at 16000 x g at 4°C. The resulting supernatant (membrane fraction) was removed, making sure not to disrupt the pellet, and placed into pre-chilled Eppendorf tubes and stored at -80°C.

3 AUDITORY CHARACTERISATION OF *NEDD4L*

3.1 Introduction

NEDD4L which is also known as NEDD4-2, is an E3 ligase that is highly conserved across vertebrate model organisms and its main function is to target membrane-associated proteins for degradation. As a member of the NEDD4 family of E3 ubiquitin ligase protein ligases, it contains the characteristic N-terminally located C2 phospholipid binding domain, 4 WW binding domains and the catalytic HECT domain at its C-terminus. In addition, a "short" NEDD4L protein isoform is also translated which lacks the C2 domain (Figure 3.1) (Dunn *et al.*, 2002). Whilst NEDD4L has been extensively researched, its potential role in the mammalian process of hearing was only recently suggested; *Nedd4l* was one of 52 identified genes as a potential, novel deafness-causing gene by the IMPC programme (Bowl *et al.*, 2017). As part of the broad-based phenotyping pipeline, ABR tests performed at 14-weeks of age identified that both male and female that were homozygous for the *Nedd4l*^{tm1b} KO null allele (*Nedd4l*$^{tm1b/tm1b}$) display profoundly elevated hearing thresholds compared to *Nedd4l*$^{+/+}$ (strain- sex- and age-matched) control mice (Figure 3.2a, Figure 3.3) (Brown & Moore, 2012) Furthermore, IMPC phenotyping also reported that *Nedd4l*$^{tm1b/tm1b}$ mice are significantly under-represented at weaning age (P21) compared to the expected Mendelian ratio of 1:2:1 (*Nedd4l*$^{+/+}$: *Nedd4l*$^{tm1b/+}$: *Nedd4l*$^{tm1b/tm1b}$ mice respectively) (Figure 3.2b, Figure 3.3; https://www.mousephenotype.org/data/genes/MGI:1933754).



Figure 3.1: Diagrammatic representation of the domain structure of the short and long isoforms of NEDD4L protein. Domains present in the short and long protein isoforms of NEDD4L. The short NEDD4L protein isoform contains four WW substrate binding domains and the catalytic HECT domain found at the C-terminus. In the long NEDD4L isoform contains all domains in the short isoform and an N-terminally located C2 phospholipid binding domain.

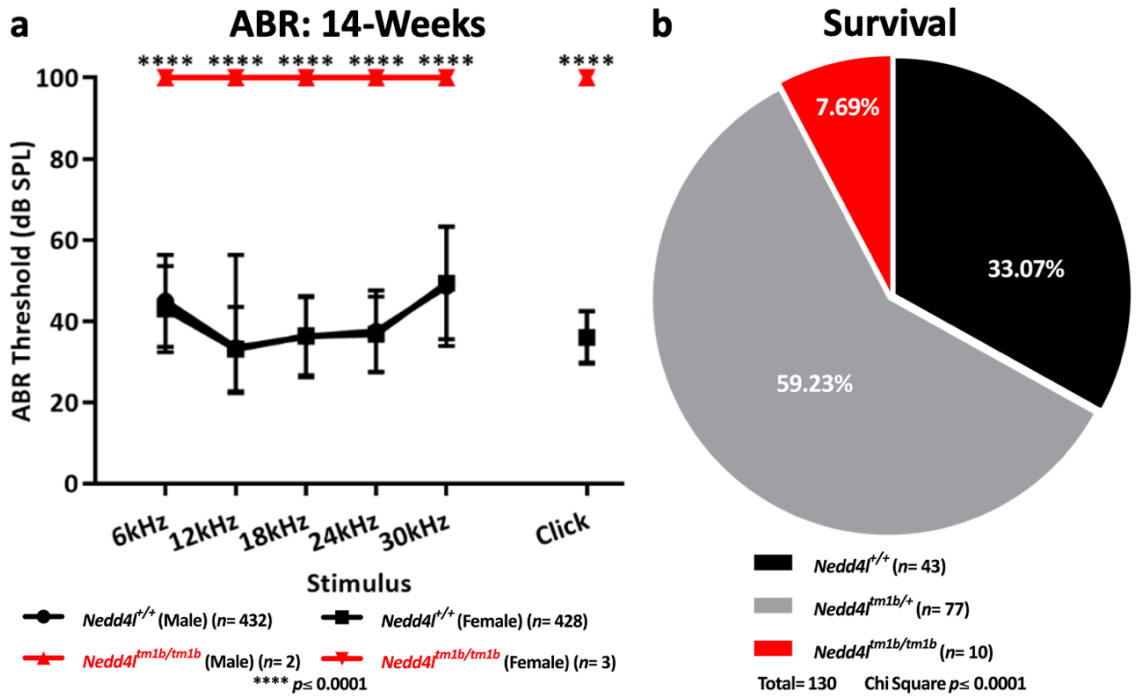

Figure 3.2: Summary of relevant results of IMPC phenotyping of Nedd4l$^{tm1b/tm1b}$ mice. **(a)** Auditory brainstem response tests performed at 14-weeks of age revealed that both male (red, upright triangles) and female (red, upside down triangles) *Nedd4l*$^{tm1b/tm1b}$ mice have profoundly elevated hearing thresholds. Data presented as averages ± standard deviation and analysed using Unpaired t tests with Welch's Correction. Statistical significance denoted by **** ($p \leq 0.0001$). **(b)** The number of mice of each possible genotype born through intercrosses between *Nedd4l*$^{tm1b/+}$ mice to generate the phenotyping cohort. Significantly fewer number of *Nedd4l*$^{tm1b/tm1b}$ mice reached P21, suggesting that there are postnatal, sub-viability concerns with *Nedd4l*$^{tm1b/tm1b}$ mice. Chi-Square tests were performed to compare the number of *Nedd4l*$^{tm1b/tm1b}$ born to the expected 25% Mendelian ratio.

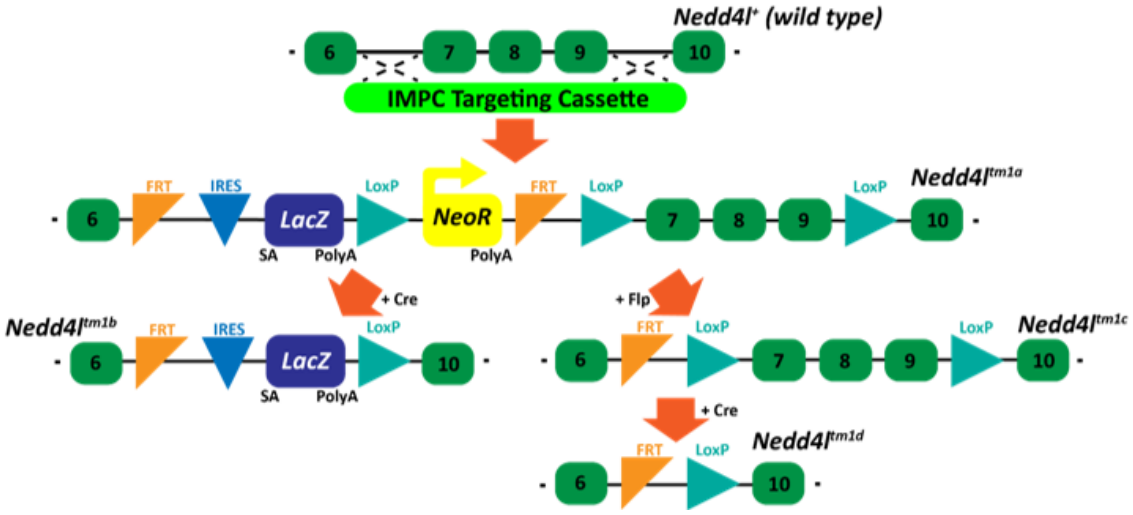

Figure 3.3: Diagrammatic representation of the Nedd4l KO alleles generated by the IMPC. The "KO-first" *Nedd4l*^{tm1a} is generated through a gene trap of the *Nedd4l* gene in ESCs, which introduces the *lacZ* reporter gene-trap cassette after exon 6, multiple *loxP* and *FRT* recombination sequences surrounding critical exons 7 – 9. The *Nedd4l*^{tm1b} "KO null" allele is generated by crossing *Nedd4l*^{tm1a}-carrying mice to a mouse line that ubiquitously expresses Cre recombinase, resulting in a *Nedd4l* allele that lacks exons 7 – 9, and a *lacZ*-tagged *Nedd4l* gene. Crossing *Nedd4l*^{tm1a}-carrying mice to a ubiquitous-expressing *Flp* recombinase mouse line generates the *Nedd4l*^{tm1c} allele, where exons 7 – 9 are flanked by *loxP* sequences but removes the *lacZ* reporter gene-trap cassette, thus restoring endogenous *Nedd4l* gene function. Subsequently, mice carrying the *Nedd4l*^{tm1c} allele can be crossed to a tissue-specific, *Cre*-expressing mouse line, generating the KO *Nedd4l*^{tm1d} allele in all *Cre*-expressing cells.

Numerous reports have investigated the potential association between the incidence of SNVs found on the human *NEDD4L* gene in patients and different populations, with different diseases. NEDD4L protein in rat cochlear tissue is reportedly detected in the OoC, SGN, Spiral Limbus (SLim), SL and SV, but the specific requirement of *NEDD4L* for mammalian process of hearing has not been explored (Zhong *et al.*, 2014). Broix *et al.* reported that two specific patients with Periventricular Heterotopia (PVH), which is characterised by the presence of bilateral, ectopic grey matter, which surrounds the lateral ventricles of the brain, carry a missense SNV in the *NEDD4L* HECT domain also experienced a "hearing impairment". The severity of the impaired hearing was not explored further (Broix *et al.*, 2016). Reports of other PVH patients have identified numerous SNVs which are found across the coding region of the human *NEDD4L* gene, but they did not report of any SNV-carrying individuals that also experienced a loss of hearing (Kato *et al.*, 2017; Elbracht *et al.*, 2018; Stouffs *et al.*, 2020). Earlier articles

regarding SNVs found within the coding region of *NEDD4L* also do not describe any individuals with auditory impairment, and instead describe a genetic association with dysregulations of blood pressure (Russo *et al.*, 2005; Fava *et al.*, 2006; Luo *et al.*, 2009).

Literature regarding previously generated KO mouse lines that carry mutant alleles of the *Nedd4l* gene have also not reported any involvement in the mammalian process of hearing. Several constitutive hypomorphic *Nedd4l* KO mouse lines, in which the longer C2 domain containing NEDD4L protein isoform is absent, are reported to display renal and neuronal phenotypes. These mice experience increased blood pressure, sensitivity to a high salt diet, water consumption, urine output and susceptibility to inducible seizures (Shi *et al.*, 2008; Minegishi *et al.*, 2016; Jewett *et al.*, 2016; Zhu *et al.*, 2017). Constitutive *Nedd4l* KO null mouse models that express neither NEDD4L protein isoform also have not been reported to have an auditory phenotype, with publications instead focussing on the lethal consequences of the allele (Boase *et al.*, 2011). Mice homozygous for the *Nedd4l* (*Nedd4l*^{tm1Shkr}) KO null allele developed normally and were present in the expected Mendelian ratio at embryonic ages, but died at early postnatal ages due to pulmonary dysfunction. Histological examination of the population of mice that survived up to weaning ages found extensive fibrosis in alveolar spaces, that were also infiltrated by inflammatory cells such as macrophages and neutrophils (Boase *et al.*, 2011).

As *Nedd4l* is a recently identified, candidate deafness-causing gene and that prior literature has not explored its functional requirement in the auditory system, I aim to use the *Nedd4l*$^{tm1b/tm1b}$ KO null mouse model to characterise its role within the mammalian process of hearing. To this end, I performed molecular experiments (RT-PCR, Western blots) to confirm that the *Nedd4l*^{tm1b} allele is a KO null mutation and that

Nedd4l$^{tm1b/tm1b}$ mice do not express any NEDD4L protein. I conducted inner ear phenotyping techniques (ABR, DPOAE and Vestibular Swim Tests) to further investigate the auditory phenotype and pathological studies (SEM, H&E staining, Immunohistochemistry against cochlear tissues) to assess the morphological effects of cochlear tissue in *Nedd4l*$^{tm1b/tm1b}$ mice. *Sox10*- and *Myo15*-driven, *Nedd4l* conditional KO (cKO) mice were also generated to investigate the requirement of *Nedd4l* in specific cochlear tissues.

3.2 Results

3.2.1 NEDD4L Expression in Cochlear Tissue

3.2.1.1 NEDD4L Transcript and Protein Expression

Characterization of mouse NEDD4L expression in cochlear tissue was performed for two reasons. Firstly, *Nedd4l* is a novel candidate, deafness causing-gene and little is known regarding its expression in cochlear tissue. Furthermore, confirmation was required to determine that the "computer-assisted" design of the *Nedd4l*^{tm1b} allele is a KO null mutation of the *Nedd4l* gene. To ascertain expression in cochlear tissue, RT-PCRs were conducted using isoform-specific primers against the longer and shorter isoform (Figure 3.4a, b; RNA Transcript; *Nedd4l-215* and *Nedd4l-201* respectively). As the *Nedd4l-215* and *Nedd4l-201* isoforms differ at the first two exons, isoform-specific primers were designed against these regions (Figure 3.4b; DNA; RNA Transcript). RT-PCR experiments showed that transcripts for both *Nedd4l* isoform were expressed in cochlear tissue, as both were readily amplified from cochlear-derived cDNA from *Nedd4l*$^{+/+}$ mice (Figure 3.4b). These transcripts were also amplified in *Nedd4l*$^{tm1b/tm1b}$-derived cDNA as they are 5' to the critical exons that are deleted in the *Nedd4l*^{tm1b} allele.

Western blots using a NEDD4L-specific antibody were also performed to determine if a specific isoform of NEDD4L protein was expressed in cochlear tissue and to verify that the *Nedd4l*^{tm1b} allele is a KO null mutation of *Nedd4l*. An anti-NEDD4L antibody was used which was raised against the amino acid sequence between the first two WW domains of the NEDD4L isoforms (Figure 3.4a; Protein Isoforms). Both isoforms were detected in *Nedd4l*$^{+/+}$ mice-derived cochlear lysates, with greater abundance of the long over the short isoform (Figure 3.4a, c; 130 and 110kDa, respectively). Compared to the amount of expression observed in *Nedd4l*$^{+/+}$ mice, less of both NEDD4L isoforms could be

detected in cochlear protein lysates derived from *Nedd4l*$^{tm1b/+}$ mice. Neither isoform could be detected in the cochlear protein lysates derived from *Nedd4l*$^{tm1b/tm1b}$ mice, which suggest that the *Nedd4l*^{tm1b} allele is a KO null mutation.

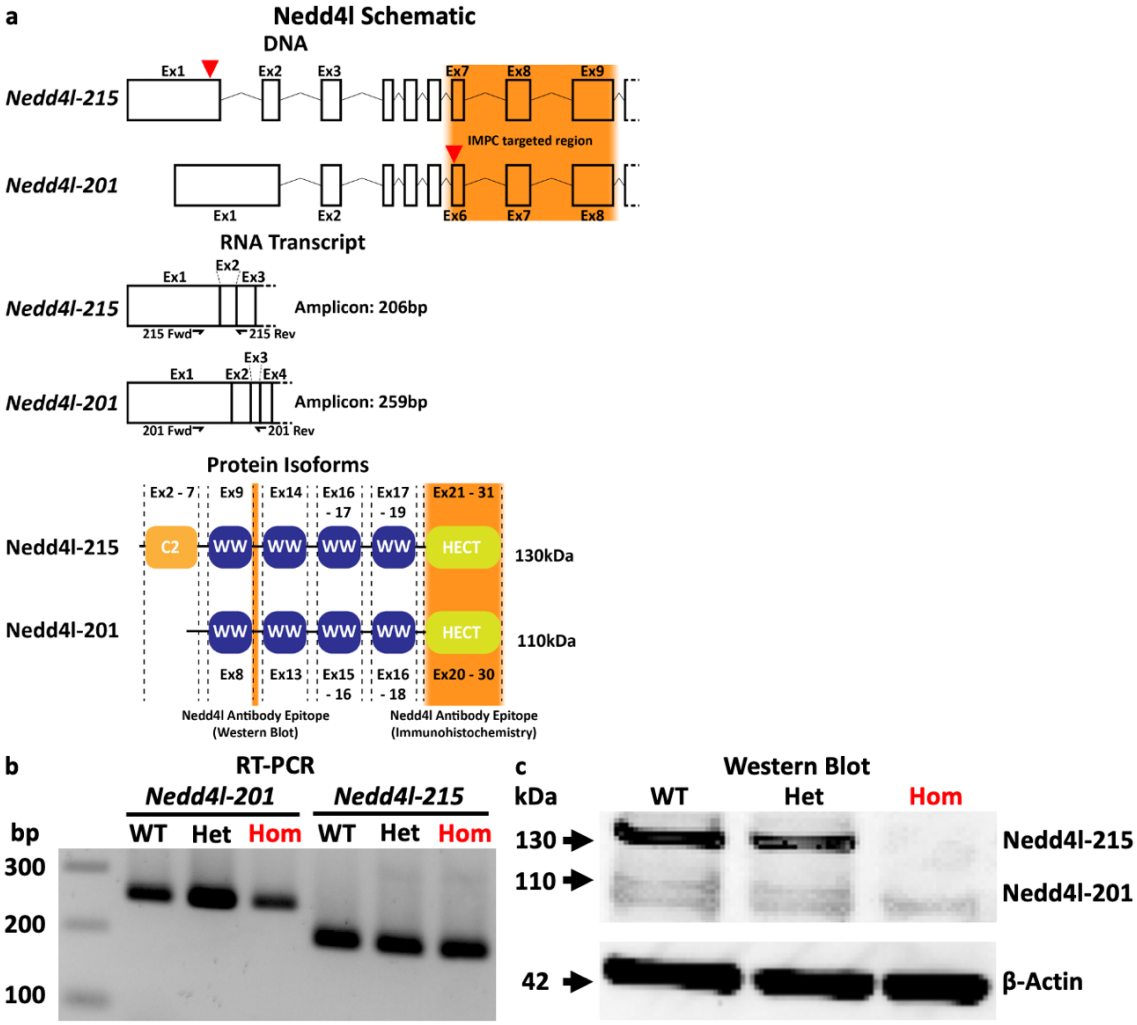

Figure 3.4: Molecular characterisation of NEDD4L transcript and protein expression in cochlear tissue. **(a)** Overview of the long and short NEDD4L isoform (*Nedd4l-215* and *Nedd4l-201*, respectively). The two isoforms are highly homologous, with exception to the first two exons (Ex); RT-PCR primers amplified these regions. Translation of the *Nedd4l-215* begins at Ex1, generating a C2-domain containing NEDD4L protein isoform, whereas *Nedd4l-201* translation begins later at Ex6, (red triangles indicate a start codon). The exons that encode for domains found in the *Nedd4l-215* and *-201* are indicated above and below the diagram, respectively. **(b)** RT-PCR using isoform-specific forward and reverse primers, found no transcriptional preference for either *Nedd4l* isoform in cochlear tissue, as both were readily amplified from cDNA synthesised from RNA derived from the cochlear tissue of *Nedd4l*$^{+/+}$ mice. Both isoforms were also amplified from cDNA generated from *Nedd4l*$^{tm1b/tm1b}$ cochlear tissue, but likely not translating for endogenous NEDD4L protein. **(c)** Both long (130kDa) and short (110kDa) isoforms were detected in anti-NEDD4L protein Western blots in *Nedd4l*$^{+/+}$ mice-derived cochlear protein lysates. Expression of both isoforms was reduced in *Nedd4l*$^{tm1b/+}$ mice, and absent in cochlear protein lysates of *Nedd4l*$^{tm1b/tm1b}$ mice, suggesting that the *Nedd4l*^{tm1b} allele is a KO null mutation. For RT-PCR and Western blots *n*= 3 for mice of each genotype.

3.2.1.2 Spatiotemporal Expression of NEDD4L

Additional experiments were performed to determine which cochlear tissue expressed NEDD4L. Using the *Nedd4l*^{tm1b} allele, expression of the *lacZ* reporter gene is determined by endogenous *Nedd4l* expression (Figure 3.3). Therefore X-Gal stains of *Nedd4l*$^{tm1b/+}$-derived cochlear tissue could faithfully track *Nedd4l* expression (Figure 3.5). X-Gal stains of cryosectioned cochlear tissue of E13.5-aged *Nedd4l*$^{tm1b/+}$ embryos, found little X-Gal staining in the developing cochlear duct (Figure 3.5b), but was found at an extra-cochlear tissue known as the endolymphatic sac (Figure 3.5d). In newborn (P0) *Nedd4l*$^{tm1b/+}$ pups, *lacZ* expression was detected in a non-sensory epithelial tissue known as interdental cells (IdCs) , which are found atop of the SLim (Figure 3.5f). However, no *Nedd4l* expression was found in older mice, as 8-week aged *Nedd4l*$^{tm1b/+}$ stained cochlear tissue was comparable to *Nedd4l*$^{+/+}$ controls (Figure 3.5g, h). No X-Gal staining was observed in all age-matched control *Nedd4l*$^{+/+}$ mice (Figure 3.5a, c, e, g).

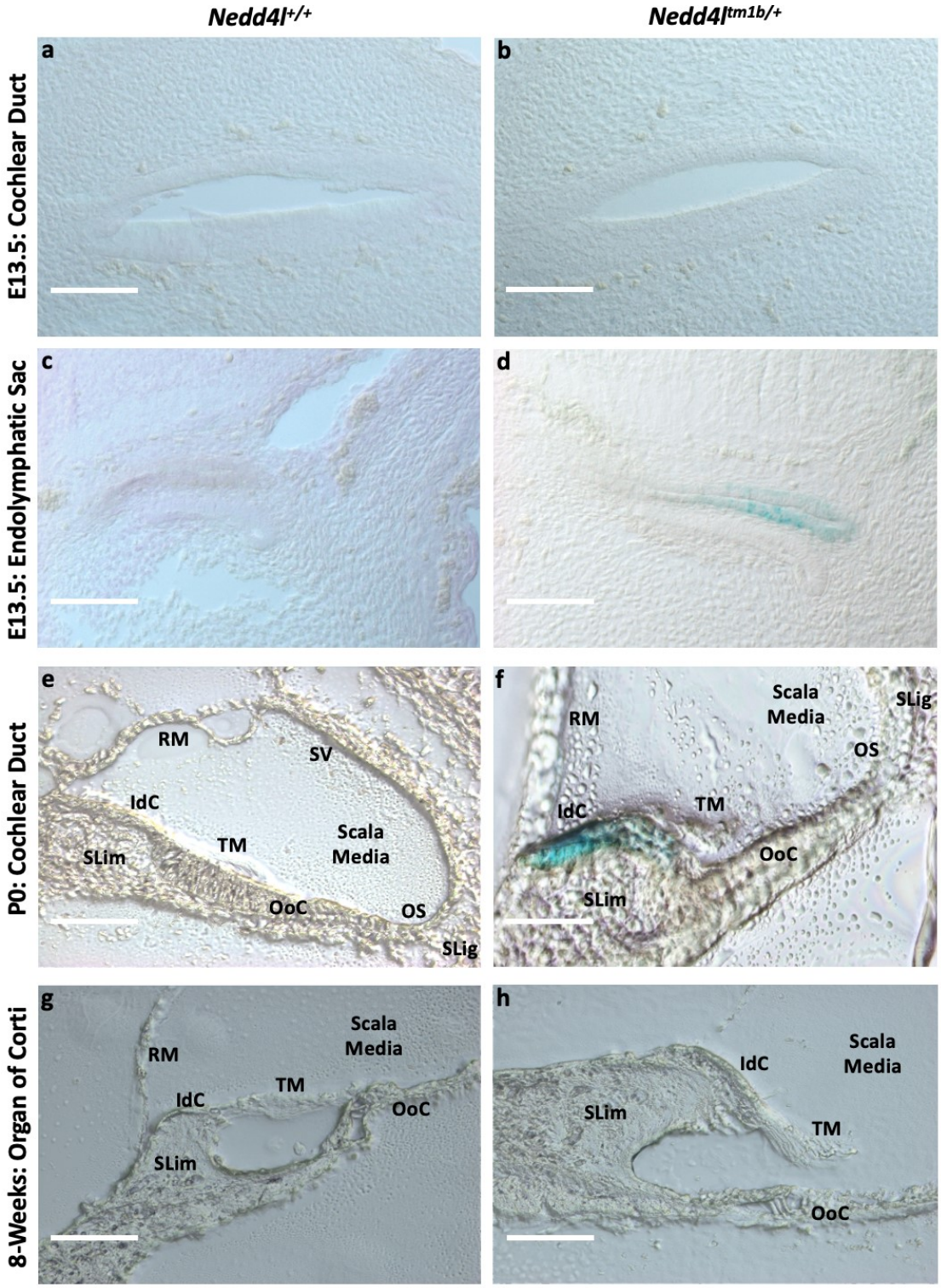

IdC: Interdental Cells; **OoC:** Organ of Corti; **OS:** Outer Sulcus; **RM:** Reissner's Membrane; **SLig:** Spiral Ligament; **SLim:** Spiral Limbus; **SV:** Stria Vascularis; **TM:** Tectorial Membrane

Figure 3.5: Spatiotemporal investigations of Nedd4l expression in cochlear tissue. X-Gal stains of *lacZ* expression under the control of endogenous *Nedd4l* expression at E13.5 (a – d), P0 (e, f) and 8-weeks of age (g, h). **(a – d)** At E13.5, X-Gal staining was found in the endolymphatic sac of *Nedd4l*$^{tm1b/+}$ mice (d) but not within developing cochlear tissue (d). **(e, f)** In P0-aged *Nedd4l*$^{tm1b/+}$ mice , X-Gal staining in *Nedd4l*$^{tm1b/+}$ was detected in IdCs, medial to the sensory epithelium. **(g, h)** X-Gal staining was undetectable at older ages in cochlear tissue. Scale bars = 35µm. For X-Gal stains of *Nedd4l*$^{+/+}$ mice-derived cochlear tissue, *n*= 2 for all ages tested. For X-Gal stains of *Nedd4l*$^{tm1b/+}$ mice, *n*= 3, 4, 3 when performed on E13.5-, P0 and 8-week old cochlear tissue, respectively.

To verify the observed expression of *Nedd4l* within IdCs of P0-aged mice, immunohistochemistry stains using an antibody against NEDD4L protein was performed (Figure 3.6). As the anti-NEDD4L antibody used for Western blots was not suitable for immunolabelling of tissue, a different anti-NEDD4L antibody was used that was raised against the NEDD4L HECT domain (Figure 3.4a). DAPI stains were presented to indicate that cochlear cells were being imaged.

NEDD4L staining in IdCs appeared punctate in *Nedd4l*$^{+/+}$ and *Nedd4l*$^{tm1b/+}$ mice-derived cochlear tissue (Figure 3.6c', d'). When NEDD4L and DAPI staining are overlapped, the punctate staining did not appear to be localised to a specific cellular location. Upon closer inspection, the location of many puncta also appeared to be outside of the IdC, suggesting that the punctate staining was non-specific (Figure 3.6c''', d'''). Further evidence that supports that the punctate staining pattern was unspecific is the detection of puncta in *Nedd4l*$^{tm1b/tm1b}$ mice-derived cochlear tissue where no NEDD4L protein should be detected (Figure 3.6e', Figure 3.4c). As expected, no staining was detected in a secondary antibody only control (Figure 3.6f'-f''').

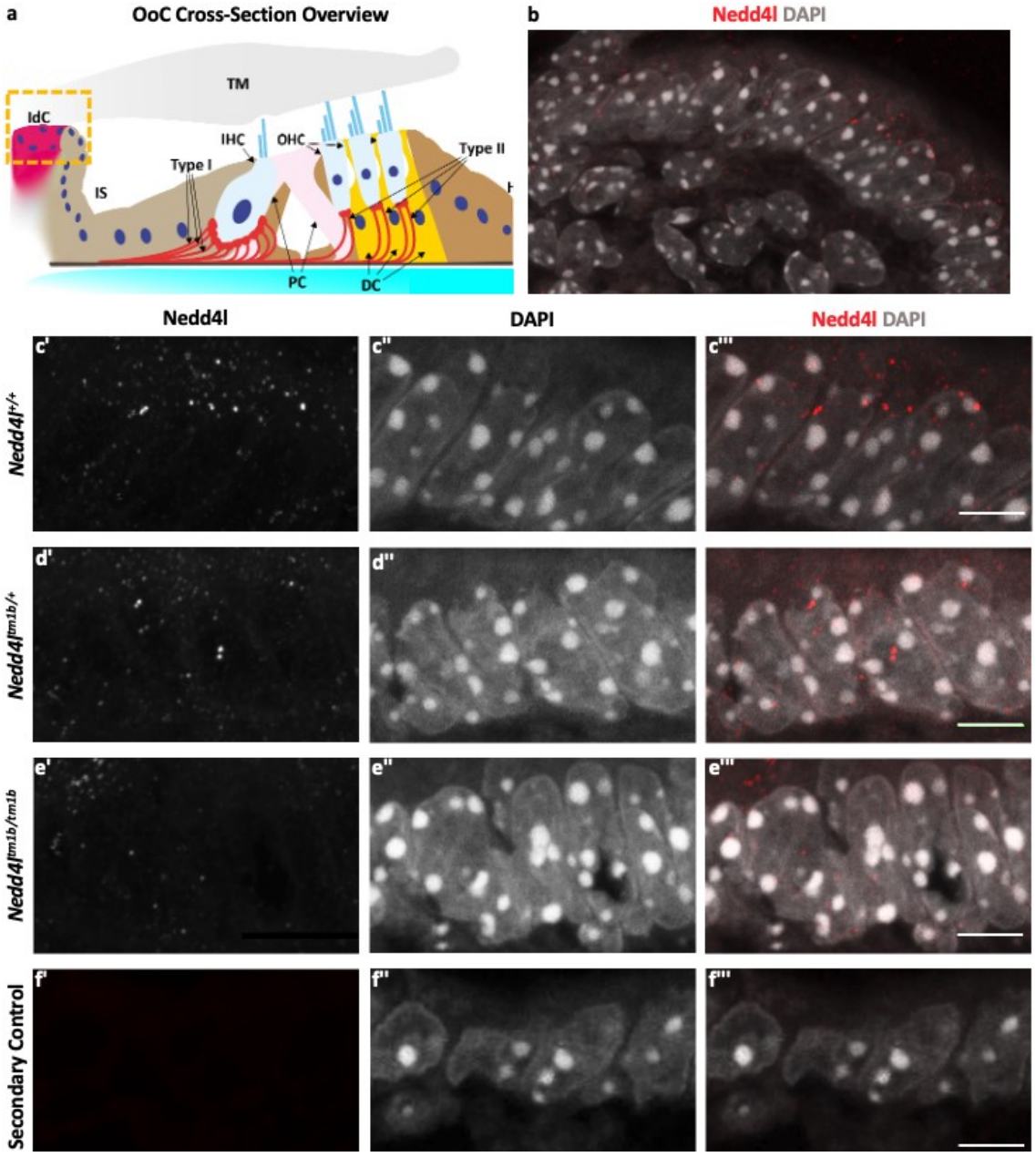

Figure 3.6: Immunohistochemistry stains against NEDD4L in cochlear tissue. Representative confocal microscopy images against an anti-NEDD4L antibody (greyscale, c' – f') and DAPI stain (greyscale, c'' – f'') in IdCs, of cryosectioned cochlear tissue from P0-aged *Nedd4l*$^{+/+}$ (c' – c'''), *Nedd4l*$^{tm1b/+}$ (d' – d''') and *Nedd4l*$^{tm1b/tm1b}$ (e' – e''') mice. A secondary-only control was performed on *Nedd4l*$^{+/+}$ mice-derived cryosections (f' – f'''). NEDD4l (red) and DAPI (greyscale) staining is overlapped in images c''' – f'''. All images were taken using the same settings. **(a)** A diagram of a cochlear cross-section. An orange, dotted box over the IdC indicate where on the cochlear section that confocal images were taken. **(c – e)** Anti-NEDD4L staining appeared to be punctate but was not localised to the IdC nucleus or within the IdC. **(f)** No staining could be detected in the secondary control condition. *n*= 3 for mice of each genotype. Scale bar = 5µm.

3.2.2 Viability of *Nedd4l*$^{tm1b/tm1b}$ Mice

Nedd4l$^{tm1b/tm1b}$ mice were generated via an intercross breed between *Nedd4l*$^{tm1b/+}$mice. The expected Mendelian ratio of *Nedd4l*$^{+/+}$, *Nedd4l*$^{tm1b/+}$ and *Nedd4l*$^{tm1b/tm1b}$ mice born from this breeding scheme is 1:2:1, respectively. However, the number of mice of each genotype, that survived to up to and past 3-weeks of age, was significantly different from the Mendelian ratios expected from this breeding strategy. Less *Nedd4l*$^{tm1b/tm1b}$ mice (15.70%) were born than expected, supporting the subviability phenotype identified through IMPC-performed phenotyping (Figure 3.7). However, this result also imply that the sub-viability concerns are not as severe as previously suggested as only 7.69% of mice that survived past 3-weeks of age carried the *Nedd4l*$^{tm1b/tm1b}$ genotype.

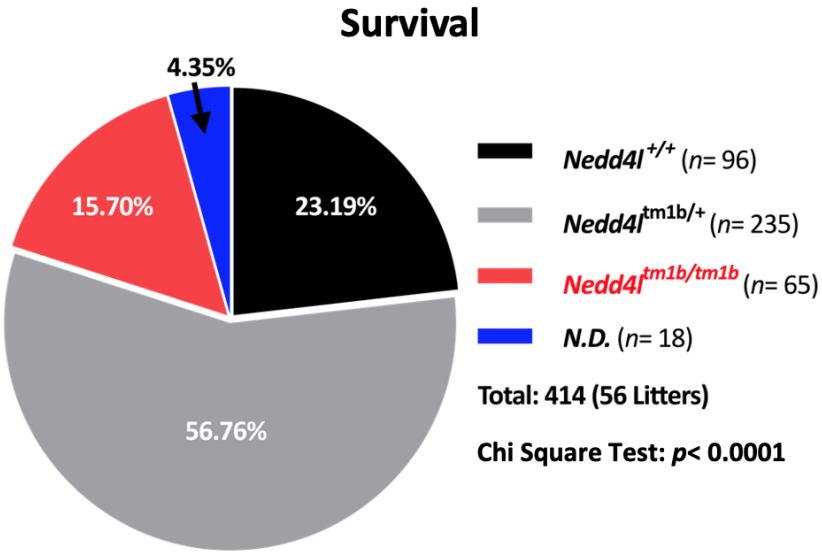

Figure 3.7: Nedd4l*$^{tm1b/tm1b}$ *mice experience sub-viability issues. Litters generated through an intercross between *Nedd4l*$^{tm1b/+}$ mice, produced fewer *Nedd4l*$^{tm1b/tm1b}$ mice than the expected Mendelian ratio. The number of mice born per genotype was compared to the expected Mendelian ratio of 1:2:1 of *Nedd4l*$^{+/+}$, *Nedd4l*$^{tm1b/+}$ and *Nedd4l*$^{tm1b/tm1b}$ mice respectively, and analysed for statistical significance using a Chi-Square test. *N.D.* refers to a mouse that had tissue submitted for genotyping, but results were inconclusive.

The weight of *Nedd4l*$^{tm1b/tm1b}$ mice was also compared to control *Nedd4l*$^{+/+}$ and *Nedd4l*$^{tm1b/+}$ mice, as a general indicator of their health (Figure 3.8). The average weight of mice of different age, sex and genotype are summarised in Table 3.1.

At 3-weeks of age, the average weight of both female and male *Nedd4l*$^{tm1b/tm1b}$ mice is less but not significantly different to their respective, sex-matched *Nedd4l*$^{+/+}$ and *Nedd4l*$^{tm1b/+}$ mice controls (female: p= 0.8055 and p= 0.2385, respectively; male: p= 0.1699 for both comparisons; Figure 3.8a, b). At 8-weeks old, both female and male *Nedd4l*$^{tm1b/tm1b}$ mice weigh less than, but are not significantly different compared to, sex-matched *Nedd4l*$^{+/+}$ and *Nedd4l*$^{tm1b/+}$ mice controls (female: p= 0.2372 for both comparisons; male: p= 0.2590 and 0.8949 respectively; Figure 3.8c, d). Overall, this suggests that *Nedd4l*$^{tm1b/tm1b}$ mice are slightly lighter than control mice and that they could be experiencing some physiological dysfunction.

Age	Female weight (g)			Male weight (g)		
	***Nedd4l*$^{+/+}$**	***Nedd4l*$^{tm1b/+}$**	***Nedd4l*$^{tm1b/tm1b}$**	***Nedd4l*$^{+/+}$**	***Nedd4l*$^{tm1b/+}$**	***Nedd4l*$^{tm1b/tm1b}$**
3-Weeks	7.43 ± 0.99	8.03 ± 1.01	6.91 ± 1.43	9.60 ± 0.51	9.57 + 1.19	8.04 ± 1.54
8-Weeks	19.66 ± 0.39	19.16 ± 1.64	18.15 ± 0.82	27.09 ± 2.65	25.44 ± 2.01	24.84 ± 0.69

Table 3.1: The average weight of mice in the Nedd4l*$^{tm1b/tm1b}$ *phenotyping cohort. Weights of female and male *Nedd4l*$^{+/+}$, *Nedd4l*$^{tm1b/+}$, *Nedd4l*$^{tm1b/tm1b}$ mice presented in grams (g) ± the standard deviation. For female mice, mice n= 3, 7 and 5 for *Nedd4l*$^{+/+}$, *Nedd4l*$^{tm1b/+}$, *Nedd4l*$^{tm1b/tm1b}$ mice, respectively. For male mice, n= 4 for mice of all genotypes.

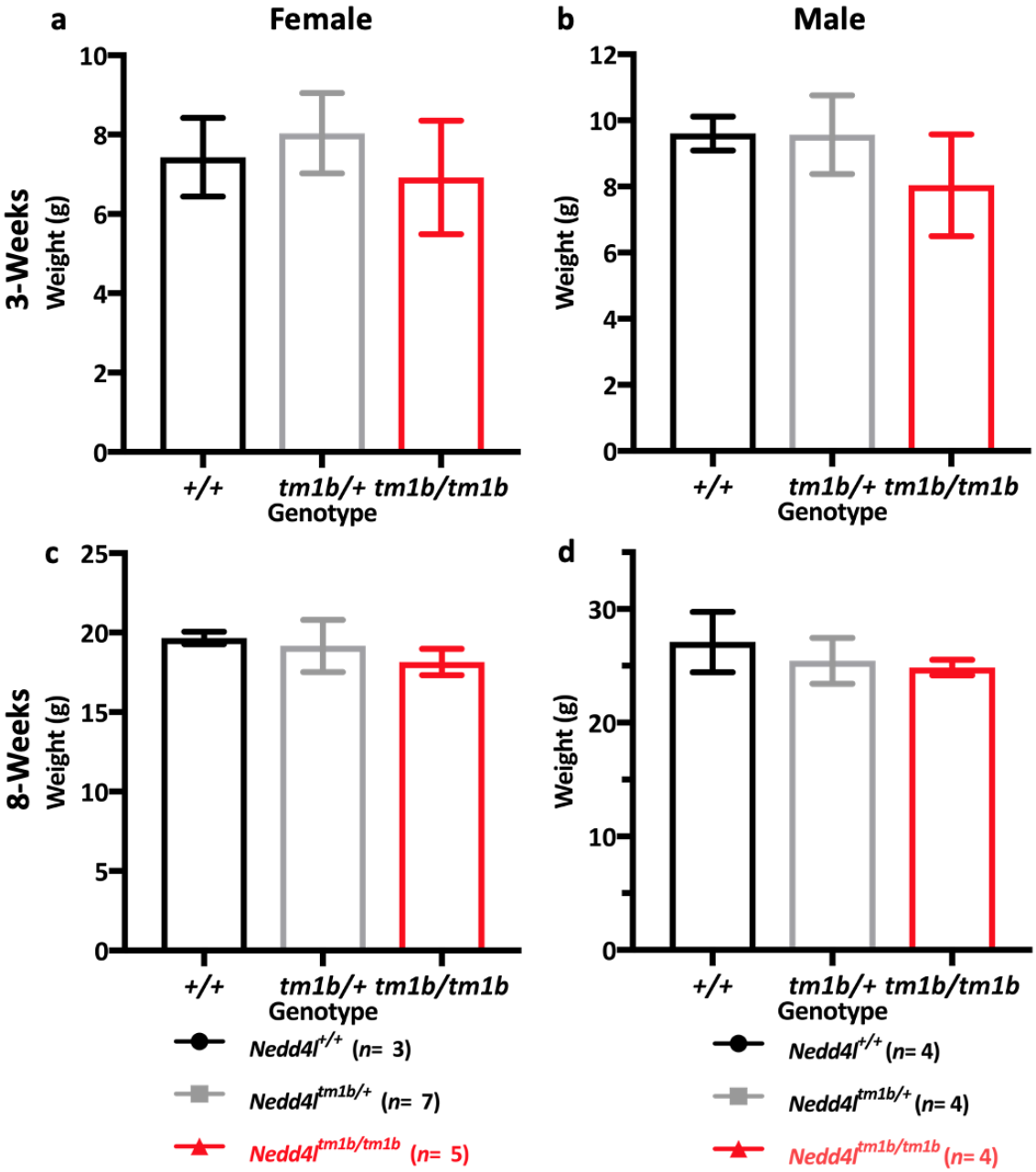

Figure 3.8: Both female and male Nedd4l$^{tm1b/tm1b}$ mice are not significantly lighter than Nedd4l$^{+/+}$ and Nedd4l$^{tm1b/+}$ mice. The body weights of 3- (a, b) and 8-week (c, d) old female (a, c) and male (b, d) mice of all genotypes. At both 3- and 8-weeks of age, female and male *Nedd4l$^{tm1b/tm1b}$* mice (red columns) are lighter compared to *Nedd4l$^{+/+}$* and *Nedd4l$^{tm1b/+}$* (black and grey columns, respectively). Data presented as averages ± standard deviation, and analysed using Ordinary one-way ANOVA tests with Sidak's multiple comparisons test, as comparisons were made to the averaged weight of *Nedd4l$^{tm1b/tm1b}$* mice.

3.2.3 Auditory Phenotyping of *Nedd4l*$^{tm1b/tm1b}$ Mice

3.2.3.1 ABR Tests

As IMPC phenotyping only performed ABR tests at 14-weeks of age, it was unable to ascertain the nature of the hearing loss experienced by *Nedd4l*$^{tm1b/tm1b}$ mice. To determine if *Nedd4l*$^{tm1b/tm1b}$ mice experience congenital hearing loss or an early-onset, progressive loss of auditory function, ABR tests were performed on P16 *Nedd4l*$^{tm1b/tm1b}$ mice (Figure 3.9a). As P16 is just after the onset of mouse hearing (~P12), auditory thresholds of mice have yet to stabilize and may account for the elevated ABR thresholds of *Nedd4l*$^{tm1b/+}$ and *Nedd4l*$^{tm1b/tm1b}$ mice in response to a 16 and 32kHz and click stimulus. However, the ABR thresholds recorded from *Nedd4l*$^{tm1b/tm1b}$ mice are not significantly different compared to those recorded from *Nedd4l*$^{+/+}$ and *Nedd4l*$^{tm1b/+}$ mice controls (Figure 3.9a).

Additional ABR tests were performed to ascertain the profile of auditory function loss within *Nedd4l*$^{tm1b/tm1b}$ mice. ABR measurements undertaken on 3-week old animals found that compared to controls, *Nedd4l*$^{tm1b/tm1b}$ mice had significantly elevated thresholds in response to all but a 16kHz stimuli (Figure 3.9b). By 8-weeks of age, the ABR thresholds of *Nedd4l*$^{tm1b/tm1b}$ mice were found to be elevated further for all frequencies tested and the broadband click stimulus, showing similar thresholds to those reported by the IMPC 14-week ABR phenotyping (Figure 3.9c). Furthermore, at 8-weeks of age, *Nedd4l*$^{tm1b/+}$ mice displayed significantly elevated hearing thresholds in response to high frequency stimuli compared to *Nedd4l*$^{+/+}$ mice (Figure 3.9c).

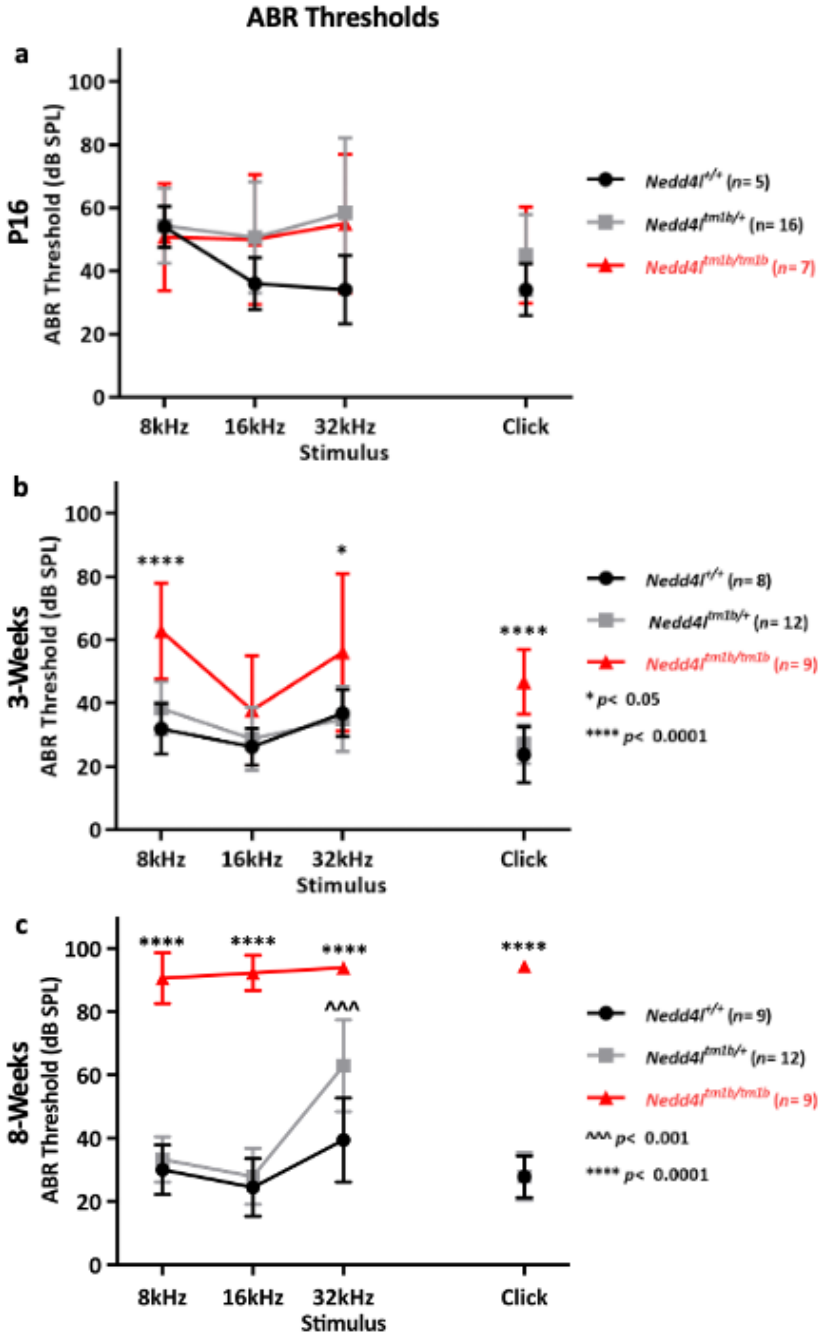

Figure 3.9: Auditory dysfunction of Nedd4l$^{tm1b/tm1b}$ mice. ABR thresholds recorded from mice at P16 (a), 3-weeks (b) and 8-weeks of age (c). **(a)** Auditory function of *Nedd4l*$^{tm1b/tm1b}$ mice (red triangles) is comparable to *Nedd4l*$^{+/+}$ (black circles) and *Nedd4l*$^{tm1b/+}$ (grey squares) mice controls at P16 in response to all stimuli. **(b)** At 3-weeks of age, *Nedd4l*$^{tm1b/tm1b}$ mice ABR thresholds are significantly elevated compared to *Nedd4l*$^{+/+}$ and *Nedd4l*$^{tm1b/+}$ mice in response to all but the 16kHz frequency. **(c)** 8-week aged *Nedd4l*$^{tm1b/tm1b}$ mice ABR thresholds are profoundly elevated in response to all stimuli. Furthermore, *Nedd4l*$^{tm1b/+}$ mice displayed high-frequency hearing loss in comparison to control *Nedd4l*$^{+/+}$ mice (p= 0.0013). Data presented as averages ± standard deviation and analysed using Ordinary one-way ANOVA with Tukey's Multiple Comparisons tests to compare thresholds recorded in response to each stimulus. Statistical significance denoted by *(p< 0.05), ^^^ (p< 0.001) and **** (p< 0.00001). * and ^ represent significant differences between *Nedd4l*$^{+/+}$ and *Nedd4l*$^{tm1b/tm1b}$ or *Nedd4l*$^{tm1b/+}$ mice respectively.

As a novel candidate deafness-causing gene, investigations were performed to determine if there were any sexual dimorphic differences in the auditory dysfunction experienced by *Nedd4l*$^{tm1b/tm1b}$ mice (Figure 3.10). At 3-weeks of age, auditory thresholds recorded from female *Nedd4l*$^{tm1b/tm1b}$ mice were elevated compared to *Nedd4l*$^{+/+}$ and *Nedd4l*$^{tm1b/+}$ female control mice (Figure 3.10a). In contrast, auditory thresholds recorded from male *Nedd4l*$^{tm1b/tm1b}$ mice were comparable to those recorded from *Nedd4l*$^{+/+}$ and *Nedd4l*$^{tm1b/+}$ male controls, except in response to a broadband click stimulus. These data indicate that female *Nedd4l*$^{tm1b/tm1b}$ begin to lose their hearing earlier than male *Nedd4l*$^{tm1b/tm1b}$ mice (Figure 3.10b). By 8-weeks of age, auditory thresholds of both female and male *Nedd4l*$^{tm1b/tm1b}$ mice were both profoundly elevated compared to their respective controls (Figure 3.10c, d). Overall, the ABR phenotyping data suggests that the development of cochlear function and onset of hearing is unaffected in *Nedd4l*$^{tm1b/tm1b}$, but then there is a rapid deterioration of hearing function, such that they become profoundly deaf by 8-weeks of age.

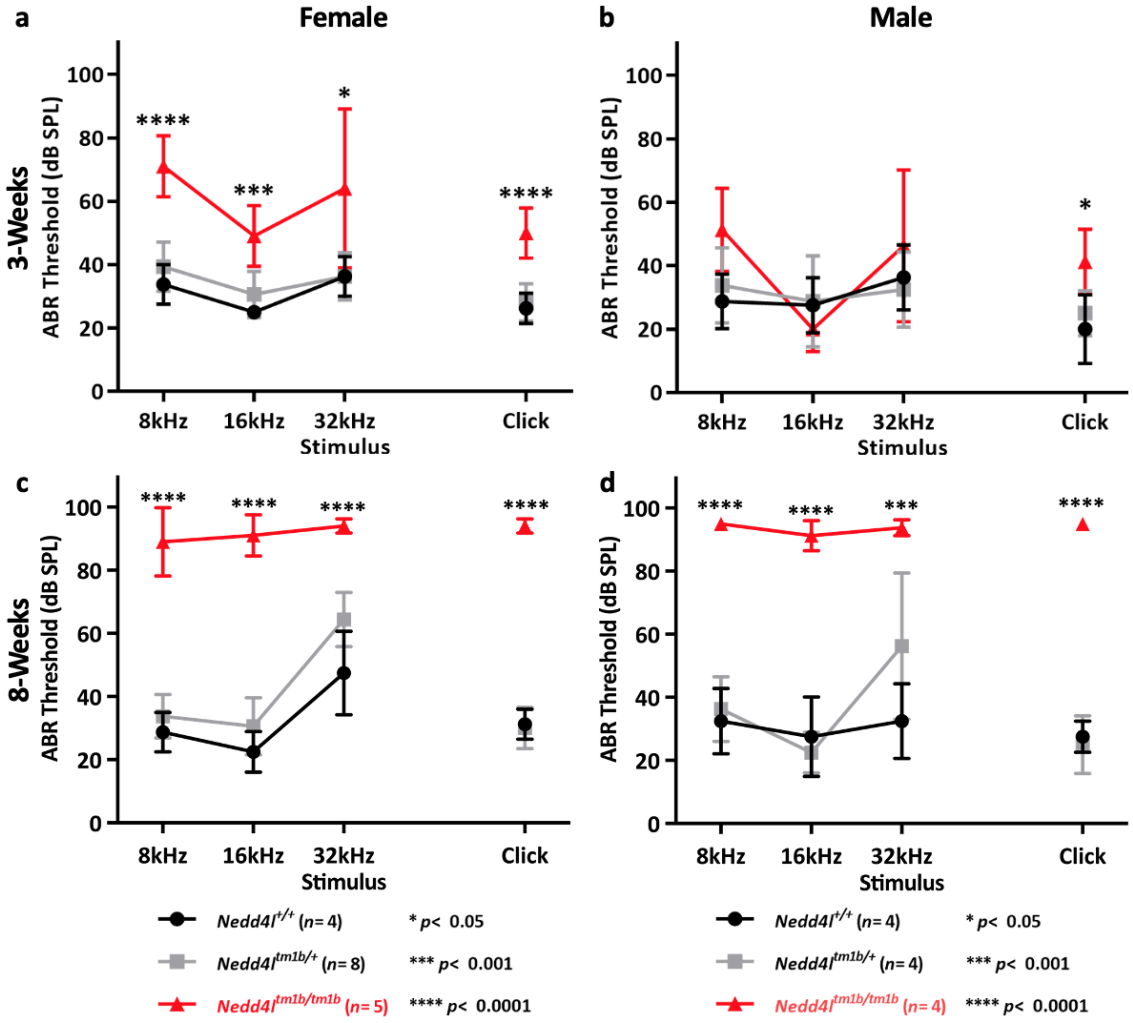

Figure 3.10: Sexual dimorphism of auditory dysfunction of Nedd4l$^{tm1b/tm1b}$ mice. ABR thresholds of female (a, c) and male (b, d) mice at 3-weeks (a, b) and 8-weeks of age (c, d). **(a, c)** Female *Nedd4l*$^{tm1b/tm1b}$ mice (red triangles) show elevated ABR thresholds at 3-weeks of age in response to all stimuli compared to female *Nedd4l*$^{+/+}$ (black circles) and *Nedd4l*$^{tm1b/+}$ controls (grey squares), which progress to profound loss at 8-weeks of age. **(b, d)** At 3-weeks of age, male *Nedd4l*$^{tm1b/tm1b}$ mice (red triangles) ABR thresholds are comparable to control male *Nedd4l*$^{+/+}$ (black circles) and *Nedd4l*$^{tm1b/+}$ mice (grey squares), except in response to a click stimulus. By 8-weeks of age, male *Nedd4l*$^{tm1b/tm1b}$ mice have profoundly elevated thresholds compared to controls, in response to all stimuli. Data presented as averages ± standard deviation and analysed using Ordinary one-way ANOVA with Tukey's Multiple Comparisons tests to compare thresholds recorded in response to each stimulus. Statistical significance denoted by * (p< 0.05), ** (p< 0.01), *** (p< 0.001) and **** (p< 0.00001).

3.2.3.2 ABR Wave Analysis

Analysis of genotype-averaged ABR waveforms was performed to investigate the hearing loss observed in *Nedd4l*$^{tm1b/tm1b}$ mice and determine the origin of the dysfunction. ABR traces recorded from 3-week old *Nedd4l*$^{tm1b/tm1b}$ mice in response to broadband click stimuli, at 30dB above their respective thresholds, were averaged and compared to controls. ABR waves were determined as outlined in Ingham *et al.*, 2011.

With exception to wave III, the peak onset of ABR waves I – IV recorded from *Nedd4l*$^{tm1b/tm1b}$ mice was earlier compared to their onset in ABR traces recorded from *Nedd4l*$^{+/+}$ and *Nedd4l*$^{tm1b/+}$ mice. Furthermore, with exception to ABR wave II, the magnitude of each ABR wave recorded from *Nedd4l*$^{tm1b/tm1b}$ mice appeared to be lower than control mice. (Figure 3.11). General inspection of the averaged traces recorded from *Nedd4l*$^{tm1b/tm1b}$ mice indicates there is impaired propagation of acoustic stimuli along the CAS. Consequently, more in-depth analysis of the individual ABR waves was performed.

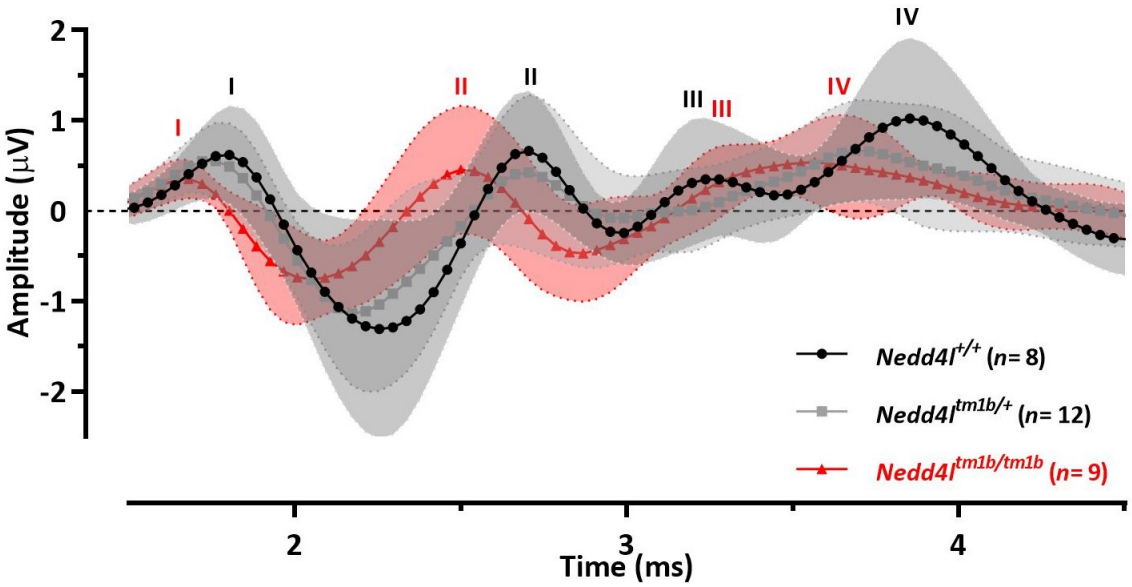

Figure 3.11: Diminished ABR waveform of Nedd4l$^{tm1b/tm1b}$ mice. Plots of an averaged ABR trace from 3-week aged *Nedd4l*$^{+/+}$ (black circles), *Nedd4l*$^{tm1b/+}$ (grey squares) and *Nedd4l*$^{tm1b/tm1b}$ (red triangles) mice, 30dB above the determined auditory threshold in response to a click stimulus. The averaged ABR trace of *Nedd4l*$^{tm1b/tm1b}$ mice show that the characteristic ABR waves I – IV are smaller in amplitude and occurred earlier than the control *Nedd4l*$^{+/+}$ or *Nedd4l*$^{tm1b/+}$ mice. The black (*Nedd4l*$^{+/+}$) and red (*Nedd4l*$^{tm1b/tm1b}$) I, II, III and IV labels denote the location of ABR wave I, II, III and IV respectively. Areas shaded in light and dark grey, or red represent the standard deviation of the averaged ABR trace for *Nedd4l*$^{+/+}$, *Nedd4l*$^{tm1b/+}$ and *Nedd4l*$^{tm1b/tm1b}$ mice respectively.

Further analysis of the onset and magnitude (latency and amplitude) of individual ABR waves corroborated earlier results. For mice of all genotypes, all ABR traces that were recorded up to the auditory threshold in response to a broadband click stimulus were extracted for analysis. In each trace, the ABR waves I – IV were identified and their

latency and amplitude measurements were extracted and averaged by genotype. Inspection of the latency data extracted from *Nedd4l*$^{tm1b/tm1b}$ mice indicated that the onset of ABR waves I - IV is earlier compared to control *Nedd4l*$^{+/+}$ and *Nedd4l*$^{tm1b/+}$ mice (Figure 3.12a, c, e, g). In addition, amplitude measurements recorded from *Nedd4l*$^{tm1b/tm1b}$ mice were lower compared to controls, except for wave II (Figure 3.12b, d, f, h).

Non-linear regression analysis of the ABR waves I – IV latency and amplitude data showed that the majority of these data could be fitted to a first-order curve (straight line) (Table 3.2). The only exception was the ABR Wave III amplitude data recorded from *Nedd4l*$^{tm1b/+}$ mice was fitted to a second-order curve. Additional non-linear regression analysis was also conducted to further determine the similarity of the latency and amplitude measurements of ABR waves I – IV, between *Nedd4l*$^{+/+}$, *Nedd4l*$^{tm1b/+}$ and *Nedd4l*$^{tm1b/tm1b}$ mice. With exception to the amplitude measurement of Wave II, a single curve could not adequately describe the latency and amplitude measurements recorded from *Nedd4l*$^{+/+}$, *Nedd4l*$^{tm1b/+}$ and *Nedd4l*$^{tm1b/tm1b}$ mice (Table 3.2). Overall, the analysis indicated that the propagation of auditory stimuli is diminished, but is quicker in *Nedd4l*$^{tm1b/tm1b}$ mice.

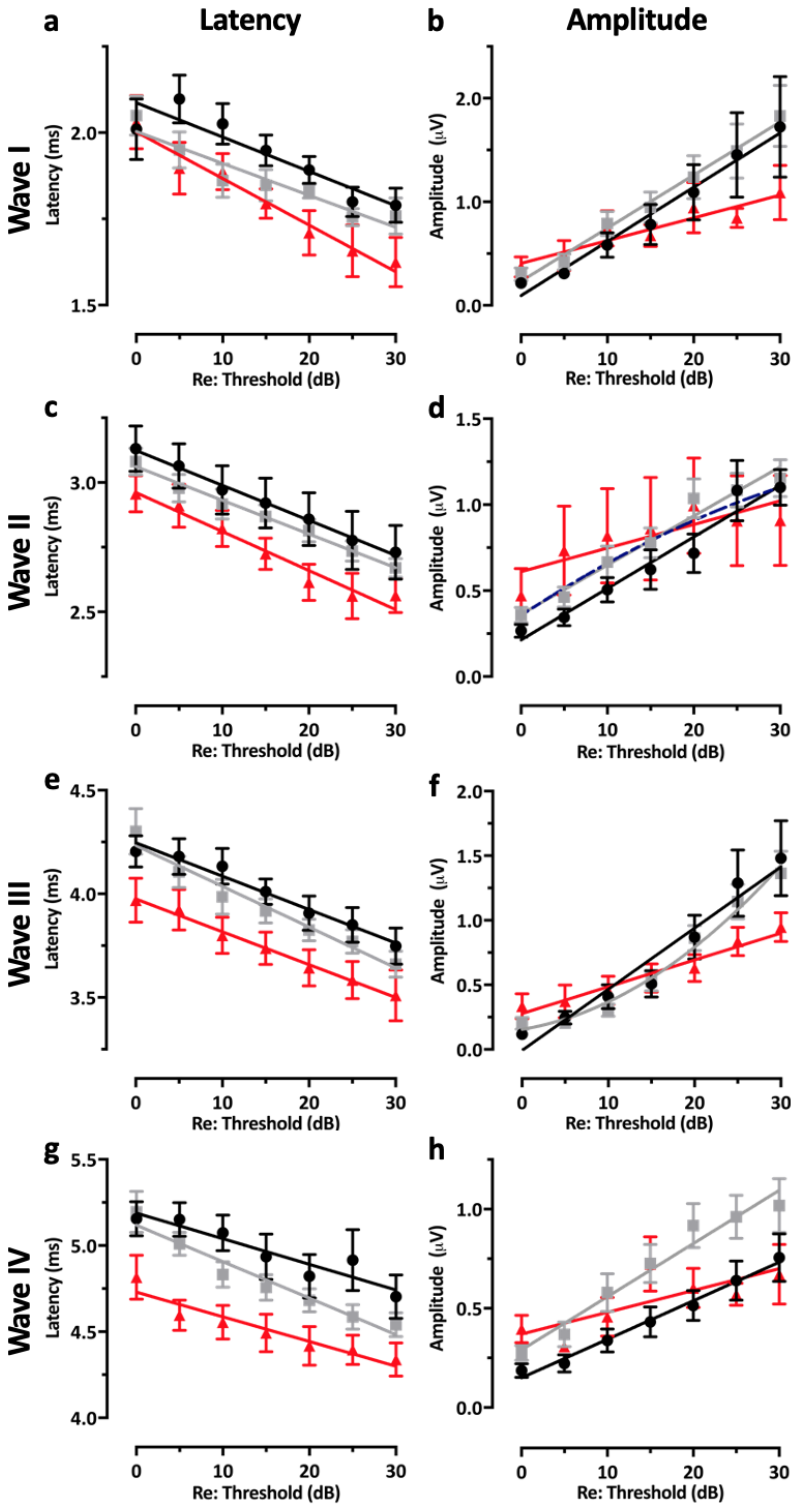

Figure 3.12: Diminished ABR wave latency and amplitude recorded from Nedd4l$^{tm1b/tm1b}$ mice. Latency (a, c, e, g) and amplitude (b, d, f, h) measurements of ABR waves I – IV of 3-weeks of age mice, in response to click stimulus. Plotted data points for waves I – IV latency and amplitude could be fit to either a first or second order polynomial line (detailed in Table 3.2). With the exception to wave II amplitude, a shared curve (blue, dotted line) could not faithfully describe the measurements extracted from ABR traces recorded from *Nedd4l*$^{+/+}$ (black circle and line), *Nedd4l*$^{tm1b/+}$ (grey square and line) and *Nedd4l*$^{tm1b/tm1b}$ (red triangle and line) mice. **(a, c, e, g)** ABR wave latency measurements of *Nedd4l*$^{tm1b/tm1b}$ mice for all waves was decreased compared to control mice. **(b, d, f, h)** ABR wave amplitude measurements of *Nedd4l*$^{tm1b/tm1b}$ mice were lower and the gradients of lines were flatter compared to controls. Data presented as averages ± standard error mean and analysed using nonlinear regression with Extra sum-of-squares F test comparison. *n*= 8, 12 and 9 for *Nedd4l*$^{+/+}$, *Nedd4l*$^{tm1b/+}$ and *Nedd4l*$^{tm1b/tm1b}$ mice respectively.

		Nedd4l$^{+/+}$		*Nedd4l*$^{tm1b/+}$		*Nedd4l*$^{tm1b/tm1b}$		Shared Curve	
		Order	*p* Value	Order	*p* Value	Order	*p* Value	Shared	*p* Value
Wave 1	**Latency**	1st	0.3013	1st	0.1585	1st	0.6420	No	0.0005
	Amplitude	1st	0.5261	1st	0.6416	1st	0.7534	No	0.0101
Wave 2	**Latency**	1st	0.8778	1st	0.8334	1st	0.6129	No	0.0010
	Amplitude	1st	0.4762	1st	0.4134	1st	0.3942	Yes	0.0984
Wave 3	**Latency**	1st	0.5844	1st	0.2889	1st	0.8980	No	<0.0001
	Amplitude	1st	0.1651	2nd	0.0156	1st	0.3434	No	0.0025
Wave 4	**Latency**	1st	0.9075	1st	0.1208	1st	0.3331	No	<0.0001
	Amplitude	1st	0.5372	1st	0.2909	1st	0.4007	No	<0.0001

Table 3.2: Summary of the ABR wave I – IV latency and amplitude linear regression analyses. Non-linear regression analysis was performed to determine whether a first order (null hypothesis) or a second order (alternative hypothesis) polynomial curve would fit the data points of ABR wave latency and amplitude measurements. p values of the analysis indicate the significance of each test, with rejection of the null hypothesis when the *p* value < 0.05. Additional analysis was performed to determine if a single, shared (null hypothesis) or different (alternative hypothesis) curve could accurately describe the ABR wave latency and amplitude measurements extracted from ABR traces recorded from *Nedd4l*$^{+/+}$, *Nedd4l*$^{tm1b/+}$ and *Nedd4l*$^{tm1b/tm1b}$ mice. *n*= 8, 12 and 9 for *Nedd4l*$^{+/+}$, *Nedd4l*$^{tm1b/+}$, *Nedd4l*$^{tm1b/tm1b}$ mice, respectively.

Additional analysis was conducted to determine whether the reduced ABR wave latency and amplitude experienced by *Nedd4l*$^{tm1b/tm1b}$ mice is the result of PAS or CAS dysfunction. To this end, the inter-wave latency between Wave I and Wave IV (time taken for ABR wave I and IV peak onset) and the ratio of Wave IV and Wave I amplitude (Wave IV: Wave I) were calculated and plotted (Figure 3.13). Changes in inter-wave latency and lower wave amplitude ratios are suggestive of disruptions to the CAS (Steinhoff *et al.*, 1988; Musiek *et al.*, 1984).

Similar non-linear regression analyses were also conducted to determine whether the data could be fit to a first or second order curve, and whether a single curve could accurately describe the data from mice of all genotypes. The inter-wave latency was reduced in *Nedd4l*$^{tm1b/tm1b}$ mice compared to control *Nedd4l*$^{+/+}$ and *Nedd4l*$^{tm1b/+}$ mice, with a different curve describing the latencies from mice of each genotype (Figure 3.13a). This indicates that the propagation of auditory stimuli through the CAS is affected. On the other hand, the Wave IV:I ratios were similar between mice of all

genotypes, which suggests that cochlear dysfunction also contributes to the auditory phenotype of *Nedd4l*$^{tm1b/tm1b}$ mice (Figure 3.13b).

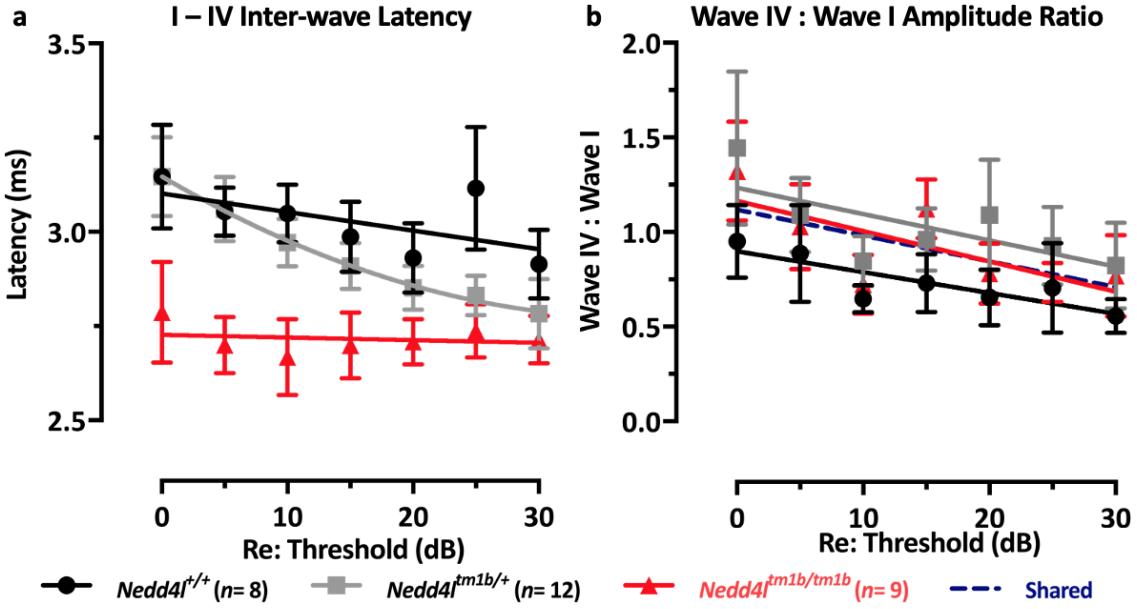

Figure 3.13: Disruptions to both PAS and CAS function is attributable to the auditory phenotypes of Nedd4l$^{tm1b/tm1b}$ mice. Inter-wave latency between ABR wave I and IV (a) and Wave IV: Wave I amplitude ratios (b) were calculated, indicating that auditory dysfunction of *Nedd4l*$^{tm1b/tm1b}$ mice affects the peripheral and central auditory system. **(a)** The ABR Wave I-IV inter-wave latency is lower in *Nedd4l*$^{tm1b/tm1b}$ mice compared to controls. Calculated inter-wave latencies from *Nedd4l*$^{+/+}$ and *Nedd4l*$^{tm1b/tm1b}$ mice were fit to first order curve (p= 0.6123 and 0.1175, respectively), whereas a second order curve was fit to measures calculated from *Nedd4l*$^{tm1b/+}$ mice (p= 0.0029). A single curve could not be fit to all inter-wave latency curves (p< 0.0001). **(b)** Wave IV: Wave I amplitude ratios were comparable to each other indicating that auditory dysfunction of *Nedd4l*$^{tm1b/tm1b}$ mice can also be attributed to disruptions in PAS too. A first order curve was fit to ratios calculated from *Nedd4l*$^{+/+}$, *Nedd4l*$^{tm1b/+}$ and *Nedd4l*$^{tm1b/tm1b}$ mice (p= 0.6541, 0.4533 and 0.4126, respectively). A single curve could adequately describe the ratios calculated from mice of each genotype (p= 0.1656). All data was presented as averages ± standard error mean and analysed using nonlinear regression with Extra sum-of-squares F test comparison. n= 8, 12 and 9 for *Nedd4l*$^{+/+}$, *Nedd4l*$^{tm1b/+}$ and *Nedd4l*$^{tm1b/tm1b}$ mice respectively.

3.2.3.3 DPOAE Tests

Additional auditory assessment of *Nedd4l*$^{tm1b/tm1b}$ mice was performed by DPOAE tests, which assesses the health of OHCs. The DPOAE responses recorded from 3-week old *Nedd4l*$^{tm1b/tm1b}$ mice were comparable to age-matched controls (Figure 3.14a). At 8-weeks of age, the DPOAE response level of *Nedd4l*$^{tm1b/tm1b}$ mice was diminished compared to controls (Figure 3.14b). Due to the large standard deviation and comparable response levels recorded in responses to a 16 and 32kHz stimuli respectively, DPOAE response levels of *Nedd4l*$^{tm1b/tm1b}$ mice were only significantly different to control *Nedd4l*$^{+/+}$ and *Nedd4l*$^{tm1b/+}$ mice at the lowest frequency used (8

kHz, p= 0.0078 and 0.0016, respectively). Whilst DPOAE tests also show that *Nedd4l*$^{tm1b/tm1b}$ mice experience auditory dysfunction, the progression of hearing loss does not mirror the ABR results (Figure 3.9), suggesting that OHC dysfunction is not the cause of deafness in *Nedd4l*$^{tm1b/tm1b}$ mice.

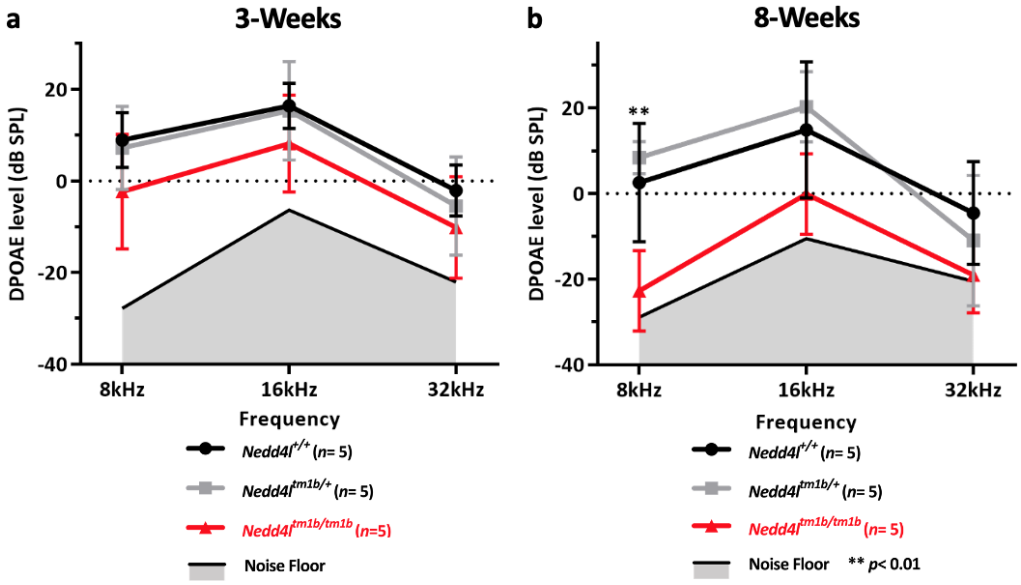

Figure 3.14: OHC dysfunction of Nedd4l$^{tm1b/tm1b}$ mice. DPOAE tests of mice at 3- (a) and 8-weeks of age (b). **(a)** Measured DPOAE response from 3-week old *Nedd4l*$^{tm1b/tm1b}$ mice (red triangles) was not significantly different to *Nedd4l*$^{+/+}$ (black circles) and *Nedd4l*$^{tm1b/+}$ (grey squares) mice controls. **(b)** Reduced DPOAE response measured from 8-week old *Nedd4l*$^{tm1b/tm1b}$ mice was significantly different to levels recorded from *Nedd4l*$^{+/+}$ and *Nedd4l*$^{tm1b/+}$ mice in response to the 8kHz stimulus. Data presented as averages ± standard deviation and analysed using Ordinary one-way ANOVA with Tukey's Multiple Comparisons tests to compare DPOAE response levels recorded in response to each stimulus. Statistical significance denoted by ** (p< 0.01) between *Nedd4l*$^{+/+}$ and *Nedd4l*$^{tm1b/tm1b}$ mice.

3.2.4 Vestibular Phenotyping of *Nedd4l*$^{tm1b/tm1b}$ mice

In order to determine if *Nedd4l*$^{tm1b/tm1b}$ mice exhibit generalized inner ear dysfunction, Vestibular Swim tests were performed on 6–month old *Nedd4l*$^{tm1b/tm1b}$ mice. There were no overt differences to the swimming behaviour observed between *Nedd4l*$^{tm1b/tm1b}$ mice and age-matched controls (Figure 3.15). As a result, no additional vestibular phenotyping tests were performed. With consideration to the results of all phenotyping tests performed, the effects of losing NEDD4L protein in *Nedd4l*$^{tm1b/tm1b}$ mice appear to be limited to the cochlea rather than affecting the entire inner ear function.

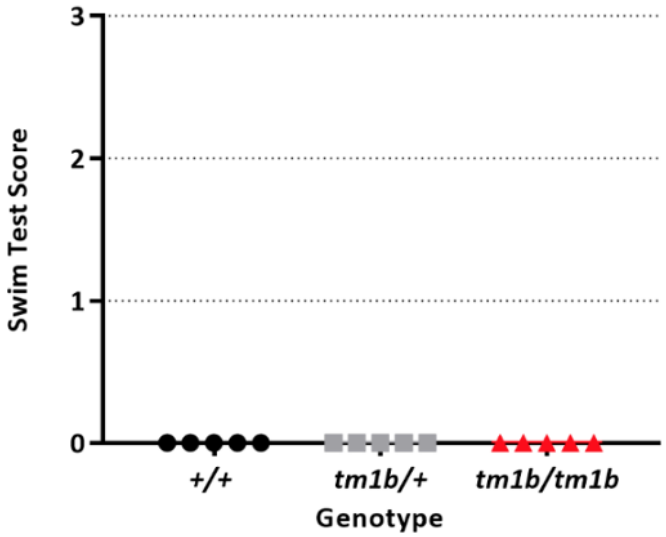

Figure 3.15: Vestibular function appears unaffected in Nedd4l$^{tm1b/tm1b}$ mice. Vestibular Swim tests of 6-month old mice show no differences in the swimming behaviour displayed by *Nedd4l*$^{+/+}$ (black circles), *Nedd4l*$^{tm1b/+}$ (grey squares) and *Nedd4l*$^{tm1b/tm1b}$ (red triangles) mice. *n*= 5 for mice of each genotype.

3.2.5 Cochlear Pathology of *Nedd4l*$^{tm1b/tm1b}$ mice

3.2.5.1 Progressive Loss of Hair Cell Bundles

As phenotypic characterization of the *Nedd4l*$^{tm1b/tm1b}$ mice suggest that auditory dysfunction likely originates in cochlear tissue, studies to identify pathophysiological changes in cochlear tissue were undertaken. SEM images were taken to visualise the stereocilia bundles of cochlear hair cells (Figure 3.16 – Figure 3.19). The number of IHC and OHC per 10 pillar cells was counted and quantified (Figure 3.20). In P16 and 3-week old *Nedd4l*$^{tm1b/tm1b}$ mice, IHC and OHC bundles could be observed at the apical, mid and basal turns of the cochlea and were comparable in number, organisation and structure to those observed in control *Nedd4l*$^{+/+}$ and *Nedd4l*$^{tm1b/+}$ mice (Figure 3.16, Figure 3.17). At 8-weeks of age, the number of IHC bundles was not affected at all cochlear turns in *Nedd4l*$^{tm1b/tm1b}$ mice. Furthermore, the number of OHC bundles was comparable between mice of different genotype at apical and mid cochlear turns (Figure 3.18a – f, 20). However, fewer OHC bundles were present at basal turns (10.6 ± 2.881) compared to apical (22.8 ± 1.304) and mid (20.2 ± 2.490) in the cochleae of *Nedd4l*$^{tm1b/tm1b}$ mice. By 6-months of age, no hair cells or bundles could be found at any turns of the *Nedd4l*$^{tm1b/tm1b}$ cochleae, as the highly ordered cellular architecture of the OoC is lost (Figure 3.19g – i, Figure 3.20).

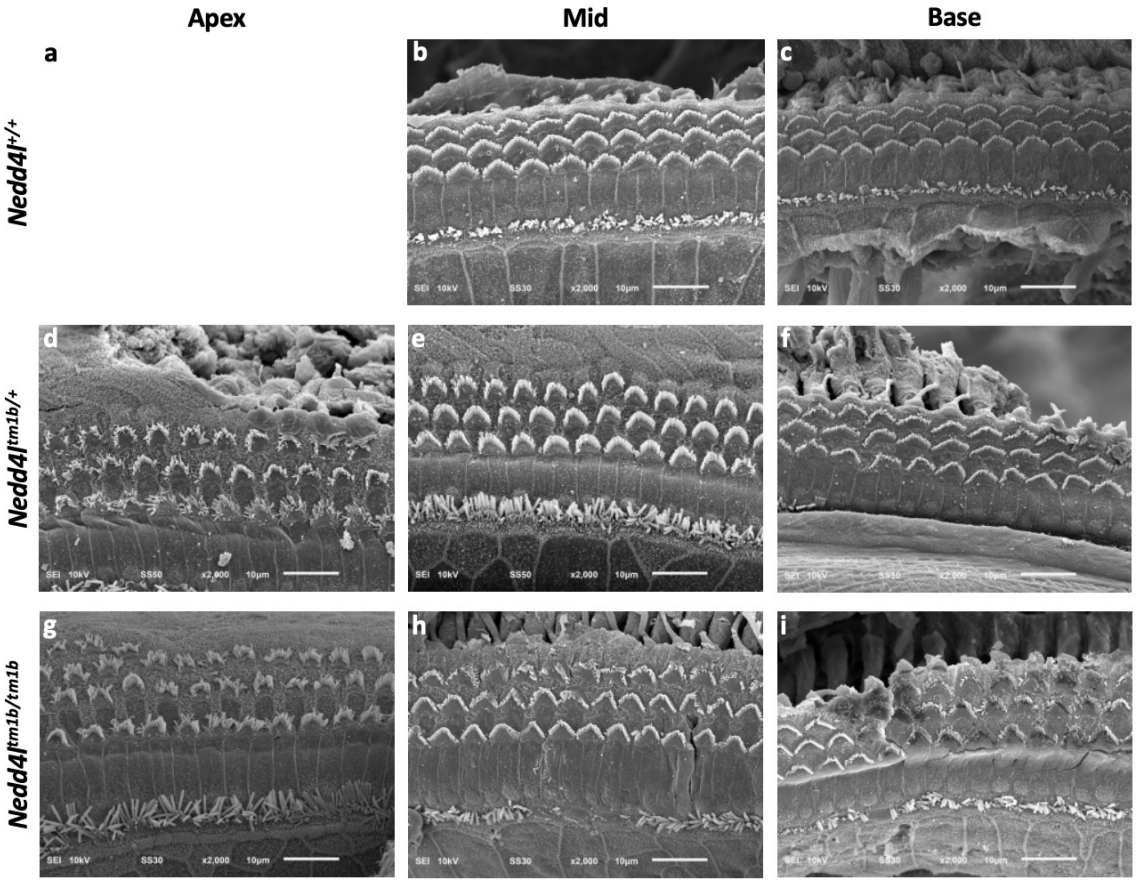

Figure 3.16: Hair cell morphology unaffected at P16-aged Nedd4l$^{tm1b/tm1b}$ mice. Representative SEM images of the sensory epithelium and hair cell bundles of *Nedd4l*$^{+/+}$ (a – c), *Nedd4l*$^{tm1b/+}$ (d – f) and *Nedd4l*$^{tm1b/tm1b}$ mice (g – i) at apical (a, d, g), mid (b, e, h) and basal (c, f, i) regions of the cochlea. Stereocilia bundles of *Nedd4l*$^{tm1b/tm1b}$ mice hair cells are comparable to *Nedd4l*$^{+/+}$ and *Nedd4l*$^{tm1b/+}$ control mice in all regions of the cochlea. A suitable image of apical-located hair cell bundles from *Nedd4l*$^{+/+}$ mice was not acquired and one could not be taken due to the Covid19 pandemic. *n*= 3, 4 and 3 for *Nedd4l*$^{+/+}$, *Nedd4l*$^{tm1b/+}$ and *Nedd4l*$^{tm1b/tm1b}$ mice respectively.

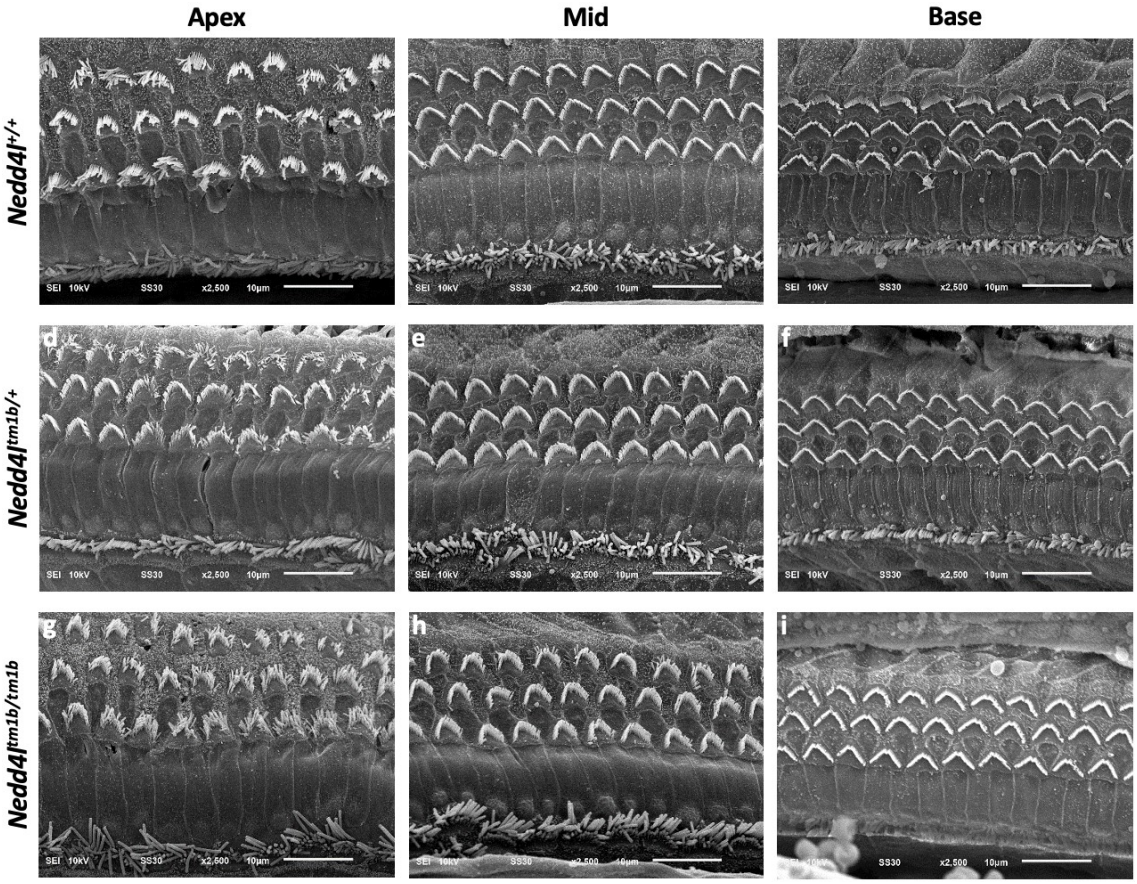

Figure 3.17: Hair cell bundle morphology unaffected in 3-weeks old Nedd4l$^{tm1b/tm1b}$ mice. Representative SEM images of the sensory epithelium and hair cell bundles of *Nedd4l*$^{+/+}$ (a – c), *Nedd4l*$^{tm1b/+}$ (d – f) and *Nedd4l*$^{tm1b/tm1b}$ mice (g – i) at apical (a, d, g), mid (b, e, h) and basal (c, f, h) regions of the cochlea. SEM images taken from *Nedd4l*$^{tm1b/tm1b}$ mice are comparable to *Nedd4l*$^{+/+}$ and *Nedd4l*$^{tm1b/+}$ control mice in all regions of the cochlea. *n*= 3, 5 and 5 for *Nedd4l*$^{+/+}$, *Nedd4l*$^{tm1b/+}$ and *Nedd4l*$^{tm1b/tm1b}$ mice respectively.

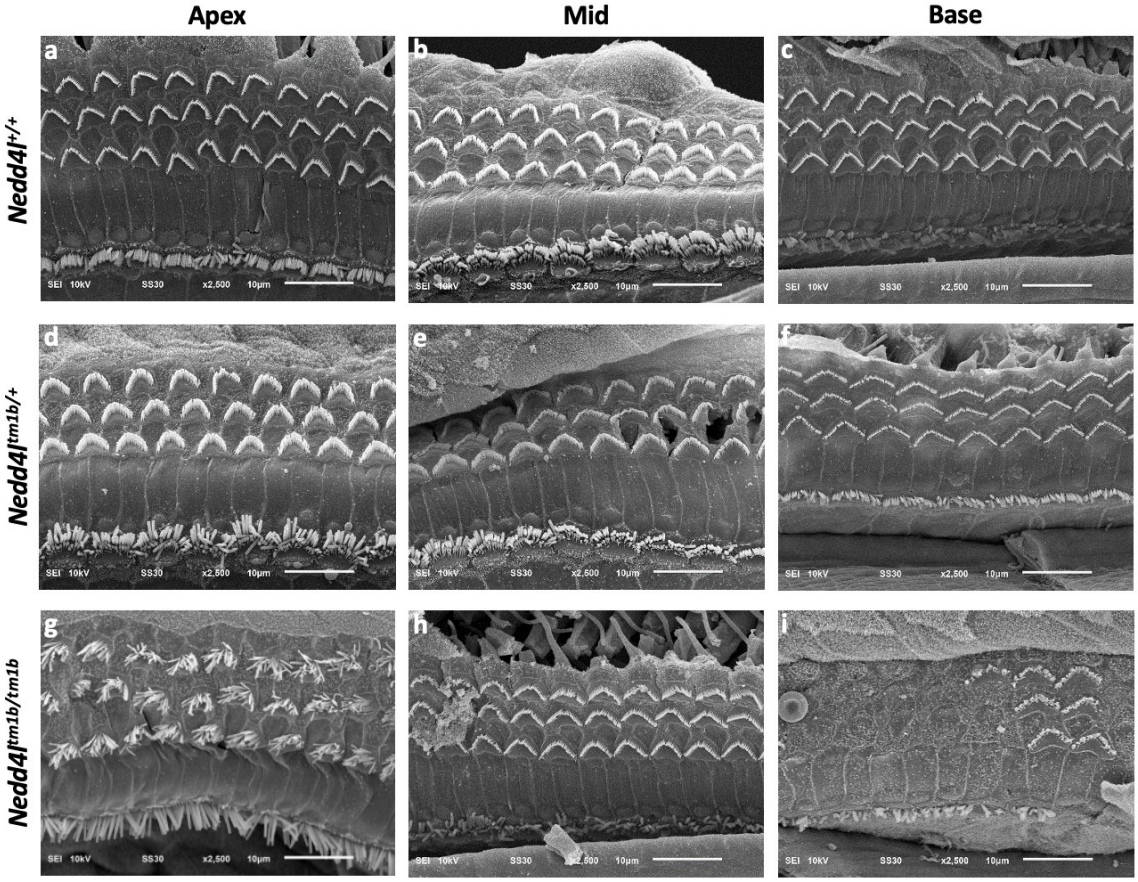

Figure 3.18: Loss of basal hair cells in 8-weeks old Nedd4l$^{tm1b/tm1b}$ mice. Representative SEM images of the sensory epithelium and hair cell bundles of *Nedd4l*$^{+/+}$ (a – c), *Nedd4l*$^{tm1b/+}$ (d – f) and *Nedd4l*$^{tm1b/tm1b}$ mice (g – i) at apical (a, d, g), mid (b, e, h) and basal (c, f, h) regions of the cochlea. **(a – f)** Hair cell bundles of *Nedd4l*$^{+/+}$ and *Nedd4l*$^{tm1b/+}$ mice looked comparable to each other and to the epithelia at earlier ages. **(g, h)** Apical and mid regions of *Nedd4l*$^{tm1b/tm1b}$ mice are comparable to similar cochlear locations in *Nedd4l*$^{+/+}$ and *Nedd4l*$^{tm1b/+}$ mice. **(i)** Loss of basal IHC and OHCs in *Nedd4l*$^{tm1b/tm1b}$ mice. *n*= 4, 3 and 5 and 5 for *Nedd4l*$^{+/+}$, *Nedd4l*$^{tm1b/+}$ and *Nedd4l*$^{tm1b/tm1b}$ mice respectively.

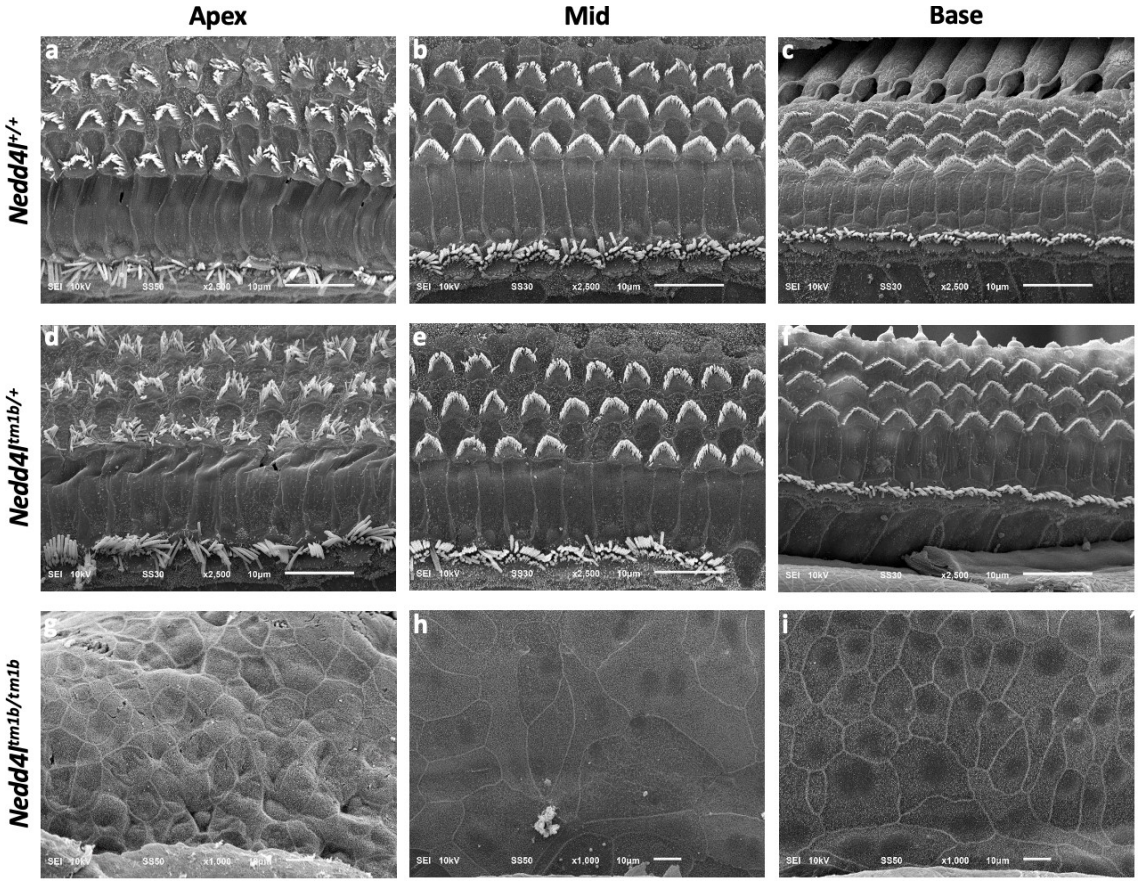

Figure 3.19: Loss of hair cell bundles and sensory epithelium morphology in 6-month old Nedd4l$^{tm1b/tm1b}$ mice. Representative SEM images of the sensory epithelium and hair cell bundles of *Nedd4l*$^{+/+}$ (a – c), *Nedd4l*$^{tm1b/+}$ (d – f) and *Nedd4l*$^{tm1b/tm1b}$ mice (g – i) at apical (a, d, g), mid (b, e, h) and basal (c, f, h) regions of the cochlea. **(a – f)** Hair cell bundles and the organised morphology of the sensory epithelium remained unchanged in *Nedd4l*$^{+/+}$ and *Nedd4l*$^{tm1b/+}$ mice. **(g – i)** Loss of IHC and OHC bundles in *Nedd4l*$^{tm1b/tm1b}$ mice had progressed to all cochlear turns. Deterioration of the sensory epithelium was also observed. *n*= 3 for all *Nedd4l*$^{+/+}$, *Nedd4l*$^{tm1b/+}$ and *Nedd4l*$^{tm1b/tm1b}$ mice.

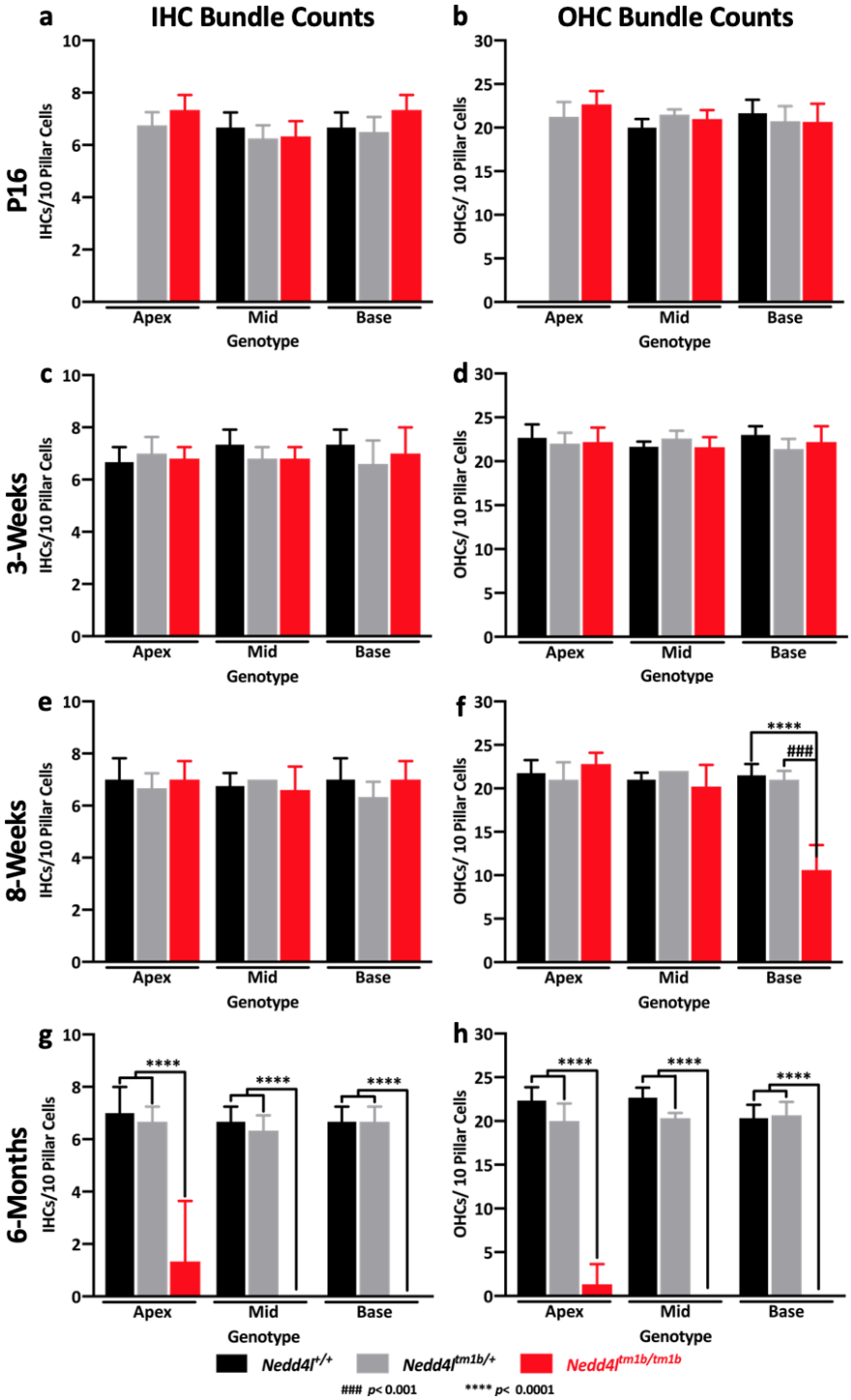

Figure 3.20: Progressive loss of IHC and OHC bundles in Nedd4l$^{tm1b/tm1b}$ mice. Counts of the number of IHC (a, c, e, g) and OHC bundles (b, d, f, h) per 10 pillar cells, at all turns of the cochlea in P16 (a, b), 3-week (c, d), 8-week (e, f) and 6-month old mice (g, h). **(a – d)** The number of IHC and OHC bundles at P16 and 3-weeks was comparable across mice of all genotypes. **(e)** The number of IHC bundles present in 8-week old mice was comparable across each genotypes. **(f)** Fewer basal OHC bundles were observed in 8-week old *Nedd4l*$^{tm1b/tm1b}$ mice (red bars), while the number of OHC bundles at apical and mid turns was comparable to control *Nedd4l*$^{+/+}$ (black bars) and *Nedd4l*$^{tm1b/+}$ (grey bars) mice. **(g, h)** By 6-months of age, the number of IHC and OHC bundles at all turns of the cochlea were fewer in *Nedd4l*$^{tm1b/tm1b}$ mice than *Nedd4l*$^{+/+}$ and *Nedd4l*$^{tm1b/+}$ mice. Counts are plotted as averages ± standard deviation and analysed using Ordinary one-way ANOVA with Tukey's Multiple Comparisons tests for specific regions of the cochlea. * and # indicates statistically significant differences between *Nedd4l*$^{+/+}$ or *Nedd4l*$^{tm1b/+}$ respectively, to *Nedd4l*$^{tm1b/tm1b}$. The *n* number for each genotype and age are specified in Figure 3.16 – Figure ***3.19***, for P16-, 3-week, 8-week and 6-month old mice, respectively.

3.2.5.2 Progressive Loss of SGN Nuclei

A progressive degeneration of the SGNs was also observed in *Nedd4l*$^{tm1b/tm1b}$ mice (Figure 3.21 – Figure 3.24). H&E stains of sectioned cochlear tissue showed that the number of SGN nuclei present in *Nedd4l*$^{tm1b/tm1b}$ mice at P16 or 3-weeks of age is comparable to age-matched controls (Figure 3.21, Figure 3.22 respectively). By 8-weeks of age, some loss of SGN nuclei is detected at all turns of the cochlea in *Nedd4l*$^{tm1b/tm1b}$ mice (Figure 3.23g – i), and when assessed at 6-months of age, few SGN nuclei remain (Figure 3.24g – i). Calculating SGN nuclei density in 8-week and 6-month old *Nedd4l*$^{tm1b/tm1b}$ mice illustrated this progressive decrease in SGN nuclei number, which is significantly lower at all turns of the cochlea when compared to age-matched controls (Figure 3.25).

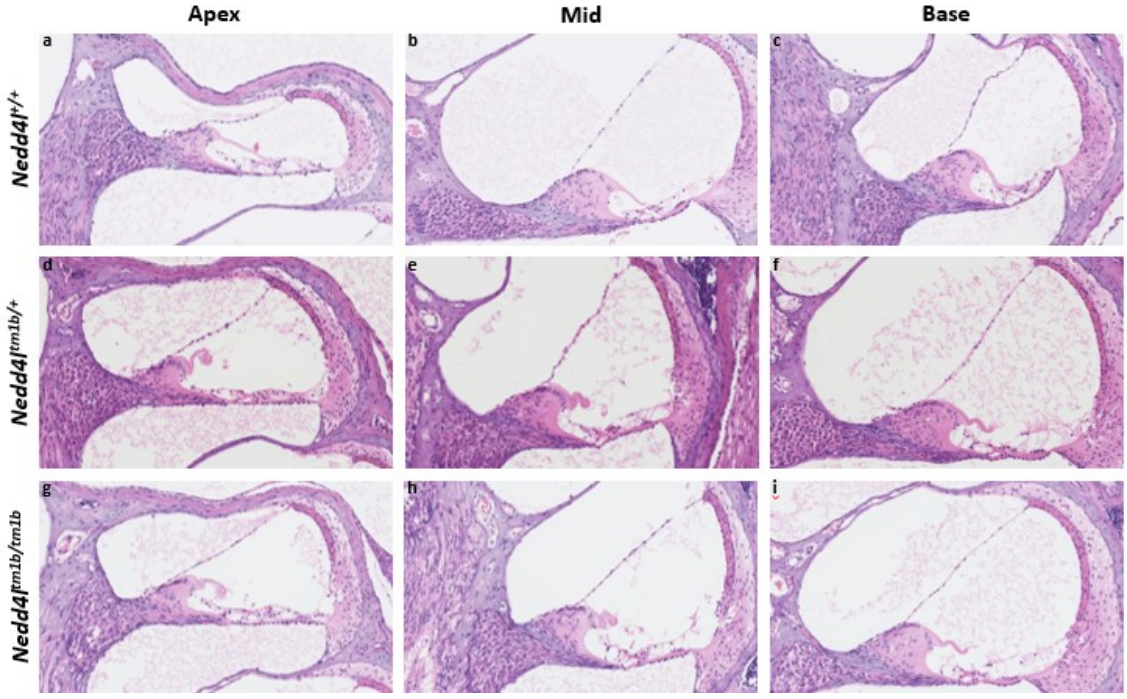

Figure 3.21: Cochlear morphology was unaffected in P16-aged Nedd4l$^{tm1b/tm1b}$ mice. Representative images of H&E-stained cochlear tissue sections from P16-aged mice. Cochlear morphology of *Nedd4l*$^{+/+}$ (a – c), *Nedd4l*$^{tm1b/+}$ (d – f) and *Nedd4l*$^{tm1b/tm1b}$ mice (g – i) looked comparable to each other, at the apical (a, d, g), mid (b, e, h) and basal (c, f, i) cochlear turns of the cochlea. For mice of each genotype, *n*= 5.

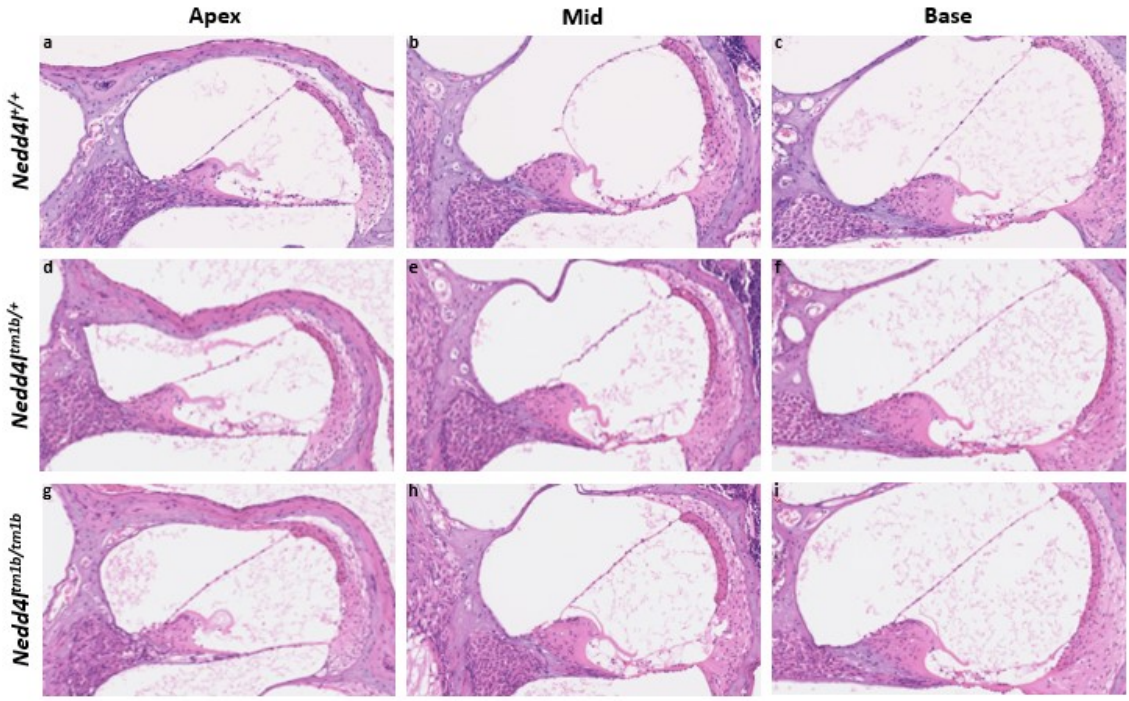

Figure 3.22: Cochlear morphology was unaffected in 3-week old Nedd4l$^{tm1b/tm1b}$ mice. Representative images of H&E-stained cochlear tissue sections from mice of 3-weeks of age. Cochlear morphology of *Nedd4l*$^{+/+}$ (a – c), *Nedd4l*$^{tm1b/+}$ (d – f) and *Nedd4l*$^{tm1b/tm1b}$ mice (g – i) looked comparable to each other, at the apical (a, d, g), mid (b, e, h) and basal (c, f, i) cochlear turns of the cochlea. For mice of each genotype, *n*= 5.

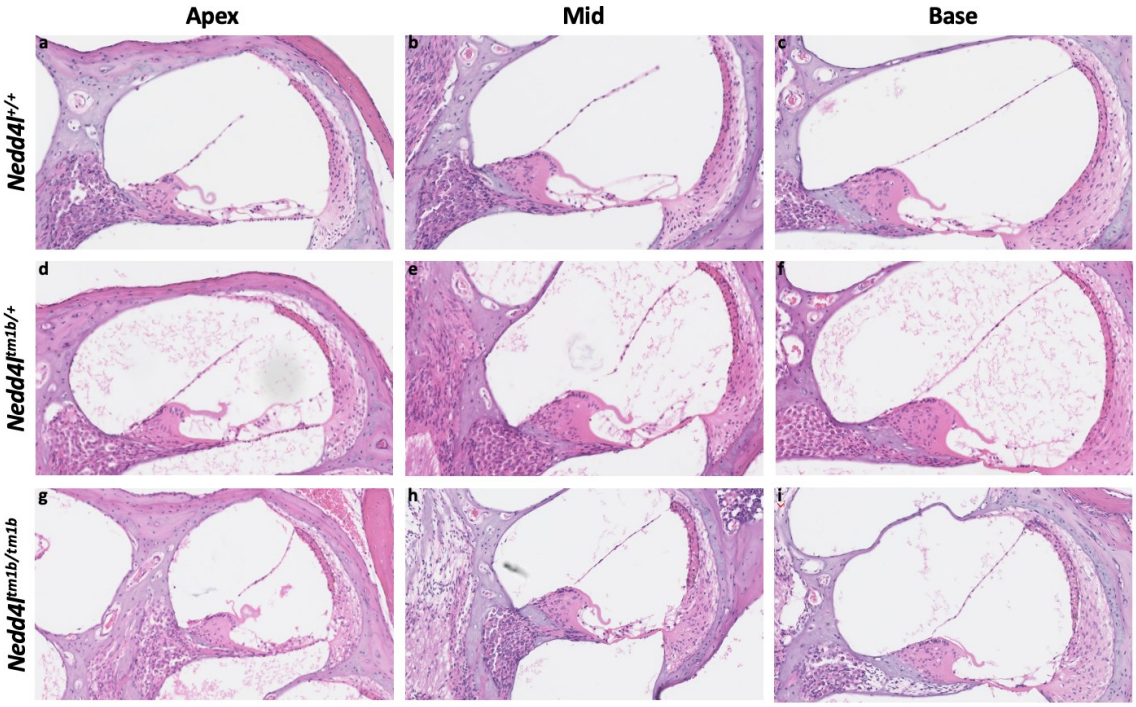

Figure 3.23: Loss of SGN in 8-week old Nedd4l$^{tm1b/tm1b}$ mice. Representative images of H&E-stained cochlear tissue sections of 8-week aged mice. Cochlear morphology of *Nedd4l*$^{+/+}$ (a – c) and *Nedd4l*$^{tm1b/+}$ (d – f) looks as expected, however *Nedd4l*$^{tm1b/tm1b}$ mice (g – h) have fewer SGN at all cochlear turns. Other cochlear structures looked similar to control *Nedd4l*$^{+/+}$ and *Nedd4l*$^{tm1b/+}$ mice. For mice of each genotype, *n*= 5.

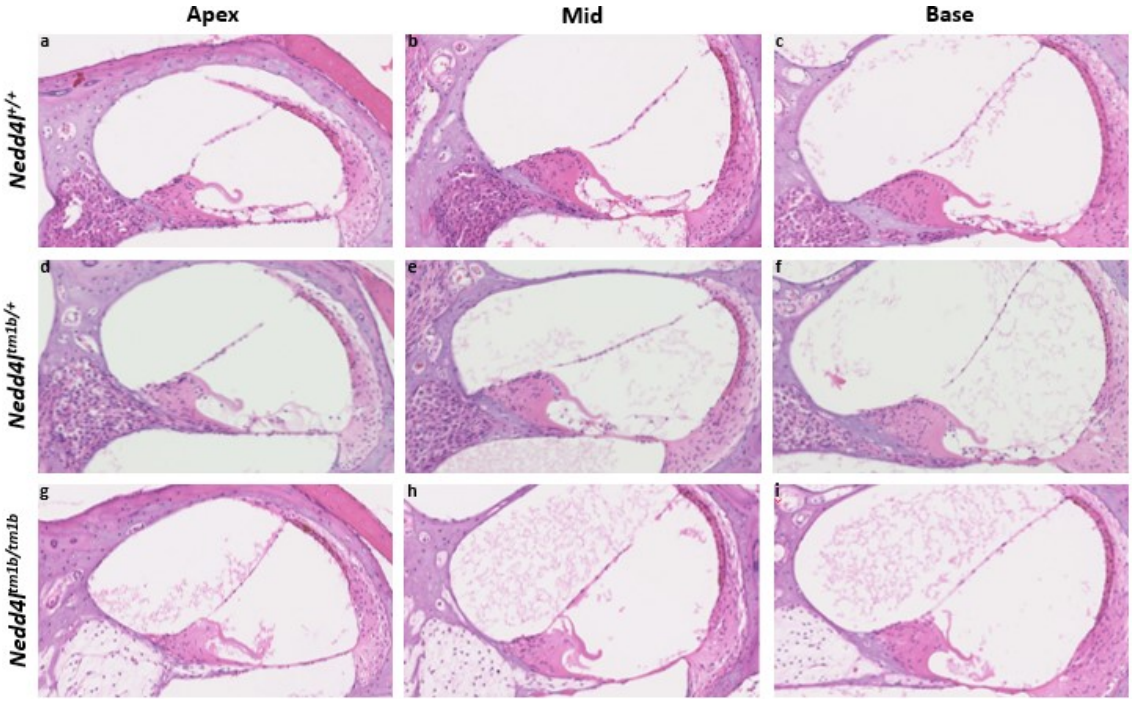

Figure 3.24: Further loss of SGNs in 6-month old Nedd4l$^{tm1b/tm1b}$ mice. H&E-stained cochlear tissue sections from 6-month aged *Nedd4l$^{tm1b/tm1b}$* mice (g – h) shows that loss of SGNs had progressed with even fewer SGN remaining at all cochlear turns compared to control *Nedd4l$^{+/+}$* (a – c) and *Nedd4l$^{tm1b/+}$* (d – f) mice. For mice of each genotype, *n*= 5.

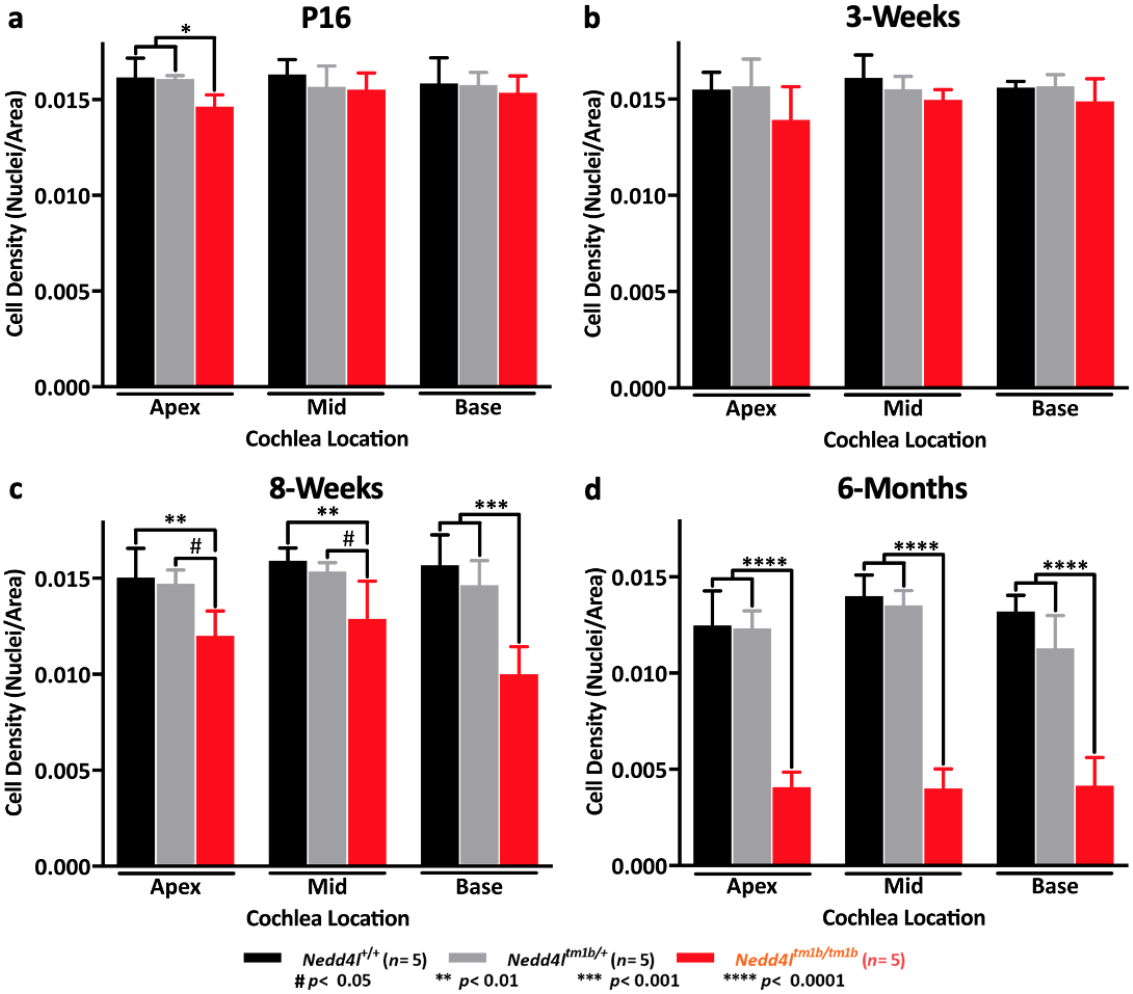

Figure 3.25: Progressive loss of SGN in Nedd4l$^{tm1b/tm1b}$ mice. SGN nuclei density within a 2500µm^2 region at all turns of the cochlea in P16 (a), 3-week (b), 8-week (c) and 6-month old (d) *Nedd4l*$^{+/+}$ (black bars), *Nedd4l*$^{tm1b/+}$ (grey bars) and *Nedd4l*$^{tm1b/tm1b}$ (red bars) mice. Counts were made from images of H&E-stained, sectioned cochlear tissue as shown in Figure 3.21 – Figure ***3.24***. **(a)** At P16, SGN nuclei density at apical turns of the cochleae in *Nedd4l*$^{tm1b/tm1b}$ mice is significantly decreased (p= 0.0111) compared to *Nedd4l*$^{+/+}$ and *Nedd4l*$^{tm1b/+}$ controls. No significant differences in the SGN nuclei density were observed at other cochlear regions. **(b)** At 3-weeks of age, no significant differences in SGN nuclei density were observed between mice of all genotypes, at all cochlear turns. **(c)** Decreased SGN nuclei density at all turns of the cochlea in 8-week old *Nedd4l*$^{tm1b/tm1b}$ mice compared to measurements from *Nedd4l*$^{+/+}$ and *Nedd4l*$^{tm1b/+}$ controls. **(d)** Further loss of SGNs at all turns of the cochlea in 6-month old *Nedd4l*$^{tm1b/tm1b}$ mice compared to controls. Counts are plotted as averages ± standard deviation and analysed using Ordinary one-way ANOVA with Tukey's Multiple Comparisons tests to compare nuclei density at specific regions of the cochlea. Statistical significance denoted by */# (p< 0.05), ** (p< 0.01), *** (p< 0.001) and **** (p<0.00001). * and # represent significant differences between *Nedd4l*$^{tm1b/tm1b}$ and *Nedd4l*$^{+/+}$ or *Nedd4l*$^{tm1b/+}$ mice, respectively.

3.2.5.3 Assessment of Afferent IHC Ribbon Synapses

Immunohistochemistry against pre- (Ribeye) and post- (GluR2) synaptic proteins were performed to assess the morphology of IHC ribbon synapses, found in the apical-mid cochlear turn of 3-week old mice (Figure 3.26). The number of functional ribbon synapses were counted, which was determined by the close proximity of Ribeye and

GluR2 signals. Co-localised, punctate staining of Ribeye and GluR2 is detectable in mice of each genotype, but fewer were present in *Nedd4l*$^{tm1b/tm1b}$ mice than control mice (Figure 3.26a – c). The co-localised puncta were quantified (Figure 3.26d), showing that on average, there are 19.4 ± 2.5 and 19.8 ± 2.5 matched Ribeye-GluR2 puncta per IHC in *Nedd4l*$^{+/+}$ and *Nedd4l*$^{tm1b/+}$ mice, but significantly less in *Nedd4l*$^{tm1b/tm1b}$ mice (15.1 ± 1.4).

Furthermore, more "orphaned" Ribeye puncta were detected in *Nedd4l*$^{tm1b/tm1b}$ mice, whereby a GluR2 puncta was not found in close proximity (Figure 3.26e). On average, 0.5 ± 0.7 and 0.7 ± 0.9 orphaned Ribeye puncta were detected in *Nedd4l*$^{+/+}$ and *Nedd4l*$^{tm1b/+}$ mice respectively, but was significantly higher in *Nedd4l*$^{tm1b/tm1b}$ mice (1.4 ± 0.9; Figure 3.26e). Orphaned GluR2 puncta were also detected but there were no significant differences in the average number of orphaned GluR2 puncta between *Nedd4l*$^{+/+}$, *Nedd4l*$^{tm1b/+}$ and *Nedd4l*$^{tm1b/tm1b}$ (0.3 ± 0.6, 0.3 ± 0.5 and 0.5 ± 0.7 respectively; Figure 3.26f).

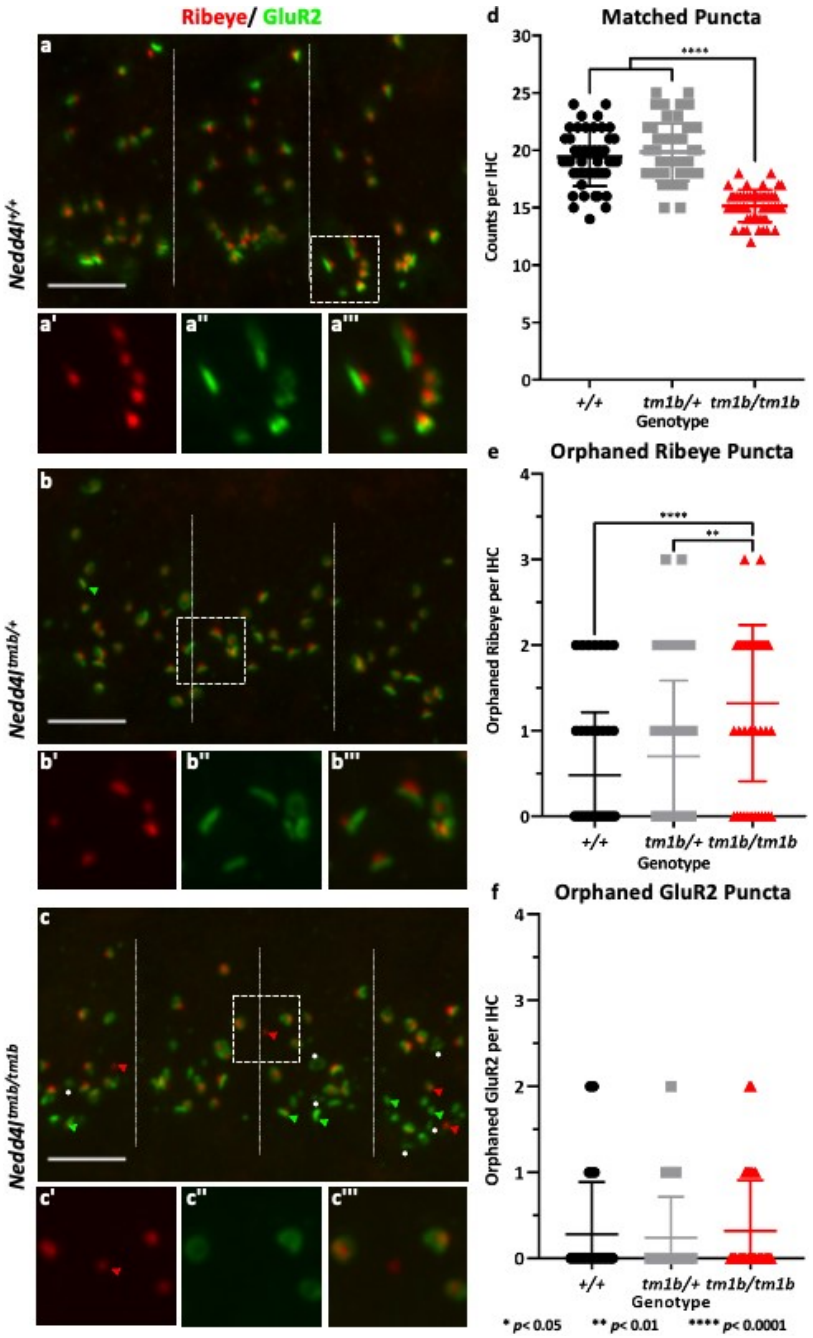

Figure 3.26: Decreased number of matched ribbon synapses at inner hair cells in Nedd4l$^{tm1b/tm1b}$ mice. Representative confocal microscopy images of Immunohistochemistry stains against pre- (Ribeye) and post- (GluR2) synaptic proteins of the IHC ribbon synapse in *Nedd4l*$^{+/+}$ (a), *Nedd4l*$^{tm1b/+}$ (b) and *Nedd4l*$^{tm1b/tm1b}$ (c) mice. The intensity of the Ribeye and GluR2 staining were increased in images displayed in (c) so that matched puncta could be visualised. White boxes demark regions of the image that are displayed below in a' – a''', b' – b''' and c' – c'''. Figures a' – c' and a'' – c'' only show Ribeye and GluR2 puncta, respectively. Figures a''' – c''' displays both Ribeye and GluR2 puncta. Counts of matched (d) and orphaned Ribeye (e) and GluR2 (f) puncta are also shown. **(a – c)** *Nedd4l*$^{tm1b/tm1b}$ mice have fewer matched Ribeye - GluR2 puncta per IHC compared to *Nedd4l*$^{+/+}$ and *Nedd4l*$^{tm1b/+}$ mice. Vertical white bars indicate different IHCs. White scale bars= 5µm. Red and green arrowheads indicate orphaned Ribeye and GluR2 puncta respectively. White asterisks indicate GluR2 puncta that could not be seen in an unaltered image. **(d)** Quantification of matched Ribeye and GluR2 puncta show that *Nedd4l*$^{tm1b/tm1b}$ mice (red triangles) have significantly fewer compared matched Ribeye and GluR2 puncta compared to control *Nedd4l*$^{+/+}$ (black circles) and *Nedd4l*$^{tm1b/+}$ mice (grey squares). **(e)** The number of orphaned Ribeye puncta was significantly higher in *Nedd4l*$^{tm1b/tm1b}$ mice compared to controls. **(f)** The number of orphaned GluR2 puncta was comparable across mice of all genotypes. Individual datapoints, the average ± standard deviation were plotted and analysed using Ordinary one-way ANOVA with Tukey's multiple comparisons test. For each genotype, *n*= 5 with puncta counted from 10 IHC per mouse.

3.2.5.4 Assessment of Cochlear Innervation

Immunohistochemistry was performed to determine if the innervation of hair cells was affected in 3-week old *Nedd4l*$^{tm1b/tm1b}$ mice. To visualise both hair cells and the innervating cochlear fibres, antibodies that were specific to α-Parvalbumin and NF200 (Neurofilament Heavy Polypeptide). α-Parvalbumin is a known Ca^{2+}-buffer protein that is expressed in both hair cell populations but with stronger expression in IHCs (Soto-Prior *et al.*, 1995; Yang *et al.*, 2004; Hackney *et al.*, 2005). NF200 is a widely used marker for neuronal intermediate filaments and for innervating fibres in cochlear tissue (Hafidi *et al.*, 1990). Images showed that both IHC and OHC populations in apical-mid cochlear regions are innervated in mice of all genotypes. However, it appears that the extent of their innervation is decreased in *Nedd4l*$^{tm1b/tm1b}$ mice (Figure 3.27a' – c'). The density of α-Parvalbumin staining detected in *Nedd4l*$^{tm1b/tm1b}$ mice appears to be clustered towards the basolateral membrane of IHCs, compared to control *Nedd4l*$^{+/+}$ and *Nedd4l*$^{tm1b/+}$ mice (Figure 3.27a – c).

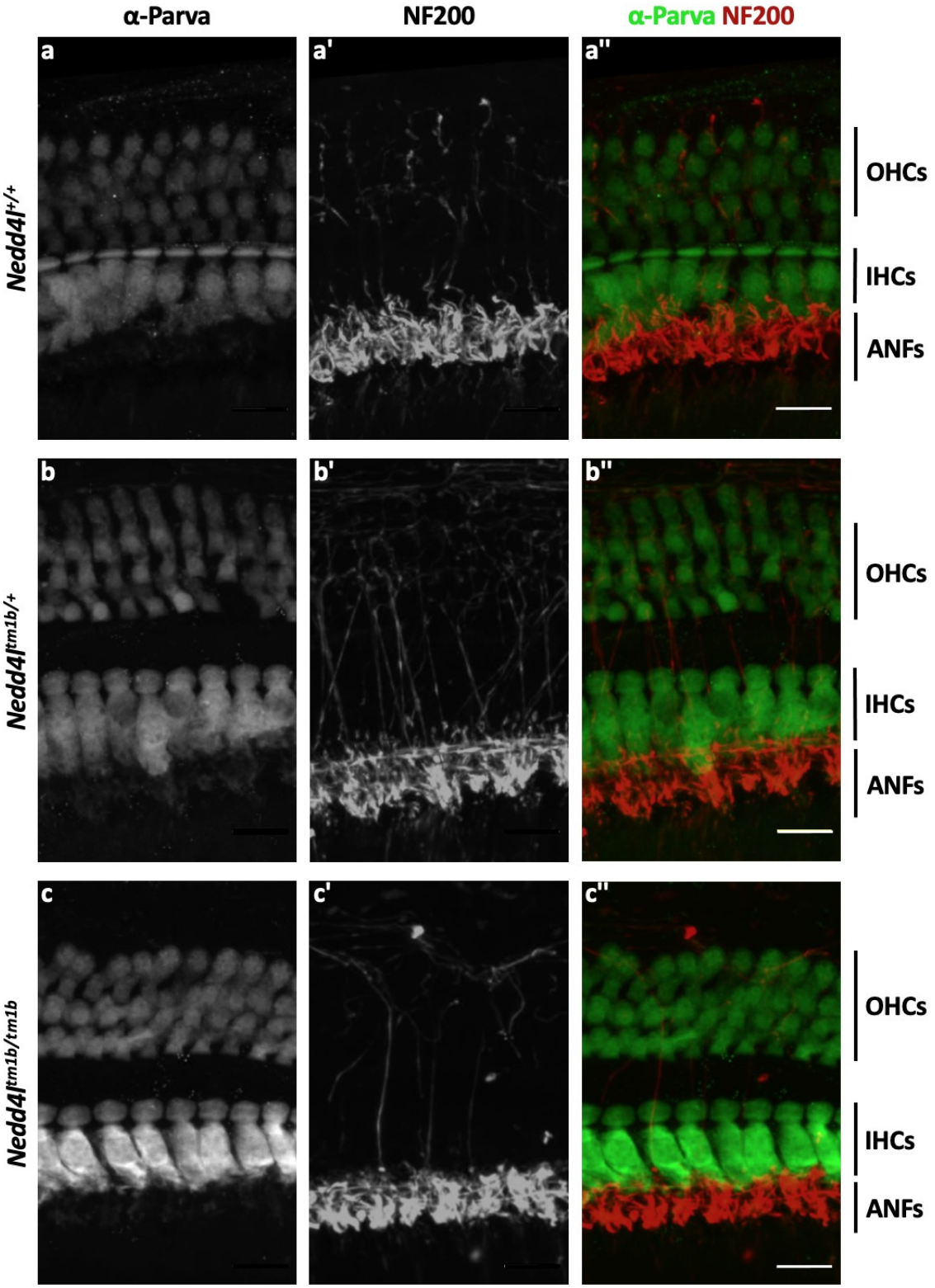

Figure 3.27: Clustered α-Parvalbumin abundance in IHCs of Nedd4l$^{tm1b/tm1b}$ mice. Representative confocal microscopy images of double Immunohistochemistry against the hair cell marker α-Parvalbumin (greyscale/green; a, b and c), and the neuronal marker NF200 (greyscale/ red; a', b' and c') in 3-week old *Nedd4l*$^{+/+}$ (a), *Nedd4l*$^{tm1b/+}$ (b) and *Nedd4l*$^{tm1b/tm1b}$ (c) mice. Labels pointing to IHC, OHC and Auditory Nerve Fibres (ANFs) populations in each image are shown on the side. **(a – c)** Intensity of α-Parvalbumin staining appears to be greater in *Nedd4l*$^{tm1b/tm1b}$ (c') compared to *Nedd4l*$^{+/+}$ (a') and *Nedd4l*$^{tm1b/+}$ (b') control mice. **(a' – c')** NF200 staining of ANFs in *Nedd4l*$^{tm1b/tm1b}$ mice suggests that IHC and OHC are less densely innervated compared to control mice. For each genotype, *n*= 3. Scale bar = 15µm.

3.2.6 Cochlear-Specific cKO of *Nedd4l*

3.2.6.1 Generation of the Auditory Phenotyping Cohort

The *Nedd4l*^{tm1b} allele is a global and constitutive KO of *Nedd4l*. Therefore a cochlear-specific *Nedd4l* cKO was generated to determine whether the hearing loss exhibited by *Nedd4l*$^{tm1b/tm1b}$ mice has a sensorineural basis. To achieve this, mice carrying the IMPC-designed, floxed *Nedd4l* allele (*Nedd4l*^{tm1c}) was crossed to a transgenic mouse line where *Cre* recombinase expression is driven by the *Sox10* promoter (*Sox10-Cre*; Jax Stock No: 025807. Imported B6;CBA-Tg(*Sox10-Cre*)1Wdr/J) Due to time constraints, mice carrying the *Sox10-Cre* transgene were backcrossed to C57BL/6N mice for only two generations before crossing to mice carrying the *Nedd4l*^{tm1c} allele. (Matsuoka *et al.*, 2005). *Sox10* expression is required for development of migratory neural crest cell progenitor and is consistently expressed in cochlear tissue during embryonic and adult ages, except for sensory hair cells from E16.5 (Watanabe *et al.*, 2000; Wakaoka *et al.*, 2013).

A specific breeding strategy was adopted to generate a *Sox10*-driven *Nedd4l* cKO phenotyping cohort to ensure that the *Sox10-Cre* transgene was inherited maternally. This is based on expression studies that were conducted to characterise the profile of *Cre* expression in *Sox10-Cre* transgenic mice by crossing them to an Cre-inducible *lacZ* reporter KI mouse line (*R26R-lacZ*; Jax Stock No: 003474; Imported as B6.129S4-*Gt(ROSA)26Sor*^{tm1Sor}/J). X-Gal stains of cochlear tissue derived from mice that carry the *Sox10-Cre* transgene and the *R26R-lacZ* KI allele, were performed (Figure 3.28). When the *Sox10-Cre* transgene is paternally inherited, X-Gal stain was detected in cochlear tissues that endogenously express *Sox10* such as the SCs of the OoC, Reissner's

membrane (RM), SV, SL and innervating fibres of SGNs (Figure 3.28b). However, *Cre* expression was also detected in IHC and OHC populations which do not endogenously express *Sox10*, as demonstrated by Wakaoka *et al.*, 2013 (Figure 3.28b, e).

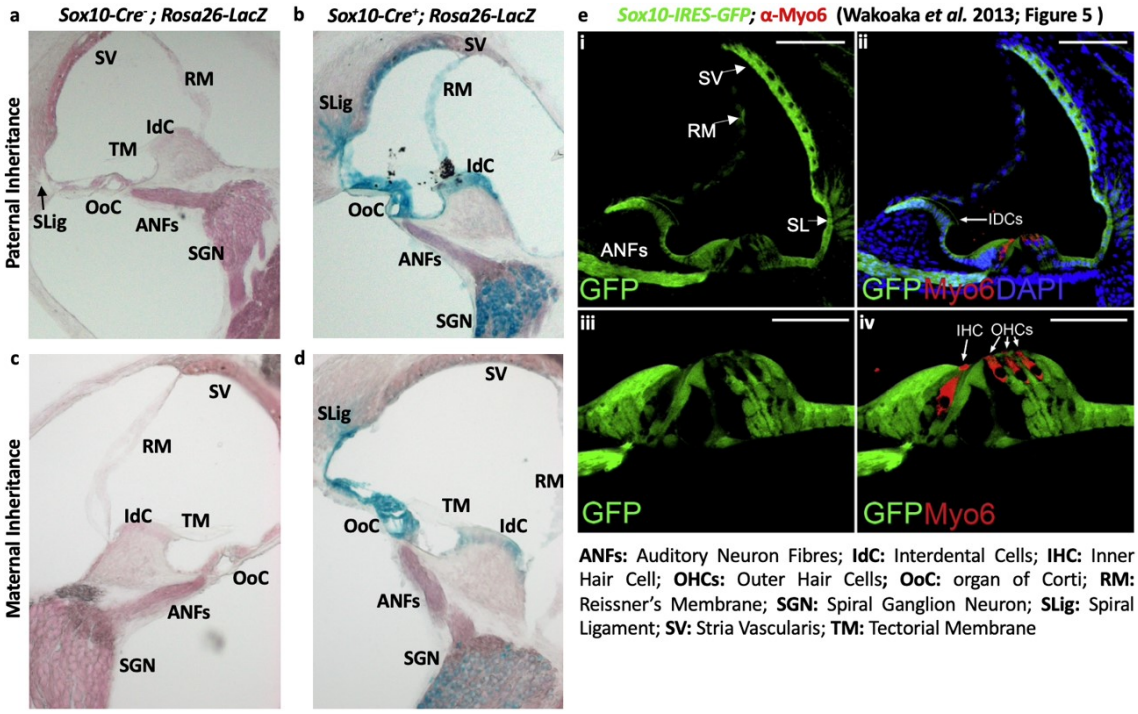

Figure 3.28: Unspecific expression of the Sox10-Cre transgene in non-Sox10 expressing cochlear tissues. X-Gal stains of sectioned cochlear tissue from mice that carry the *Rosa26-lacZ* KI allele, and paternally (b) or maternally (d) inherited the *Sox10-Cre* transgene. Their respective genetic controls which do not carry the *Sox10-Cre* transgene (a, c). Adapted from Wakaoka et al., 2013, immunohistochemistry images of sectioned cochlear tissue from P21-aged mice that carry a "*Sox10-IRES-GFP"* KI allele, in which GFP demarks locations of endogenous *Sox10* expression (e). **(a, b)** Paternal inheritance of the *Sox10-Cre* transgene resulted in *lacZ* expression across the entire OoC, SGN, SV, SLig, IdC, RM and ANF. No X-Gal staining was detected in mice that only carry the *Rosa26-lacZ* allele. *n*= 2 and 1, for mice that do and do not carry the *Sox10-Cre* transgene. **(c, d)** Maternal inheritance of the *Sox10-Cre* transgene resulted in X-Gal staining in the OoC, SGN, SL, RM, IdC and ANFs. *n*= 2 and 1, for mice that do and do not carry the *Sox10-Cre* transgene. **(e)** Immunohistochemistry images published by Wakaoka et al., 2013, which depicts GFP (marker of endogenous *Sox10* expression) fluorescence in numerous cochlear tissues, including SV, SL and ANFs (i, ii). GFP/Sox10 expression is also detected in IdCs (ii) and the SCs surrounding the Myo6a-expressing hair cells (iii, iv). Scale bars = 100µm in i and ii. Scale bars = 50µm in iii and iv.

When the *Sox10-Cre* transgene is maternally inherited, X-Gal staining was also detected in the SCs, RM, SL and IdCs too (Figure 3.28d). Maternal inheritance of the *Sox10-Cre* transgene resulted in a more faithful recapitulation of endogenous *Sox10* cochlear expression as presented by Wakaoka *et al.*, 2013, compared with paternal inheritance of the *Sox10-Cre* transgene, as no X-Gal staining could be detected in IHCs (Figure 3.28d, e). As expected, no staining was detected in mice that do not carry the *Sox10-Cre*

transgene but do carry the *Rosa26-lacZ* KI allele (Figure 3.28a, c). By ensuring that the *Sox10-Cre* transgene is maternally inherited, Cre expression and recombination of the *Nedd4l*^{tm1c} allele would be restricted to the post-migratory, post-otic neural crest population of mouse embryonic development. Therefore, in the instance that hearing loss is detected in these cKO mice, it would suggest that *Nedd4l* is required in these cells for hearing function.

The *Sox10*-driven *Nedd4l* cKO phenotyping cohort was generated by crossing male, heterozygous *Nedd4l*^{tm1c} mice that did not carry the *Sox10-Cre* allele (*Nedd4l*$^{tm1c/+}$; *Sox10-Cre*$^{-}$) to female, *Nedd4l*$^{tm1c/+}$ mice that also carried the *Sox10-Cre* transgene (*Nedd4l*$^{tm1c/+}$; *Sox10-Cre*$^{+}$). Surprisingly, inspection of the genotypes of mice produced showed that a *Sox10*-driven cKO of *Nedd4l* results in lethality, as only one homozygous *Nedd4l*^{tm1c} mouse that carried the *Sox10-Cre* transgene (*Nedd4l*$^{tm1c/tm1c}$; *Sox10-Cre*$^{+}$) survived (Figure 3.29). The ratio of the number of mice of each genotype born through this breeding strategy was significantly different to the expected Mendelian ratios, as demonstrated by Chi-square tests.

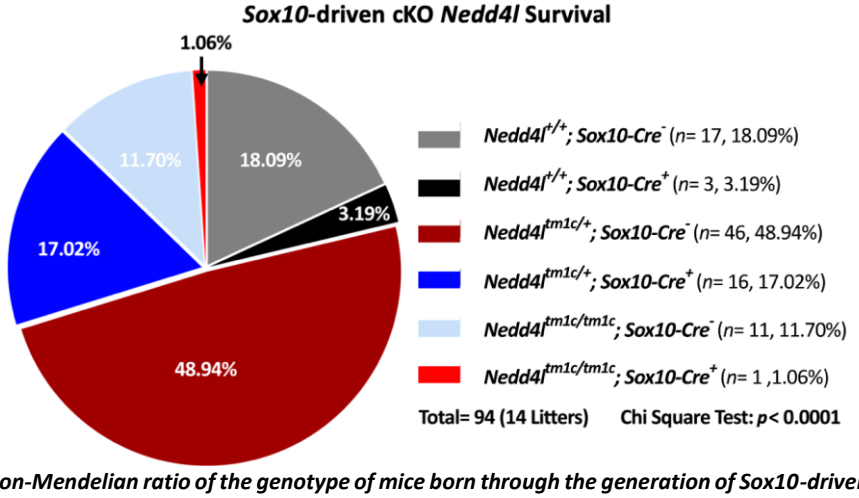

Figure 3.29: Non-Mendelian ratio of the genotype of mice born through the generation of Sox10-driven, cKO Nedd4l mice. The ratio of mice of each possible genotype that was born and survived to weaning age, generated from intercross breeds between *Nedd4l*$^{tm1c/+}$; *Sox10-Cre*$^{+}$ and *Nedd4l*$^{tm1c/+}$; *Sox10-Cre*$^{-}$ mice. Only 1 *Nedd4l*$^{tm1c/tm1c}$; *Sox10-Cre*$^{+}$ (red) mouse was counted, which is significantly fewer than the number expected (12 of the 94 mice born). Chi-Square tests were performed to determine if the phenotyping cohort produced was significantly different from the expected Mendelian ratio of genotypes of mice, born from the intercross breeds.

3.2.6.2 Auditory Phenotyping

Longitudinal auditory phenotyping was conducted despite the underrepresentation of *Nedd4l*$^{tm1c/tm1c}$*; Sox10-Cre*$^{+}$ mice from the intercrosses. At 3-weeks of age, the ABR thresholds of mice carrying the wild type *Nedd4l* allele and the *Sox10-Cre* transgene (*Nedd4l*$^{+/+}$*; Sox10-Cre*$^{+}$) is not elevated and comparable to thresholds recorded from wild type mice indicating that the presence of the *Sox10-Cre* does not impact auditory function (*Nedd4l*$^{+/+}$*; Sox10-Cre*$^{-}$) (Figure 3.30a). At 3-weeks of age, *Nedd4l*$^{tm1c/+}$*; Sox10-Cre*$^{+}$ mice had significantly elevated hearing thresholds compared to control *Nedd4l*$^{tm1c/+}$ mice that did not carry the *Sox10-Cre* transgene (*Nedd4l*$^{tm1c/+}$*; Sox10-Cre*$^{-}$), but only in response to 8kHz frequency stimulus (Figure 3.30b).

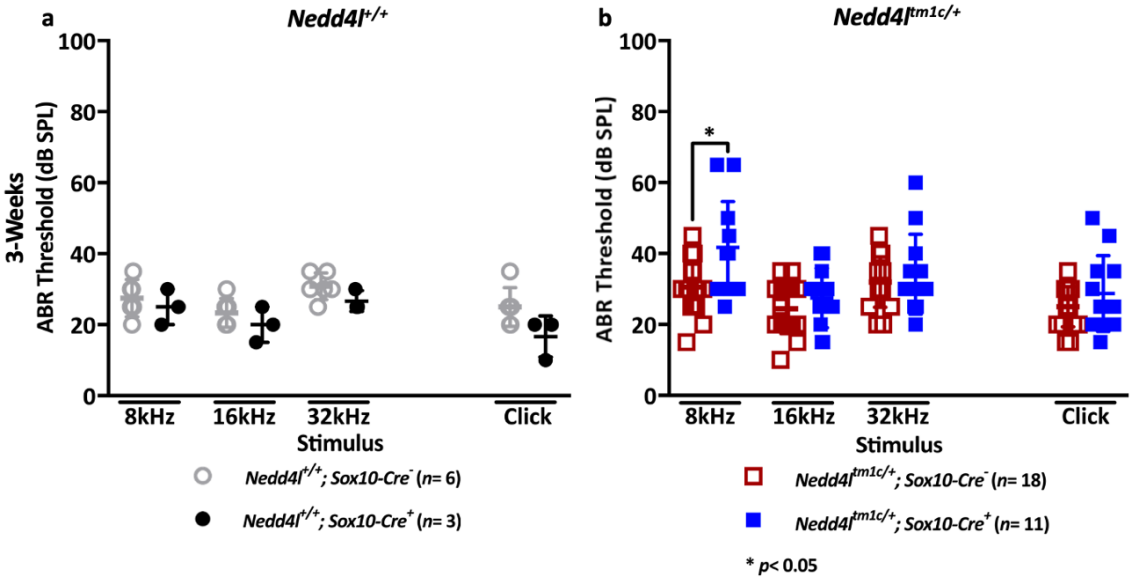

Figure 3.30: 3-Week old Nedd4l*$^{tm1c/+}$*; Sox10-Cre*$^{+}$ *mice display low frequency hearing loss. Recorded ABR thresholds of 3-week old mice in the *Sox10*-driven, *Nedd4l* cKO phenotyping cohort. **(a)** No difference in ABR thresholds between *Nedd4l*$^{+/+}$*; Sox10-Cre*$^{-}$ (grey, hollow circles) and *Nedd4l*$^{+/+}$*; Sox10-Cre*$^{+}$ (black, filled circles) mice. **(b)** Compared to control *Nedd4l*$^{tm1c/+}$*; Sox10-Cre*$^{-}$ (brown, hollow squares) mice, *Nedd4l*$^{tm1c/+;}$ *Sox10-Cre*$^{+}$ (blue, hollow squares) mice displayed elevated ABR thresholds only in response to an 8kHz frequency stimulus (p= 0.0164). Individual thresholds of each mouse were plotted along with the average threshold (central line) ± standard deviation. Average thresholds between mice of different genotypes were analysed using Unpaired T test with Welch's Correction to compare thresholds recorded in response to each stimulus. Statistical significance was denoted with * which indicated that p< 0.05.

At 8-weeks of age, the hearing loss of *Nedd4l*$^{tm1c/+}$*; Sox10-Cre*$^{+}$ mice had progressed to mid frequency (16kHz) and broadband click stimuli too (Figure 3.31a). The large standard deviation of recorded thresholds suggested that two populations of *Nedd4l*$^{tm1c/+}$*; Sox10-Cre*$^{+}$ mice existed; they either experienced profound hearing loss (HL) or displayed normal hearing (NH) that was comparable to control *Nedd4l*$^{tm1c/+}$*;Sox10-Cre*$^{-}$ mice (Figure 3.31b). Auditory thresholds of *Nedd4l*$^{tm1c/+}$*; Sox10-Cre*$^{+}$ (HL) mice were significantly elevated when compared to *Nedd4l*$^{tm1c/+}$*; Sox10-Cre*$^{+}$ (NH) mice and *Nedd4l*$^{tm1c/+}$*;Sox10-Cre*$^{-}$ mice. Overall, this suggests that *Nedd4l* function could be required in *Sox10*-expressing cochlear cells.

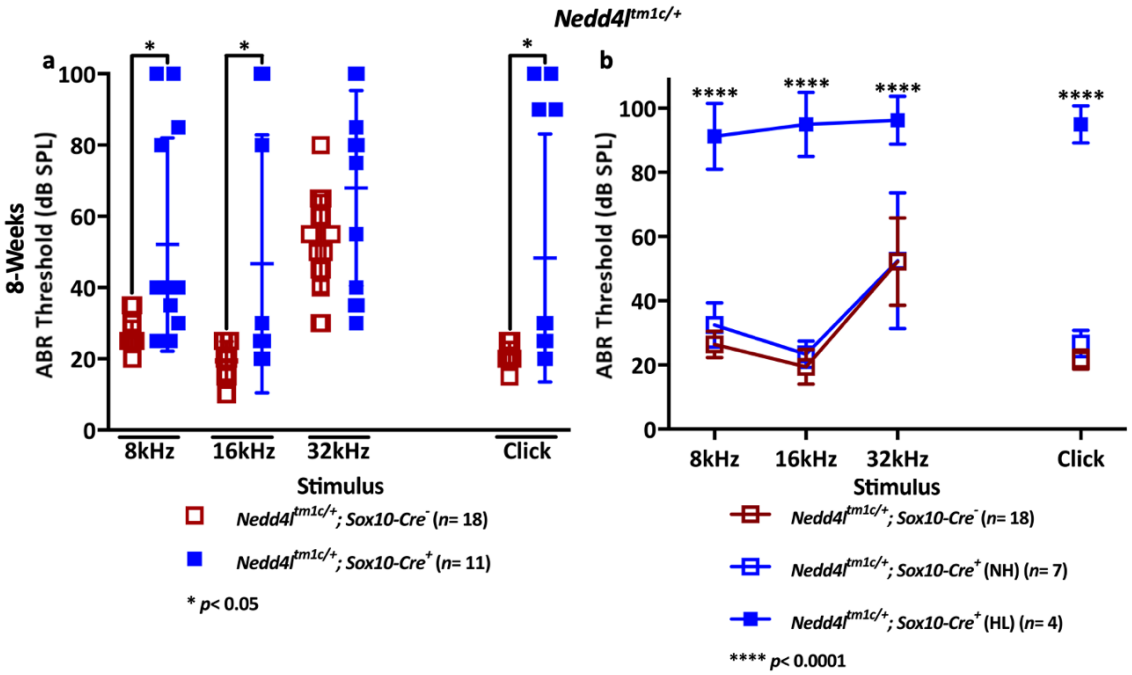

Figure 3.31: Nedd4l*$^{tm1c/+}$*; Sox10-Cre*$^{+}$ *mice experience variable profound hearing loss. **(a)** The averaged ABR thresholds of *Nedd4l*$^{tm1c/+}$*; Sox10-Cre*$^{+}$ mice were significantly elevated compared to control *Nedd4l*$^{tm1c/+}$*; Sox10-Cre*$^{-}$ mice, in response to an 8 and 16kHz and click stimuli (p= 0.015, 0.0261 and 0.0232, respectively). Individual thresholds were plotted along with averages (central line) ± standard deviation. Average thresholds between mice of different genotypes were analysed using Unpaired T test with Welch's Correction to compare thresholds recorded in response to each stimulus. **(b)** Two distinct population of *Nedd4l*$^{tm1c/+}$*; Sox10-Cre*$^{+}$ mice could be separated based on their recorded auditory thresholds. *Nedd4l*$^{tm1c/+}$*; Sox10-Cre*$^{+}$ (HL) mice (blue squares) display profoundly elevated thresholds in response to all stimuli that is statistically significant compared to *Nedd4l*$^{tm1c/+}$*; Sox10-Cre*$^{+}$ (NH) and *Nedd4l*$^{tm1c/+}$*; Sox10-Cre*$^{-}$ mice (p< 0.0001). Average thresholds ± standard deviation was plotted and analysed using Ordinary one-way ANOVA tests with Tukey's multiple comparisons test. Statistical significance denoted by * and **** when p< 0.05 and 0.0001, respectively.

DPOAE responses recorded from 3-months of age *Nedd4l*$^{tm1c/+}$*; Sox10-Cre*$^{+}$ mice were lower compared to those recorded in control *Nedd4l*$^{tm1c/+}$*; Sox10-Cre*$^{-}$ mice (Figure 3.32), but the differences were not statistically significant.

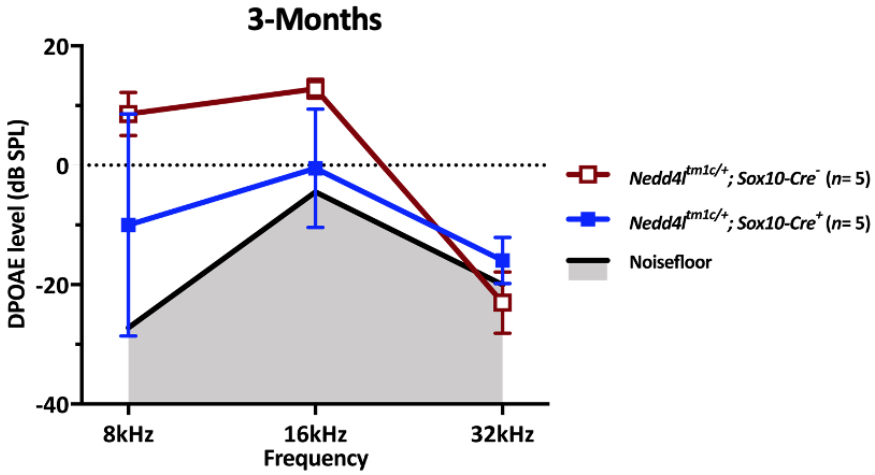

Figure 3.32: Reduced DPOAE response of Nedd4l*$^{tm1c/+}$*; Sox10-Cre*$^{+}$ *mice. Decreased OHC function in *Sox10*-driven cKO of *Nedd4l* mice. DPOAE response levels of *Nedd4l*$^{tm1c/+}$*; Sox10-Cre*$^{+}$ (blue, filled squares) mice are not significantly different to control *Nedd4l*$^{tm1c/+}$*; Sox10-Cre*$^{-}$ (brown, hollow squares) mice, in response to an 8 and 16kHz stimuli. Data presented as averages ± standard deviation and analysed Unpaired T test with Welch's Correction to compare DPOAE response levels recorded in response to each stimulus.

ABR thresholds were also recorded from the single *Nedd4l*$^{tm1c/tm1c}$*; Sox10-Cre*$^{+}$ mouse that survived past weaning ages (Figure 3.33). At 3-weeks of age, recorded thresholds of the *Nedd4l*$^{tm1c/tm1c}$*; Sox10-Cre*$^{+}$ mouse was comparable to control *Nedd4l*$^{tm1c/tm1c}$*; Sox10-Cre*$^{-}$ mice, but had elevated to profound levels of hearing loss when tested again at 8-weeks of age (Figure 3.33). As only one *Nedd4l*$^{tm1c/tm1c}$*; Sox10-Cre*$^{+}$ mouse underwent auditory phenotyping, no statistical analysis was performed.

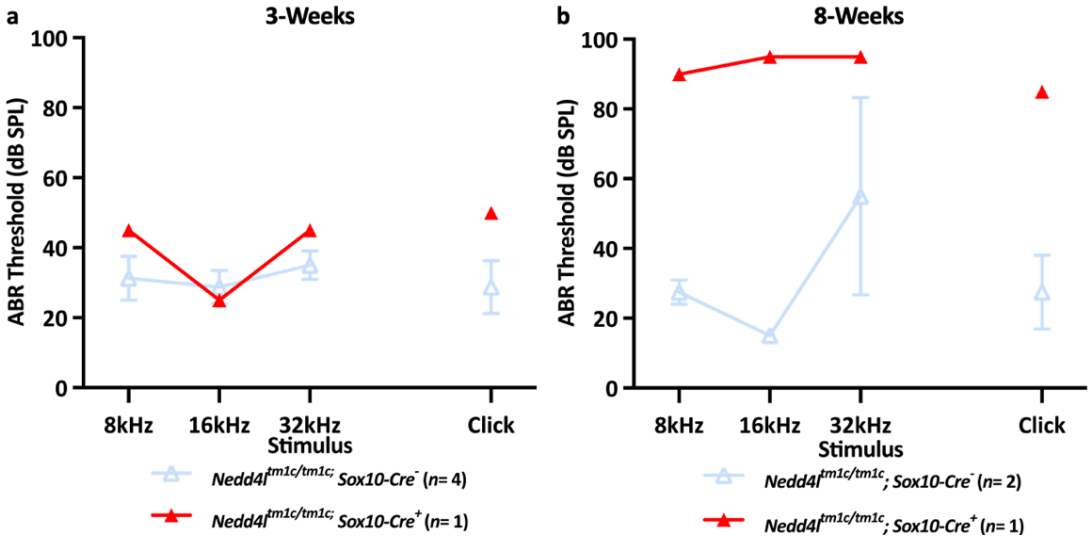

Figure 3.33: A Sox10-driven, cKO Nedd4l mouse displayed profound loss of auditory function. Recorded ABR thresholds of *Nedd4l$^{tm1c/tm1c}$; Sox10-Cre^{-}* (blue, hollow triangles) and *Nedd4l$^{tm1c/tm1c}$; Sox10-Cre^{+}* (red, filled triangles) mice at 3- (a) and 8-weeks of age (b). **(a)** ABR thresholds recorded at 3-weeks of age was statistically comparable between mice of both genotypes. **(b)** At 8-weeks of age, the *Nedd4l$^{tm1c/tm1c}$; Sox10-Cre^{+}* mouse exhibited profoundly elevated hearing thresholds.

3.2.6.3 Cochlear Pathology

Histological assessment of *Nedd4l$^{tm1c/+}$; Sox10-Cre^{+}* mice cochlear tissue was performed to determine the primary cause of their auditory dysfunction. Cochlear morphology was assessed by H&E staining. The cochlear morphology of *Nedd4l$^{tm1c/+}$; Sox10-Cre^{+}* mice looked comparable to control *Nedd4l$^{tm1c/+}$; Sox10-Cre^{-}* mice (Figure 3.34a – f). Counts of SGN nuclei and the density measurements were calculated too. There were no significant differences in SGN nuclei density at all turns of the cochlea in *Nedd4l$^{tm1c/+}$; Sox10-Cre^{+}* mice (Figure 3.34g).

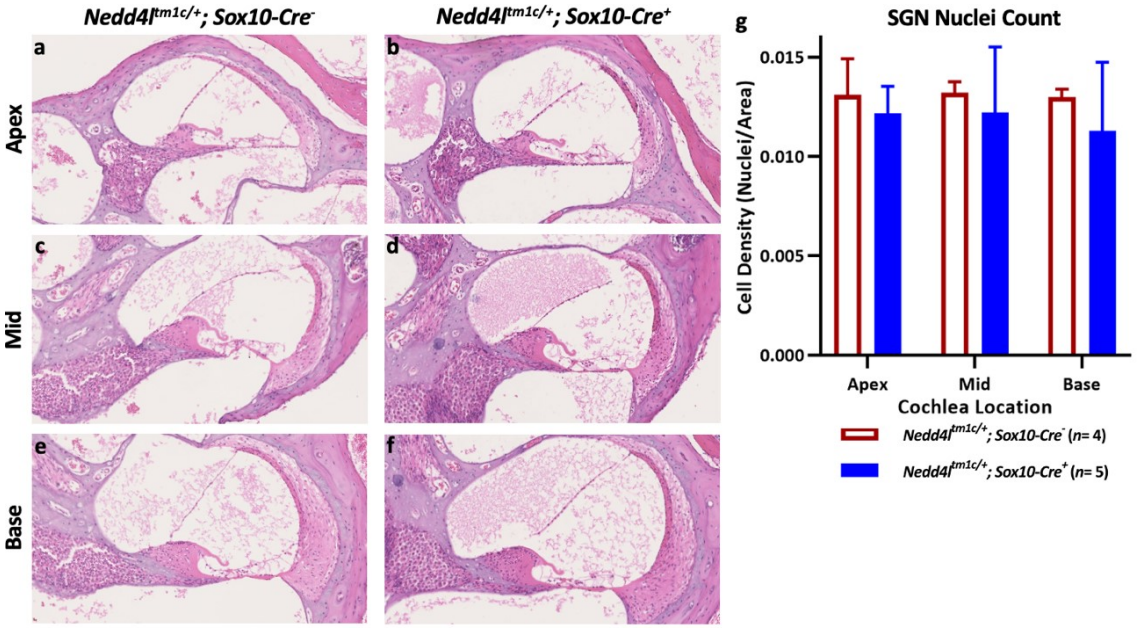

Figure 3.34: Cochlear morphology appears unaffected in Nedd4l$^{tm1c/+}$; Sox10-Cre^{+} mice. Representative images of H&E-stained, cochlear tissue sections from 3-months of age *Nedd4l$^{tm1c/+}$; Sox10-Cre^{-}* (a – c) and *Nedd4l$^{tm1c/+}$; Sox10-Cre^{+}* mice (d – f). Images of the apical (a, d), mid (b, e) and basal (c, f) cochlear turns, from mice of both genotypes are displayed. SGN nuclei density within a 2500µm^2 region, at all turns of the cochlea, is quantified and displayed (g). **(a – f)** Cochlear morphology appears unperturbed in *Nedd4l$^{tm1c/+}$; Sox10-Cre^{+}* mice compared to *Nedd4l$^{tm1c/+}$; Sox10-Cre^{-}* controls, at all turns of the cochlea. **(g)** Quantification of SGN nuclei density showed no significant differences between *Nedd4l$^{tm1c/+}$; Sox10-Cre^{-}* (brown, hollow bars) and *Nedd4l$^{tm1c/+}$; Sox10-Cre^{+}* (blue, filled bars). Density is presented as averages ± standard deviation and analysed using Unpaired T test with Welch's Correction to compare nuclei density at specific cochlear turns.

3.2.7 Hair Cell-Specific cKO of *Nedd4l*

3.2.7.1 Generation of the Auditory Phenotyping Cohort

A hair cell specific *Nedd4l* cKO was also generated to determine if *Nedd4l* expression is required for hair cell function. To this end, the *Nedd4l*^{tm1c} mouse line was crossed to mice heterozygous for a KI allele in which the *Myo15* coding region was replaced with the Cre recombinase protein (*Myo15-Cre)* (Caberlotto *et al.*, 2011). The *Myo15* gene is well-documented for its hair cell specific, early postnatal age onset of expression (Liang *et al.*, 1999; Caberlotto *et al.*, 2011). Robust Cre expression from the *Myo15-Cre* KI allele is first detected in both hair cell populations at P4.

The phenotyping cohort of hair cell specific *Nedd4l* cKO mice were generated through an intercross breed between *Nedd4l*$^{tm1c/+}$ mice that either do or do not carry the *Myo15-Cre* allele (*Nedd4l*$^{tm1c/+}$*; Myo15-Cre*$^{+}$ and *Nedd4l*$^{tm1c/+}$*; Myo15-Cre*$^{-}$ respectively). Litters of mice were produced in the expected Mendelian ratios and a proportionate number of *Myo15-Cre*-driven *Nedd4l* KO (*Nedd4l*$^{tm1c/tm1c}$*; Myo15-Cre*$^{+}$) mice were born. (Figure 3.35).

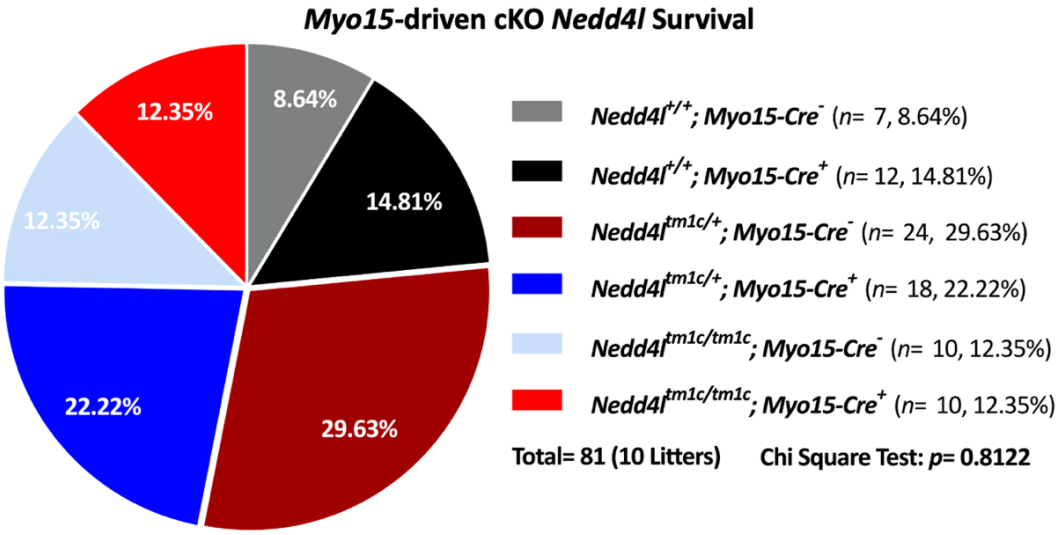

Figure 3.35: Mendelian ratio of genotypes of mice born through the generation of Myo15-driven, Nedd4l cKO mice. The ratio of mice of each possible genotype that was born and survived to weaning age, generated from intercross breeds between *Nedd4l*$^{tm1c/+}$*; Myo15-Cre*$^{+}$ and *Nedd4l*$^{tm1c/+}$*; Myo15-Cre*$^{-}$ mice. A Chi-Square test showed that the ratio of genotypes is statistically comparable to the expected Mendelian ratio of genotypes of the adopted breeding strategy.

3.2.7.2 Auditory Phenotyping

Longitudinal ABR tests were performed at 3- and 8-weeks of age to assess the auditory function of *Myo15*-driven *Nedd4l* cKO mice (*Nedd4l*$^{tm1c/tm1c}$; *Myo15-Cre*$^{+}$). Recorded ABR thresholds of wild type *Nedd4l* mice that carry the *Myo15-Cre* KI allele (*Nedd4l*$^{+/+}$*; Myo15-Cre*$^{+}$) were comparable to those recorded from its appropriate control wild type (*Nedd4l*$^{+/+}$*; Myo15-Cre*$^{-}$), at both time points tested (Figure 3.36a, b respectively). This result suggests that if any measurable auditory dysfunction is observed in *Nedd4l*$^{tm1c/tm1c}$; *Myo15-Cre*$^{+}$ mice, it would be due to the loss of *Nedd4l* in hair cells and not the presence of the *Myo15-Cre* KI allele. Both *Nedd4l*$^{tm1c/+}$; *Myo15-Cre*$^{+}$ (blue squares) and *Nedd4l*$^{tm1c/tm1c}$; *Myo15-Cre*$^{+}$ mice (red triangles) display statistically comparable auditory thresholds to their respective controls at 3- and 8-weeks of age (Figure 3.36c – f). Overall, this indicates that *Nedd4l* is not required for hair cell function of mice older than P4.

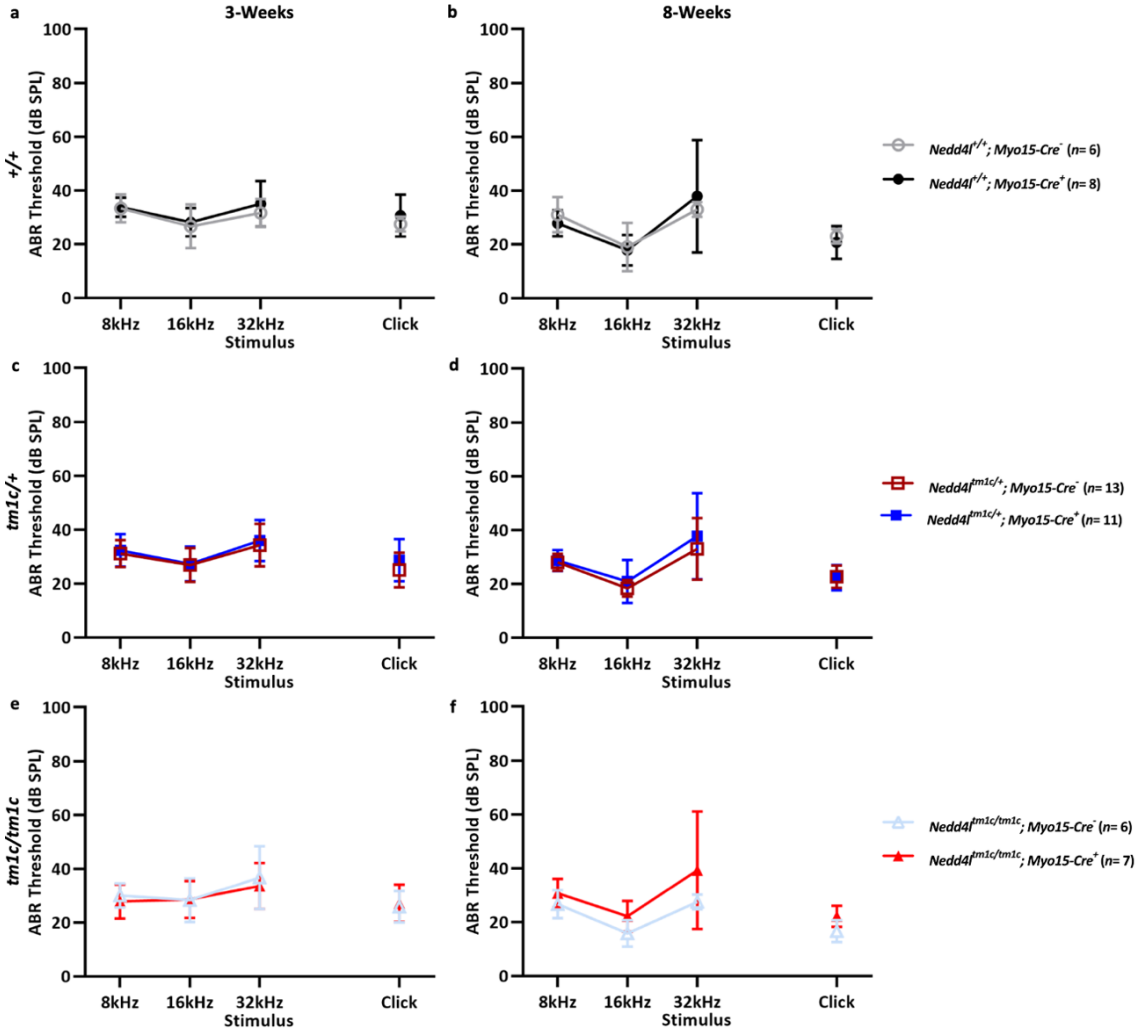

Figure 3.36: Myo15-driven loss of Nedd4l does not cause profound hearing loss. ABR thresholds of all mice born from intercrosses to generate *Myo15*-driven cKO *Nedd4l* mice. ABR tests were performed at 3- (a, c, e) and 8- (b, d, f) weeks of age. **(a, c, e)** At 3-weeks of age, there was no difference in ABR thresholds between mice of all genotypes. **(b, d, f)** At 8-weeks of age, the auditory thresholds recorded are statistically similar between *Myo15*-Cre KI allele carriers and their respective controls. Data presented as averages ± standard deviation and analysed using Unpaired T test with Welch's Correction to compare thresholds recorded in response to each stimulus.

DPOAE tests performed on 3-months old *Nedd4l*$^{tm1c/tm1c}$*; Myo15-Cre*$^{+}$ mice also showed no difference in OHC function to *Nedd4l*$^{tm1c/tm1c}$*; Myo15-Cre*$^{-}$ controls, as the recorded DPOAE responses were comparable. However, the DPOAE level in response to high frequency stimuli recorded from mice of both genotypes were at similar levels to the noisefloor (Figure 3.37).

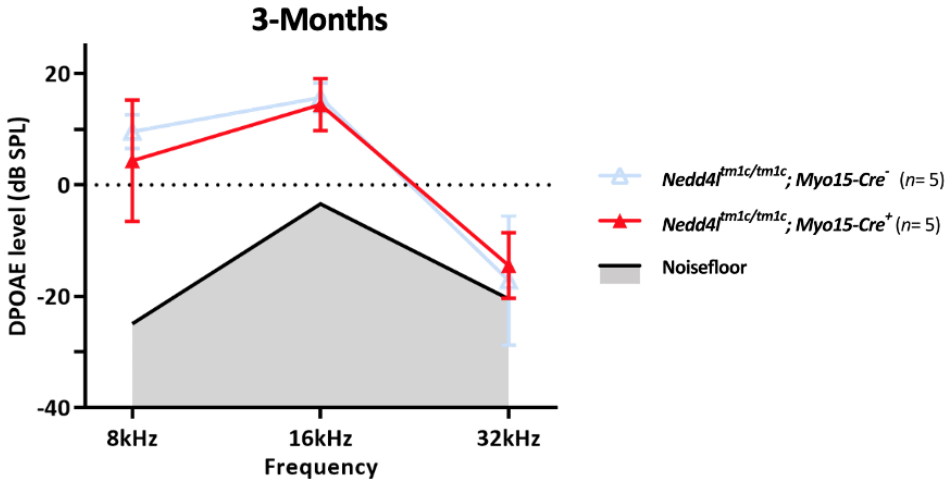

Figure 3.37: Reduced DPOAE response of both Nedd4l$^{tm1c/tm1c}$; Myo15-Cre^{-} and Nedd4l$^{tm1c/tm1c}$; Myo15-Cre^{+} mice. DPOAE levels of 3-months of age *Nedd4l$^{tm1c/tm1c}$; Myo15-Cre^{+}* (red, filled triangles) and *Nedd4l$^{tm1c/tm1c}$; Myo15-Cre^{-}* (blue, hollow triangles) mice. Recorded DPOAE levels from both mice are comparable to each other. Data presented as averages ± standard deviation and analysed Unpaired T test with Welch's Correction to compare DPOAE response levels recorded in response to each stimulus.

3.2.7.3 Cochlear Pathology

The morphology of cochlear tissue from *Nedd4l$^{tm1c/tm1c}$; Myo15-Cre^{+}* mice was assessed by H&E staining of cochlear sections. The cochlear tissue of *Nedd4l$^{tm1c/tm1c}$; Myo15-Cre^{+}* and *Nedd4l$^{tm1c/tm1c}$; Myo15-Cre^{-}* mice were comparable to each other with no degeneration or abnormalities in cochlear tissue observed in either genotype (Figure 3.38a – c, d – f respectively). In addition, the calculated SGN nuclei density showed that there was little difference in the number of SGN found in cochlear tissue of *Nedd4l$^{tm1c/tm1c}$; Myo15-Cre^{+}* and *Nedd4l$^{tm1c/tm1c}$; Myo15-Cre^{-}* mice (Figure 3.38g). Overall, this suggests that loss of *Nedd4l* in *Myo15*-expressing hair cells does not affect auditory function.

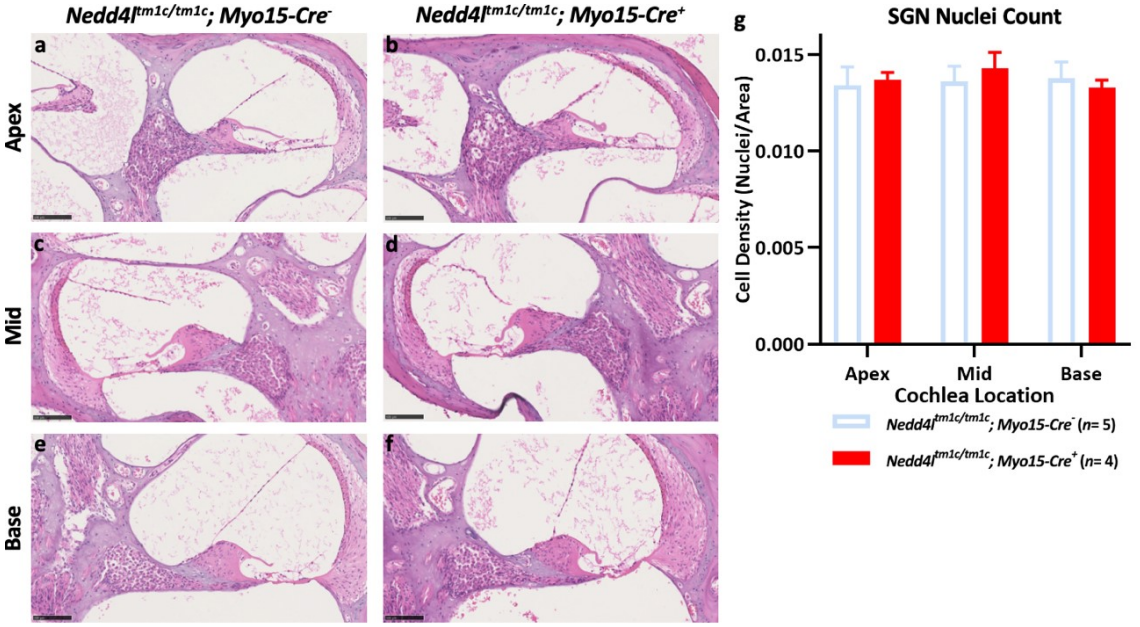

Figure 3.38: Cochlear morphology appears unaffected in Nedd4l$^{tm1c/tm1c}$; Myo15-Cre^{+} mice. Representative images of apical (a, d), mid (b, e) and basal (c, f) cochlear turns of H&E stained cochlear tissue sections from 3-months of age *Nedd4l$^{tm1c/tm1c}$; Myo15-Cre^{-}* (a – c) and *Nedd4l$^{tm1c/tm1c}$; Myo15-Cre^{+}* mice (d – f). The SGN nuclei density within a 2500µm^2 region, at all turns of the cochlea, is quantified (g). **(a – f)** Cochlear morphology in *Nedd4l$^{tm1c/tm1c}$; Myo15-Cre^{+}* mice look comparable to the morphology observed in control *Nedd4l$^{tm1c/tm1c}$; Myo15-Cre^{-}* mice, at all turns of the cochlea. **(g)** No significant differences in SGN nuclei density were observed between *Nedd4l$^{tm1c/tm1c}$; Myo15-Cre^{-}* (blue, hollow bars) and *Nedd4l$^{tm1c/tm1c}$; Myo15-Cre^{+}* (red, filled bars) mice of both genotypes. Data presented as averages ± standard deviation and analysed using Unpaired T test with Welch's Correction to compare nuclei density at specific regions of the cochlea.

3.3 Discussion

3.3.1 *Nedd4l* is a Deafness-Causing Gene

Nedd4l$^{tm1b/tm1b}$ mice experience an early-onset, progressive hearing loss, with elevated ABR thresholds first recorded in 3-week old mice. Hearing loss deteriorates to profound levels by 8-weeks of age, which is earlier than previously reported (Figure 3.9) (Bowl *et al.*, 2017). In-depth analysis of ABR traces recorded from 3-week old *Nedd4l*$^{tm1b/tm1b}$ mice, in response to a click stimulus, suggests that both the PAS and CAS are affected (Figure 3.11 – Figure 3.13). The lack of overt vestibular dysfunction displayed by 6-month old *Nedd4l*$^{tm1b/tm1b}$ mice suggests that *Nedd4l* function is restricted to cochlear tissue of the inner ear (Figure 3.15). Assessment of cochlear morphology found that 3-week aged *Nedd4l*$^{tm1b/tm1b}$ mice have fewer functional ribbon synapses and nerve fibres innervating IHC and OHC, at apical-mid cochlear regions (Figure 3.26, Figure 3.27). In addition, *Nedd4l*$^{tm1b/tm1b}$ mice experience a progressive loss of hair cell bundles and SGN nuclei from 8-weeks of age. By 6-months of age, the highly organised architecture of the OoC is lost and few SGN remain (Figure 3.16 – Figure 3.25).

3.3.2 Cochlear Synaptopathy of *Nedd4l*$^{tm1b/tm1b}$ mice

The auditory phenotypes and cochlear pathology displayed by 3-week old *Nedd4l*$^{tm1b/tm1b}$ mice are similar to the cochlear synaptopathy displayed by mice that are exposed to moderate levels of noise. Both *Nedd4l*$^{tm1b/tm1b}$ and noise-exposed mice have decreased ABR wave I amplitude, along with fewer matched pre- and post-synaptic ribbon proteins and IHC afferent innervation (Figure 3.12, Figure 3.26) (Kujawa & Liberman, 2009; Furman *et al.*, 2013). Previous literature has also described increases in $[Ca^{2+}_i]$ of hair cells following exposure to noise (Fridberger & Ulfendahl, 1996; Fridberger

et al., 1998; Zuo *et al.*, 2008). It can perhaps be inferred that there is increased Ca^{2+}_i in the hair cells of *Nedd4l*$^{tm1b/tm1b}$ mice due to the increased abundance of the Ca^{2+} buffer protein, α-Parvalbumin (Figure 3.27) (Soto-Prior *et al.*, 1995; Yang *et al.*, 2004; Hackney *et al.*, 2005). Physiologically, increased [Ca^{2+}_i] could stimulate excess glutamate neurotransmitter release and cause ototoxic effects in *Nedd4l*$^{tm1b/tm1b}$ mice (Ruel *et al.*, 2000). Increased glutamate release has been shown to decrease the abundance of GluR2 protein and could account for the increased number of orphaned Ribeye puncta at the presynaptic membrane, observed in 3-week old *Nedd4l*$^{tm1b/tm1b}$ mice (Figure 3.26e) (Chen *et al.*, 2007; 2009).

In *Nedd4l*$^{tm1b/tm1b}$ mice, the first observable loss of bundles and SGN nuclei is detected in 8-week old mice, which is 5 weeks after the onset of hearing loss and when mice are profoundly deaf (Figure 3.18, Figure 3.23). In a similar fashion, loss of hair cell bundle and SGN in noise exposed mice is detected months after their noise exposure. Overall, the similarity in phenotypes suggests that auditory dysfunction and cochlear pathology of *Nedd4l*$^{tm1b/tm1b}$ mice is a consequence of similar mechanisms to those initiated when mice are exposed to noise.

Conclusions of the auditory characterisation of *Nedd4l*$^{tm1b/tm1b}$ mice suggests they have decreased cochlear output, which could be verified by measuring the membrane capacitance of the IHC presynaptic membrane and compound action potential of type I afferent neurons in *Nedd4l*$^{tm1b/tm1b}$ mice. In the literature surrounding the onset of tinnitus, decreased activity of cochlear tissue can result in changes to CAS function as shown by increased activity of neurons of the inferior colliculus in response to cochlear trauma (Vogler *et al.*, 2014; Noreña, 2015). Furthermore, sodium salicylate-induced

tinnitus in mice resulted in decreased latency of ABR waves II – IV and inter-wave latency (Lowe & Walton, 2015). To determine whether decreased cochlear output of *Nedd4l*$^{tm1b/tm1b}$ mice results in central auditory deficits, the mechanisms which decrease cochlear activity could be inhibited. Following from a previous conclusion made, suggesting that similar noise-induced mechanisms are involved in the cause of auditory dysfunction in *Nedd4l*$^{tm1b/tm1b}$ mice, mice that are exposed to moderate levels of noise experience temporary threshold shifts (TTS) which are the result of ATP signalling through $P2X_2$ purinergic receptors (Housley *et al.*, 2013). Therefore, *Nedd4l*$^{tm1b/tm1b}$ mice could be treated with a $P2X_2$ receptor antagonist to investigate whether cochlear and CAS dysfunction is rescued.

Further experiments would have to be conducted to determine if a specific subpopulation of IHC innervation is lost in *Nedd4l*$^{tm1b/tm1b}$ mice (Figure 3.27). In noise-challenged mouse models, ribbon synapses associated with low-SR type I afferent fibres are preferentially lost (Furman *et al.*, 2013). One method of investigating whether similar preferential loss of neuronal structures occurs in *Nedd4l*$^{tm1b/tm1b}$ mice would be to conduct immunohistochemistry on sectioned cochlear tissue, against markers of high- and low-SR type I afferent fibres such as CALB2 and LYPD1 (Petitpré *et al.*, 2018; Shrestha *et al.*, 2018; Sun *et al.*, 2018). If low-SR fibres are preferentially lost, I would expect to observe reduced anti-LYPD1 staining in *Nedd4l*$^{tm1b/tm1b}$ mice, with no change to the signal detected for CALB2.

Additional immunohistochemistry should be conducted to determine whether there is an increased abundance of Oncomodulin protein (ß-Parvalbumin) OHC population of *Nedd4l*$^{tm1b/tm1b}$ mice. Like α-Parvalbumin, Oncomodulin is a Ca^{2+} buffer protein but is

preferentially expressed in OHCs instead of IHCs (Yang *et al.*, 2004; Hackney *et al.*, 2005). In OHCs, α9α10 ACh receptors permit Ca^{2+} influx which results in the attenuation of OHC electromotility (Oliver *et al.*, 2000). The hypothesised increased glutamate release in *Nedd4l*$^{tm1b/tm1b}$ mice could result in MOC-mediated attenuation of OHC electromotility, accounting for the decreased DPOAE levels recorded. To determine whether *Nedd4l*$^{tm1b/tm1b}$ mice have increased MOC efferent feedback on OHC function, inhibitory postsynaptic currents could be recorded.

3.3.3 Requirement of *Nedd4l* in IdCs

However, it is difficult to determine whether the cochlear synaptopathy is a consequence of, or the primary cause of hearing loss in *Nedd4l*$^{tm1b/tm1b}$ mice. One line of evidence to suggest that cochlear synaptopathy is not the primary cause of hearing loss in *Nedd4l*$^{tm1b/tm1b}$ mice is that *Nedd4l* expression is not detected at or in close proximity to hair cells (Figure 3.5f). *Nedd4l*-controlled *lacZ* reporter gene expression was detected in the IdCs which are found atop of the SLim. This correlates with a previous report detailing the localisation of *Nedd4l* in cochlear tissue and scRNA-seq transcriptomic data found on the gEAR database (Figure 3.39) (Zhong *et al.*, 2014; Orvis *et al.*, 2020; Kolla *et al.*, 2020). It is more likely that the loss of NEDD4L protein in IdCs results in global changes to cochlear function, which results in the loss of ribbon synapses. Another reason to suggest cochlear synaptopathy may not be the primary cause of hearing loss in *Nedd4l*$^{tm1b/tm1b}$ mice is the progressive nature of their hearing loss. Cochlear synaptopathy is associated with hidden hearing loss, in which auditory nerve activity is disrupted but does not result in increased auditory thresholds (Shi *et al.*, 2016).

However, *Nedd4l*$^{tm1b/tm1b}$ mice experience progressive increases in ABR thresholds, indicating that they do not experience hidden hearing loss.

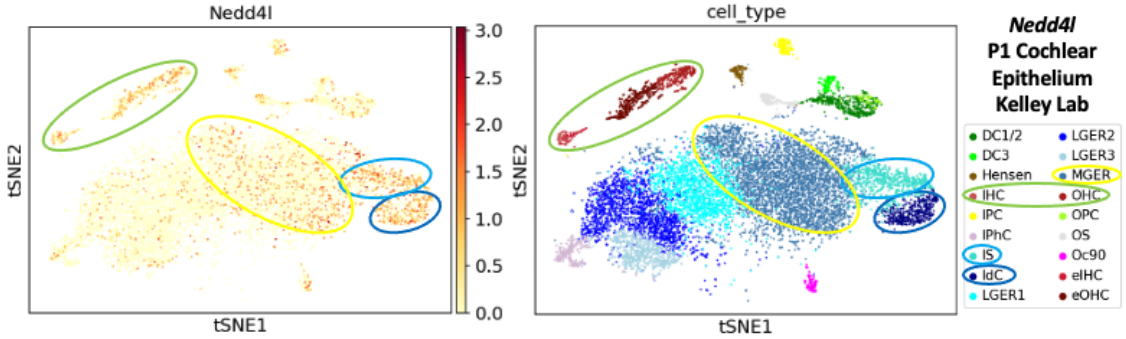

Figure 3.39: gEAR Database: scRNA-seq reported Nedd4l expression in mouse cochlear tissue. scRNA-seq transcript expression data generated by the Kelley lab, for *Nedd4l* in cochlear epithelium tissue derived from P1-aged, CD1 mice. *Nedd4l* transcripts expression were enriched in numerous cochlear cell types, with its expression highest in interdental cells (dark blue circle) and both IHC and OHC (green circle). Expression was also detected in the IS (light blue circle) and Medial Greater Epithelial Ridge (MGER, yellow circle).

The dispensable role of *Nedd4l* in hair cell function is illustrated by the auditory phenotyping and characterisation of a hair cell-specific *Nedd4l* cKO mice showed that auditory function and morphology is not disrupted and does not phenocopy the auditory deficits of the constitutive *Nedd4l*$^{tm1b/tm1b}$ KO mice (Figure 3.36 – Figure 3.38). As the *Myo15*-driven recombination of the *Nedd4l*^{tm1c} alleles occurs at early post-natal ages (P4), it is not possible to exclude the possibility that *Nedd4l* function is required during hair cell development and maturation prior to P4 (Caberlotto *et al.*, 2011). However, this is unlikely as *Nedd4l*-controlled *lacZ* expression indicated that *Nedd4l* is not expressed in hair cells at early postnatal ages (Figure 3.5f).

The auditory phenotypes displayed by the *Sox10*-driven *Nedd4l* cKO mice suggests that *Nedd4l* is required in *Sox10*-expressing cochlear cells, which includes IdCs (Figure 3.28). A variable and profound hearing loss is observed in *Nedd4l*$^{tm1c/+}$*; Sox10-Cre*$^{+}$ mice and the one *Nedd4l*$^{tm1c/tm1c}$; *Sox10-Cre*$^{+}$ mouse respectively (Figure 3.31, Figure 3.33). The variable auditory phenotypes displayed by *Nedd4l*$^{tm1c/+}$*; Sox10-Cre*$^{+}$ mice could be a

consequence of variable *Sox10-Cre* transgene expression. In experiments to characterise the expression of the *Sox10-Cre* transgene using the *R26R-lacZ* reporter KI allele, the intensity of the X-Gal stain found in IdCs varied between mice (Figure 3.40). It is possible that higher amounts of *Sox10-Cre* transgene expression were present in *Nedd4l*$^{tm1c/+}$*; Sox10-Cre*$^{+}$ (HL) mice, resulting in robust recombination of the *Nedd4l*^{tm1c} allele in IdCs and the auditory phenotypes. On the other hand, the auditory thresholds of *Nedd4l*$^{tm1c/+}$*; Sox10-Cre*$^{+}$ (NH) mice that were comparable to control *Nedd4l*$^{tm1c/+}$*; Sox10-Cre*$^{-}$ mice could be a consequence of lower levels of *Sox10-Cre* transgene expression in IdCs and decreased likelihood for recombination of the *Nedd4l*^{tm1c} allele.

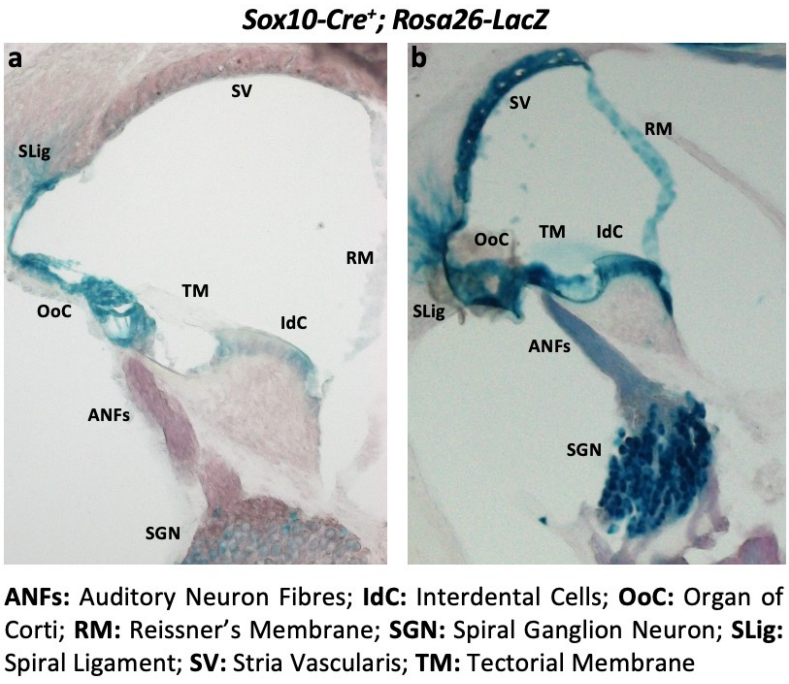

Figure 3.40: Variable level of Sox10-Cre transgene expression. Different levels of lacZ reporter gene expression in mice that carry the *R26R-LacZ* KI allele and the maternally inherited, *Sox10-Cre* transgene. Cochlear tissue was incubated in X-Gal staining solution for the same length of time and conditions, but either displayed low (a) or high (b) levels of X-Gal staining in cochlear tissue, indicating variable levels in *Sox10-Cre* transgene expression.

The auditory and viability phenotypes observed in *Sox10*-driven *Nedd4l* cKO mice are more severe than those observed in constitutive *Nedd4l* KO mice. The elevation in auditory thresholds of 8-week old *Nedd4l*$^{tm1c/+}$*; Sox10-Cre*$^{+}$ (HL) mice is more severe than age-matched, *Nedd4l*$^{tm1b/+}$ mice, and is comparable to age-matched *Nedd4l*$^{tm1b/tm1b}$ mice

(Figure 3.9, Figure 3.31). In addition, there was decreased viability of *Nedd4l*$^{tm1c/tm1c}$; *Sox10-Cre*$^{+}$ mice compared to *Nedd4l*$^{tm1b/tm1b}$ mice (Figure 3.29). Both could be a consequence of the mixed C57BL/6N-CBA background strain of mice in the *Sox10*-driven *Nedd4l* cKO phenotyping cohort, compared to the congenic C57BL/6N background of mice in the constitutive *Nedd4l* KO phenotyping cohort. Previous literature has shown that the background strain of mice can affect the severity of a phenotype and the viability of mutant mouse models (Zheng *et al.*, 1999; Heiman-Patterson *et al.*, 2015; Percival *et al.*, 2017; Alcaraz *et al.*, 2020). For example, mutations of the *Zfp423* gene, which encodes a transcriptional regulatory protein, on a C57BL/6 background results in perinatal lethality, but not when on a BALB/C-C57BL/6 mixed background (Alcaraz *et al.*, 2020). The *Sox10-Cre* transgenic mouse line was generated on C57BL/6N-CBA mixed background strain and due to time constraints of generating congenic mutant mouse lines, the *Sox10-Cre* transgenic was only backcrossed for two generations to C57BL/6N. Therefore, the increased severity of the hearing loss experienced by *Nedd4l*$^{tm1c/+}$*; Sox10-Cre*$^{+}$ (HL) mice could be that the loss of a single functional allele of *Nedd4l* in *Sox10*-expressing cochlear cells is less tolerable in non-C57BL/6N, congenic mice. In a similar fashion, the decreased viability of *Sox10*-driven *Nedd4l* cKO mice could be explained by the decreased tolerance to the loss of *Nedd4l* in migratory neuronal crest cells on a mixed C57BL/6N-CBA background (Matsuoka *et al.*, 2005).

3.3.4 Haploinsufficiency of *Nedd4l* in Mammalian Hearing

Auditory phenotyping also identified that 8-week old *Nedd4l*$^{tm1b/+}$ mice also experience decreased auditory function, as shown by their significantly elevated ABR thresholds in response to high frequency stimuli when compared to *Nedd4l*$^{+/+}$ mice controls (Figure

3.9c). Recorded DPOAE levels from *Nedd4l*$^{tm1b/+}$ are also lower compared to *Nedd4l*$^{+/+}$ mice, but this was not significantly different (Figure 3.14b). A possible explanation for the elevated ABR thresholds is the presence of the hypomorphic *Cadherin23* allele (*Cdh23*^{ahl}) which is present in the C57BL/6 mouse strains, which includes all the IMPC-generated KO mouse models and all mice carrying the *Nedd4l*^{tm1b} allele (Skarnes *et al.*, 2011; Bowl *et al.*, 2017). Mice homozygous for the *Cdh23*^{ahl} allele experience progressive hearing loss which begins at high frequencies from ~3 months of age (Hequembourg & Liberman, 2001; Kane *et al.*, 2012). However, it is unlikely that the presence of the *Cdh23*^{ahl} is causing the decreased auditory function in *Nedd4l*$^{tm1b/+}$ mice, as all mice in the phenotyping cohort (*Nedd4l*$^{+/+}$, *Nedd4l*$^{tm1b/+}$ and *Nedd4l*$^{tm1b/tm1b}$) are homozygous for the *Cdh23*^{ahl} allele and the *Nedd4l*$^{+/+}$ mice do not show any elevation of any auditory thresholds.

It is possible that *Nedd4l* haploinsufficiency could account for the high-frequency hearing loss experienced by 8-week old *Nedd4l*$^{tm1b/+}$ mice. This could also explain the auditory dysfunction that is experienced by *Nedd4l*$^{tm1c/+}$; *Sox10-Cre*$^{+}$ mice (Figure 3.31b). The differences in the ABR thresholds recorded from *Nedd4l*$^{tm1b/+}$ and *Nedd4l*$^{tm1c/+}$; *Sox10-Cre*$^{+}$ mice in response to 8kHz, 16kHz and click stimulus could be due to the different background strain of these mice, which was previously discussed. Further support of the haploinsufficiency of *Nedd4l* in auditory function is that the PVH patients which experience a “hearing impairment” are heterozygous for the missense SNV on the *NEDD4L* gene (Broix *et al.*, 2016). An alternative explanation could be that there is a possible genetic interaction between the hypomorphic *Cdh23*^{ahl} and the KO null *Nedd4l*^{tm1b} alleles. However, this is less plausible given that CDH23 is involved in hair cell

function and that hair cell-driven *Nedd4l* cKO mice do not display any auditory phenotypes (Figure 3.36, Figure 3.37). To resolve the cause of high-frequency hearing loss in *Nedd4l*$^{tm1b/+}$ mice, the *Nedd4l*^{tm1b} allele should be placed on a mouse strain background that do not carry the *Cdh23*^{ahl} alleles, such as the "repaired" C57BL/6N strain (Mianné *et al.*, 2016). If on the "repaired" C57BL/6N background, *Nedd4l*$^{tm1b/+}$ mice do not phenocopy the auditory phenotype displayed by C57BL/6N background *Nedd4l*$^{tm1b/+}$ mice, a single functional copy of the *Nedd4l* is not sufficient for proper auditory function.

4 INVESTIGATION OF NEDD4L COCHLEAR SUBSTRATES

4.1 Introduction

NEDD4L is a well-known E3 ubiquitin ligase protein that is reported to ubiquitinate membrane-localised proteins (Goel *et al.*, 2015). These target proteins are involved in various cellular processes, such as: establishing cell polarity; channel and transporter proteins responsible for ion flux; and, signalling pathways (Raikwar *et al.*, 2010; Arroyo *et al.*, 2011; Y. Kim *et al.*, 2018). The most well characterized NEDD4L substrate is the ENaC, which has been demonstrated to be crucial for reabsorption of Na^+ ions and fluid in the kidney and lung (Hummler *et al.*, 1996; Hummler *et al.*, 1997; Mcdonald *et al.*, 1999). Publications that describe previously generated *Nedd4l* KO mouse models have reported increased expression and activity of ENaC, which results in renal and pulmonary dysfunction (Ronzaud *et al.*, 2013; Minegishi *et al.*, 2016; Henshall *et al.*, 2017; Boase *et al.*, 2011; Kimura *et al.*, 2011).

The localization and functional requirement of ENaC in cochlear tissue has previously been investigated, with expression of all three ENaC subunits found in RM where it is required for Na^+ absorption from the scala media (Kim *et al.*, 2009). Another report details expression of ENaC subunits in the SLim and the SV, and confirmed its activity in the endolymph-facing, apical membrane of ENaC-expressing cells (Couloigner *et al.*, 2001). Increased expression of the ENaC subunits was also detected in KO mice for the *Pendrin* gene, which encodes an anion exchange protein required to maintain the endolymphatic pH (Kim *et al.*, 2014; Kim & Wangemann, 2011). Expression of other known NEDD4L substrates have also been reported in cochlear tissue too. Many of these proteins are ion channels and transporters, such as the K^+-specific KCNQ1 channel, Cl^--

specific Barttin and ClC-Ka channel, the Na^+-K^+-Cl^- cotransporter NKCC1 and the Aquaporin2 channel (Neyroud *et al.*, 1997; Estévez *et al.*, 2001; Crouch *et al.*, 1997; Mhatre *et al.*, 2002).

As *Nedd4l* is a newly identified deafness-causing gene, it is not yet known what the cochlear substrates of NEDD4L are and whether these include any of the substrates that have been reported in other tissues or if there are any cochlear-specific target proteins. To gain insights into the cochlear function of NEDD4L and to determine the molecular cause of hearing loss in *Nedd4l*$^{tm1b/tm1b}$ mice, I conducted experiments designed to elaborate upon the *in vivo* cochlear substrates of NEDD4L. To enable this, I utilized a surrogate MEFs line to identify potential NEDD4L substrates with a view to then validate these interactions in cochlear tissue from wild-type and *Nedd4l*$^{tm1b/tm1b}$ mice.

4.2 Results

4.2.1 Decreased ENaC Expression in *Nedd4l*$^{tm1b/tm1b}$ Cochlear Tissue

ENaC expression was investigated to determine if it is dysregulated in cochlear tissue of *Nedd4l*$^{tm1b/tm1b}$ mice. Based on the previously published literature, which reports an *in vivo* interaction between ENaC and NEDD4L (Kimura *et al.*, 2011; Boase *et al.*, 2011; Ronzaud *et al.*, 2013; Minegishi *et al.*, 2016; Henshall *et al.*, 2017), one could hypothesise that if NEDD4L ubiquitinates ENaC in cochlear tissue, the absence of NEDD4L protein in *Nedd4l*$^{tm1b/tm1b}$ mice would result in greater abundance of ENaC compared to control *Nedd4l*$^{+/+}$ mice. To test this, Western blots of whole cochlear protein lysates prepared from *Nedd4l*$^{tm1b/tm1b}$ and *Nedd4l*$^{+/+}$ mice were undertaken (Figure 4.1). This showed a lower abundance of the αENaC subunit in *Nedd4l*$^{tm1b/tm1b}$ mice compared to age-matched control *Nedd4l*$^{+/+}$ mice (Figure 4.1a). The lower abundance was quantified showing that the relative abundance of αENaC in cochlear tissue derived from P0-aged *Nedd4l*$^{tm1b/tm1b}$ mice is ~50% of the level found in *Nedd4l*$^{+/+}$-derived cochlear tissue (Figure 4.1b).

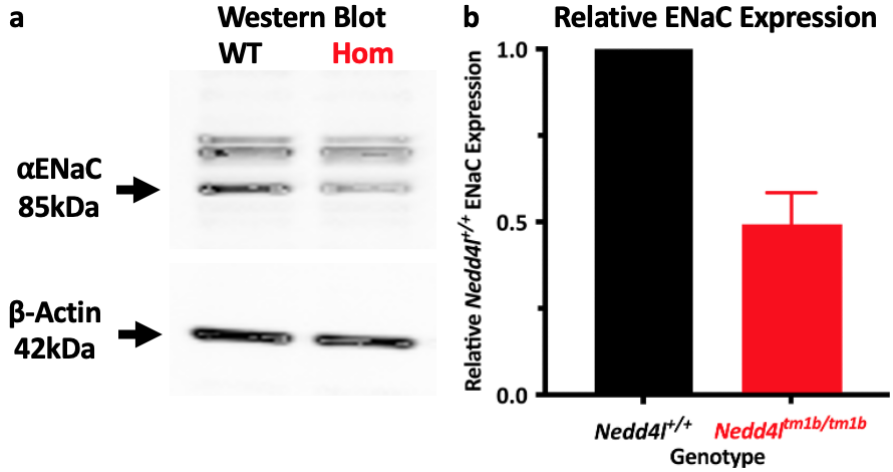

Figure 4.1: Decreased αENaC subunit protein abundance in Nedd4l$^{tm1b/tm1b}$ mice. Representative Western blot against the αENaC subunit in *Nedd4l*$^{tm1b/tm1b}$ mice (a) and its quantified abundance compared to αENaC subunit abundance in *Nedd4l*$^{+/+}$ mice (b). **(a)** The αENaC subunit protein (85kDa) is detected in total protein cochlear lysates derived from P0-aged *Nedd4l*$^{+/+}$ mice, but its abundance appears to be lower in *Nedd4l*$^{tm1b/tm1b}$ mice. **(b)** Comparison of αENaC subunit expression indicated that its expression is 50% lower in *Nedd4l*$^{tm1b/tm1b}$ mice than control *Nedd4l*$^{+/+}$ mice. *n*= 2 *Nedd4l*$^{tm1b/tm1b}$ mice.

4.2.2 NEDD4L Antibodies are Unsuitable for Immunoprecipitation

As an alternative to investigating known NEDD4L substrates individually in an attempt to elucidate the primary cause of auditory dysfunction experienced by *Nedd4l*$^{tm1b/tm1b}$ mice, an unbiased approach was adopted to identify proteins that physically interact with NEDD4L protein. To this end, immunoprecipitation reactions using anti-NEDD4L antibodies were performed to pull-down NEDD4L interacting proteins. Immunoprecipitated proteins would then be identified via MS (Figure 4.2a). These experiments were conducted using protein lysates extracted from MEFs, derived from embryos that carry the *Nedd4l*$^{tm1c/tm1c}$ genotype (*Nedd4l*$^{tm1c/tm1c}$ MEFs; Figure 4.2b). Any interactions identified between NEDD4L, and potential substrates can be validated by inducing *in vitro* recombination of the *Nedd4l* gene (Figure 4.2a, b). This can be achieved by treating MEFs with a soluble, recombinant Cre recombinase protein (Cre), which effectively generates *Nedd4l* KO (*Nedd4l*$^{tm1d/tm1d}$; Figure 4.2b) MEF populations. Additional experiments would then be conducted to verify any interactions between NEDD4L and potential substrates in cochlear tissue derived from *Nedd4l*$^{+/+}$ and *Nedd4l*$^{tm1b/tm1b}$ KO mice.

Numerous reasons informed this experimental design. Firstly, the use of MEFs was required as the total yield of protein able to be extracted from cochlear tissue would not be sufficient for this combined immunoprecipitation/MS approach. Secondly, the restricted expression of *Nedd4l* in the cochlea, which is limited to IdCs (Figure 3.5f), means that NEDD4L protein is not present in a majority of cells, effectively diluting NEDD4L and its interacting proteins. *Nedd4l*$^{tm1c/tm1c}$ MEFs also represents a flexible

system that provides a suitable negative control, in the form of Cre treated MEFs that originated from the same embryo.

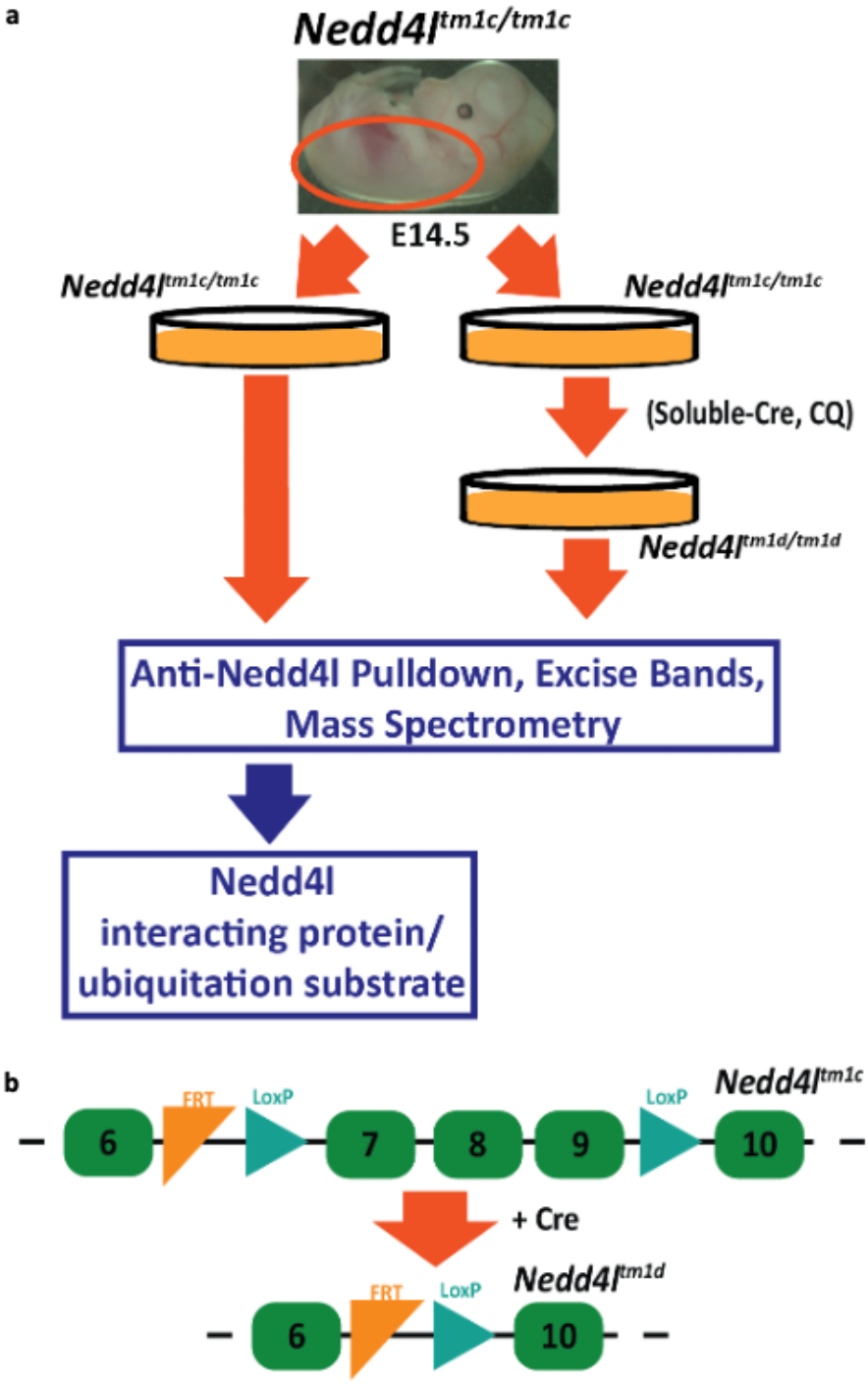

Figure 4.2: Proposed workflow of Cre treatment of Nedd4l$^{tm1c/tm1c}$ MEFs to identify in vivo NEDD4L substrates. **(a)** Identification of *in vivo* NEDD4L substrates, using MEFs generated from *Nedd4l*$^{tm1c/tm1c}$ embryos. *In vitro* recombination of *Nedd4l*$^{tm1c/tm1c}$ MEFs to generate KO *Nedd4l*$^{tm1d/tm1d}$ MEFs through treatment with Cre and CQ. Protein lysates extracted from MEFs of both conditions are used for anti-NEDD4L protein immunoprecipitation reactions and specific protein bands are submitted for MS. The list of proteins identified from treated and untreated *Nedd4l*$^{tm1c/tm1c}$ MEFs will be compared, with proteins that are unique to the untreated MEFs are considered potential *in vivo* NEDD4L substrates. **(b)** Overview of the *Nedd4l* exons removed from *Nedd4l*^{tm1c} allele upon *in vitro* recombination by Cre treatment.

Initial experiments were first conducted to determine if MEF cell populations expressed NEDD4L protein. Anti-NEDD4L Western blots indicate that both isoforms of NEDD4L protein are detected in Whole Cell (WC) protein lysates extracted from *Nedd4l*$^{tm1c/tm1c}$ MEFs. The similarity in banding pattern between the protein lysates extracted from the cochlear tissue of *Nedd4l*$^{+/+}$ mice and *Nedd4l*$^{tm1c/tm1c}$ MEFs indicate that MEFs are suitable model identifying *in vivo* NEDD4L substrates (Figure 4.3).

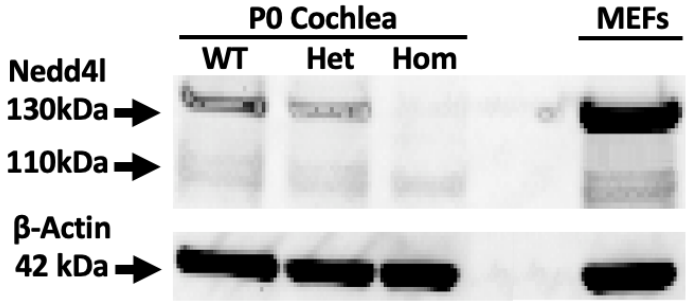

Figure 4.3: Nedd4l*$^{tm1c/tm1c}$ *MEFs express NEDD4L protein. Anti-NEDD4L Western blots showing that *Nedd4l*$^{tm1c/tm1c}$ MEFs express the long (130kDa) and short (110kDa) protein isoform of NEDD4L. The protein band pattern detected in WC protein lysates of *Nedd4l*$^{tm1c/tm1c}$ MEFs looked comparable to the band pattern obtained from cochlear protein lysates of P0-aged *Nedd4l*$^{+/+}$ (WT) and *Nedd4l*$^{tm1b/+}$ (Het) mice. Neither NEDD4L isoform could be detected in cochlear protein lysates from P0-aged *Nedd4l*$^{tm1b/tm1b}$ (Hom) mice. *n*= 1 to validate the presence of NEDD4L protein in MEF cells.

In addition, experiments were also conducted to determine if anti-NEDD4L antibodies that were utilised for Western blot and immunohistochemistry purposes (Figure 3.4a), were suitable for immunoprecipitation reactions. Two anti-NEDD4L antibodies were separately incubated with 500µg of precleared WC protein lysates extracted from *Nedd4l*$^{tm1c/tm1c}$ MEFs and pulled-down using Protein G Sepharose beads. The pull-down lysates were then immunoblotted with an anti-NEDD4L antibody to assess if NEDD4L could be detected (Figure 4.4). Neither anti-NEDD4L antibody (CS #4013s and PTG-13690-1-AP) could pulldown, nor enrich for, NEDD4L protein, as indicated by the lack of an expected protein band at approximately 130kDa, the molecular weight of NEDD4L protein (Figure 4.4, lanes i, ii and v). The protein bands that were present were also observed in the control lane, in which 500µg of precleared WC protein lysates extracted

from *Nedd4l*$^{tm1c/tm1c}$ MEFs was incubated with rabbit serum. The rationale behind this was that the anti-NEDD4L antibodies used for immunoprecipitation reactions were generated in a rabbit host. Overall, this suggests that protein bands present in the anti-NEDD4L antibody-incubated protein lysate lanes i and ii were due to proteins binding non-specifically to the protein G Sepharose beads.

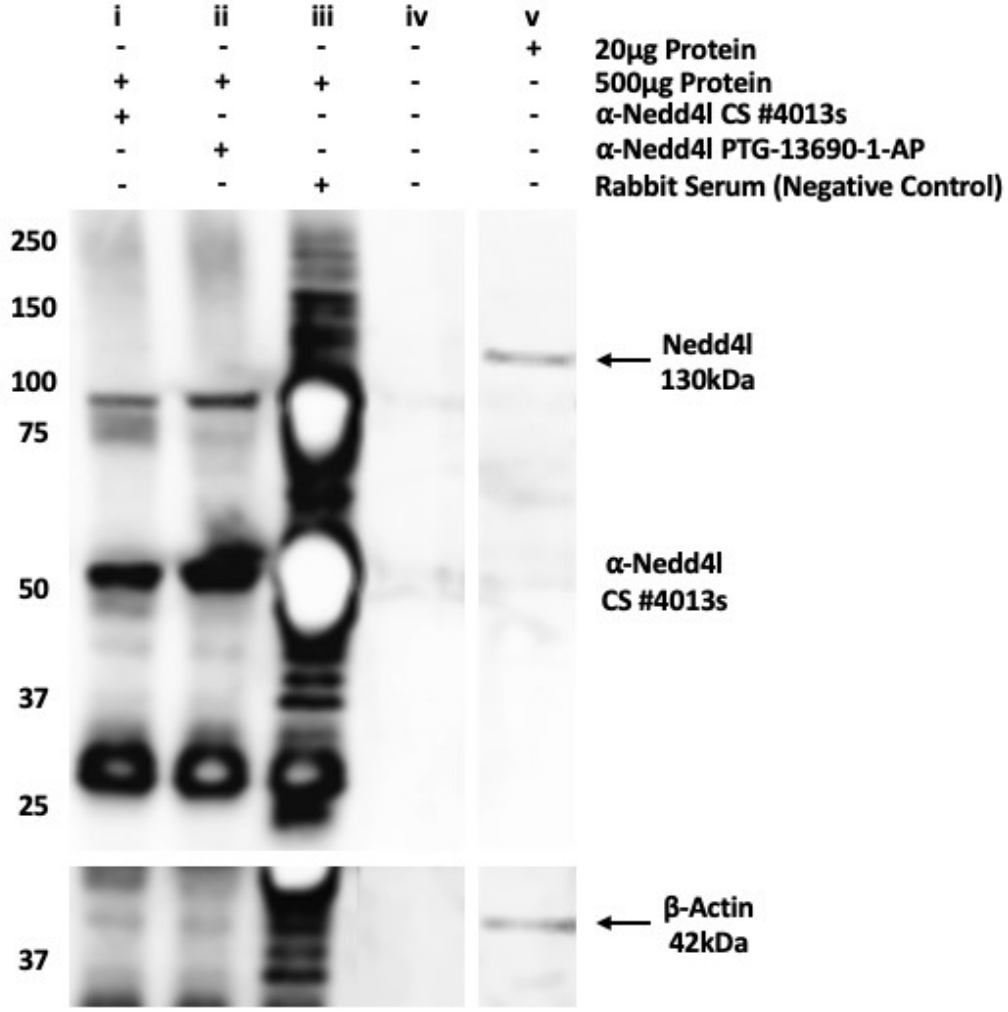

Figure 4.4: Immunoprecipitation reactions against NEDD4L are unspecific. Western blots against NEDD4L protein show that two, previously utilised anti-NEDD4L antibodies (CS #4013s and PTG-13690-1-AP; lanes i and ii, respectively) are not suitable for immunoprecipitation reactions. Neither lane have a band present at 130kDa (the expected molecular weight of NEDD4L; lane v) and instead display a similar band pattern to the negative control rabbit serum condition in lane iii. *n*= 2 for attempts to utilise anti-NEDD4L antibodies for immunoprecipitation reactions.

4.2.3 Cre Treatment of *Nedd4l*$^{tm1c/tm1c}$ MEFs

4.2.3.1 Proposed Anti-Ubiquitinated Protein Immunoprecipitations

As the commercially-available anti-NEDD4L antibodies were deemed unsuitable for immunoprecipitation purposes, the experimental plan was changed such that NEDD4L substrates would now be identified by pulling-down ubiquitinated proteins instead. This approach would follow the same workflow outlined in Figure 4.2. Like the initial workflow, untreated *Nedd4l*$^{tm1c/tm1c}$ MEFs would express mature NEDD4L protein that would ubiquitinate its substrates, a cellular event that would not occur in Cre-treated *Nedd4l*$^{tm1c/tm1c}$ (effectively *Nedd4l*$^{tm1d/tm1d}$ MEFs). Therefore, potential *in vivo* NEDD4L substrates could be identified by comparing the proteins that are ubiquitinated in untreated *Nedd4l*$^{tm1c/tm1c}$ MEFs, to proteins that are ubiquitinated in Cre-treated *Nedd4l*$^{tm1c/tm1c}$ MEFs.

This approach would be better served using MEFs derived from *Nedd4l*$^{tm1c/tm1c}$ mice instead from constitutive KO *Nedd4l*$^{tm1b/tm1b}$ embryonic mice. There are concerns that constitutive KO *Nedd4l*$^{tm1b/tm1b}$ MEFs would compensate for the loss of NEDD4L which could affect the global, cellular profile of ubiquitinated proteins. By performing the experiments using Cre-treated *Nedd4l*$^{tm1c/tm1c}$ MEFs, the loss of NEDD4L function would lead to acute changes that would only affect its substrates, rather than the changes to the entire cell.

Initial experiments were conducted to determine the optimal conditions for Cre treatment of *Nedd4l*$^{tm1c/tm1c}$ MEFs. The desired result is to induce the complete recombination of the *Nedd4l* gene while not producing a cytotoxic environment for MEFs. Numerous variables were investigated, such as the concentration of the Cre, the

length of the treatment, recombination efficacy with FBS present in the culture media, and whether the lysosomotrophic chemical CQ would aid *in vitro* recombination (Wadia *et al.*, 2004).

4.2.3.2 FBS Impairs Cre-Mediated *in vitro* Recombination

Prior literature has reported various concentrations of Cre used for treatment of various different types of cells, ranging from 250nM to 5µM (Moreno-García *et al.*, 2013; Rowe *et al.*, 2013; O'Meara *et al.*, 2013; Bao *et al.*, 2017). With this in consideration, *Nedd4l*$^{tm1c/tm1c}$ MEFs were seeded in 6-well plates and treated with 1 or 3µM Cre for 24 hours, and the efficacy of the treatment was tested by anti-NEDD4L Western blots (Figure 4.5a, b). The first test of Cre treatment of *Nedd4l*$^{tm1c/tm1c}$ MEFs showed that recombination of the *Nedd4l* gene had occurred, as seen by the reduced intensity of the NEDD4L protein band at 130kDa in 3µM Cre-treated MEFs (Figure 4.5a). A 1µM Cre treatment did not appear to result in *Nedd4l* recombination as the intensity of the NEDD4L band appeared similar to that of the control, untreated (0µM) *Nedd4l*$^{tm1c/tm1c}$ MEFs (Figure 4.5a).

To increase the efficacy of *in vitro* recombination of the *Nedd4l* gene, the same Cre treatment of *Nedd4l*$^{tm1c/tm1c}$ MEFs was performed again, but with the exclusion of FBS from the culture media (Wadia *et al.*, 2004). Previously published literature has suggested that its presence can affect the efficacy of Cre treatment. Without FBS in the culture media, treatment with 3µM Cre resulted in no detectable NEDD4L present in the protein lysate prepared from treated *Nedd4l*$^{tm1c/tm1c}$ MEFs (Figure 4.5b). Efforts to load an equal amount of total protein were made, but difficulties arose in obtaining an accurate concentration of the protein lysate extracted from other conditions.

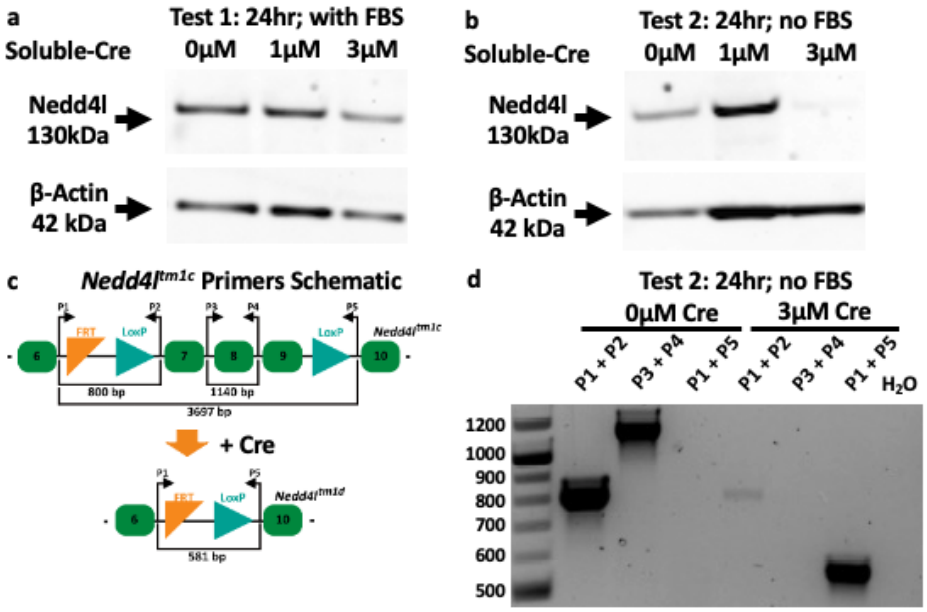

Figure 4.5: FBS impairs Cre-mediated recombination of Nedd4l$^{tm1c/tm1c}$ MEFs. Anti-NEDD4L Western blots (a, b) and PCR (d) against the *Nedd4l*^{tm1c} allele to determine the success of *in vitro* recombination of NEDD4L by treatment with Cre (Merck). **(a)** NEDD4L protein was detected in *Nedd4l*$^{tm1c/tm1c}$ MEFs after a 24-hour treatment with 1μM and 3μM Cre. The culture media was supplemented with FBS. **(b)** In the absence of FBS, no mature NEDD4L protein could be detected in 3μM Cre, 24-hour treatments of *Nedd4l*$^{tm1c/tm1c}$ MEFs. **(c)** Overview of the 5 different primers (P1 – P5) used to genotype the *Nedd4l*^{tm1c} and *Nedd4l*^{tm1d} allele. With a *Nedd4l*^{tm1c} template, the P1 + P5 combination generates a 3.7kbp amplicon, whereas the P1 + P2 and P3 + P4 combinations amplify shorter amplicons. PCR reactions against the *Nedd4l*^{tm1d} allele using the P1 + P2 and P3 + P4 primer combinations fail, as *in vitro* recombination has removed the primer binding sites. The binding sites of the P1 and P5 primers are closer in the *Nedd4l*^{tm1d} allele and PCR reactions generate a shorter amplicon. **(d)** PCR reactions using DNA extracted from untreated MEFs (0μM) using the previously described primer combination produced amplicons of the expected size, indicating that untreated cells carried the *Nedd4l*^{tm1c} allele. The P1 + P5 primer combination produced an amplicon of the expected size when PCR is performed using DNA extracted from 3μM Cre-treated cells. A faint band of the expected size was observed in the reaction where the P1 + P2 primer combination is used. For each condition, *n*= 1 as this was a preliminary test of Cre treatment conditions.

PCR amplification was also performed to verify successful recombination of the *Nedd4l*^{tm1c} allele, using three different primer combinations described in Figure 4.5c. Control reactions using DNA extracted from untreated (0μM Cre) MEFs, the P1 + P2 or P3 + P4 primer combination was successful in amplifying *Nedd4l*^{tm1c}-specific amplicons (Figure 4.5d; 0μM Cre; P1 + P2, P3 + P4). Further confirmation for the presence of the *Nedd4l*^{tm1c} allele in untreated MEFs was provided by the absence of an amplicon at 581bp, when the P1 + P5 primer combination was used to amplify from the *Nedd4l*^{tm1d} template (Figure 4.5c, d; 0μM Cre; P1 + P5). When reactions were performed using DNA extracted from 3μM Cre Cre-treated MEFs, the P1 + P2 and P3 + P4 primer combinations

failed to amplify the *Nedd4l*^{tm1c}-allele products (Figure 4.5; 3µM Cre; P1 + P2, P3 + P4). Through Cre-mediated recombination of the *Nedd4l*^{tm1c} allele, the P1 + P5 primer combination was able to amplify the *Nedd4l*^{tm1d} allele product of the expected length (Figure 4.5d; 3µM Cre; P1 + P5).

4.2.3.3 CQ does not Aid *in vitro* Recombination

As previously reported in the literature, use of CQ has aided the delivery of exogenous material into, and aided Cre-mediated recombination in cultured cell lines (Frankel & Pabo, 1988; Fawell *et al.*, 1994; Wadia *et al.*, 2004; Hashida *et al.*, 2004). Tests were performed to determine whether the addition of CQ during Cre treatments, in the absence of FBS in the culture media, could enhance the efficacy of *in vitro* recombination in *Nedd4l*$^{tm1c/tm1c}$ MEFs (Figure 4.6). Due to the concerns that high CQ concentrations and long treatments could cause cytotoxic effects, 50µM CQ was added alongside Cre in 4-hour long treatment of *Nedd4l*$^{tm1c/tm1c}$ MEFs. Different treatment conditions were also assessed too, such as using a lower concentration of Cre (2µM) to determine if it could replicate the amount of recombination observed in previous conditions (Figure 4.5b, d). Other conditions tested included performing multiple Cre treatments to compensate for the shorter length of treatment, and whether a different supplier of Cre (Excellgen) was more effective to induce *in vitro* recombination than the one previously used (Merck).

A single Cre treatment (2µM) with Merck Cre reduced the amount of NEDD4L protein by 34% and double treatments (2x 2µM) caused an 82% decrease in NEDD4L protein detected, relative to untreated cells (Figure 4.6; Merck Cre; lanes i, ii, iv respectively). In the same conditions, treatment of *Nedd4l*$^{tm1c/tm1c}$ MEFs with Excellgen Cre resulted in a

greater level of *in vitro* recombination of the *Nedd4l*^{tm1c} allele compared to Merck Cre. A 2µM and 2x 2µM treatments of MEFs using Excellgen Cre decreased the abundance of NEDD4L by 77% and 93%, respectively (Figure 4.6; Excellgen Cre; lanes vi, vii) (34% and 82% respectively, in Merck Cre treatment conditions).

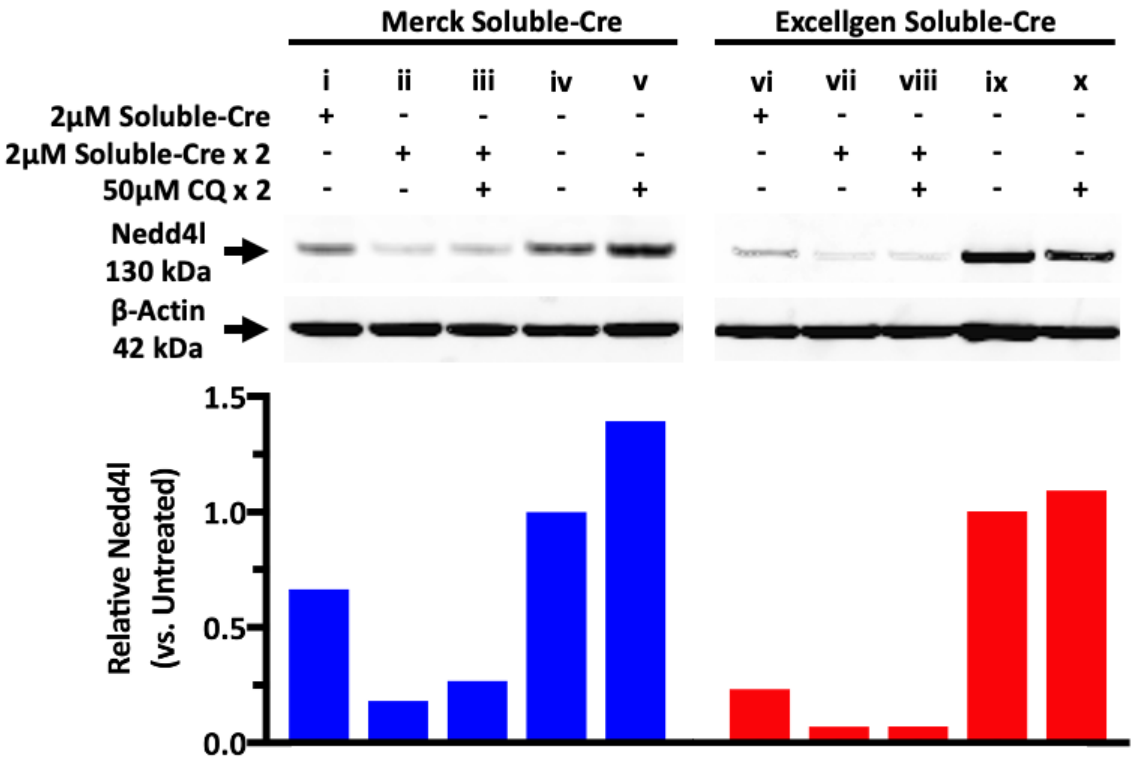

Figure 4.6: Co-treatment of Cre and CQ does not recapitulate previously observed effectiveness of in vitro recombination. Anti-NEDD4L Western blot to investigate the recombination efficacy of shorter (4-hour) Cre treatments, the effects of CQ treatment (50µM) and comparison of Merck- and Excellgen-produced Cre reagents. In all conditions tested, more NEDD4L protein was detected in *Nedd4l*$^{tm1c/tm1c}$ MEFs treated with Merck-produced Cre (lanes i, ii, iii) compared to those treated with Excellgen-produced Cre (lanes vi, vii, viii). The abundance of NEDD4L protein in cells treated twice with Cre was lower than cells that had been treated once (Merck Cre: i, ii; Excellgen Cre: vi, vii). Compared to their respective control conditions, CQ treatments increased the amount of NEDD4L protein detected (Merck: ii-v; Excellgen: vii-x). For each condition, *n*= 1 as this was a preliminary test of Cre treatment conditions.

Contrary to my assumptions that CQ would increase the efficacy of *in vitro* recombination of the *Nedd4l*^{tm1c} allele, addition of CQ to Cre treatments did not decrease the amount of NEDD4L protein present (Figure 4.6; Merck Cre; lanes iii and viii). Double cotreatment of *Nedd4l*$^{tm1c/tm1c}$ MEFs with CQ and either Merck or Excellgen Cre (2x (2µM + CQ)) did not result in a greater level of recombination compared to 2x 2µM treated cells. More NEDD4L protein was detected in Merck Cre, 2x (2µM + CQ)

cotreated than 2x 2µM treated cells (Figure 4.6; Merck Cre; lanes iii, ii; 26% vs. 18%, respectively). The reduction in NEDD4L protein detected in Excellgen Cre 2x (2µM + CQ)-cotreated and 2x 2µM-treated *Nedd4l*$^{tm1c/tm1c}$ MEFs was comparable (Figure 4.6; Excellgen Cre; lanes viii, vii; 7%). Increased NEDD4L protein was also observed in *Nedd4l*$^{tm1c/tm1c}$ MEFs treated twice with CQ, which had a greater abundance of NEDD4L protein (Figure 4.6; lane v, x; 139% and 109%, respectively) than untreated MEFs (Figure 4.6; lane iv; 100%). Overall, Western blot against NEDD4L suggested that these conditions do not cause complete *in vitro* recombination of the *Nedd4l*^{tm1c} allele in *Nedd4l*$^{tm1c/tm1c}$ MEFs. In addition, they do not result in a similar level of recombination observed in previous treatment condition where cells were treated with 3µM Merck Cre, for 24 hours (Figure 4.5b).

PCRs were performed to assess the efficacy of *in vitro* recombination and corroborated the conclusion drawn from Western blots. Using DNA extracted from treated *Nedd4l*$^{tm1c/tm1c}$ MEFs, PCRs using the P1 + P2 and P3 + P4 primer combinations produced amplicons at the expected band size if amplified from a *Nedd4l*^{tm1c} template (800bp and 1.1kbp, respectively) for all conditions tested. PCRs using the P1 + P5 primer combination also produced an amplicon at approximately 580bp if amplified from a *Nedd4l*^{tm1d} template (Figure 4.7). The presence of these three amplicons together indicates that *in vitro* recombination did not occur in all MEFs. Consistent with the Western blot results, there appeared to be more recombination of the *Nedd4l*^{tm1c} allele in Excellgen Cre-treated compared to Merck Cre-treated MEFs, as indicated by the greater abundance of the amplicon generated from the *Nedd4l*^{tm1d} allele, using the P1 + P5 primer combination (Figure 4.7a, b).

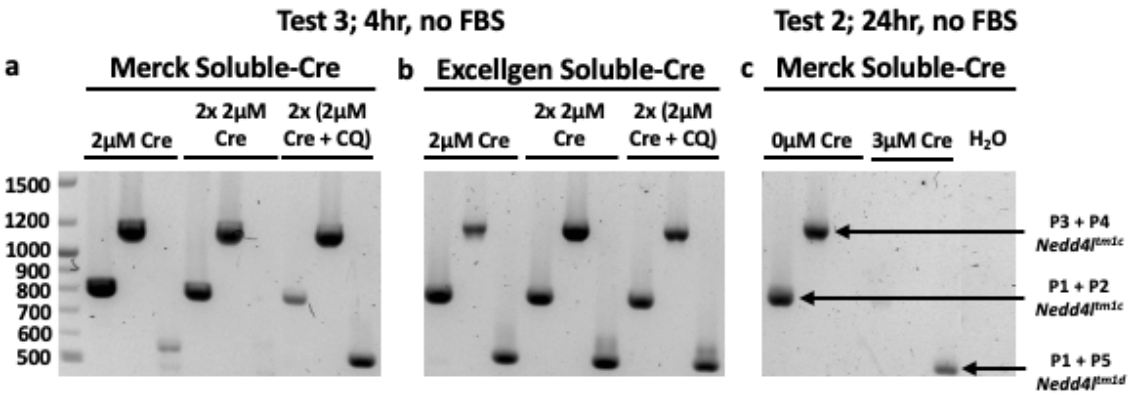

Figure 4.7: Chloroquine does not increase efficacy of recombination of the Nedd4l^{tm1c} allele. PCR assay to investigate the recombination efficacy of shorter (4-hour) Cre treatments, cotreatment with CQ (50µM) and comparison of Merck- (a) and Excellgen-produced (b) Cre reagents. *Nedd4l$^{tm1c/tm1c}$* MEFs were either treated once (2µM Cre) or twice (2x 2µM Cre) with Cre, or cotreated twice with Cre and CQ (2x 2µM Cre + CQ*). In vitro* recombination of the *Nedd4l^{tm1c}* allele was assessed by the presence of amplicons that could be amplified from the *Nedd4l^{tm1c}* allele (P1 + P2, 800bp; P3 + P4; 1.2kbp) or the *Nedd4l^{tm1d}* allele (P1 + P5; 500bp). The extent of recombination was compared the amount previously observed in test 2, where *Nedd4l$^{tm1c/tm1c}$* MEFs were treated with 3µM Cre (Merck) for 24 hours (c). **(a)** In all treatment conditions using Merck Cre, both *Nedd4l^{tm1c}* and *Nedd4l^{tm1d}* allele-specific amplicons were detected. Cotreatment with CQ resulted in a greater abundance of the *Nedd4l^{tm1d}* allele amplicon, compared to cells that were not treated with CQ. **(b)** In all treatment conditions using Excellgen Cre, both *Nedd4l^{tm1c}* and *Nedd4l^{tm1d}* allele-specific amplicons were detected. **(c)** PCR reactions using DNA extracted from untreated *Nedd4l$^{tm1c/tm1c}$* MEFs could amplify the *Nedd4l^{tm1c}*-specific amplicons at 800bp and 1.2kbp, but not the *Nedd4l^{tm1d}*-specific amplicon at 500bp. PCR using DNA extracted from 3µM Merck Cre-treated MEFs could not amplify *Nedd4l^{tm1c}*-specific amplicons but could amplify the *Nedd4l^{tm1d}*-specific amplicon. For each condition, *n*= 1 as this was a preliminary test of Cre treatment conditions.

The extent of *Nedd4l^{tm1c}* recombination in MEFs cotreated with Merck Cre and CQ appeared to be greater than cells treated with Merck Cre alone (Figure 4.7a). This is evident by the presence of an amplicon at around 550bp using the P1 + P5 primer combination (Figure 4.7a; 2x (2µM Cre + CQ)), but its absence (Figure 4.7a; 2x 2µM Cre) or decreased abundance (Figure 4.7a; 2µM Cre) of the *Nedd4l^{tm1d}*-specific amplicon in cells not treated with CQ. The absence of an amplicon in Merck Cre 2x 2µM Cre-treated cells could be the result of a failed PCR (Figure 4.7a; 2x 2µM Cre).

PCR assays using DNA extracted from Excellgen Cre-treated MEFs (Figure 4.7b; 2µM Cre; 2x 2µM Cre) showed greater abundance for the *Nedd4l^{tm1c}*-specific amplicons (P1 + P2, P3 + P4 primer combination) than 2x (2µM Cre + CQ) treated cells. The abundance of the *Nedd4l^{tm1d}*-specific amplicon was comparable when PCR reactions were undertaken using DNA extracted from 2x 2µM Cre and 2x (2µM Cre + CQ) treated MEFs (Figure 4.7b;

2x 2µM; 2x (2µM Cre + CQ)). This correlates with the comparable amount of NEDD4L protein detected by Western blots from treated cells (Figure 4.6; lanes vii, viii).

4.2.3.4 Inconsistent Efficacy of Nedd4l^{tm1c} In Vitro Recombination

Previous tests had shown that a single 24-hour treatment of *Nedd4l*$^{tm1c/tm1c}$ MEFs with 3µM Cre (Merck), maintained in culture media without FBS, appeared to cause complete *in vitro* recombination of *Nedd4l* (Figure 4.5b, d). This test condition was repeated, and treated cells were expanded so that the necessary amounts of total protein required for the immunoprecipitation, and subsequent MS, could be harvested. Before further downstream experiments were performed, Western blot (anti-NEDD4L) and PCR (*Nedd4l*^{tm1c} and *Nedd4l*^{tm1d} alleles) were performed for molecular confirmation of successful recombination of the *Nedd4l*^{tm1c} allele.

Anti-NEDD4L Western blots identified a reduced abundance of NEDD4L protein in Cre-treated cells but did not fully recapitulate the results previously observed (Figure 4.8a, c). This indicated that *Nedd4l in vitro* recombination had not occurred in all treated *Nedd4l*$^{tm1c/tm1c}$ MEFs. As such, PCR amplification using DNA extracted from treated MEFs was not performed. Cre treatment of MEFs was repeated again using previous volumes and concentrations, but extending the duration of the Cre treatment from 24- to 48-hours. The rationale to increasing the duration of treatment was to provide more time for MEF cell uptake of Cre and *in vitro* recombination of *Nedd4l* in all *Nedd4l*$^{tm1c/tm1c}$ MEFs. However, this adjustment was unsuccessful at increasing the amount of *in vitro* recombination of the *Nedd4l*^{tm1c} allele. NEDD4L protein was still detectable in the protein lysates extracted from 48 hour-treated *Nedd4l*$^{tm1c/tm1c}$ MEF, and in greater abundance compared to the previous attempt (Figure 4.8a, b).

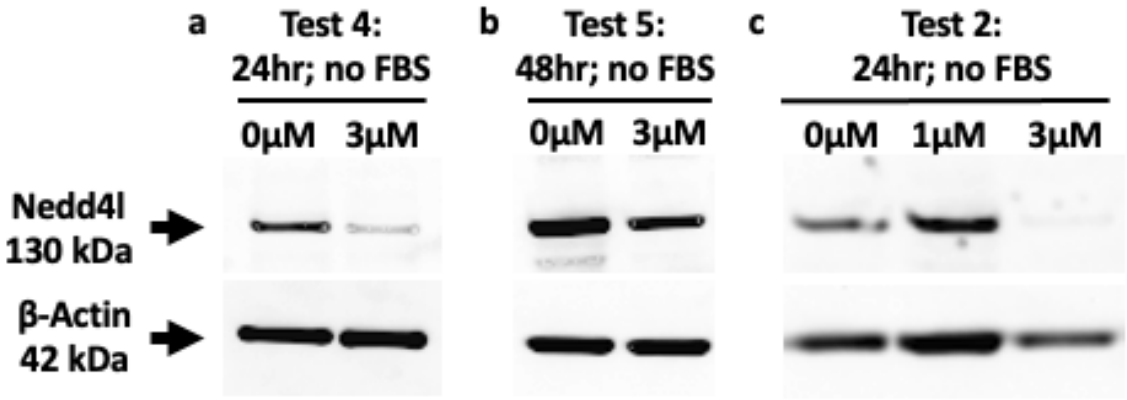

Figure 4.8: Inconsistent levels of Nedd4l recombination in Cre-treated Nedd4l$^{tm1c/tm1c}$ MEFs. 24- (a) and 48-hour (b) Cre treatments did not recapitulate the same level of *Nedd4l^{tm1c}* recombination observed in previous treatments (c). **(a)** NEDD4L protein was present in lysates extracted from *Nedd4l$^{tm1c/tm1c}$* MEFs treated with Merck-produced, Cre for 24-hours. No FBS was present in the culture media. **(b)** NEDD4L protein was still detected in MEFs when the duration of Cre treatment was doubled. **(c)** For comparison, anti-NEDD4L Western blots that were performed against protein lysates that were extracted in a previous Cre treatment test; images were previously shown in Figure 4.5. For each condition, *n*= 1 as this was a preliminary test of Cre treatment conditions.

4.2.4 Use of *Nedd4l*$^{tm1b/tm1b}$ MEFs to Identify Nedd4l *In Vivo* Cochlear Substrates

4.2.4.1 *Nedd4l*$^{tm1b/tm1b}$ MEFs are Suitable Model

As inducing *in vitro* recombination of *Nedd4l*$^{tm1c/tm1c}$ MEFs with Cre yielded inconsistent results, E14.5-aged *Nedd4l*$^{tm1b/tm1b}$ embryos were obtained and used to generate MEF cell populations. This approach eliminates the need to induce *in vitro* recombination of the *Nedd4l* gene using Cre. An overview of the workflow is shown in Figure 4.9a. Initial hesitancy in using *Nedd4l*$^{tm1b/tm1b}$ mice was centred on the lack of flexibility in using MEFs that carry a constitutive *Nedd4l* KO allele and the assumed global affects this has on the profile of ubiquitinated proteins. Furthermore, there was some apprehension due to the IMPC-reported sub-viability in *Nedd4l*$^{tm1b/tm1b}$ mice and whether that would affect the culturing of *Nedd4l*$^{tm1b/tm1b}$ MEFs. No issues were experienced with regards to obtaining and maintaining *Nedd4l*$^{tm1b/tm1b}$ MEFs, which grew and divided in a similar fashion to *Nedd4l*$^{+/+}$ and *Nedd4l*$^{tm1b/+}$ MEFs.

Anti-NEDD4L Western blots were performed to confirm that *Nedd4l*$^{tm1b/tm1b}$ MEFs do not express any mature NEDD4L protein (Figure 4.9b; WC). NEDD4L protein was detected in WC protein lysates extracted from *Nedd4l*$^{+/+}$ (WT) and *Nedd4l*$^{tm1b/+}$ (Het) MEFs. Less NEDD4L protein could be detected in *Nedd4l*$^{tm1b/+}$ MEFs and none was observed in *Nedd4l*$^{tm1b/tm1b}$ (Hom) MEFs (Figure 4.9b; WC).

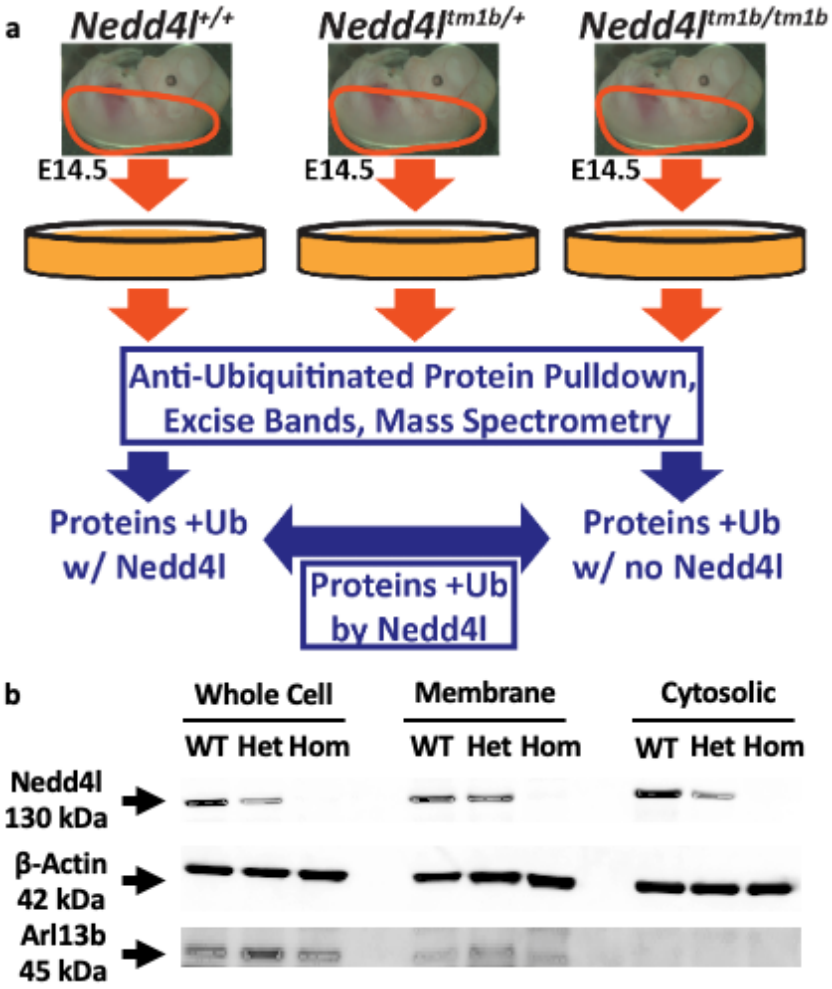

Figure 4.9: Nedd4l$^{tm1b/tm1b}$ MEFs do not express NEDD4L protein. A proposed workflow to use *Nedd4l*$^{tm1b/tm1b}$ MEFs to identify *in vivo* NEDD4L substrates (a) and confirmation that MEFs derived from *Nedd4l*$^{tm1b/tm1b}$ embryos do not express any NEDD4L protein (b). **(a)** *Nedd4l*$^{tm1b/tm1b}$ MEFs would be used to harvest the necessary amount of protein necessary for anti-ubiquitinated protein immunoprecipitation and MS. **(b)** Western blots detected mature NEDD4L protein in *Nedd4l*$^{+/+}$ (WT) and *Nedd4l*$^{tm1b/+}$ (Het) but not *Nedd4l*$^{tm1b/tm1b}$ (Hom) MEFs in WC lysates, membrane or cytosolic protein fractions. Membrane protein ARL13B was only detected in WC protein lysates and the membrane protein fraction. For MEF cells of each genotype, *n*= 1 in order to validate the absence of NEDD4L protein in *Nedd4l*$^{tm1b/tm1b}$ MEF cells.

As NEDD4L protein is well known to ubiquitinate transmembrane proteins, cytosolic and membrane protein fractions were extracted from MEFs of all genotypes, for downstream immunoprecipitation and MS steps (Goel *et al.*, 2015). No NEDD4L protein was detected in the membrane nor cytosolic fraction of *Nedd4l*$^{tm1b/tm1b}$ MEFs, but was present in the fractions derived from *Nedd4l*$^{+/+}$ and *Nedd4l*$^{tm1b/+}$ MEFs (Figure 4.9b; Membrane, Cytosolic). Interestingly, a difference in abundance of Nedd4l protein was not evident between membrane fractions from *Nedd4l*$^{+/+}$ and *Nedd4l*$^{tm1b/+}$ MEFs, but

was evident between cytosolic fractions showing that abundance of cytosolic-localised Nedd4l protein is lower in *Nedd4l*$^{tm1b/+}$ MEFs.

To confirm successful fractionation of cytosolic and membrane fractions, Western blots were performed against the ARL13B protein which is a known ciliary membrane-associated protein (Larkins *et al.*, 2011). ARL13B protein was identified in WC and membrane protein lysates, but not in the cytosolic lysates, indicating a successful fractionation of protein lysates (Figure 4.9b).

4.2.4.2 Subtle Changes to the Ubiquitinated Proteins in *Nedd4l*$^{tm1b/tm1b}$ MEFs

Membrane and cytosolic fractions extracted from *Nedd4l*$^{+/+}$ (WT) and *Nedd4l*$^{tm1b/tm1b}$ (Hom) MEFs were used for anti-ubiquitin immunoprecipitation reactions (Figure 4.10). Whilst NEDD4L is well known to target proteins for degradation, its function within cochlear tissue has not been characterised and could have non-degradative functions. Therefore, the FK2 antibody which recognises both mono- and poly-ubiquitinated protein species was used for the immunoprecipitation reactions. Ubiquitinated proteins from cytosolic and membrane fractions were extracted from *Nedd4l*$^{+/+}$- and *Nedd4l*$^{tm1b/tm1b}$ MEFs, ran on a 3-8% Tris-Acetate gel and Coomassie stained. As the FK2 antibody was generated from a mouse host and has the IgG_1 isotype, mouse IgG_1 serum was incubated with WC protein lysate in the negative control condition.

In an attempt to identify potential *in vivo* NEDD4L substrates, the protein banding pattern of *Nedd4l*$^{+/+}$ and *Nedd4l*$^{tm1b/tm1b}$ MEFs was compared, looking for differences between the two conditions. Banding patterns of membrane and cytosolic proteins were not compared to each other. Due to its reported E3 ubiquitin ligase activity, *in vivo*

NEDD4L substrates would not be ubiquitinated in *Nedd4l*$^{tm1b/tm1b}$ MEFs and consequently would not be enriched by FK2 immunoprecipitations or detected by Coomassie stains. Therefore, a protein band was selected for MS if it was present in *Nedd4l*$^{+/+}$ MEFs, but absent in *Nedd4l*$^{tm1b/tm1b}$ MEFs. Furthermore, if a particular protein band is more intense in *Nedd4l*$^{+/+}$ than in *Nedd4l*$^{tm1b/tm1b}$ MEFs, it was also selected for MS. The rationale for this criterion is that there are likely other active E3 Ubiquitin ligases, besides NEDD4L. Their ubiquitinated substrates would be pulled down by the anti-ubiquitinated protein FK2 immunoprecipitation. Therefore, reduced intensity of a protein band in *Nedd4l*$^{tm1b/tm1b}$ MEFs could be due to a NEDD4L substrate not being ubiquitinated, and a different protein substrate of a similar molecular weight that is ubiquitinated by other E3 Ubiquitin ligases. However, if a particular protein band that fits these criteria, but is also present in the IgG1-negative control lane, it was no longer considered for MS analysis.

The intensity of the Coomassie stain of anti-FK2 pulled down proteins presented difficulties in identifying differences in the protein banding pattern between *Nedd4l*$^{+/+}$ and *Nedd4l*$^{tm1b/tm1b}$ cytosolic and membrane fractions (Figure 4.10a). To aid in identifying the differences in protein banding pattern, the image of Coomassie stain was altered using ImageJ. The image was altered several times to allow optimal analysis of different regions of the Coomassie stained gel, these defined regions are denoted by the orange lines (Figure 4.10b). No differences in banding pattern were detected between cytosolic fractions extracted from *Nedd4l*$^{+/+}$ and *Nedd4l*$^{tm1b/tm1b}$ MEFs (Figure 4.10b; Cytosolic). The banding pattern observed for the membrane fractions of *Nedd4l*$^{+/+}$ and *Nedd4l*$^{tm1b/tm1b}$ MEFs largely looked similar too, save for some differences in the

intensity of some protein bands that were detected (Figure 4.10b; Membrane; orange dotted line box). An enlarged image of this section of the gel is shown in Figure 4.10c. The bands indicated by the orange arrows (at approximately 130kDa and 115kDa) were excised and submitted for MS.

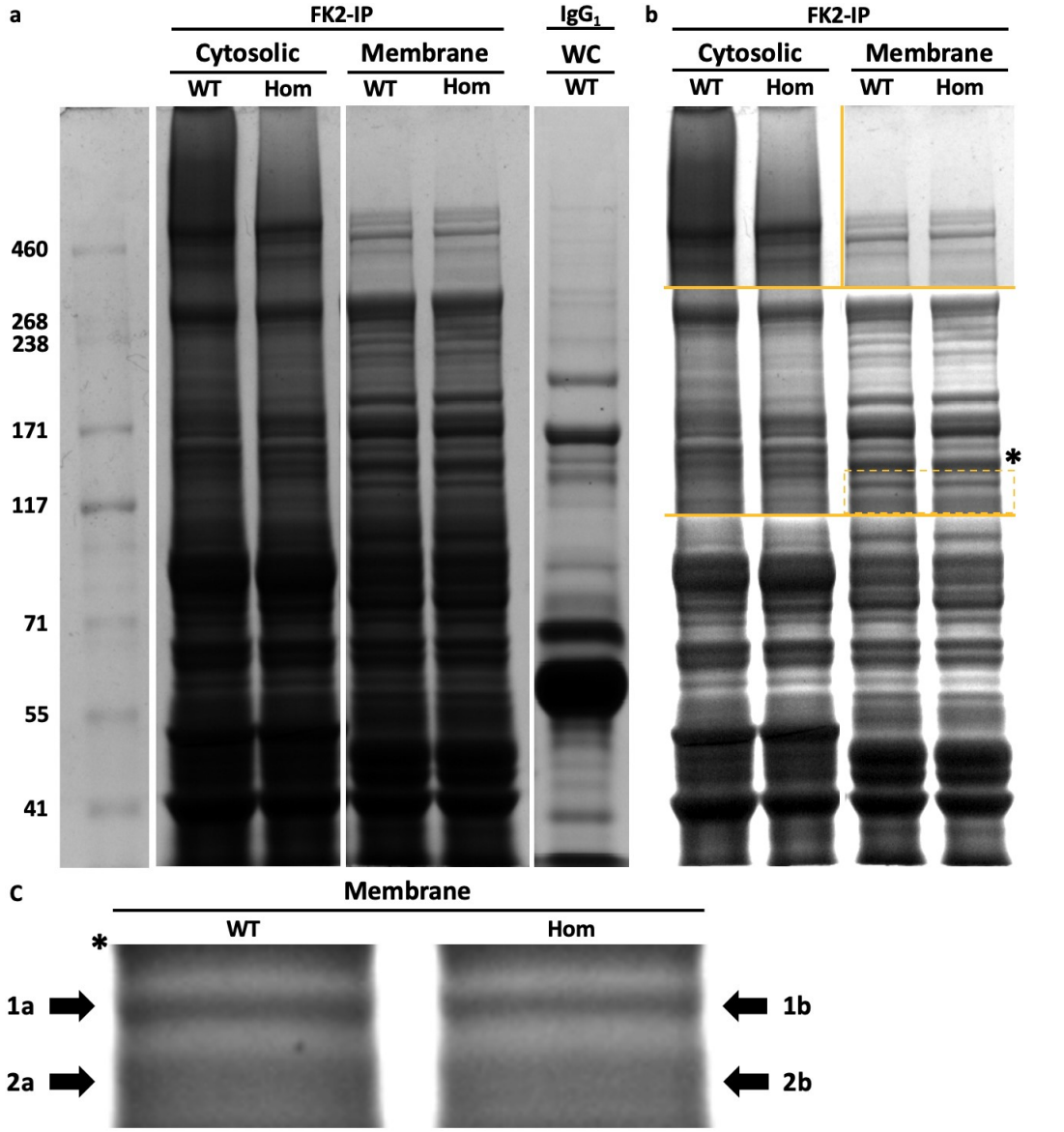

Figure 4.10: Subtle differences in protein ubiquitination in Nedd4l$^{tm1b/tm1b}$ MEFs. Coomassie stains of FK2 immunoprecipitation reactions against mono- and polyubiquitinated (FK2) cytosolic and membrane proteins extracted from *Nedd4l*$^{+/+}$ (WT) and *Nedd4l*$^{tm1b/tm1b}$ (Hom) MEFs. **(a)** The intensity of the Coomassie stain against FK2-immunoprecipitated proteins was too intense to identify any differences in the ubiquitinated proteins of cytosolic and membrane protein extracted from *Nedd4l*$^{+/+}$ and *Nedd4l*$^{tm1b/tm1b}$ MEFs. WC protein lysates incubated with mouse IgG_1 protein was used as a negative control against the FK2 antibody. **(b)** The intensity of the Coomassie stained gel shown in (a) was altered using ImageJ to detect any differences in ubiquitinated proteins. Orange lines delineate different regions of the gel that were altered differently. Differences in the protein banding pattern observed in mono- and polyubiquitinated membrane proteins are highlighted with the dotted line, orange box (*). **(c)** A closeup image of a section of the Coomassie-stained gel highlighted with the dotted line, orange box in (b). The black arrows indicate the protein bands, 1a, 1b, 2a, 2b, that were cut from the gel and sent for MS analysis. For MEF cells of each genotype, *n*= 1.

4.2.4.3 MG132 Treatment did not Aid Selection of Protein Bands

Difficulties arose when trying to identify differences in the Coomassie stain protein banding patterns between *Nedd4l*$^{+/+}$ and *Nedd4l*$^{tm1b/tm1b}$ MEFs. To overcome this and obtain a more representative profile of the ubiquitinated protein species, more *Nedd4l*$^{+/+}$ and *Nedd4l*$^{tm1b/tm1b}$ MEFs were cultured and treated with the proteasomal inhibitor, MG132 (Figure 4.11a). Consequently, extracted protein lysates would have a greater concentration of ubiquitinated protein species, compared to lysates extracted from untreated MEFs. As no differences could be observed in the ubiquitinated proteins found in the cytosolic fraction (Figure 4.10b), only membrane-localised proteins were used for anti-ubiquitinated protein immunoprecipitation reactions.

Following MG132 treatment of *Nedd4l*$^{+/+}$- and *Nedd4l*$^{tm1b/tm1b}$ MEFs and extraction of WC and membrane protein lysates, preliminary Western blots were conducted before lysates were used for downstream immunoprecipitation and MS steps. Anti-NEDD4L Western blots were performed against WC lysates of MG132-treated and untreated, *Nedd4l*$^{+/+}$- and *Nedd4l*$^{tm1b/tm1b}$ MEFs. As expected, *Nedd4l*$^{tm1b/tm1b}$ MEFs did not express any NEDD4L protein. Both NEDD4L protein isoforms were detectable in MG132-treated, *Nedd4l*$^{+/+}$ MEF cell lysates, with the larger, 130kDa NEDD4L protein is the predominant isoform in MEFs (Figure 4.11b). The abundance of the smaller isoform was greater in MG132-treated than untreated cells (Figure 4.11b; WT; 110kDa). Western blots were also performed to confirm that a successful extraction of the membrane protein fraction of MG132-treated and untreated, *Nedd4l*$^{+/+}$- and *Nedd4l*$^{tm1b/tm1b}$ MEFs. Antibodies directed against the Na^+-K^+-ATPase α_1 and α-Tubulin proteins were used to assess the presence of membrane and cytosolic-localised proteins, respectively. Both Na^+-K^+-

ATPase α_1 and α-Tubulin could be detected in control WC protein lysates extracted from MG132-treated and untreated, *Nedd4l*$^{+/+}$- and *Nedd4l*$^{tm1b/tm1b}$ MEFs (Figure 4.11c; WC). No cytosolic α-Tubulin protein was detected in the membrane protein lysates. Na^+-K^+-ATPase α_1 protein was detected and more abundant in the membrane fraction compared to the WC lysate, suggesting enrichment of membrane proteins (Figure 4.11c; Membrane).

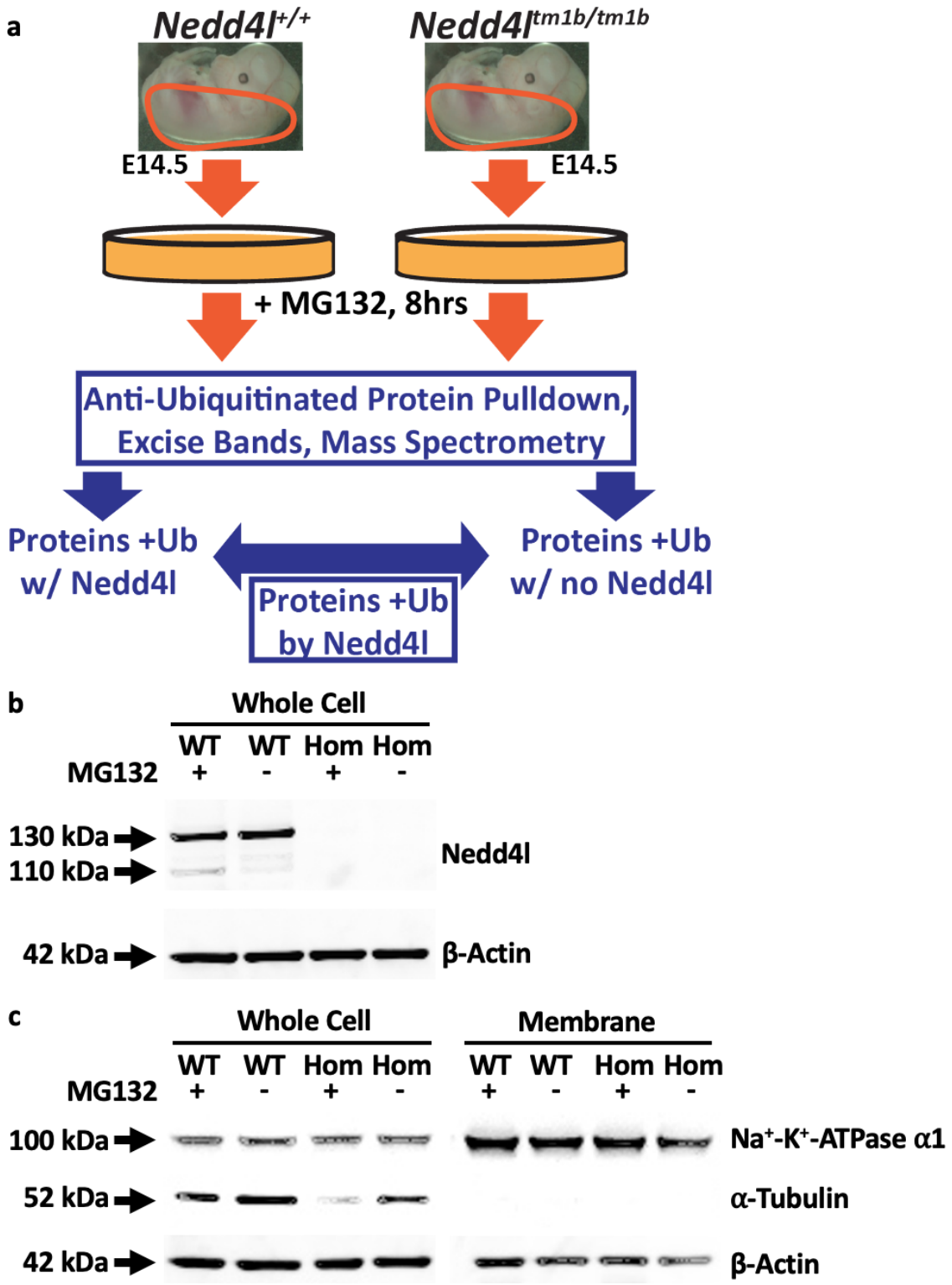

Figure 4.11: Proposed workflow for proteasome inhibitor, MG132, treatment of Nedd4l$^{tm1b/tm1b}$ MEFs. The proposed workflow to identify *in vivo* NEDD4L cochlear substrates from MG132-treated *Nedd4l*$^{+/+}$ (WT) and *Nedd4l*$^{tm1b/tm1b}$ (Hom) MEFs (a), Western blot confirmation that treated *Nedd4l*$^{tm1b/tm1b}$ MEFs do not express mature Nedd4l protein (b) and the successful extraction of membrane fractions from MEFs (c). **(a)** The proposed workflow includes an 8 hour MG132 treatment, before membrane protein lysates are extracted. **(b)** Expression of both NEDD4L isoforms is not affected in MG132-treated and untreated *Nedd4l*$^{+/+}$ MEFs. **(c)** Successful enrichment of membrane-localised proteins as indicated by the presence of membrane protein Na^+K^+ATPase α_1 subunit, and the absence of cytosolic protein α-Tubulin, in the membrane protein fractions of treated and untreated *Nedd4l*$^{+/+}$ and *Nedd4l*$^{tm1b/tm1b}$ MEFs. For MEF cells of each genotype, *n*= 1 in order to validate the absence of NEDD4L protein in *Nedd4l*$^{tm1b/tm1b}$ MEF cells.

Coomassie stains against immunoprecipitated mono- and poly-ubiquitinated membrane proteins was conducted as previously described (Figure 4.10). The overall intensity of the Coomassie stain of membrane proteins was lower compared to the previous Coomassie stain (Figure 4.10, Figure 4.12). However, the protein banding pattern between all conditions and to the IgG_1 negative control appeared identical. No protein bands unique to the MG132-treated *Nedd4l*$^{+/+}$-derived MEFs could be detected (Figure 4.12; lane i) and consequently, no protein bands were excised and submitted for MS analysis.

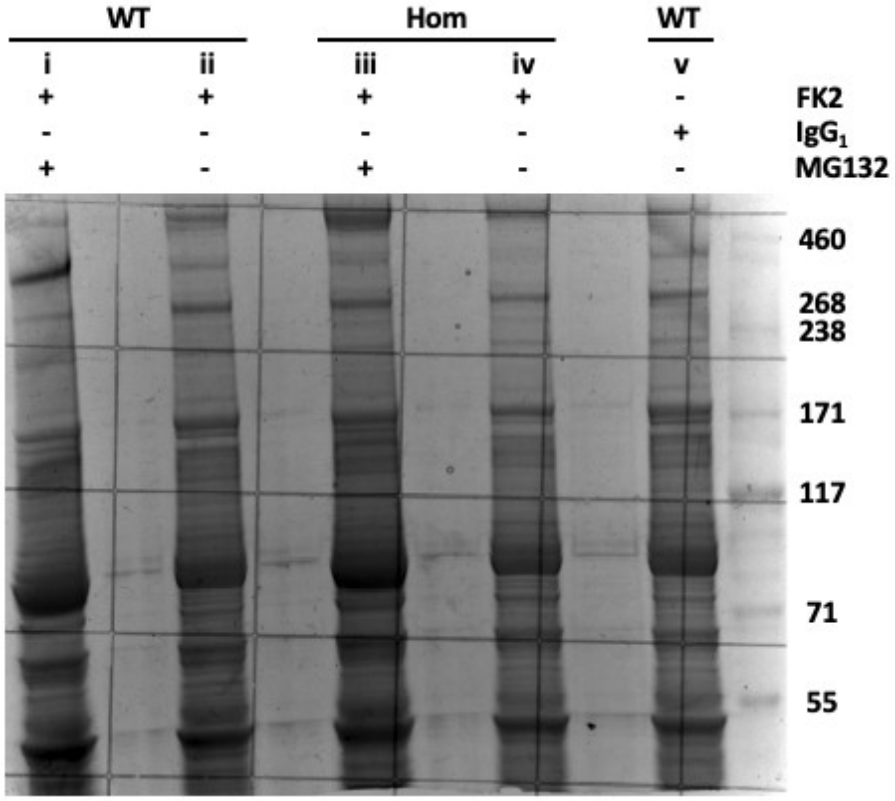

Figure 4.12: Unique protein bands in MG132-treated Nedd4l$^{+/+}$ MEFs could not be detected following an anti-ubiquitinated immunoprecipitation. Comparable Coomassie-stained protein banding pattern of MG132-treated and untreated *Nedd4l*$^{+/+}$ (WT) and *Nedd4l*$^{tm1b/tm1b}$ (Hom) MEFs. In addition, the banding pattern of protein lysates extracted untreated *Nedd4l*$^{+/+}$ MEFs that were incubated with the IgG_1 negative control looked comparable with the protein band pattern observed in all test conditions. For MEF cells of each genotype and condition, *n*= 1.

4.2.5 In silico Analysis of Potential NEDD4L cochlear substrates

4.2.5.1 Identification of Potential NEDD4L Substrates

MS was undertaken on four protein bands (1a, 1b, 2a and 2b) excised from the gel-separated, FK2-immunoprecipitated membrane fractions prepared from *Nedd4l*$^{+/+}$- and *Nedd4l*$^{tm1b/tm1b}$-derived MEFs (Figure 4.10c). From protein bands 1a and 2a that were identified and excised from the membrane fraction of *Nedd4l*$^{+/+}$-derived MEFs, MS returned 326 and 263 protein hits, respectively (Figure 4.10c, Figure 4.13a; Appendix Table 5, Appendix Table 7). Protein bands 2a and 2b that were identified and excised from the membrane fraction of *Nedd4l*$^{tm1b/tm1b}$-derived MEFs, MS returned 387 and 375 protein hits, respectively (Figure 4.10c, Figure 4.13a; Appendix Table 6, Appendix Table 8). Overall, 1351 individual protein hits were identified from the four excised protein bands.

To identify potential *in vivo* NEDD4L substrates, many sorting parameters were applied to the list of protein hits identified from bands 1a, 1b, 2a and 2b. The first sorting parameter was to consider proteins that are unique to the *Nedd4l*$^{+/+}$ immunoprecipitated bands, which were not present in the protein list from their respective control *Nedd4l*$^{tm1b/tm1b}$ protein bands (Figure 4.13a). Proteins that were common to immunoprecipitated bands obtained from both MEFs populations were disregarded. In a comparison of the 326 and 387 protein hits identified from protein bands 1a and 1b, 96 and 157 were only reported in their respective list of protein hits. In a similar comparison of the initial 263 and 375 protein hits identified from bands 2a and 2b, 38 and 150 were specific to their respective list of protein hits. Furthermore, only unique protein hits that were identified from the membrane protein fraction

prepared from *Nedd4l*$^{+/+}$-derived MEFs were considered. My rationale was that in *Nedd4l*$^{tm1b/tm1b}$-derived MEFs, NEDD4L protein is not present to ubiquitinate its substrates and would not be pulled-down in FK2-immunoprecipitations. Therefore, it would not be included in the list of protein hits identified in MS. As such, only the 96 and 38 unique protein hits returned from protein bands 1a and 2a respectively, were also considered (Figure 4.13b).

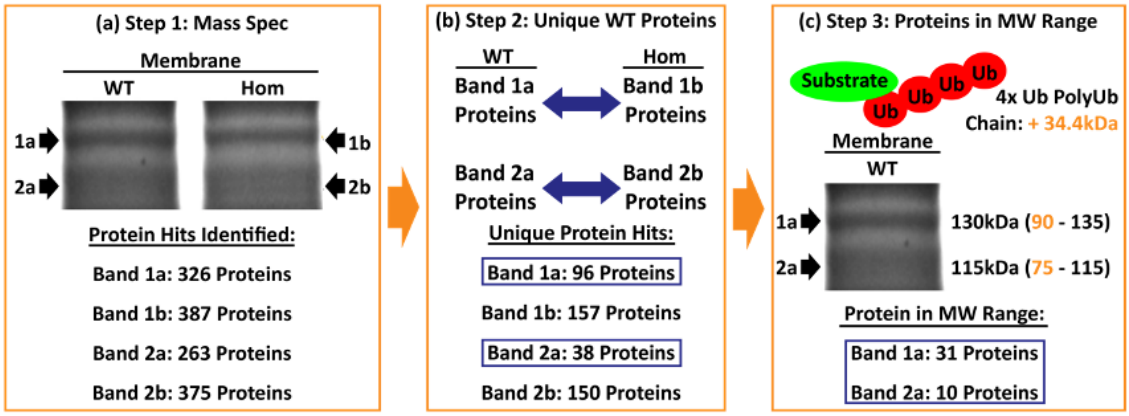

Figure 4.13: Overview of sorting MS protein hits to identify potential NEDD4L substrates. A workflow of how MS-identified, protein hits were sorted, in the process of identifying potential NEDD4L substrates. **(a)** MS of protein bands 1a and 2a, which were excised from membrane fractions prepared from *Nedd4l*$^{+/+}$-derived MEFs, returned 326 and 263 proteins, respectively. MS of protein bands 1b and 2b, which were excised from membrane fractions prepared from *Nedd4l*$^{tm1b/tm1b}$-derived MEFs, returned 387 and 375 proteins, respectively. **(b)** Potential NEDD4L substrates would only be present in membrane fractions prepared from *Nedd4l*$^{+/+}$-derived cells; protein hits that were identified only in bands 1a and 2a were considered. Comparison of the list of proteins identified from bands 1a and 2a, to the list of proteins identified from bands 1b and 2b respectively, returned 96 and 38 unique protein hits from bands 1a and 2a, respectively. **(c)** Addition of a polyubiquitin chain, containing 4 Ub moieties, would add 34.4kDa to the native molecular weight of potential NEDD4L substrate. With consideration to the MW of bands 1a and 2a (130 and 115kDa, respectively), only proteins that were between 90 – 135kDa identified from band 1a, and between 75 – 115kDa identified from band 2a were considered. As a result, 31 proteins were identified from band 1a, and 10 proteins were identified from band 2a.

Another selection criterion is the molecular weight of protein bands 1a and 2a, and of the proteins in the unique hits identified in bands 1a and 2a (Figure 4.13b). The 1a and 2a bands were approximately at 130kDa and 115kDa in size, respectively. Accounting for the resolution and scale of the Coomassie-stained, FK2-immunoprecipitated protein gel, proteins that were between 125 – 135kDa and 110 – 120kDa were considered for bands 1a and 2a. However, additional considerations had to be made due to increases in a protein's native weight due to its ubiquitination, its effects on migration of proteins

down a protein gel and that MS does not identify whether a protein has been modified by a Ub moiety. A single Ub moiety is 8.6kDa, and previous literature has described that a polyubiquitin chain consisting of up to four Ub moieties (34.4kDa) can initiate its degradation. At the maximum theoretical limit, a NEDD4L substrate carrying a polyubiquitin chain which consists of four Ub moieties, could be running higher than it would if it was running only on its native weight. Consequently, proteins that were between 90 – 135kDa and 75 – 120kDa were selected from the unique protein hits identified from bands 1a or 2a, respectively. Overall, 31 proteins (Table 4.1) were within the 90 – 135kDa from the unique protein hits from band 1a, and 10 proteins (Table 4.2) were within the 75 – 120 kDa range from the list of unique protein hits identified from band 2a (Figure 4.13c). Interestingly, one of the substrates identified from the unique protein hits from 2a was NEDD4L, which provided additional evidence that the *Nedd4l*$^{tm1b/tm1b}$ genotype is a homozygous KO null mutation of the *Nedd4l* gene.

Protein Name	Gene Name	MW (kDa)
V-type Proton ATPase Subunit a	*Tcirg1*	93.4
Aftiphilin	*Aftph*	101.1
Leucyl-tRNA Synthetase 2	*Lars2*	101.4
Little Elongation Complex Subunit 2	*Ice2*	109.8
Integrin Alpha-9	*Itga9*	114.3
Pleckstrin Homology Domain-containing Family M Member 2	*Plekhm2*	114.3
Alpha V Integrin	*Itgav*	115.2
PUM-HD Domain-containing Protein	*Pum1*	116.3
SWI/SNF-related Matrix-Associated Actin-dependent Regulator of Chromatin Subfamily A containing DEAD/H Box 1	*Smarcad1*	116.4
Pleckstrin Homology Domain-containing Family G Member 5	*Plekhg5*	118.9
Caspase Recruitment Domain-containing Protein	*Card10*	119.1
Solute Carrier Family 12, Member 7, KCC4	*Slc12a7*	119.4
Lysine-Specific Demethylase 4A	*Kdm4a*	120.3
Transcription Elongation Factor SPT5	*Supt5h*	120.6
Nuclear Export Mediator Factor	*Nemf*	121.1
DNA Helicase B	*Helb*	121.4
TATA Element Modulatory Factor 1	*Tmf1*	121.7
Histone Deacetylase 5	*Hdac5*	121.9

Protein Name	Gene Name	MW (kDa)
Platelet-derived Growth Factor Receptor Alpha	*Pdgfra*	122.6
OTU Domain-containing Protein 4	*Otud4*	123
Formin-Like Protein 2	*Fmnl2*	123
SLIT-ROBO Rho GTPase-activating protein 2	*Srgap2*	124.6
Eukaryotic Translation Initiation Factor 2-Alpha Kinase 3	*Eif2ak3*	124.6
Suppression of Tumorigenicity 5 Protein	*St5*	126.8
Phosphatidylinositide Phosphatase SAC2	*Inpp5f*	127.5
Ankyrin Repeat and FYVE Domain-containing 1	*Ankfy1*	128.6
Mannosidase Alpha Class 2A Member 2	*Man2a2*	130.6
Solute Carrier Family 12, Member 2 NKCC1	*Slc12a2*	130.6
Ubiquitin Carboxyl-Terminal Hydrolase 7	*Usp7*	132.8
Nuclear Exosome Regulator NRDE2	*Nrde2*	133.4
F-Box only Protein 38	*Fbxo38*	133.8

Table 4.1: The 31 protein hits identified by MS of FK2-immunoprecipitated protein fraction band 1a, prepared from Nedd4l$^{+/+}$-derived MEFs. These proteins were identified as potential NEDD4L substrates were selected as their native molecular weight was between 90 – 135kDa.

Protein Name	Gene Name	MW (kDa)
Coiled-Coil Domain-containing Protein R3HCC1L	*R3hcc1l*	84.4
A-Kinase Anchor Protein 1, Mitochondrial	*Akap1*	92.1
Integrator Complex Subunit 6-Like	*Ints6l*	96.9
Phosphofurin Acidic Cluster Sorting Protein 2	*Pacs2*	98.1
Disks Large Homolog 1	*Dlg1*	100.8
Band 4.1-Like Protein 3	*Epb41l3*	101.4
Staphylococcal Nuclease Domain-containing Protein	*Snd1*	102
Adaptor Protein 2-Associated Protein Kinase 1	*Aak1*	103.3
Discs, Large Homolog 3 (Drosophila)	*Dlg3*	103.8
Pumilio Homolog 2	*Pum2*	114.2
E3 Ubiquitin-Protein Ligase NEDD4-Like	*Nedd4l*	115.3

Table 4.2: The 10 protein hits identified by MS of FK2-immunoprecipitated membrane protein fraction band 2a, prepared from Nedd4l$^{+/+}$-derived MEFs. These proteins were identified as potential NEDD4L substrates were selected as their native molecular weight was between 75 – 120kDa.

4.2.5.2 In Silico Analysis of Potential Substrate Expression in Cochlear Tissue

The final sorting parameter was to identify whether any of the 41 (Table 4.1, Table 4.2) proteins could be a target of NEDD4L within cochlear tissue. For a protein to be substrate of NEDD4L within the cochlea, it would need to be expressed in the same cell type as NEDD4L. Therefore, to determine if any of the 41 candidate protein substrates could be ubiquitinated by NEDD4L, an assessment of their respective gene expression within the cochlear tissue was undertaken utilizing the gEAR database (umgear.org); (Orvis *et al.*, 2020). Their expression was compared to that of *Nedd4l* to see they are both expressed

in IdCs, which is where *Nedd4l* expression was detected in cochlear tissue of P0-aged mice (Figure 3.5f). A transcriptomic dataset generated from the cochlear tissue of P1 mice, which includes data for IdCs, was used (Kolla *et al.*, 2020). This dataset was generated by the Kelley lab, and was used as it closely age-matches with the *Nedd4l* cochlear expression studies that I performed.

Nedd4l transcripts are detected in IdCs in the Kelley lab-generated scRNA-seq dataset (Figure 4.14; blue circle, "IdC"). This corroborates the X-Gal staining observed in P0 cochlear tissue (Figure 3.5). Interestingly, the scRNA-seq data also indicated increased levels of *Nedd4l* transcripts in both hair cell populations, IS and medial greater epithelial ridge cells (MGER) compared to other cochlear cell types (Figure 4.14; green circle, "IHC" and "OHC"; light blue circle, "IS"; yellow circle, "MGER"). Therefore, transcript expression of potential substrates was assessed on whether its expression was detected in the IdCs, IHCs, MGER, IS and OHCs.

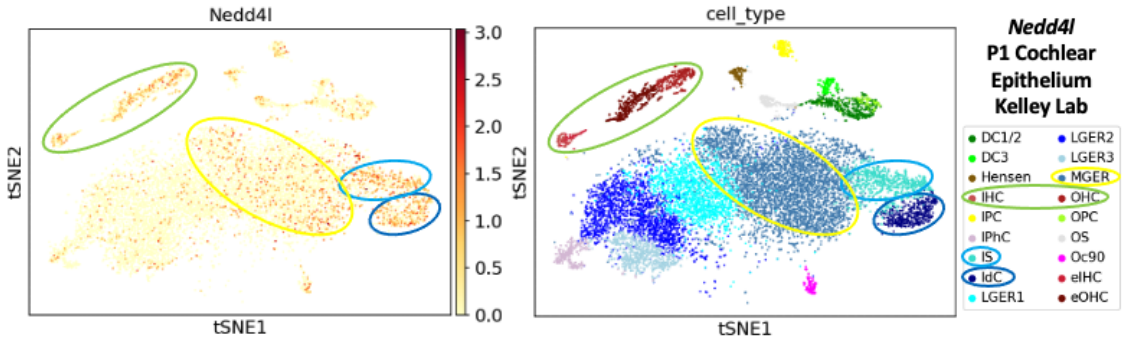

Figure 4.14: gEAR Database: scRNA-seq reported Nedd4l expression in mouse cochlear tissue. scRNA-seq transcript expression data generated by the Kelley lab, for *Nedd4l* in cochlear epithelium tissue derived from P1-aged, CD1 mice. *Nedd4l* transcripts expression were enriched in numerous cochlear cell types, with its expression highest in IdC (dark blue circle) and both IHC and OHC (green circle). Expression was also detected in the IS (light blue circle) and Medial Greater Epithelial Ridge (MGER, yellow circle).

Many potential substrates were deemed improbable cochlear NEDD4L substrates and so were not followed-up. For example, some transcripts were not expressed in the same cochlear cell types as *Nedd4l*. This included proteins such as Transcription Elongation Factor SPT5 (*Supt5h*) and Integrin Alpha-9 (*Itga9*), in which their transcripts were either

not detected in cochlear tissue or their transcripts were not detected in *Nedd4l*-expressing cochlear cell types, respectively (Figure 4.15). In other cases, transcripts of other potential NEDD4L substrates appeared to have ubiquitous expression across all cochlear cell types from P1-aged mice and not enriched in any cochlear cell type. This included potential substrates such as Nuclear Export Mediator Factor (*Nemf*) and SWI/SNF-related matrix-associated actin-dependent regulator of chromatin subfamily A containing DEAD/H Box 1 (*Smarcad1*) (Figure 4.16a, b respectively).

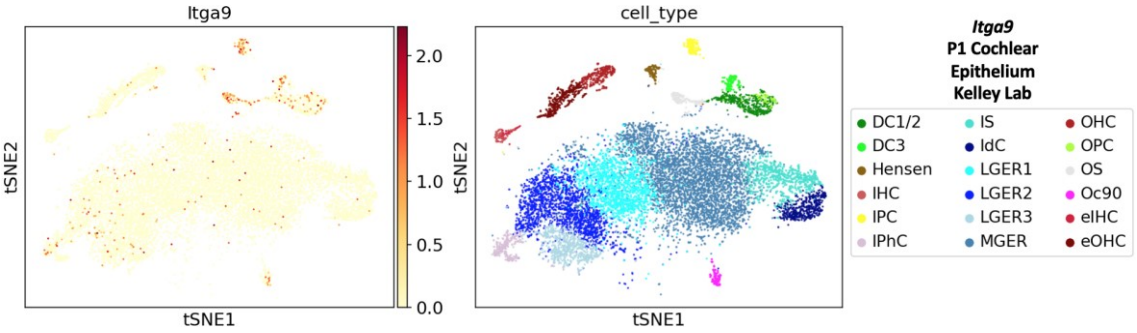

Figure 4.15: gEAR Database: transcript expression of potential NEDD4L substrates Itga9, does not overlap with Nedd4l transcript expression in P1-aged mouse cochlear epithelial tissue. The cochlear cell enrichment of transcripts for potential NEDD4L substrate Integrin Alpha-9 (*Itga9*) did not match where *Nedd4l* transcripts are detected, indicating that neither are substrates of NEDD4L in cochlear tissue. Transcripts for *Itga9* are detected in Deiter Cells (DC1/2, DC3), Hensen's Cells, Inner Pharyngeal and Pillar Cells (IPhC, IPC respectively).

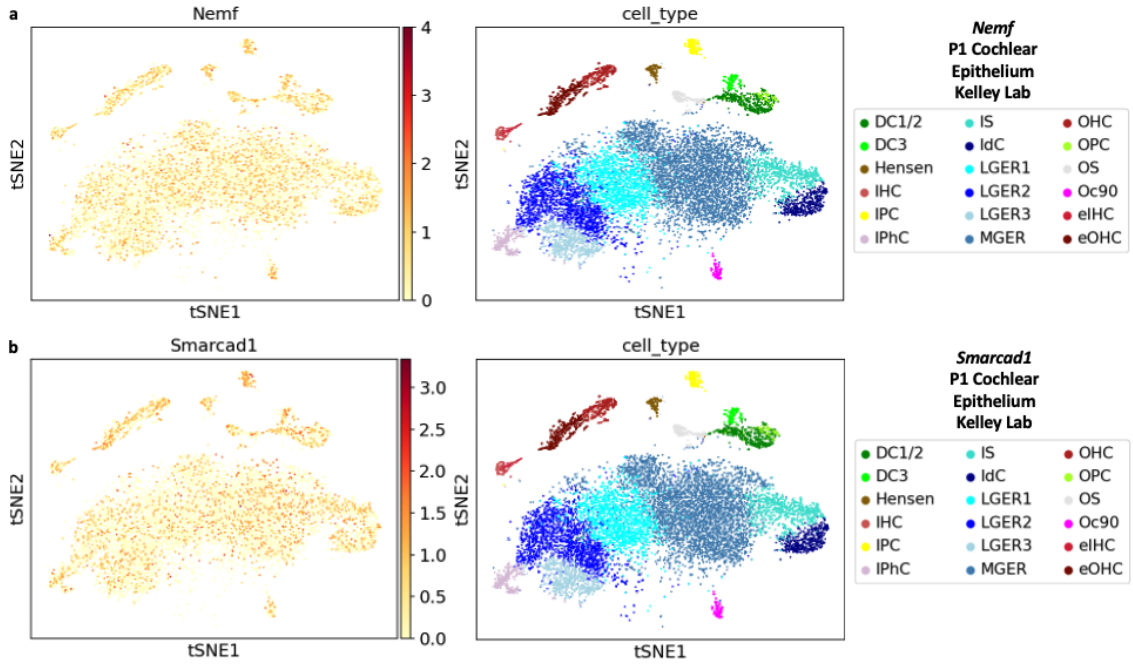

Figure 4.16: gEAR Database: location of transcript expression of potential NEDD4L substrates, Nemf and Smarcad1 is ubiquitously expressed in P1-aged mouse cochlear epithelial tissue. The cochlear cell enrichment of transcripts of the potential NEDD4L substrates, Nuclear Export Mediator Factor (*Nemf*, a) and SWI/SNF-related Matrix-Associated Actin-dependent Regulator of Chromatin Subfamily A containing DEAD/ H Box 1 (*Smarcad1*, b) are not enriched in a particular cochlear cell type of P1-aged cochlear epithelial tissue. As transcript location did not match where *Nedd4l* transcripts are enriched, they were no longer considered potential NEDD4L substrate.

The only potential substrate which appeared to match *Nedd4l* transcript expression was Solute carrier family 12 member 2 (*Slc12a2*), which is also known as the Na^+-K^+-Cl^- Cotransporter 1 (NKCC1) (Figure 4.17a). *Slc12a2* is a known deafness-causing gene, whose expression and function has been previously described in the K^+ recycling pathway (Crouch *et al.*, 1997; Dixon *et al.*, 1999; Delpire *et al.*, 1999). There were plans to perform anti-NKCC1 immunohistochemistry stains on the cochlear tissue of *Nedd4l*$^{tm1b/tm1b}$ mice, to investigate if NKCC1 protein expression is disrupted, but unfortunately this was not conducted due to the Covid-19 pandemic.

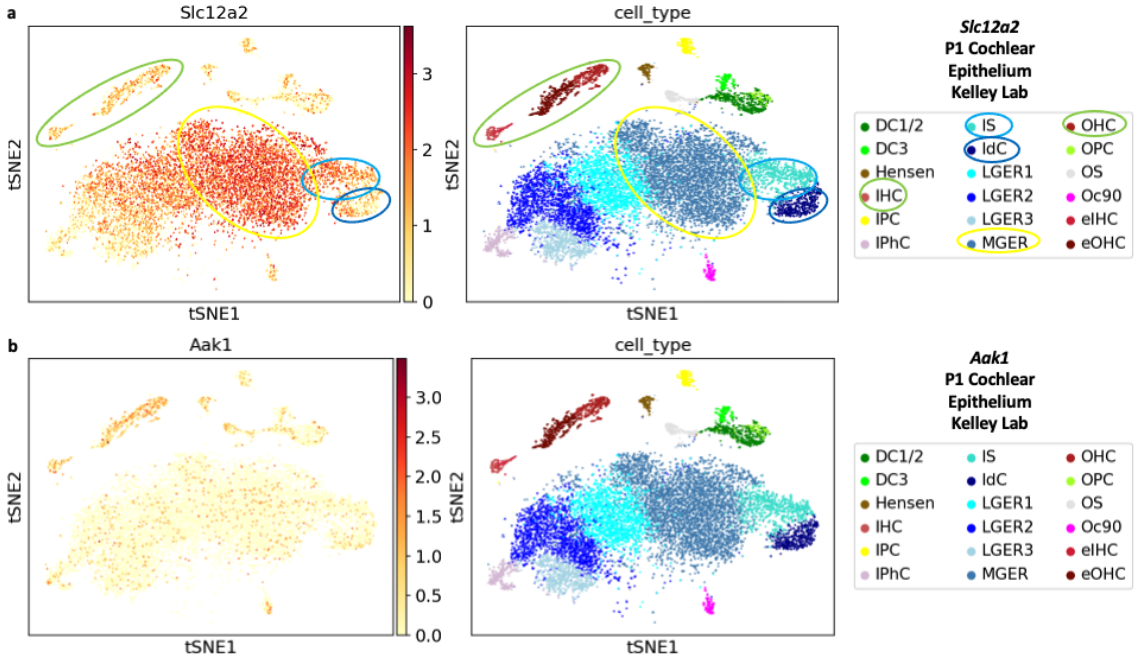

Figure 4.17: gEAR Database: the location of transcript expression of potential NEDD4L substrates, Slc12a2 and Aak1, in P1-aged mouse cochlear epithelial tissue. The cochlear cell enrichment for transcripts of the potential NEDD4L substrates, Solute Carrier Family 12, Member 2 (*Slc12a2*, a) and Adaptor Protein 2-Associated Protein Kinase 1 (*Aak1*, b). **(a)** *Slc12a2* transcripts were enriched in the IdCs (dark blue circle), IS (light blue circle), IHC and OHC (green circle) and MGER (MGER, yellow circle). This matched the location where *Nedd4l* transcripts are enriched in the cochlear epithelial tissue of P1-aged mice. **(b)** *Aak1* transcripts enriched in both IHC and OHCs populations. Whilst this did not match the location where *Nedd4l* transcripts are enriched, *Aak1* is a candidate deafness-causing gene that was identified by the IMPC.

A literature review was also conducted to investigate if any of the other 40 potential *in vivo* NEDD4L substrates had any known cochlear function or involved in hearing loss onset when mutated. AP2-associated protein kinase 1 (*Aak1*) was identified alongside *Nedd4l*, as one of 52 novel deafness-causing genes identified by the IMPC (Bowl *et al.*, 2017). Despite the transcript expression of *Aak1* not matching *Nedd4l*'s reported transcript expression profile (Figure 4.17b), there were also plans to investigate if AAK1 protein expression was altered in *Nedd4l*$^{tm1b/tm1b}$ mice. Again, this was not conducted due to the Covid-19 pandemic.

4.2.5.3 Investigation of Previously Reported NEDD4L Substrates

There are published reviews which discuss the function of NEDD4L and its previously reported interacting proteins (Goel *et al.*, 2015; Manning & Kumar, 2018). Using reviews

published by Goel *et al.* and Manning and Kumar, there were 66 (not including ENaC or NKCC1) previously reported NEDD4L substrates (Appendix Table 9). *In silico* investigation was conducted to determine where the transcripts of these 66 previously reported NEDD4L interacting protein are expressed in cochlear tissue, using the Kelley lab-generated scRNA-seq from P1-aged cochlear epithelial tissue. The expression of transcripts of previously reported, NEDD4L interacting proteins was then compared to the expression of *Nedd4l* transcripts, to determine if they could potentially interact in cochlear tissue. In addition, a literature review was also conducted to determine if any of the previously reported, NEDD4L interacting proteins are involved in cochlear function or implicated in hearing loss.

Only two previously reported NEDD4L interacting protein overlapped with the location of *Nedd4l* transcripts and had a reported role in cochlear function; Potassium Voltage-Gated Channel Subfamily Q Member 1 (KCNQ1) and Occludin proteins. *Kcnq1* transcripts were detected in the IdCs and IS and is involved in maintaining endolymphatic K^+ (Figure 4.18a) (Neyroud *et al.*, 1997). Occludin is noteworthy given that published articles have described its requirement for cochlear function (Figure 4.18b) (Kitajiri *et al.*, 2014). Like NKCC1 and AAK1, there were plans to characterise KCNQ1 and Occludin protein in the cochlear tissue of *Nedd4l*$^{tm1b/tm1b}$ mice, but could not be conducted due to the Covid-19 pandemic.

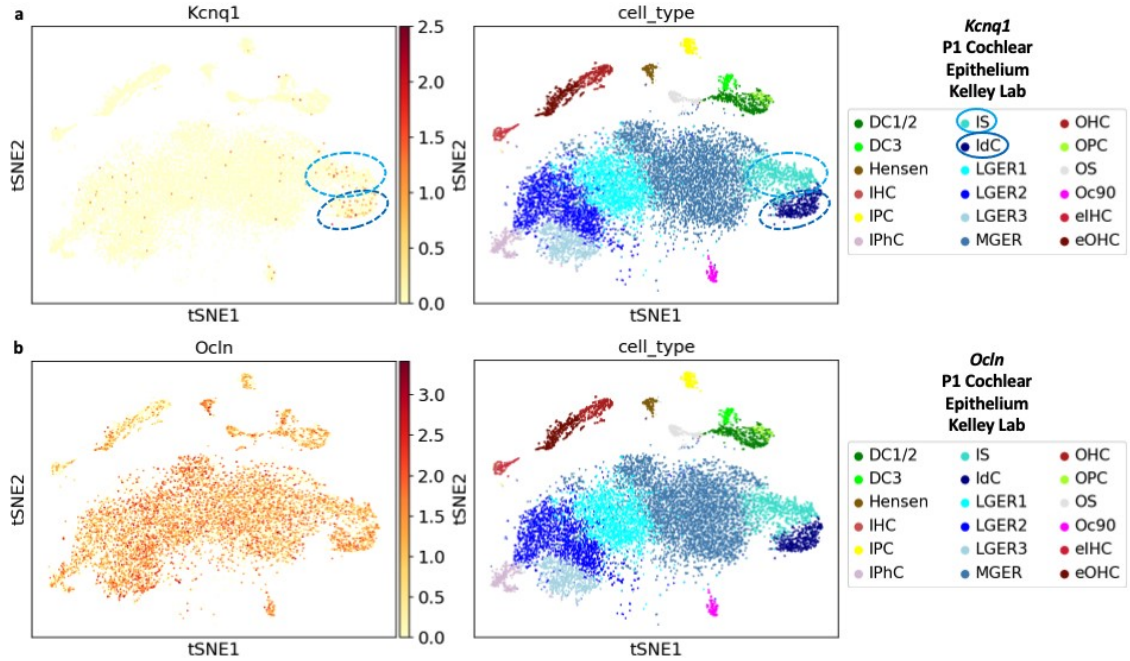

Figure 4.18: gEAR Database: the location of transcript expression of the previously reported NEDD4L substrates, Potassium Voltage-Gated Channel Subfamily Q Member 1 and Occludin. Reported expression of transcripts for Potassium Voltage-Gated Channel Subfamily Q Member 1 (*Kcnq1*, a) and Occludin (*Ocln*, b). Both proteins have been reported to be involved in cochlear function. **(a)** Transcripts for *Kcnq1* were found specifically in IdCs (dark blue circle) and IS (light blue circle). **(b)** *Ocln* transcripts were detected ubiquitously in the cochlear epithelial tissue of P1-aged CD-1 mice.

4.3 Discussion

4.3.1 Potential Non-Canonical Regulation of ENaC by NEDD4L

A functional ENaC channel is composed of the channel pore-containing αENaC and the two regulatory ß and γENaC subunits. NEDD4L-mediated ubiquitination and degradation of all three ENaC channel subunit proteins have been well characterised (Manning & Kumar, 2018). Therefore, the observation of decreased αENaC subunit protein in P0-aged, *Nedd4l*$^{tm1b/tm1b}$ mice-derived cochlear tissue was particularly striking, given that its abundance was expected to increase in the absence of NEDD4L protein. This result does raise questions regarding the cause and mechanism by which αENaC subunit protein abundance is decreased in cochlear tissue of *Nedd4l*$^{tm1b/tm1b}$ mice. Decreased αENaC could be mediated through another ubiquitin ligase protein, such as the NEDD4 protein that is also expressed in cochlear tissue and could have some compensatory activity in the absence of NEDD4L (Zhong *et al.*, 2014). Alternatively, another protein of the NEDD4 E3 Ubiquitin Ligase family, WWP2, could also be responsible, as its interaction and inhibition of ENaC activity has been described (McDonald *et al.*, 2002). In addition, it has been shown that the Serine/Threonine Protein Kinase WNK4 can also regulate the activity and abundance of all three ENaC subunits (Yu *et al.*, 2013).

The regulation of the other ENaC subunits in cochlear tissue by NEDD4L has also not been investigated either. Previous reports have described specific ENaC subunit regulation at the transcriptional and translational level. Tissue and hormone-specific regulation of the different ENaC subunits has been previously described. For example, increased transcription of the ß and γ, but not αENaC subunits was observed upon vasopressin treatment of kidney cortical collecting duct cell line, derived from rats

(Djelidi *et al.*, 1997). Other reports have described the Mitogen-activated protein kinase (MAPK)-mediated repression of αENaC transcription (Zentner *et al.*, 1998; Lin *et al.*, 1999). There has also been a disparity in the regulation of different ENaC subunits in previously generated *Nedd4l* KO lines. Only ßENaC protein was disrupted in the lungs of a constitutive *Nedd4l* KO mouse line, but not observed in other tissues such as the kidney, whereas decreased abundance of all ENaC subunits was reported in the kidneys of a hypomorphic *Nedd4l* KO mice (Boase *et al.*, 2011; Shi *et al.*, 2008). Further investigation of ENaC channel in cochlear tissue will be discussed in Chapter 6.

4.3.2 Cochlear Function of Potential NEDD4L Cochlear Substrates

Identifying NEDD4L substrates through immunoprecipitation reactions against mono- and polyubiquitinated proteins was an unbiased, global approach designed to elaborate upon NEDD4L function, which may highlight its role within the cochlea. Through this approach, NKCC1 was identified as a potential *in vivo* NEDD4L substrate, and also has an overlapping expression pattern in cochlear tissue. NKCC1 represents an interesting candidate to further investigate as the basolateral-localised cotransporter is a well characterised membrane protein in cochlear tissues that is required for ion homeostasis (Crouch *et al.*, 1997; Delpire *et al.*, 1999; Dixon *et al.*, 1999; Flagella *et al.*, 1999). In cochlear tissue, NKCC1 (encoded by *Slc12a2*) is involved in maintaining the endolymph ionic composition, as indicated by its expression in the SL, SLim, SV (Diaz *et al.*, 2007; Crouch *et al.*, 1997; Mizuta *et al.*, 1997). This is also evident when the *Slc12a2* gene is mutated, resulting in gross pathological disruptions to the endolymph spaces and hearing loss in both mice and humans (Delpire *et al.*, 1999; Dixon *et al.*, 1999; Flagella *et al.*, 1999; Diaz *et al.*, 2007; Macnamara *et al.*, 2019; Mutai *et al.*, 2020; McNeill *et al.*, 2020; Koumangoye *et al.*, 2020). In addition, NKCC1 abundance is known to be regulated by NEDD4L, with a previous report detailing its increased expression in the colon tissue of the mice that carry an intestinal epithelium-specific KO of *Nedd4l* (Jiang *et al.*, 2017).

KCNQ1 protein subunits are located in the endolymph-facing, marginal cells of the SV (Neyroud *et al.*, 1997). When mutated in mice, the scala media space collapses, indicating disruption of K^+ recycling back into endolymphatic spaces following hair cell MET (Rivas & Francis, 2005). Reported *Kcnq1* expression is specific to the IdCs, suggesting that it could be involved in the hypothesised medial pathway of K^+ recycling

back into endolymphatic spaces (Spicer & Schulte, 1998). This pathway involves K^+ transport through the IS, SLim and IdCs, where it can be returned to endolymphatic spaces. Disruptions to the *Ocln* gene in mice also causes hearing loss phenotype, which is characterised by the disruptions of the deafness associated Tricellulin protein that is found at tricellular tight junctions (Kitajiri *et al.*, 2014; Riazuddin *et al.*, 2006). In addition to validating potential interactions with NEDD4L, experiments must also be designed to determine the pathological consequences of dysregulated ubiquitination of KCNQ1 and Occludin. These should include investigations to determine if their abundance is perturbed in *Nedd4l*$^{tm1b/tm1b}$ mice. If so, it would be pertinent to perform *in vivo* phenotyping to determine if the ionic composition of endolymph is affected and whether this affects the EP in *Nedd4l*$^{tm1b/tm1b}$ mice.

4.3.3 Suitability of MEFs to Identify NEDD4L Cochlear Substrates

Many factors influenced the use of MEFs as a surrogate model to identify NEDD4L *in vivo* cochlear substrates. The profile of *Nedd4l* expression discovered by *Nedd4l*-controlled *lacZ* expression studies was restricted to the IdCs. With considerations to the small number of cells found within a mature cochlea, identifying NEDD4L substrates in cochlear tissue through the use of cochlear tissue would be challenging. Use of MEFs was able to identify a potential NEDD4L *in vivo* substrate (NKCC1), whose absence of regulation in *Nedd4l*$^{tm1b/tm1b}$ mice could be the cause of auditory dysfunction. However, it is possible that more NEDD4L *in vivo* cochlear substrates could have been identified if a cell model which more accurately modelled cochlear tissue was used. The cochlea is highly organised with numerous cell types that are specialised for a particular role in the process of hearing. As a result, it must be asked how accurate the *Nedd4l*$^{tm1b/tm1b}$ MEF cell and its proteome is to model the *Nedd4l*-expressing IdCs of cochlear tissue. Whilst plans also included validation of potential substrate interactions in cochlear tissues, it is possible that using MEFs will not identify IdC-specific interactions between NEDD4L and its substrates in the first place.

On the other hand, there are few alternative *in vitro* cochlear cell lines available, and none appear appropriate to model the cochlear IdC population. Cell lines such as UB/OC1 and 2, and HEI-OC1 cell lines have been previously described but represent a model for the OoC and sensory hair cells than the non-sensory IdCs (Rivolta & Holley, 2002; Kalinec *et al.*, 2003). Another alternative cell model that would be a more accurate representation of the cochlea and of IdCs could be to generate Conditionally Reprogrammed Otic Stem Cells (CROSCs) from *Nedd4l*$^{tm1b/tm1b}$ mice. Overexpression of

the pro-hair cell transcription factor ATOH1 in CROSCs was shown to upregulate transcription of hair cell-specific genes such as Otoferlin and Myosin VI, indicating that CROSCs could be directed towards a specific cochlear cell lineage (Walters *et al.*, 2015). However, using this approach to direct CROSCs towards an IdC fate would be technically challenging due to insufficient understanding of their development (Iyer & Groves, 2021). Clonal analysis has identified that *Eya1*-expressing otic progenitors give rise to the IdC population, but also to non-sensory cells of the OoC, the surrounding epithelial ridge cells and the SGNs (Xu *et al.*, 2017).

4.3.4 Underreporting of NEDD4L Cochlear Substrates

Numerous steps and techniques were utilised to try to identify NEDD4L *in vivo* substrates from MEFs. However, some difficulties arose along the way that hindered the identification of potential substrates. For example, identifying differences in protein banding pattern between immunoprecipitated ubiquitinated proteins from *Nedd4l*$^{+/+}$ and *Nedd4l*$^{tm1b/tm1b}$ MEFs was difficult due to the overall intensity of the Coomassie stain. More intensely stained protein bands could be masking the presence of less intense, adjacent protein bands, and unfortunately these cannot be revealed by altering the contrast or saturation of the gel image using ImageJ. Furthermore, the overall similarity of the banding pattern has contributed to the difficulty in selecting bands to be excised for MS.

Attempts to enrich for ubiquitinated proteins extracted from MEFs through MG132-mediated proteasomal inhibition did not benefit the identification of protein bands either. Whilst stained protein bands were less intense, no differences could be detected between the membrane fractions of MG132 treated *Nedd4l*$^{+/+}$ and *Nedd4l*$^{tm1b/tm1b}$ MEFs. This could be due to lysosomal- and autophagy-based protein degradation pathways which are utilised for membrane-localised proteins, as opposed to the proteasome-mediated degradation of cytosolic proteins (Seglen *et al.*, 1979; Huber & Teis, 2016; Cichanover, 2005). Future attempts to enrich for membrane-localised proteins should include treatment with lysosome and autophagy inhibitors such as CQ.

The activity of CQ to inhibit these degradative pathways could also explain the results observed in treatment of *Nedd4l*$^{tm1c/tm1c}$ MEFs with CQ to aid *in vitro* recombination of the *Nedd4l*^{tm1c} allele. Combined treatment of *Nedd4l*$^{tm1c/tm1c}$ MEF cell with Cre and CQ

aided in the recombination of *Nedd4l*^{tm1c} allele as shown in the PCR reactions but CQ also inhibited the clearance of NEDD4L protein that was translated before *in vitro* recombination of *Nedd4l.*

Decisions made during the *in silico* portion of analysis may have also hindered the identification of potential substrates. One reservation to the sorting of the initial list of 41 potential substrates using transcriptomic, scRNA-seq data to inform of potential protein interactions. Previous studies have shown that the level of transcription does not necessarily correlate with the level of translation (absolute concentration of mRNA and protein, respectively) (Vogel & Marcotte, 2012; Liu *et al.*, 2016; Buccitelli & Selbach, 2020). However, the scRNA-seq data was only used to determine the cellular location of *Nedd4l* transcripts or a potential substrate within cochlear tissue, and infer potential interactions if they overlapped.

5 AUDITORY CHARACTERISATION OF *NEDD4*

5.1 Introduction

Nedd4 was one of ten genes identified as expressed in embryonic mouse neuronal precursor cells that show decreased transcripts after E10 (Kumar *et al.*, 1992). As the namesake of the HECT-domain containing family of E3 Ubiquitin Ligase enzymes, *Nedd4* is well characterized, with numerous publications describing its role in targeting proteins for proteasomal degradation and its physiological requirement (Boase & Kumar, 2015).

More recently, through whole exome sequencing (WES) of patients with adult-onset hearing loss, *NEDD4* was identified as a novel candidate deafness-causing gene. Across five patients, out of the 30-patient cohort, two novel coding lesions were identified that are predicted to cause pathogenic residue substitutions within the encoded NEDD4 protein (Lewis *et al.*, 2018). None of the five patients have a family history of hearing loss. Furthermore, these five patients were placed in the "sensory hearing loss" subgroup as audiometric tests identified elevated auditory thresholds in response to only higher frequency stimuli (4 – 8kHz) (Dubno *et al.*, 2013; Lewis *et al.*, 2018). While previously published reports describe associations between single nucleotide polymorphisms found in the *NEDD4* gene and the incidence of schizophrenia, hypertension and the severity of keloid scars, this is the first report to suggest that mutations in the *NEDD4* gene causes loss of auditory function (Han *et al.*, 2019; Li *et al.*, 2010; Nakashima *et al.*, 2010).

Nedd4 is broadly expressed at embryonic ages, including the facial primordia, heart, lung, spinal cord, muscle and skin (Liu *et al.*, 2009; Fouladkou *et al.*, 2010; Wiszniak *et al.*, 2013). Several different *Nedd4* KO null mouse models have been generated and

characterized, but none have implicated *Nedd4* in the process of mammalian hearing. This is due to the lack of opportunity to assess their auditory capabilities, as all published *Nedd4* KO null models are reported to exhibit fully penetrant embryonic lethality occurring between E18.5 and P0 (Cao *et al.*, 2008; Liu *et al.*, 2009; Kawabe *et al.*, 2010). The auditory function of mice that are heterozygous for a *Nedd4* KO allele has also not been reported. Characterisation studies of *Nedd4* haploinsufficient mice have instead reported of disrupted lipid metabolism and abnormal gait (Li *et al.*, 2015; Camera *et al.*, 2014).

As part of the IMPC programme a new *Nedd4* KO mouse model was generated utilizing a *lacZ*-tagged deletion allele (*Nedd4*^{tm2b}, Figure 5.1). Consistent with results from previously generated *Nedd4* KO mice, no homozygous *Nedd4*^{tm2b} (*Nedd4*$^{tm2b/tm2b}$) mice were born from an intercross of heterozygous *Nedd4*^{tm2b} (*Nedd4*$^{tm2b/+}$) mice (Figure 5.2b). Consequently, *Nedd4*$^{tm2b/+}$ mice entered the IMPC adult phenotyping pipeline, which included an ABR test at 14-weeks of age (Figure 5.2a). Recorded ABR hearing thresholds for the two male *Nedd4*$^{tm2b/+}$ mice (inverted grey triangles) that were tested show they have comparable hearing thresholds to sex-matched, wild type (*Nedd4*$^{+/+}$) control mice (black squares). On the other hand, the two female *Nedd4*$^{tm2b/+}$ mice (upright grey triangles) that were tested appear to exhibit mildly elevated thresholds in response to a 18, 24 and 30kHz auditory stimuli compared to control female *Nedd4*$^{+/+}$ mice (black circles), but this is stated to not be statistically significant (https://www.mousephenotype.org/data/genes/MGI:97297). Overall, according to the IMPC portal it appears that a single functional *Nedd4* allele is likely sufficient to support auditory function.

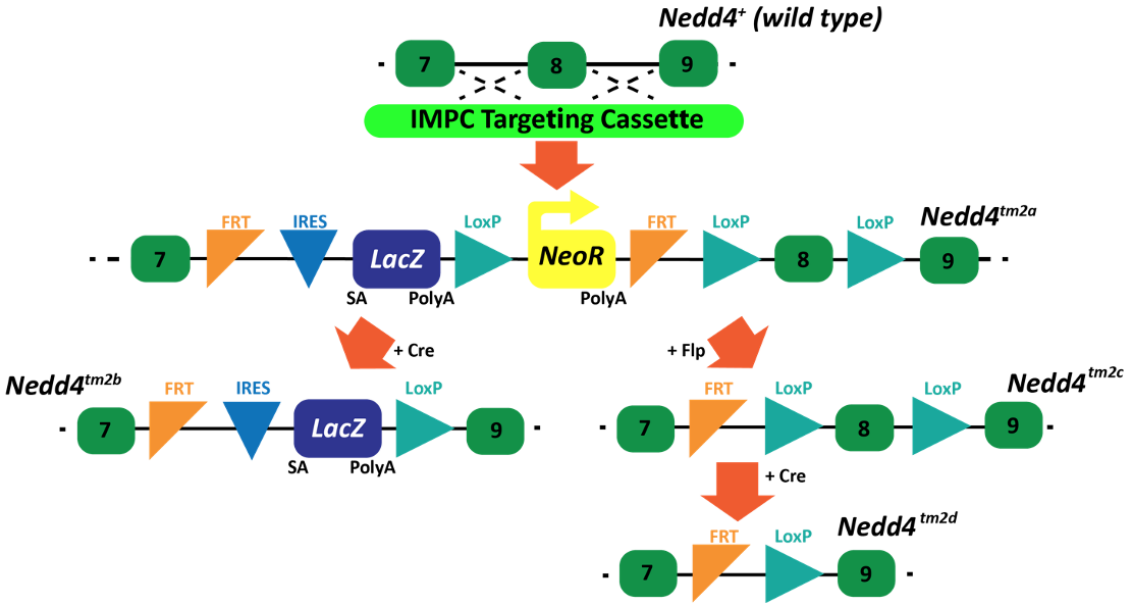

Figure 5.1: Diagrammatic representation of the IMPC-generated Nedd4 KO alleles. The "KO first" *Nedd4*^{tm2a} allele is generated through a *Nedd4* gene trap cassette in mouse C57BL/6N ES cells, introducing the *lacZ* reporter gene, and multiple *loxP* and *FRT* recombination sequences surrounding critical exon (exon 8). Introduction of Cre recombinase to mice carrying the *Nedd4*^{tm2a} allele recombines out the genetic sequence between the first and third *loxP* sites, leaving a *lacZ*-tagged *Nedd4* gene which lacks exon 8 (*Nedd4*^{tm2b}). Alternatively, introduction of Flp recombinase to *Nedd4*^{tm2a} allele-carriers generates the *Nedd4*^{tm2c} allele which results in a floxed exon 8. Mice that carry the *Nedd4*^{tm2c} allele can be crossed to a *Cre*-expressing mouse line to cause recombination of the allele, generating the *Nedd4*^{tm2d} null allele.

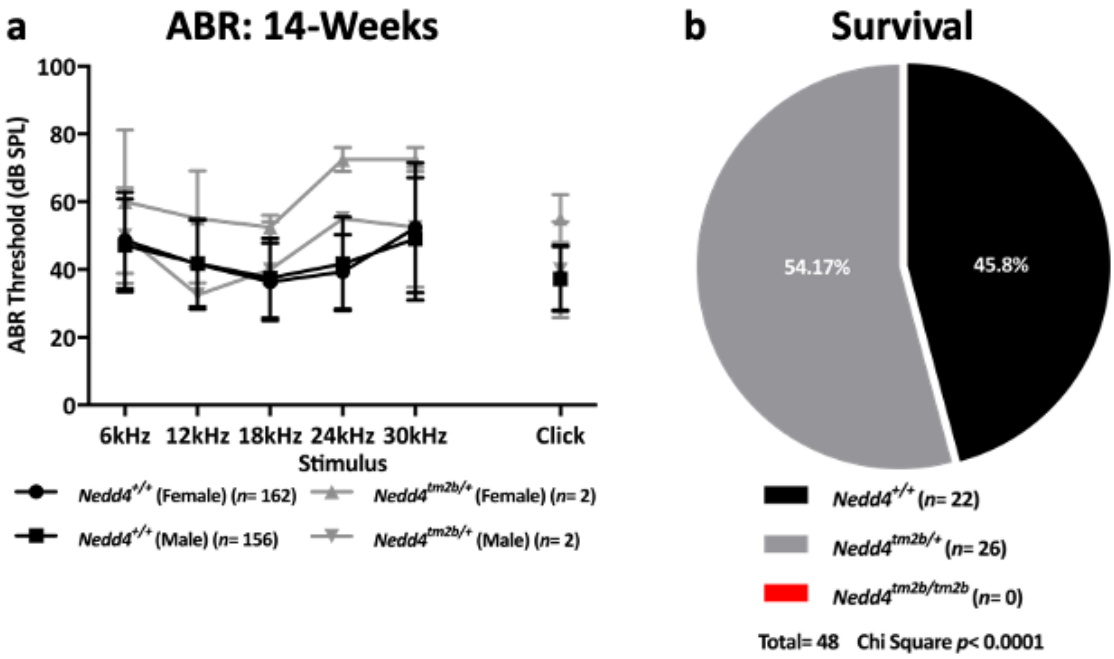

Figure 5.2: Summary of relevant results of IMPC-performed phenotyping of Nedd4$^{tm2b/+}$ mice. **(a)** ABR tests performed at 14-weeks of age *Nedd4*$^{tm2b/+}$ mice. Thresholds were determined for two female and two male *Nedd4*$^{tm2b/+}$ mice. ABR thresholds of *Nedd4*$^{tm2b/+}$ mice are reported to not be significantly different to sex-matched, control *Nedd4*$^{+/+}$ mice. Data presented as averages ± standard deviation. **(b)** The proportion of mice of each genotype born from intercross matings of *Nedd4*$^{tm2b/+}$ mice that were set up to generate a mouse phenotyping cohort. Of the 48 offspring born, no *Nedd4*$^{tm2b/tm2b}$ mice were found. Chi-square tests were performed, showing significantly different proportion of mice of different genotypes born compared to the expected Mendelian genotype proportions (25% *Nedd4*$^{+/+}$, 50% *Nedd4*$^{tm2b/+}$ and 25% *Nedd4*$^{tm2b/tm2b}$ mice).

Nedd4 is widely expressed in cochlear tissues, as reported by the various transcriptomic datasets available on the gEAR Database (Figure 5.3; umgear.org) (Orvis *et al.*, 2020; Kolla *et al.*, 2020; Korrapati *et al.*, 2019; Li *et al.*, 2020). Given that *Nedd4*$^{tm2b/tm2b}$ mice are not viable, I generated *Nedd4* cKO mouse lines to determine if *Nedd4* has a critical role within the mammalian auditory system. To enable this, I utilized mice that carry the IMPC-generated *floxed Nedd4* allele (*Nedd4*^{tm2c}, Figure 5.1) and two *Cre*-expressing mouse lines: the *Sox10-Cre* and the *Myo15-Cre* lines (Matsuoka *et al.*, 2005; Caberlotto *et al.*, 2011). *Sox10* is consistently expressed in all cochlear tissue during embryonic and adult ages, except for sensory hair cells from E16.5 (Wakaoka *et al.*, 2013). Outside of cochlear tissue, *Sox10* is also involved in the formation of neural crest cell-derived tissues, such as bone, ligament and muscle of the neck and shoulder, glial cells and melanocytes (Matsuoka *et al.*, 2005; Mollaaghababa & Pavan, 2003). On the other hand,

Myo15 is exclusively expressed in the cochlear hair cells from E15.5 and in the adult pituitary gland (Liang *et al.*, 1999; Anderson *et al.*, 2000).

Generation of tissue-specific *Nedd4* KO mice will hopefully avoid the lethality issues that confound the use of the constitutive *Nedd4*^{tm2b} KO allele, thus providing an opportunity to investigate the requirement of *Nedd4* for mammalian auditory function. By generating a *Myo15*- and *Sox10*-driven *Nedd4* cKO mice, I can assess the requirement of *Nedd4* in hair cell and non-hair cell populations within cochlear tissue. As previously described, when maternally inherited, the *Sox10-Cre* transgene expression is detected in all cochlear tissues except for IHCs (Figure 3.28). Robust *Cre* expression from the *Myo15-Cre* KI allele was detected in all cochlear hair cells in P4-aged mice (Caberlotto *et al.*, 2011). Through the investigation of these two *Nedd4* cKO mouse lines, I aim to determine whether *Nedd4* is required for hair cell function or in other cochlear tissues.

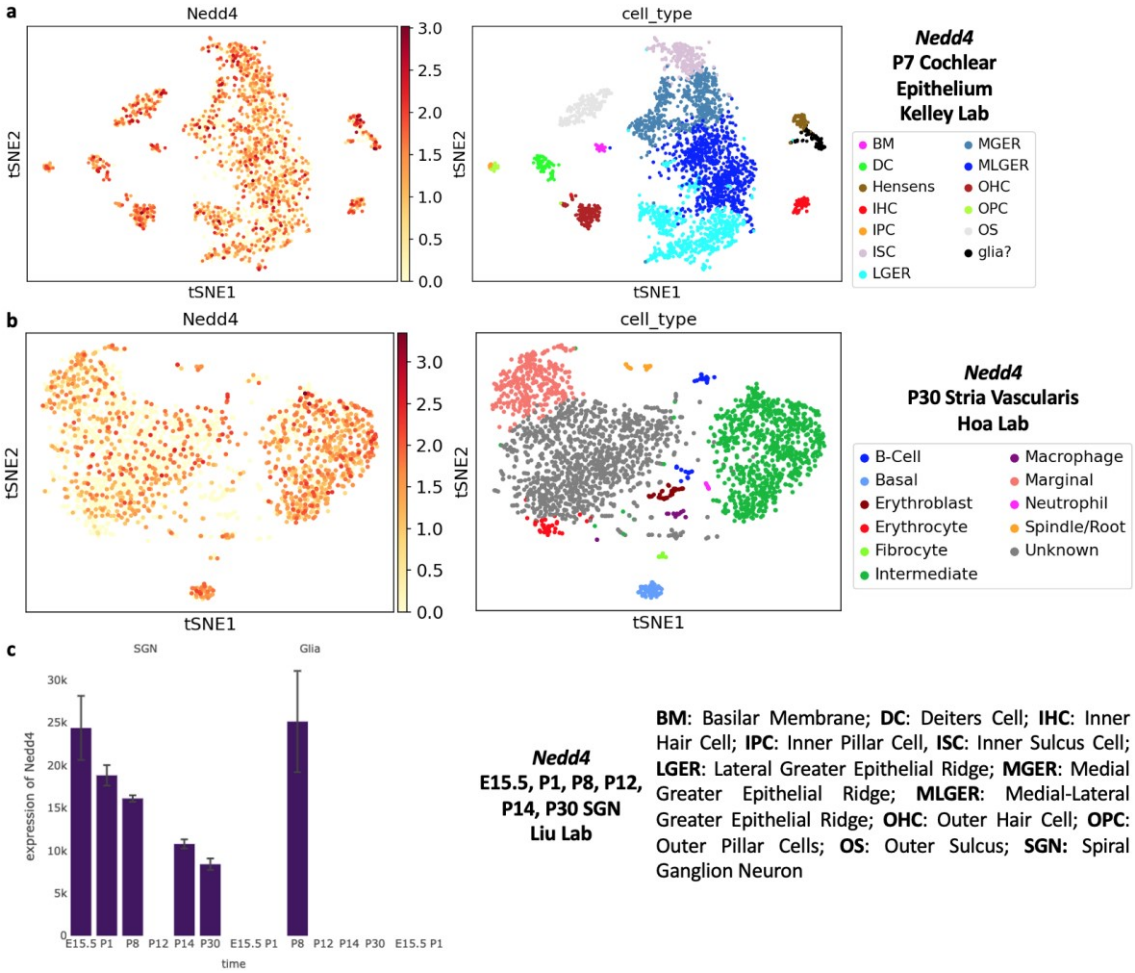

Figure 5.3: gEAR Database: reported transcriptomic data regarding Nedd4 expression in mouse cochlear tissue. Transcriptomic data describing *Nedd4* expression in the cochlear epithelium in P7-aged CD1 mice (a), SV in P30-aged CBA/J mice (b) and SGN derived from mice of various ages (c), generated from the Kelley, Hoa and Liu lab respectively. **(a, b)** scRNA-seq identified *Nedd4* expression in all cochlear cell types of cochlear epithelium and SV. **(c)** *Nedd4* expression is detected in SGN and glia cells that are present in cochlear tissue, with the highest *Nedd4* expression detected at E15.5 and P8, respectively.

5.2 Results

5.2.1 Auditory Characterisation of *Myo15*-Driven cKO *Nedd4* Mice

5.2.1.1 Generation of the Auditory Phenotyping Cohort

Myo15-driven *Nedd4* cKO mice were generated to assess the requirement of *Nedd4* in hair cell function. This was achieved through ABR and DPOAE phenotyping tests. The phenotyping cohort was generated by intercross breeds between *Nedd4*$^{tm2c/+}$ mice, one of which also carries the *Myo15-Cre* KI allele (*Nedd4*$^{tm2c/+}$; *Myo15-Cre*$^{+}$). As a result, the spatiotemporal regulated expression of Cre recombinase would cause recombination of the *Nedd4*^{tm2c} allele only in *Myo15*-expressing hair cells (Liang *et al.*, 1999). Through this breeding strategy, the mice could have one of six possible genotypes. Homozygous *Nedd4*^{tm2c} mice that carry the *Myo15-Cre* KI allele (*Nedd4*$^{tm2c/tm2c}$; *Myo15-Cre*$^{+}$) were expected to make up 12.5% of all mice born. As such, of the 102 mice that were born from 15 litters, 12 were expected to carry the *Nedd4*$^{tm2c/tm2c}$; *Myo15-Cre*$^{+}$ genotype, but just eight were born (Figure 5.4). However, a Chi-Square test indicates that the overall ratio of the number of mice of each genotype, is not significantly different from the expected Mendelian ratio.

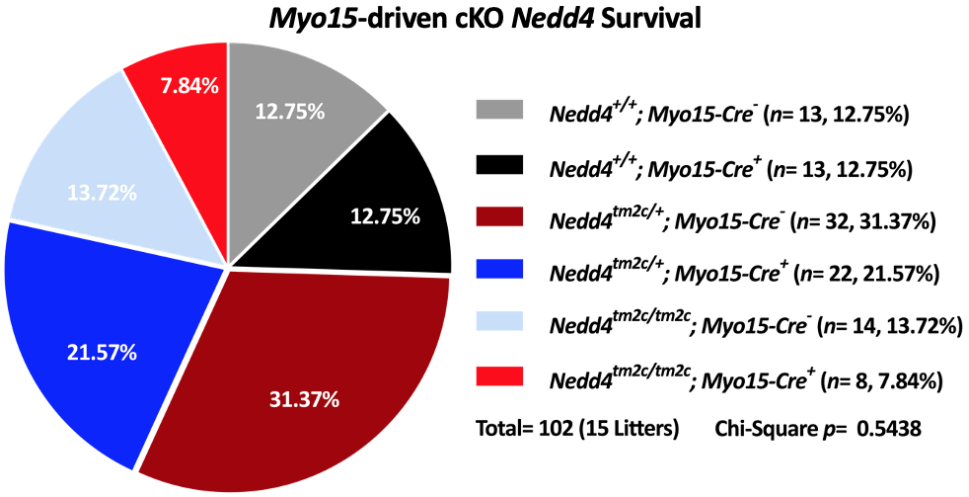

Figure 5.4: Generation of Myo15-driven Nedd4 cKO mouse litters produced a Mendelian ratio of mice. Mice of all possible genotypes were identified and survived past the weaning age, in the litters produced through the intercross between *Nedd4*$^{tm2c/+}$; *Myo15-Cre*$^{+}$ and *Nedd4*$^{tm2c/+}$; *Myo15-Cre*$^{-}$ mice. A chi-square test shows that the ratio of genotypes of the mice born is not significantly different to the expected Mendelian ratio of genotypes (p= 0.5438).

5.2.1.2 Auditory Phenotyping of *Myo15*-driven *Nedd4* cKO Mice

The IMPC-performed broad-based phenotyping suggests that female *Nedd4*$^{tm2b/+}$ mice may have elevated ABR thresholds in response to 18, 24 and 30kHz stimuli compared to female control *Nedd4*$^{+/+}$ mice (Figure 5.2a). To determine if a similar finding is observed in *Nedd4*$^{tm2c/tm2c}$;*Myo15-Cre*$^{+}$ mice, longitudinal ABR tests were performed when mice were 3-weeks, 8-weeks, and 3-months old to assess whether the auditory function was affected (Figure 5.5). The ABR thresholds of wild type (*Nedd4*$^{+/+}$) and *Nedd4*$^{tm2c/+}$ mice that carry the *Myo15-Cre* KI allele (black filled circles and blue filled squares, respectively) is statistically comparable to their respective control mice at all ages tested (Figure 5.5a, b, d, e, g and h). While ABR thresholds of 3-week old *Nedd4*$^{tm2c/tm2c}$; *Myo15-Cre*$^{+}$ mice (filled red triangles) are elevated in response to a click stimulus compared to *Nedd4*$^{tm2c/tm2c}$; *Myo15-Cre*$^{-}$ control mice (light blue hollow triangles), their hearing thresholds at older ages, and for other stimuli, did not show any significant differences to controls (Figure 5.5c, f, i). By 3-months of age all mice show elevated high-frequency hearing thresholds in response to a 32kHz stimuli, which is due to the hypomorphic *Cdh23*^{ahl} allele present in the C57BL/6N strain background (Figure 5.5g – i).

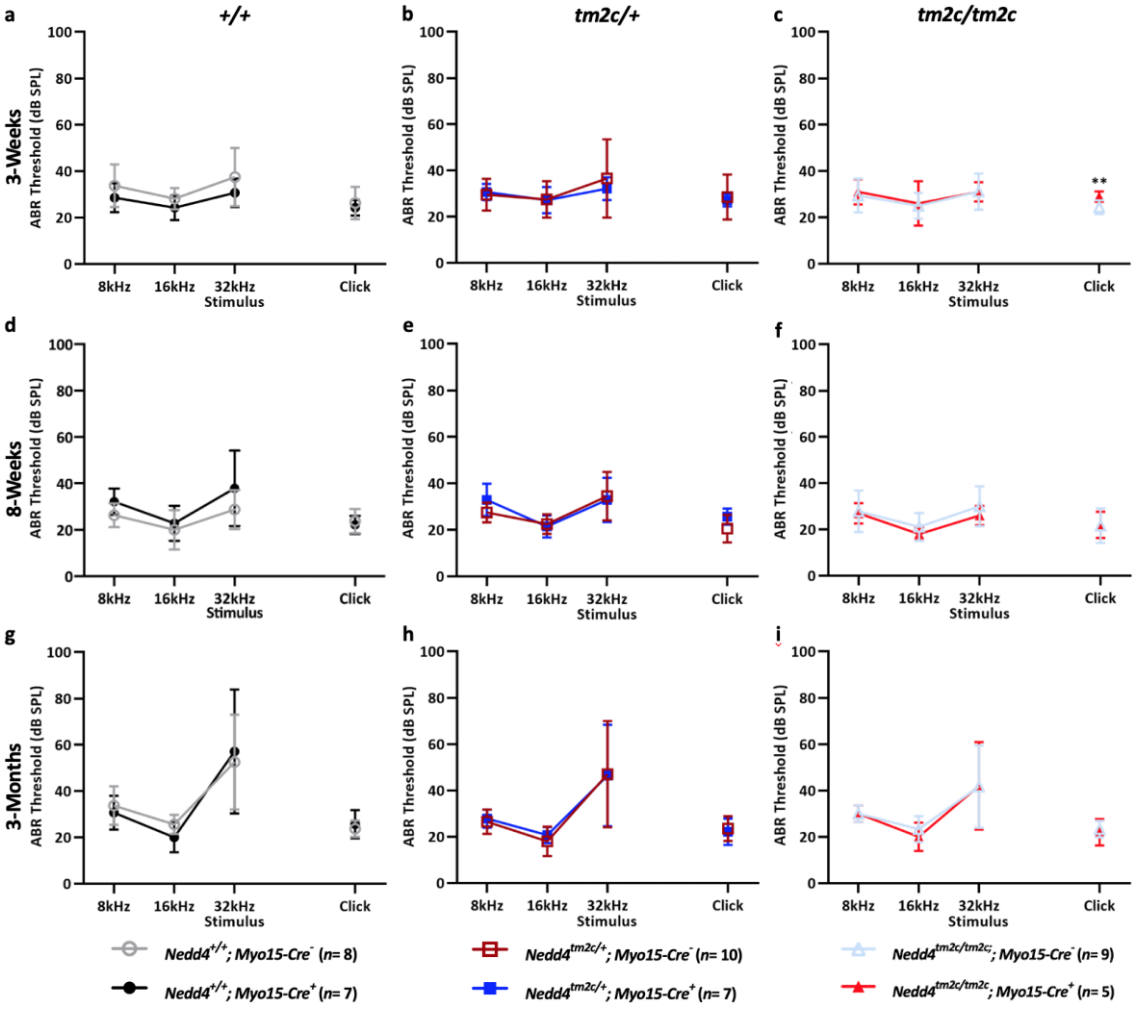

Figure 5.5: Myo15-driven Nedd4 cKO mice display normal ABR thresholds. All mice in *Myo15*-driven cKO *Nedd4* phenotyping cohort underwent ABR tests at 3- (a – c) and 8-weeks (d – f), and 3-months (g – i) of age. **(a, b)** At 3-weeks old, ABR thresholds of *Nedd4$^{+/+}$; Myo15-Cre^{+}* (a, black filled circles) and *Nedd4$^{tm2c/+}$; Myo15-Cre^{+}* (b, blue filled circles) were comparable to their respective controls, at all stimuli tested. **(c)** ABR thresholds recorded from *Nedd4$^{tm2c/tm2c}$; Myo15-Cre^{+}* (red filled triangles) mice are significantly elevated only in response to a click stimulus is significantly different to control *Nedd4$^{tm2c/tm2c}$; Myo15-Cre^{-}* mice (p= 0.0085). **(d – f)** At 8-weeks of age, ABR thresholds of *Nedd4$^{+/+}$; Myo15-Cre^{+}* (d), *Nedd4$^{tm2c/+}$; Myo15-Cre^{+}* (e) and *Nedd4$^{tm2c/tm2c}$; Myo15-Cre^{+}* (f) mice are similar to their respective controls. **(g – i)** Mice of all genotypes have increased ABR thresholds in response to a 32kHz stimulus when tests are performed at 3-months of age. All data presented as averages ± standard deviation error bars. Unpaired T test with Welch's Correction were performed to determine if the recorded auditory thresholds in response to each stimulus, was significantly different between mice of different genotypes.

DPOAE tests were also performed to assess if OHC function is affected in *Nedd4$^{tm2c/tm2c+}$; Myo15-Cre^{+}* mice. Similar to the ABR tests, recorded DPOAE levels from *Nedd4$^{tm2c/tm2c}$; Myo15-Cre^{+}* mice are comparable to control *Nedd4$^{tm2c/tm2c}$; Myo15-Cre^{-}* mice (Figure 5.6). In response to a high frequency stimulus, the DPOAE levels recorded from mice of both genotypes were comparable to the noise floor. Again, this is likely a consequence of the strain-specific *Cdh23^{ahl}* allele.

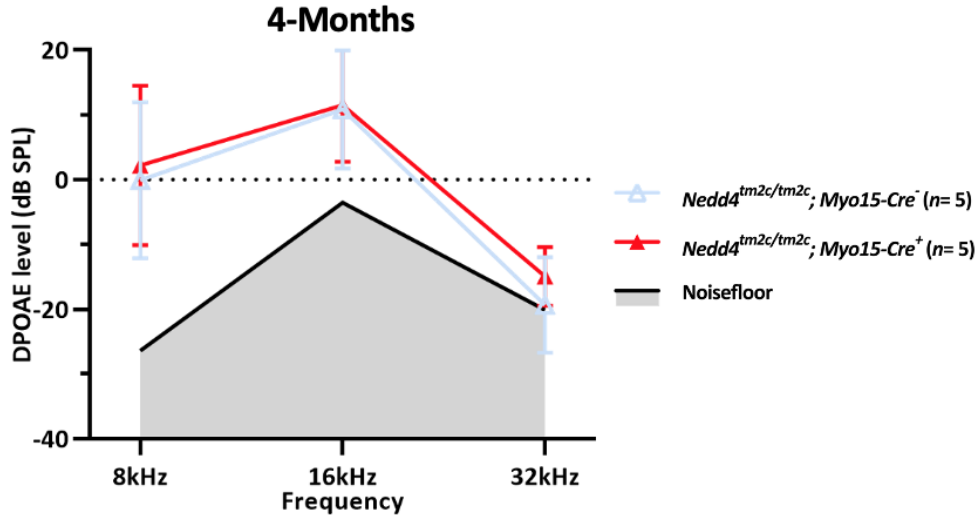

Figure 5.6: Decreased DPOAE levels of Myo15-driven Nedd4 cKO mice. Recorded DPOAE responses from 4-month old *Nedd4$^{tm2c/tm2c}$; Myo15-Cre^{-}* (light blue hollow triangles) and *Nedd4$^{tm2c/tm2c}$; Myo15-Cre^{+}* (red filled triangles) mice. DPOAE levels from mice of both genotypes are comparable at all frequencies tested. DPOAE levels presented as averages ± standard deviation error bars. Unpaired T tests with Welch's Corrections were performed, showing no significant differences in the recorded DPOAE levels from mice of each genotype.

5.2.1.3 Cochlear Pathology of *Myo15*-driven *Nedd4* cKO Mice

H&E staining of histological cochlear sections prepared from 4-month old *Nedd4$^{tm2c/tm2c}$*; *Myo15-Cre^{+}* mice was also performed. At all cochlear turns, H&E stained tissue from *Nedd4$^{tm2c/tm2c}$; Myo15-Cre^{+}* mice look comparable to control *Nedd4$^{tm2c/tm2c}$*; *Myo15-Cre^{-}* mice (Figure 5.7a – f). All cochlear structures, including the OoC, SGN and SV were present in mice of both genotypes. The similarity of the cochlear tissue in mice of both genotypes is further reflected in the calculated density of SGN nuclei, which is comparable between mice of both genotypes at all cochlear turns (Figure 5.7g). Unfortunately, due to the Covid19 pandemic, SEM images of the *Nedd4$^{tm2c/tm2c}$; Myo15-Cre^{+}* mice hair cell bundles could not be taken.

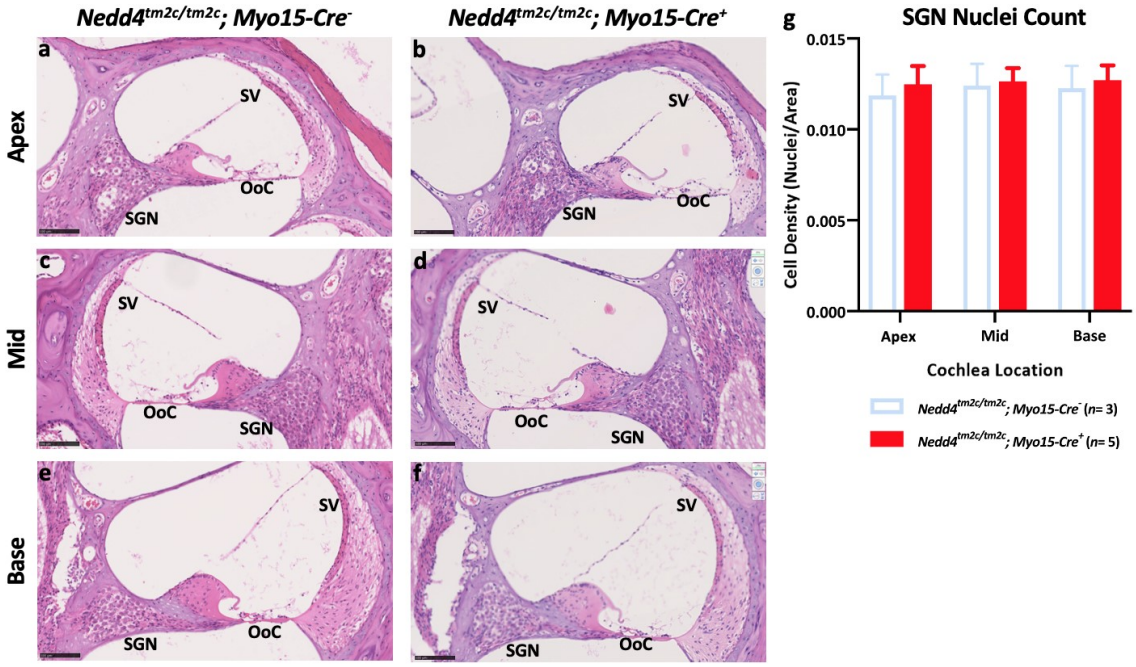

OoC: organ of Corti; SGN: Spiral Ganglion Neuron; SV: Stria Vascularis

Figure 5.7: 4-month old, Nedd4$^{tm2c/tm2c}$; Myo15-Cre^{+} mice show no loss of cochlear structures. Representative images of H&E-stained cochlear sections from a single *Nedd4$^{tm2c/tm2c}$; Myo15-Cre^{-}* (a, c, e) and *Nedd4$^{tm2c/tm2c}$; Myo15-Cre^{+}* (b, d, f) mouse. Images of the cochlear apical (a, b), mid (c, d) and basal (e, f) turns are shown. For mice of both genotypes, the SGN density within a 2500µm^2 area was calculated at each cochlear turn (g). **(a – f)** At all turns, *Nedd4$^{tm2c/tm2c}$; Myo15-Cre^{-}* and *Nedd4$^{tm2c/tm2c}$; Myo15-Cre^{+}* cochlear tissue looks comparable to each other. **(g)** The calculated SGN density is comparable between mice of each genotype. The average calculated density is presented + standard deviation error bars. Unpaired T tests with Welch's Correction identified no statistically significant differences between the calculated density at each cochlear turn, between mice of each genotype.

5.2.2 Auditory Characterisation of *Sox10*-driven *Nedd4* cKO Mice

5.2.2.1 Generation of the Auditory Phenotyping Cohort

To investigate the requirement of *Nedd4* in non-hair cell cochlear tissues, *Sox10*-driven *Nedd4* cKO were generated. To generate the *Sox10*-driven *Nedd4* cKO phenotyping cohort, female *Nedd4*$^{tm2c/+}$ mice that carry a single copy of the *Sox10-Cre* transgene (*Nedd4*$^{tm2c/+}$; *Sox10-Cre*$^{+}$) were crossed to male *Nedd4*$^{tm2c/+}$ mice that do not carry the *Sox10-Cre* transgene. This specific breeding strategy was adopted as paternal inheritance of the *Sox10-Cre* transgene results in 'leaky' Cre expression that does not recapitulate endogenous *Sox10* cochlear expression as faithfully as when the *Sox10-Cre* transgene is maternally inherited (Figure 3.28).

Based on the aforementioned breeding strategy, there are six possible genotypes for the offspring. Following Mendelian ratios, it is expected that *Nedd4*$^{tm2c/tm2c}$ mice which also carry the *Sox10-Cre* transgene (*Nedd4*$^{tm2c/tm2c}$; *Sox10-Cre*$^{+}$) should account for 12.5% of all mice born. However, no *Nedd4*$^{tm2c/tm2c}$; *Sox10-Cre*$^{+}$ mice are found in the 48 pups born (Figure 5.8, red). In addition, *Nedd4*$^{tm2c/tm2c}$ mice that do not carry the *Sox10-Cre* transgene (*Nedd4*$^{tm2c/tm2c}$; *Sox10-Cre*$^{-}$) are also underrepresented in the seven litters born (Figure 5.8, light blue); for the expected Mendelian ratio, six of the 48 mice would have the *Nedd4*$^{tm2c/tm2c}$; *Sox10-Cre*$^{-}$ genotype. Chi-square tests showed that the overall ratio of the number of mice of each genotype is significantly different from the expected Mendelian ratio.

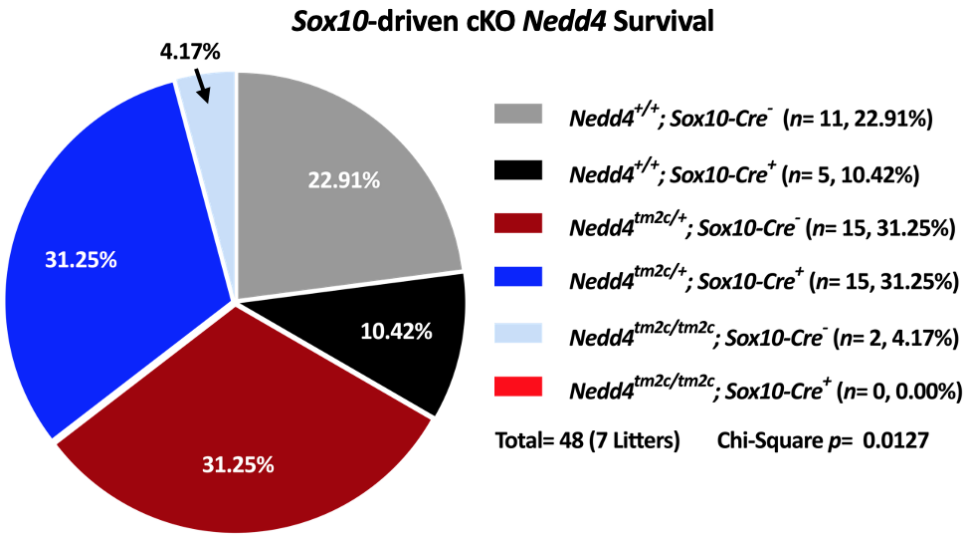

Figure 5.8: Sox10-driven, homozygous Nedd4 cKO is a lethal mutation. No *Nedd4$^{tm2c/tm2c}$; Sox10-Cre^{+}* mice were present in the *Sox10*-driven Nedd4 cKO phenotyping cohort, indicating that *Sox10*-driven, *Nedd4* cKO is a lethal mutation. Of the 48 total mice born through intercross breeds, 6 *Nedd4$^{tm2c/tm2c}$; Sox10-Cre^{+}* mice were expected to born. A Chi-square test shows that the ratio of genotypes of the mice born is significantly different from the expected Mendelian ratio (p= 0.0127).

As *Nedd4$^{tm2c/tm2c}$; Sox10-Cre^{-}* mice are significantly underrepresented in the phenotyping cohort, their body weights at 3-months of age were compared to mice of other genotypes in the phenotyping cohort. Decreased weight could indicate that *Nedd4$^{tm2c/tm2c}$; Sox10-Cre^{-}* mice are experiencing some physiological dysfunction. The average weight of female and male mice of each genotype are listed in Table 5.1. Only one female *Nedd4$^{tm2c/tm2c}$; Sox10-Cre^{-}* mouse was born, which was lighter (20.09g) than other female mice. One male *Nedd4$^{tm2c/tm2c}$; Sox10-Cre^{-}* mouse (27.82g) was also born, which aside from *Nedd4$^{tm2c/+}$; Sox10-Cre^{+}* mice (27.39g ± 0.95), was lighter than all the other mice in the phenotyping cohort (Figure 5.9a).

Genotype	Female Weight (g)	Male Weight (g)
Nedd4$^{+/+}$; *Sox10-Cre*$^{-}$	22.77 ± 0.82	29.12 ± 3.20
Nedd4$^{+/+}$; *Sox10-Cre*$^{+}$	23.94 ± 1.39	31.02 ± 0
Nedd4$^{tm2c/+}$; *Sox10-Cre*$^{-}$	23.48 ± 2.92	31.29 ± 3.72
Nedd4$^{tm2c/+}$; *Sox10-Cre*$^{+}$	21.01 ± 2.72	27.39 ± 0.95
Nedd4$^{tm2c/tm2c}$; *Sox10-Cre*$^{-}$	20.09 ± 0	27.82 ± 0
Nedd4$^{tm2c/tm2c}$; *Sox10-Cre*$^{+}$	-	-

Table 5.1: The body weight of female and male mice of each genotype born in the Sox10-driven Nedd4 cKO phenotyping cohort. Average body weight presented in grams (g) ± standard deviation. The number of mice of each genotype and sex are detailed in Figure 5.9.

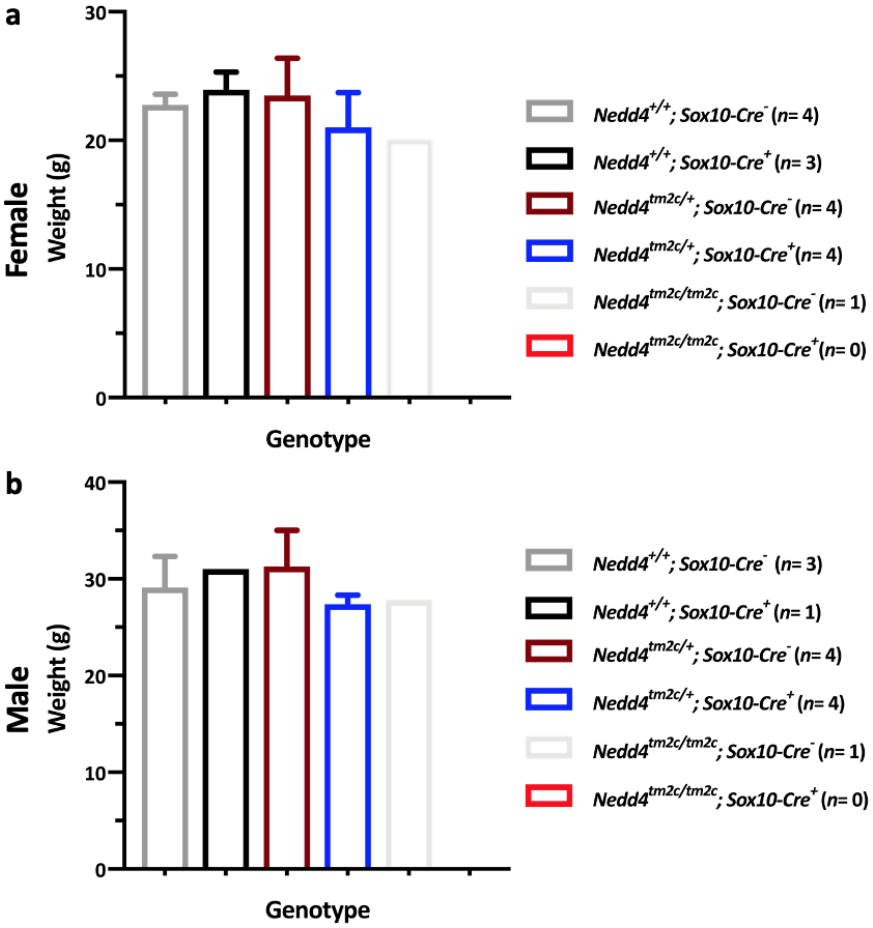

Figure 5.9: Nedd4$^{tm2c/tm2c}$; Sox10-Cre^{-} mice are lighter than other mice in the Sox10-driven Nedd4 cKO phenotyping cohort. The average weight of 3-month old female (a) and male (b) mice of all genotypes present in the *Sox10*-driven, *Nedd4* cKO phenotyping cohort. (a) The female *Nedd4*$^{tm2c/tm2c}$*; Sox10-Cre*$^{-}$ mouse (20.09g) was lighter than other female mice that different genotypes. (b) With the exception to *Nedd4*$^{tm2c/+}$*; Sox10-Cre*$^{+}$ mice (27.39g) the male *Nedd4*$^{tm2c/tm2c}$*; Sox10-Cre*$^{-}$ mouse (27.39g) was lighter than all male of other genotypes. Error bars represent the standard deviation.

5.2.2.2 Auditory Phenotyping of *Sox10*-driven *Nedd4* cKO Mice

To determine if *Nedd4*$^{tm2c/tm2c}$; *Sox10-Cre*$^{-}$ mice experience any auditory dysfunction, longitudinal ABR tests were performed at 3- and 8-weeks, and 3-months of age (Figure 5.10). At all ages tested, in response to all stimuli the auditory thresholds of mice that carry the *Sox10-Cre* transgene (Figure 5.10a, b, d, e, g and h; black filled circles and blue filled squares for *Nedd4*$^{+/+}$ and *Nedd4*$^{tm2c/+}$ mice, respectively) are not significantly different to their respective controls. 8-weeks old *Nedd4*$^{tm2c/tm2c}$; *Sox10-Cre*$^{-}$ mice display a variable high-frequency hearing loss in response to a 32kHz auditory stimulus (Figure 5.10f). By 3-months of age, mice of all genotypes show mildly elevated high-frequency hearing thresholds, which is likely due to the *Cdh23*^{ahl} allele (Figure 5.10g, h). However, at 3-months of age the two *Nedd4*$^{tm2c/tm2c}$; *Sox10-Cre*$^{-}$ mice display a profound high-frequency hearing loss (Figure 5.10i).

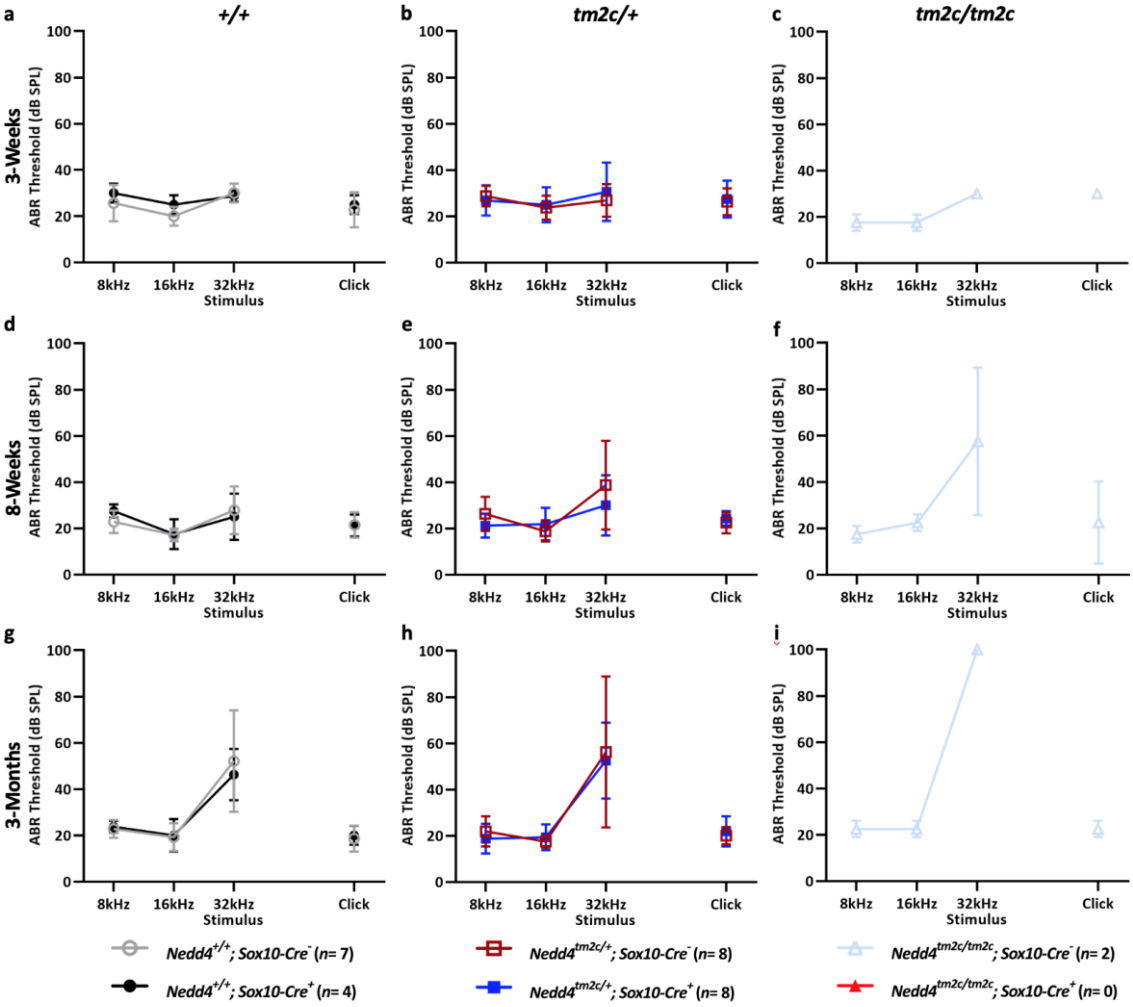

Figure 5.10: Nedd4$^{tm2c/tm2c}$; Sox10-Cre^{-} mice display a high-frequency hearing loss phenotype. ABR thresholds of mice in the *Sox10*-driven *Nedd4* cKO phenotyping cohort. ABR tests were performed at 3- (a, d, g) and 8-weeks (b, e, h), and 3-months (c, f, i) of age. **(a – c)** At 3-weeks of age, the recorded ABR thresholds from mice of all genotypes, in response to all stimuli, is comparable to each other. **(d - f)** Increased ABR thresholds recorded only in response to a high frequency stimulus, is recorded in 8-week old *Nedd4$^{tm2c/tm2c}$; Sox10-Cre^{-}* (f, light blue hollow triangles) mice. In response to all stimuli, mice of other genotypes have comparable auditory thresholds to those previously recorded at 3-weeks of age. **(g – i)** All mice show varying degrees of high-frequency hearing loss. All data presented as averages ± standard deviation error bars. Significant differences in the recorded auditory thresholds in response to each stimulus, between mice of different genotypes is assessed using Unpaired T test with Welch's Correction.

As only two *Nedd4$^{tm2c/tm2c}$*; *Sox10-Cre^{-}* mice were born and there was not a suitable genetic control, further auditory characterisation of these mice was not performed. Instead, OHC function of *Nedd4$^{tm2c/+}$*; *Sox10-Cre^{+}* mice was assessed by DPOAE tests. Compared to *Nedd4$^{tm2c/+}$*; *Sox10-Cre^{-}* mice, the recorded DPOAE levels are not significantly different to each other (Figure 5.11).

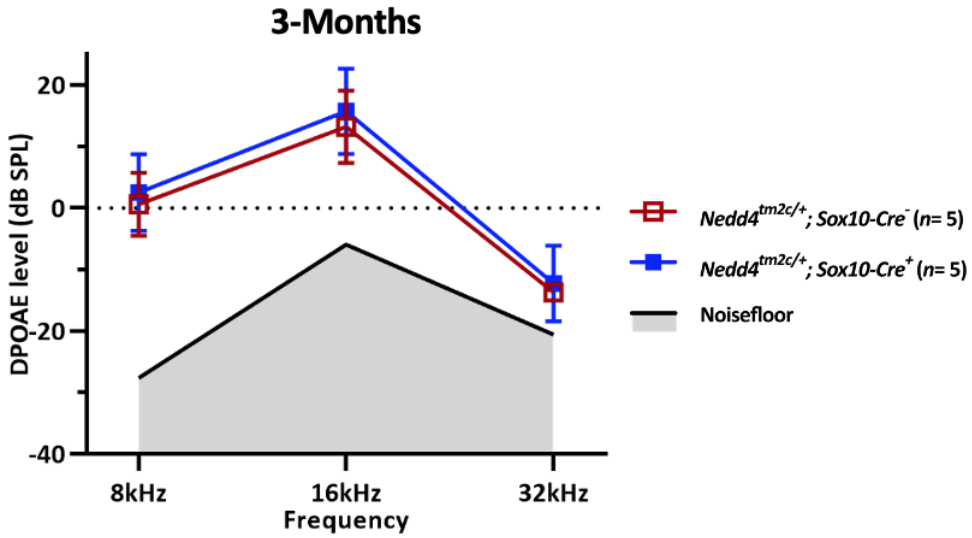

Figure 5.11: Decreased DPOAE levels of Nedd4$^{tm2c/+}$; Sox10-Cre^{-} and Nedd4$^{tm2c/+}$; Sox10-Cre^{+} mice in response to high frequency stimuli. DPOAE levels of 3-months of age *Nedd4$^{tm2c/+}$; Sox10-Cre^{-}* and *Nedd4$^{tm2c/+}$; Sox10-Cre^{+}* mice are comparable to each other. DPOAE levels presented as averages ± standard deviation error bars. Unpaired T test with Welch's Correction found that recorded DPOAE levels of both mice are not significantly different.

5.2.2.3 Cochlear Pathology of *Sox10*-driven *Nedd4* cKO Mice

Histological assessment of H&E staining sectioned cochlear tissue of 3-month old *Nedd4$^{tm2c/+}$*; *Sox10-Cre^{+}* mice was also conducted. The cochlear morphology of *Nedd4$^{tm2c/+}$*; *Sox10-Cre^{+}* mice appears comparable to control *Nedd4$^{tm2c/+}$*; *Sox10-Cre^{-}* mice (Figure 5.12a – f). The OoC, SGN and SV tissue is observable in mice of both genotypes. In addition, at all cochlear turns the SGN nuclei density in mice of both genotypes is not significantly different to each other (Figure 5.12g).

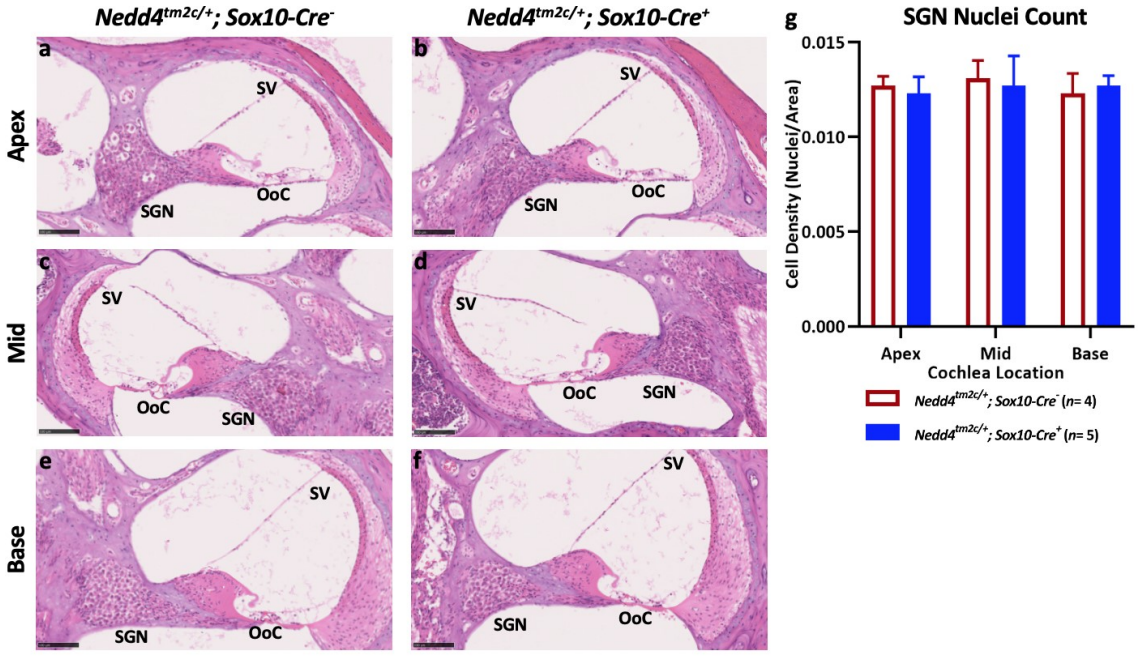

OoC: organ of Corti; SGN: Spiral Ganglion Neuron; SV: Stria Vascularis

Figure 5.12: Histological sections of Nedd4$^{tm2c/+}$; Sox10-Cre^{+} cochlear tissue appears similar to control Nedd4$^{tm2c/+}$; Sox10-Cre^{-} mice. Representative images of H&E-stained sectioned cochlear tissue from a single *Nedd4$^{tm2c/+}$; Sox10-Cre^{-}* (a, c, e) and *Nedd4$^{tm2c/+}$; Sox10-Cre^{+}* (b, d, f) mouse. Images of the apical (a, b), mid (c, d) and basal (e, f) turns for each mouse are shown. Calculated SGN density within a 2500µm^2 area at all cochlear turns, for mice of both genotypes is also shown (g). **(a – f)** H&E-stained cochlear tissue of *Nedd4$^{tm2c/+}$; Sox10-Cre^{+}* mice look comparable to control cochlear tissue from *Nedd4$^{tm2c/+}$; Sox10-Cre^{-}* mice, with no sign of pathological changes to the OoC, SGN or SV. **(g)** The calculated SGN density is comparable between mice of both genotypes. The average calculated density is presented + standard deviation error bars. Unpaired t tests with Welch's Correction found no statistically significant differences in the nuclei density at all cochlear turns between mice of both genotypes.

5.3 Discussion

5.3.1 *Nedd4* is a Potential Deafness-Causing Gene

Nedd4 was identified as novel candidate deafness-causing gene through WES of patients with adult-onset hearing loss. As *Nedd4*$^{tm2b/tm2b}$ mice are not viable and the IMPC report *Nedd4*$^{tm2b/+}$ mice to have normal hearing, *Myo15*- and *Sox10*-driven *Nedd4* cKO mice were generated to investigate the requirement of *Nedd4* in the mammalian process of hearing. As a novel candidate deafness-causing gene, its functional requirement in cochlear tissue is not known. gEAR transcriptomic data indicates that *Nedd4* is expressed all in cochlear tissues between embryonic ages and up to P7, which is corroborated by a previous report detailing wide cochlear expression in the OoC, RM, SGN, SL and SLim (Zhong *et al.*, 2014; Kolla *et al.*, 2020).

Auditory phenotyping of hair cell-specific, *Myo15*-driven *Nedd4* cKO mice indicates that they have comparable auditory function to their genetic controls. In addition, histological assessment of cochlear tissue revealed no overt changes to cochlear morphology. Overall, these data suggest that *Nedd4* is dispensable for cochlear hair cell function from P4 onwards in mice (Caberlotto *et al.*, 2011). However, to rule out that *Nedd4* function is not required in prenatal hair cells, a different hair cell-specific Cre driver line that expresses at embryonic ages should be utilized. For instance, the *Barhl1-Cre* transgene could be utilized as this line expresses Cre recombinase specifically in IHC at OHC during embryonic development ages (Chellappa *et al.*, 2008). However, I did not have this line available to me for my studies.

Investigations into the requirement of *Nedd4* in *Sox10*-expressing cells in cochlear tissue are inconclusive. The phenotyping cohort did not include any *Nedd4*$^{tm2c/tm2c}$; *Sox10-Cre*$^{+}$

mice and as such their auditory function could not be assessed. Their lethality could be explained by the involvement of *Nedd4* during delamination of neural crest cells from the neural tube during embryonic development (Wiszniak *et al.*, 2013). The auditory thresholds of *Nedd4*$^{tm2c/+}$; *Sox10-Cre*$^{+}$ mice are comparable to genetic controls. Interestingly, *Nedd4*$^{tm2c/tm2c}$; *Sox10-Cre*$^{-}$ mice display a profound, high frequency hearing loss phenotype by 3-months of age. Mice of this genotype were not expected to display an auditory phenotype as they do not carry the Cre driver allele and therefore no recombination of the *Nedd4*^{tm2c} allele should occur.

Mice of all genotypes did display some high frequency hearing loss, which is likely attributable to their C57BL/6N genetic background strain (Skarnes *et al.*, 2011). At the Mary Lyon Centre, the *Nedd4*^{tm2c}, and both the *Myo15-Cre* KI and *Sox10-Cre* transgenic mouse lines, were maintained by backcrossing to C57BL/6N. Therefore, these mice will carry the well-documented *ahl* polymorphism in the *Cdh23* gene, that predisposes to early-onset hearing loss that begins at the higher frequencies (Noben-Trauth *et al.*, 2003; Kane *et al.*, 2012). This strain-specific allele likely accounts for the elevated high-frequency thresholds recorded by ABR and reduced high-frequency otoacoustic emissions recorded in mice of all genotypes at the oldest timepoint tested.

5.3.2 The Role of *Nedd4* Function in Cochlear Tissue

Several pieces of evidence suggest that *Nedd4*$^{tm2c/tm2c}$; *Sox10-Cre*$^{-}$ mice are experiencing some physiological dysfunction, despite not possessing the *Sox10-Cre* transgene. They were underrepresented in the *Sox10*-driven, *Nedd4* cKO phenotyping cohort, with only two out of 48 mice carrying the *Nedd4*$^{tm2c/tm2c}$; *Sox10-Cre*$^{-}$ genotype (Figure 5.8). This does not appear to be a consequence of being homozygous carriers of the *Nedd4*^{tm2c} allele, as *Nedd4*$^{tm2c/tm2c}$; *Myo15-Cre*$^{-}$ mice were born at expected Mendelian ratio in the *Myo15*-driven cKO of *Nedd4* phenotyping cohort (Figure 5.4). In addition, at 3-months of age, the two (one female and male) *Nedd4*$^{tm2c/tm2c}$; *Sox10-Cre*$^{-}$ mice were underweight compared to other, sex-matched mice (Figure 5.9). Finally, *Nedd4*$^{tm2c/tm2c}$; *Sox10-Cre*$^{-}$ mice display a progressive high-frequency hearing loss (Figure 5.10f, i). In response to a 32kHz stimulus, the hearing threshold of *Nedd4*$^{tm2c/tm2c}$; *Sox10-Cre*$^{-}$ mice is already elevated (~60dB SPL) by 8-weeks of age, which is higher than the thresholds recorded for age-matched mice (Figure 5.10d, e, f). Indeed, the high-frequency hearing threshold of *Nedd4*$^{tm2c/tm2c}$; *Sox10-Cre*$^{-}$ mice at 8-weeks of age is similar to the high-frequency hearing thresholds seen across the other genotypes at 3-months of age (Figure 5.10f, g, h). These data suggest that the *Nedd4*$^{tm2c/tm2c}$; *Sox10-Cre*$^{-}$ mice have a progressive high-frequency hearing loss that exceeds what would be expected as an effect of the *Cdh23*^{ahl} allele alone. As such, these results led me to consider whether recombination of the *Nedd4*^{tm2c} allele could have occurred in these mice, even though they do not carry the *Sox10-Cre* transgene.

One potential explanation for how recombination could have occurred in *Nedd4*$^{tm2c/tm2c}$; *Sox10-Cre*$^{-}$ mice could be that some maternally-inherited Cre transcript or protein was

present at the earliest stages of embryonic development. Mice of the *Sox10*-driven *Nedd4* cKO phenotyping cohort maternally inherited the *Sox10-Cre* transgene and it is possible that some *Cre* transcript or protein is present in the fertilised egg cells. In addition, the amount of *Sox10-Cre* transgene expression and the rate of *Nedd4*^{tm2c} recombination are unknown. Given that the *Sox10-Cre* transgene did not faithfully recapitulate endogenous *Sox10* expression in cochlear tissue, it is possible this is true in other tissues (Figure 3.28).

The survival of two *Nedd4*$^{tm2c/tm2c}$; *Sox10-Cre*$^{-}$ mice into adult ages could depend on how long maternally-derived *Sox10-Cre* transgene transcripts or proteins are present at early stages of embryonic development and in which embryo cells they are found in. Degradation of maternal-derived transcripts and proteins is necessary for embryonic development (Li *et al.*, 2010). However, the degradation dynamics of an exogenous transcript or protein is not known, and it is possible that the lifespan of Cre transcripts and proteins could persist for longer compared to other maternally-derived species. In addition, the embryonic location of where Cre transcripts or proteins are, and the embryonic cells that they are located in is likely to be stochastic due to the random nature of how cellular contents are divided during mitosis.

The *Nedd4*$^{tm2c/tm2c}$; *Sox10-Cre*$^{-}$ mice could be mosaic for the *Nedd4*^{tm2c} and *Nedd4*^{tm2d} alleles. The maternally-derived Cre could have resulted in recombination of the *Nedd4*^{tm2c} allele in a cell, whose lineage can tolerate the loss of *Nedd4* and it does not affect the survival of the mouse, but is required for cochlear development. Consequently, the *Nedd4*^{tm2d} allele may be present in the cochlear tissue of the two *Nedd4*$^{tm2c/tm2c}$; *Sox10-Cre*$^{-}$ mice. One method of determining if maternally-derived Cre

from the *Sox10-Cre* transgene accounts for the observed phenotypes of *Nedd4*$^{tm2c/tm2c}$; *Sox10-Cre*$^{-}$ mice is to change the breeding strategy, so that the *Sox10-Cre* transgene is paternally inherited.

The auditory phenotyping of mice from the *Sox10*-driven *Nedd4* cKO phenotyping cohort does suggest that more experiments will be warranted to fully characterise the role of *Nedd4* in cochlear function. Based on the cochlear location of *Sox10-Cre* transgene expression, *Nedd4* function could be required in the SCs of the OoC, the SL, SGN, RM or in IdCs (Figure 3.28d). Given that *Nedd4*$^{tm2c/tm2c}$; *Myo15-Cre*$^{+}$ mice did not display any auditory dysfunction, the possibility that *Nedd4* is required in postnatal IHC or OHCs was not considered (Figure 5.5 – Figure 5.7).

6 DISCUSSION

6.1 Auditory Dysfunction of *Nedd4l*$^{tm1b/tm1b}$ Mice

Following the identification of *Nedd4l* as a novel, candidate deafness-causing gene, experiments were conducted to fully characterise the role of *Nedd4l* in the process of hearing. Molecular characterisation confirmed that the *Nedd4l*^{tm1b} allele is a KO null mutation, and through *Nedd4l*-controlled, *lacZ*-reporter gene expression, *Nedd4l* expression was detected in IdCs of the cochlea in P0-aged mice (Figure 3.4Figure 3.5). Auditory phenotyping of *Nedd4l*$^{tm1b/tm1b}$ mice revealed that they experience an early-onset, hearing loss which deteriorates to profound levels in 8-week old mice. Decreased latency and amplitude of ABR waves recorded from *Nedd4l*$^{tm1b/tm1b}$ mice are indicative of cochlear and CAS dysfunction (Figure 3.9 – Figure 3.13).

Pathological assessment of *Nedd4l*$^{tm1b/tm1b}$ mice identified decreased colocalisation of pre- and postsynaptic proteins at the IHC ribbon synapse and nerve fibres making contact to IHCs (Figure 3.25,Figure 3.26). Degeneration of hair cell bundles and SGN is also observed but the onset of loss occurred when *Nedd4l*$^{tm1b/tm1b}$ mice display profound levels of hearing loss (Figure 3.9,Figure 3.17 –Figure 3.24). The cochlear degeneration of *Nedd4l*$^{tm1b/tm1b}$ mice share similar characteristics to the cochlear synaptopathy of previously reported noise-exposed mouse models, which could indicate a shared pathway of auditory dysfunction. Noise-exposed mice have fewer matched pre- and postsynaptic proteins at the IHC ribbon synapse and IHC-innervating afferent fibres, followed by SGN degeneration at later ages, (Kujawa & Liberman, 2009; Furman *et al.*, 2013).

To determine the requirement of *Nedd4l* in the process of hearing, *Sox10*- and *Myo15*-driven *Nedd4l* cKO mice were generated. Investigating the requirement of *Nedd4l* in *Sox10*-expressing cochlear tissue was hindered by the decreased viability of *Nedd4l*$^{tm1c/tm1c}$; *Sox10-Cre*$^{+}$ mice, but auditory phenotyping did suggest that *Nedd4l* is required in *Sox10*-expressing cochlear cell types, which includes IdCs (Figure 3.28, Figure 3.31). *Myo15*-driven *Nedd4l* cKO mice did not experience any auditory dysfunction, suggesting that *Nedd4l* function is dispensable in adult hair cell function and maintenance (Figure 3.34).

A MS approach was taken to identify the mechanism of hearing loss in *Nedd4l*$^{tm1b/tm1b}$ mice. A surrogate MEF model was used to identify potential substrates of NEDD4L, with plans to validate their interactions in *Nedd4l*$^{tm1b/tm1b}$ mice-derived cochlear tissue. These experiments were able to identify the NKCC1 protein, which is well known for its requirement in K^{+} recycling pathways within cochlear tissue (Figure 4.17). Decreased abundance of the αENaC subunit was also detected in cochlear protein lysates extracted from *Nedd4l*$^{tm1b/tm1b}$ mice (Figure 4.1). Collectively, these data suggest that the auditory dysfunction of *Nedd4l*$^{tm1b/tm1b}$ mice could be a consequence of impaired ion homeostatic mechanisms in non-sensory cells of the cochleae.

6.1.1 IMPC-Generated *Nedd4l*^{tm1b} KO Null Allele

The *Nedd4l*^{tm1b} allele is a constitutive KO null mutation, as verified via Western blot of *Nedd4l*$^{tm1b/tm1b}$ mice-derived cochlear protein lysates (Figure 3.4c). Previous *Nedd4l* KO null models described by Boase *et al.* (*Nedd4l*$^{15\Delta/15\Delta}$) and Yanpallewar *et al.* (*Nedd4l*$^{10\Delta/10\Delta}$), also do not express either NEDD4L protein isoforms, but were reported to experience respiratory distress instead (Boase *et al.*, 2011; Yanpallewar *et al.*, 2016).

Both heterozygous *Nedd4l*$^{15\Delta}$ and *Nedd4l*$^{10\Delta}$ display haploinsufficient phenotypes like *Nedd4l*$^{tm1b/+}$ mice. Whereas *Nedd4l*$^{tm1b/+}$ mice experience high-frequency hearing loss at 8-weeks old, heterozygous *Nedd4l*$^{15\Delta}$ and *Nedd4l*$^{10\Delta}$ mice show elevated blood pressure and hyperactivity, respectively (Figure 3.9c) (Boase *et al.*, 2011; Yanpallewar *et al.*, 2016). Collectively, this suggests that *Nedd4l* is haploinsufficient for mammalian physiology.

Nedd4l$^{tm1b/tm1b}$ mice are less viable compared to their respective littermates, which is reported in previous literature (Figure 3.7). However, the *Nedd4l* KO null mutation carried by the *Nedd4l*$^{15\Delta/15\Delta}$ and *Nedd4l*$^{10\Delta/10\Delta}$ models resulted in lethality in all mice by P21. Lethality in these models were attributed to the inability to inflate their lungs (Boase *et al.*, 2011; Yanpallewar *et al.*, 2016). One explanation for the difference in viability of the *Nedd4l* KO null models is that the *Nedd4l*^{tm1b}, *Nedd4l*$^{15\Delta/15\Delta}$ and *Nedd4l*$^{10\Delta/10\Delta}$ models were generated on the C57BL/6N, 6J and 6CR strains, respectively (Skarnes *et al.*, 2011; Boase *et al.*, 2011; Yanpallewar *et al.*, 2016). Despite the genetic similarity between the C57BL/6 strains, the different strains can cause variation in phenotypic severity and survival even when carrying the same genetic mutation (Mekada *et al.*, 2009; Simon *et al.*, 2013; Cooper *et al.*, 2018; Kang *et al.*, 2019). For example, C57BL/6N mice heterozygous for a *Scn1a* gene mutation are more viable than C57BL/6J mice carrying the same gene mutation (Kang *et al.*, 2019).

6.1.2 NEDD4L Cochlear Expression

X-gal staining against *Nedd4l*-controlled, *lacZ* reporter gene expression was only observed in IdCs of P0-aged, cochlear tissue (Figure 3.5). Whilst transcriptomic data available on the gEAR database corroborated my findings, it also indicated that *Nedd4l*

is more widely expressed through cochlear tissues; *Nedd4l* transcript was identified in hair cells and IS too (Figure 4.14) (Kolla *et al.*, 2020). Hoa lab-generated single nucleus RNA-seq data of tissue extracted from the cochlear lateral wall of P30-aged mice also identified *Nedd4l* expression at RM and all three cell layers (basal, intermediate, marginal) of the SV (Figure 6.1; Korrapati *et al.*, 2019; Orvis *et al.*, 2020). X-Gal staining could have provided a more restrictive profile of *Nedd4l* expression due to the method of imaging used, which gives images a slight blue hue. Weaker X-Gal stains could be masked and therefore, weaker *Nedd4l* expression in non-IdC cochlear tissues could go undetected. As an alternative to X-gal stains, fluorescent or chromogenic immunohistochemistry stains could be performed using antibodies against the translated LacZ protein. However, *lacZ*-reporter studies and scRNA-seq data are assessments of *Nedd4l* gene expression which is not an indicator of protein abundance (Liu *et al.*, 2016). Future investigation of *Nedd4l* function in cochlear tissue should include more direct methods to assess the cochlear location of NEDD4L protein, such as utilizing an anti-NEDD4L antibody that is suitable for immunohistochemistry on wholemount or cryosectioned tissue.

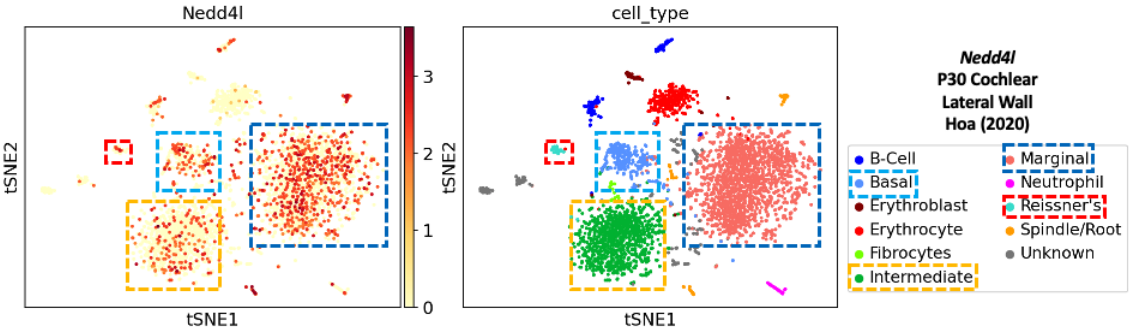

Figure 6.1: scRNA-seq data of Nedd4l transcripts in the cochlear lateral wall. *Nedd4l* expression was detected in the Marginal (dark blue square), Intermediate (orange square), Basal (light blue) of the Stria Vascularis and Reissner's membrane (red square), as reported by Korrapati *et al.* 2019.

6.1.3 NEDD4L and TM Function

Previous literature exploring the functional requirement of IdCs in mammalian auditory function is sparse compared to other cochlear tissues. Some research has investigated the role of IdC in the context of TM function. Ultrastructural observations identified microvilli-lined ducts within the IdC epithelial layer within secretory vesicles emanating from them (Lim, 1970; Thorn *et al.*, 1979). As IdCs are a point of contact and anchorage for the TM in the OoC, the vesicles are believed to deliver proteins that constitute the TM and maintain its function (Prieto *et al.*, 1990; Lim, 1970; Thorn *et al.*, 1979). Crucial to the attachment of TM and keeping it positioned above hair cell bundles is the expression of numerous membrane-bound, Glycosylphosphatidylinositol (GPI)-anchor containing proteins such as α-tectorin and otoancorin, which have been identified in IdCs (Legan *et al.*, 2000; Zwaenepoel *et al.*, 2002; Moreno-Pelayo *et al.*, 2008; Lukashkin *et al.*, 2012).

One hypothesis to explain the auditory dysfunction of *Nedd4l*$^{tm1b/tm1b}$ mice is the dysregulated abundance of GPI-anchor proteins. The abundance of α-tectorin and otoancorin could be assessed through Western blot or immunohistochemistry, to determine if their abundance is disrupted in *Nedd4l*$^{tm1b/tm1b}$ mice. However, when assessing *Nedd4l*$^{tm1b/tm1b}$ mice cochlear pathology, there were no indications to suggest that TM was affected. It was present when tissue was processed to expose hair cell bundles for SEM and wholemount immunohistochemistry stains. In addition, the TM of of *Nedd4l*$^{+/+}$, *Nedd4l*$^{tm1b/+}$ and *Nedd4l*$^{tm1b/tm1b}$ mice looked comparable upon gross observation of the cross-sectioned cochleae. Furthermore, computational protein-protein interaction analysis of novel and previously identified, deafness-causing genes,

placed NEDD4L and α-Tectorin far apart from each other on an interaction map, indicating that their interaction is unlikely (Bowl *et al.*, 2017).

6.1.4 Endolymphatic Ion Homeostasis in *Nedd4l*$^{tm1b/tm1b}$ Mice

Investigations of the mechanism of hearing loss in *Nedd4l*$^{tm1b/tm1b}$ mice suggests that the ionic composition of the endolymph is disrupted. In support of this hypothesis is the 50% decrease in abundance of the αENaC subunit of P0-aged cochlear tissue of *Nedd4l*$^{tm1b/tm1b}$ mice compared to control *Nedd4l*$^{+/+}$ mice (Figure 4.1). During this early postnatal timepoint, the ionic composition of the endolymph is undergoing a transition from a low [K^+], high [Na^+] to a high [K^+], low [Na^+], with increases in [K^+] correlating with the increasing magnitude of the EP (Li *et al.*, 2013; 2020). Published literature has implied that ENaC is required in maintaining low endolymphatic [Na^+] and that the decreased abundance of the αENaC subunit, which is crucial for ENaC activity, suggests that endolymphatic [Na^+] is disrupted in *Nedd4l*$^{tm1b/tm1b}$ mice (Figure 6.2a, b) (Canessa *et al.*, 1994; Lee & Marcus, 2003). Previous literature has reported that increases in ENaC expression correlates with increases in endolymphatic volume.

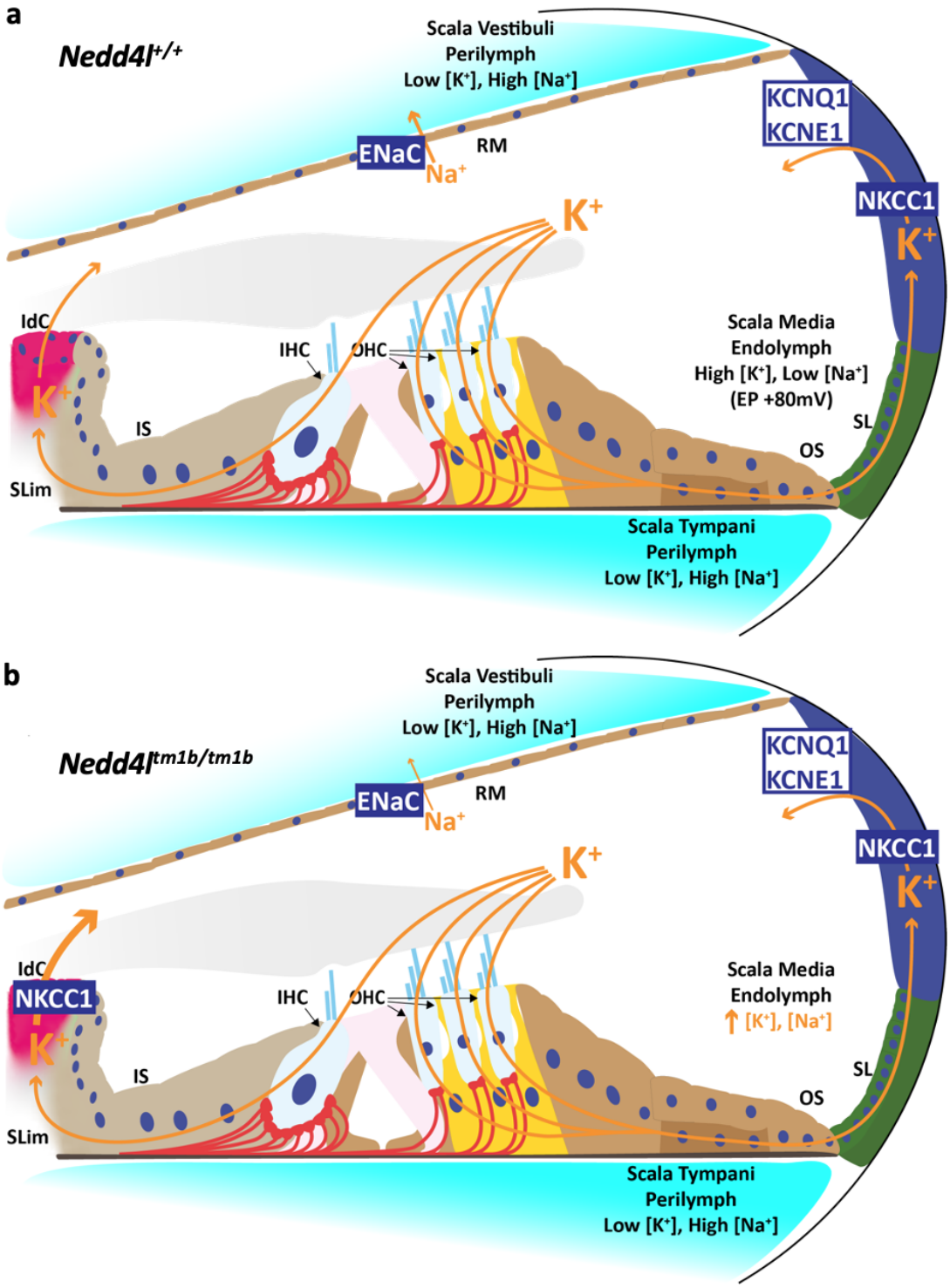

Cl⁻: Chloride Ion; **ENaC:** Epithelial Sodium Channel; **IdC:** Interdental Cells; **IS:** Inner Sulcus; **IHC:** Inner Hair Cell; **K⁺:** Potassium Ions; **Na⁺:** Sodium Ions; **NKCC1:** Na⁺-K⁺-Cl⁻ Cotransporter 1; **OHC:** Outer Hair Cells; **OS:** Outer Sulcus; **RM:** Reissner's Membrane; **SL:** Spiral Ligament; **SLim:** Spiral Ligament; **SV:** Stria Vascularis

Figure 6.2: Hypothesised increased endolymphatic [K⁺] and [Na⁺] in Nedd4l$^{tm1b/tm1b}$ mice. Hypothesised K^+ and Na^+ flux in *Nedd4l*$^{+/+}$ (a) and *Nedd4l*$^{tm1b/tm1b}$ (b) mice. **(a)** Replenishment of endolymphatic K^+ influx through medial (IS, Slim and IdC) and lateral (OS, SL, SV) K^+ recycling pathways. Na^+ efflux out of endolymphatic spaces via RM-localised ENaC. **(b)** Increased abundance of NKCC1 in *Nedd4l*$^{tm1b/tm1b}$ mice could result in increased K^+ recycling through medial pathways and increased endolymphatic [K^+]. Decreased abundance of αENaC subunit suggests decreased ENaC activity and increased endolymphatic [Na^+].

Additional evidence to suggest that the endolymph ionic composition is disrupted in *Nedd4l*$^{tm1b/tm1b}$ mice is the identification of NKCC1 as a potential NEDD4L substrate (Figure 4.17). Expression of NKCC1 has been well characterised in cochlear tissue, specifically at the SL fibrocytes and in the SV (Figure 6.2a) (Crouch *et al.*, 1997; Dixon *et al.*, 1999; Delpire *et al.*, 1999). In these tissues, NKCC1-mediated transport of Na^+, K^+ and Cl^- ions, is coupled with the activity of Na^+-K^+-ATPase and ClC-Barttin channels to replenish K^+ in endolymphatic spaces (Figure 1.6b; Schulte & Steel, 1994; Wangemann *et al.*, 1995; Estévez *et al.*, 2001). NKCC1 protein is also detected in IdCs at early postnatal time points, which correlates with the spatiotemporal expression of *Nedd4l* and the establishment of high [K^+] in endolymphatic spaces (Sakaguchi *et al.*, 1998; Li *et al.*, 2013). Increased NKCC1 protein has been demonstrated in the colon tissue of intestine-specific *Nedd4l* KO mice but has not been validated in cochlear tissues (Jiang *et al.*, 2017). Increased NKCC1 expression in the cochlea could result in elevated endolymphatic [K^+] and disrupt the ionic composition of the endolymph in *Nedd4l*$^{tm1b/tm1b}$ mice (Figure 6.2b), which is discussed further in 6.2.

Whether the hypothesised change to the endolymph ionic composition in *Nedd4l*$^{tm1b/tm1b}$ mice also disrupts the EP is unclear. Previous research in mouse models of metabolic age-related hearing loss where the EP is pharmacologically reduced via furosemide application, has shown that recorded DPOAEs are also reduced (Schmiedt *et al.*, 2002; Mills & Schmiedt, 2004; Lang *et al.*, 2010). However, 3-week old *Nedd4l*$^{tm1b/tm1b}$ mice have significantly elevated ABR thresholds but comparable DPOAEs to control mice (Figure 3.9, Figure 3.14). Overall, this suggests that the EP of *Nedd4l*$^{tm1b/tm1b}$ mice is not affected, but EP measurements are required for validation.

6.1.4.1 Further Investigation of ENaC and NKCC1 Activity in *Nedd4l*$^{tm1b/tm1b}$ Mice

Molecular characterisation should be conducted to gain a better understanding of how ENaC and NKCC1 protein abundance is affected in P0- and 3-week old *Nedd4l*$^{tm1b/tm1b}$ mice. Whilst the αENaC subunit is necessary for ENaC channel conductance, the presence of the β- and γENaC subunits enhance its activity and should also be investigated in P0-aged *Nedd4l*$^{tm1b/tm1b}$ mice via Western blots. Furthermore, if the abundance of all ENaC subunits is also decreased at 3-weeks of age, it suggests that endolymphatic [Na^+] is consistently disrupted. Anti-NKCC1 immunohistochemistry stains should be conducted to determine whether NKCC1 expression is detected in IdCs past postnatal ages. As previous research has identified NKCC1 is involved in the replenishment of K^+ in the endolymph, investigations should be conducted to determine if NKCC1 expression is also affected in the SV (Delpire *et al.*, 1999; Dixon *et al.*, 1999; Hibino & Kurachi, 2006; Nin *et al.*, 2008).

To determine how these molecular changes affects cochlear physiology in *Nedd4l*$^{tm1b/tm1b}$ mice, the endolymph ionic composition and EP should also be measured at P0- and 3-weeks old mice. These experiments would address if endolymphatic [Na^+] and [K^+] is increased and whether that translates to changes to the EP. This could determine whether loss of auditory function in *Nedd4l*$^{tm1b/tm1b}$ mice is due to dysregulation of either or both ENaC and NKCC1 proteins in cochlear tissue.

A pharmacological approach could also be adopted to gain insights into the contribution of NKCC1 and ENaC in the auditory dysfunction of *Nedd4l*$^{tm1b/tm1b}$ mice. If elevated NKCC1 activity is the primary cause of hearing loss in *Nedd4l*$^{tm1b/tm1b}$ mice, treatment

with the NKCC1 inhibitor bumetanide, could prevent the development of auditory dysfunction. Modulation of ENaC channel activity can be achieved by treating *Nedd4l*$^{tm1b/tm1b}$ mice with amiloride or the synthetic glucocorticoid hormone, Dexamethasone (Dex), which can inhibit or promote ENaC channel activity, respectively (Kleyman & Cragoe, 1988; Lin *et al.*, 1999). If impaired ENaC function is involved in the cause of auditory dysfunction of *Nedd4l*$^{tm1b/tm1b}$ mice, one would expect amiloride treatment to worsen the hearing loss phenotype. By extension, treatment with Dex could attenuate the hearing loss phenotype observed in *Nedd4l*$^{tm1b/tm1b}$ mice (Figure 6.3).

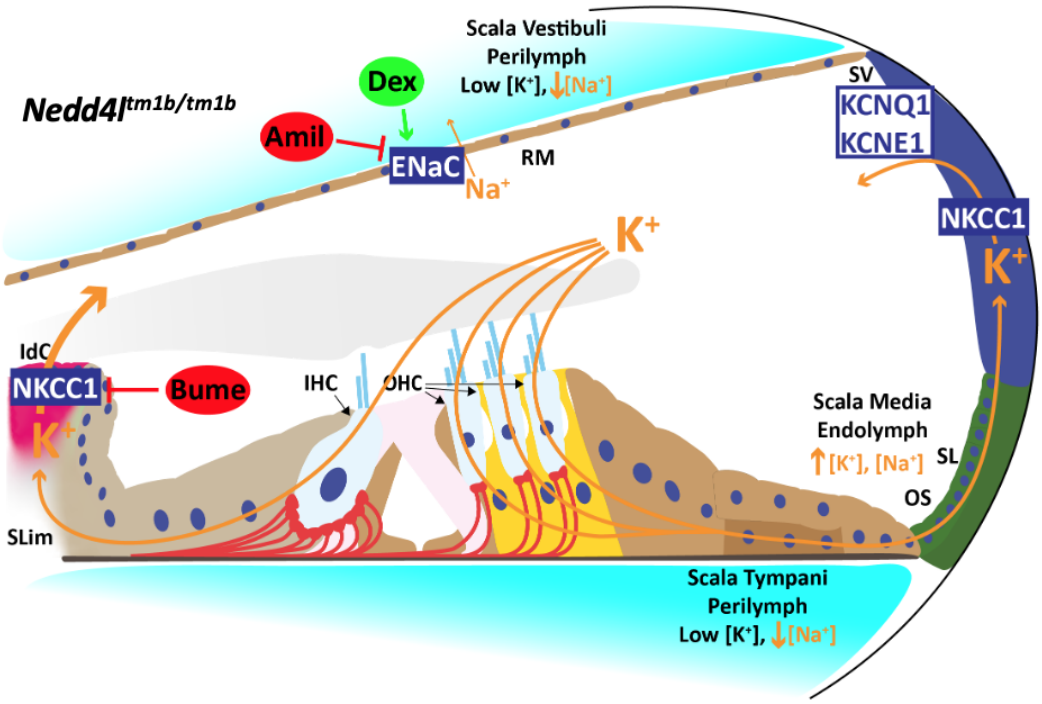

Amil: Amiloride; **Bume:** Bumetanide; **Cl⁻:** Chloride Ion; **Dex:** Dexamethasone; **ENaC:** Epithelial Sodium Channel; **IdC:** Interdental Cells; **IS:** Inner Sulcus; **IHC:** Inner Hair Cell; **K⁺:** Potassium Ions; **Na⁺:** Sodium Ions; **NKCC1:** Na⁺-K⁺-Cl⁻ Cotransporter 1; **OHC:** Outer Hair Cells; **OS:** Outer Sulcus; **RM:** Reissner's Membrane; **SL:** Spiral Ligament; **SLim:** Spiral Ligament; **SV:** Stria Vascularis

Figure 6.3: Pharmacological treatment of Nedd4l*$^{tm1b/tm1b}$ *mice. The involvement of ENaC and NKCC1 in auditory dysfunction of *Nedd4l*$^{tm1b/tm1b}$ mice could be investigated by treating *Nedd4l*$^{tm1b/tm1b}$ mice with agonists (Dex for NKCC1) and antagonists (Amil and Bume for ENaC and NKCC1, respectively).

Impaired ion homeostasis can cause increases in endolymphatic volume (endolymphatic hydrops), which is also observed alongside cochlear synaptopathy in noise-exposed

mice (Neyroud *et al.*, 1997; Dixon *et al.*, 1999; Delpire *et al.*, 1999; Kim *et al.*, 2018). Attempts were made to determine the presence of endolymphatic hydrops in *Nedd4l*$^{tm1b/tm1b}$ mice by assessing H&E-stained, paraffin-embedded cochlear section, but was abandoned as RM was disrupted in cochleae from mice of all genotypes. Previous reports have identified endolymphatic hydrops in cryosectioned cochlear tissue, which could be performed in *Nedd4l*$^{tm1b/tm1b}$ mice. However, the presence of endolymphatic hydrops typically results in vestibular dysfunction, which was not observed in *Nedd4l*$^{tm1b/tm1b}$ mice (Figure 3.15) suggesting that disrupted ENaC or NKCC1 regulation may not change the endolymphatic volume.

6.2 Increased Purinergic Signalling in *Nedd4l*$^{tm1b/tm1b}$ Mice?

The hypothesised ectopic NKCC1 expression in the cochlear tissue of *Nedd4l*$^{tm1b/tm1b}$ mice could result in elevated endolymphatic [K^+]. Previous research has shown that this can stimulate the release of ATP-filled vesicles from the endolymph-facing marginal cells of the SV, which initiates otoprotective, purinergic signalling pathways in the cochlea by temporarily dampening cochlear function (White *et al.*, 1995; Munoz *et al.*, 2001; Järlebark *et al.*, 2002; Thorne *et al.*, 2004; Housley *et al.*, 2013). Increased ATP in endolymphatic spaces in *Nedd4l*$^{tm1b/tm1b}$ mice could account for how the loss of NEDD4L protein in the small population of IdCs, can result in a profound hearing loss phenotype (Figure 6.4).

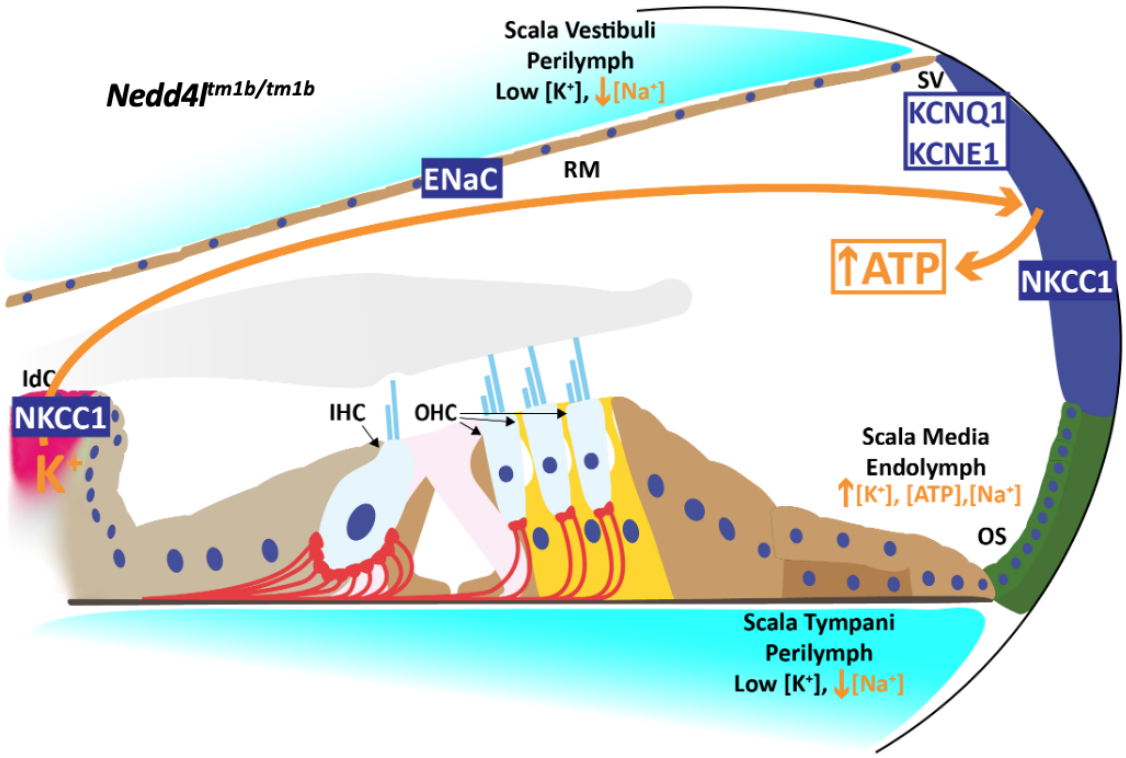

Cl^-: Chloride Ion; **ENaC:** Epithelial Sodium Channel; **IdC:** Interdental Cells; **IHC:** Inner Hair Cell; **K^+:** Potassium Ion; **Na^+:** Sodium Ion; **NKCC1:** Na^+-K^+-Cl^- Cotransporter 1; **OHC:** Outer Hair Cell; **OS:** Outer Sulcus; **RM:** Reissner's Membrane; **SV:** Stria Vascularis

Figure 6.4: Increased endolymphatic [ATP] in Nedd4l$^{tm1b/tm1b}$ mice. Auditory dysfunction of *Nedd4l*$^{tm1b/tm1b}$ mice is hypothesised to be a consequence of increased endolymphatic [ATP] from marginal cells of the SV, due to increased endolymphatic K^+ from ectopic NKCC1 expression in IdC.

Within cochlear tissue, ATP release can stimulate metabotropic P2Y and ionotropic P2X receptors (Lee & Marcus, 2008). Inappropriate activation of the $P2X_2$ and G-protein complex coupled, P2Y receptors could desensitise the cochlear function of *Nedd4l*$^{tm1b/tm1b}$ mice. ATP binding to P2Y receptors initiates its nucleotide exchange factor activity, which exchanges a GDP for a GTP molecule on the G_α subunit of the heterotrimeric $G_{\alpha\beta\gamma}$ protein complex (Erb & Weisman, 2012). Consequently, G_α dissociates from the heterotrimeric complex, activating the membrane-bound Phospholipase C (PLC) protein. PLC catalyses the hydrolysis of Phosphatidylinositol 4,5-bisphosphate (PIP_2) into the secondary messengers, Diacylglycerol (DAG) and Inositol 1, 4, 5-triphosphate (IP_3) (Bartlett *et al.*, 2005). DAG activates PKC and the MAPK pathway. ATP binding to P2X receptors opens non-selective channels, permitting the influx of monovalent and divalent cations.

6.2.1 Cochlear Synaptopathy

The hypothesised elevated concentration of ATP within the endolymph would affect IHC and OHC function. Activation of $P2X_2$ and P2Y ($P2Y_{1,\ 2}$ or $_4$) receptors could increase intracellular [Ca^{2+}_i] ([Ca^{2+}_i]) in both IHC and OHCs, via non-selective cation influx or IP_3-mediated release of Ca^{2+} from intracellular stores, respectively (Figure 6.5) (Mammano *et al.*, 1999; Sugasawa *et al.*, 1996; Szücs *et al.*, 2004; Huang *et al.*, 2010). Increased [Ca^{2+}_i] could be the cause of increased density of α-Parvalbumin staining towards the basolateral IHC of of *Nedd4l*$^{tm1b/tm1b}$ mice (Figure 3.27). α-Parvalbumin and other Ca^{2+} buffer proteins such as the Calbindin and Calretinin are involved in the rate and magnitude of glutamate exocytosis (Hackney *et al.*, 2005; Pangrsic *et al.*, 2015). Their increased abundance could be a compensatory mechanism to sequester Ca^{2+} away from

the presynaptic ribbon structures and prevent glutamate ototoxic effects. Whether the expression and localisation of all mobile Ca^{2+} buffer proteins are affected in *Nedd4l*$^{tm1b/tm1b}$ mice is unknown and would require additional immunohistochemistry to be confirmed.

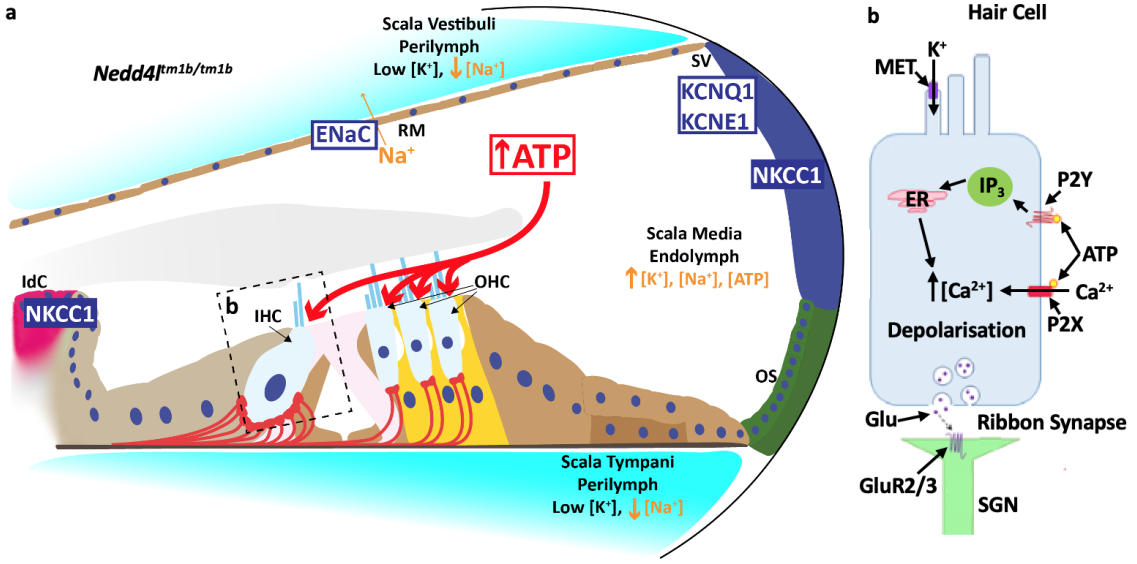

Ca^{2+}: Calcium Ion; **Cl^-:** Chloride Ion; **ENaC:** Epithelial Sodium Channel; **ER:** Endoplasmic Reticulum; **Glu:** Glutamate; **GluR2/3:** Glutamate Receptor 2/3; **IdC:** Interdental Cells; **IP_3:** Inositol Triphosphate; **IHC:** Inner Hair Cell; **K^+:** Potassium Ion; **MET:** Mechanoelectrical Transduction Channel; **NKCC1:** Na^+-K^+-Cl^- Cotransporter 1; **OHC:** Outer Hair Cell; **OS:** Outer Sulcus; **RM:** Reissner's Membrane; **SGN:** Spiral Ganglion Neuron; **SV:** Stria Vascularis

Figure 6.5: Increased [Ca^{2+}_i] at IHC and OHC of Nedd4l$^{tm1b/tm1b}$ mice. **(a)** Increased endolymphatic ATP can act at the IHC and OHC. **(b)** Activation of P2Y and P2X receptors results in increased [Ca^{2+}_i], via release from intracellular stores or its influx. Consequentially, increased [Ca^{2+}_i] can stimulate excessive glutamate exocytosis, leading to ototoxic effects at the pre- and postsynaptic membrane.

The proposed molecular studies would provide insight to the dynamics of Ca^{2+} signalling in *Nedd4l*$^{tm1b/tm1b}$ mice, but are indirect approaches methods to investigating [Ca^{2+}_i] in hair cells. Alternative methods to investigate hair cell [Ca^{2+}_i] could be to perform *ex vivo* Ca^{2+} imaging of explanted cochlear tissue from *Nedd4l*$^{tm1b/tm1b}$ mice using Ca^{2+}-specific fluorescent dyes such as Fura-2-AM or Fluo4-AM. In addition to assessing [Ca^{2+}_i] in hair cells, this approach could also determine whether waves of Ca^{2+} are detected in the SCs of the OoC and the OS which could indicate that there is damage and increased endolymphatic ATP signalling in the cochlear tissue of *Nedd4l*$^{tm1b/tm1b}$ mice (Gale *et al.*, 2004; Piazza *et al.*, 2007).

Inappropriate stimulation of purinergic receptors on hair cells and increased [Ca^{2+}_i] could provide an explanation for the degeneration of different cochlear tissues in *Nedd4l*$^{tm1b/tm1b}$ mice. Increased [Ca^{2+}_i] could lead to excessive glutamate ototoxicity and result in the cochlear synaptopathy of *Nedd4l*$^{tm1b/tm1b}$ mice. At 3-weeks of age, *Nedd4l*$^{tm1b/tm1b}$ mice have decreased number of matched pre- and postsynaptic puncta in IHCs which is due to fewer GluR2 puncta (Figure 3.26). This correlated with decreased ABR wave I latency and amplitude recorded in response to a click stimulus, and decreased afferent neurons contacting IHCs (Figure 3.12b,Figure 3.27). The loss of functional ribbon synapses was observed five weeks earlier than any other signs of cochlear degeneration, which mirrors findings found in mouse models of noise-induced hearing loss (Kujawa & Liberman, 2009; Furman *et al.*, 2013).

6.2.2 Decreased ENaC Abundance

Excessive ATP signalling in *Nedd4l*$^{tm1b/tm1b}$ mice could also explain the observed decrease in αENaC subunit abundance (Figure 4.1, Figure 6.6). Previous research has explored physiological and molecular inhibition of ENaC inhibition via a purinergic receptor-mediated mechanism. At RM, activation of $P2Y_4$ receptors decreased the amiloride-sensitive Na^+ current recorded from RM tissue (Kim *et al.*, 2010). It has been previously shown that activation of the PKC-MAPK signalling cascade in parotid epithelial cells lead to transcriptional repression of the α-ENaC subunit (Zentner *et al.*, 1998; Lin *et al.*, 1999). MAPK signalling pathways can also phosphorylate the β- and γ-ENaC subunits too, which promotes their ubiquitination (Stockand *et al.*, 2000; Booth & Stockand, 2003). As previously discussed, future experiments will need to determine if all ENaC subunits are similarly affected in *Nedd4l*$^{tm1b/tm1b}$ mice.

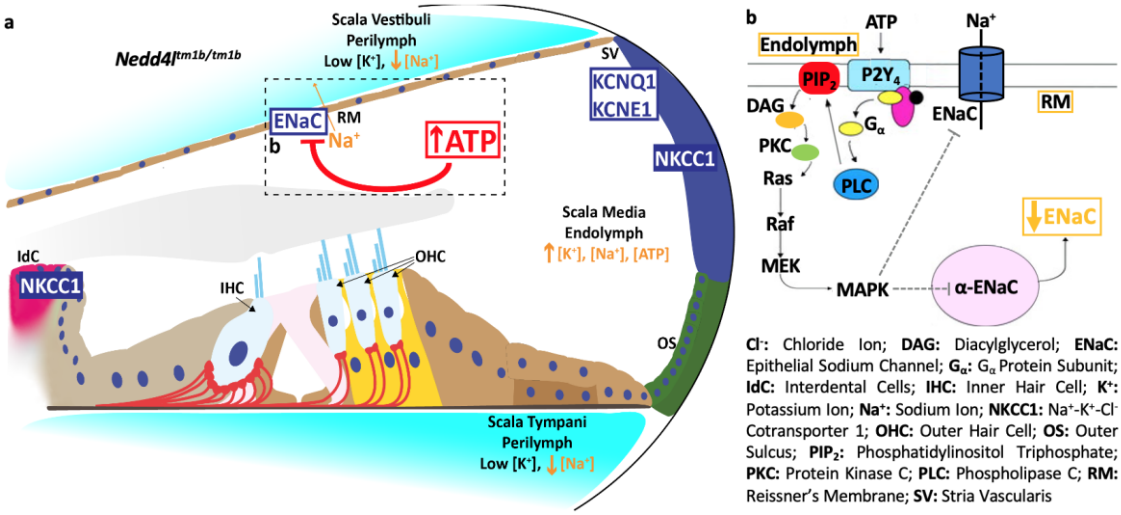

Figure 6.6: Decreased ENaC activity via activation of P2Y$_4$ receptors at RM. **(a)** Increased endolymphatic ATP in *Nedd4l*$^{tm1b/tm1b}$ mice could result in repression of ENaC activity. **(b)** Inappropriate activation of P2Y$_4$ activation results in G$_\alpha$-mediated activation of PLC, generating the secondary messenger DAG and stimulating PKC and the MAPK signalling pathway. MAPK pathway activation results in transcriptional repression of the αENaC subunit, or inhibit ENaC activity by phosphorylating the β- and γENaC subunits, thus promoting their ubiquitination.

6.2.3 Investigating Puringeric Signalling Pathways

Experiments should be conducted to verify whether increased purinergic signalling is involved in the hearing loss of *Nedd4l*$^{tm1b/tm1b}$ mice. A molecular indicator of elevated ATP in endolymphatic spaces in *Nedd4l*$^{tm1b/tm1b}$ mice could be increased expression of ectonucleotidases, NTPDase1 and NTPDase2, which are known to regulate the abundance of ATP within the endolymph and perilymph. Ectonucleotidase expression in the cochlear tissue of *Nedd4l*$^{tm1b/tm1b}$ mice could be assessed via Western blot or Immunohistochemistry methods. An alternative approach could be to assess whether P2Y-activated intracellular signalling pathways are affected in *Nedd4l*$^{tm1b/tm1b}$ mice. Western blots could also be performed against phosphorylated and unphosphorylated kinases of the MAPK pathway to assess whether they are more active in the cochlear tissue of *Nedd4l*$^{tm1b/tm1b}$ mice.

A pharmacological approach could also be adopted. For example, decreased ABR thresholds of *Nedd4l*$^{tm1b/tm1b}$ mice that were treated with P2X and P2Y antagonists such

as suramin or PPDAS compared to untreated *Nedd4l*$^{tm1b/tm1b}$ mice, could indicate that inappropriate stimulation of purinergic receptors is involved in the hearing loss in *Nedd4l*$^{tm1b/tm1b}$ mice. Alternatively, *Nedd4l*$^{tm1b/tm1b}$ mice could be exposed to a moderate level of noise that is known to cause temporary threshold shifts (TTS) in ABR thresholds. Previous reports have shown that noise-induced TTS is the result of $P2X_2$ receptors temporarily dampening auditory function in response to noise exposure (Housley *et al.*, 2013). If purinergic signalling is involved in the loss of auditory function of *Nedd4l*$^{tm1b/tm1b}$ mice, noise exposure of *Nedd4l*$^{tm1b/tm1b}$ mice could result in permanent threshold shifts or an accelerated onset of profound hearing loss.

Another approach could be to measure excitatory postsynaptic currents (EPSCs) from the type II afferent neurons of *Nedd4l*$^{tm1b/tm1b}$ mice. Previous research has shown that in response to cochlear damage and ATP release, EPSCs could be recorded from type II neurons which have previously shown little activity in response to sound (Robertson, 1984; Weisz *et al.*, 2009; Liu *et al.*, 2015). If *Nedd4l*$^{tm1b/tm1b}$ mice have increased endolymphatic ATP, there could be increased type II afferent neuronal activity.

6.3 Characterisation of *Nedd4* in Mammalian Cochlear Function

NEDD4 was identified as a novel candidate deafness-causing gene through a WES study of patients with adult-onset high-frequency hearing loss. Auditory characterisation was conducted on a *Nedd4* KO mouse model to investigate the role of *Nedd4* within the mammalian auditory system. No *Nedd4*$^{tm2b/tm2b}$ mice were born in the IMPC phenotyping cohort suggesting that constitutive *Nedd4* KO results in embryonic lethality (Figure 5.2b). This is consistent with lethality issues reported in other *Nedd4* KO mouse models (Cao *et al.*, 2008; Liu *et al.*, 2009; Kawabe *et al.*, 2010).

IMPC phenotyping of *Nedd4*$^{tm2b/+}$ mice did not detect any significant phenotypes, which is not consistent with published reports describing a previously generated, heterozygous *Nedd4* KO mouse model (*Nedd4*$^{17\Delta/+}$) (Camera *et al.*, 2014; Li *et al.*, 2015). Camera *et al*. described subtle gait phenotypes in *Nedd4*$^{17\Delta/+}$ mice that was detected using specialised video analysis software (Camera *et al.*, 2014). However, neither gait analysis nor video analysis is included in the broad-based IMPC phenotyping pipeline, and as such would explain why gait phenotypes were not detected in *Nedd4*$^{tm2b/+}$ mice (Brown & Moore, 2012). Li *et al.* described increased concentration of insulin in *Nedd4*$^{17\Delta/+}$ mice, a physiological measure that would be recorded as part of the IMPC phenotyping pipeline. The absence of elevated insulin in *Nedd4*$^{tm2b/+}$ mice could be because they were maintained on a congenic C57BL/6N background, whereas *Nedd4*$^{17\Delta/+}$ were were on a mixed C57BL/6J-129S5/SvEvBrd background.

To elucidate if *Nedd4* is involved in cochlear function, auditory characterisation of tissue-specific *Nedd4* cKO mice was conducted to circumvent the lethality experienced by

Nedd4$^{tm2b/tm2b}$ mice. A hair cell-specific, *Myo15*-driven *Nedd4* cKO mouse was generated, but auditory phenotyping did not identify auditory dysfunction in *Nedd4*$^{tm2c/tm2c}$; *Myo15-Cre*$^{+}$ mice and no signs of pathological changes to cochlear tissue were observed (Figure 5.5 – Figure 5.7). This indicated that *Nedd4* is not required for hair cell function in mice that are older than P4.

Investigations into the requirement of *Nedd4* in *Sox10*-expressing cochlear cells was also conducted. However, the role of *Nedd4* in *Sox10*-expressing cochlear cells is difficult to ascertain. Firstly, no *Nedd4*$^{tm2c/tm2c}$; *Sox10-Cre*$^{+}$ mice were born and therefore their auditory function could not be assessed (Figure 5.8) (Wiszniak *et al.*, 2013). In addition, two *Nedd4*$^{tm2c/tm2c}$; *Sox10-Cre*$^{-}$ mice, that were expected to display comparable auditory function to other control mice that do not carry the *Sox10-Cre* transgene, exhibited a high-frequency hearing loss at 8-weeks of age (Figure 5.10). It was hypothesised that the auditory phenotype displayed by *Nedd4*$^{tm2c/tm2c}$; *Sox10-Cre*$^{-}$ mice was a consequence of partial *Nedd4*^{tm2c} recombination *in utero*. Supporting this hypothesis is that *Nedd4*$^{tm2c/tm2c}$; *Sox10-Cre*$^{-}$ mice had decreased body weight compared to mice of other genotype, suggesting some physiological dysfunction in these mice (Figure 5.9). Overall, it appears that *Nedd4* is involved in mammalian auditory system, in non-sensory, adult hair cells.

6.4 Further Auditory Characterisation of *Nedd4*

To further investigate the role of *Nedd4* in cochlear function, auditory characterisation should be performed using different *Nedd4* KO models. As *NEDD4* was identified as a novel candidate age-related hearing loss gene in patients, one approach could be to investigate the auditory function of *Nedd4*$^{tm2b/+}$ mice on the "repaired" C57BL/6N background strain. The the C57BL/6N repair line carries a corrected *Cdh23*^{ahl} allele and do not experience high-frequency hearing loss that "unrepaired" C57BL/6N background strain mice would (Zheng *et al.*, 1999; Kane *et al.*, 2012; Mianné *et al.*, 2016). As IMPC-conducted ABRs of *Nedd4*$^{tm2b/+}$ mice on the "unrepaired" C57BL/6N background were conducted at 14-weeks of age, longitudinal auditory phenotyping of *Nedd4*$^{tm2b/+}$ mice on the "repaired" C57BL/6N background could begin at similar ages and reassessed every two months.

An alternative approach would be to utilise a tamoxifen-inducible, *Cre*-expressing driver line to generate an inducible KO (iKO) of *Nedd4*. Induction of Cre activity and *Nedd4* recombination at postnatal ages would not disrupt embryonic development and could potentially avoid the lethality display by previous *Nedd4* KO models. To generate *Nedd4* iKO mice, a tamoxifen-inducible, ubiquitous *Cre*-expressing (*Cre-ER*; Jax Stock No: 004682; Guo *et al.*, 2002) could be utilized. By generating *Nedd4*$^{tm2c/tm2c}$ mice that carry the *Cre-ER* transgene (*Nedd4*$^{tm2c/tm2c}$*; Cre-ER*$^{+}$) and inducing Cre activity at postnatal ages, it would allow investigation into *Nedd4* function in a fully developed auditory system. ABR tests of P21-aged, *Nedd4*$^{tm2c/tm2c}$; *Cre-ER*$^{+}$ mice could be performed to determine if they experience an early-onset hearing loss phenotype, with auditory function being reassessed every two weeks to determine whether *Nedd4*$^{tm2c/tm2c}$; *Cre-*

ER^{+} mice experience progressive phenotypes. If early-onset phenotypes are not detected, *Nedd4*$^{tm2c/tm2c}$; *Cre-ER*$^{+}$ mice could be placed onto the "repaired" C57BL/6N background to fully characterise the adult-onset, high-frequency hearing loss. Furthermore, conducting more ABR tests would provide the opportunity to assess how acoustic stimuli propagates through the CAS through ABR wave analysis.

To complement the phenotyping studies, cochlear pathology of *Nedd4*$^{tm2c/tm2c}$*; Cre-ER*$^{+}$ mice could be undertaken such as performing SEM and H&E staining to visualise hair cell bundles and overall cochlear morphology, respectively. Previous reports have detailed that a specific population of type I afferent neurons are preferentially lost as mice age (Furman *et al.*, 2013; Shrestha *et al.*, 2018). As *Nedd4*$^{tm2c/tm2c}$; *Sox10-Cre*$^{-}$ mice experience a later-onset hearing loss phenotype, investigations in *Nedd4*$^{tm2c/tm2c}$*; Cre-ER*$^{+}$ mice should be conducted to determine whether there is a preferential loss of specific population of type I afferents. This could be achieved by conducting Immunohistochemistry against LYPD1- and CALB2-expressing which display low SR/ high threshold and high SR/low threshold electrophysiological activity, respectively (Petitpré *et al.*, 2018; Shrestha *et al.*, 2018; Sun *et al.*, 2018). Furthermore, this could be complimented by assessing the ribbon synapse of *Nedd4*$^{tm2c/tm2c}$*; Cre-ER*$^{+}$ mice and whether there are fewer matched pre- and postsynaptic ribbon structures.

If alternative KO models are generated to investigate the requirement of *Nedd4* in cochlear function are conducted, molecular characterisation should also be conducted to determine that NEDD4 expression is disrupted at the gene and protein level. If *Nedd4*$^{tm2c/tm2c}$; *Cre-ER*$^{+}$ mice are generated, genotyping of mice should be conducted before tamoxifen administration to determine that they carry the *Nedd4*^{tm2c} allele.

Following induction of Cre activity, recombination efficacy should be assessed to determine that cochlear tissue of tamoxifen-treated, *Nedd4*$^{tm2c/tm2c}$; *Cre-ER*$^{+}$ mice should only carry the *Nedd4*^{tm2d} KO allele. This could be assessed by utilizing the IMPC-designed qPCR genotyping assay that was used to genotype the *Nedd4* cKO mouse lines.

Anti-NEDD4 Western blots should also be conducted to verify that tamoxifen-treated, *Nedd4*$^{tm2c/tm2c}$; *Cre-ER*$^{+}$ mice do not express any NEDD4 protein in cochlear tissue. If *Nedd4*$^{tm2b/+}$ mice on the "repaired" C57BL/6N background are generated, anti-NEDD4 Western blots should be performed to confirm they express less NEDD4 protein instead. Anti-NEDD4 immunohistochemistry stains should also be conducted, which would also inform where NEDD4 is expressed within cochlear tissue. Its cochlear expression has previously been investigated but appeared to overlap with NEDD4L expression (Zhong *et al.*, 2014). Determining where NEDD4 protein is located within the cochlea could provide insights into what its requirement for cochlear function is.

6.5 Conclusion

Investigation of the NEDD4 family of E3 Ubiquitin Ligase proteins suggest different levels of requirement for cochlear function. Auditory phenotyping of *Nedd4* cKO mice indicates that loss of NEDD4 could result in adult-onset, high-frequency hearing loss due to dysfunction in non-sensory cells. To elucidate *Nedd4*'s requirement in mammalian auditory function, alternative KO models are required due to the lethality experienced by *Sox10*-driven cKO *Nedd4* mice. Anti-NEDD4 immunohistochemistry should be conducted to determine its cochlear expression. On the other hand, auditory phenotyping of constitutive and cochlear-specific cKO mice confirmed that *Nedd4l* is required for mammalian auditory function. In the absence of *Nedd4l*, mice experience an early-onset, progressive hearing loss phenotype, which progresses to profound deafness by 8-weeks of age. Experiments designed to determine the mechanism of hearing loss in *Nedd4l*$^{tm1b/tm1b}$ mice identified dysregulation of αENaC subunit of the ENaC channel. Additional investigations also identified the NKCC1 cotransporter as a potential substrate of NEDD4L in cochlear tissue. Based on previous literature, NEDD4L is likely involved in regulating the endolymph composition and the EP. To validate this hypothesis, future experiments should include additional characterisation of NEDD4L expression in cochlear tissue, and characterisation of ENaC and NKCC1 abundance in *Nedd4l* KO mice.

BIBLOGRAPHY

Agnew, T., Goldsworthy, M., Aguilar, C., Taylor, R.W., Bowl, M.R. & Cox Correspondence, R.D. (2018) A Wars2 Mutant Mouse Model Displays OXPHOS Deficiencies and Activation of Tissue-Specific Stress Response Pathways. *CellReports* **25**, pp.3315-3328.e6.

Ahituv, N. & Avraham, K.B. (2002) Mouse models for human deafness: Current tools for new fashions. *Trends in Molecular Medicine* **8(9)**, pp.447–451.

Ahmed, Z.M., Goodyear, R., Riazuddin, Saima, Lagziel, A., Legan, P.K., Behra, M., Burgess, S.M., Lilley, K.S., Wilcox, E.R., Riazuddin, Sheikh, Griffith, A.J., Frolenkov, G.I., Belyantseva, I.A., Richardson, G.P. & Friedman, T.B. (2006) The tip-link antigen, a protein associated with the transduction complex of sensory hair cells, is protocadherin-15. *Journal of Neuroscience* **26(26)**, pp.7022–7034.

Akil, O., Dyka, F., Calvet, C., Emptoz, A., Lahlou, G., Nouaille, S., De Monvel, J.B., Hardelin, J.P., Hauswirth, W.W., Avan, P., Petit, C., Safieddine, S. & Lustig, L.R. (2019) Dual AAV-mediated gene therapy restores hearing in a DFNB9 mouse model. *Proceedings of the National Academy of Sciences of the United States of America* **116(10)**, pp.4496–4501.

Akil, O., Seal, R.P., Burke, K., Wang, C., Alemi, A., During, M., Edwards, R.H. & Lustig, L.R. (2012) Restoration of Hearing in the VGLUT3 Knockout Mouse Using Virally Mediated Gene Therapy. *Neuron* **75(2)**, pp.283–293.

Alagramam, K.N., Goodyear, R.J., Geng, R., Furness, D.N., van Aken, A.F.J., Marcotti, W., Kros, C.J. & Richardson, G.P. (2011) Mutations in protocadherin 15 and cadherin 23 affect tip links and mechanotransduction in mammalian sensory hair cells. *PLoS ONE* **6(4)**, p.19183.

Alcaraz, W.A., Liu, Z., Valdes, P., Chen, E., Gonzalez, A.G.V., Wade, S., Wong, C., Kim, E., Chen, H.H.M., Ponn, A., Concepcion, D. & Hamilton, B.A. (2020) Strain-Dependent Modifier Genes Determine Survival in Zfp423 Mice. *G3: Genes|Genomes|Genetics* **10(11)**, p.4241.

Anderson, D.W., Probst, F.J., Belyantseva, I.A., Fridell, R.A., Beyer, L., Martin, D.M., Wu, D., Kachar, B., Friedman, T.B., Raphael, Y. & Camper, S.A. (2000) The motor and tail regions of myosin XV are critical for normal structure and function of auditory and vestibular hair cells. *Human Molecular Genetics* **9(12)**, pp.1729–1738.

Anniko, M. & Wikström, S.O. (1984) Pattern formation of the otic placode and morphogenesis of the otocyst. *American Journal of Otolaryngology--Head and*

Neck Medicine and Surgery **5(6)**, pp.373–381.

Arnold, T., Oestreicher, E., Ehrenberger, K. & Felix, D. (1998) GABA(A) receptor modulates the activity of inner hair cell afferents in guinea pig cochlea. *Hearing Research* **125(1–2)**, pp.147–153.

Arroyo, J.P., Lagnaz, D., Ronzaud, C., Vázquez, N., Ko, B.S., Moddes, L., Ruffieux-Daidié, D., Hausel, P., Koesters, R., Yang, B., Stokes, J.B., Hoover, R.S., Gamba, G. & Staub, O. (2011) Nedd4-2 modulates renal Na+-Cl- cotransporter via the aldosterone-SGK1-Nedd4-2 pathway. *Journal of the American Society of Nephrology* **22(9)**, pp.1707–1719.

Ashmore, J.F. (1987) A fast motile response in guinea-pig outer hair cells: the cellular basis of the cochlear amplifier. *The Journal of Physiology* **388(1)**, pp.323–347.

Assad, J.A., Shepherd, G.M.G. & Corey, D.P. (1991) Tip-link integrity and mechanical transduction in vertebrate hair cells. *Neuron* **7(6)**, pp.985–994.

Bao, X., Lian, X., Hacker, T.A., Schmuck, E.G., Qian, T., Bhute, V.J., Han, T., Shi, M., Drowley, L., Plowright, A.T., Wang, Q.D., Goumans, M.J. & Palecek, S.P. (2017) Long-term self-renewing human epicardial cells generated from pluripotent stem cells under defined xeno-free conditions. *Nature Biomedical Engineering* **1(1)**, p.3.

Bartlett, P.J., Young, K.W., Nahorski, S.R. & Challiss, R.A.J. (2005) Single cell analysis and temporal profiling of agonist-mediated inositol 1,4,5-trisphosphate, Ca2+, diacylglycerol, and protein kinase C signaling using fluorescent biosensors. *Journal of Biological Chemistry* **280(23)**, pp.21837–21846.

Bartsch, T.F., Hengel, F.E., Oswald, A., Dionne, G., Chipendo, I. V., Mangat, S.S., Shatanofy, M. El, Shapiro, L., Müller, U. & Hudspeth, A.J. (2019) Elasticity of individual protocadherin 15 molecules implicates tip links as the gating springs for hearing. *Proceedings of the National Academy of Sciences of the United States of America* **166(22)**, pp.11048–11056.

Basch, M.L., Brown, R.M., Jen, H.I. & Groves, A.K. (2016) Where hearing starts: The development of the mammalian cochlea. *Journal of Anatomy* **228(2)**, pp.233–254.

Basu, A., Lagier, S., Vologodskaia, M., Fabella, B.A. & Hudspeth, A.J. (2016) Direct mechanical stimulation of tip links in hair cells through DNA tethers. *eLife* **5(JUN2016)**.

Batta, T.J., Panyi, G., Szucs, A. & Sziklai, I. (2004) Regulation of the lateral wall stiffness by acetylcholine and GABA in the outer hair cells of the guinea pig. *European Journal of Neuroscience* **20(12)**, pp.3364–3370.

Beck, J.A., Lloyd, S., Hafezparast, M., Lennon-Pierce, M., Eppig, J.T., Festing, M.F.W. & Fisher, E.M.C. (2000) Genealogies of mouse inbred strains. *Nature Genetics* **24(1)**, pp.23–25.

Becker, L., Schnee, M.E., Niwa, M., Sun, W., Maxeiner, S., Talaei, S., Kachar, B., Rutherford, M.A. & Ricci, A.J. (2018) The presynaptic ribbon maintains vesicle populations at the hair cell afferent fiber synapse. *eLife* **7**.

Békésy, G. (1960) *Experiments in Hearing*, New York: McGraw-Hill.

Belyantseva, I.A., Adler, H.J., Curi, R., Frolenkov, G.I. & Kachar, B. (2000) Expression and localization of prestin and the sugar transporter GLUT-5 during development of electromotility in cochlear outer hair cells. *The Journal of neuroscience : the official journal of the Society for Neuroscience* **20(24)**, p.RC116.

Belyantseva, I.A., Boger, E.T., Naz, S., Frolenkov, G.I., Sellers, J.R., Ahmed, Z.M., Griffith, A.J. & Friedman, T.B. (2005) Myosin-XVa is required for tip localization of whirlin and differential elongation of hair-cell stereocilia. *Nature Cell Biology* **7(2)**, pp.148–156.

Berglund, A.M. & Ryugo, D.K. (1987) Hair cell innervation by spiral ganglion neurons in the mouse. *The Journal of Comparative Neurology* **255(4)**, pp.560–570.

Bermingham, N.A., Hassan, B.A., Price, S.D., Vollrath, M.A., Ben-Arie, N., Eatock, R.A., Bellen, H.J., Lysakowski, A. & Zoghbi, H.Y. (1999) Math 1: An essential gene for the generation of inner ear hair cells. *Science* **284(5421)**, pp.1837–1841.

Beurg, M., Michalski, N., Safieddine, S., Bouleau, Y., Schneggenburger, R., Chapman, E.R., Petit, C. & Dulon, D. (2010) Control of exocytosis by synaptotagmins and otoferlin in auditory hair cells. *Journal of Neuroscience* **30(40)**, pp.13281–13290.

Beurg, M., Fettiplace, R., Nam, J.H. & Ricci, A.J. (2009) Localization of inner hair cell mechanotransducer channels using high-speed calcium imaging. *Nature Neuroscience* **12(5)**, pp.553–558.

Blanchet, C., Eróstegui, C., Sugasawa, M. & Dulon, D. (1996) Acetylcholine-induced potassium current of guinea pig outer hair cells: Its dependence on a calcium influx through nicotinic-like receptors. *Journal of Neuroscience* **16(8)**, pp.2574–2584.

Boase, Natasha A, Rychkov, G.Y., Townley, S.L., Dinudom, A., Candi, E., Voss, A.K., Tsoutsman, T., Semsarian, C., Melino, G., Koentgen, F., Cook, D.I. & Kumar, S. (2011) Respiratory distress and perinatal lethality in Nedd4-2-deficient mice. *Nature Communications* **2**, p.287.

Boase, Natasha A., Rychkov, G.Y., Townley, S.L., Dinudom, A., Candi, E., Voss, A.K., Tsoutsman, T., Semsarian, C., Melino, G., Koentgen, F., Cook, D.I. & Kumar, S. (2011) Respiratory distress and perinatal lethality in Nedd4-2-deficient mice. *Nature Communications* **2(1)**, p.287.

Boase, N.A. & Kumar, S. (2015) NEDD4: The founding member of a family of ubiquitin-protein ligases. *Gene* **557(2)**, pp.113–122.

Booth, R.E. & Stockand, J.D. (2003) Targeted degradation of ENaC in response to PKC activation of the ERK1/2 cascade. *American Journal of Physiology-Renal Physiology* **284(5)**, pp.F938–F947.

Bowl, M.R., Simon, M.M., Ingham, N.J., Greenaway, S., Santos, L., Cater, H., Taylor, S., Mason, J., Kurbatova, N., Pearson, S., Bower, L.R., Clary, D.A., Meziane, H., Reilly, P., Minowa, O., Kelsey, L., Tocchini-Valentini, G.P., Gao, X., Bradley, A., Skarnes, W.C., Moore, M., Beaudet, A.L., Justice, M.J., Seavitt, J., Dickinson, M.E., Wurst, W., de Angelis, M.H., Herault, Y., Wakana, S., Nutter, L.M.J., Flenniken, A.M., McKerlie, C., Murray, S.A., Svenson, K.L., Braun, R.E., West, D.B., Lloyd, K.C.K., Adams, D.J., White, J., Karp, N., Flicek, P., Smedley, D., Meehan, T.F., Parkinson, H.E., Teboul, L.M., Wells, S., Steel, K.P., Mallon, A.M. & Brown, S.D.M. (2017) A large scale hearing loss screen reveals an extensive unexplored genetic landscape for auditory dysfunction. *Nature Communications* **8(1)**, p.886.

Brandt, A., Khimich, D. & Moser, T. (2005) Few CaV1.3 channels regulate the exocytosis of a synaptic vesicle at the hair cell ribbon synapse. *Journal of Neuroscience* **25(50)**, pp.11577–11585.

Brandt, A., Striessnig, J. & Moser, T. (2003) Cav1.3 Channels Are Essential for Development and Presynaptic Activity of Cochlear Inner Hair Cells. *Journal of Neuroscience* **23(34)**, pp.10832–10840.

Broix, L., Jagline, H., Ivanova, E.L., Schmucker, S., Drouot, N., Clayton-Smith, J., Pagnamenta, A.T., Metcalfe, K.A., Isidor, B., Louvier, U.W., Poduri, A., Taylor, J.C., Tilly, P., Poirier, K., Saillour, Y., Lebrun, N., Stemmelen, T., Rudolf, G., Muraca, G., Saintpierre, B., Elmorjani, A., Moïse, M., Weirauch, N.B., Guerrini, R., Boland, A., Olaso, R., Masson, C., Tripathy, R., Keays, D., Beldjord, C., Nguyen, L., Godin, J., Kini, U., Nischké, P., Deleuze, J.F., Bahi-Buisson, N., Sumara, I., Hinckelmann, M.V. & Chelly, J. (2016) Mutations in the HECT domain of NEDD4L lead to AKT-mTOR pathway deregulation and cause periventricular nodular heterotopia. *Nature Genetics* **48(11)**, pp.1349–1358.

Brooker, R., Hozumi, K. & Lewis, J. (2006) Notch ligands with contrasting function:

Jagged1 and Delta1 in the mouse inner ear. *Development* **133(7)**, pp.1277–1286.

Brown, M.C., Nuttall, A.L. & Masta, R.I. (1983) Intracellular recordings from cochlear inner hair cells: Effects of stimulation of the crossed olivocochlear efferents. *Science* **222(4619)**, pp.69–72.

Brown, S.D.M. & Moore, M.W. (2012) The International Mouse Phenotyping Consortium: Past and future perspectives on mouse phenotyping. *Mammalian Genome* **23(9–10)**, pp.632–640.

Buccitelli, C. & Selbach, M. (2020) mRNAs, proteins and the emerging principles of gene expression control. *Nature Reviews Genetics* **21(10)**, pp.630–644.

Buchwald, J.S. & Huang, C.M. (1975) Far-field acoustic response: Origins in the cat. *Science* **189(4200)**, pp.382–384.

Butler, B.E. & Lomber, S.G. (2013) Functional and structural changes throughout the auditory system following congenital and early-onset deafness: implications for hearing restoration. *Frontiers in Systems Neuroscience* **7**.

Caberlotto, E., Michel, V., Foucher, I., Bahloul, A., Goodyear, R.J., Pepermans, E., Michalski, N., Perfettini, I., Alegria-Prévot, O., Chardenoux, S., Cruzeiro, M. Do, Hardelin, J.P., Richardson, G.P., Avan, P., Weil, D. & Petit, C. (2011) Usher type 1G protein sans is a critical component of the tip-link complex, a structure controlling actin polymerization in stereocilia. *Proceedings of the National Academy of Sciences of the United States of America* **108(14)**, pp.5825–5830.

Camera, D., Boase, N.A., Kumar, S., Pow, D. V. & Poronnik, P. (2014) Subtle gait abnormalities in Nedd4 heterozygous mice. *Behavioural Brain Research* **260**, pp.15–24.

Canessa, C.M., Schild, L., Buell, G., Thorens, B., Gautschi, I., Horisberger, J.D. & Rossier, B.C. (1994) Amiloride-sensitive epithelial Na + channel is made of three homologous subunits. *Nature 1994 367:6462* **367(6462)**, pp.463–467.

Cao, Xiao R., Lill, N.L., Boase, N., Shi, P.P., Croucher, D.R., Shan, H., Qu, J., Sweezer, E.M., Place, T., Kirby, P.A., Daly, R.J., Kumar, S. & Yang, B. (2008) Nedd4 controls animal growth by regulating IGF-1 signaling. *Science Signaling* **1(38)**.

Cao, X. R., Lill, N.L., Boase, N., Shi, P.P., Croucher, D.R., Shan, H., Qu, J., Sweezer, E.M., Place, T., Kirby, P.A., Daly, R.J., Kumar, S. & Yang, B. (2008) Nedd4 Controls Animal Growth by Regulating IGF-1 Signaling. *Science Signaling* **1(38)**, pp.ra5–ra5.

Carrott, L., Bowl, M.R., Aguilar, C., Johnson, S.L., Chessum, L., West, M., Morse, S., Dorning, J., Smart, E., Hardisty-Hughes, R., Ball, G., Parker, A., Barnard, A.R.,

MacLaren, R.E., Wells, S., Marcotti, W. & Brown, S.D.M. (2016) Absence of neuroplastin-65 affects synaptogenesis in mouse inner hair cells and causes profound hearing loss. *Journal of Neuroscience* **36(1)**, pp.222–234.

Chakrabarti, R., Michanski, S. & Wichmann, C. (2018) Vesicle sub-pool organization at inner hair cell ribbon synapses. *EMBO reports* **19(11)**.

Chan, D.K. & Hudspeth, A.J. (2005) Ca2+ current-driven nonlinear amplification by the mammalian cochlea in vitro. *Nature Neuroscience* **8(2)**, pp.149–155.

Chellappa, R., Li, S., Pauley, S., Jahan, I., Jin, K. & Xiang, M. (2008) Barhl1 Regulatory Sequences Required for Cell-Specific Gene Expression and Autoregulation in the Inner Ear and Central Nervous System. *Molecular and Cellular Biology* **28(6)**, pp.1905–1914.

Chen, P., Johnson, J.E., Zoghbi, H. & Segil, N. (2002) The role of Math1 in inner ear development: Uncoupling the establishment of the sensory primordium from hair cell fate determination. *Development*.

Chen, P. & Segil, N. (1999) p27(Kip1) links cell proliferation to morphogenesis in the developing organ of Corti. *Development*.

Chen, Z., Peppi, M., Kujawa, S.G. & Sewell, W.F. (2009) Regulated Expression of Surface AMPA Receptors Reduces Excitotoxicity in Auditory Neurons. *Journal of Neurophysiology* **102(2)**, p.1152.

Chen, Z., Kujawa, S.G. & Sewell, W.F. (2007) Auditory sensitivity regulation via rapid changes in expression of surface AMPA receptors. *Nature Neuroscience 2007 10:10* **10(10)**, pp.1238–1240.

Cheng, D., Hoogenraad, C.C., Rush, J., Ramm, E., Schlager, M.A., Duong, D.M., Xu, P., Wijayawardana, S.R., Hanfelt, J., Nakagawa, T., Sheng, M. & Peng, J. (2006) Relative and absolute quantification of postsynaptic density proteome isolated from rat forebrain and cerebellum. *Molecular and Cellular Proteomics* **5(6)**, pp.1158–1170.

Cheng, Y.F., Tong, M. & Edge, A.S.B. (2016) Destabilization of Atoh1 by E3 ubiquitin ligase Huwe1 and casein kinase 1 is essential for normal sensory hair cell development. *Journal of Biological Chemistry* **291(40)**, pp.21096–21109.

Chessum, L., Matern, M.S., Kelly, M.C., Johnson, S.L., Ogawa, Y., Milon, B., McMurray, M., Driver, E.C., Parker, A., Song, Y., Codner, G., Esapa, C.T., Prescott, J., Trent, G., Wells, S., Dragich, A.K., Frolenkov, G.I., Kelley, M.W., Marcotti, W., Brown, S.D.M., Elkon, R., Bowl, M.R. & Hertzano, R. (2018) Helios is a key transcriptional

regulator of outer hair cell maturation. *Nature* **563(7733)**, pp.696–724.

Cichanover, A. (2005) Intracellular protein degradation: From a vague idea thru the lysosome and the ubiquitin-proteasome system and onto human diseases and drug targeting. *Cell Death and Differentiation* **12(9)**, pp.1178–1190.

Coate, T.M., Spita, N.A., Zhang, K.D., Isgrig, K.T. & Kelley, M.W. (2015) Neuropilin-2/semaphorin-3F-mediated repulsion promotes inner hair cell innervation by spiral ganglion neurons. *eLife* **4(AUGUST2015)**, pp.1–24.

Cooper, M.A., O'Meara, B., Jack, M.M., Elliot, D., Lamb, B., Khan, Z.W., Menta, B.W., Ryals, J.M., Winter, M.K. & Wright, D.E. (2018) Intrinsic Activity of C57BL/6 Substrains Associates with High-Fat Diet-Induced Mechanical Sensitivity in Mice. *The journal of pain : official journal of the American Pain Society* **19(11)**, p.1285.

Corey, D.P. & Hudspeth, A.J. (1979) Ionic basis of the receptor potential in a vertebrate hair cell. *Nature* **281(5733)**, pp.675–677.

Couloigner, V., Fay, M., Djelidi, S., Farman, N., Escoubet, B., Runembert, I., Sterkers, O., Friedlander, G. & Ferrary, E. (2001) Location and function of the epithelial Na channel in the cochlea. *American Journal of Physiology - Renal Physiology* **280(2 49-2)**.

Crouch, J.J., Sakaguchi, N., Lytle, C. & Schulte, B.A. (1997) Immunohistochemical localization of the Na-K-Cl co-transporter (NKCC1) in the gerbil inner ear. *Journal of Histochemistry and Cytochemistry* **45(6)**, pp.773–778.

Cunningham, C.L. & Müller, U. (2019) Molecular structure of the hair cell mechanoelectrical transduction complex. *Cold Spring Harbor Perspectives in Medicine* **9(5)**.

d'Aldin, C., Puel, J.L., Leducq, R., Crambes, O., Eybalin, M. & Pujol, R. (1995) Effects of a dopaminergic agonist in the guinea pig cochlea. *Hearing Research* **90(1–2)**, pp.202–211.

Dabdoub, A., Puligilla, C., Jones, J.M., Fritzsch, B., Cheah, K.S.E., Pevny, L.H. & Kelley, M.W. (2008) Sox2 signaling in prosensory domain specification and subsequent hair cell differentiation in the developing cochlea. *Proceedings of the National Academy of Sciences of the United States of America* **105(47)**, pp.18395–18401.

Dallos, P., Wu, X., Cheatham, M.A., Gao, J., Zheng, J., Anderson, C.T., Jia, S., Wang, X., Cheng, W.H.Y., Sengupta, S., He, D.Z.Z. & Zuo, J. (2008) Prestin-Based Outer Hair Cell Motility Is Necessary for Mammalian Cochlear Amplification. *Neuron* **58(3)**, pp.333–339.

Darrow, K.N., Simons, E.J., Dodds, L. & Liberman, M.C. (2006) Dopaminergic innervation of the mouse inner ear: Evidence for a separate cytochemical group of cochlear efferent fibers. *The Journal of Comparative Neurology* **498(3)**, pp.403–414.

Darrow, K.N., Maison, S.F. & Liberman, M.C. (2007) Selective removal of lateral olivocochlear efferents increases vulnerability to acute acoustic injury. *Journal of Neurophysiology* **97(2)**, pp.1775–1785.

Davies, C., Tingley, D., Kachar, B., Wenthold, R.J. & Petralia, R.S. (2001) Distribution of members of the PSD-95 family of MAGUK proteins at the synaptic region of inner and outer hair cells of the guinea pig cochlea. *Synapse* **40(4)**, pp.258–268.

Defourny, J., Poirrier, A.L., Lallemend, F., Sánchez, S.M., Neef, J., Vanderhaeghen, P., Soriano, E., Peuckert, C., Kullander, K., Fritzsch, B., Nguyen, L., Moonen, G., Moser, T. & Malgrange, B. (2013) Ephrin-A5/EphA4 signalling controls specific afferent targeting to cochlear hair cells. *Nature Communications* **4(1)**, pp.1–12.

Delhez, A., Lefebvre, P., Péqueux, C., Malgrange, B. & Delacroix, L. (2020) Auditory function and dysfunction: estrogen makes a difference. *Cellular and Molecular Life Sciences* **77(4)**, pp.619–635.

Delpire, E., Lu, J., England, R., Dull, C. & Thorne, T. (1999) Deafness and imbalance associated with inactivation of the secretory Na- K-2Cl co-transporter. *Nature Genetics* **22(2)**, pp.192–195.

Deol, K.K., Lorenz, S. & Strieter, E.R. (2019) Enzymatic Logic of Ubiquitin Chain Assembly. *Frontiers in Physiology* **10**.

Diaz, R.C., Vazquez, A.E., Dou, H., Wei, D., Cardell, E. Lou, Lingrel, J., Shull, G.E., Doyle, K.J. & Yamoah, E.N. (2007) Conservation of hearing by simultaneous mutation of Na,K-ATPase and NKCC1. *JARO - Journal of the Association for Research in Otolaryngology* **8(4)**, pp.422–434.

Dickerson, I.M., Bussey-Gaborski, R., Holt, J.C., Jordan, P.M. & Luebke, A.E. (2016) Maturation of suprathreshold auditory nerve activity involves cochlear CGRP–receptor complex formation. *Physiological Reports* **4(14)**.

Dixon, M.J., Gazzard, J., Chaudhry, S.S., Sampson, N., Schulte, B.A. & Steel, K.P. (1999) Mutation of the Na-K-Cl co-transporter gene Slc12a2 results in deafness in mice. *Human Molecular Genetics* **8(8)**, pp.1579–1584.

Djelidi, S., Fay, M., Cluzeaud, F., Escoubet, B., Eugene, E., Capurro, C., Bonvalet, J.P., Farman, N. & Blot-Chabaud, M. (1997) Transcriptional regulation of sodium

transport by vasopressin in renal cells. *Journal of Biological Chemistry* **272(52)**, pp.32919–32924.

Driver, E.C. & Kelley, M.W. (2020) Development of the cochlea. *Development (Cambridge)* **147(12)**.

Dubno, J.R., Eckert, M.A., Lee, F.S., Matthews, L.J. & Schmiedt, R.A. (2013) Classifying human audiometric phenotypes of age-related hearing loss from animal models. *JARO - Journal of the Association for Research in Otolaryngology* **14(5)**, pp.687–701.

Dunbar, L.A., Patni, P., Aguilar, C., Mburu, P., Corns, L., Wells, H.R., Delmaghani, S., Parker, A., Johnson, S., Williams, D., Esapa, C.T., Simon, M.M., Chessum, L., Newton, S., Dorning, J., Jeyarajan, P., Morse, S., Lelli, A., Codner, G.F., Peineau, T., Gopal, S.R., Alagramam, K.N., Hertzano, R., Dulon, D., Wells, S., Williams, F.M., Petit, C., Dawson, S.J., Brown, S.D., Marcotti, W., El-Amraoui, A. & Bowl, M.R. (2019) Clarin-2 is essential for hearing by maintaining stereocilia integrity and function. *EMBO Molecular Medicine* **11(9)**.

Dunn, D.M., Ishigami, T., Pankow, J., von Niederhausern, A., Alder, J., Hunt, S.C., Leppert, M.F., Lalouel, J.M. & Weiss, R.B. (2002) Common variant of human NEDD4L activates a cryptic splice site to form a frameshifted transcript. *Journal of Human Genetics* **47(12)**, pp.665–676.

Elbracht, M., Kraft, F., Begemann, M., Holschbach, P., Mull, M., Kabat, I.M., Müller, B., Häusler, M., Kurth, I. & Hehr, U. (2018) Familial *NEDD4L* variant in periventricular nodular heterotopia and in a fetus with hypokinesia and flexion contractures. *Molecular Genetics & Genomic Medicine* **6(6)**, pp.1255–1260.

Elgoyhen, A.B., Vetter, D.E., Katz, E., Rothlin, C. V., Heinemann, S.F. & Boulter, J. (2001) α10: A determinant of nicotinic cholinergic receptor function in mammalian vestibular and cochlear mechanosensory hair cells. *Proceedings of the National Academy of Sciences of the United States of America* **98(6)**, pp.3501–3506.

Elgoyhen, A.B., Johnson, D.S., Boulter, J., Vetter, D.E. & Heinemann, S. (1994) α9: An acetylcholine receptor with novel pharmacological properties expressed in rat cochlear hair cells. *Cell* **79(4)**, pp.705–715.

Emptoz, A., Michel, V., Lelli, A., Akil, O., De Monvel, J.B., Lahlou, G., Meyer, A., Dupont, T., Nouaille, S., Ey, E., De Barros, F.F., Beraneck, M., Dulon, D., Hardelin, J.P., Lustig, L., Avan, P., Petit, C. & Safieddine, S. (2017) Local gene therapy durably restores vestibular function in a mouse model of Usher syndrome type 1G. *Proceedings of the National Academy of Sciences of the United States of America*

114(36), pp.9695–9700.

Erb, L. & Weisman, G.A. (2012) Coupling of P2Y receptors to G proteins and other signaling pathways. *Wiley Interdisciplinary Reviews: Membrane Transport and Signaling* **1(6)**, pp.789–803.

Estévez, R., Boettger, T., Stein, V., Birkenhäger, R., Otto, E., Hildebrandt, F. & Jentsch, T.J. (2001) Barttin is a Cl- channel β-subunit crucial for renal Cl- reabsorption and inner ear K+ secretion. *Nature* **414(6863)**, pp.558–561.

Eybalin, M. (1993) Neurotransmitters and neuromodulators of the mammalian cochlea. *Physiological Reviews* **73(2)**, pp.309–374.

Fava, C., Von Wowern, F., Berglund, G., Carlson, J., Hedblad, B., Rosberg, L., Burri, P., Almgren, P. & Melander, O. (2006) 24-h ambulatory blood pressure is linked to chromosome 18q21-22 and genetic variation of NEDD4L associates with cross-sectional and longitudinal blood pressure in Swedes. *Kidney International* **70(3)**, pp.562–569.

Fawell, S., Seery, J., Daikh, Y., Moore, C., Chen, L.L., Pepinsky, B. & Barsoum, J. (1994a) Tat-mediated delivery of heterologous proteins into cells. *Proceedings of the National Academy of Sciences of the United States of America* **91(2)**, pp.664–668.

Fawell, S., Seery, J., Daikh, Y., Moore, C., Chen, L.L., Pepinsky, B. & Barsoum, J. (1994b) Tat-mediated delivery of heterologous proteins into cells. *Proceedings of the National Academy of Sciences of the United States of America* **91(2)**, pp.664–668.

Felix, D. & Ehrenberger, K. (1992) The efferent modulation of mammalian inner hair cell afferents. *Hearing Research* **64(1)**, pp.1–5.

Fettiplace, R. (2017) Hair cell transduction, tuning, and synaptic transmission in the mammalian cochlea. *Comprehensive Physiology* **7(4)**, pp.1197–1227.

Fettiplace, R. & Hackney, C.M. (2006) The sensory and motor roles of auditory hair cells. *Nature Reviews Neuroscience* **7(1)**, pp.19–29.

Flagella, M., Clarke, L.L., Miller, M.L., Erway, L.C., Giannella, R.A., Andringa, A., Gawenis, L.R., Kramer, J., Duffy, J.J., Doetschman, T., Lorenz, J.N., Yamoah, E.N., Cardell, E. Lou & Shull, G.E. (1999) Mice lacking the basolateral Na-K-2Cl cotransporter have impaired epithelial chloride secretion and are profoundly deaf. *Journal of Biological Chemistry* **274(38)**, pp.26946–26955.

Flores, E.N., Duggan, A., Madathany, T., Hogan, A.K., Márquez, F., Kumar, G., Seal, R., Edwards, R., Liberman, M.C. & García-Añoveros, J. (2015) A Non-canonical Pathway from Cochlea to Brain Signals Tissue-damaging Noise. *Current biology :*

CB **25(5)**, p.606.

Fotia, A.B., Ekberg, J., Adams, D.J., Cook, D.I., Poronnik, P. & Kumar, S. (2004) Regulation of neuronal voltage-gated sodium channels by the ubiquitin protein ligases Nedd4 and Nedd4-2. *Journal of Biological Chemistry* **279(28)**, pp.28930–28935.

Fotia, A.B., Cook, D.I. & Kumar, S. (2006) The ubiquitin-protein ligases Nedd4 and Nedd4-2 show similar ubiquitin-conjugating enzyme specificities. *International Journal of Biochemistry and Cell Biology* **38(3)**, pp.472–479.

Fouladkou, F., Lu, C., Jiang, C., Zhou, L., She, Y., Walls, J.R., Kawabe, H., Brose, N., Henkelman, R.M., Huang, A., Bruneau, B.G. & Rotin, D. (2010) The Ubiquitin Ligase Nedd4-1 Is Required for Heart Development and Is a Suppressor of Thrombospondin-1. *The Journal of Biological Chemistry* **285(9)**, p.6770.

Frank, T., Rutherford, M.A., Strenzke, N., Neef, A., Pangršič, T., Khimich, D., Fetjova, A., Gundelfinger, E.D., Liberman, M.C., Harke, B., Bryan, K.E., Lee, A., Egner, A., Riedel, D. & Moser, T. (2010) Bassoon and the synaptic ribbon organize Ca2+ channels and vesicles to add release sites and promote refilling. *Neuron* **68(4)**, pp.724–738.

Frank, T., Khimich, D., Neef, A. & Moser, T. (2009) Mechanisms contributing to synaptic Ca2+ signals and their heterogeneity in hair cells. *Proceedings of the National Academy of Sciences of the United States of America* **106(11)**, pp.4483–4488.

Frankel, A.D. & Pabo, C.O. (1988) Cellular uptake of the tat protein from human immunodeficiency virus. *Cell* **55(6)**, pp.1189–1193.

Fridberger, A., Flock, Åke, Ulfendahl, M. & Flock, B. (1998) Acoustic overstimulation increases outer hair cell Ca2+ concentrations and causes dynamic contractions of the hearing organ. *Proceedings of the National Academy of Sciences of the United States of America* **95(12)**, p.7127.

Fridberger, A. & Ulfendahl, M. (1996) Acute mechanical overstimulation of isolated outer hair cells causes changes in intracellular calcium levels without shape changes. *Acta oto-laryngologica* **116(1)**, pp.17–24.

Fritzsch, B., Matei, V.A., Nichols, D.H., Bermingham, N., Jones, K., Beisel, K.W. & Wang, V.Y. (2005) Atoh1 null mice show directed afferent fiber growth to undifferentiated ear sensory epithelia followed by incomplete fiber retention. In *Developmental Dynamics*. NIH Public Access, pp. 570–583.

Frolenkov, G.I. (2006) Regulation of electromotility in the cochlear outer hair cell.

Journal of Physiology **576(1)**, pp.43–48.

Fuchs, P.A. & Murrow, B.W. (1992) Cholinergic inhibition of short (outer) hair cells of the chick's cochlea. *Journal of Neuroscience* **12(3)**, pp.800–809.

Furman, A.C., Kujawa, S.G. & Liberman, M.C. (2013) Noise-induced cochlear neuropathy is selective for fibers with low spontaneous rates. *https://doi.org/10.1152/jn.00164.2013* **110(3)**, pp.577–586.

Gale, J.E., Piazza, V., Ciubotaru, C.D. & Mammano, F. (2004) A mechanism for sensing noise damage in the inner ear. *Current Biology* **14(6)**, pp.526–529.

Gaskill, S.A. & Brown, A.M. (1990) The behavior of the acoustic distortion product, 2f1−f2, from the human ear and its relation to auditory sensitivity. *The Journal of the Acoustical Society of America* **88(2)**, p.821.

Glowatzki, E. & Fuchs, P.A. (2002) Transmitter release at the hair cell ribbon synapse. *Nature Neuroscience* **5(2)**, pp.147–154.

Goel, P., Manning, J.A. & Kumar, S. (2015) NEDD4-2 (NEDD4L): The ubiquitin ligase for multiple membrane proteins. *Gene* **557(1)**, pp.1–10.

Grati, M. & Kachar, B. (2011) Myosin VIIa and sans localization at stereocilia upper tip-link density implicates these Usher syndrome proteins in mechanotransduction. *Proceedings of the National Academy of Sciences of the United States of America* **108(28)**, pp.11476–11481.

Groff, J.A. & Liberman, M.C. (2003) Modulation of Cochlear Afferent Response by the Lateral Olivocochlear System: Activation Via Electrical Stimulation of the Inferior Colliculus. *Journal of Neurophysiology* **90(5)**, pp.3178–3200.

Guinan, J.J., Warr, W.B. & Norris, B.E. (1983) Differential olivocochlear projections from lateral versus medial zones of the superior olivary complex. *The Journal of Comparative Neurology* **221(3)**, pp.358–370.

Guo, C., Yang, W. & Lobe, C.G. (2002) A cre recombinase transgene with mosaic, widespread tamoxifen-inducible action. *genesis* **32(1)**, pp.8–18.

Haas, A.L., Warms, J. V., Hershko, A. & Rose, I.A. (1982) Ubiquitin-activating enzyme. Mechanism and role in protein-ubiquitin conjugation. *Journal of Biological Chemistry* **257(5)**, pp.2543–2548.

Hackney, C.M., Mahendrasingam, S., Penn, A. & Fettiplace, R. (2005) The concentrations of calcium buffering proteins in mammalian cochlear hair cells. *Journal of Neuroscience* **25(34)**, pp.7867–7875.

Hackney, C.M. & Furness, D.N. (2013) The composition and role of cross links in mechanoelectrical transduction in vertebrate sensory hair cells. *Journal of Cell Science* **126(8)**, pp.1721–1731.

Hafidi, A., Despres, G. & Romand, R. (1990) Cochlear innervation in the developing rat: An immunocytochemical study of neurofilament and spectrin proteins. *Journal of Comparative Neurology* **300(2)**, pp.153–161.

Han, C., Cui, K., Bi, X., Wang, L., Sun, M., Yang, L. & Liu, L. (2019) Association between polymorphism of the NEDD4 gene and cognitive dysfunction of schizophrenia patients in Chinese Han population. *BMC Psychiatry* **19(1)**, p.405.

Hardisty-Hughes, R.E., Parker, A. & Brown, S.D.M. (2010) A hearing and vestibular phenotyping pipeline to identify mouse mutants with hearing impairment. *Nature Protocols* **5(1)**, pp.177–190.

Harvey, K.F., Dinudom, A., Cook, D.I. & Kumar, S. (2001) The Nedd4-like Protein KIAA0439 is a Potential Regulator of the Epithelial Sodium Channel. *Journal of Biological Chemistry* **276(11)**, pp.8597–8601.

Hashida, H., Miyamoto, M., Cho, Y., Hida, Y., Kato, K., Kurokawa, T., Okushiba, S., Kondo, S., Dosaka-Akita, H. & Katoh, H. (2004) Fusion of HIV-1 Tat protein transduction domain to poly-lysine as a new DNA delivery tool. *British Journal of Cancer* **90(6)**, pp.1252–1258.

Hatstat, A.K., Pupi, M.D. & Mccafferty, D.G. (2020) Bioinformatic and computational analysis reveals the prevalence and nature of PY motif-mediated protein-protein interactions in the Nedd4 family of ubiquitin ligases. *bioRxiv*, p.2020.11.12.380584.

Heiman-Patterson, T.D., Blankenhorn, E.P., Sher, R.B., Jiang, J., Welsh, P., Dixon, M.C., Jeffrey, J.I., Wong, P., Cox, G.A. & Alexander, G.M. (2015) Genetic Background Effects on Disease Onset and Lifespan of the Mutant Dynactin p150Glued Mouse Model of Motor Neuron Disease. *PLOS ONE* **10(3)**, p.e0117848.

Henshall, T.L., Manning, J.A., Alfassy, O.S., Goel, P., Boase, N.A., Kawabe, H. & Kumar, S. (2017) Deletion of Nedd4-2 results in progressive kidney disease in mice. *Cell Death and Differentiation* **24(12)**, pp.2150–2160.

Hequembourg, S. & Liberman, M.C. (2001) Spiral ligament pathology: A major aspect of age-related cochlear degeneration in C57BL/6 mice. *JARO - Journal of the Association for Research in Otolaryngology* **2(2)**, pp.118–129.

Hibino, H., Horio, Y., Inanobe, A., Doi, K., Ito, M., Yamada, M., Gotow, T., Uchiyama, Y.,

Kawamura, M., Kubo, T. & Kurachi, Y. (1997) An ATP-dependent inwardly rectifying potassium channel, K(AB)-2 (Kir4.1), in cochlear stria vascularis of inner ear: Its specific subcellular localization and correlation with the formation of endocochlear potential. *Journal of Neuroscience* **17(12)**, pp.4711–4721.

Hibino, H. & Kurachi, Y. (2006) Molecular and physiological bases of the K+ circulation in the mammalian inner ear. *Physiology* **21(5)**, pp.336–345.

Housley, G.D., Morton-Jones, R., Vlajkovic, S.M., Telang, R.S., Paramananthasivam, V., Tadros, S.F., Wong, A.C.Y., Froud, K.E., Cederholm, J.M.E., Sivakumaran, Y., Snguanwongchai, P., Khakh, B.S., Cockayne, D.A., Thorne, P.R. & Ryan, A.F. (2013) ATP-gated ion channels mediate adaptation to elevated sound levels. *Proceedings of the National Academy of Sciences of the United States of America* **110(18)**, pp.7494–7499.

Housley, G.D. & Ashmore, J.F. (1991) Direct measurement of the action of acetylcholine on isolated outer hair cells of the guinea pig cochlea. *Proceedings of the Royal Society B: Biological Sciences* **244(1310)**, pp.161–167.

Huang, L.C., Thorne, P.R., Vlajkovic, S.M. & Housley, G.D. (2010) Differential expression of P2Y receptors in the rat cochlea during development. *Purinergic Signalling* **6(2)**, pp.231–248.

Huber, L.A. & Teis, D. (2016) Lysosomal signaling in control of degradation pathways. *Current Opinion in Cell Biology* **39**, pp.8–14.

Hudspeth, A.J. & Corey, D.P. (1977) Sensitivity, polarity, and conductance change in the response of vertebrate hair cells to controlled mechanical stimuli. *Proceedings of the National Academy of Sciences of the United States of America* **74(6)**, pp.2407–2411.

Huibregtse, J.M., Scheffner, M., Beaudenon, S. & Howley, P.M. (1995) A family of proteins structurally and functionally related to the E6-AP ubiquitin-protein ligase. *Proceedings of the National Academy of Sciences of the United States of America* **92(7)**, pp.2563–2567.

Hummler, E., Barker, P., Talbot, C., Wang, Q., Verdumo, C., Grubb, B., Gatzy, J., Burnier, M., Horisberger, J.D., Beermann, F., Boucher, R. & Rossier, B.C. (1997) A mouse model for the renal salt-wasting syndrome pseudohypoaldosteronism. *Proceedings of the National Academy of Sciences of the United States of America* **94(21)**, pp.11710–11715.

Hummler, E., Barker, P., Galzy, J., Beermann, F., Verdumo, C., Schmidt, A., Boucher, R.

& Rossier, B.C. (1996) Early death due to defective neonatal lung liquid clearance in αENaC-deficient mice. *Nature Genetics* **12(3)**, pp.325–328.

Ingham, N.J., Pearson, S. & Steel, K.P. (2011) Using the Auditory Brainstem Response (ABR) to Determine Sensitivity of Hearing in Mutant Mice. *Current Protocols in Mouse Biology* **1(2)**, pp.279–287.

Ingham, R.J., Gish, G. & Pawson, T. (2004) The Nedd4 family of E3 ubiquitin ligases: Functional diversity within a common modular architecture. *Oncogene* **23(11 REV. ISS. 1)**, pp.1972–1984.

Isgrig, K., Shteamer, J.W., Belyantseva, I.A., Drummond, M.C., Fitzgerald, T.S., Vijayakumar, S., Jones, S.M., Griffith, A.J., Friedman, T.B., Cunningham, L.L. & Chien, W.W. (2017) Gene Therapy Restores Balance and Auditory Functions in a Mouse Model of Usher Syndrome. *Molecular Therapy* **25(3)**, pp.780–791.

Iyer, A.A. & Groves, A.K. (2021) Transcription Factor Reprogramming in the Inner Ear: Turning on Cell Fate Switches to Regenerate Sensory Hair Cells. *Frontiers in Cellular Neuroscience* **15**, p.660748.

Järlebark, L.E., Housley, G.D., Raybould, N.P., Vlajkovic, S. & Thorne, P.R. (2002) ATP-gated ion channels assembled from P2X2 receptor subunits in the mouse cochlea. *NeuroReport* **13(15)**, pp.1979–1984.

Jean, P., de la Morena, D.L., Michanski, S., Tobón, L.M.J., Chakrabarti, R., Picher, M.M., Neef, J., Jung, S.Y., Gültas, M., Maxeiner, S., Neef, A., Wichmann, C., Strenzke, N., Grabner, C. & Moser, T. (2018) The synaptic ribbon is critical for sound encoding at high rates and with temporal precision. *eLife* **7**.

Jewett, K.A., Christian, C.A., Bacos, J.T., Lee, K.Y., Zhu, J. & Tsai, N.P. (2016) Feedback modulation of neural network synchrony and seizure susceptibility by Mdm2-p53-Nedd4-2 signaling. *Molecular Brain* **9(1)**, p.32.

Jiang, C., Kawabe, H. & Rotin, D. (2017) The ubiquitin ligase Nedd4L regulates the Na/K/2Cl co-transporter NKCC1/SLC12A2 in the colon. *Journal of Biological Chemistry* **292(8)**, pp.3137–3145.

Johnson, C.P. & Chapman, E.R. (2010) Otoferlin is a calcium sensor that directly regulates SNARE-mediated membrane fusion. *Journal of Cell Biology* **191(1)**, pp.187–197.

Johnson, K.R., Zheng, Q.Y. & Erway, L.C. (2000) A major gene affecting age-related hearing loss is common to at least ten inbred strains of mice. *Genomics* **70(2)**, pp.171–180.

Johnson, K.R., Zheng, Q.Y. & Noben-Trauth, K. (2006) Strain background effects and genetic modifiers of hearing in mice. *Brain Research* **1091(1)**, pp.79–88.

Johnson, S.L., Franz, C., Kuhn, S., Furness, D.N., Rüttiger, L., Münkner, S., Rivolta, M.N., Seward, E.P., Herschman, H.R., Engel, J., Knipper, M. & Marcotti, W. (2010) Synaptotagmin IV determines the linear Ca 2+ dependence of vesicle fusion at auditory ribbon synapses. *Nature Neuroscience* **13(1)**, pp.45–52.

Jones, C., Roper, V.C., Foucher, I., Qian, D., Banizs, B., Petit, C., Yoder, B.K. & Chen, P. (2008) Ciliary proteins link basal body polarization to planar cell polarity regulation. *Nature Genetics* **40(1)**, pp.69–77.

Justice, M.J., Noveroske, J.K., Weber, J.S., Zheng, B. & Bradley, A. (1999) Mouse ENU mutagenesis. *Human Molecular Genetics* **8(10)**, pp.1955–1963.

Justice, M.J., Siracusa, L.D. & Stewart, A.F. (2011) Technical approaches for mouse models of human disease. *DMM Disease Models and Mechanisms* **4(3)**, pp.305–310.

Kalinec, G.M., Webster, P., Lim, D.J. & Kalinec, F. (2003) A cochlear cell line as an in vitro system for drug ototoxicity screening. *Audiology and Neuro-Otology* **8(4)**, pp.177–189.

Kamadurai, H.B., Souphron, J., Scott, D.C., Duda, D.M., Miller, D.J., Stringer, D., Piper, R.C. & Schulman, B.A. (2009) Insights into Ubiquitin Transfer Cascades from a Structure of a UbcH5B∼Ubiquitin-HECTNEDD4L Complex. *Molecular Cell* **36(6)**, pp.1095–1102.

Kamynina, E., Debonneville, C., Hirt, R.P. & Staub, O. (2001) Liddle's syndrome: A novel mouse Nedd4 isoform regulates the activity of the epithelial Na+ channel. *Kidney International* **60(2)**, pp.466–471.

Kane, K.L., Longo-Guess, C.M., Gagnon, L.H., Ding, D., Salvi, R.J. & Johnson, K.R. (2012) Genetic background effects on age-related hearing loss associated with Cdh23 variants in mice. *Hearing Research* **283(1–2)**, pp.80–88.

Kang, S.K., Hawkins, N.A. & Kearney, J.A. (2019) C57BL/6J and C57BL/6N substrains differentially influence phenotype severity in the Scn1a+/− mouse model of Dravet syndrome. *Epilepsia Open* **4(1)**, p.164.

Kato, K., Miya, F., Hori, I., Ieda, D., Ohashi, K., Negishi, Y., Hattori, A., Okamoto, N., Kato, M., Tsunoda, T., Yamasaki, M., Kanemura, Y., Kosaki, K. & Saitoh, S. (2017) A novel missense mutation in the HECT domain of NEDD4L identified in a girl with periventricular nodular heterotopia, polymicrogyria and cleft palate. *Journal of*

Human Genetics **62(9)**, pp.861–863.

Kawabe, H., Neeb, A., Dimova, K., Young, S.M., Takeda, M., Katsurabayashi, S., Mitkovski, M., Malakhova, O.A., Zhang, D.E., Umikawa, M., Kariya, K. ichi, Goebbels, S., Nave, K.A., Rosenmund, C., Jahn, O., Rhee, J.S. & Brose, N. (2010) Regulation of Rap2A by the Ubiquitin Ligase Nedd4-1 Controls Neurite Development. *Neuron* **65(3)**, pp.358–372.

Kawashima, Y., Géléoc, G.S.G., Kurima, K., Labay, V., Lelli, A., Asai, Y., Makishima, T., Wu, D.K., Della Santina, C.C., Holt, J.R. & Griffith, A.J. (2011) Mechanotransduction in mouse inner ear hair cells requires transmembrane channel-like genes. *Journal of Clinical Investigation* **121(12)**, pp.4796–4809.

Kazmierczak, P., Sakaguchi, H., Tokita, J., Wilson-Kubalek, E.M., Milligan, R.A., Müller, U. & Kachar, B. (2007) Cadherin 23 and protocadherin 15 interact to form tip-link filaments in sensory hair cells. *Nature* **449(7158)**, pp.87–91.

Kemp, D.T. (2002) Otoacoustic emissions, their origin in cochlear function, and use. *British Medical Bulletin* **63**, pp.223–241.

Kemp, D.T. (1978) Stimulated acoustic emissions from within the human auditory system. *Journal of the Acoustical Society of America* **64(5)**, pp.1386–1391.

Kharkovets, T., Dedek, K., Maier, H., Schweizer, M., Khimich, D., Nouvian, R., Vardanyan, V., Leuwer, R., Moser, T. & Jentsch, T.J. (2006) Mice with altered KCNQ4 K+ channels implicate sensory outer hair cells in human progressive deafness. *EMBO Journal* **25(3)**, pp.642–652.

Khimich, D., Nouvtan, R., Pujol, R., Diesk, S.T., Egner, A., Gundelfinger, E.D. & Moser, T. (2005) Hair cell synaptic ribbons are essential for synchronous auditory signalling. *Nature* **434(7035)**, pp.889–894.

Kiernan, A.E., Pelling, A.L., Leung, K.K.H., Tang, A.S.P., Bell, D.M., Tease, C., Lovell-Badge, R., Steel, K.P. & Cheah, K.S.E. (2005) Sox2 is required for sensory organ development in the mammalian inner ear. *Nature* **434(7036)**, pp.1031–1035.

Kiernan, A.E., Xu, J. & Gridley, T. (2006) The Notch Ligand JAG1 Is Required for Sensory Progenitor Development in the Mammalian Inner Ear D. Beier, ed. *PLoS Genetics* **2(1)**, p.e4.

Kim, B.G., Kim, J.Y., Kim, H.N., Bok, J., Namkung, W., Choi, J.Y. & Kim, S.H. (2014) Developmental changes of ENaC expression and function in the inner ear of pendrin knock-out mice as a perspective on the development of endolymphatic hydrops. *PLoS ONE* **9(4)**, p.95730.

Kim, C.H., Kim, H.Y., Lee, H.S., Chang, S.O., Oh, S.H. & Lee, J.H. (2010) P2Y4-mediated regulation of Na+ absorption in the Reissner's membrane of the cochlea. *Journal of Neuroscience* **30(10)**, pp.3762–3769.

Kim, H.M. & Wangemann, P. (2011) Epithelial Cell Stretching and Luminal Acidification Lead to a Retarded Development of Stria Vascularis and Deafness in Mice Lacking Pendrin E. Abdelhay, ed. *PLoS ONE* **6(3)**, p.e17949.

Kim, J., Xia, A., Grillet, N., Applegate, B.E. & Oghalai, J.S. (2018) Osmotic stabilization prevents cochlear synaptopathy after blast trauma. *Proceedings of the National Academy of Sciences* **115(21)**, pp.E4853–E4860.

Kim, S.H., Kim, K.X., Raveendran, N.N., Wu, T., Pondugula, S.R. & Marcus, D.C. (2009) Regulation of ENaC-mediated sodium transport by glucocorticoids in Reissner's membrane epithelium. *American Journal of Physiology-Cell Physiology* **296(3)**, pp.C544–C557.

Kim, W.Y., Fritzsch, B., Serls, A., Bakel, L.A., Huang, E.J., Reichardt, L.F., Barth, D.S. & Lee, J.E. (2001) NeuroD-null mice are deaf due to a severe loss of the inner ear sensory neurons during development. *Development* **128(3)**, pp.417–426.

Kim, Y., Yoo, H., Hong, A., Kwon, M., Kang, S., Kim, K. & Song, Y. (2018) NEDD4L limits cAMP signaling through ubiquitination of CREB-regulated transcription coactivator 3. *The FASEB Journal* **32(7)**, pp.4053–4062.

Kimura, T., Kawabe, H., Jiang, C., Zhang, W., Xiang, Y.Y., Lu, C., Salter, M.W., Brose, N., Lu, W.Y. & Rotin, D. (2011) Deletion of the ubiquitin ligase Nedd4L in lung epithelia causes cystic fibrosis-like disease. *Proceedings of the National Academy of Sciences of the United States of America* **108(8)**, pp.3216–3221.

Kitajiri, S.I., Katsuno, T., Sasaki, H., Ito, J., Furuse, M. & Tsukita, S. (2014) Deafness in occludin-deficient mice with dislocation of tricellulin and progressive apoptosis of the hair cells. *Biology Open* **3(8)**, pp.759–766.

Kleyman, T.R. & Cragoe, E.J. (1988) Amiloride and its analogs as tools in the study of ion transport. *The Journal of Membrane Biology* **105(1)**, pp.1–21.

Kolla, L., Kelly, M.C., Mann, Z.F., Anaya-Rocha, A., Ellis, K., Lemons, A., Palermo, A.T., So, K.S., Mays, J.C., Orvis, J., Burns, J.C., Hertzano, R., Driver, E.C. & Kelley, M.W. (2020) Characterization of the development of the mouse cochlear epithelium at the single cell level. *Nature Communications* **11(1)**, pp.1–16.

Komura, Y., Tamura, R., Uwano, T., Nishijo, H. & Ono, T. (2005) Auditory thalamus integrates visual inputs into behavioral gains. *Nature Neuroscience* **8(9)**, pp.1203–

1209.

Korrapati, S., Taukulis, I., Olszewski, R., Pyle, M., Gu, S., Singh, R., Griffiths, C., Martin, D., Boger, E., Morell, R.J. & Hoa, M. (2019) Single Cell and Single Nucleus RNA-Seq Reveal Cellular Heterogeneity and Homeostatic Regulatory Networks in Adult Mouse Stria Vascularis. *Frontiers in Molecular Neuroscience* **12**.

Koumangoye, R., Bastarache, L. & Delpire, E. (2020) NKCC1: Newly Found as a Human Disease-Causing Ion Transporter. *Function* **2(1)**, p.28.

Koundakjian, E.J., Appler, J.L. & Goodrich, L. V. (2007) Auditory neurons make stereotyped wiring decisions before maturation of their targets. *Journal of Neuroscience* **27(51)**, pp.14078–14088.

Kujawa, S.G. & Liberman, M.C. (2009) Adding insult to injury: Cochlear nerve degeneration after "temporary" noise-induced hearing loss. *Journal of Neuroscience* **29(45)**, pp.14077–14085.

Kumar, S., Tomooka, Y. & Noda, M. (1992) Identification of a set of genes with developmentally down-regulated expression in the mouse brain. *Biochemical and Biophysical Research Communications*.

Kurima, K., Ebrahim, S., Pan, B., Sedlacek, M., Sengupta, P., Millis, B.A., Cui, R., Nakanishi, H., Fujikawa, T., Kawashima, Y., Choi, B.Y., Monahan, K., Holt, J.R., Griffith, A.J. & Kachar, B. (2015) TMC1 and TMC2 Localize at the Site of Mechanotransduction in Mammalian Inner Ear Hair Cell Stereocilia. *Cell Reports* **12(10)**, pp.1606–1617.

Lanford, P.J., Lan, Y., Jiang, R., Lindsell, C., Weinmaster, G., Gridley, T. & Kelley, M.W. (1999) Notch signalling pathway mediates hair cell development in mammalian cochlea. *Nature Genetics* **21(3)**, pp.289–292.

Lang, H., Jyothi, V., Smythe, N.M., Dubno, J.R., Schulte, B.A. & Schmiedt, R.A. (2010) Chronic Reduction of Endocochlear Potential Reduces Auditory Nerve Activity: Further Confirmation of an Animal Model of Metabolic Presbyacusis. *Journal of the Association for Research in Otolaryngology 2010 11:3* **11(3)**, pp.419–434.

Laos, M., Sulg, M., Herranen, A., Anttonen, T. & Pirvola, U. (2017) Indispensable role of Mdm2/p53 interaction during the embryonic and postnatal inner ear development. *Scientific Reports* **7**.

Laplantine, E., Fontan, E., Chiaravalli, J., Lopez, T., Lakisic, G., Véron, M., Agou, F. & Israël, A. (2009) NEMO specifically recognizes K63-linked poly-ubiquitin chains through a new bipartite ubiquitin-binding domain. *EMBO Journal* **28(19)**,

pp.2885–2895.

Larkins, C.E., Gonzalez Aviles, G.D., East, M.P., Kahn, R.A. & Caspary, T. (2011) Arl13b regulates ciliogenesis and the dynamic localization of Shh signaling proteins. *Molecular Biology of the Cell* **22(23)**, pp.4694–4703.

Lee, J.H. & Marcus, D.C. (2003) Endolymphatic sodium homeostasis by Reissner's membrane. *Neuroscience* **119(1)**, pp.3–8.

Lee, J.H. & Marcus, D.C. (2008) Purinergic signaling in the inner ear. *Hearing Research* **235(1–2)**, pp.1–7.

Lee, Y.S., Liu, F. & Segil, N. (2006) A morphogenetic wave of p27Kip1 transcription directs cell cycle exit during organ of Corti development. *Development* **133(15)**, pp.2817–2826.

Legan, P.K., Lukashkina, V.A., Goodyear, R.J., Kössl, M., Russell, I.J. & Richardson, G.P. (2000) A targeted deletion in α-tectorin reveals that the tectorial membrane is required for the gain and timing of cochlear feedback. *Neuron* **28(1)**, pp.273–285.

Lelli, A., Michel, V., De Monvel, J.B., Cortese, M., Bosch-Grau, M., Aghaie, A., Perfettini, I., Dupont, T., Avan, P., El-Amraoui, A. & Petit, C. (2016) Class III myosins shape the auditory hair bundles by limiting microvilli and stereocilia growth. *Journal of Cell Biology* **212(2)**, pp.231–244.

Lenzi, D. & Von Gersdorff, H. (2001) Structure suggests function: The case for synaptic ribbons as exocytotic nanomachines. *BioEssays* **23(9)**, pp.831–840.

Lewis, M.A., Nolan, L.S., Cadge, B.A., Matthews, L.J., Schulte, B.A., Dubno, J.R., Steel, K.P. & Dawson, S.J. (2018) Whole exome sequencing in adult-onset hearing loss reveals a high load of predicted pathogenic variants in known deafness-associated genes and identifies new candidate genes. *BMC Medical Genomics* **11(1)**, p.77.

Li, C., Li, X., Bi, Z., Sugino, K., Wang, G., Zhu, T. & Liu, Z. (2020) Comprehensive transcriptome analysis of cochlear spiral ganglion neurons at multiple ages. *eLife* **9**.

Li, J.J., Jr, R.J.F., Diao, S., Xue, B., Bahouth, S.W. & Liao, F.F. (2015) Nedd4 haploinsufficient mice display moderate insulin resistance, enhanced lipolysis, and protection against high-fat diet-induced obesity. *Endocrinology* **156(4)**, pp.1283–1291.

Li, L., Zheng, P. & Dean, J. (2010) Maternal control of early mouse development. *Development (Cambridge, England)* **137(6)**, p.859.

Li, N., Guo, Y., Zhou, L., Wang, H., Yao, X., Luo, W. & Chang, J. (2010) Genetic variation and association analyses of NEDD4 gene in Kazak Chinese patients with hypertension. *International journal of molecular epidemiology and genetics* **1(3)**, pp.226–35.

Li, X., Zhou, F., Marcus, D.C. & Wangemann, P. (2013) Endolymphatic Na+ and K+ Concentrations during Cochlear Growth and Enlargement in Mice Lacking Slc26a4/pendrin B. Sokolowski, ed. *PLoS ONE* **8(5)**, p.e65977.

Li, Y., Liu, H., Zhao, X. & He, D.Z. (2020) Endolymphatic Potential Measured From Developing and Adult Mouse Inner Ear. *Frontiers in Cellular Neuroscience* **14**, p.584928.

Liang, Y., Wang, A., Belyantseva, I.A., Anderson, D.W., Probst, F.J., Barber, T.D., Miller, W., Touchman, J.W., Jin, L., Sullivan, S.L., Sellers, J.R., Camper, S.A., Lloyd, R. V., Kachar, B., Friedman, T.B. & Fridell, R.A. (1999) Characterization of the human and mouse unconventional myosin XV genes responsible for hereditary deafness DFNB3 and shaker 2. *Genomics* **61(3)**, pp.243–258.

Liberman, L.D. & Liberman, M.C. (2016) Postnatal maturation of auditory-nerve heterogeneity, as seen in spatial gradients of synapse morphology in the inner hair cell area. *Hearing Research* **339**, pp.12–22.

Liberman, L.D., Wang, H. & Liberman, M.C. (2011) Opposing Gradients of Ribbon Size and AMPA Receptor Expression Underlie Sensitivity Differences among Cochlear-Nerve/Hair-Cell Synapses. *The Journal of Neuroscience* **31(3)**, p.801.

Liberman, M.C. (1978) Auditory-nerve response from cats raised in a low-noise chamber. *Journal of the Acoustical Society of America* **63(2)**, pp.442–455.

Liberman, M.C. (1980) Morphological differences among radial afferent fibers in the cat cochlea: An electron-microscopic study of serial sections. *Hearing Research* **3(1)**, pp.45–63.

Liberman, M.C., Gao, J., He, D.Z.Z., Wu, X., Jia, S. & Zuo, J. (2002) Prestin is required for electromotility of the outer hair cell and for the cochlear amplifier. *Nature* **419(6904)**, pp.300–304.

Liberman, M.C. (1982) Single-neuron labeling in the cat auditory nerve. *Science* **216(4551)**, pp.1239–1241.

Lim, D.J. (1970) Morphology and function of the interdental cell —An ultrastructural observation. *The Journal of Laryngology & Otology* **84(12)**, pp.1241–1256.

Lim, D.J. & Anniko, M. (1985) Developmental morphology of the mouse inner ear: A

scanning electron microscopic observation. *Acta Oto-Laryngologica* **99(S422)**, pp.5–69.

Lin, H.H., Zentner, M.D., Ho, H.L.L., Kim, K.J. & Ann, D.K. (1999) The gene expression of the amiloride-sensitive epithelial sodium channel α-subunit is regulated by antagonistic effects between glucocorticoid hormone and Ras pathways in salivary epithelial cells. *Journal of Biological Chemistry* **274(31)**, pp.21544–21554.

Lin, Q., Jo, D., Gebre-Amlak, K.D. & Ruley, H.E. (2004) Enhanced cell-permeant Cre protein for site-specific recombination in cultured cells. *BMC Biotechnology* **4**, p.25.

Liu, C., Glowatzki, E. & Fuchs, P.A. (2015) Unmyelinated type II afferent neurons report cochlear damage. *Proceedings of the National Academy of Sciences of the United States of America* **112(47)**, pp.14723–14727.

Liu, P., Gan, W., Su, S., Hauenstein, A. V., Fu, T.M., Brasher, B., Schwerdtfeger, C., Liang, A.C., Xu, M. & Wei, W. (2018) K63-linked polyubiquitin chains bind to DNA to facilitate DNA damage repair. *Science Signaling* **11(533)**, p.8133.

Liu, Y., Oppenheim, R.W., Sugiura, Y. & Lin, W. (2009) Abnormal development of the neuromuscular junction in Nedd4-deficient mice. *Developmental Biology* **330(1)**, pp.153–166.

Liu, Y., Beyer, A. & Aebersold, R. (2016) On the Dependency of Cellular Protein Levels on mRNA Abundance. *Cell* **165(3)**, pp.535–550.

Lowe, A.S. & Walton, J.P. (2015) Alterations in Peripheral and Central Components of the Auditory Brainstem Response: A Neural Assay of Tinnitus. *PLOS ONE* **10(2)**, p.e0117228.

Lukashkin, A.N., Legan, P.K., Weddell, T.D., Lukashkina, V.A., Goodyear, R.J., Welstead, L.J., Petit, C., Russell, I.J. & Richardson, G.P. (2012) A mouse model for human deafness DFNB22 reveals that hearing impairment is due to a loss of inner hair cell stimulation. *Proceedings of the National Academy of Sciences of the United States of America* **109(47)**, pp.19351–19356.

Luo, F., Wang, Y., Wang, X., Sun, K., Zhou, X. & Hui, R. (2009) A functional variant of NEDD4L is associated with hypertension, antihypertensive response, and orthostatic hypotension. *Hypertension (Dallas, Tex. : 1979)* **54(4)**, pp.796–801.

Ma, Q., Chen, Z., Barrantes, I.D.B., De La Pompa, J.L. & Anderson, D.J. (1998) neurogenin1 is essential for the determination of neuronal precursors for proximal cranial sensory ganglia. *Neuron* **20(3)**, pp.469–482.

Macnamara, E.F., Koehler, A.E., D'Souza, P., Estwick, T., Lee, P., Vezina, G., Fauni, H., Braddock, S.R., Torti, E., Holt, J.M., Sharma, P., Malicdan, M.C. V. & Tifft, C.J. (2019) Kilquist syndrome: A novel syndromic hearing loss disorder caused by homozygous deletion of *SLC12A2*. *Human Mutation* **40(5)**, pp.532–538.

Maeda, R., Kindt, K.S., Mo, W., Morgan, C.P., Erickson, T., Zhao, H., Clemens-Grisham, R., Barr-Gillespie, P.G. & Nicolson, T. (2014) Tip-link protein protocadherin 15 interacts with transmembrane channel-like proteins TMC1 and TMC2. *Proceedings of the National Academy of Sciences of the United States of America* **111(35)**, pp.12907–12912.

Magupalli, V.G., Schwarz, K., Alpadi, K., Natarajan, S., Seigel, G.M. & Schmitz, F. (2008) Multiple RIBEYE-RIBEYE interactions create a dynamic scaffold for the formation of synaptic ribbons. *Journal of Neuroscience* **28(32)**, pp.7954–7967.

Maison, S., Liberman, L.D. & Liberman, M.C. (2016) Type II Cochlear Ganglion Neurons Do Not Drive the Olivocochlear Reflex: Re-Examination of the Cochlear Phenotype in Peripherin Knock-Out Mice. *eNeuro* **3(4)**.

Maison, S.F., Liu, X.P., Eatock, R.A., Sibley, D.R., Grandy, D.K. & Charles Liberman, M. (2012) Dopaminergic signaling in the cochlea: Receptor expression patterns and deletion phenotypes. *Journal of Neuroscience* **32(1)**, pp.344–355.

Maison, S.F., Luebke, A.E., Liberman, M.C. & Zuo, J. (2002) Efferent protection from acoustic injury is mediated via α9 nicotinic acetylcholine receptors on outer hair cells. *Journal of Neuroscience* **22(24)**, pp.10838–10846.

Maison, S.F., Rosahl, T.W., Homanics, G.E. & Liberman, M.C. (2006) Functional role of GABAergic innervation of the cochlea: Phenotypic analysis of mice lacking GABAA receptor subunits α1, α2, α5, β6, β2, β3, or δ. *Journal of Neuroscience* **26(40)**, pp.10315–10326.

Maison, S.F., Liu, X.P., Vetter, D.E., Eatock, R.A., Nathanson, N.M., Wess, J. & Liberman, M.C. (2010) Muscarinic signaling in the cochlea: Presynaptic and postsynaptic effects on efferent feedback and afferent excitability. *Journal of Neuroscience* **30(19)**, pp.6751–6762.

Mammano, F., Frolenkov, G.I., Lagostena, L., Belyantseva, I.A., Kurc, M., Dodane, V., Colavita, A. & Kachar, B. (1999) ATP-Induced Ca2+ Release in Cochlear Outer Hair Cells: Localization of an Inositol Triphosphate-Gated Ca2+ Store to the Base of the Sensory Hair Bundle. *Journal of Neuroscience* **19(16)**, pp.6918–6929.

Manning, J.A. & Kumar, S. (2018) Physiological Functions of Nedd4-2: Lessons from

Knockout Mouse Models. *Trends in Biochemical Sciences* **43(8)**, pp.635–647.

Marcus, D.C., Wu, T., Wangemann, P. & Kofuji, P. (2002) KCNJ10 (kir4.1) potassium channel knockout abolishes endocochlear potential. *American Journal of Physiology - Cell Physiology* **282(2 51-2)**.

Martin, G.K., Vazquez, A.E., Jimenez, A.M., Stagner, B.B., Howard, M.A. & Lonsbury-Martin, B.L. (2007) Comparison of distortion product otoacoustic emissions in 28 inbred strains of mice. *Hearing Research* **234(1–2)**, pp.59–72.

Martin, G.K., Stagner, B.B. & Lonsbury-Martin, B.L. (2006) Assessment of Cochlear Function in Mice: Distortion-Product Otoacoustic Emissions. *Current Protocols in Neuroscience* **34(1)**, pp.8.21C.1-8.21C.18.

Martinez-Monedero, R., Liu, C., Weisz, C., Vyas, P., Fuchs, P.A. & Glowatzki, E. (2016) GluA2-containing AMPA receptors distinguish ribbon-associated from ribbonless afferent contacts on rat cochlear hair cells. *eNeuro* **3(2)**, pp.11080–11085.

Masterton, R.B. (1992) Role of the central auditory system in hearing: the new direction. *Trends in Neurosciences* **15(8)**, pp.280–285.

Matei, V., Pauley, S., Kaing, S., Rowitch, D., Beisel, K.W., Morris, K., Feng, F., Jones, K., Lee, J. & Fritzsch, B. (2005) Smaller inner ear sensory epithelia in Neurog1 null mice are related to earlier hair cell cycle exit. *Developmental Dynamics* **234(3)**, pp.633–650.

Matsubara, A., Laake, J.H., Davanger, S., Usami, S.I. & Ottersen, O.P. (1996) Organization of AMPA receptor subunits at a glutamate synapse: A quantitative immunogold analysis of hair cell synapses in the rat organ of corti. *Journal of Neuroscience* **16(14)**, pp.4457–4467.

Matsuoka, T., Ahlberg, P.E., Kessaris, N., Iannarelli, R., Dennehy, U., Richardson, W.D., McMahon, A.P. & Koentges, G. (2005) Neural crest origins of the neck and shoulder. *Nature* **436(7049)**, pp.347–355.

Mcdonald, F.J., Yang, B., Hrstka, R.F., Drummond, H.A., Tarr, D.E., Mccray, P.B., Stokes, J.B., Welsh, M.J. & Williamson, R.A. (1999) Disruption of the β subunit of the epithelial Na+ channel in mice: Hyperkalemia and neonatal death associated with a pseudohypoaldosteronism phenotype. *Proceedings of the National Academy of Sciences of the United States of America* **96(4)**, pp.1727–1731.

McDonald, F.J., Western, A.H., McNeil, J.D., Thomas, B.C., Olson, D.R. & Snyder, P.M. (2002) Ubiquitin-protein ligase WWP2 binds to and downregulates the epithelial Na+ channel. *American Journal of Physiology - Renal Physiology* **283(3 52-3)**,

pp.431–436.

McNeill, A., Iovino, E., Mansard, L., Vache, C., Baux, D., Bedoukian, E., Cox, H., Dean, J., Goudie, D., Kumar, A., Newbury-Ecob, R., Fallerini, C., Renieri, A., Lopergolo, D., Mari, F., Blanchet, C., Willems, M., Roux, A.F., Pippucci, T. & Delpire, E. (2020) SLC12A2 variants cause a neurodevelopmental disorder or cochleovestibular defect. *Brain* **143(8)**, pp.2380–2387.

Mekada, K., Abe, K., Murakami, A., Nakamura, S., Nakata, H., Moriwaki, K., Obata, Y. & Yoshiki, A. (2009) Genetic differences among C57BL/6 substrains. *Experimental animals* **58(2)**, pp.141–149.

Meyer, A.C., Frank, T., Khimich, D., Hoch, G., Riedel, D., Chapochnikov, N.M., Yarin, Y.M., Harke, B., Hell, S.W., Egner, A. & Moser, T. (2009) Tuning of synapse number, structure and function in the cochlea. *Nature Neuroscience* **12(4)**, pp.444–453.

Mhatre, A.N., Jero, J., Chiappini, I., Bolasco, G., Barbara, M. & Lalwani, A.K. (2002) Aquaporin-2 expression in the mammalian cochlea and investigation of its role in Meniere's disease. In *Hearing Research*. Elsevier, pp. 59–69.

Mianné, J., Chessum, L., Kumar, S., Aguilar, C., Codner, G., Hutchison, M., Parker, A., Mallon, A.M., Wells, S., Simon, M.M., Teboul, L., Brown, S.D.M. & Bowl, M.R. (2016) Correction of the auditory phenotype in C57BL/6N mice via CRISPR/Cas9-mediated homology directed repair. *Genome Medicine* **8(1)**, p.16.

Michalski, N., Goutman, J.D., Auclair, S.M., de Monvel, J.B., Tertrais, M., Emptoz, A., Parrin, A., Nouaille, S., Guillon, M., Sachse, M., Ciric, D., Bahloul, A., Hardelin, J.P., Sutton, R.B., Avan, P., Krishnakumar, S.S., Rothman, J.E., Dulon, D., Safieddine, S. & Petit, C. (2017) Otoferlin acts as a Ca2+ sensor for vesicle fusion and vesicle pool replenishment at auditory hair cell ribbon synapses. *eLife* **6**.

Mills, D.M. & Schmiedt, R.A. (2004) Metabolic Presbycusis: Differential Changes in Auditory Brainstem and Otoacoustic Emission Responses with Chronic Furosemide Application in the Gerbil. *JARO: Journal of the Association for Research in Otolaryngology* **5(1)**, p.1.

Minegishi, S., Ishigami, T., Kino, T., Chen, L., Nakashima-Sasaki, R., Araki, N., Yatsu, K., Fujita, M. & Umemura, S. (2016) An isoform of Nedd4-2 is critically involved in the renal adaptation to high salt intake in mice. *Scientific Reports* **6**.

Minsky, N., Shema, E., Field, Y., Schuster, M., Segal, E. & Oren, M. (2008) Monoubiquitinated H2B is associated with the transcribed region of highly

expressed genes in human cells. *Nature Cell Biology* **10(4)**, pp.483–488.

Mizuta, K., Adachi, M. & Iwasa, K.H. (1997) Ultrastructural localization of the Na-K-Cl cotransporter in the lateral wall of the rabbit cochlear duct. *Hearing Research* **106(1–2)**, pp.154–162.

Mollaaghababa, R. & Pavan, W.J. (2003) The importance of having your SOX on: role of SOX10 † in the development of neural crest-derived melanocytes and glia. *Oncogene 2003 22:20* **22(20)**, pp.3024–3034.

Moore, D.R. (1988) Auditory brainstem of the ferret: Sources of projections to the inferior colliculus. *The Journal of Comparative Neurology* **269(3)**, pp.342–354.

Moreno-García, M.E., Sommer, K., Rincon-Arano, H., Brault, M., Ninomiya-Tsuji, J., Matesic, L.E. & Rawlings, D.J. (2013) Kinase-Independent Feedback of the TAK1/TAB1 Complex on BCL10 Turnover and NF-κB Activation. *Molecular and Cellular Biology* **33(6)**, pp.1149–1163.

Moreno-Pelayo, M.Á., Goodyear, R.J., Mencía, A., Modamio-Høybjør, S., Legan, P.K., Olavarrieta, L., Moreno, F. & Richardson, G.P. (2008) Characterization of a spontaneous, recessive, missense mutation arising in the Tecta gene. *JARO - Journal of the Association for Research in Otolaryngology* **9(2)**, pp.202–214.

Morsli, H., Choo, D., Ryan, A., Johnson, R. & Wu, D.K. (1998) Development of the mouse inner ear and origin of its sensory organs. *Journal of Neuroscience* **18(9)**, pp.3327–3335.

Moser, T. & Beutner, D. (2000) Kinetics of exocytosis and endocytosis at the cochlear inner hair cell afferent synapse of the mouse. *Proceedings of the National Academy of Sciences of the United States of America* **97(2)**, pp.883–888.

Mouse Genome Sequencing Consortium, Waterston, R.H., Lindblad-Toh, K., Birney, E., Rogers, J., Lander, E.S., et al. (2002) Initial sequencing and comparative analysis of the mouse genome. *Nature* **420(6915)**, pp.520–562.

Munoz, D.J.B., Kendrick, I.S., Rassam, M. & Thorne, P.R. (2001) Vesicular storage of adenosine triphosphate in the guinea-pig cochlear lateral wall and concentrations of ATP in the endolymph during sound exposure and hypoxia. *Acta Oto-Laryngologica* **121(1)**, pp.10–15.

Murata, J., Tokunaga, A., Okano, H. & Kubo, T. (2006) Mapping of notch activation during cochlear development in mice: Implications for determination of prosensory domain and cell fate diversification. *The Journal of Comparative Neurology* **497(3)**, pp.502–518.

Musiek, F.E., Kibbe, K., Rackliffe, L. & Weider, D.J. (1984) The auditory brain stem response I–V amplitude ratio in normal, cochlear, and retrocochlear ears. *Ear and Hearing* **5(1)**, pp.52–55.

Mutai, H., Wasano, K., Momozawa, Y., Kamatani, Y., Miya, F., Masuda, S., Morimoto, N., Nara, K., Takahashi, S., Tsunoda, T., Homma, K., Kubo, M. & Matsunaga, T. (2020) Variants encoding a restricted carboxy-terminal domain of SLC12A2 cause hereditary hearing loss in humans. *PLoS Genetics* **16(4)**.

Nakagawa, T., Akaike, N., Kimitsuki, T., Komune, S. & Arima, T. (1990) ATP-induced current in isolated outer hair cells of guinea pig cochlea. *Journal of Neurophysiology* **63(5)**, pp.1068–1074.

Nakajima, H.H., Dong, W., Olson, E.S., Merchant, S.N., Ravicz, M.E. & Rosowski, J.J. (2009) Differential intracochlear sound pressure measurements in normal human temporal bones. *JARO - Journal of the Association for Research in Otolaryngology* **10(1)**, pp.23–36.

Nakano, Y., Kim, S.H., Kim, H.M., Sanneman, J.D., Zhang, Y., Smith, R.J.H., Marcus, D.C., Wangemann, P., Nessler, R.A. & Bánfi, B. (2009) A claudin-9-based ion permeability barrier is essential for hearing. *PLoS Genetics* **5(8)**, p.1000610.

Nakashima, M., Chung, S., Takahashi, A., Kamatani, N., Kawaguchi, T., Tsunoda, T., Hosono, N., Kubo, M., Nakamura, Y. & Zembutsu, H. (2010) A genome-wide association study identifies four susceptibility loci for keloid in the japanese population. *Nature Genetics* **42(9)**, pp.768–772.

Nalefski, E.A. & Falke, J.J. (1996) The C2 domain calcium-binding motif: Structural and functional diversity. *Protein Science* **5(12)**, pp.2375–2390.

Narimatsu, M., Bose, R., Pye, M., Zhang, L., Miller, B., Ching, P., Sakuma, R., Luga, V., Roncari, L., Attisano, L. & Wrana, J.L. (2009) Regulation of Planar Cell Polarity by Smurf Ubiquitin Ligases. *Cell* **137(2)**, pp.295–307.

Nelson, R.F., Glenn, K.A., Zhang, Y., Wen, H., Knutson, T., Gouvion, C.M., Robinson, B.K., Zhou, Z., Yang, B., Smith, R.J.H. & Paulson, H.L. (2007) Selective cochlear degeneration in mice lacking the F-box protein, Fbx2, a glycoprotein-specific ubiquitin ligase subunit. *Journal of Neuroscience* **27(19)**, pp.5163–5171.

Neyroud, N., Tesson, F., Denjoy, I., Leibovici, M., Donger, C., Barhanin, J., Fauré, S., Gary, F., Coumel, P., Petit, C., Schwartz, K. & Guicheney, P. (1997) A novel mutation in the potassium channel gene KVLQT1 causes the Jervell and Lange-Nielsen cardioauditory syndrome. *Nature Genetics* **15(2)**, pp.186–189.

Niedzielski, A.S. & Wenthold, R.J. (1995) Expression of AMPA, kainate, and NMDA receptor subunits in cochlear and vestibular ganglia. *Journal of Neuroscience* **15(3 II)**, pp.2338–2353.

Nin, F., Hibino, H., Doi, K., Suzuki, T., Hisa, Y. & Kurachi, Y. (2008) The endocochlear potential depends on two K+ diffusion potentials and an electrical barrier in the stria vascularis of the inner ear. *Proceedings of the National Academy of Sciences of the United States of America* **105(5)**, pp.1751–1756.

Noben-Trauth, K., Zheng, Q.Y. & Johnson, K.R. (2003) Association of cadherin 23 with polygenic inheritance and genetic modification of sensorineural hearing loss. *Nature Genetics* **35(1)**, pp.21–23.

Nordeen, K.W., Killackey, H.P. & Kitzes, L.M. (1983) Ascending auditory projections to the inferior colliculus in the adult gerbil, Meriones unguiculatus. *Journal of Comparative Neurology* **214(2)**, pp.131–143.

Noreña, A.J. (2015) Revisiting the Cochlear and Central Mechanisms of Tinnitus and Therapeutic Approaches. *Audiology and Neurotology* **20(Suppl. 1)**, pp.53–59.

Nouvian, R., Neef, J., Bulankina, A. V., Reisinger, E., Pangršié, T., Frank, T., Sikorra, S., Brose, N., Binz, T. & Moser, T. (2011) Exocytosis at the hair cell ribbon synapse apparently operates without neuronal SNARE proteins. *Nature Neuroscience* **14(4)**, pp.411–413.

O'Meara, R.W., Michalski, J.P., Anderson, C., Bhanot, K., Rippstein, P. & Kothary, R. (2013) Integrin-linked kinase regulates process extension in oligodendrocytes via control of actin cytoskeletal dynamics. *Journal of Neuroscience* **33(23)**, pp.9781–9793.

Ohlemiller, K.K., Jones, S.M. & Johnson, K.R. (2016) Application of Mouse Models to Research in Hearing and Balance. *Journal of the Association for Research in Otolaryngology* **17(6)**, pp.493–523.

Ohyama, T., Basch, M.L., Mishina, Y., Lyons, K.M., Segil, N. & Groves, A.K. (2010) BMP signaling is necessary for patterning the sensory and nonsensory regions of the developing mammalian cochlea. *Journal of Neuroscience* **30(45)**, pp.15044–15051.

Oliver, D., Klöcker, N., Schuck, J., Baukrowitz, T., Ruppersberg, J.P. & Fakler, B. (2000) Gating of Ca2+-activated K+ channels controls fast inhibitory synaptic transmission at auditory outer hair cells. *Neuron* **26(3)**, pp.595–601.

Olsen, S.K. & Lima, C.D. (2013) Structure of a Ubiquitin E1-E2 Complex: Insights to E1-

E2 Thioester Transfer. *Molecular Cell* **49(5)**, pp.884–896.

Ono, K., Kita, T., Sato, S., O'Neill, P., Mak, S.S., Paschaki, M., Ito, M., Gotoh, N., Kawakami, K., Sasai, Y. & Ladher, R.K. (2014) FGFR1-Frs2/3 Signalling Maintains Sensory Progenitors during Inner Ear Hair Cell Formation. *PLoS Genetics* **10(1)**, p.1004118.

Orvis, J., Gottfried, B., Kancherla, J., Adkins, R.S., Song, Y., Dror, A.A., Olley, D., Rose, K., Chrysostomou, E., Kelly, M.C., Milon, B., Matern, M.S., Azaiez, H., Herb, B., Colantuoni, C., Carter, R.L., Ament, S.A., Kelley, M.W., White, O., Bravo, H.C., Mahurkar, A. & Hertzano, R. (2020) gEAR: gene Expression Analysis Resource portal for community-driven, multi-omic data exploration. *bioRxiv*.

Palma, F. Di, Holme, R.H., Bryda, E.C., Belyantseva, I.A., Pellegrino, R., Kachar, B., Steel, K.P. & Noben-Trauth, K. (2001) Mutations in Cdh23, encoding a new type of cadherin, cause stereocilia disorganization in waltzer, the mouse model for Usher syndrome type 1D. *Nature Genetics* **27(1)**, pp.103–107.

Pan, B., Askew, C., Galvin, A., Heman-Ackah, S., Asai, Y., Indzhykulian, A.A., Jodelka, F.M., Hastings, M.L., Lentz, J.J., Vandenberghe, L.H., Holt, J.R. & Géleóc, G.S. (2017) Gene therapy restores auditory and vestibular function in a mouse model of Usher syndrome type 1c. *Nature Biotechnology* **35(3)**, pp.264–272.

Pan, N., Jahan, I., Kersigo, J., Kopecky, B., Santi, P., Johnson, S., Schmitz, H. & Fritzsch, B. (2011) Conditional deletion of Atoh1 using Pax2-Cre results in viable mice without differentiated cochlear hair cells that have lost most of the organ of Corti. *Hearing Research* **275(1–2)**, pp.66–80.

Pangrsic, T., Gabrielaitis, M., Michanski, S., Schwaller, B., Wolf, F., Strenzke, N. & Moser, T. (2015) EF-hand protein Ca2+ buffers regulate Ca2+ influx and exocytosis in sensory hair cells. *Proceedings of the National Academy of Sciences of the United States of America* **112(9)**, pp.E1028–E1037.

Pangšrič, T., Lasarow, L., Reuter, K., Takago, H., Schwander, M., Riedel, D., Frank, T., Tarantino, L.M., Bailey, J.S., Strenzke, N., Brose, N., Müller, U., Reisinger, E. & Moser, T. (2010) Hearing requires otoferlin-dependent efficient replenishment of synaptic vesicles in hair cells. *Nature Neuroscience* **13(7)**, pp.869–876.

Peng, A.W., Belyantseva, I.A., Hsu, P.D., Friedman, T.B. & Heller, S. (2009) Twinfilin 2 regulates actin filament lengths in cochlear stereocilia. *Journal of Neuroscience* **29(48)**, pp.15083–15088.

Peng, B.G., Li, Q.X., Ren, T.Y., Ahmad, S., Chen, S.P., Chen, P. & Lin, X. (2004) Group I

metabotropic glutamate receptors in spiral ganglion neurons contribute to excitatory neurotransmissions in the cochlea. *Neuroscience* **123(1)**, pp.221–230.

Pepermans, E., Michel, V., Goodyear, R., Bonnet, C., Abdi, S., Dupont, T., Gherbi, S., Holder, M., Makrelouf, M., Hardelin, J., Marlin, S., Zenati, A., Richardson, G., Avan, P., Bahloul, A. & Petit, C. (2014) The CD 2 isoform of protocadherin-15 is an essential component of the tip-link complex in mature auditory hair cells . *EMBO Molecular Medicine* **6(7)**, pp.984–992.

Peppi, M., Landa, M. & Sewell, W.F. (2012) Cochlear kainate receptors. *JARO - Journal of the Association for Research in Otolaryngology* **13(2)**, pp.199–208.

Percival, C.J., Marangoni, P., Tapaltsyan, V., Klein, O. & Hallgrímsson, B. (2017) The Interaction of Genetic Background and Mutational Effects in Regulation of Mouse Craniofacial Shape. *G3: Genes|Genomes|Genetics* **7(5)**, p.1439.

Perkins, R.E. & Morest, D.K. (1975) A study of cochlear innervation patterns in cats and rats with the Golgi method and Nomarski optics. *The Journal of Comparative Neurology* **163(2)**, pp.129–158.

Persaud, A., Alberts, P., Amsen, E.M., Xiong, X., Wasmuth, J., Saadon, Z., Fladd, C., Parkinson, J. & Rotin, D. (2009) Comparison of substrate specificity of the ubiquitin ligases Nedd4 and Nedd4-2 using proteome arrays. *Molecular Systems Biology* **5**.

Petitpré, C., Wu, H., Sharma, A., Tokarska, A., Fontanet, P., Wang, Y., Helmbacher, F., Yackle, K., Silberberg, G., Hadjab, S. & Lallemend, F. (2018) Neuronal heterogeneity and stereotyped connectivity in the auditory afferent system. *Nature Communications* **9(1)**, pp.1–13.

Pettitt, S.J., Liang, Q., Rairdan, X.Y., Moran, J.L., Prosser, H.M., Beier, D.R., Lloyd, K.C., Bradley, A. & Skarnes, W.C. (2009) Agouti C57BL/6N embryonic stem cells for mouse genetic resources. *Nature Methods* **6(7)**, pp.493–495.

Piazza, V., Ciubotaru, C.D., Gale, J.E. & Mammano, F. (2007) Purinergic signalling and intercellular Ca2+ wave propagation in the organ of Corti. *Cell Calcium* **41(1)**, pp.77–86.

Pickart, C.M., Kasperek, E.M., Beal, R. & Kim, A. (1994) Substrate properties of site-specific mutant ubiquitin protein (G76a) reveal unexpected mechanistic features of ubiquitin-activating enzyme (E1). *Journal of Biological Chemistry* **269(10)**, pp.7115–7123.

Pirvola, U., Ylikoski, J., Trokovic, R., Hébert, J.M., McConnell, S.K. & Partanen, J. (2002)

FGFR1 is required for the development of the auditory sensory epithelium. *Neuron* **35(4)**, pp.671–680.

Potter, P.K., Bowl, M.R., Jeyarajan, P., Wisby, L., Blease, A., Brown, S.D.M., et al. (2016) Novel gene function revealed by mouse mutagenesis screens for models of age-related disease. *Nature Communications* **7(1)**, pp.1–13.

Prieto, J.J., Rueda, J. & Merchan, J.A. (1990) Two different secretion mechanisms in the inner ear's interdental cells. *Hearing Research* **45(1–2)**, pp.51–61.

Pruneda, J.N., Littlefield, P.J., Soss, S.E., Nordquist, K.A., Chazin, W.J., Brzovic, P.S. & Klevit, R.E. (2012) Structure of an E3:E2∼Ub Complex Reveals an Allosteric Mechanism Shared among RING/U-box Ligases. *Molecular Cell* **47(6)**, pp.933–942.

Puel, J.L. (1995) Chemical synaptic transmission in the cochlea. *Progress in Neurobiology* **47(6)**.

Raikwar, N.S., Vandewalle, A. & Thomas, C.P. (2010) Nedd4–2 interacts with occludin to inhibit tight junction formation and enhance paracellular conductance in collecting duct epithelia. *American Journal of Physiology-Renal Physiology* **299(2)**, pp.F436–F444.

Rajan, R. & Johnstone, B.M. (1988) Binaural acoustic stimulation exercises protective effects at the cochlea that mimic the effects of electrical stimulation of an auditory efferent pathway. *Brain Research* **459(2)**, pp.241–255.

Rauschecker, J.P. (2012) Ventral and dorsal streams in the evolution of speech and language. *Frontiers in Evolutionary Neuroscience* **4(MAY)**, p.7.

Regus-Leidig, H., Ott, C., Löhner, M., Atorf, J., Fuchs, M., Sedmak, T., Kremers, J., Fejtová, A., Gundelfinger, E.D. & Brandstätter, J.H. (2013) Identification and Immunocytochemical Characterization of Piccolino, a Novel Piccolo Splice Variant Selectively Expressed at Sensory Ribbon Synapses of the Eye and Ear K. W. Koch, ed. *PLoS ONE* **8(8)**, p.e70373.

Ren, Y., Landegger, L.D. & Stankovic, K.M. (2019) Gene therapy for human sensorineural hearing loss. *Frontiers in Cellular Neuroscience* **13**, p.323.

Riazuddin, Saima, Ahmed, Z.M., Fanning, A.S., Lagziel, A., Kitajiri, S.I., Ramzan, K., Khan, S.N., Chattaraj, P., Friedman, P.L., Anderson, J.M., Belyantseva, I.A., Forge, A., Riazuddin, Sheikh & Friedman, T.B. (2006) Tricellulin is a tight-junction protein necessary for hearing. *American Journal of Human Genetics* **79(6)**, pp.1040–1051.

Richard, T.J.C., Herzog, L.K., Vornberger, J., Rahmanto, A.S., Sangfelt, O., Salomons, F.A. & Dantuma, N.P. (2020) K63-linked ubiquitylation induces global sequestration of

mitochondria. *Scientific Reports* **10(1)**, pp.1–12.

Rickheit, G., Maier, H., Strenzke, N., Andreescu, C.E., De Zeeuw, C.I., Muenscher, A., Zdebik, A.A. & Jentsch, T.J. (2008) Endocochlear potential depends on Cl- channels: Mechanism underlying deafness in Bartter syndrome IV. *EMBO Journal* **27(21)**, pp.2907–2917.

Rivas, A. & Francis, H.W. (2005) Inner ear abnormalities in a Kcnq1 (Kvlqt1) knockout mouse: A model of Jervell and Lange-Nielsen syndrome. *Otology and Neurotology* **26(3)**, pp.415–424.

Rivolta, M.N. & Holley, M.C. (2002) Cell lines in inner ear research. *Journal of Neurobiology* **53(2)**, pp.306–318.

Robertson, D. (1984) Horseradish peroxidase injection of physiologically characterized afferent and efferent neurones in the guinea pig spiral ganglion. *Hearing Research* **15(2)**, pp.113–121.

Ronzaud, C., Loffing-Cueni, D., Hausel, P., Debonneville, A., Malsure, S.R., Fowler-Jaeger, N., Boase, N.A., Perrier, R., Maillard, M., Yang, B., Stokes, J.B., Koesters, R., Kumar, S., Hummler, E., Loffing, J. & Staub, O. (2013) Renal tubular NEDD4-2 defciency causes NCC-mediated salt-dependent hypertension. *Journal of Clinical Investigation* **123(2)**, pp.657–665.

Rosenthal, N. & Brown, S. (2007) The mouse ascending: Perspectives for human-disease models. *Nature Cell Biology* **9(9)**, pp.993–999.

Roux, I., Safieddine, S., Nouvian, R., Grati, M., Simmler, M.C., Bahloul, A., Perfettini, I., Le Gall, M., Rostaing, P., Hamard, G., Triller, A., Avan, P., Moser, T. & Petit, C. (2006) Otoferlin, Defective in a Human Deafness Form, Is Essential for Exocytosis at the Auditory Ribbon Synapse. *Cell* **127(2)**, pp.277–289.

Rowe, I., Chiaravalli, M., Mannella, V., Ulisse, V., Quilici, G., Pema, M., Song, X.W., Xu, H., Mari, S., Qian, F., Pei, Y., Musco, G. & Boletta, A. (2013) Defective glucose metabolism in polycystic kidney disease identifies a new therapeutic strategy. *Nature Medicine* **19(4)**, pp.488–493.

Ruel, J., Chabbert, C., Nouvian, R., Bendris, R., Eybalin, M., Leger, C.L., Bourien, J., Mersel, M. & Puel, J.L. (2008) Salicylate enables cochlear arachidonic-acid-sensitive NMDA receptor responses. *Journal of Neuroscience* **28(29)**, pp.7313–7323.

Ruel, J., Bobbin, R.P., Vidal, D., Pujol, R. & Puel, J.L. (2000) The selective AMPA receptor antagonist GYKI 53784 blocks action potential generation and excitotoxicity in the

guinea pig cochlea. *Neuropharmacology* **39(11)**, pp.1959–1973.

Russell, W.L., Kelly, E.M., Hunsicker, P.R., Bangham, J.W., Maddux, S.C. & Phipps, E.L. (1979) Specific-locus test shows ethylnitrosourea to the the most potent mutagen in the mouse. *Proceedings of the National Academy of Sciences of the United States of America* **76(11)**, pp.5818–5819.

Russo, C.J., Melista, E., Cui, J., DeStefano, A.L., Bakris, G.L., Manolis, A.J., Gavras, H. & Baldwin, C.T. (2005) Association of NEDD4L ubiquitin ligase with essential hypertension. *Hypertension* **46(3)**, pp.488–491.

Safieddine, S., El-Amraoui, A. & Petit, C. (2012) The Auditory Hair Cell Ribbon Synapse: From Assembly to Function. *Annual Review of Neuroscience* **35(1)**, pp.509–528.

Safieddine, S. & Wenthold, R.J. (1999) SNARE complex at the ribbon synapses of cochlear hair cells: Analysis of synaptic vesicle- and synaptic membrane-associated proteins. *European Journal of Neuroscience* **11(3)**, pp.803–812.

Sai, X. & Ladher, R.K. (2015) Early steps in inner ear development: induction and morphogenesis of the otic placode. *Frontiers in Pharmacology* **6(FEB)**, p.19.

Sakaguchi, N., Crouch, J.J., Lytle, C. & Schulte, B.A. (1998) Na-K-Cl cotransporter expression in the developing and senescent gerbil cochlea. *Hearing Research* **118(1–2)**, pp.114–122.

Salt, A.N., Melichar, I. & Thalmann, R. (1987) Mechanisms of endocochlear potential generation by stria vascularis. *Laryngoscope* **97(8)**, pp.984–991.

Sanes, D.H. (1990) An in vitro analysis of sound localization mechanisms in the gerbil lateral superior olive. *Journal of Neuroscience* **10(11)**, pp.3494–3506.

Schmiedt, R.A., Lang, H., Okamura, H. oki & Schulte, B.A. (2002) Effects of Furosemide Applied Chronically to the Round Window: A Model of Metabolic Presbyacusis. *The Journal of Neuroscience* **22(21)**, p.9643.

Schrott-Fischer, A., Kammen-Jolly, K., Scholtz, A., Rask-Andersen, H., Glueckert, R. & Eybalin, M. (2007) Efferent neurotransmitters in the human cochlea and vestibule. *Acta Oto-Laryngologica* **127(1)**, pp.13–19.

Schulte, B.A. & Steel, K.P. (1994) Expression of α and β subunit isoforms of Na,K-ATPase in the mouse inner ear and changes with mutations at the Wv or Sld loci. *Hearing Research* **78(1)**, pp.65–76.

Schwander, M., Xiong, W., Tokita, J., Lelli, A., Elledge, H.M., Kazmierczak, P., Sczaniecka, A., Kolatkar, A., Wiltshire, T., Kuhn, P., Holt, J.R., Kachar, B., Tarantino,

L. & Müller, U. (2009) A mouse model for nonsyndromic deafness (DFNB12) links hearing loss to defects in tip links of mechanosensory hair cells. *Proceedings of the National Academy of Sciences of the United States of America* **106(13)**, pp.5252–5257.

Schwander, M., Kachar, B. & Müller, U. (2010) The cell biology of hearing. *Journal of Cell Biology* **190(1)**, pp.9–20.

Seglen, P.O., Grinde, B. & Solheim, A.E. (1979) Inhibition of the Lysosomal Pathway of Protein Degradation in Isolated Rat Hepatocytes by Ammonia, Methylamine, Chloroquine and Leupeptin. *European Journal of Biochemistry* **95(2)**, pp.215–225.

Sekerková, G., Richter, C.P. & Bartles, J.R. (2011) Roles of the espin actin-bundling proteins in the morphogenesis and stabilization of hair cell stereocilia revealed in CBA/CaJ congenic jerker mice. *PLoS Genetics* **7(3)**.

Shi, L., Chang, Y., Li, X., Aiken, S., Liu, L. & Wang, J. (2016) Cochlear Synaptopathy and Noise-Induced Hidden Hearing Loss. *Neural Plasticity* **2016**.

Shi, P.P., Cao, X.R., Sweezer, E.M., Kinney, T.S., Williams, N.R., Husted, R.F., Nair, R., Weiss, R.M., Williamson, R.A., Sigmund, C.D., Snyder, P.M., Staub, O., Stokes, J.B. & Yang, B. (2008) Salt-sensitive hypertension and cardiac hypertrophy in mice deficient in the ubiquitin ligase Nedd4-2. *American Journal of Physiology - Renal Physiology* **295(2)**, pp.462–470.

Shore, S.E., Helfert, R.H., Bledsoe, S.C., Altschuler, R.A. & Godfrey, D.A. (1991) Descending projections to the dorsal and ventral divisions of the cochlear nucleus in guinea pig. *Hearing Research* **52(1)**, pp.255–268.

Shrestha, B.R., Chia, C., Wu, L., Kujawa, S.G., Liberman, M.C. & Goodrich, L. V. (2018) Sensory Neuron Diversity in the Inner Ear Is Shaped by Activity. *Cell* **174(5)**, pp.1229-1246.e17.

Siemens, J., Lillo, C., Dumont, R.A., Reynolds, A., Williams, D.S., Gillespie, P.G. & Müller, U. (2004) Cadherin 23 Is a component of the tip link in hair-cell stereocilla. *Nature* **428(6986)**, pp.950–955.

Simon, M.M., Greenaway, S., White, J.K., Fuchs, H., Gailus-Durner, V., Brown, S.D., et al. (2013) A comparative phenotypic and genomic analysis of C57BL/6J and C57BL/6N mouse strains. *Genome Biology 2013 14:7* **14(7)**, pp.1–22.

Skarnes, William C, Rosen, B., West, A.P., Koutsourakis, M., Bushell, W., Iyer, V., Mujica, A.O., Thomas, M., Harrow, J., Cox, T., Jackson, D., Severin, J., Biggs, P., Fu, J., Nefedov, M., de Jong, P.J., Stewart, A.F. & Bradley, A. (2011) A conditional

knockout resource for the genome-wide study of mouse gene function. *Nature* **474(7351)**, pp.337–42.

Skarnes, William C., Rosen, B., West, A.P., Koutsourakis, M., Bushell, W., Iyer, V., Mujica, A.O., Thomas, M., Harrow, J., Cox, T., Jackson, D., Severin, J., Biggs, P., Fu, J., Nefedov, M., De Jong, P.J., Stewart, A.F. & Bradley, A. (2011) A conditional knockout resource for the genome-wide study of mouse gene function. *Nature* **474(7351)**, pp.337–344.

Smith, C.A. & Sjöstrand, F.S. (1961) A synaptic structure in the hair cells of the guinea pig cochlea. *Journal of Ultrasructure Research* **5(2)**, pp.184–192.

Soto-Prior, A., Cluzel, M., Renard, N., Ripoll, C., Lavigne-Rebillard, M., Eybalin, M. & Hamel, C.P. (1995) Molecular cloning and expression of α parvalbumin in the guinea pig cochlea. *Molecular Brain Research* **34(2)**, pp.337–342.

Spicer, S.S. & Schulte, B.A. (1998) Evidence for a medial K+ recycling pathway from inner hair cells. *Hearing Research* **118(1–2)**, pp.1–12.

Steel, K.P. & Bock, G.R. (1980) The nature of inherited deafness in deafness mice. *Nature* **288(5787)**, pp.159–161.

Steinhoff, H.J., Böhnke, F. & Janssen, T. (1988) Click ABR intensity-latency characteristics in diagnosing conductive and cochlear hearing losses. *Archives of Oto-Rhino-Laryngology* **245(5)**, pp.259–265.

Stockand, J.D., Hui-Fang, B., Schenck, J., Malik, B., Middleton, P., Schlanger, L.E. & Eaton, D.C. (2000) Differential effects of protein kinase C on the levels of epithelial Na+ channel subunit proteins. *Journal of Biological Chemistry* **275(33)**, pp.25760–25765.

Stouffs, K., Verloo, P., Brock, S., Régal, L., Beysen, D., Ceulemans, B., Jansen, A.C. & Meuwissen, M.E.C. (2020) Recurrent NEDD4L Variant in Periventricular Nodular Heterotopia, Polymicrogyria and Syndactyly. *Frontiers in Genetics* **11**, p.26.

Sudol, M., Chen, H.I., Bougeret, C., Einbond, A. & Bork, P. (1995) Characterization of a novel protein-binding module - the WW domain. *FEBS Letters* **369(1)**, pp.67–71.

Sugasawa, M., Erostegui, C., Blanchet, C. & Dulon, D. (1996) ATP activates non-selective cation channels and calcium release in inner hair cells of the guinea-pig cochlea. *Journal of Physiology* **491(3)**, pp.707–718.

Sun, S., Babola, T., Pregernig, G., So, K.S., Nguyen, M., Su, S.S.M., Palermo, A.T., Bergles, D.E., Burns, J.C. & Müller, U. (2018) Hair Cell Mechanotransduction Regulates Spontaneous Activity and Spiral Ganglion Subtype Specification in the

Auditory System. *Cell* **174(5)**, pp.1247-1263.e15.

Swatek, K.N. & Komander, D. (2016) Ubiquitin modifications. *Cell Research* **26(4)**, pp.399–422.

Szücs, A., Szappanos, H., Tóth, A., Farkas, Z., Panyi, G., Csernoch, L. & Sziklai, I. (2004) Differential expression of purinergic receptor subtypes in the outer hair cells of the guinea pig. In *Hearing Research*. Elsevier, pp. 2–7.

Taranda, J., Maison, S.F., Ballestero, J.A., Katz, E., Savino, J., Vetter, D.E., Boulter, J., Liberman, M.C., Fuchs, P.A. & Elgoyhen, A.B. (2009) A Point Mutation in the Hair Cell Nicotinic Cholinergic Receptor Prolongs Cochlear Inhibition and Enhances Noise Protection R. W. Aldrich, ed. *PLoS Biology* **7(1)**, p.e1000018.

Testa, G., Schaft, J., Van Der Hoeven, F., Glaser, S., Anastassiadis, K., Zhang, Y., Hermann, T., Stremmel, W. & Stewart, A.F. (2004) A Reliable lacZ Expression Reporter Cassette for Multipurpose, Knockout-First Alleles. *Genesis* **38(3)**, pp.151–158.

The International Mouse Knockout Consortium (2007) A Mouse for All Reasons. *Cell* **128(1)**, pp.9–13.

Thorn, L., Arnold, W., Schinko, I. & Wetzstein, R. (1979) The limbus spiralis and its relationship to the developing tectorial membrane in the cochlear duct of the guinea pig fetus. *Anatomy and Embryology* **155(3)**, pp.303–310.

Thorne, P.R., Muñoz, D.J.B. & Housley, G.D. (2004) Purinergic Modulation of Cochlear Partition Resistance and Its Effect on the Endocochlear Potential in the Guinea Pig. *JARO - Journal of the Association for Research in Otolaryngology* **5(1)**, pp.58–65.

Uthaiah, R.C. & Hudspeth, A.J. (2010) Molecular anatomy of the hair cell's ribbon synapse. *Journal of Neuroscience* **30(37)**, pp.12387–12399.

Vetter, D.E., Liberman, M.C., Mann, J., Barhanin, J., Boulter, J., Brown, M.C., Saffiote-Kolman, J., Heinemann, S.F. & Elgoyhen, A.B. (1999) Role of α9 nicotinic ACh receptor subunits in the development and function of cochlear efferent innervation. *Neuron* **23(1)**, pp.93–103.

Vetter, D.E., Katz, E., Maison, S.F., Taranda, J.N., Turcan, S., Ballestero, J., Liberman, M.C., Elgoyhen, A.B.N. & Boulter, J. (2007) The α10 nicotinic acetylcholine receptor subunit is required for normal synaptic function and integrity of the olivocochlear system. *Proceedings of the National Academy of Sciences of the United States of America* **104(51)**, pp.20594–20599.

Vogel, C. & Marcotte, E.M. (2012) Insights into the regulation of protein abundance from proteomic and transcriptomic analyses. *Nature Reviews Genetics* **13(4)**, pp.227–232.

Vogler, D.P., Robertson, D. & Mulders, W.H.A.M. (2014) Hyperactivity following unilateral hearing loss in characterized cells in the inferior colliculus. *Neuroscience* **265**, pp.28–36.

Vyas, P., Wood, M.B., Zhang, Y., Goldring, A.C., Chakir, F.Z., Fuchs, P.A. & Hiel, H. (2020) Characterization of HA-tagged α9 and α10 nAChRs in the mouse cochlea. *Scientific Reports* **10(1)**, pp.1–15.

Wadia, Jehangir S., Stan, R. V. & Dowdy, S.F. (2004) Transducible TAT-HA fusogenic peptide enhances escape of TAT-fusion proteins after lipid raft macropinocytosis. *Nature Medicine* **10(3)**, pp.310–315.

Wadia, Jehangir S, Stan, R. V & Dowdy, S.F. (2004) Transducible TAT-HA fusogenic peptide enhances escape of TAT-fusion proteins after lipid raft macropinocytosis. *Nature Medicine* **10(3)**, pp.310–315.

Wakaoka, T., Motohashi, T., Hayashi, H., Kuze, B., Aoki, M., Mizuta, K., Kunisada, T. & Ito, Y. (2013) Tracing Sox10-expressing cells elucidates the dynamic development of the mouse inner ear. *Hearing Research* **302**, pp.17–25.

Walters, Brandon J., Diao, S., Zheng, F., Walters, Bradley J., Layman, W.S. & Zuo, J. (2015) Pseudo-immortalization of postnatal cochlear progenitor cells yields a scalable cell line capable of transcriptionally regulating mature hair cell genes. *Scientific Reports* **5(1)**, pp.1–13.

Wang, J.C.C., Raybould, N.P., Luo, L., Ryan, A.F., Cannell, M.B., Thorne, P.R. & Housley, G.D. (2003) Noise induces up-regulation of P2X2 receptor subunit of ATP-gated ion channels in the rat cochlea. *NeuroReport* **14(6)**, pp.817–823.

Wangemann, P. (2006) Supporting sensory transduction: Cochlear fluid homeostasis and the endocochlear potential. *Journal of Physiology* **576(1)**, pp.11–21.

Wangemann, P., Liu, J. & Marcus, D.C. (1995) Ion transport mechanisms responsible for K+ secretion and the transepithelial voltage across marginal cells of stria vascularis in vitro. *Hearing Research* **84(1–2)**, pp.19–29.

Wangemann, P. & Schacht, J. (1996) Homeostatic mechanisms in the cochlea. In P. Dallos, A. Popper, & R. Fay, eds. *Springer Handbook of Auditory Research: The Cochlea*. Springer New York, pp. 130–185.

Watanabe, K. ichi, Takeda, K., Katori, Y., Ikeda, K., Oshima, T., Yasumoto, K. ichi, Saito,

H., Takasaka, T. & Shibahara, S. (2000) Expression of the Sox10 gene during mouse inner ear development. *Molecular Brain Research* **84(1–2)**, pp.141–145.

Webber, J.L., Clancy, J.C., Zhou, Y., Yraola, N., Homma, K. & García-Añoveros, J. (2021) Axodendritic versus axosomatic cochlear efferent termination is determined by afferent type in a hierarchical logic of circuit formation. *Science Advances* **7(4)**, p.eabd8637.

Wedemeyer, C., Martín, J.Z. de S., Ballestero, J., Gómez-Casati, M.E., Torbidoni, A.V., Fuchs, P.A., Bettler, B., Elgoyhen, A.B. & Katz, E. (2013) Activation of presynaptic GABAb(1a,2) receptors inhibits synaptic transmission at mammalian inhibitory cholinergic olivocochlear-hair cell synapses. *Journal of Neuroscience* **33(39)**, pp.15477–15487.

Weisz, C., Glowatzki, E. & Fuchs, P. (2009) The postsynaptic function of type II cochlear afferents. *Nature* **461(7267)**, pp.1126–1129.

Weisz, C.J.C., Lehar, M., Hiel, H., Glowatzki, E. & Fuchs, P.A. (2012) Synaptic transfer from outer hair cells to type II afferent fibers in the rat cochlea. *Journal of Neuroscience* **32(28)**, pp.9528–9536.

Weisz, C.J.C., Glowatzki, E. & Fuchs, P.A. (2014) Excitability of type II cochlear afferents. *Journal of Neuroscience* **34(6)**, pp.2365–2373.

Wenzel, G.I., Anvari, B., Mazhar, A., Pikkula, B. & Oghalai, J.S. (2007) Laser-induced collagen remodeling and deposition within the basilar membrane of the mouse cochlea. *Journal of Biomedical Optics* **12(2)**, p.021007.

White, P.N., Thorne, P.R., Housley, G.D., Mockett, B., Billett, T.E. & Burnstock, G. (1995) Quinacrine staining of marginal cells in the stria vascularis of the guinea-pig cochlea: a possible source of extracellular ATP? *Hearing Research* **90(1–2)**, pp.97–105.

Wilcox, E.R., Burton, Q.L., Naz, S., Riazuddin, Saima, Smith, T.N., Ploplis, B., Belyantseva, I., Ben-Yosef, T., Liburd, N.A., Morell, R.J., Kachar, B., Wu, D.K., Griffith, A.J., Riazuddin, Sheikh & Friedman, T.B. (2001) Mutations in the gene encoding tight junction claudin-14 cause autosomal recessive deafness DFNB29. *Cell* **104(1)**, pp.165–172.

Winter, I.M., Robertson, D. & Yates, G.K. (1990) Diversity of characteristic frequency rate-intensity functions in guinea pig auditory nerve fibres. *Hearing Research* **45(3)**, pp.191–202.

Wiszniak, S., Kabbara, S., Lumb, R., Scherer, M., Secker, G., Harvey, N., Kumar, S. &

Schwarz, Q. (2013) The ubiquitin ligase Nedd4 regulates craniofacial development by promoting cranial neural crest cell survival and stem-cell like properties. *Developmental Biology* **383(2)**, pp.186–200.

Woods, C., Montcouquiol, M. & Kelley, M.W. (2004) Math1 regulates development of the sensory epithelium in the mammalian cochlea. *Nature Neuroscience* **7(12)**, pp.1310–1318.

Xiong, W., Grillet, N., Elledge, H.M., Wagner, T.F.J., Zhao, B., Johnson, K.R., Kazmierczak, P. & Müller, U. (2012) TMHS is an integral component of the mechanotransduction machinery of cochlear hair cells. *Cell* **151(6)**, pp.1283–1295.

Xu, J., Ueno, H., Xu, C.Y., Chen, B., Weissman, I.L. & Xu, P.X. (2017) Identification of mouse cochlear progenitors that develop hair and supporting cells in the organ of Corti. *Nature Communications* **8(1)**, pp.1–17.

Xu, P., Duong, D.M., Seyfried, N.T., Cheng, D., Xie, Y., Robert, J., Rush, J., Hochstrasser, M., Finley, D. & Peng, J. (2009) Quantitative Proteomics Reveals the Function of Unconventional Ubiquitin Chains in Proteasomal Degradation. *Cell* **137(1)**, pp.133–145.

Yang, D., Thalmann, I., Thalmann, R. & Simmons, D.D. (2004) Expression of α and β Parvalbumin Is Differentially Regulated in the Rat Organ of Corti during Development. *Journal of Neurobiology* **58(4)**, pp.479–492.

Yanpallewar, S., Wang, T., Koh, D.C.I., Quarta, E., Fulgenzi, G. & Tessarollo, L. (2016) Nedd4-2 haploinsufficiency causes hyperactivity and increased sensitivity to inflammatory stimuli. *Scientific Reports* **6(1)**, pp.1–9.

Yeh, W.H., Shubina-Oleinik, O., Levy, J.M., Pan, B., Newby, G.A., Wornow, M., Burt, R., Chen, J.C., Holt, J.R. & Liu, D.R. (2020) In vivo base editing restores sensory transduction and transiently improves auditory function in a mouse model of recessive deafness. *Science Translational Medicine* **12(546)**, p.9101.

Yoshiki, A. & Moriwaki, K. (2006) Mouse phenome research: Implications of genetic background. *ILAR Journal* **47(2)**, pp.94–102.

Yu, L., Cai, H., Yue, Q., Alli, A.A., Wang, D., Al-Khalili, O., Bao, H.F. & Eaton, D.C. (2013) WNK4 inhibition of ENaC is independent of Nedd4-2-mediated ENaC ubiquitination. *American Journal of Physiology - Renal Physiology* **305(1)**, p.F31.

Zentner, M.D., Lin, H.H., Wen, X., Kim, K.J. & Ann, D.K. (1998) The amiloride-sensitive epithelial sodium channel α-subunit is transcriptionally down-regulated in rat parotid cells by the extracellular signal-regulated protein kinase pathway. *Journal*

of Biological Chemistry **273(46)**, pp.30770–30776.

Zhao, B., Wu, Z., Grillet, N., Yan, L., Xiong, W., Harkins-Perry, S. & Müller, U. (2014) TMIE is an essential component of the mechanotransduction machinery of cochlear hair cells. *Neuron* **84(5)**, pp.954–967.

Zheng, J., Shou, J., Guillemot, F., Kageyama, R. & Gao, W. (2000) Hes1 is a negative regulator of inner ear hair cell differentiation. *Development*.

Zheng, Q.Y., Johnson, K.R. & Erway, L.C. (1999) Assessment of hearing in 80 inbred strains of mice by ABR threshold analyses. *Hearing Research* **130(1–2)**, pp.94–107.

Zhong, S.X., Hu, G.H. & Liu, Z.H. (2014) Expression of ENaC, SGK1 and Nedd4 isoforms in the cochlea of guinea pig. *Folia Histochemica et Cytobiologica* **52(2)**, pp.144–148.

Zhu, J., Lee, K.Y., Jewett, K.A., Man, H.Y., Chung, H.J. & Tsai, N.P. (2017) Epilepsy-associated gene Nedd4-2 mediates neuronal activity and seizure susceptibility through AMPA receptors W. N. Frankel, ed. *PLOS Genetics* **13(2)**, p.e1006634.

Zhu, Q., Pao, G.M., Huynh, A.M., Suh, H., Tonnu, N., Nederlof, P.M., Gage, F.H. & Verma, I.M. (2011) BRCA1 tumour suppression occurs via heterochromatin-mediated silencing. *Nature* **477(7363)**, pp.179–184.

Zuo, H., Cui, B., She, X. & Wu, M. (2008) Changes in Guinea pig cochlear hair cells after sound conditioning and noise exposure. *Journal of occupational health* **50(5)**, pp.373–379.

Zwaenepoel, I., Mustapha, M., Leibovici, M., Verpy, E., Goodyear, R., Liu, X.Z., Nouaille, S., Nance, W.E., Kanaan, M., Avraham, K.B., Tekaia, F., Loiselet, J., Lathrop, M., Richardson, G. & Petit, C. (2002) Otoancorin, an inner ear protein restricted to the interface between the apical surface of sensory epithelia and their overlying acellular gels, is defective in autosomal recessive deafness DFNB22. *Proceedings of the National Academy of Sciences of the United States of America* **99(9)**, pp.6240–6245.

APPENDIX

Appendix Table 1: All reagents and chemicals used in the experiments described. The supplier of reagents and chemicals, and their respective catalog number is also detailed.

Reagent	Supplier	Catalog Number
AQ Eosin Y	Thermo Scientific™	6766007
Acetone	Acros Organics™	13277983
Agarose	Thermo Scientific™	17850
Amersham ECL Select Western Blotting Detection Reagent	GE Healthcare	RPN2235
Bio Rad DC Assay	Bio Rad	5000111
BSA	New England Biolabs	B9000S
Blue Ribbon Paraffin	Leica	3801360
Carbon Discs	Agar Scientific Ltd.	AGG3347N
Cell-Culture Grade DMSO	Sigma	D2650
Countess™ Cell Counting Chamber Slides	Invitrogen™	C10228
Chloroquine	Sigma	C6628
Clearium	Leica	3801100
DAPI (4', 6-Diamidono-2-Phenylindole)	Biolegend	422801
DC Protein Assay	Bio-rad	5000111
D.F.B decalcifying agent	Pioneer Research Chemicals	PRC/R/12
DMEM, high glucose, GlutaMAX™	Gibco™	10566016
DNeasy Blood and Tissue Kit	Qiagen	69504
Donkey Serum	Sigma-Aldrich	D9663
dPBS	Gibco™	14190144
EDTA (Ethylenediamine Tetracetic Acid)	VWR Chemicals	280214S
Ethanol	Fisher Bioreagents	BP8202-1
FBS	Gibco™	26140-079
Geneclean® II Kit	MPBio	111001400
Goat Anti-Rabbit IgG (H + L)-HRP Conjugate	Bio-Rad	1706515
Glutaraldehyde	TAAB Laboratories	G002
Haematoxylin Gills III	Thermo Scientific™	M1051740500
High-Capacity cDNA Reverse Transcription Kit	Applied Biosystems™	10400745
Hotshot Diamond PCR Reaction Mixture	Clent Life Science	HS002
ImmEdge® Hydrophobic Barrier PAP Pen	Vector Laboratories	H-4000
Industrial Denatured Alcohol	Pioneer Research Chemicals	PRC/R/101
IGEPAL	Sigma-Aldrich	I8896
Isopropanol	Fisher Scientific	S25372

Reagent	Supplier	Catalog Number
Lithium Carbonate	Acros Organics™	197785000
2mM Magnesium Chloride	VWR	10128-298
Mem-PER™ Plus Membrane Protein Extraction Kit	Thermo Scientific™	89842
2-Mercaptoethanol	Sigma-Aldrich	M6250
Methanol	Fisher Scientific	A412-500
MG132	Enzo Life Sciences	BML-PI102-0005
Milk Powder	Marvel	-
M-PER™ Mammalian Protein Extraction Reagent	Thermo Scientific™	78501
10% Neutral Buffered Formalin	Leica	3800770
Nitrocellulose/Filter Paper Sandwich, 0.45µm, 8.3 x 7.3 cm	Thermo Fisher	LC2001
NuPAGE™ 3-8% Tris-Acetate Protein Gel, 10-well	Thermo Fisher	EA0375BOX
NuPAGE™ 4-12% Bis-Tris Protein Gels, 10-well	Thermo Fisher	NP0321BOX
NuPAGE™ Antioxidant	Thermo Fisher	NP0005
NuPAGE™ MOPS SDS Running Buffer (20x)	Thermo Fisher	NP0001
NuPAGE™ LDS Sample Buffer (4x)	Thermo Fisher	NP0007
NuPAGE™ Sample Reducing Agent (10x)	Thermo Fisher	NP0004
NuPAGE™ Transfer Buffer (20x)	Thermo Fisher	NP0006
NuPAGE™ Tris-Acetate SDS Running Buffer (20x)	Thermo Fisher	LA0041
O.C.T Compound	VWR Chemicals	00411243
Osmium Tetraoxide	TAAB Laboratories	O015
Paraformaldehyde (PFA)	Sigma-Aldrich	158127
Penicillin/Streptomycin	Gibco™	15070063
Ponceau S	Sigma-Aldrich	P7170
Potassium Ferricyanide	Fluka™	15616750
Potassium Ferrocyanide	Sigma-Aldrich	P3289
Protein G Sepharose, Fast Flow	Millipore	P3296
RNAlater™	Invitrogen™	AM7020
RNeasy Plus Mini Kit	Qiagen	74134
Scanning Electron Microscopy Specimen Stubs	Agar Scientific Ltd	AGG301
Silver Paint	Agar Scientific Ltd	AGG3790
Slowfade™ Antifade Mountant	Invitrogen™	S36936
Sodium Deoxycholate	Sigma-Aldrich	D6750
Soluble-Cre	Merck Millipore	SCR508
Soluble-Cre	Excellgen	EG-1001
Sucrose	Fisher Scientific	S25590
Super Frost Plus™ Adhesion Slides	Fisher Scientific	10149870

Reagent	Supplier	Catalog Number
TaqMan™ GTXpress™ Master mix	Applied Biosystems™	4403311
TaqMan® Sample-to-SNP™	Applied Biosystems™	4403313
Thiocarbohydrazide	Sigma-Aldrich	223220
Tris Base	Sigma-Aldrich	10708976001
Triton X-100	Sigma-Aldrich	11332481001
Tween 20	Sigma-Aldrich	P1379
0.4% Trypan Blue Stain	Gibco™	15250061
Trypsin/EDTA (0.05%)	Gibco™	25300062
Trypsin/EDTA (0.25%)	Gibco™	25200056
Viscotears®	Novartis	-
Xylene	Pioneer Research Chemicals	PRC/R/201

Appendix Table 2: All solutions used in the experiments described. The recipe of the solutions is also noted, with concentration, volumes, temperature and other steps included, where required.

Solution	Recipe
Blocking Solution	10% (volume/volume) Donkey Serum, 1% (volume/volume) BSA in PBS with 0.1% Triton X-100/ PBS with 0.3% Triton X-100.
200mM Chloroquine	2.58g Chloroquine in 25mL of sterile H_2O
4% EDTA	4% (weight/volume) EDTA in PBS
4.3% EDTA	4.3% (weight/volume) EDTA in Phosphate Buffer
Ethanol Solution	Ethanol (weight/volume) in ddH_2O
0.1% Formic Acid	Formic acid (volume/volume) in ddH_2O
Industrial Denatured Alcohol (IDA)	IDA (volume/volume) in ddH_2O
2.5% Glutaraldehyde (GTA)	2.5% (volume/volume) GTA in Phosphate Buffer
Lithium Carbonate	100mL Saturated Lithium Carbonate in 500mL ddH_2O
5% Milk Solution	5% (weight/volume) Milk powder in TBS with 0.1% Tween20
MEF Culture Media	DMEM, 10% (volume/volume) FBS, 1% (volume/volume) Pencillin/Streptomycin
10mM MG132	5mg MG132 in 1mL cell culture-grade DMSO
MOPS Buffer	50mL of 20x MOPS buffer + 950mL of H_2O
Paraformaldehyde (PFA)	4% (weight/volume) PFA in PBS
PBS with 0.1% Triton X-100	PBS (1L) + 1mL 100% Triton X-100
PBS with 0.3% Triton X-100	PBS (1L) + 3mL 100% Triton X-100
0.1M Phosphate Buffer	4.44g Sodium Phosphate Monobasic Anhydrous, 17.04g Sodium Phosphate Dibasic Anhydrous in 789mL H_2O
5mM Potassium Ferricyanide	3.29g Potassium Ferricyanide in 100mL of PBS
5mM Potassium Ferrocyanide	4.22g in Potassium Ferrocyanide in 100 of PBS
Reagent A’	20µL Reagent S + 1 mL Reagent A
RIPA Lysis	150mM NaCl, 1% (volume/volume) NP-40, 0.5% (volume/volume) Sodium Deoxycholate, 0.1% (volume/volume) Sodium Dodecyl sulphate, 50mM Tris pH 7.5
0.1M Sodium Cacodylate	2.14g Sodium Cacodylate in 100mL of ddH_2O
10% Sodium Deoxycholate	10% (weight/volume) Sodium Deoxycholate in 50mL of ddH_2O.
Solvent B	0.1% (volume/volume) formic acid in 100% acetonitrile
Sucrose	30% (weight/volume) in PBS

Solution	Recipe
Tris-Acetate (TA) Buffer	50mL of 20x TA Buffer + 950mL of ddH_2O
TE Buffer	1mM EDTA, 10mM Tris-Cl in 100mL of ddH_2O
PBS with 0.1% Tween20	PBS (1L) + 1mL 100% of Tween20
1% Thiocarbohydrazide	0.15g Thiocarbohydrazide + 15mL of ddH_2O. Syringe filtered before use.
Transfer Buffer	25mL 20x Transfer Buffer + 50mL Methanol + 500µL antioxidant + 425mL ddH_2O
Western Blocking Solution	5% (weight/volume) milk powder in TBS with 0.1% Tween20
X-Gal Solution (96mL)	200µL of 2mM MgCl2, 200µL of 0.02% (volume/volume) IGEPAL, 5mL of 5mM Potassium Ferrocyanide, 5mL of 5mM Potassium Ferricyanide, 100µL of 10% Sodium Deoxycholate, 2.5mL of 0.1% (1 mg/mL) X-Gal in DMF, 4°C PBS pH 8.0, 83mL of 4°C PBS.

Appendix Table 3: All the equipment used in the experiments described. The name of the equipment and the manufacturer for said equipment is noted.

Equipment	Manufacturer
ABI 7900 HT Fast Real-Time PCR System	Applied Biosystems™
Acclaim™ PepMap™ 100 C18 precolumn	Dionex
Automated Tissue Processor EM TP	Leica
Automatic Stainer	Sakura
ChemiDoc™ Imaging System	Bio-Rad
Countess Cell Counting Cell Chamber Slides	Invitrogen™
Cryostat Microtome HM525	Thermo Scientific™
Epoch BioTek Spectrophotometer	BioTek
ER10B+ Low-Noise Probe Microphone	Etymotic Research
ES1 Free Field Transducer	Tucker Davis Technology
Excelsior AS Processor	Thermo Scientific™
Heat-box	Datesand Ltd
Histostar Embedding Centre	Epredia
Invitrogen Countess II	Invitrogen™
Joel LSM-6010 Scanning Electron Microscope	Joel Ltd
Leica EM CPD300 Critical Point Dryer	Leica
MF1 Speakers	Tucker Davis Technology
Millipore C18 ZipTips	Millipore
Mr. Frosty™ Freezing Container	Thermo Fisher Scientific™
Nano Series™ Standard PepMap™ 100 C18 Columns	Dionex
NanoZoomer RS Scanner	Hamamatsu
Para Trimmer™	Thermo Scientific™
Q Exactive™ HF Orbitrap Mass Spectrometer	Thermo Fisher Scientific™
Quorum Q150RS Sputter Coater	Quorum
Recording Electrodes	Grass Telefactor
Rotary Microtome HM325	Thermo Scientific™
Sakura Ident™ Labeller	Sakura Finetek Europe
Sound Attenuating Chamber	ETS-Lindgren
Superfrost Plus™ Adhesion Slides	Fischer Scientific
Triversa Nanomate Nanospray Source	Advion Biosciences
TouchTools™ PCR Wizard	TECAN
UltiMate® 3000 HPLC series	Dionex
Zeiss Axio Observer Z1 Microscope	Zeiss
Zeiss LSM 710 Fluorescence Microscope	Zeiss

Appendix Table 4: The antibodies their, application and concentration used.

Antibody	Supplier	Catalog Number	Application	Concentration
Actin	Sigma-Aldrich	A2066	Western Blot	1:3000
Arl13b	Proteintech	17711-1-AP	Western Blot	1:1000
αENaC	Stressmarq Biosciences	SPC-403	Western Blot	1:1000
FK2	Enzo	BML-PW8810	Immunoprecipitation	1µg/mg
GluR2	Merck Millipore	MAB397	Wholemount Immunohistochemistry	1:200
NEDD4L	Proteintech	13690-1-AP	Cryosection Immunohistochemistry	1:50
NEDD4L	Cell Signalling	CS4013s	Western Blot	1:1000
NF200	Sigma-Aldrich	N4142	Wholemount Immunohistochemistry	1:200
αParvalbumin	R&D Systems	AF5058	Wholemount Immunohistochemistry	1:150
Ribeye	Synaptic Systems	192103	Wholemount Immunohistochemistry	1:200

Appendix 1: The Python code used to scrape t-SNE plots from the gEAR database.

```
import openpyxl
import os
from selenium import webdriver
from selenium.webdriver.common.keys import Keys
from selenium.webdriver.common.by import By
from selenium.webdriver.support.select import Select
from time import sleep
import base64
from PIL import Image
from io import BytesIO

def img():
    count = 0
    imgs = browser.find_elements_by_xpath('//div/img')
    for img in imgs:
        src = img.get_attribute('src')
        if src[0:22] == '':
            data = src[22:len(src)]
            im = Image.open(BytesIO(base64.b64decode(data)))
            im.save(str(count) + '.png', 'PNG')
            count += 1

def scRNA1():
    dest = new_path + '/scRNA-seq (1)'
    os.chdir(dest)
    browser.execute_script('elem =
document.getElementById("selected_profile"); elem.click();')
    browser.execute_script('select = document.getElementsByClassName("form-
control input-sm"); select[0].selectedIndex = 16;')
    browser.execute_script('var event = new Event("change");
select[0].dispatchEvent(event)')
    sleep(15)
    img()
    print(gene + ' scRNA(1) scraped')

def Kelley():
    dest = new_path + '/scRNA-seq (Kelley Lab 2020)'
    os.chdir(dest)
    browser.execute_script('elem =
document.getElementById("selected_profile"); elem.click();')
    browser.execute_script('select = document.getElementsByClassName("form-
control input-sm"); select[0].selectedIndex = 17;')
    browser.execute_script('var event = new Event("change");
select[0].dispatchEvent(event)')
    sleep(15)
    img()
    print(gene + ' Kelley scraped')

databases = ['scRNA-seq (1)', 'scRNA-seq (Kelley Lab 2020)']

path = '/Users/mfbx2jl2/Documents/Thesis/gEAR_Scrape/'
os.chdir(path)
gene_list = open('Gene_List.txt')
raw_genes = gene_list.readline()
str_genes = raw_genes.strip()
```

```
genes = str_genes.split(', ')

for gene in genes:
    for database in databases:
        os.mkdirs(os.path.join(gene, database))

for gene in genes:
    new_path = path + '/' + gene
    os.chdir(new_path)
    browser = webdriver.Chrome()
    browser.get('https://umgear.org/?')
    exact_search = browser.find_element_by_id('exact_match_icon')
    exact_search.click()
    element_search = browser.find_element_by_id('search_gene_symbol_intro')
    element_search.clear()
    element_search.send_keys(gene)
    element_search.send_keys(Keys.RETURN)
    sleep(10)

    scRNA1()
    Kelley()

    browser.close()
```

Appendix Table 5: **The 326 protein hits identified through *MS of FK2-immunoprecipitated protein fraction band 1a, prepared from Nedd4l$^{+/+}$-derived MEFs.***

Protein Name	Gene Name	Molecular Weight (kDa)
Leucine-rich PPR motif-containing protein, mitochondrial	*Lrpprc*	156.5
Protein Niban 1	*Niban1*	102.6
Splicing factor 3B subunit 1	*Sf3b1*	145.7
Valine--tRNA ligase	*Vars*	140.1
Leucine--tRNA ligase, cytoplasmic	*Lars*	134.1
Fibulin-2	*Fbln2*	131.7
Neural cell adhesion molecule 1	*Ncam1*	93.6
Neural cell adhesion molecule 1	*Ncam1*	93.4
Erythrocyte protein band 4.1-like 2	*Epb41l2*	109.8
Nardilysin, N-arginine dibasic convertase, NRD convertase 1	*Nrd1*	140.5
Band 4.1-like protein 2	*Epb41l2*	101.8
Uncharacterized protein	*Hdlbp*	141.7
Nidogen-1	*Nid1*	136.5
Golgin subfamily A member 2	*Golga2*	116.2
Uncharacterized protein	*Tpp2*	138.4
Tripeptidyl-peptidase 2	*Tpp2*	139.8
Isoleucine--tRNA ligase, cytoplasmic	*Iars*	144.2
Collagen, type V, alpha 1	*Col5a1*	183.6
Hypoxia up-regulated protein 1	*Hyou1*	111.1
AP-3 complex subunit beta-1	*Ap3b1*	122.7
Eukaryotic translation initiation factor 3 subunit A	*Eif3a*	161.8
Regulator of nonsense transcripts 1	*Upf1*	123.9
SPT16, facilitates chromatin-remodeling subunit	*Supt16*	119.8
AHNAK nucleoprotein (desmoyokin)	*Ahnak*	603.9
Probable ATP-dependent RNA helicase DDX46	*Ddx46*	117.4
Low density lipoprotein receptor-related protein 1	*Lrp1*	504.4
Extended synaptotagmin-1	*Esyt1*	121.5
Golgi apparatus protein 1	*Glg1*	133.6
Coatomer subunit alpha	*Copa*	138.3
Inactive tyrosine-protein kinase 7	*Ptk7*	117.5
Epidermal growth factor receptor substrate 15	*Eps15*	102.2
MKIAA0791 protein (Fragment)	*Nup155*	158.5
Epidermal growth factor receptor substrate 15	*Eps15*	98.4
Ataxin-2-like protein	*Atxn2l*	115.2
Inverted formin-2	*Inf2*	138.5
Structural maintenance of chromosomes protein 2	*Smc2*	134.2
Ataxin-2-like protein	*Atxn2l*	105.4
Fibronectin type III domain-containing protein 3B	*Fndc3b*	132.7
Ubiquitin conjugation factor E4 B	*Ube4b*	147
Splicing factor 3b, subunit 3	*Sf3b3*	135.5
RAB11-binding protein RELCH	*Relch*	134.5
Leucine-rich repeat flightless-interacting protein 1	*Lrrfip1*	79.2
Protein transport protein Sec31A	*Sec31a*	133.5
5-oxoprolinase	*Oplah*	137.5

Protein Name	Gene Name	Molecular Weight (kDa)
DNA damage-binding protein 1	*Ddb1*	126.8
La-related protein 1	*Larp1*	121.1
Ubiquitin-associated protein 2-like	*Ubap2l*	116.7
Fibronectin	*Fn1*	272.4
RNA polymerase-associated protein CTR9 homolog	*Ctr9*	133.3
UDP-glucose:glycoprotein glucosyltransferase 1	*Uggt1*	176.3
Alpha-mannosidase 2	*Man2a1*	131.5
Plasma membrane calcium-transporting ATPase 1	*Atp2b1*	134.7
Thyroid hormone receptor-associated protein 3	*Thrap3*	108.1
Reticulon-4	*Rtn4*	126.5
Elongation factor-like GTPase 1	*Efl1*	125.7
Ubiquitin-associated protein 2	*Ubap2*	117.9
Coatomer subunit beta'	*Copb2*	102.4
Uncharacterized protein	*Ctdp1*	104.5
Sodium/potassium-transporting ATPase subunit alpha-1	*Atp1a1*	112.9
Apoptotic protease-activating factor 1 (Fragment)	*Apaf1*	141.1
Ubiquitin carboxyl-terminal hydrolase 7	*Usp7*	132.8
Chondroitin sulfate proteoglycan 4	*Cspg4*	252.2
Collagen alpha-1(XII) chain	*Col12a1*	340
Endosialin	*Cd248*	81.8
Collagen alpha-2(VI) chain	*Col6a2*	110.3
Epidermal growth factor receptor	*Egfr*	134.8
MKIAA1329 protein (Fragment)	*Sorcs2*	131.5
Filamin-A	*Flna*	281
Cytoplasmic FMR1-interacting protein 1	*Cyfip1*	145.1
Band 4.1-like protein 3	*Epb41l3*	103.3
Nodal modulator 1	*Nomo1*	133.3
Protein phosphatase 1 regulatory subunit 12A	*Ppp1r12a*	114.9
MKIAA0034 protein (Fragment)	*mKIAA0034*	192.4
ELKS/Rab6-interacting/CAST family member 1	*Erc1*	128.3
Ribosomal protein S3	*Rps3*	26.7
Codanin-1	*Cdan1*	135.8
Collagen alpha-1(I) chain	*Col1a1*	137.9
Tenascin	*Tnc*	231.7
Platelet-derived growth factor receptor beta	*Pdgfrb*	123.3
Latent-transforming growth factor beta-binding protein 3	*Ltbp3*	134.3
Elongation factor 1-alpha 1	*Eef1a1*	50.1
Nuclear export mediator factor Nemf	*Nemf*	121.1
AHNAK nucleoprotein 2 (Fragment)	*Ahnak2*	166.4
Calcium-transporting ATPase	*Atp2b4*	133
Ataxin-2	*Atxn2*	136.4
IF rod domain-containing protein	*Vim*	53.7
Alpha v integrin	*Itgav*	115.2
Leucine-rich repeat flightless-interacting protein 1	*Lrrfip1*	75
Integrin alpha-5	*Itga5*	115
Catenin beta-1	*Ctnnb1*	85.4

Protein Name	Gene Name	Molecular Weight (kDa)
Glypican-4	*Gpc4*	62.5
Bcl-2-associated transcription factor 1	*Bclaf1*	105.9
Putative helicase MOV-10	*Mov10*	120.9
Plexin-B2	*Plxnb2*	206.1
Thrombospondin-1	*Thbs1*	129.6
ATPase, Ca++ transporting, cardiac muscle, slow twitch 2, isoform CRA_b (Fragment)	*Atp2a2*	116.5
WASH complex subunit 2	*Washc2*	145.2
MCG124046	*Prss1*	26.1
Constitutive coactivator of PPAR-gamma-like protein 1	*FAM120A*	121.6
RBR-type E3 ubiquitin transferase	*Ankib1*	122.5
26S proteasome non-ATPase regulatory subunit 1	*Psmd1*	105.7
PUM-HD domain-containing protein (Fragment)	*Pum1*	116.3
AP2-associated protein kinase 1	*Aak1*	103.3
Basement membrane-specific heparan sulfate proteoglycan core protein	*Hspg2*	469.5
Synaptopodin	*Synpo*	117.4
WD_REPEATS_REGION domain-containing protein	*Dcaf5*	103.6
ATP-citrate synthase	*Acly*	120.7
Extended synaptotagmin-2	*Esyt2*	94.1
Pumilio homolog 1	*Pum1*	100.3
DNA helicase B	*Helb*	121.4
ADP/ATP translocase 1	*Slc25a4*	32.9
SWI/SNF-related matrix-associated actin-dependent regulator of chromatin subfamily A containing DEAD/H box 1	*Smarcad1*	116.4
Actin, aortic smooth muscle	*Acta2*	42
Actin, beta	*Actb*	41.7
Eukaryotic translation initiation factor 3 subunit L	*Eif3l*	66.6
Plexin-B1	*Plxnb1*	231.2
MCG11560	*Slc25a5*	32.9
Heat shock protein 90kDa beta (Grp94), member 1	*Hsp90b1*	92.4
U2 snRNP-associated SURP motif-containing protein	*U2surp*	118.2
ATP-dependent RNA helicase A	*Dhx9*	149.6
Spectrin alpha chain, non-erythrocytic 1	*Sptan1*	287.4
Nidogen-2	*Nid2*	153.8
Uncharacterized protein	*Ddx39*	49.1
Tankyrase 1 binding protein 1	*Tnks1bp1*	181.7
Heat shock protein 84b	*Hsp90ab1*	83.2
26S proteasome non-ATPase regulatory subunit 2	*Psmd2*	100.2
AP2-associated protein kinase 1 (Fragment)	*Aak1*	54
Uncharacterized protein	*Eif4a1*	46.2
Intersectin-1	*Itsn1*	194.8
Slit homolog 3 (Drosophila)	*Slit3*	167.6
Biglycan	*Bgn*	41.6
MKIAA1850 protein (Fragment)	*Vcpip1*	137.2

Protein Name	Gene Name	Molecular Weight (kDa)
Pyruvate kinase PKM	*Pkm*	57.8
KxDL motif-containing protein 1	*Kxd1*	26.8
Glutamyl-prolyl-tRNA synthetase	*Eprs*	169.9
Collagen alpha-1(XI) chain	*Col11a1*	180.9
FERM, ARHGEF and pleckstrin domain-containing protein 1	*Farp1*	118.8
Alpha glucosidase 2 alpha neutral subunit	*Ganab*	109.3
DNA-directed RNA polymerase II subunit RPB2	*Polr2b*	133.8
Arf-GAP with SH3 domain, ANK repeat and PH domain-containing protein 1	*Asap1*	127.3
Eukaryotic translation initiation factor 3 subunit B	*Eif3b*	108.9
Alpha-actinin-1	*Actn1*	103
Dynactin subunit 1	*Dctn1*	141.6
Transcription elongation factor SPT5	*Supt5h*	120.6
Interleukin-6 signal transductor	*il6st*	102.4
Nucleoporin_C domain-containing protein	*Nup133*	128.5
Ribosome-binding protein 1	*Rrbp1*	172.8
Protein transport protein Sec23A	*Sec23a*	86.1
40S ribosomal protein S2	*Rps2*	31.2
Endoplasmic reticulum chaperone BiP	*Hspa5*	72.4
Structural maintenance of chromosomes protein 3	*Smc3*	141.5
Protein flightless-1 homolog	*Flii*	144.7
Aminopeptidase	*Enpep*	107.9
Tight junction protein ZO-1	*Tjp1*	188.7
Slit homolog 2 protein	*Slit2*	171.1
Reticulon-3	*Rtn3*	103.8
Cell cycle and apoptosis regulator protein 2	*Ccar2*	102.9
GTP-binding nuclear protein Ran	*Ran*	24.4
Keratin, type I cytoskeletal 10	*Krt10*	57.7
Keratin, type II cytoskeletal 1	*Krt1*	65.6
Integrin alpha-9	*Itga9*	114.3
Anoctamin	*Ano6*	108.4
Serine/threonine-protein kinase 11-interacting protein	*Stk11ip*	117.9
Importin-9	*Ipo9*	116
Cell division cycle and apoptosis regulator protein 1	*Ccar1*	132
Alpha-actinin-4	*Actn4*	107
Sister chromatid cohesion protein PDS5 homolog A	*Pds5a*	150.1
MCG10343, isoform CRA_b	*Slc25a3*	39.7
Protein PRRC2C	*Prrc2c*	310.7
TATA element modulatory factor	*Tmf1*	121.7
Tubulin alpha-1B chain	*Tuba1b*	50.1
Intersectin-2	*Itsn2*	191.6
Pde4dip protein	*Pde4dip*	277.2
Choline transporter-like protein 2	*Slc44a2*	80.1
E3 ubiquitin-protein ligase NEDD4	*Nedd4*	127.6
Myb-binding protein 1A	*Mybbp1a*	151.9
SRGAP2 (Fragment)	*SRGAP2*	124.6

Protein Name	Gene Name	Molecular Weight (kDa)
Alpha-mannosidase	*Man2a2*	130.6
Integrin alpha-8	*Itga8*	117.5
Receptor-type tyrosine-protein phosphatase alpha	*Ptpra*	89.8
Keratin, type II cytoskeletal 2 oral	*Krt76*	62.8
Collagen alpha-2(V) chain	*Col5a2*	144.9
Aminopeptidase N	*Anpep*	109.6
Serpin H1	*Serpinh1*	46.5
O-phosphoseryl-tRNA(Sec) selenium transferase	*Sepsecs*	55.3
Secretory carrier-associated membrane protein	*Gm45927*	88.9
RNA-binding protein 27	*Rbm27*	118.5
Paralemmin A kinase anchor protein (Fragment)	*Pakap*	126
Delta-1-pyrroline-5-carboxylate synthase	*Aldh18a1*	87.2
Ankyrin repeat and FYVE domain containing 1	*Ankfy1*	128.6
Dolichyl-diphosphooligosaccharide--protein glycosyltransferase subunit 2 (Fragment)	*Rpn2*	72.1
Kinesin family member 1B, isoform CRA_a	*Kif1b*	130
Nuclear pore complex protein Nup160	*Nup160*	158.1
Protein transport protein Sec61 subunit alpha isoform 1	*Sec61a1*	52.2
Phosphatidylinositide phosphatase SAC1	*Sacm1l*	66.9
CD109 antigen	*Cd109*	161.6
Keratin 90	*Krt90*	58.2
Neuropilin-1	*Nrp1*	102.9
Platelet-derived growth factor receptor alpha	*Pdgfra*	122.6
Aftiphilin	*Aftph*	101.1
Keratin, type II cytoskeletal 79	*Krt79*	57.5
Fibrillin-1	*Fbn1*	312.1
Calcium homeostasis endoplasmic reticulum protein	*Cherp*	107.6
Golgi integral membrane protein 4	*Golim4*	79.9
Tetraspanin-6	*Tspan6*	27.3
MKIAA4231 protein (Fragment)	*Col3a1*	139.2
Myomegalin	*Pde4dip*	63.2
Protein IWS1 homolog	*Iws1*	85.2
WASH complex subunit 4	*Washc4*	136.3
Uncharacterized protein	*Slc7a5*	55.8
Coatomer subunit gamma-1	*Copg1*	97.5
OTU domain-containing protein 4	*Otud4*	123
Tetraspanin	*Cd63*	26.8
Coatomer subunit beta	*Copb1*	107
Eukaryotic translation initiation factor 3 subunit C	*Eif3c*	105.5
Nuclear pore complex protein Nup214	*Nup214*	212.8
Methionine synthase	*Mtr*	139
Protein disulfide-isomerase A3	*Pdia3*	56.6
Sec24-related gene family, member B (S. cerevisiae)	*Sec24b*	135.5
E3 ubiquitin-protein ligase PDZRN3	*Pdzrn3*	119.3
Uncharacterized protein	*Hnrnpu*	87.9
40S ribosomal protein S9	*Rps9*	22.6

Protein Name	Gene Name	Molecular Weight (kDa)
Cyclin-dependent kinase 9	*Cdk9*	42.7
Pituitary tumor-transforming gene 1 protein-interacting protein	*Pttg1ip*	20
RRP12-like protein	*Rrp12*	143
Fibrillin-2	*Fbn2*	313.6
Frizzled-2	*Fzd2*	64
Keratin, type I cytoskeletal 13	*Krt13*	47.7
MKIAA0253 protein (Fragment)	*Ncstn*	79.8
Amyloid-beta A4 protein	*App*	86.7
Protein WWC2	*Wwc2*	132.5
Junction-mediating and -regulatory protein	*Jmy*	110.5
Phosphatidylinositol 3,4,5-trisphosphate 5-phosphatase 2	*Inppl1*	138.9
Interferon-induced transmembrane protein 3	*Ifitm3*	14.9
60S ribosomal protein L3	*Rpl3*	46.1
Phosphatidylinositide phosphatase SAC2	*Inpp5f*	127.5
Transmembrane 9 superfamily member (Fragment)	*Tm9sf3*	72.1
MKIAA0536 protein (Fragment)	*Prpf4b*	117.4
CD44 antigen	*Cd44*	85.8
Ribosomal_L18_c domain-containing protein	*Rpl5*	34.3
Protein arginine N-methyltransferase 1	*Prmt1*	42.4
SEC24 related gene family, member C (S. cerevisiae), isoform CRA_a	*Sec24c*	118.5
Eukaryotic translation initiation factor 4 gamma 3	*Eif4g3*	192.7
CUG triplet repeat, RNA binding protein 1, isoform CRA_b	*Celf1*	52.1
NADH dehydrogenase [ubiquinone] 1 beta subcomplex subunit 11, mitochondrial	*Ndufb11*	17.4
Macrosialin	*Cd68*	35.9
Golgi-specific brefeldin A-resistance factor 1	*Gbf1*	206.7
Proteolipid protein 2	*Plp2*	16.6
Solute carrier family 12, member 7	*Slc12a7*	119.4
Uncharacterized protein	*Stt3a*	85.8
Rho-associated protein kinase 1	*Rock1*	158.1
Protein PRRC2A	*Prrc2a*	229.1
Collagen type V alpha 3 chain	*Col5a3*	171.9
Nascent polypeptide-associated complex subunit alpha, muscle-specific form	*Naca*	220.4
Pleckstrin homology domain-containing family M member 2	*Plekhm2*	114.3
Secretory carrier-associated membrane protein	*Scamp2*	36.4
Protein disulfide-isomerase	*P4hb*	57
Transport and Golgi organization protein 1 homolog	*Mia3*	213.5
Latent-transforming growth factor beta-binding protein 2	*Ltbp2*	195.7
Nuclear exosome regulator NRDE2	*Nrde2*	133.4
Zinc transporter 7	*Slc30a7*	41.8
SEC63	*Sec63*	87.8
Protein argonaute-2	*Ago2*	97.2
SAPS domain family, member 3, isoform CRA_c	*Ppp6r3*	97.8

Protein Name	Gene Name	Molecular Weight (kDa)
Uncharacterized protein	*Hnrnpk*	51
G_PROTEIN_RECEP_F1_2 domain-containing protein	*Agtr2*	45.1
Plectin	*Plec*	533.9
Tubulin-specific chaperone D	*Tbcd*	133.2
Leucine-rich repeat-containing protein 15	*Lrrc15*	64.1
V-type proton ATPase subunit a	*Tcirg1*	93.4
Myb/SANT-like DNA-binding domain-containing protein 1	*Msantd1*	32.1
Small nuclear ribonucleoprotein Sm D1	*Snrpd1*	13.3
Caspase recruitment domain-containing protein 10	*Card10*	119.1
Transmembrane protein 43	*Tmem43*	44.8
Eukaryotic translation initiation factor 2-alpha kinase 3	*Eif2ak3*	124.6
Solute carrier family 12 member 2	*Slc12a2*	130.6
Little elongation complex subunit 2	*Ice2*	109.8
Nestin	*Nes*	207
40S ribosomal protein S27	*Rps27*	9.5
PRA1 family protein 3	*Arl6ip5*	21.5
Nuclear autoantigenic sperm protein	*Nasp*	84
Uncharacterized protein	*Surf4*	30.4
Transmembrane 9 superfamily member 4	*Tm9sf4*	74.6
Golgin subfamily A member 3	*Golga3*	167.2
Dolichyl-diphosphooligosaccharide--protein glycosyltransferase subunit 1	*Rpn1*	68.5
Suppression of tumorigenicity 5 protein	*St5*	126.8
Lysine-specific demethylase 4A	*Kdm4a*	120.3
Zinc finger CCCH domain-containing protein 4	*Zc3h4*	140.9
Histone deacetylase	*Hdac5*	121.9
Transmembrane and coiled-coil domain-containing protein 4	*Tmco4*	67.9
HIV Tat-specific factor 1 homolog	*Htatsf1*	86.2
Uncharacterized protein	*Rps23*	16
Chromatin assembly factor 1 subunit A	*Chaf1a*	101.9
Afadin	*Afdn*	207.2
60S ribosomal protein L27	*Rpl27*	15.8
Leucyl-tRNA synthetase, mitochondrial	*Lars2*	101.4
Serine/arginine repetitive matrix protein 1	*Srrm1*	106.8
Pleckstrin homology domain-containing family G member 5	*Plekhg5*	118.9
F-box only protein 38	*Fbxo38*	133.8
Transcriptional regulator ATRX	*Atrx*	278.4
Protocadherin 7	*Pcdh7*	136.7
ATP-dependent RNA helicase DHX30	*Dhx30*	136.6
Ras-related protein Rab-1B (Fragment)	*Rab1b*	28.2
Cingulin	*Cgn*	136.5
Uncharacterized protein	*Ptbp1*	59.2
Trafficking protein particle complex subunit 10	*Trappc10*	141.5
Tubulin beta-5 chain	*Tubb5*	49.6
PKS_ER domain-containing protein	*Vat1*	43.1

Protein Name	Gene Name	Molecular Weight (kDa)
Myadm protein	*Myadm*	35.3
RIKEN cDNA 5830416A07, isoform CRA_c	*Zc3h18*	108.2
Protein RER1	*Rer1*	23
Uncharacterized protein	*Pdia6*	48.6
1-phosphatidylinositol 4,5-bisphosphate phosphodiesterase gamma-1	*Plcg1*	149.6
Eukaryotic translation initiation factor 4 gamma 1	*Eif4g1*	176
Insulin-like growth factor 2 receptor	*Igf2r*	273.7
Nucleoporin 153	*Nup153*	151.9
Neighbor of Brca1 gene 1	*Nbr1*	109.9
Placenta-specific gene 8 protein	*Plac8*	12.3
Transmembrane protein 119	*Tmem119*	29.4
Formin-like protein 2	*Fmnl2*	123
Cadherin-2	*Cdh2*	99.7
Low-density lipoprotein receptor-related protein 11	*Lrp11*	51.8
Protein kish-A	*Tmem167a*	8.1
26S proteasome non-ATPase regulatory subunit 3	*Psmd3*	60.7
Cohesin subunit SA-2	*Stag2*	145.6
TBC1 domain family member 1	*Tbc1d1*	141.9

Appendix Table 6: The 387 protein hits identified through MS of FK2-immunoprecipitated protein fraction band 1b, prepared from Nedd4l$^{tm1b/tm1b}$-derived MEFs.

Protein Name	Gene Name	Molecular Weight (kDa)
Leucine-rich PPR motif-containing protein, mitochondrial	*Lrpprc*	156.5
Leucine--tRNA ligase, cytoplasmic	*Lars*	134.1
Regulator of nonsense transcripts 1	*Upf1*	123.9
Protein Niban 1	*Niban1*	102.6
AHNAK nucleoprotein (desmoyokin)	*Ahnak*	603.9
Extended synaptotagmin-1	*Esyt1*	121.5
Golgin subfamily A member 2	*Golga2*	116.2
Fibulin-2	*Fbln2*	131.7
Protein phosphatase 1 regulatory subunit 12A	*Ppp1r12a*	114.9
Low density lipoprotein receptor-related protein 1	*Lrp1*	504.4
Eukaryotic translation initiation factor 3 subunit A	*Eif3a*	161.8
DNA damage-binding protein 1	*Ddb1*	126.8
Band 4.1-like protein 2	*Epb41l2*	101.8
Erythrocyte protein band 4.1-like 2	*Epb41l2*	109.8
Alpha-mannosidase 2	*Man2a1*	131.5
Ubiquitin carboxyl-terminal hydrolase 7	*Usp7*	128.4
RAB11-binding protein RELCH	*Relch*	134.5
Constitutive coactivator of PPAR-gamma-like protein 1	*FAM120A*	121.6
Nidogen-1	*Nid1*	136.5
Collagen, type V, alpha 1	*Col5a1*	183.6
Cell cycle and apoptosis regulator protein 2	*Ccar2*	102.9
Thyroid hormone receptor-associated protein 3	*Thrap3*	108.1
Splicing factor 3b, subunit 3	*Sf3b3*	135.5
AP-3 complex subunit beta-1	*Ap3b1*	122.7
DNA-directed RNA polymerase II subunit RPB2	*Polr2b*	133.8
Inverted formin-2	*Inf2*	138.5
HIV Tat-specific factor 1 homolog	*Htatsf1*	86.2
Neural cell adhesion molecule 1	*Ncam1*	93.6
IF rod domain-containing protein	*Vim*	53.7
Uncharacterized protein	*Hdlbp*	141.7
Neural cell adhesion molecule 1	*Ncam1*	93.4
Epidermal growth factor receptor substrate 15	*Eps15*	98.4
Protein transport protein Sec31A	*Sec31a*	133.5
ELKS/Rab6-interacting/CAST family member 1	*Erc1*	128.3
Epidermal growth factor receptor substrate 15	*Eps15*	102.2
Bcl-2-associated transcription factor 1	*Bclaf1*	105.9
Integrin alpha-V	*Itgav*	115.3
Ataxin-2-like protein	*Atxn2l*	115.2
Bcl-2-associated transcription factor 1	*Bclaf1*	100.2
Probable ATP-dependent RNA helicase DDX46	*Ddx46*	117.4
Band 4.1-like protein 3	*Epb41l3*	103.3
Ubiquitin-associated protein 2-like	*Ubap2l*	116.7
Ubiquitin conjugation factor E4 B	*Ube4b*	147
Ataxin-2-like protein	*Atxn2l*	105.4

Protein Name	Gene Name	Molecular Weight (kDa)
Coatomer subunit beta'	*Copb2*	102.4
Slit homolog 3 (Drosophila)	*Slit3*	167.6
ATP-citrate synthase	*Acly*	120.7
Collagen alpha-2(VI) chain	*Col6a2*	110.3
Cullin-associated NEDD8-dissociated protein 1	*Cand1*	136.2
Latent-transforming growth factor beta-binding protein 3	*Ltbp3*	134.3
Ubiquitin associated protein 2-like, isoform CRA_b	*Ubap2l*	103.9
Inactive tyrosine-protein kinase 7	*Ptk7*	117.5
PUM-HD domain-containing protein	*Pum1*	126.6
Splicing factor 3B subunit 1	*Sf3b1*	145.7
Leucine-rich repeat flightless-interacting protein 1	*Lrrfip1*	79.2
Pyruvate carboxylase	*Pcx*	129.7
Alpha glucosidase 2 alpha neutral subunit	*Ganab*	109.3
Sodium/potassium-transporting ATPase subunit alpha-1	*Atp1a1*	112.9
Ribosome-binding protein 1	*Rrbp1*	172.8
Actin, beta	*Actb*	41.7
Calcium homeostasis endoplasmic reticulum protein	*Cherp*	107.6
Heat shock protein 84b	*Hsp90ab1*	83.2
SPT16, facilitates chromatin-remodeling subunit	*Supt16*	119.8
ATP-dependent RNA helicase DHX30	*Dhx30*	136.6
RNA polymerase-associated protein CTR9 homolog	*Ctr9*	133.3
La-related protein 1	*Larp1*	121.1
Exportin-5	*Xpo5*	136.9
Cadherin-2	*Cdh2*	99.7
Protein IWS1 homolog	*Iws1*	85.2
Reticulon-4	*Rtn4*	126.5
Fibronectin	*Fn1*	272.4
Golgi apparatus protein 1	*Glg1*	133.6
Eukaryotic translation initiation factor 3 subunit C	*Eif3c*	105.5
Platelet-derived growth factor receptor beta	*Pdgfrb*	123.3
Endosialin	*Cd248*	81.8
Rabankyrin-5	*Ankfy1*	128.6
Golgi integral membrane protein 4	*Golim4*	79.9
Ubiquitin conjugation factor E4 A	*Ube4a*	124.4
Isoleucine--tRNA ligase, cytoplasmic	*Iars*	144.2
Heat shock protein 90kDa beta (Grp94), member 1	*Hsp90b1*	92.4
Elongation factor 1-alpha 1	*Eef1a1*	50.1
Moesin	*Msn*	67.7
Eukaryotic translation initiation factor 3 subunit B	*Eif3b*	108.9
Actin, aortic smooth muscle	*Acta2*	42
Plasma membrane calcium-transporting ATPase 1	*Atp2b1*	134.7
Catenin beta-1	*Ctnnb1*	85.4
Uncharacterized protein	*Hnrnpu*	87.9
Filamin-A	*Flna*	281
Alpha-actinin-1	*Actn1*	103
Putative helicase MOV-10	*Mov10*	120.9

Protein Name	Gene Name	Molecular Weight (kDa)
Epidermal growth factor receptor	*Egfr*	134.8
MKIAA1329 protein (Fragment)	*Sorcs2*	131.5
Palladin	*Palld*	152
Delta-1-pyrroline-5-carboxylate synthase	*Aldh18a1*	87.2
Heat shock protein HSP 90-alpha	*Hsp90aa1*	84.7
Hypoxia up-regulated protein 1	*Hyou1*	111.1
Spectrin alpha chain, non-erythrocytic 1	*Sptan1*	287.4
Staphylococcal nuclease domain-containing protein	*Snd1*	102
Importin-9	*Ipo9*	116
Uncharacterized protein	*Eif4a1*	46.2
SAPS domain family, member 3, isoform CRA_c	*Ppp6r3*	97.8
E3 ubiquitin-protein ligase NEDD4	*Nedd4*	102.6
KH type-2 domain-containing protein	*Rps3*	26.7
Collagen alpha-1(I) chain	*Col1a1*	137.9
UDP-glucose:glycoprotein glucosyltransferase 1	*Uggt1*	176.3
Synaptopodin	*Synpo*	117.4
Coatomer subunit beta	*Copb1*	107
Fibronectin type III domain-containing protein 3B	*Fndc3b*	132.7
MKIAA0031 protein (Fragment)	*Eftud2*	109.7
ATPase, Ca++ transporting, cardiac muscle, slow twitch 2, isoform CRA_b (Fragment)	*Atp2a2*	116.5
FERM, ARHGEF and pleckstrin domain-containing protein 1	*Farp1*	118.8
Rab GTPase-activating protein 1	*Rabgap1*	120.7
Apoptotic protease-activating factor 1 (Fragment)	*Apaf1*	141.1
Structural maintenance of chromosomes protein 2	*Smc2*	134.2
Thrombospondin-1	*Thbs1*	129.6
Nardilysin, N-arginine dibasic convertase, NRD convertase 1	*Nrd1*	140.5
MKIAA4141 protein (Fragment)	*Slit2*	176.5
Obscurin-like protein 1	*Obsl1*	197.8
26S proteasome non-ATPase regulatory subunit 1	*Psmd1*	105.7
MKIAA0034 protein (Fragment)	*mKIAA0034*	192.4
RBR-type E3 ubiquitin transferase	*Ankib1*	122.5
Collagen alpha-1(XII) chain	*Col12a1*	340
Nodal modulator 1	*Nomo1*	133.3
SEC24 related gene family, member C (S. cerevisiae), isoform CRA_a	*Sec24c*	118.5
Codanin-1	*Cdan1*	135.8
Coatomer subunit gamma-1	*Copg1*	97.5
ATP synthase subunit alpha, mitochondrial	*Atp5f1a*	59.7
Guanine nucleotide exchange protein SMCR8	*Smcr8*	104.9
Calcium-transporting ATPase	*Atp2b4*	133
Alpha-actinin-4	*Actn4*	107
Integrin alpha-5	*Itga5*	115
Elongation factor 2	*Eef2*	95.3
Extended synaptotagmin-2	*Esyt2*	94.1
GST C-terminal domain-containing protein	*Vars*	140.1

Protein Name	Gene Name	Molecular Weight (kDa)
Collagen alpha-1(XI) chain	*Col11a1*	180.9
Endoplasmic reticulum chaperone BiP	*Hspa5*	72.4
RNA-binding protein 26	*Rbm26*	114.1
Plectin	*Plec*	533.9
Sec24-related gene family, member D (S. cerevisiae)	*Sec24d*	112.6
Mitochondrial 10-formyltetrahydrofolate dehydrogenase	*Aldh1l2*	101.5
Serine/arginine repetitive matrix protein 1	*Srrm1*	106.8
Pyruvate kinase PKM	*Pkm*	57.8
MCG11560	*Slc25a5*	32.9
Ubiquitin-associated protein 2	*Ubap2*	117.9
Tprkb protein	*Tprkb*	17.6
Nucleoporin_C domain-containing protein	*Nup133*	128.5
ADP/ATP translocase 1	*Slc25a4*	32.9
Ribosomal_L18_c domain-containing protein	*Rpl5*	34.3
Biglycan	*Bgn*	41.6
Glypican-4	*Gpc4*	62.5
PKS_ER domain-containing protein	*Vat1*	43.1
Tripeptidyl-peptidase 2	*Tpp2*	139.8
Rho-associated protein kinase 1	*Rock1*	158.1
WASH complex subunit 2	*Washc2*	145.2
Arf-GAP with SH3 domain, ANK repeat and PH domain-containing protein 1	*Asap1*	127.3
T-complex protein 1 subunit alpha	*Tcp1*	60.4
Interleukin-6 signal transductor	*il6st*	102.4
Serpin H1	*Serpinh1*	46.5
Serine/threonine-protein kinase 11-interacting protein	*Stk11ip*	117.9
Ataxin-2	*Atxn2*	136.4
Tight junction protein ZO-1	*Tjp1*	188.7
CLIP-associating protein 1	*Clasp1*	170.9
SEC23-interacting protein	*Sec23ip*	110.7
Uncharacterized protein	*Ctdp1*	104.5
Neuropilin-2	*Nrp2*	104.6
Family with sequence similarity 120, member C	*Fam120c*	119.6
Intersectin-2	*Itsn2*	191.6
General vesicular transport factor p115	*Uso1*	106.9
Drebrin	*Dbn1*	77.2
Protein transport protein Sec23A	*Sec23a*	86.1
DNA-binding protein SMUBP-2	*Ighmbp2*	109.3
26S proteasome non-ATPase regulatory subunit 2	*Psmd2*	100.2
Eukaryotic translation initiation factor 3 subunit L	*Eif3l*	66.6
KxDL motif-containing protein 1	*Kxd1*	26.8
Thrombospondin-3	*Thbs3*	104.1
Tubulin alpha-1B chain	*Tuba1b*	50.1
WASH complex subunit 5	*Washc5*	134
Uncharacterized protein	*Pdia6*	48.6
Uncharacterized protein	*Ddx39b*	54.6

Protein Name	Gene Name	Molecular Weight (kDa)
Cell division cycle and apoptosis regulator protein 1	*Ccar1*	132
Chondroitin sulfate proteoglycan 4	*Cspg4*	252.2
5-oxoprolinase	*Oplah*	137.5
MCG124046	*Prss1*	26.1
E3 ubiquitin-protein ligase PDZRN3	*Pdzrn3*	119.3
Ataxin-2 (Fragment)	*Atxn2*	43
Elongation factor-like GTPase 1	*Efl1*	125.7
Keratin, type II cytoskeletal 79	*Krt79*	57.5
Importin-7	*Ipo7*	119.4
Vacuolar protein sorting-associated protein 29	*Vps29*	5.7
Protein disulfide-isomerase A4	*Pdia4*	72.3
WASH complex subunit 4	*Washc4*	136.3
Uncharacterized protein	*Ddx39*	49.1
Keratin, type II cytoskeletal 1	*Krt1*	65.6
Keratin 90	*Krt90*	58.2
ESF1, nucleolar pre-rRNA processing protein, homolog (S. cerevisiae)	*Esf1*	98
2-oxoglutarate dehydrogenase, mitochondrial	*Ogdh*	116.4
Adhesion G protein-coupled receptor L3	*Adgrl3*	175.6
MKIAA0791 protein (Fragment)	*Nup155*	158.5
40S ribosomal protein S2	*Rps2*	31.2
Collagen alpha-2(V) chain	*Col5a2*	144.9
Collectin-12	*Colec12*	81.3
Intersectin-1	*Itsn1*	194.8
Neuropilin-1	*Nrp1*	102.9
Keratin, type II cytoskeletal 2 oral	*Krt76*	62.8
Fibrillin-2	*Fbn2*	313.6
WD_REPEATS_REGION domain-containing protein	*Dcaf5*	103.6
T-complex protein 1 subunit eta	*Cct7*	59.6
Mutant fibrillin-1	*Fbn1*	418
MKIAA0899 protein (Fragment)	*Ap2a2*	107.3
Tenascin	*Tnc*	231.7
General transcription factor II-I	*Gtf2i*	112.2
Oxoglutarate dehydrogenase-like	*Ogdhl*	116.5
Low-density lipoprotein receptor	*Ldlr*	94.9
Phosphatidylinositide phosphatase SAC1	*Sacm1l*	66.9
Tankyrase 1 binding protein 1	*Tnks1bp1*	181.7
U2 snRNP-associated SURP motif-containing protein	*U2surp*	118.2
Trafficking protein particle complex subunit 11	*Trappc11*	128.3
Lethal(2) giant larvae protein homolog 1	*Llgl1*	115.5
Amyloid-beta A4 protein	*App*	86.7
Methionine--tRNA ligase, cytoplasmic	*Mars*	102.3
Tubulin beta-5 chain	*Tubb5*	49.6
Nidogen-2	*Nid2*	153.8
Fibroblast growth factor receptor	*Fgfr1*	92.9
Rab3 GTPase-activating protein catalytic subunit	*Rab3gap1*	110.9

Protein Name	Gene Name	Molecular Weight (kDa)
Krt2 protein	*Krt2*	70.9
Glutamyl-prolyl-tRNA synthetase	*Eprs*	169.9
Erbb2 interacting protein	*Erbin*	162.1
ATP-dependent RNA helicase A	*Dhx9*	149.6
Transcription intermediary factor 1-alpha	*Trim24*	116.6
Uncharacterized protein	*Ptbp1*	59.2
THO complex subunit 2	*Thoc2*	182.7
Cytoplasmic FMR1-interacting protein 1	*Cyfip1*	145.1
RNA-binding protein 27	*Rbm27*	118.5
CD109 antigen	*Cd109*	161.6
CD44 antigen	*Cd44*	85.8
Kinesin family member 1B, isoform CRA_a	*Kif1b*	130
Filamin-B	*Flnb*	277.7
Keratin, type I cytoskeletal 17	*Krt17*	48.1
Coatomer subunit alpha	*Copa*	139.3
Glyceraldehyde-3-phosphate dehydrogenase	*Gapdh*	38.6
MKIAA4231 protein (Fragment)	*Col3a1*	139.2
DDB1- and CUL4-associated factor 6	*Dcaf6*	97.5
Choline transporter-like protein 2	*Slc44a2*	80.1
Tetraspanin	*Cd63*	26.8
Uncharacterized protein	*Luzp1*	124.1
Serine/arginine repetitive matrix protein 1 (Fragment)	*Srrm1*	16.2
Pre-mRNA-processing factor 40 homolog A	*Prpf40a*	108.4
Secretory carrier-associated membrane protein	*Gm45927*	88.9
60S ribosomal protein L3	*Rpl3*	46.1
E3 SUMO-protein ligase RanBP2	*Ranbp2*	340.9
L-lactate dehydrogenase	*Ldha*	39.7
Dolichyl-diphosphooligosaccharide--protein glycosyltransferase subunit 1	*Rpn1*	68.5
40S ribosomal protein S9	*Rps9*	22.6
Junction-mediating and -regulatory protein	*Jmy*	110.5
AHNAK nucleoprotein 2 (Fragment)	*Ahnak2*	166.4
T-complex protein 1 subunit gamma	*Cct3*	60.6
FAS-associated factor 2	*Faf2*	52.4
Tubulin-specific chaperone D	*Tbcd*	133.2
Neighbor of Brca1 gene 1	*Nbr1*	109.9
Eukaryotic translation initiation factor 4 gamma 1	*Eif4g1*	176
Transmembrane 9 superfamily member (Fragment)	*Tm9sf3*	72.1
Protein PRRC2A	*Prrc2a*	229.1
Paralemmin A kinase anchor protein (Fragment)	*Pakap*	126
Pinin	*Pnn*	82.5
MKIAA0002 protein (Fragment)	*Cct8*	60.2
AA_TRNA_LIGASE_II_ALA domain-containing protein	*Aars*	106.8
Protein arginine N-methyltransferase 1	*Prmt1*	42.4
Chromatin assembly factor 1 subunit A	*Chaf1a*	101.9

Protein Name	Gene Name	Molecular Weight (kDa)
Dolichyl-diphosphooligosaccharide--protein glycosyltransferase 48 kDa subunit	*Ddost*	49
Reticulon-3	*Rtn3*	103.8
Eukaryotic translation initiation factor 3 subunit H	*Eif3h*	39.8
Interferon-induced transmembrane protein 3	*Ifitm3*	14.9
AP2-associated protein kinase 1	*Aak1*	103.3
Anoctamin	*Ano6*	108.4
PAX3/FKHR fusion (Fragment)	*Pax3*	8.4
Epididymis-specific alpha-mannosidase	*Man2b2*	115.5
SH3 and PX domain-containing protein 2A	*Sh3pxd2a*	124.1
Atrial natriuretic peptide receptor 2	*Npr2*	117
Zinc finger CCCH domain-containing protein 4	*Zc3h4*	140.9
Keratin, type II cuticular Hb2	*Krt82*	57.1
Ephrin type-A receptor 4	*Epha4*	109.7
Protein RER1	*Rer1*	23
Trifunctional enzyme subunit alpha, mitochondrial	*Hadha*	82.6
Ras-related protein Rab-1B (Fragment)	*Rab1b*	28.2
Pericentrin	*Pcnt*	331.1
Uncharacterized protein	*Gm9889*	11.1
RAS p21 protein activator 1	*Rasa1*	115.4
Myb/SANT-like DNA-binding domain-containing protein 1	*Msantd1*	32.1
MKIAA0253 protein (Fragment)	*Ncstn*	79.8
Proteolipid protein 2	*Plp2*	16.6
Hdac6 protein	*Hdac6*	126
Integrin alpha-8	*Itga8*	117.5
Pre-mRNA-splicing factor ATP-dependent RNA helicase DHX15	*Dhx15*	90.9
MFLJ00087 protein (Fragment)	*Rasal3*	115.8
Coronin-1B	*Coro1b*	53.9
Predicted gene 45861	*Gm45861*	215.4
NADH dehydrogenase [ubiquinone] 1 beta subcomplex subunit 11, mitochondrial	*Ndufb11*	17.4
DNA polymerase delta catalytic subunit	*Pold1*	123.7
Dedicator of cytokinesis protein 7	*Dock7*	241.3
GDT1 family protein	*Tmem165*	34.8
Small nuclear ribonucleoprotein Sm D1	*Snrpd1*	13.3
F-box only protein 41	*Fbxo41*	94.3
WD repeat and HMG-box DNA-binding protein 1	*Wdhd1*	124.3
Paternally-expressed gene 3 protein	*Peg3*	178.8
Dolichyl-diphosphooligosaccharide--protein glycosyltransferase subunit 2 (Fragment)	*Rpn2*	72.1
Transitional endoplasmic reticulum ATPase	*Vcp*	89.3
Tyrosine-protein kinase	*Jak1*	133.3
Solute carrier family 12 member 6	*Slc12a6*	127.4
Rpl7a protein (Fragment)	*Rpl7a*	30.5
Transmembrane protease serine 11A	*Tmprss11a*	43.6

Protein Name	Gene Name	Molecular Weight (kDa)
Nascent polypeptide-associated complex subunit alpha, muscle-specific form	*Naca*	220.4
Plexin-B2	*Plxnb2*	206.1
Protein disulfide-isomerase	*P4hb*	57
Protein WWC2	*Wwc2*	132.5
Rps16 protein	*Rps16*	19.3
Rap guanine nucleotide exchange factor (GEF) 1	*Rapgef1*	136.4
Family with sequence similarity 40, member B	*Strip2*	96.2
MCG10343, isoform CRA_b	*Slc25a3*	39.7
Leucine-rich repeats and immunoglobulin-like domains protein 3	*Lrig3*	122.6
Transportin-1	*Tnpo1*	102.3
Protein argonaute-2	*Ago2*	97.2
Anti-VIPase light chain variable region (Fragment)	*Ap1b1*	12.2
AP complex subunit beta	*Car12*	104.9
Alpha-carbonic anhydrase domain-containing protein	*Arf4*	42.4
ADP-ribosylation factor 4	*Wdr11*	20.4
Bromodomain and WD repeat domain containing 2, isoform CRA_a	*Irf9*	135.9
Interferon regulatory factor 9	*Sfpq*	51.5
Splicing factor, proline- and glutamine-rich	*Sec63*	75.4
SEC63	*Aak1*	87.8
AP2-associated protein kinase 1 (Fragment)	*Calr*	54
Calreticulin	*Cand2*	48
TIP120 domain-containing protein	*Sec61a1*	135.5
Protein transport protein Sec61 subunit alpha isoform 1	*Mical1*	52.2
[F-actin]-monooxygenase MICAL1	*Stat2*	116.7
Signal transducer and activator of transcription	*Ppp4r1*	106.3
Serine/threonine-protein phosphatase 4 regulatory subunit 1	*NARS1*	106.3
Asparagine--tRNA ligase, cytoplasmic	*Myh9*	64.2
Myosin-9	*Hdac4*	226.2
Histone deacetylase 4	*Usp25*	118.5
Ubiquitin carboxyl-terminal hydrolase 25	*Rpl27*	121.3
60S ribosomal protein L27	*Arcn1*	15.8
Coatomer subunit delta	*Asph*	57.1
Aspartyl/asparaginyl beta-hydroxylase	*Prrc2c*	83
Protein PRRC2C	*Try10*	310.7
MCG140784	*Yipf4*	26.2
Protein YIPF4	*Dmd*	27.3
Dystrophin	*Afdn*	425.6
KOW domain-containing protein	*Hspa8*	17.2
Afadin	*Iqgap1*	207.2
Heat shock cognate 71 kDa protein	*Ifih1*	70.8
MKIAA0051 protein (Fragment)	*Colgalt1*	191.2
Melanoma differentiation-associated protein 5	*Dhx16*	115.9
Procollagen galactosyltransferase 1	*Anpep*	71

Protein Name	Gene Name	Molecular Weight (kDa)
DEAH (Asp-Glu-Ala-His) box polypeptide 16	*Col1a2*	119
Aminopeptidase N	*Myo1c*	109.6
Collagen alpha-2(I) chain	*Psmd6*	129.5
Unconventional myosin-Ic	*Adgrl2*	121.9
26S proteasome non-ATPase regulatory subunit 6	*Rps11*	45.5
Adhesion G protein-coupled receptor L2	*Prpf4b*	166.5
Ribosomal_S17_N domain-containing protein	*Eif2s1*	19.4
MKIAA0536 protein (Fragment)	*Sec24a*	117.4
Eukaryotic translation initiation factor 2 subunit 1	*Hectd1*	36.1
Protein transport protein Sec24A	*Hadhb*	118.7
E3 ubiquitin-protein ligase HECTD1	*Enpep*	289.9
Trifunctional enzyme subunit beta, mitochondrial	*Sptbn1*	51.4
Aminopeptidase	*Dcn*	107.9
Spectrin beta chain, non-erythrocytic 1	*Col27a1*	274.1
Decorin	*Cgn*	39.8
Collagen alpha-1(XXVII) chain	*Myadm*	186.2
Cingulin	*Zc3h18*	136.5
Myadm protein	*Slc7a5*	35.3
RIKEN cDNA 5830416A07, isoform CRA_c	*Dctn1*	108.2
Uncharacterized protein	*Pdia3*	55.8
Dynactin subunit 1	*Krt10*	141.6
Protein disulfide-isomerase A3	*Pabpc6*	56.6
Keratin, type I cytoskeletal 10	*Clcn3*	57.7
Polyadenylate-binding protein	*Tmem119*	71
H(+)/Cl(-) exchange transporter 3	*Wdr6*	90.8
Transmembrane protein 119	*Dars*	29.4
WD_REPEATS_REGION domain-containing protein	*Arl6ip5*	121.8
AA_TRNA_LIGASE_II domain-containing protein	*Surf4*	57.1
PRA1 family protein 3	*Kpnb1*	21.5
Uncharacterized protein	*Tm9sf4*	30.4
Importin subunit beta-1	*Gbf1*	97.1
Transmembrane 9 superfamily member 4	*Lrpprc*	74.6
Golgi-specific brefeldin A-resistance factor 1	*Lars*	206.7
Leucine-rich PPR motif-containing protein, mitochondrial	*Upf1*	156.5

Appendix Table 7: The 263 protein hits identified through MS of FK2-immunoprecipitated protein fraction band 2a, prepared from Nedd4l$^{+/+}$-derived MEFs.

Protein Name	Gene Name	Molecular Weight (kDa)
Extended synaptotagmin-1	*Esyt1*	121.5
Constitutive coactivator of PPAR-gamma-like protein 1	*FAM120A*	121.6
Drebrin	*Dbn1*	72.5
ADF-H domain-containing protein	*Dbn1*	72.4
Importin-7	*Ipo7*	119.4
DNA damage-binding protein 1	*Ddb1*	126.8
Uncharacterized protein	*Rab3gap1*	110.1
SAP domain-containing protein	*Sf3b2*	98.1
Protein transport protein Sec31A	*Sec31a*	133.5
AHNAK nucleoprotein (desmoyokin)	*Ahnak*	603.9
Squamous cell carcinoma antigen recognized by T-cells 3	*Sart3*	109.6
DNA helicase	*Mcm2*	103.1
Band 4.1-like protein 3 (Fragment)	*Epb41l3*	91.3
SEC23-interacting protein	*Sec23ip*	110.7
Vimentin	*Vim*	53.7
Band 4.1-like protein 3	*Epb41l3*	101.4
Eukaryotic translation initiation factor 3 subunit A	*Eif3a*	161.8
Cullin-associated NEDD8-dissociated protein 1	*Cand1*	136.2
Importin-9	*Ipo9*	116
Disks large homolog 1	*Dlg1*	100.8
Golgi integral membrane protein 4	*Golim4*	79.9
Non-SMC condensin I complex, subunit G	*Ncapg*	112.8
Rabankyrin-5	*Ankfy1*	128.6
Signal transducer and activator of transcription	*Stat2*	106.3
Golgin subfamily A member 2	*Golga2*	116.2
Regulator of nonsense transcripts 1	*Upf1*	123.9
Exportin-4	*Xpo4*	129.9
Fibulin-2	*Fbln2*	131.7
Coatomer subunit beta'	*Copb2*	102.4
Ubiquitin-like modifier-activating enzyme 6	*Uba6*	117.9
MKIAA0031 protein (Fragment)	*Eftud2*	109.7
Pyruvate carboxylase	*Pcx*	129.7
Coiled-coil and C2 domain-containing protein 1B	*Cc2d1b*	93
Serine/threonine-protein phosphatase 4 regulatory subunit 1	*Ppp4r1*	106.3
MKIAA1329 protein (Fragment)	*Sorcs2*	131.5
Leucine-rich PPR motif-containing protein, mitochondrial	*Lrpprc*	156.5
Sodium/potassium-transporting ATPase subunit alpha-1	*Atp1a1*	112.9
Neural cell adhesion molecule 1	*Ncam1*	119.4
Prostaglandin F2 receptor negative regulator	*Ptgfrn*	98.7
Uncharacterized protein	*Ror2*	104.8

Protein Name	Gene Name	Molecular Weight (kDa)
Serrate RNA effector molecule homolog	*Srrt*	100.4
FERM, ARHGEF and pleckstrin domain-containing protein 1	*Farp1*	118.8
Neural cell adhesion molecule 1	*Ncam1*	93.6
Thyroid hormone receptor-associated protein 3	*Thrap3*	108.1
SEC24 related gene family, member C (S. cerevisiae), isoform CRA_a	*Sec24c*	118.5
MKIAA1352 protein (Fragment)	*Lars*	137.7
Ankycorbin	*Rai14*	108.8
26S proteasome non-ATPase regulatory subunit 1	*Psmd1*	105.7
Putative helicase MOV-10	*Mov10*	120.9
Uncharacterized protein	*Hnrnpu*	87.9
Splicing factor 3b, subunit 3	*Sf3b3*	135.5
Low-density lipoprotein receptor	*Ldlr*	94.9
Neurabin-2	*Ppp1r9b*	89.5
Pumilio homolog 2	*Pum2*	114.2
Alpha v integrin	*Itgav*	115.2
Integrin beta-1	*Itgb1*	88.2
Nucleoprotein TPR	*Tpr*	273.8
ATP-citrate synthase	*Acly*	120.7
Uncharacterized protein	*Hdlbp*	141.7
Platelet-derived growth factor receptor beta	*Pdgfrb*	123.3
Eukaryotic translation initiation factor 4 gamma 1	*Eif4g1*	176
Actin, beta	*Actb*	41.7
CAP-Gly domain-containing linker protein 2	*Clip2*	115.8
Keratin, type II cytoskeletal 6A	*Krt6a*	59.3
Low density lipoprotein receptor-related protein 1	*Lrp1*	504.4
WASH complex subunit 5	*Washc5*	134
Elongation factor 1-alpha 1	*Eef1a1*	50.1
Reticulon-4	*Rtn4*	126.5
Eukaryotic translation initiation factor 3 subunit B	*Eif3b*	108.9
Ribosome-binding protein 1	*Rrbp1*	172.8
Smooth muscle gamma-actin	*Krt90*	42.9
Keratin 90	*Ipo4*	58.2
Importin-4	*Ccar2*	119.2
Cell cycle and apoptosis regulator protein 2	*Zfr*	102.9
Zinc finger RNA-binding protein	*Cwc22*	116.8
Pre-mRNA-splicing factor CWC22 homolog	*Krt5*	104.7
Keratin 5	*Krt79*	61.7
Keratin, type II cytoskeletal 79	*Atxn2l*	57.5
Ataxin-2-like protein	*Atxn2l*	115.2
Ataxin-2-like protein	*Ncstn*	105.4
MKIAA0253 protein (Fragment)	*Actn1*	79.8
Alpha-actinin-1	*Synpo*	103
Synaptopodin	*Pold1*	117.4
DNA polymerase delta catalytic subunit	*Man2a1*	123.7

Protein Name	Gene Name	Molecular Weight (kDa)
Alpha-mannosidase 2	*Eps15l1*	131.5
Epidermal growth factor receptor substrate 15-like 1	*Nrp2*	99.2
Neuropilin-2	*Ganab*	104.6
Alpha glucosidase 2 alpha neutral subunit	*Eif3c*	109.3
Eukaryotic translation initiation factor 3 subunit C	*Prss1*	105.5
MCG124046	*Rnf20*	26.1
E3 ubiquitin-protein ligase BRE1A	*Col5a1*	113.5
Collagen, type V, alpha 1	*Krt14*	183.6
Keratin, type I cytoskeletal 14	*Ube4a*	52.8
Ubiquitin conjugation factor E4 A	*Tnc*	124.4
Tenascin	*Krt1*	231.7
Keratin, type II cytoskeletal 1	*Rnf40*	65.6
E3 ubiquitin-protein ligase BRE1B	*Ece1*	113.9
Endothelin-converting enzyme 1	*Epha3*	87
Eph receptor A3	*Krt15*	110
Keratin 15, isoform CRA_a	*Mtrex*	49.5
Exosome RNA helicase MTR4	*Ubap2l*	117.6
Ubiquitin-associated protein 2-like	*Krt42*	116.7
Keratin, type I cytoskeletal 42	*Sf3b1*	50.1
Splicing factor 3B subunit 1	*Krt10*	145.7
Keratin, type I cytoskeletal 10	*Ctnnb1*	57.7
Catenin beta-1	*Krt2*	85.4
Krt2 protein	*Hsp90b1*	70.9
Heat shock protein 90kDa beta (Grp94), member 1	*Thbs1*	92.4
Thrombospondin-1	*Slit3*	129.6
Slit homolog 3 (Drosophila)	*Atp2a2*	167.6
ATPase, Ca++ transporting, cardiac muscle, slow twitch 2, isoform CRA_b (Fragment)	*Ranbp6*	116.5
Ran-binding protein 6	*Esyt2*	124.5
Extended synaptotagmin-2	*Adgrl2*	94.1
Adhesion G protein-coupled receptor L2	*Krt76*	166.5
Keratin, type II cytoskeletal 2 oral	*Itga6*	62.8
Itga6 protein (Fragment)	*Pkn1*	126.6
Serine/threonine-protein kinase N1	*Pakap*	104.3
Paralemmin A kinase anchor protein (Fragment)	*Slc25a5*	126
MCG11560	*Cdh2*	32.9
Cadherin-2	*Jak1*	99.7
Tyrosine-protein kinase	*Gaa*	133.3
Lysosomal alpha-glucosidase	*Tut1*	106.2
Speckle targeted PIP5K1A-regulated poly(A) polymerase	*Mia3*	94.5
Transport and Golgi organization protein 1 homolog	*Erc1*	213.5
ELKS/Rab6-interacting/CAST family member 1	*Col11a1*	128.3
Collagen alpha-1(XI) chain	*Aars*	180.9
AA_TRNA_LIGASE_II_ALA domain-containing protein	*Sec24a*	106.8
Protein transport protein Sec24A	*Epb41l2*	118.7

Protein Name	Gene Name	Molecular Weight (kDa)
Erythrocyte protein band 4.1-like 2	*Usp15*	109.8
Ubiquitin carboxyl-terminal hydrolase 15	*Ephb2*	112.3
Ephrin type-B receptor 2	*Pcdhgc3*	109.8
Protocadherin gamma C3	*Cd248*	101
Endosialin	*Krt78*	81.8
Keratin 78	*Kxd1*	112.2
KxDL motif-containing protein 1	*Bgn*	26.8
Biglycan	*Obsl1*	41.6
Obscurin-like protein 1	*Lig1*	197.8
DNA ligase	*Gm5478*	104
Predicted pseudogene 5478	*Specc1*	57.9
Cytospin-B	*Nedd4*	118
E3 ubiquitin-protein ligase NEDD4	*Flna*	102.6
Filamin-A	*Pum1*	281
PUM-HD domain-containing protein	*Slc25a4*	126.6
ADP/ATP translocase 1	*Ubap2*	32.9
Ubiquitin-associated protein 2	*Alkbh2*	117.9
DNA oxidative demethylase ALKBH2	*Cherp*	27.1
Calcium homeostasis endoplasmic reticulum protein	*Bclaf1*	107.6
Bcl-2-associated transcription factor 1	*Nedd4l*	105.9
E3 ubiquitin-protein ligase NEDD4-like	*Col3a1*	115.3
Type I epidermal keratin mRNA, 3'end (Fragment)	*Pttg1ip*	10.7
MKIAA4231 protein (Fragment)	*Ahnak2*	139.2
Pituitary tumor-transforming gene 1 protein-interacting protein	*Glg1*	20
AHNAK nucleoprotein 2 (Fragment)	*Xpo5*	166.4
Golgi apparatus protein 1	*Matr3*	133.6
Exportin 5	*Tbcd*	136.8
MCG121979, isoform CRA_c (Fragment)	*Map1s*	95.2
Tubulin-specific chaperone D	*Vcl*	133.2
Microtubule-associated protein 1S	*Usp7*	103
Vinculin	*Rbm19*	116.6
Ubiquitin carboxyl-terminal hydrolase 7	*Rps3*	132.8
Probable RNA-binding protein 19	*Emilin1*	106
KH type-2 domain-containing protein	*Niban1*	26.7
Uncharacterized protein	*Fnbp4*	107.5
Protein Niban 1	*K16*	102.6
Formin-binding protein 4	*Hspg2*	116.2
Keratin intermediate filament 16a	*Sec24d*	52
Basement membrane-specific heparan sulfate proteoglycan core protein	*Uba1*	469.5
Sec24-related gene family, member D (S. cerevisiae)	*App*	112.6
UBA_e1_C domain-containing protein	*Cd44*	124.2
Amyloid-beta A4 protein	*Cd63*	86.7
CD44 antigen	*Rtn3*	85.8
Tetraspanin	*Pacs1*	26.8

Protein Name	Gene Name	Molecular Weight (kDa)
Reticulon-3	*Fbn1*	103.8
Phosphofurin acidic cluster sorting protein 1	*Map7d1*	104.8
Fibrillin-1	*Ppfibp1*	312.1
MAP7 domain-containing protein 1	*Cand2*	93.2
Liprin-beta-1 (Fragment)	*Ppp1r12a*	20.5
TIP120 domain-containing protein	*U2surp*	135.5
Protein phosphatase 1 regulatory subunit 12A	*Ints6l*	114.9
U2 snRNP-associated SURP motif-containing protein	*Taok1*	118.2
Integrator complex subunit 6-like	*Atp2b4*	96.9
MCG124812	*Atp2b2*	116
Calcium-transporting ATPase	*Eprs*	133
Calcium-transporting ATPase	*Eif4a2*	136.7
Glutamyl-prolyl-tRNA synthetase	*Col6a1*	169.9
Eukaryotic initiation factor 4A-II	*Oga*	46.4
Collagen alpha-1(VI) chain	*Eif3l*	108.4
Protein O-GlcNAcase	*Nrp1*	103.1
Eukaryotic translation initiation factor 3 subunit L	*Pdgfra*	66.6
Neuropilin-1	*Rpl3*	102.9
Platelet-derived growth factor receptor alpha	*Dlg3*	122.6
60S ribosomal protein L3	*Tuba1b*	46.1
Discs, large homolog 3 (Drosophila), isoform CRA_c (Fragment)	*Tm9sf3*	103.8
Tubulin alpha-1B chain	*Cald1*	50.1
Transmembrane 9 superfamily member (Fragment)	*Psmd2*	72.1
Caldesmon 1	*Gpc4*	89.2
26S proteasome non-ATPase regulatory subunit 2	*Prpf40a*	100.2
Glypican-4	*Hectd1*	62.5
Pre-mRNA-processing factor 40 homolog A	*Tmem119*	108.4
E3 ubiquitin-protein ligase HECTD1	*Dhx30*	289.9
Transmembrane protein 119	*Try10*	29.4
ATP-dependent RNA helicase DHX30	*Llgl1*	136.6
MCG140784	*Srrm1*	26.2
Lethal(2) giant larvae protein homolog 1	*Fn1*	115.5
Serine/arginine repetitive matrix protein 1 (Fragment)	*Msn*	16.2
Fibronectin	*Ifitm3*	272.4
Moesin	*Nes*	67.7
Interferon-induced transmembrane protein 3	*Radil*	14.9
Nestin	*Xntrpc*	207
Ras-associating and dilute domain-containing protein	*Ddx39b*	120.3
Xndc1-transient receptor potential cation channel, subfamily C, member 2 readthrough	*Hsp90aa1*	140.6
Uncharacterized protein	*Pacs2*	54.6
Heat shock protein HSP 90-alpha	*Nol4*	84.7
Phosphofurin acidic cluster sorting protein 2	*Ppfibp1*	98.1
Uncharacterized protein (Fragment)	*Lrrc15*	46
Liprin-beta-1 (Fragment)	*R3hcc1l*	26.8

Protein Name	Gene Name	Molecular Weight (kDa)
Leucine-rich repeat-containing protein 15	*Snd1*	64.1
Coiled-coil domain-containing protein R3HCC1L	*Nsun2*	84.4
Staphylococcal nuclease domain-containing protein	*Ogdhl*	102
SAM_MT_RSMB_NOP domain-containing protein	*Slc25a3*	88
Oxoglutarate dehydrogenase-like	*Aak1*	116.5
MCG10343, isoform CRA_b	*Thbd*	39.7
AP2-associated protein kinase 1	*Akap1*	103.3
Thbd protein	*Hspa5*	61.8
A-kinase anchor protein 1, mitochondrial	*Peg3*	92.1
Endoplasmic reticulum chaperone BiP	*Tspan6*	72.4
Paternally-expressed gene 3 protein	*Gm45927*	178.8
Tetraspanin-6	*Heatr6*	27.3
Secretory carrier-associated membrane protein	*Spag9*	88.9
HEAT repeat-containing protein 6	*Ktn1*	128.8
C-Jun-amino-terminal kinase-interacting protein 4	*Styxl1*	146.1
Kinectin	*Cast*	152.4
Serine/threonine/tyrosine interacting-like 1, isoform CRA_c	*Apba1*	37.6
Calpastatin	*Cc2d1a*	84.9
Uncharacterized protein	*Rps2*	93
Coiled-coil and C2 domain-containing protein 1A	*Rer1*	103.6
40S ribosomal protein S2	*Slc7a5*	32.1
Protein RER1	*Pnisr*	23
Uncharacterized protein	*Col1a2*	55.8
Arginine/serine-rich protein PNISR	*Erbin*	93.1
Collagen alpha-2(I) chain	*Insrr*	129.5
Erbb2 interacting protein	*Ipo5*	162.1
Insulin receptor-related protein	*Oxr1*	144.8
Importin-5	*Itsn1*	123.5
Oxidation resistance protein 1	*Col1a1*	95.9
Intersectin-1	*Ran*	194.8
Collagen alpha-1(I) chain	*Sulf2*	137.9
GTP-binding nuclear protein Ran	*Calr*	24.4
MKIAA1247 protein (Fragment)	*Tubb5*	108.1
Calreticulin	*2210010C04Rik*	48
Tubulin beta-5 chain	*Ano6*	49.6
RIKEN cDNA 2210010C04 gene	*Sacm1l*	26.4
Anoctamin	*Uso1*	108.4
Phosphatidylinositide phosphatase SAC1	*Itga3*	66.9
General vesicular transport factor p115	*Colec12*	106.9
Integrin alpha-3	*Lamp1*	116.7
Collectin-12	*Chtf18*	81.3
Lysosomal membrane glycoprotein 1, isoform CRA_a	*Ndufb11*	43.9
Chromosome transmission fidelity protein 18 homolog	*Sec23a*	108.1
NADH dehydrogenase [ubiquinone] 1 beta subcomplex subunit 11, mitochondrial	*Aak1*	17.4

Protein Name	Gene Name	Molecular Weight (kDa)
Protein transport protein Sec23A	*Esyt1*	86.1
AP2-associated protein kinase 1 (Fragment)	*FAM120A*	54
Extended synaptotagmin-1	*Dbn1*	121.5

Appendix Table 8: The 375 protein hits identified through MS of FK2-immunoprecipitated protein fraction band 2b, prepared from Nedd4l$^{tm1b/tm1b}$-derived MEFs.

Protein Name	Gene Name	Molecular Weight (kDa)
Extended synaptotagmin-1	*Esyt1*	121.5
SAP domain-containing protein	*Sf3b2*	98.1
SAP domain-containing protein	*Sf3b2*	98.2
AHNAK nucleoprotein (desmoyokin)	*Ahnak*	603.9
Squamous cell carcinoma antigen recognized by T-cells 3	*Sart3*	109.6
Protein transport protein Sec31A	*Sec31a*	133.5
Drebrin	*Dbn1*	72.5
ADF-H domain-containing protein	*Dbn1*	72.4
Uncharacterized protein	*Rab3gap1*	110.1
Constitutive coactivator of PPAR-gamma-like protein 1	*FAM120A*	121.6
Cullin-associated NEDD8-dissociated protein 1	*Cand1*	136.2
DNA helicase	*Mcm2*	103.1
Vimentin	*Vim*	53.7
Protein transport protein Sec31A (Fragment)	*Sec31a*	101
DNA damage-binding protein 1	*Ddb1*	126.8
SEC23-interacting protein	*Sec23ip*	110.7
Disks large homolog 1	*Dlg1*	100.1
130kDa Protein 4.1B MEF cell isoform	*Epb41l3*	97.5
Eukaryotic translation initiation factor 3 subunit A	*Eif3a*	161.8
Band 4.1-like protein 3 (Fragment)	*Epb41l3*	91.3
Golgi integral membrane protein 4	*Golim4*	79.9
Importin-7	*Ipo7*	119.4
Non-SMC condensin I complex, subunit G	*Ncapg*	112.8
ATP-citrate synthase	*Acly*	120.7
Eukaryotic translation initiation factor 3 subunit B	*Eif3b*	108.9
Alpha glucosidase 2 alpha neutral subunit	*Ganab*	109.3
Importin-9	*Ipo9*	116
MKIAA0031 protein (Fragment)	*Eftud2*	109.7
Eukaryotic translation initiation factor 3 subunit C	*Eif3c*	105.5
Coatomer subunit beta'	*Copb2*	102.4
Golgin subfamily A member 2	*Golga2*	116.2
Leucine-rich PPR motif-containing protein, mitochondrial	*Lrpprc*	156.5
Rabankyrin-5	*Ankfy1*	128.6
Uncharacterized protein	*Hnrnpu*	87.9
Pyruvate carboxylase	*Pcx*	129.7
Nucleoprotein TPR	*Tpr*	273.8
Ubiquitin-like modifier-activating enzyme 6	*Uba6*	117.9
WASH complex subunit 5	*Washc5*	134
Regulator of nonsense transcripts 1	*Upf1*	123.9
E3 ubiquitin-protein ligase NEDD4	*Nedd4*	102.6
Reticulon	*Rtn4*	38.5

Protein Name	Gene Name	Molecular Weight (kDa)
Serine/threonine-protein phosphatase 4 regulatory subunit 1	*Ppp4r1*	106.3
Alpha-actinin-1	*Actn1*	103
Putative helicase MOV-10	*Mov10*	120.9
Fibulin-2	*Fbln2*	131.7
Heat shock protein 90kDa beta (Grp94), member 1	*Hsp90b1*	92.4
Vinculin	*Vcl*	116.6
Zinc finger RNA-binding protein	*Zfr*	116.8
Sodium/potassium-transporting ATPase subunit alpha-1	*Atp1a1*	112.9
MKIAA1329 protein (Fragment)	*Sorcs2*	131.5
Actin, beta	*Actb*	41.7
E3 ubiquitin-protein ligase BRE1B	*Rnf40*	113.9
Thyroid hormone receptor-associated protein 3	*Thrap3*	108.1
Catenin beta-1	*Ctnnb1*	85.4
E3 ubiquitin-protein ligase BRE1A	*Rnf20*	113.5
Uncharacterized protein	*Ror2*	104.8
Coiled-coil and C2 domain-containing protein 1B	*Cc2d1b*	93
Ankycorbin	*Rai14*	108.8
Uncharacterized protein	*Hdlbp*	141.7
Exportin-4	*Xpo4*	129.9
Signal transducer and activator of transcription	*Stat2*	106.3
SEC24 related gene family, member C (S. cerevisiae), isoform CRA_a	*Sec24c*	118.5
Ribosome-binding protein 1	*Rrbp1*	172.8
Staphylococcal nuclease domain-containing protein	*Snd1*	102
Elongation factor 1-alpha 1	*Eef1a1*	50.1
Pumilio homolog 2	*Pum2*	114
Splicing factor 3b, subunit 3	*Sf3b3*	135.5
MKIAA1352 protein (Fragment)	*Lars*	137.7
Alpha v integrin	*Itgav*	115.2
FERM, ARHGEF and pleckstrin domain-containing protein 1	*Farp1*	118.8
2-oxoglutarate dehydrogenase, mitochondrial	*Ogdh*	116.4
Moesin	*Msn*	67.7
Filamin-A	*Flna*	281
Coatomer subunit beta	*Copb1*	107
CAP-Gly domain-containing linker protein 2	*Clip2*	115.8
Ataxin-2-like protein	*Atxn2l*	115.2
Neurabin-2	*Ppp1r9b*	89.5
Heat shock protein 84b	*Hsp90ab1*	83.2
Actin, alpha cardiac muscle 1	*Actc1*	42
Neural cell adhesion molecule 1	*Ncam1*	119.4
Elongation factor 2	*Eef2*	95.3
Low density lipoprotein receptor-related protein 1	*Lrp1*	504.4
Ataxin-2-like protein	*Atxn2l*	105.4

Protein Name	Gene Name	Molecular Weight (kDa)
Platelet-derived growth factor receptor beta	*Pdgfrb*	123.3
Synaptopodin	*Synpo*	117.4
General vesicular transport factor p115	*Uso1*	106.9
Neural cell adhesion molecule 1	*Ncam1*	93.6
Keratin, type I cytoskeletal 10	*Krt10*	57.7
Delta-1-pyrroline-5-carboxylate synthase	*Aldh18a1*	87.2
26S proteasome non-ATPase regulatory subunit 1	*Psmd1*	105.7
Cell cycle and apoptosis regulator protein 2	*Ccar2*	102.9
ATPase, Ca++ transporting, cardiac muscle, slow twitch 2, isoform CRA_b (Fragment)	*Atp2a2*	116.5
UBA_e1_C domain-containing protein	*Uba1*	124.2
Uncharacterized protein	*Emilin1*	107.5
Low-density lipoprotein receptor	*Ldlr*	94.9
Sec24-related gene family, member D (S. cerevisiae)	*Sec24d*	112.6
Bcl-2-associated transcription factor 1	*Bclaf1*	105.9
Alpha-actinin-4	*Actn4*	107
Exosome RNA helicase MTR4	*Mtrex*	117.6
Prostaglandin F2 receptor negative regulator	*Ptgfrn*	98.7
SAPS domain family, member 3, isoform CRA_c	*Ppp6r3*	97.8
Erythrocyte protein band 4.1-like 2	*Epb41l2*	109.8
Caldesmon 1	*Cald1*	89.2
Integrin beta-1	*Itgb1*	88.2
Heat shock protein HSP 90-alpha	*Hsp90aa1*	84.7
Probable RNA-binding protein 19	*Rbm19*	106
Adhesion G protein-coupled receptor L2	*Adgrl2*	166.5
Keratin 5	*Krt5*	61.7
Transport and Golgi organization protein 1 homolog	*Mia3*	213.5
MCG124046	*Prss1*	26.1
PUM-HD domain-containing protein	*Pum1*	126.6
Eukaryotic translation initiation factor 4 gamma 1	*Eif4g1*	176
Epidermal growth factor receptor substrate 15-like 1	*Eps15l1*	99.2
Collagen, type V, alpha 1	*Col5a1*	183.6
Keratin, type II cytoskeletal 1	*Krt1*	65.6
T-complex protein 1 subunit alpha	*Tcp1*	60.4
ADP/ATP translocase 1	*Slc25a4*	32.9
ATP synthase subunit alpha, mitochondrial	*Atp5f1a*	59.7
Extended synaptotagmin-2	*Esyt2*	94.1
Collagen alpha-1(XI) chain	*Col11a1*	180.9
AA_TRNA_LIGASE_II_ALA domain-containing protein	*Aars*	106.8
Cadherin-2	*Cdh2*	99.7
Paralemmin A kinase anchor protein (Fragment)	*Pakap*	126
Neuropilin-2	*Nrp2*	104.6
Coatomer subunit gamma-1	*Copg1*	97.5
Uncharacterized protein	*Eif4a1*	46.2
MKIAA0899 protein (Fragment)	*Ap2a2*	107.3
Microtubule-associated protein 1S	*Map1s*	103

Protein Name	Gene Name	Molecular Weight (kDa)
Ubiquitin conjugation factor E4 A	*Ube4a*	124.4
Inactive phospholipase C-like protein 1	*Plcl1*	122.6
MKIAA0034 protein (Fragment)	*mKIAA0034*	192.4
Glypican-4	*Gpc4*	62.5
Pyruvate kinase PKM	*Pkm*	57.8
Keratin, type II cytoskeletal 1b	*Krt77*	61.3
Oxoglutarate dehydrogenase-like	*Ogdhl*	116.5
AP complex subunit beta	*Ap2b1*	105.7
Ribosomal protein S3	*Rps3*	26.7
MCG11560	*Slc25a5*	32.9
26S proteasome non-ATPase regulatory subunit 2	*Psmd2*	100.2
Keratin, type I cytoskeletal 13	*Krt13*	47.7
Golgi apparatus protein 1	*Glg1*	133.6
Splicing factor 3B subunit 1	*Sf3b1*	145.7
Promyelocytic leukemia	*Pml*	98.2
Serrate RNA effector molecule homolog	*Srrt*	100.4
Protein transport protein Sec24A	*Sec24a*	118.7
Ephrin type-A receptor 3	*Epha3*	109.9
Pre-mRNA-processing factor 40 homolog A	*Prpf40a*	108.4
Eph receptor A3	*Epha3*	110
MKIAA0253 protein (Fragment)	*Ncstn*	79.8
Calcium homeostasis endoplasmic reticulum protein	*Cherp*	107.6
Endothelin-converting enzyme 1	*Ece1*	87
Obscurin-like protein 1	*Obsl1*	197.8
Keratin, type II cytoskeletal 2 oral	*Krt76*	62.8
DNA ligase	*Lig1*	104
Tyrosine-protein kinase	*Jak1*	133.3
Thrombospondin-1	*Thbs1*	129.6
Speckle targeted PIP5K1A-regulated poly(A) polymerase	*Tut1*	94.5
ELKS/Rab6-interacting/CAST family member 1	*Erc1*	128.3
Cytospin-B	*Specc1*	117
Ephrin type-B receptor 2	*Ephb2*	109.8
Mitochondrial 10-formyltetrahydrofolate dehydrogenase	*Aldh1l2*	101.5
Importin-5	*Ipo5*	123.5
Ubiquitin-associated protein 2-like	*Ubap2l*	116.7
Kinectin	*Ktn1*	152.4
Krt2 protein	*Krt2*	70.9
MKIAA4231 protein (Fragment)	*Col3a1*	139.2
Tubulin-specific chaperone D	*Tbcd*	133.2
AP complex subunit beta	*Ap1b1*	104.9
Amyloid-beta A4 protein	*App*	86.7
Eukaryotic translation initiation factor 3 subunit L	*Eif3l*	66.6
AP-2 complex subunit alpha-1	*Ap2a1*	107.6
Importin-4	*Ipo4*	119.2

Protein Name	Gene Name	Molecular Weight (kDa)
Keratin 90	*Krt90*	58.2
Collagen alpha-1(VI) chain	*Col6a1*	108.4
Serpin H1	*Serpinh1*	46.5
Lysosomal alpha-glucosidase	*Gaa*	106.2
PKS_ER domain-containing protein	*Vat1*	43.1
Endosialin	*Cd248*	81.8
Protein Niban 1	*Niban1*	102.6
Platelet-derived growth factor receptor alpha	*Pdgfra*	122.6
Caldesmon 1 (Fragment)	*Cald1*	41.3
Integrin alpha-3	*Itga3*	116.7
Aspartyl/asparaginyl beta-hydroxylase	*Asph*	83
Keratin, type II cytoskeletal 79	*Krt79*	57.5
Ubiquitin carboxyl-terminal hydrolase 7	*Usp7*	132.8
Exportin 5	*Xpo5*	136.8
DNA polymerase delta catalytic subunit	*Pold1*	123.7
Pre-mRNA-splicing factor CWC22 homolog	*Cwc22*	104.7
Tubulin alpha-1B chain	*Tuba1b*	50.1
Slit homolog 3 (Drosophila)	*Slit3*	167.6
Nidogen-1	*Nid1*	136.5
RAS p21 protein activator 1	*Rasa1*	115.4
Tubulin beta-5 chain	*Tubb5*	49.6
Ran-binding protein 6	*Ranbp6*	124.5
Serine/threonine-protein kinase N1	*Pkn1*	104.3
Tenascin	*Tnc*	231.7
Biglycan	*Bgn*	41.6
MCG124812	*Taok1*	116
Uncharacterized protein	*Ddx39*	49.1
Uncharacterized protein	*Ddx39b*	54.6
Transmembrane protein 119	*Tmem119*	29.4
Methionine--tRNA ligase, cytoplasmic	*Mars*	102.3
Nck-associated protein 1	*Nckap1*	129.4
Protein transport protein Sec23A	*Sec23a*	86.1
ATP-dependent RNA helicase DHX30	*Dhx30*	136.6
Protein phosphatase 1 regulatory subunit 12A	*Ppp1r12a*	114.9
Keratin, type I cytoskeletal 14	*Krt14*	52.8
Ubiquitin-associated protein 2	*Ubap2*	117.9
Transitional endoplasmic reticulum ATPase	*Vcp*	89.3
Predicted pseudogene 5478	*Gm5478*	57.9
C230096C10Rik protein	*Emc1*	111.6
Formin-binding protein 4	*Fnbp4*	116.2
Alpha-mannosidase 2	*Man2a1*	131.5
Arginine/serine-rich protein PNISR	*Pnisr*	93.1
MCG140784	*Try10*	26.2
Uncharacterized protein	*Ptbp1*	59.2
DEAH (Asp-Glu-Ala-His) box polypeptide 37	*Dhx37*	128.2
MAP7 domain-containing protein 1	*Map7d1*	93.2

Protein Name	Gene Name	Molecular Weight (kDa)
Inactive tyrosine-protein kinase 7	*Ptk7*	117.5
Keratin 78	*Krt78*	112.2
CD44 antigen	*Cd44*	85.8
Itga6 protein (Fragment)	*Itga6*	126.6
MKIAA1247 protein (Fragment)	*Sulf2*	108.1
KxDL motif-containing protein 1	*Kxd1*	26.8
Dolichyl-diphosphooligosaccharide--protein glycosyltransferase subunit 1	*Rpn1*	68.5
Collectin-12	*Colec12*	81.3
Fibrillin-1	*Fbn1*	312.1
T-complex protein 1 subunit eta	*Cct7*	59.6
Tetraspanin	*Cd63*	26.8
Calcium-transporting ATPase	*Atp2b2*	136.7
Phosphofurin acidic cluster sorting protein 1	*Pacs1*	104.8
Phosphatidylinositide phosphatase SAC1	*Sacm1l*	66.9
Anoctamin	*Ano6*	108.4
Erbb2 interacting protein	*Erbin*	162.1
60S ribosomal protein L3	*Rpl3*	46.1
Neuropilin-1	*Nrp1*	102.9
Protein disulfide-isomerase A3	*Pdia3*	56.6
Ubiquitin carboxyl-terminal hydrolase 15	*Usp15*	112.3
Glutamyl-prolyl-tRNA synthetase	*Eprs*	169.9
Intersectin-1	*Itsn1*	194.8
Coiled-coil and C2 domain-containing protein 1A	*Cc2d1a*	103.6
Protein disulfide-isomerase A4	*Pdia4*	72.3
Oxidation resistance protein 1	*Oxr1*	95.9
Lethal(2) giant larvae protein homolog 1	*Llgl1*	115.5
AHNAK nucleoprotein 2 (Fragment)	*Ahnak2*	166.4
L-lactate dehydrogenase	*Ldha*	39.7
Ephrin type-B receptor 3	*Ephb3*	109.6
Protein O-GlcNAcase	*Oga*	103.1
ARHGEF2 (Fragment)	*ARHGEF2*	112.1
Leucine-rich repeat-containing protein 15	*Lrrc15*	64.1
MCG10343, isoform CRA_b	*Slc25a3*	39.7
Leucine-rich repeat flightless-interacting protein 1	*Lrrfip1*	79.2
Endoplasmic reticulum chaperone BiP	*Hspa5*	72.4
Splicing factor 3A subunit 1	*Sf3a1*	88.5
Uncharacterized protein	*Ddx21*	93.5
Tr-type G domain-containing protein	*Eif2s3x*	51.1
Very low-density lipoprotein receptor	*Vldlr*	96.3
La-related protein 1	*Larp1*	121.1
Serine/arginine repetitive matrix protein 1 (Fragment)	*Srrm1*	16.2
Keratin, type I cytoskeletal 42	*Krt42*	50.1
E3 ubiquitin-protein ligase HECTD1	*Hectd1*	289.9
Uncharacterized protein	*Pdia6*	48.6
Trifunctional enzyme subunit alpha, mitochondrial	*Hadha*	82.6

Protein Name	Gene Name	Molecular Weight (kDa)
Lysosomal membrane glycoprotein 1, isoform CRA_a	*Lamp1*	43.9
40S ribosomal protein S2	*Rps2*	31.2
Cell division cycle and apoptosis regulator protein 1	*Ccar1*	132
Thbd protein	*Thbd*	61.8
Integrin alpha-7	*Itga7*	129.2
Chromosome transmission fidelity protein 18 homolog	*Chtf18*	108.1
MKIAA0002 protein (Fragment)	*Cct8*	60.2
Collagen alpha-2(VI) chain	*Col6a2*	110.3
Calreticulin	*Calr*	48
GTP-binding nuclear protein Ran	*Rasl2-9*	24.4
Collagen alpha-1(I) chain	*Col1a1*	137.9
Coatomer subunit delta	*Arcn1*	57.1
Protocadherin gamma C3	*Pcdhgc3*	101
Ribosomal_L18_c domain-containing protein	*Rpl5*	34.3
Basement membrane-specific heparan sulfate proteoglycan core protein	*Hspg2*	469.5
Collagen alpha-2(V) chain	*Col5a2*	144.9
Uncharacterized protein	*Slc7a5*	55.8
Lysosomal membrane glycoprotein 2, isoform CRA a	*Lamp2*	45.8
Procollagen galactosyltransferase 1	*Colgalt1*	71
40S ribosomal protein S9	*Rps9*	22.6
Polyadenylate-binding protein	*Pabpc6*	71
SAM and SH3 domain-containing protein 1	*Sash1*	135.5
Fibronectin	*Fn1*	272.4
Dolichyl-diphosphooligosaccharide--protein glycosyltransferase subunit 2 (Fragment)	*Rpn2*	72.1
Ubiquitin carboxyl-terminal hydrolase 47	*Usp47*	157.1
Protein argonaute-2	*Ago2*	97.2
T-complex protein 1 subunit delta	*Cct4*	58
U2 snRNP-associated SURP motif-containing protein	*U2surp*	118.2
Uncharacterized protein	*Gm6994*	16.2
Sodium/potassium-transporting ATPase subunit alpha	*Atp4a*	114
Uncharacterized protein	*Ror1*	104.1
Ral GTPase-activating protein subunit alpha-2	*Ralgapa2*	218.9
DNA helicase	*Mcm3*	91.5
Cytosolic phospholipase A2	*Pla2g4a*	85.2
Nascent polypeptide-associated complex subunit alpha, muscle-specific form	*Naca*	220.4
ADP-ribosylation factor 4	*Arf4*	20.4
Liprin-beta-1 (Fragment)	*Ppfibp1*	20.5
Tetraspanin-6	*Tspan6*	27.3
CD98 heavy chain	*Slc3a2*	58.8
Family with sequence similarity 40, member B	*Strip2*	96.2
RIKEN cDNA C330023M02, isoform CRA_a	*Naa25*	111.6
Citrate synthase, mitochondrial	*Cs*	51.7
MCG121979, isoform CRA_c (Fragment)	*Matr3*	95.2

Protein Name	Gene Name	Molecular Weight (kDa)
Receptor-type tyrosine-protein kinase FLT3	*Flt3*	113.3
Latent-transforming growth factor beta-binding protein 3	*Ltbp3*	134.3
Laminin B1 subunit 1	*Lamb1*	202.3
Coronin-1B	*Coro1b*	53.9
Transportin-1	*Tnpo1*	102.3
Splicing factor, proline- and glutamine-rich	*Sfpq*	75.4
Lysosomal-trafficking regulator	*Lyst*	425
DNA-directed RNA polymerase II subunit RPB2	*Polr2b*	133.8
Manganese-transporting ATPase 13A1	*Atp13a1*	132.3
Transmembrane 9 superfamily member (Fragment)	*Tm9sf3*	72.1
Rps16 protein	*Rps16*	19.3
Focal ashension kinase 1	*Ptk2*	121
Tankyrase 1 binding protein 1	*Tnks1bp1*	181.7
Protein transport protein Sec61 subunit alpha isoform 1	*Sec61a1*	52.2
Calpastatin	*Cast*	84.9
Nodal modulator 1	*Nomo1*	133.3
GON-4-like protein	*Gon4l*	248.6
Fibrillin-2	*Fbn2*	313.6
Integrator complex subunit 3	*Ints3*	117.9
HEAT repeat-containing protein 6	*Heatr6*	128.8
Glyceraldehyde-3-phosphate dehydrogenase	*Gapdh*	38.6
Serine/threonine-protein phosphatase 4 regulatory subunit 3A	*Ppp4r3a*	95.3
Uncharacterized protein	*Apba1*	93
Uncharacterized protein	*Surf4*	30.4
Choline transporter-like protein 2	*Slc44a2*	80.1
MKIAA0051 protein (Fragment)	*Iqgap1*	191.2
ATP-dependent RNA helicase DDX24	*Ddx24*	101.3
SAM_MT_RSMB_NOP domain-containing protein	*Nsun2*	88
Axotomy induced glycoprotein 2	*Serinc1*	50.5
Armadillo repeat protein deleted in velo-cardio-facial syndrome homolog	*Arvcf*	105
Zinc finger CCCH type-containing 7B	*Zc3h7b*	110.2
Interferon-induced transmembrane protein 3	*Ifitm3*	14.9
R3H domain-containing 1	*R3hdm1*	124.3
ATP-binding cassette sub-family E member 1	*Abce1*	67.3
E3 ubiquitin-protein ligase TRIP12	*Trip12*	224
Reticulon-3	*Rtn3*	103.8
Asparagine--tRNA ligase, cytoplasmic	*NARS1*	64.2
Ataxin-2	*Atxn2*	136.4
Eukaryotic translation initiation factor 2 subunit 1	*Eif2s1*	36.1
5'-nucleotidase domain-containing 2	*Nt5dc2*	63.8
Eukaryotic translation initiation factor 3 subunit H	*Eif3h*	39.8
WD_REPEATS_REGION domain-containing protein	*Wdr6*	121.8

Protein Name	Gene Name	Molecular Weight (kDa)
Trifunctional purine biosynthetic protein adenosine-3	*Gart*	107.4
AP-3 complex subunit beta-1	*Ap3b1*	122.7
Tripeptidyl-peptidase 2	*Tpp2*	139.8
Transforming acidic coiled-coil-containing protein 2	*Tacc2*	305
GDT1 family protein	*Tmem165*	34.8
Ankyrin repeat and KH domain-containing 1	*Ankhd1*	269.5
H(+)/Cl(-) exchange transporter 3	*Clcn3*	90.8
Uncharacterized protein	*Arl6ip1*	23.3
GTPase-activating protein and VPS9 domain-containing protein 1	*Gapvd1*	162.3
Proteolipid protein 2	*Plp2*	16.6
Coiled-coil domain-containing protein 154	*Ccdc154*	76.1
Cytoskeleton-associated protein 4	*Ckap4*	63.7
Secretory carrier-associated membrane protein	*Gm45927*	88.9
Zinc finger and BTB domain-containing protein 42	*Zbtb42*	46.7
Ras-related protein Rab-1B (Fragment)	*Rab1b*	28.2
MKIAA1995 protein (Fragment)	*Nek9*	109
Protein IWS1 homolog	*Iws1*	85.2
Arf-GAP with SH3 domain, ANK repeat and PH domain-containing protein 2	*Asap2*	111.1
Protein PRRC2C	*Prrc2c*	310.7
Igh protein	*Igh*	51.9
Eukaryotic peptide chain release factor GTP-binding subunit ERF3A	*Gspt1*	68.6
Nucleoporin 153	*Nup153*	151.9
Alpha-1,4 glucan phosphorylase	*Pygb*	96.6
Type I epidermal keratin mRNA, 3'end (Fragment)	*N/A*	10.7
Decorin	*Dcn*	39.8
RIKEN cDNA 2210010C04 gene	*2210010C04Rik*	26.4
Inosine-5'-monophosphate dehydrogenase	*Impdh2*	55.7

***Appendix Table 9: Previous Nedd4l substrates reported by Goel et al. and Manning and Kumar* (Goel *et al.*, 2015; Manning & Kumar, 2018).**

Goel *et al.* 2015	**Manning and Kumar 2018**
Aquaporin 2	Arrestin Domain Containing 1
Barttin CLCNK Type Accessory Subunit Beta	Arrestin Domain Containing 4
Cystic Fibrosis Transmembrane Conductance Regulator	cAMP Response Element-Binding Regulated Transcription Coactivator 3
Chloride Voltage-Gated Channel 5	Divalent Metal Transporter 1
Disks Large Homolog 4	Potassium Voltage-Gated Channel Subfamily H Member 2
Disks Large-Associated Protein 1	Solute Carrier Family 9 Member 3 (Sodium-Hydrogen Antiporter 3)
Dihydropyrimidinase-Related Protein 2	Solute Carrier Family 22 Member 6 Organic Anion Transporter 1
Dishevelled Segment Polarity Protein 2	Solute Carrier Family 22 Member 8 Organic Anion Transporter 3
G Protein-Coupled Receptor Kinase 2	Unc-51 Like Autophagy Activating Kinase 1
Potassium Voltage-Gated Channel Subfamily Q Member 1	
Potassium Voltage-Gated Channel Subfamily Q Member 2	
Potassium Voltage-Gated Channel Subfamily Q Member 3	
Potassium Voltage-Gated Channel Subfamily Q Member 5	
Lysophosphatidic Acid Receptor 1	
Nedd4 Family Interacting Protein 1	
Nedd4 Family Interacting Protein 2	
Nuclear Factor I X	
Neurotrophic Receptor Tyrosine Kinase 1	
Occludin	
Sodium Voltage-Gated Channel Alpha Subunit 10	
Sodium Voltage-Gated Channel Alpha Subunit 2	
Sodium Voltage-Gated Channel Beta Subunit 2	
Sodium Voltage-Gated Channel Alpha Subunit 3	
Sodium Voltage-Gated Channel Beta Subunit 3	
Sodium Voltage-Gated Channel Alpha Subunit 5	
Sodium Voltage-Gated Channel Alpha Subunit 9	
Stratifin	
Surfactant Protein C	
Serum Glucocorticoid Kinase 1	
SH3 and Multiple Ankyrin Repeat Domains 3	

Solute Carrier Family 12 Member 3 (Sodium Chloride Cotransporter 1)	
Solute Carrier Family 1 Member 2 (Excitatory Amino Acid Transporter 2)	
Solute Carrier Family 1 Member 3 (Excitatory Amino Acid Transporter 1)	
Solute Carrier Family 38 Member 2 (Sodium-dependent Amino Acid Transporter)	
Solute Carrier Family 5 Member 1 (Sodium/Glucose Cotransporter 1)	
Solute Carrier Family 6 Member 3 (Sodium-Dependent Dopamine Transporter 1)	
Mothers against Decapentaplegic Homolog 2	
Mothers against Decapentaplegic Homolog 3	
Mothers against Decapentaplegic Homolog 4	
Mothers against Decapentaplegic Homolog 7	
Transforming Growth Factor Beta Receptor 1	
Activated CDC42 Kinase 1	
Tweety Family Member 1	
Tweety Family Member 2	
Tweety Family Member 3	
Ubiquitin Carboxyl-Terminal Hydrolase 45	
WW Domain Binding Protein 1 Like	
WNK Lysine Deficient Protein Kinase 1	
Wnk Lysine Deficient Protein Kinase 3	
Y-Box Binding Protein 1	
14-3-3 Beta	
14-3-3 Epsilon	
14-3-3 Gamma	
14-3-3 Eta	
14-3-3 Theta	
14-3-3 Sigma	
14-3-3 Zeta	